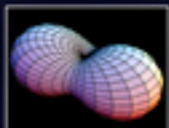
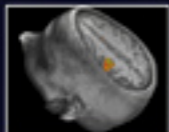


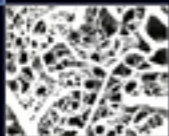
Richard B. Buxton



# Introduction to Functional Magnetic Resonance Imaging

Principles and Techniques

SECOND EDITION



CAMBRIDGE

CAMBRIDGE

[www.cambridge.org/9780521899956](http://www.cambridge.org/9780521899956)

This page intentionally left blank

# Introduction to Functional Magnetic Resonance Imaging

## Principles and Techniques

---

Functional magnetic resonance imaging (fMRI) has become a standard tool for mapping the working brain's activation patterns, both in health and in disease. It is an interdisciplinary field and crosses the borders of neuroscience, psychology, psychiatry, radiology, mathematics, physics, and engineering. Developments in techniques, procedures and our understanding of this field are expanding rapidly. In this second edition of *Introduction to Functional Magnetic Resonance Imaging*, Richard Buxton – a leading authority on fMRI – provides an invaluable guide to how fMRI works, from introducing the basic ideas and principles to the underlying physics and physiology. He covers the relationship between fMRI and other imaging techniques and includes a guide to the statistical analysis of fMRI data. This book will be useful both to the experienced neuroscientist, and the clinician or researcher with no previous knowledge of the technology.

RICHARD B. BUXTON is Professor of Radiology at the University of California at San Diego.



# **Introduction to Functional Magnetic Resonance Imaging**

## **Principles and Techniques**

---

SECOND EDITION

**Richard B. Buxton**

University of California, San Diego, USA



**CAMBRIDGE**  
UNIVERSITY PRESS

CAMBRIDGE UNIVERSITY PRESS  
Cambridge, New York, Melbourne, Madrid, Cape Town, Singapore,  
São Paulo, Delhi, Dubai, Tokyo

Cambridge University Press  
The Edinburgh Building, Cambridge CB2 8RU, UK

Published in the United States of America by Cambridge University Press, New York

[www.cambridge.org](http://www.cambridge.org)

Information on this title: [www.cambridge.org/9780521899956](http://www.cambridge.org/9780521899956)

© R. B. Buxton 2009

This publication is in copyright. Subject to statutory exception and to the provision of relevant collective licensing agreements, no reproduction of any part may take place without the written permission of Cambridge University Press.

First published in print format 2009

ISBN-13 978-0-511-60520-8 eBook (NetLibrary)

ISBN-13 978-0-521-89995-6 Hardback

Cambridge University Press has no responsibility for the persistence or accuracy of urls for external or third-party internet websites referred to in this publication, and does not guarantee that any content on such websites is, or will remain, accurate or appropriate.

*For Lynn*





# Contents

*Preface to the second edition* ix

*Preface to the first edition* xi

---

- Part I** An overview of functional magnetic resonance imaging 1
- Part IA** Introduction to the physiological basis of functional neuroimaging 3
- 1 **Neural activity and energy metabolism** 5
- 2 **Cerebral blood flow and brain activation** 34
- Part IB** Introduction to functional magnetic resonance imaging 65
- 3 **Nuclear magnetic resonance** 67
- 4 **Magnetic resonance imaging** 85
- 5 **Imaging functional activity** 101
- Part II** Principles of magnetic resonance imaging 117
- Part IIA** The nature of the magnetic resonance signal 119
- 6 **Basic physics of magnetism and NMR** 121
- 7 **Relaxation and contrast in MRI** 147
- 8 **Diffusion and the MR signal** 173
- Part IIB** Magnetic resonance imaging 203
- 9 **Mapping the MR signal** 205
- 10 **Techniques in MRI** 232
- 11 **Noise and artifacts in MR images** 252
- Part III** Principles of functional magnetic resonance imaging 277
- Part IIIA** Perfusion imaging 279
- 12 **Contrast agent techniques** 281
- 13 **Arterial spin labeling techniques** 307
- Part IIIB** Blood oxygenation level dependent imaging 339
- 14 **The BOLD effect** 341
- 15 **Design and analysis of BOLD experiments** 368
- 16 **Interpreting the BOLD response** 400
- 

*Appendix* The physics of nuclear magnetic resonance 425

*Index* 440

The color plates are between pages 231 and 232



# Preface to the second edition

The field of functional magnetic resonance imaging (fMRI) has expanded enormously since the mid-1990s. The field is still dominated by basic neuroscience research, but increasingly fMRI is being used to study disease, and clinical applications are growing rapidly. This book is intended as an introduction to the basic ideas and techniques of fMRI. My goal was to provide a guide to the principles of fMRI with sufficient depth to be useful to the active neuroscience investigator using fMRI in research, but also to make the material accessible to the new investigator or clinician with no prior knowledge of the field. To this end, the key ideas are all presented in [Part I](#) as a general overview and then developed in more detail in [Parts II](#) and [III](#).

The second edition has been extensively revised to reflect new developments in the field since publication of the first edition in 2002. As in the first edition, the emphasis is on examples that illustrate the basic principles rather than a comprehensive review of the field. The viewpoint of the book reflects my own background as a physicist, focusing on how the techniques work and the physiological mechanisms underlying fMRI. The early sections on the basic connections between neural activity, blood flow, and energy metabolism have been completely revised to reflect the large body of the new work since the first edition was published. The final chapter addresses what I think is the primary challenge for fMRI today: how can we take fMRI from a mapping tool to a quantitative probe of brain physiology?

I have been fortunate to be able to work with an exceptional group of colleagues at UCSD, and over the years the material in the book has been shaped by many helpful discussions with Eric Wong, Larry Frank, Tom Liu, David Dubowitz, Miriam Scandeng, Giedrius Buracas, Kun Lu, Adina Roskies, Karla Miller, Kamil Uludag, Marty Sereno, Joan Stiles, Frank Haist, Greg Brown, Anna Devor, and Anders Dale. I have also benefited from numerous stimulating discussions with other colleagues in the field, particularly on ideas related to the physiological foundations of fMRI, including Peter Bandettini, David Boas, Noam Harel, Joe Mandeville, Marcus Raichle, Robert Turner, Essa Yacoub and many others.

Finally, this book could not have been completed without the loving support of Lynn Hall, and the book is dedicated to her.

Richard B. Buxton



# Preface to the first edition

The field of functional magnetic resonance imaging (fMRI) is intrinsically interdisciplinary, involving neuroscience, psychology, psychiatry, radiology, physics, and mathematics. For me, this is part of the pleasure in working in this area, providing an opportunity to collaborate with scientists and clinicians with a wide range of backgrounds. This book is intended as an introduction to the basic ideas and techniques of fMRI. My goal was to provide a guide to the principles of fMRI with sufficient depth to be useful to the active neuroscience investigator using fMRI in their research, but also to make the material accessible to the new investigator or clinician with no prior knowledge of the field. The viewpoint of the book reflects my own background as a physicist, focusing on how the techniques work. The emphasis is on examples that illustrate the basic principles rather than a more comprehensive review of the field or a more rigorous mathematical treatment of the fundamentals.

This book grew out of courses I taught with my colleagues L. R. Frank and E. C. Wong, and their insights have significantly shaped the way in which the material is presented. Our courses were geared toward graduate students in neuroscience and psychology, but the book should also be useful for clinicians who want to understand the basis of the new fMRI techniques and potential clinical applications, and for physicists and engineers who are looking for an overview of the ideas of fMRI. Some of the techniques described are not yet part of the mainstream of basic neuroscience applications, such as arterial spin labeling, bolus tracking, and diffusion tensor imaging. However, the clinical application of these techniques is rapidly growing, and I think that over the next few years they will become an integral part of many neuroscience fMRI studies. This book should also serve as an introduction to recent excellent multiauthor works that present some of this material in greater depth, such as *Functional MRI* edited by C. T. W. Moonen and P. A. Bandettini (published in 1999 by Springer).

In writing this book, I have benefited from helpful discussions and critical readings from several of my close colleagues, including Eric Wong, Larry Frank, Tom Liu, Karla Miller, Antigona Martinez, and David Dubowitz. I am also fortunate to be able to work with faculty and students in the San Diego neuroscience community, including Geoff Boynton, Greg Brown, Adina Roskies, Marty Sereno, Joan Stiles, Dave Swinney, and many others. Their insights, comments, and questions have stimulated me to think about many of the topics discussed in the book. In addition, I have also benefited from numerous discussions with colleagues in the field over the years, including Peter Bandettini, Anders Dale, Arno Villringer, Robert Weisskoff, Joe Mandeville, Van Wedeen, Bruce Rosen, Ken Kwong, Robert Turner, Gary Glover, Robert Edelman, Mark Henkelman, and many others. Although these individuals have strongly influenced my own thinking, they are not responsible for what appears here, particularly any errors that may remain.

Finally, this could not have been completed without the loving support of Lynn Hall, and the book is dedicated to her.

Richard B. Buxton



**Part**

# **An overview of functional magnetic resonance imaging**

## **Part IA Introduction to the physiological basis of functional neuroimaging**

- 1 Neural activity and energy metabolism
- 2 Cerebral blood flow and brain activation

## **Part IB Introduction to functional magnetic resonance imaging**

- 3 Nuclear magnetic resonance
- 4 Magnetic resonance imaging
- 5 Imaging functional activity





Part

# IA

## Introduction to the physiological basis of functional neuroimaging

The subject to be observed lay on a delicately balanced table which could tip downwards either at the head or at the foot if the weight of either end were increased. The moment emotional or intellectual activity began in the subject, down went the balance at the head-end, in consequence of the redistribution of blood in his system ...

... We must suppose a very delicate adjustment whereby the circulation follows the needs of the cerebral activity. Blood very likely may rush to each region of the cortex according as it is most active, but of this we know nothing.

*William James (1890) The Principles of Psychology*



# Neural activity and energy metabolism

<b>Introduction</b>	<i>page</i> 5
Metabolic activity accompanies neural activity	5
Functional MRI	7
<b>Neural signaling</b>	7
Neural activity	8
The membrane potential	9
Synaptic activity	10
Electrophysiology measurements	12
<b>Recovery from neural activity</b>	14
Neural signaling is a thermodynamically downhill process	14
Metabolism of ATP is required to restore ionic gradients following neural activity	14
The sodium/potassium pump	15
Astrocytes play a key role in recycling neurotransmitter	16
An ATP energy budget for neural activity	16
<b>Energy metabolism</b>	18
Glycolysis in the cytosol	18
Lactate production and the lactate shuttle	20
Mitochondrial pyruvate metabolism and the electron transfer chain	20
Delivery of glucose and O <sub>2</sub> by blood flow	22
<b>Measuring energy metabolism with PET</b>	23
The deoxyglucose technique for measuring glucose metabolism	23
Measuring the cerebral metabolic rate for glucose	23
Increased glucose metabolism is closely associated with functional activity	24
Measuring cerebral blood flow and O <sub>2</sub> metabolism	25
Balance of blood flow, glucose metabolism and O <sub>2</sub> use in the brain at rest and during activation	26

## Introduction

### Metabolic activity accompanies neural activity

The goal of understanding the functional organization of the human brain has motivated neuroscientists for well over 100 years, but the experimental tools to measure and map brain activity have been slow to develop. Neural activity is difficult to localize without placing electrodes directly in the brain. Fluctuating electric and magnetic fields measured at the scalp or near the head provide information on electrical events within the brain, and from these data the location of a few sources of activity can be estimated, but the information is not

sufficient to produce a detailed map of the pattern of activation. However, precise localization of the *metabolic* activity and blood flow changes that follow neural activity are much more feasible and form the basis for most of the functional neuroimaging techniques in use today, including positron emission tomography (PET) and functional magnetic resonance imaging (fMRI). Although comparatively new, fMRI techniques are now a primary tool for basic studies of the organization of the working human brain, and clinical applications are growing.

In 1890, William James published *The Principles of Psychology*, a landmark in the development of psychology as a science grounded in physiology. The possibility of measuring changes in brain blood flow associated with mental activity clearly lay behind the experiment performed by Angelo Mosso and recounted by James in the quotation at the beginning of this section. By current standards of blood flow measurement, this experiment is quaintly crude, but it indicates that the idea of inferring neural activity in the brain from a measurement of changes in local blood flow long preceded the ability to do such measurements (Raichle 1998).

In fact, this experiment is unlikely to have worked reliably for an important reason. The motivation for this experiment may have been an analogy with muscle activity. Vigorous exercise produces substantial muscle swelling through increased blood volume, and thus a redistribution in weight. But the brain is surrounded by fluid and encased in a hard shell, so the overall fluid volume within the cranium must remain nearly constant, a principle often referred to as the Munro–Kellie doctrine. Blood volume changes do occur in the brain, and the brain does move with cardiac pulsations, but these changes most likely involve shifts of cerebrospinal fluid (CSF) as well. As a result, the weight of the head should remain approximately constant.

Furthermore, this experiment depends on a change in blood volume, rather than blood flow, and blood flow and blood volume are distinct quantities. *Blood flow* refers to the volume per minute moving through the vessels, while *blood volume* is the volume occupied by the vessels. In principle, there need be no fixed relation between blood flow and blood volume; flow through a set of pipes can be increased by increasing the driving pressure without changing the volume of the plumbing. Physiologically, however, experiments typically show a strong correlation between cerebral blood flow (CBF) and cerebral blood volume (CBV), and functional neuroimaging techniques are now available for measuring both of these quantities.

The working brain requires a continuous supply of glucose and oxygen ( $O_2$ ), which must be supplied by CBF. The human brain receives approximately 15% of the total cardiac output of blood (approximately 700 mL/min) and yet accounts for only 2% of the total body weight. Within the brain, the distribution of blood flow is heterogeneous, with gray matter receiving several times more flow per gram of tissue than white matter. Indeed, the flow per gram of tissue to gray matter is comparable to that in heart muscle, the most energetic organ in the body. The activity of the brain generates approximately 11 W/kg of heat, and glucose and  $O_2$  provide the fuel for this energy generation. Yet the brain has virtually no reserve store of  $O_2$ , and is therefore dependent on continuous delivery by CBF. If the supply of  $O_2$  to the brain is cut off, loss of consciousness quickly follows.

Table 1.1 lists the primary physiological variables associated with brain energy metabolism and blood flow, along with approximate values for the resting human brain. With brain activation, glucose metabolism,  $O_2$  metabolism, blood flow and blood volume all increase in the active area. Unexpectedly, however, the oxygen extraction fraction (OEF) – the fraction of the delivered  $O_2$  that leaves the blood and is metabolized in the cells – *decreases* with activation, and this phenomenon is exploited in fMRI.

**Table 1.1.** Typical energy metabolism and blood flow variables for the resting human brain

Physiological variable	Abbreviation	Typical value
Cerebral blood flow	CBF	0.5 mL/(g·min)
Cerebral blood volume	CBV	4%
Cerebral metabolic rate of glucose	CMRGlc	8.5 $\mu$ mol/(g·min)
Cerebral metabolic rate of oxygen	CMRO <sub>2</sub>	1.6 $\mu$ mol/(g·min)
Oxygen extraction fraction	OEF (or $E$ )	40%
Arterial oxygen content	[O <sub>2</sub> ] <sub>a</sub>	8 $\mu$ mol/mL

## Functional MRI

Positron emission tomography provided the first technology for mapping patterns of activation in the human brain with high spatial resolution by measuring changes in blood flow and energy metabolism, and these methods are described later in this chapter. More recently, fMRI methods have dominated the field of functional neuroimaging, primarily based on a phenomenon called the blood oxygenation level dependent (BOLD) effect. This effect arises because of two distinct phenomena. The first is that when hemoglobin, the molecule in blood that carries O<sub>2</sub>, loses that O<sub>2</sub> to become deoxyhemoglobin, the magnetic properties change in a subtle way. The effect of this is that the MR signal changes slightly, increasing when the blood becomes more oxygenated. This phenomenon alone, while interesting from a biophysical point of view, only becomes useful when combined with a second, physiological phenomenon: when an area of brain is activated, the blood flow increases much more than the O<sub>2</sub> metabolic rate (CMRO<sub>2</sub>). This leads to a reduction of the OEF, a seemingly paradoxical scenario in which the venous blood is more oxygenated – despite the increase in CMRO<sub>2</sub> – because the blood flow has increased more. Taken together, these two phenomena produce the BOLD effect, a local increase of the MR signal owing to a reduction of the OEF during increased neural activity.

Functional MRI based on the BOLD effect is the most widely used method for exploring brain function in human subjects, but MRI offers several additional techniques as well. Although the term fMRI is often taken in a narrow sense to mean BOLD imaging, in this book the term is taken in a broader sense to mean any MRI technique that moves beyond anatomical imaging and provides information on physiological function. [Chapters 1 and 2](#) provide an introduction to the physiological basis of these methods, as well as background on other techniques such as PET. The connection between neural activity, energy metabolism, and blood flow is the foundation of functional neuroimaging, yet this area of physiology is still not well understood. Recent research has emphasized the key role played by astrocytes, cells that have processes projecting to both neurons and blood vessels. This has led to the concept of the *neurovascular unit*, a close interaction between neurons, astrocytes, and blood vessels. The first two chapters describe these current results and ideas.

## Neural signaling

Like all organs, energy metabolism in the brain is necessary for the basic processes of cellular work, such as chemical synthesis and chemical transport. But the particular work done by the brain, which requires the high level of energy metabolism, is the generation of electrical

activity required for neuronal signaling. We begin by reviewing the basic processes involved in neural activity from the perspective of thermodynamics, in order to emphasize the essential role of energy metabolism. A more complete description can be found in standard neuroscience texts (Nicholls *et al.* 1992).

## Neural activity

Neurons have a complex structure, with an intricate tree of fine *dendrites* extending outward from the cell body, and a single *axon* that carries outgoing signals (Fig. 1.1A). **The axon divides into many branches, and a branch makes contact with a dendrite or cell body of another neuron at a *synapse*.** In the primate brain, a neuron may have on the order of 10 000 synapses where it can receive signals from other neurons. Most of these connections are with nearby neurons (within a few millimeters), but some connections are much longer.

A key aspect of all cells, but in particular for neurons, is the *membrane potential*. Electrodes placed inside and outside the cell record an electric potential difference across the cell membrane of approximately  $-70$  mV, with the potential more negative inside. One can think of the membrane potential as the medium of neuronal signaling: it is the physiological property altered in one neuron when it receives a signal from another neuron. An *action potential* or *spike* is a transient disturbance of that potential, a rapid depolarization of the membrane near the origin of the axon, initiated by a partial depolarization of the membrane potential. For example, if positive current is injected into the cell, the membrane potential will slowly increase (depolarize, approaching zero) until a threshold is reached that

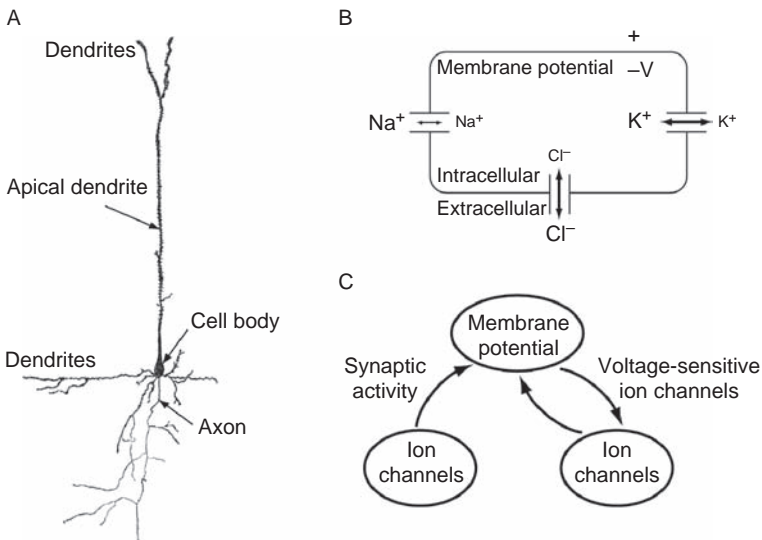


**Fig. 1.1.** Neuronal signaling. (A) The schematic diagram shows the dendrites, cell body, and axon for a pyramidal cell, the principal neuron of the cortex. Axons from other neurons make contact at synapses on the dendrites and cell body, causing ion channels to open and current to flow into or out of the cell. If a sufficient depolarizing current reaches the cell body, an action potential is generated that travels along the axon to signal other neurons. (B) Ions have different extracellular and intracellular concentrations. The membrane potential depends on these distributions plus the permeability of the cell membrane to each ion. Synaptic activity leads to transient opening or closing of specific ion channels, producing fluctuations of the membrane potential. (C) A source of the non-linear complexity of neuronal signaling, including the generation of an action potential, is that other ion channels are voltage dependent and so are affected by the membrane potential, creating a feedback loop.

triggers the action potential, an abrupt further depolarization that quickly recovers. This rapid depolarization triggers an action potential in a nearby section of the axon, and in this way the action potential propagates down the axon until it reaches a junction with another neuron at a synapse.

The arrival of the action potential then influences the firing of the second neuron by creating a local fluctuation in the membrane potential of the post-synaptic neuron. With an *excitatory post-synaptic potential* (EPSP), the potential inside is raised, creating a slight depolarization, and for an *inhibitory post-synaptic potential* (IPSP) the potential inside is decreased, creating a slight hyperpolarization. Each neuron thus has the capacity to integrate the inputs from many other neurons through their cumulative effect on the post-synaptic potential. A new action potential is generated by the post-synaptic neuron if the membrane potential in the region where the axon originates becomes sufficiently depolarized. From an electrical viewpoint, the working neuron is an intricate pattern of continuously fluctuating membrane potentials caused by synaptic activity punctuated by occasional sharp action potentials.

## The membrane potential

The membrane potential depends on two factors: the extracellular/intracellular distribution of ions across the cell membrane, and the permeability of the membrane to each of those ions (Fig. 1.1 B, C). In general, ions cannot freely diffuse across the membrane but instead must pass through *ion channels* created by specialized proteins embedded in the membrane. Ion channels can be very specific and can be modulated by chemical messengers such as neurotransmitters, or by the membrane potential itself. The interesting complexity of neuronal signaling is that permeability to specific ions determines the membrane potential, but the membrane potential, in turn, affects the permeability of voltage-sensitive ion channels. For example, a voltage-sensitive sodium ( $\text{Na}^+$ ) channel will open if the membrane in its vicinity becomes depolarized, and this will lead to an additional  $\text{Na}^+$  influx that will further depolarize the membrane. This non-linear cooperative behavior is a key part of the generation of an action potential.

In addition to  $\text{Na}^+$ , the other principal ions involved in neuronal signaling are potassium ( $\text{K}^+$ ), calcium ( $\text{Ca}^{2+}$ ) and chloride ( $\text{Cl}^-$ ), which are distributed with higher concentrations of  $\text{Na}^+$ ,  $\text{Ca}^{2+}$  and  $\text{Cl}^-$  outside the cell and a higher concentration of  $\text{K}^+$  inside the cell. Whenever there is a concentration difference across a membrane, there is a tendency for the ions to diffuse from the side with the higher concentration to the side with the lower concentration. However, this tendency is offset by the membrane potential; a negative potential inside the cell will favor a higher intracellular concentration of positive ions. For a given intracellular/extracellular distribution of an ion, the *equilibrium potential* is the membrane potential that would balance that distribution so that there is no tendency for a net movement across the membrane. For example, a typical distribution of  $\text{Cl}^-$  is an extracellular/intracellular concentration ratio of approximately 12:1, a ratio that is in equilibrium with a membrane potential of approximately  $-70$  mV. Because this is close to what is observed as the existing membrane potential in resting neurons, we conclude that even if the membrane is highly permeable to  $\text{Cl}^-$  there will nevertheless be no tendency for a net flux of ions through the membrane.

Sodium has a similarly high extracellular/intracellular concentration ratio, approximately 10:1, but because  $\text{Na}^+$  is positively charged the equilibrium potential is approximately  $+60$  mV, substantially different from  $\text{Cl}^-$ . At rest, the permeability of the membrane to

$\text{Na}^+$  is low, so there is little flux of  $\text{Na}^+$  down its gradient (although there is a slow leak). If membrane ion channels open to allow passage of  $\text{Na}^+$ , making the membrane permeable to  $\text{Na}^+$ , there is a strong inward current because both the concentration gradient and the negative potential drive a  $\text{Na}^+$  flux into the cell. Potassium has an even more asymmetric distribution, with an extracellular/intracellular concentration ratio of approximately 1:40, and the corresponding equilibrium potential is approximately  $-95$  mV. Opening a  $\text{K}^+$  channel will lead to an outward flux of  $\text{K}^+$  down its gradient. In short, relative to the resting membrane potential, the  $\text{Cl}^-$  distribution is near equilibrium; the  $\text{K}^+$  distribution is somewhat out of equilibrium; and the  $\text{Na}^+$  distribution is far from equilibrium.

Given this complex non-equilibrium system with multiple ions in different distributions, what actually determines the membrane potential? Ultimately, the membrane potential depends on a very slight imbalance of charge inside and outside the cell, but the amount of charge involved is much smaller than the fluxes of charge across the membrane through ion channels. One can think of the neuron as being in a *steady state* in which the net flux of charge across the membrane is zero. That is, positive and negative charges are moving back and forth through membrane channels, and for any particular ion there may be a steady flux in one direction, such as a slow but steady leak of  $\text{Na}^+$  into the cell. Overall, however, there is no net charge transfer across the membrane. Because the membrane potential is highly sensitive to any imbalance of charge across the membrane, any departure from this steady state, leading to a net flux of charge, will quickly alter the membrane potential. Then, for any combination of ion distributions and membrane permeabilities, the membrane potential takes on the value that will create this steady state with no net flux of charge.

For example, if the membrane is highly permeable to one ion, but only weakly permeable to the others, the membrane potential will approach the equilibrium potential of that ion, because that ion alone determines the net flux of charge. However, if the membrane also is permeable to another ion with a different equilibrium potential, the resulting membrane potential will be intermediate between the two equilibrium potentials, weighted by the relative permeability to each of the different ions. That is, as the permeability to the second ion increases, the membrane potential will shift toward the equilibrium potential of that ion. In this case, because the membrane is permeable to both ions but the membrane potential does not match either equilibrium potential, there will be a steady leak of ions that tends to degrade the ionic distributions across the membrane, even though there is no net flux of charge. The stability of the cell depends on maintaining these ionic distributions, so homeostasis requires that the ions be pumped back against their gradient, requiring energy metabolism (see below). In short, the membrane potential depends on the ion distributions across the membrane and the permeability of the membrane to each ion, and these ion permeabilities are altered in neuronal signaling.

## Synaptic activity

An action potential arriving at a synapse with another neuron initiates a process that causes ion channels on the post-synaptic neuron to open or close (Fig. 1.2). This process begins on the pre-synaptic side when the incoming action potential triggers an increase of the membrane permeability to  $\text{Ca}^{2+}$ , allowing  $\text{Ca}^{2+}$  entry into the pre-synaptic terminal. Within the pre-synaptic terminal, *neurotransmitter* molecules are concentrated in small packages called *vesicles*, and the influx of  $\text{Ca}^{2+}$  triggers these vesicles to merge with the cell membrane and spill their contents into the synaptic cleft separating the pre- and post-synaptic membranes. The neurotransmitter molecules diffuse across this thin (20–40 nm) gap and bind to receptor



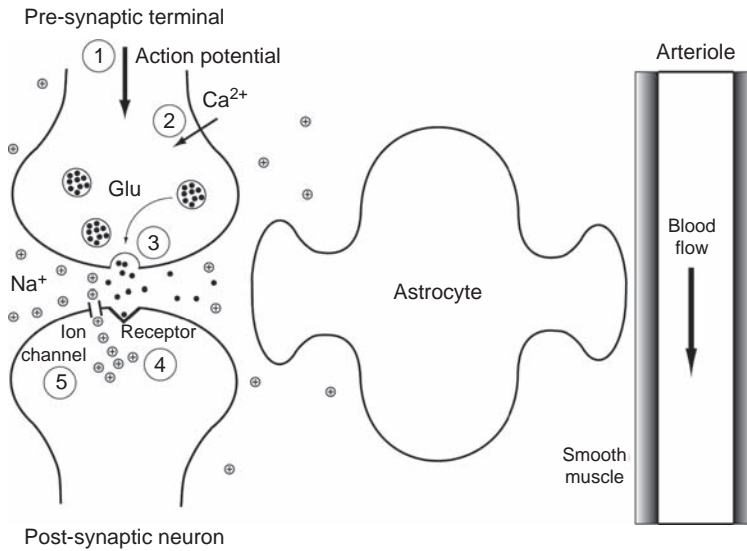


**Fig. 1.2.** Synaptic signaling. An action potential arriving at the pre-synaptic terminal (1) initiates  $Ca^{2+}$  influx (2), triggering neurotransmitter (glutamate [Glu]) release into the synaptic cleft (3), binding of neurotransmitter to receptors on the post-synaptic neuron (4), opening of  $Na^+$  channels (5), and creation of a strong influx of  $Na^+$  into the post-synaptic neuron. Astrocytes have processes that project to neuronal synapses and also to blood vessels, and are involved in clearing neurotransmitter and signaling blood flow changes (illustrated in Figs. 1.4 and 2.4).

sites on the post-synaptic membrane. At each synapse, the neurotransmitter released is characteristic of the pre-synaptic neuron. Glutamate is the most common excitatory neurotransmitter in mammalian cortex, and gamma-aminobutyric acid (GABA) is a common inhibitory neurotransmitter (Erecinska and Silver 1990). Glutamatergic neurons include the *pyramidal cells*, the principal neurons of the cortex. GABAergic neurons include a diverse class of *interneurons* that are important for controlling the net activity of ensembles of neurons.

There are two general classes of receptor. *Ionotropic* receptors are proteins that are themselves ion channels, so binding of neurotransmitter leads to a conformational change of the receptor that opens the ion channel, and the channel remains open while the neurotransmitter is bound. These receptors are very fast, operating on a time scale of milliseconds, and many glutamate and GABA receptors operate in this way. In contrast, at *metabotropic* receptors, binding of the neurotransmitter initiates a chemical cascade that changes the concentration of intracellular *second messengers*, such as cyclic adenosine monophosphate (cAMP), cyclic guanosine monophosphate (cGMP), and  $Ca^{2+}$ . These receptors are also called *G-protein-coupled receptors*, because the initiating step involves guanosine triphosphate (GTP), an energy-rich molecule that is a close relative of ATP, which is discussed later in this chapter. These signaling molecules then gate ion channels or exert other modulatory effects on the post-synaptic neuron, and the time scale for these effects can be much slower and longer lasting (seconds to minutes or more) compared with ionotropic receptors. For this reason, activation of these receptors is often described as having a *neuromodulatory* role, affecting different aspects of neuronal signaling from neurotransmitter release to post-synaptic effects, and these synapses are thought to play an important role in learning and

memory. Examples include different types of glutamate and GABA receptor as well as a wide range of other receptors including those for serotonin (5-hydroxytryptamine [5-HT]), histamine, and dopamine.

In summary, binding of neurotransmitter to a receptor on the post-synaptic membrane initiates a process that opens or modulates particular ion channels either directly or through the action of second messengers. Opening  $\text{Na}^+$  channels creates a strong inward positive current, which will tend to depolarize the membrane potential in the vicinity of the synapse, creating an EPSP. If, however, the action at the synapse is to open  $\text{K}^+$  channels, the effect is to make the potential more negative – hyperpolarizing the membrane – because the equilibrium potential for  $\text{K}^+$  is more negative, creating an IPSP. If  $\text{Cl}^-$  channels are opened, there may be no change in the membrane potential itself, because the resting membrane potential is already close to the  $\text{Cl}^-$  equilibrium potential. However, this also has an inhibitory effect on the post-synaptic neuron, because now opening the same  $\text{Na}^+$  channels will have less of an effect on the membrane potential. Opening  $\text{Cl}^-$  channels pulls the potential more strongly toward the  $\text{Cl}^-$  equilibrium potential, which happens to be approximately the resting potential. For this reason, more  $\text{Na}^+$  channels would need to open to achieve the same depolarization as when the  $\text{Cl}^-$  channels are not open. In short, opening many  $\text{Na}^+$  channels will depolarize the membrane; opening many  $\text{K}^+$  channels will hyperpolarize the membrane; and opening many  $\text{Cl}^-$  channels will tend to peg the membrane potential near the resting value.

At any moment, the neuron may be receiving signals from many other neurons, creating a complex pattern of flickering fluctuations of the membrane potential on the dendritic tree. Along a dendrite, the currents and associated membrane potentials combine; and if there is a sufficient net current that reaches the cell body, the membrane potential there will be depolarized, generating an action potential and sending a new signal to other neurons. Note, though, that there is likely to be a great deal of sub-threshold synaptic activity that may not lead to spiking. Excitatory synapses generally are located on the dendrites, while inhibitory synapses are generally closer to the cell body. Because of the complex geometry of a neuron, incoming excitatory currents down a dendrite toward the cell body can be dissipated by IPSPs nearer the cell body. For this reason, the output of the post-synaptic cell is a complex combination of the inputs, and it is important to keep in mind the distinction between synaptic activity and spiking activity. As discussed below, much of the energy cost of neural signaling is thought to lie in the recovery from synaptic activity.

## Electrophysiology measurements

The opening and closing of ion channels creates currents across the cell membrane and also within the extracellular space. Because of Ohm's law, these fluctuating currents are associated with fluctuating electric potentials (Fig. 1.3). These *extracellular potentials* can be measured invasively with an electrode with high temporal resolution. For example, opening a  $\text{Na}^+$  channel at a synapse near the electrode, creating a positive current into the cell, creates a negative deflection of the potential at the location of the electrode. Extracellular potentials are often analyzed by dividing the signal into low- and high-frequency components. The low-frequency components, called *local field potentials* (LFPs), primarily reflect synaptic activity, while the high-frequency activity, called *multi-unit activity* (MUA), primarily reflects spiking activity (Logothetis 2002). While electrode studies are primarily carried out in animal models, implanted electrodes in patients with epilepsy have made possible human recordings as well.

In addition, some components of extracellular potentials are detectable outside the head with non-invasive techniques. The *electroencephalogram* (EEG) is produced from

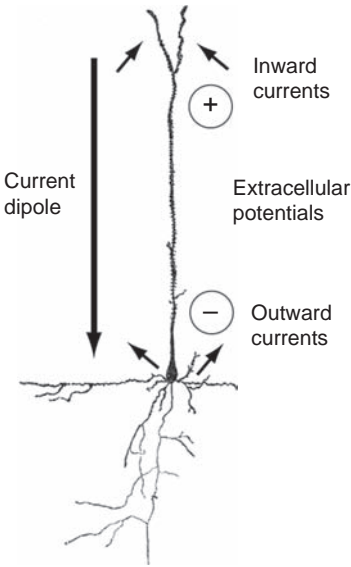


**Fig. 1.3.** Extracellular potentials. Pyramidal neurons, the principal neurons of the cortex, have a long apical dendrite extending from the cell body toward the cortical surface. Excitatory activity near the top creates inward positive currents toward the cell body. This current dipole in the apical dendrite creates extracellular return currents that can be detected as fluctuations of the extracellular potential using implanted electrodes. If the dendritic currents in a patch of cortex are sufficiently coherent, the activity can be detected on the surface of the head. Electroencephalography is sensitive to the extracellular currents and magnetoencephalography is sensitive to the magnetic field created by the current dipole.

measurements with sensitive electrodes on the scalp. The primary source of these measured potentials is coherent activity of the cortical pyramidal cells, which have a long apical dendrite extending perpendicularly through the layers of cortex. Current entering the dendritic tree at the top and exiting in the cell body creates a large current dipole within the apical dendrite and a distributed extracellular return current through the rest of the head. When a patch of cortex is active, the coherent activity of the roughly aligned pyramidal cells produces currents that are detectable as potential fluctuations on the scalp, and from measurements with an array of scalp electrodes the source location can be estimated. The EEG signals are dominated by synaptic currents, rather than action potentials, and do not distinguish between excitatory and inhibitory activity. In addition, the strength of the detected potential depends on the geometry of the dendritic currents; an active neuron with a more symmetric dendritic tree would not generate a strong net current dipole and so likely would not be detected.

Another non-invasive technique for detecting electrical activity is *magnetoencephalography* (MEG), a technique for measuring very weak magnetic fields outside the head. The MEG signal also is dominated by the current dipoles along the apical dendrites of the pyramidal cells, but here it is the magnetic field produced by that dendritic current that is measured. An important distinction between MEG and EEG is that with EEG the measured potentials result from currents flowing through the head between the site of the activity and the electrodes. For this reason, the electrodes must be in electrical contact with the scalp. In addition, any variations in electrical conductivity, such as between the brain and the skull, must be taken into account when modeling the source of the potentials from the measured values on the scalp. In contrast, the magnetic field created by the current dipole in the cortex extends through space, so the detectors do not need to be in contact with the head, and the effects of intervening tissues are much less of a problem.

Temporal resolution with EEG and MEG is excellent, on the order of milliseconds. However, spatial localization with EEG and MEG is more problematic because of the

difficulty of solving the *inverse problem*: taking a set of measured potentials or magnetic fields on the surface of the head and working backwards to deduce what pattern of activity in the brain could give rise to the observed pattern of measurements. The central problem is that potentially many distributions of activity within the brain could produce similar measured EEG and MEG signals, and because of the intrinsic noise in the measurements these brain spatial patterns cannot be distinguished. Nevertheless, substantial progress has been made on this problem, particularly when high-resolution anatomical MRI data are used to constrain the possible solutions of the inverse problem. In summary, current EEG and MEG methods provide a useful window on brain function, particularly for analyzing the temporal evolution of the response to a stimulus.

## Recovery from neural activity

### Neural signaling is a thermodynamically downhill process

From a thermodynamic point of view, each of the steps in neuronal signaling is a downhill reaction in which a system held far from equilibrium is allowed to approach closer to equilibrium. The high extracellular  $\text{Na}^+$  concentration leads to a spontaneous inward ion flow once the trigger of a permeability increase occurs. Similarly, the  $\text{Ca}^{2+}$  influx occurs spontaneously once its membrane permeability is increased, and the neurotransmitter is already tightly bundled in a small package waiting to disperse freely once the package is opened. We can think of neuronal signaling as a spontaneous, but controlled, process. Nature's trick in each case is to maintain a system away from equilibrium, waiting for the right trigger to allow it to move toward equilibrium.

The set of intracellular and extracellular ionic concentrations is a thermodynamic system whose equilibrium state would be one of zero potential difference across the cell membrane, with equal ionic concentrations on either side. Any chemical system that is removed from equilibrium has the capacity to do useful work, and this capacity is called the *free energy* of the system (see [Box 1.1](#) at the end of this chapter). The neuronal system, with its unbalanced ionic concentrations, has the potential to do work in the form of neuronal signaling. But with each action potential and release of neurotransmitter at a synapse, the available free energy is reduced. Returning the neurons to their prior state, with the original ion gradients and neurotransmitter distributions, requires energy metabolism.

### Metabolism of ATP is required to restore ionic gradients following neural activity

Restoring the ion gradients requires active transport of each ion against its natural drift direction, which is thermodynamically an uphill process, moving the system away from equilibrium and increasing the free energy of the system ([Fig. 1.4](#)). For such a change to occur, the transport must be coupled to another system whose free energy decreases sufficiently in the process so that the total free energy decreases (see [Box 1.1](#) at the end of this chapter). The re-establishment of ionic gradients thus requires a source of free energy, and in biological systems free energy is primarily stored in the relative proportions of the three phosphorylated forms of adenosine: adenosine triphosphate (ATP), adenosine diphosphate (ADP), and adenosine monophosphate (AMP) (Siesjo 1978). Inorganic phosphate ( $\text{P}_i$ ) can combine with ADP to form ATP, but the thermal equilibrium of this system at body temperature strongly favors the ADP form. Yet in the body, the ATP/ADP ratio is

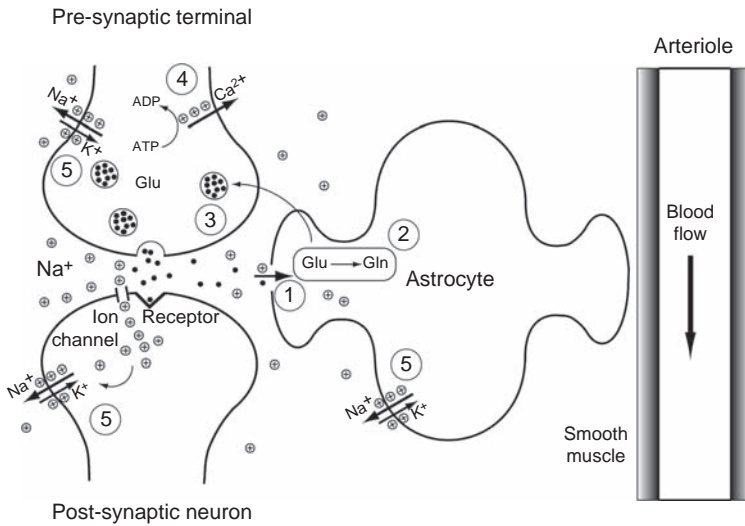


**Fig. 1.4.** Recovery from neuronal signaling. Glutamate (Glu) is taken up from the synaptic cleft by the astrocyte, with free energy supplied by the Na<sup>+</sup> gradient (1), converted to glutamine in the astrocyte with free energy supplied by ATP (2), and transported back to the pre-synaptic terminal and repackaged into vesicles with the consumption of ATP (3). Calcium ions are pumped out of the pre-synaptic terminal using free energy supplied by ATP (4) or the Na<sup>+</sup> gradient (not shown), and Na<sup>+</sup> is pumped out of the cells by the Na<sup>+</sup>/K<sup>+</sup> pump using ATP (5).

maintained at a far higher value, approximately 10:1 in the mammalian brain (Erecinska and Silver 1994). The conversion of ATP to ADP, therefore, involves a large release of free energy, enough to drive other uphill reactions. Despite the large free energy change associated with the reaction  $\text{ATP} \rightarrow \text{ADP}$ , the ATP form is relatively stable against a spontaneous reaction. In order to make use of this stored free energy, the conversion of ATP to ADP is coupled to other uphill reactions through the action of particular enzymes, generically referred to as an ATPase. The ATP/ADP system is used throughout the body as a common free energy storage system.

## The sodium/potassium pump

The transport of Na<sup>+</sup> and K<sup>+</sup> against their existing gradients is accomplished by coupling the transport of these ions to the breakdown of ATP to ADP. The enzyme Na<sup>+</sup>/K<sup>+</sup>-ATPase, also known as the Na<sup>+</sup>/K<sup>+</sup> pump, performs this task by transporting three Na<sup>+</sup> out of the cell and two K<sup>+</sup> into the cell for each ATP molecule consumed. The Na<sup>+</sup>/K<sup>+</sup> pump is critical not just for energetic recovery from an action potential or a fluctuating post-synaptic potential but also simply to maintain the cell's resting potential. The resting permeability to Na<sup>+</sup> is small, but not zero, so there is a constant leak of Na<sup>+</sup> into the cell. This excess Na<sup>+</sup> must be pumped out continuously by the Na<sup>+</sup>/K<sup>+</sup> requiring a constant source of ATP.

The Na<sup>+</sup> gradient itself can also serve as a source of free energy to drive other uphill processes. For example, excess intracellular Ca<sup>2+</sup> can be pumped out of the pre-synaptic terminal by two transport systems (Blaustein 1988). One mechanism directly involves ATP, transporting one Ca<sup>2+</sup> out of the cell for each ATP consumed. The second system is driven by the Na<sup>+</sup> gradient, transporting one Ca<sup>2+</sup> out in exchange for an inward flux of three

$\text{Na}^+$ . Note that one ATP is required to move one  $\text{Ca}^{2+}$  out of the cell by either transport system because in the second system the  $\text{Na}^+/\text{K}^+$  will ultimately be required to consume one ATP to transport the three  $\text{Na}^+$  back out of the cell.

## Astrocytes play a key role in recycling neurotransmitter

At the synapse, neurotransmitter must be taken up by the pre-synaptic terminal, and repackaged into vesicles. For glutamate, the process of re-uptake involves a shuttle between the astrocytes and the neurons (Erecinska and Silver 1990; Iadecola and Nedergaard 2007). Astrocytes are one of the most common glial cells in the brain, frequently located in areas of high synaptic density. The glutamate from the synapse is transported into the astrocytes by coupling the passage of one glutamate with the movement of three  $\text{Na}^+$  down the  $\text{Na}^+$  gradient. The transport of the  $\text{Na}^+$  back out of the cell requires the action of the  $\text{Na}^+/\text{K}^+$  and consumption of one ATP. In the astrocyte, the glutamate is converted to glutamine, which requires an additional ATP, and the glutamine is then released.

The glutamine is passively taken up by the pre-synaptic terminal, where it is converted back to glutamate. Repackaging the glutamate into the vesicles then requires transporting the neurotransmitter against a strong concentration gradient, a process that requires more ATP. One proposed mechanism for accomplishing this is that a strong concentration gradient of hydrogen ions ( $\text{H}^+$ ) ions is first created, with the  $\text{H}^+$  concentration high inside the vesicle (Erecinska and Silver 1990). The inward transport of neurotransmitter is then coupled to a degradation of this gradient. The  $\text{H}^+$  gradient itself is created by an ATP-powered pump.

## An ATP energy budget for neural activity

Theoretical estimates of the energy cost of different aspects of neuronal signaling by Attwell and colleagues have provided a useful and influential guide in thinking about the energetics of brain activity (Attwell and Iadecola 2002; Attwell and Laughlin 2001). To frame this argument, consider the following basic processes: (1) maintenance of the cell at rest; (2) the generation of an action potential and the propagation of that action potential to many synapses with other neurons; (3) recovery on the pre-synaptic side of the synapse, including  $\text{Ca}^{2+}$  clearance and neurotransmitter recycling through the astrocytes; and (4) recovery from post-synaptic potentials, primarily related to pumping  $\text{Na}^+$  out of the cell against its gradient. We can think of the first process as basic housekeeping of the cell, and this component is not directly related to neuronal signaling. The other three components are directly related to signaling, broken down as the spiking activity and pre- and post-synaptic activity. The overall costs of this signaling component will depend on the average spiking rate in the brain, because this drives all three components. In addition, the relative costs of spiking and synaptic activity will depend on the average number of synapses reached by each action potential. For these reasons, the distribution of energy costs across these components is estimated to be different for rats and primates because the primate brain has a lower average spiking rate but approximately a three-fold larger ratio of synapses to neurons.

The estimates derived by Attwell and colleagues (Attwell and Iadecola 2002; Attwell and Laughlin 2001) are based on a wide range of data, primarily from rat studies, relating the different neuronal and glial processes to the ATP required for recovery and for maintenance of the cell. For the primate brain, the dominant energy cost is recovery from post-synaptic potentials (~74%). The costs of maintaining the cell, generating and transmitting action potentials, and recycling neurotransmitter at the synapse are all relatively inexpensive

compared with post-synaptic costs. At first glance this seems surprising, because we tend to think of the essence of neural activity as spiking, and we might have expected that to be the dominant energy cost. The overall energy consumption is closely related to the spiking rate (Laughlin and Sejnowski 2003), but it is the downstream synaptic activity rather than the generation of the spike itself that is costly. By these estimates, it is the integrative activity associated with a neuron receiving many inputs that is costly.

The idea that synaptic activity dominates the energy costs potentially affects how we should interpret a measured spatial distribution of changes in energy metabolism. Based on this picture, the energy cost associated with the generation of a particular neuronal spike is spatially distributed, depending on the projections from that neuron to synapses with other neurons. Some of these projections are quite long, creating the possibility that the location where the spike originated may not be detected, with energy metabolism changes seen only at the downstream synaptic terminals. In practice, this phenomenon of missing the site of generation of the spikes is probably rare in functional neuroimaging, because most of the synaptic connections a neuron receives are from nearby neurons. Given the typical resolution of neuroimaging methods of a few millimeters, most of the synaptic activity within a resolution element of the imaging technique arises from spiking within that same element.

However, Raichle and Mintun (2006) have emphasized an example of missing the spiking location in a study by Schwartz and colleagues (1979). In this early deoxyglucose (DG) study in rats, the animals were exposed to an osmotic load that would stimulate neurons in the hypothalamus that have long-range projections to the pituitary gland. The result was that there was no measurable change in glucose metabolism in the hypothalamus, the location of the spiking neurons, while there was a strong increase in glucose metabolism in the pituitary, the location of the synapses. This result supports the general picture that energy metabolism changes are strongest at the site of increased synaptic activity, rather than the site of increased spiking activity.

The high cost of post-synaptic processes reflects the need to pump  $\text{Na}^+$  out of the cell. Estimates are that at least half of the ATP used in the brain is consumed in driving the  $\text{Na}^+/\text{K}^+$  pump (Ames 2000). One way to think about this high cost of  $\text{Na}^+$  pumping is to look at the synapse as an amplifier for an excitatory signal. The action potential arriving at the synapse is a weak electrical signal, which is first converted to an intracellular  $\text{Ca}^{2+}$  signal and then converted to a chemical signal in the form of neurotransmitter released into the synaptic cleft. These stages are relatively inexpensive because the number of molecules that must be transported in the recovery phase is relatively small. The major amplification comes when a neurotransmitter binds to a post-synaptic receptor and opens a  $\text{Na}^+$  channel, which may let a thousand ions pass through before it closes again. In this way, the weak signal associated with one neurotransmitter molecule binding to a receptor is amplified a thousand-fold. But all that  $\text{Na}^+$  must be pumped back in the recovery stage. Very roughly, moving any molecule against its gradient requires about one ATP, so it is perhaps not so surprising that the primary signal amplification stage is the dominant energy cost in neural signaling.

In brief, a source of free energy is not required for the production of a neuronal signal, but rather for the re-establishment of chemical and ionic gradients reduced by the signaling, particularly the costs of ion pumping for synaptic activity. Without this replenishment, the system eventually runs down like an old battery in need of charging. The restoration of chemical gradients is driven either directly or indirectly by the conversion of ATP to ADP. To maintain their activity, the cells must restore their supply of ATP by

reversing this reaction and converting ADP back to ATP. This requires that the strongly uphill conversion of ADP to ATP must be coupled to an even more strongly downhill reaction. In the brain, virtually all of the ATP used to fuel cellular work is derived from the metabolism of glucose and  $O_2$  (Siesjo 1978). Both  $O_2$  and glucose are in short supply in the brain, and continued brain function requires continuous delivery of these metabolic substrates by CBF.

## Energy metabolism

In the discussion above and in [Box 1.1](#) (at end of this chapter), neural activity is discussed in terms of a thermodynamic framework, in which uphill chemical processes are coupled to other, downhill, processes. For virtually all cellular processes, this chain of thermodynamic coupling leads to the ATP/ADP system within the body. But the next step in the chain, the restoration of the ATP/ADP ratio, requires coupling the body to the outside world through intake of glucose and  $O_2$ . Despite the fact that a bowl of sugar on the dining room table surrounded by air appears to be quite stable, glucose and  $O_2$  together are far removed from equilibrium. When burned, glucose and  $O_2$  are converted into water and  $CO_2$ , releasing a substantial amount of heat. If a more controlled conversion is performed, much of the free energy can be used to drive the conversion of ATP to ADP, with metabolism of one glucose molecule generating enough free energy change to convert as many as 38 ADP to ATP. As far as maintaining neural activity is concerned, the chain of thermodynamically coupled systems ends with glucose and  $O_2$ . As long as we eat and breathe, we can continue to think.

The mechanisms for harnessing the free energy of glucose and  $O_2$  in oxidative metabolism can be divided into four stages: (1) *glycolysis* in the cytosol, in which glucose breaks down into two pyruvate molecules; (2) the *trans-carboxylic acid* (TCA) cycle (also called the *Kreb's cycle* or the *citric acid cycle*) in the mitochondria, in which pyruvate is broken down to form carbon dioxide ( $CO_2$ ) with the storage of energy in the form of reduced nicotinamide adenine dinucleotide (NADH) and related compounds; (3) the *electron transfer chain* in the mitochondria, in which the transfer of electrons from NADH to  $O_2$  to form water is coupled to pumping of  $H^+$  across the inner membrane of the mitochondria against its gradient and thus storing energy in the  $H^+$  gradient; and (4) the movement of  $H^+$  down its gradient coupled with the combination of ADP and  $P_i$  to form ATP ([Fig 1.5](#)). Glycolysis does not require  $O_2$  and produces only a small amount of ATP through reactions in the cytosol. The further metabolism of pyruvate in the mitochondria produces much more ATP. Oxidative glucose metabolism involves many steps, and the following is a sketch of only a few key features. A more complete discussion can be found in Siesjo (1978).

## Glycolysis in the cytosol

In glycolysis, the breakdown of a glucose molecule into two molecules of pyruvate is coupled to the net conversion of two molecules of ADP to ATP. The process involves several steps, with each step catalyzed by a particular enzyme. The first step in this process is the addition of a phosphate group to the glucose, catalyzed by the enzyme *hexokinase*. The phosphate group is made available by the conversion of ATP to ADP, so in this stage of glycolysis one ATP is consumed and fructose 6-phosphate is produced. A second phosphorylation stage, catalyzed by *phosphofructokinase* (PFK), consumes one more ATP molecule. Up to this point, two ATP molecules have been consumed, but in the remaining steps the complex is broken down into



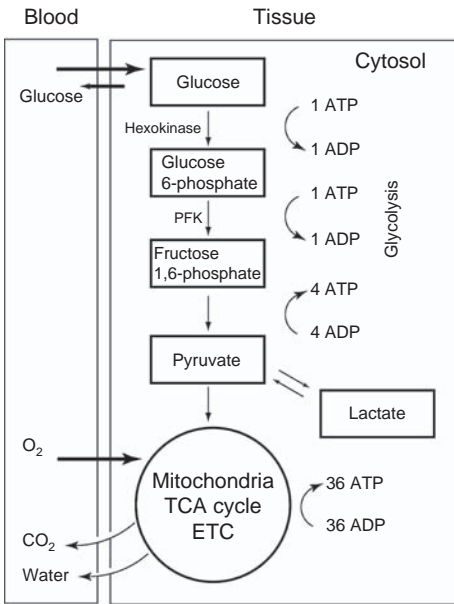


**Fig. 1.5.** Energy metabolism. The major steps of cerebral energy metabolism are illustrated. Glucose is taken up from blood and first undergoes glycolysis (the steps in boxes) to produce pyruvate, for a net conversion of two ADP to ATP. If pyruvate is not further metabolized, it interchanges reversibly with lactate. Oxidative metabolism occurs in the mitochondria, where pyruvate enters the tricarboxylic acid (TCA) cycle and is broken down to CO<sub>2</sub> with electrons transferred to the electron transfer chain (ETC). Electrons move down the ETC to a final combination with O<sub>2</sub>, using the free energy available to pump H<sup>+</sup> across an internal membrane in the mitochondria (not shown in the figure). Finally, the H<sup>+</sup> gradient is tapped to convert an additional 36 ADP to ATP. The waste products CO<sub>2</sub> and heat are cleared from the tissue by blood flow.

two pyruvate molecules accompanied by the conversion of four ADP to ATP. The net production of ATP is then two ATP for each glucose molecule undergoing glycolysis.

The cerebral metabolic rate of glucose (CMRGlc) is defined as the number of moles of glucose metabolized per gram of tissue per minute. The activities of the key enzymes are sensitive to the local environment and so provide several avenues for local control of CMRGlc. Hexokinase is inhibited by its own product, so unless the fructose 6-phosphate continues down the metabolic path, the activity of hexokinase is curtailed. The step catalyzed by PFK is the major control point in glycolysis (Bradford 1986). The enzyme PFK is stimulated by the presence of ADP and inhibited by the presence of ATP. In this way, there is a simple mechanism for increasing glycolysis when the stores of ATP need to be replenished. In addition, many other factors influence the activity of PFK, including inhibition when the pH decreases, so CMRGlc can be adjusted to meet a variety of demands.

In addition to storing energy in ATP, a second important mechanism for storing free energy comes into play during glycolysis. The molecule nicotinamide adenine dinucleotide (NAD<sup>+</sup>) can accept electrons to form NADH, a thermodynamically uphill process. During glycolysis, the conversion of glucose to two pyruvate molecules is coupled to the conversion of two NAD<sup>+</sup> molecules to two molecules of NADH. Essentially, two electrons are transferred to each NAD<sup>+</sup> molecule, and the NAD<sup>+</sup> also picks up an H<sup>+</sup> to make the neutral form NADH. At equilibrium, NAD<sup>+</sup> is present in higher concentration than NADH, so the thermodynamically downhill process of glucose conversion to two pyruvate molecules is coupled to the uphill process of NAD<sup>+</sup> → NADH. The NADH serves as an intermediate mechanism to carry electrons to other processes, donating the electrons and reverting to the NAD<sup>+</sup> form. The NADH/NAD<sup>+</sup> system thus contains stored free energy that can be tapped by other processes.

## Lactate production and the lactate shuttle

The end point of glycolysis is the production of two pyruvate molecules, two ATP, and two NADH. For glycolysis to proceed, the negative free energy change associated with converting glucose to pyruvate must be larger than the positive free energy changes associated with  $\text{ADP} \rightarrow \text{ATP}$  and  $\text{NAD}^+ \rightarrow \text{NADH}$ . If the  $\text{NADH}/\text{NAD}^+$  ratio grows too large, the free energy required to convert more  $\text{NAD}^+$  to NADH will become too high to be provided by the conversion of  $\text{glucose} \rightarrow \text{pyruvate}$ , and glycolysis will stop. In each case, the free energies of the individual reactions depend on ratios of reactants and products (see [Box 1.1](#) at the end of this chapter), so glycolysis is energetically favored if the glucose/pyruvate ratio is high or the  $\text{NADH}/\text{NAD}^+$  ratio is low. Most of the pyruvate produced diffuses into the mitochondria, where it is further metabolized (see the next section), and this tends to keep the glucose/pyruvate ratio high. In addition, a transport mechanism, called the *malate/aspartate shuttle*, transfers NADH from the cytosol to the mitochondria in exchange for  $\text{NAD}^+$ , which tends to keep the  $\text{NADH}/\text{NAD}^+$  ratio from getting too high in the cytosol.

These mechanisms both shuffle the products of glycolysis off to the mitochondria, as fuel for oxidative metabolism. However, if the rate of pyruvate production by glycolysis exceeds the rate of pyruvate metabolism in the mitochondria, the pyruvate concentration in the cytosol will grow and another reaction becomes important: pyruvate is converted to lactate by a reaction coupled to  $\text{NADH} \rightarrow \text{NAD}^+$ , reducing the problems of both pyruvate and NADH build-up. This reversible reaction is catalyzed by the enzyme *lactate dehydrogenase*, and the lactate produced diffuses out of the cell and is carried away in the blood. In principle, this can also happen in reverse, with lactate from the blood diffusing into the cell, converting to pyruvate, and diffusing into the mitochondria for further metabolism, and there is some evidence that the brain can be a net consumer as well as producer of lactate during exercise (Quistorff *et al.* 2008).

From the description above, the production of lactate may be a sign of an imbalance in energy metabolism, indicating an over-metabolism of glucose relative to  $\text{O}_2$  metabolism. In hypoxia, for example, glycolysis could continue to provide some ATP when  $\text{O}_2$  is scarce, with the resulting production of lactate. In fact, though, lactate production may play a more direct role in healthy energy metabolism through the action of a *lactate shuttle* (Pellerin *et al.* 2007). Astrocytes play a key role in neuronal signaling by clearing neurotransmitter from the synaptic cleft. There is a growing body of evidence indicating that astrocytes have a high glucose metabolic rate compared with their  $\text{O}_2$  metabolic rate, with production of lactate. However, rather than diffusing into the blood, the lactate diffuses into the neurons where it is used as fuel. Lactate dehydrogenase converts the lactate to pyruvate, which is then metabolized in the mitochondria of the neuron.

In summary, the end point of glycolysis is the production of two ATP molecules and two pyruvate molecules from each glucose molecule, plus the conversion of two  $\text{NAD}^+$  molecules to two NADH molecules. But glycolysis alone taps only a small fraction of the available free energy in the glucose, and utilization of this additional energy requires further metabolism of pyruvate in the TCA cycle.

## Mitochondrial pyruvate metabolism and the electron transfer chain

In the healthy resting brain, nearly all of the pyruvate produced by glycolysis is destined for the TCA cycle. The TCA cycle involves many steps, each catalyzed by a different enzyme, and the machinery of the process is housed in the mitochondria. The net balance sheet for the

TCA cycle is that one pyruvate molecule is broken down to three molecules of  $\text{CO}_2$  with the conversion of 12 molecules of  $\text{NAD}^+$  to  $\text{NADH}$  (or a related electron storage compound). These molecular transformations do not involve molecular  $\text{O}_2$ . At this point, the free energy is concentrated in the  $\text{NADH}/\text{NAD}^+$  system. In the next stage, this free energy is converted to free energy of the  $\text{H}^+$  gradient in the mitochondria by the electron transfer chain.

Historically, the conversion of free energy from the metabolism of pyruvate and  $\text{O}_2$  to free energy of ATP presented a difficult puzzle, if nothing else, because of the numbers of molecules involved: how can the metabolism of one pyruvate and three  $\text{O}_2$  be coupled to the conversion of 18 ADP to ATP? For the free energy to be captured, the individual reactions must be tightly coupled together so that at each step the net free energy change is negative. It is unlikely that all of these molecules could be involved in one coupled reaction, so there must exist another intermediate store of free energy that could be raised by coupling it to the metabolism of pyruvate, and which could then be tapped to drive individual conversions of ADP to ATP. In the early 1960s, Peter Mitchell made the radical proposal that the missing intermediate was not a chemical reaction, but instead was a concentration gradient. In this *chemiosmotic hypothesis*, the intermediate storage of free energy is an  $\text{H}^+$  (proton) gradient across an inner membrane in the mitochondria. This proton gradient, with  $\text{H}^+$  at a higher concentration in the intermembrane space, stores free energy both in the  $\text{H}^+$  concentration difference and additionally in the electric potential difference that results from pumping positively charged  $\text{H}^+$  across the membrane. This idea is now viewed as the central concept underlying energy metabolism in the mitochondria (Nicholls and Ferguson 2002).

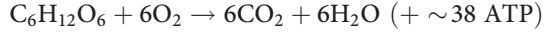
A mitochondrion is a complex organelle approximately  $1\ \mu\text{m}$  in diameter, and it is thought to have originated as an independent cell that merged with early eukaryotic cells in a symbiotic relationship. Over time, much of the original DNA of the mitochondria has moved to the cell nucleus, but some mitochondrial DNA remains. The potential advantage of a cell merger may have been that mitochondria were excellent machines for scavenging  $\text{O}_2$ . Today, the mitochondria are the powerhouses of the cell. The structure of a mitochondrion is important: there are two membranes defining an inner matrix, and an intermembrane space. The inner membrane is highly folded, with a large surface area, and contains several molecular complexes that span the membrane. These complexes function as pumps, transporting  $\text{H}^+$  from the matrix to the intermembrane space, creating the strong gradient of both  $\text{H}^+$  concentration and electric potential. The free energy to drive this uphill pumping is provided by the  $\text{NADH}/\text{NAD}^+$  system, by the transfer of electrons from  $\text{NADH}$  to the complexes, leaving  $\text{NAD}^+$ . These complexes are arranged in a chain, and the electrons are passed along the chain. At each step in the complex this electron transfer is a thermodynamically downhill process that is coupled to the uphill process of pumping  $\text{H}^+$  across the membrane against its gradient.

At the end of the electron transfer chain, the electron reaches an enzyme called *cytochrome oxidase*, and the final step in this process is the transfer of four electrons from cytochrome oxidase to an  $\text{O}_2$  molecule to form two molecules of water. The net result of the electron transfer chain is that free energy has been transferred between different forms, ending with the  $\text{H}^+$  gradient in the mitochondria and the conversion of  $\text{O}_2$  to water. The necessary  $\text{O}_2$ , of course, must be delivered by blood flow to the capillary bed, from which it diffuses to the mitochondria.

Finally, the  $\text{H}^+$  gradient in the mitochondria is coupled to *ATP synthase*, located in the inner membrane, to produce ATP. The ATP synthase has two components, a stalk that

penetrates the membrane and serves as a channel for  $H^+$ , and a head that couples this  $H^+$  transfer to the conversion of ADP to ATP.

At the end of the process, pyruvate and  $O_2$  are consumed, and  $CO_2$  and water are produced, and up to an additional 36 ATP molecules are created by combining ADP and  $P_i$ . The full oxidative metabolism of glucose thus produces approximately 18 times as much ATP as glycolysis alone. The overall metabolism of glucose is then:



From a thermodynamic viewpoint, the original free energy that drives this process is based on the conversion of glucose and  $O_2$  to  $CO_2$  and water. All of the other components of the system are cycled:  $NAD^+$  to NADH and back,  $H^+$  pumped across the mitochondrial membrane and back, etc. These other systems serve as intermediate storage for the free energy but at the end of the process are left where they started. The key to harnessing the original free energy is that the seemingly simple conversion, as written above, is broken into a long chain of coupled reactions that make possible the transfer of free energy from one system to another. The biological machinery underlying energy metabolism is a complex mechanism for combining the slow burning of glucose and  $O_2$  in a stepwise fashion that captures the free energy in a form which can then be coupled to the conversion of ADP to ATP.

## Delivery of glucose and $O_2$ by blood flow

Blood flow delivers glucose to the brain, carried in the plasma, but only approximately 30% or less of the glucose that enters the capillary is extracted from the blood (Oldendorf 1971). Glucose does not easily cross the blood-brain barrier, and a transporter system is required (Robinson and Rapoport 1986). This type of transport is called *facilitated diffusion*, rather than active transport, because no energy metabolism is required to move the glucose out of the blood. Glucose simply diffuses down its gradient from a higher concentration in blood to a lower concentration in tissue through particular channels (transporters) in the capillary wall. The channels have no preference for which way the glucose is transported, and so also transport unmetabolized glucose out of the tissue and back into the blood. Once across the capillary wall, the glucose must diffuse through the interstitial space separating the blood vessels and the cells and enter the intracellular environment. There the glucose enters into the first steps of glycolysis. However, not all of the glucose that leaves the blood is metabolized. Approximately half of the extracted glucose diffuses back out into the blood and is carried away by venous flow (Gjedde 1987). That is, glucose is delivered in excess of what is required at rest. The net extraction of glucose, the fraction of glucose delivered to the capillary bed that is actually metabolized, is only approximately 15%.

Oxygen is carried by blood primarily in the erythrocytes, where most of it is bound to hemoglobin. A small fraction (~2%) of total  $O_2$  is carried as dissolved gas in the plasma. While this fraction typically is not important in terms of the amount of  $O_2$  carried by the blood, the plasma concentration is important for  $O_2$  transport into the tissue. Oxygen diffuses into the tissue down a concentration gradient between dissolved gas in capillary plasma and dissolved gas in tissue. In the blood, the two pools of  $O_2$  – bound to hemoglobin and dissolved in plasma – are in fast equilibrium, so that  $O_2$  diffusing out of the capillary is quickly replenished by the release of hemoglobin-bound  $O_2$ . In the healthy human brain, with subjects relaxed and lying still, the OEF is approximately 40%. Remarkably, this fraction is relatively uniform across the brain in this basal state despite a several-fold variation of the resting  $CMRO_2$  in different regions (Gusnard and Raichle 2001).

Carbon dioxide, the end product of oxidative glucose metabolism, diffuses out of the cell, into the blood, and is carried off to the lungs to be cleared from the body. In addition, heat generated by metabolism is also carried away by the blood.

## Measuring energy metabolism with PET

### The deoxyglucose technique for measuring glucose metabolism

The development of the DG technique was a landmark in the evolution of functional neuroimaging techniques (Sokoloff 1977; Sokoloff *et al.* 1977). With this method, it became possible to map the pattern of glucose utilization in the brain with a radioactive tracer, whose distribution in an animal brain can be measured by a process called *autoradiography*. In autoradiography, a radioactive nucleus is attached to a molecule of interest and injected into an animal. After waiting for a time to allow the tracer to distribute, the animal is sacrificed and the brain cut into thin sections. Each section is laid on photographic film to allow the photons produced in the decay of the radioactive nucleus to expose the film. The result is a picture of the distribution of the agent at the time of sacrifice.

However, autoradiography cannot be used with labeled glucose itself because the brain concentration of the tracer at any single time point is never a good reflection of the glucose metabolic rate. Suppose that glucose is labeled with a radioactive isotope of carbon (e.g.,  $^{14}\text{C}$ ). At early times after injection, the amount of tracer in the tissue does not reflect the local metabolic rate because some of that tracer will diffuse back out into the blood and will not be metabolized. If we wait a longer time, the unmetabolized tracer may have cleared, but some of the  $^{14}\text{C}$  tracer that was attached to the glucose that *was* metabolized has also cleared as  $\text{CO}_2$ . In short, to measure the glucose metabolic rate with labeled glucose, measurements at multiple time points are required, and this cannot be done with autoradiography.

It is this central problem of estimating the metabolic rate from a single concentration measurement that was solved with the DG method. Deoxyglucose differs from glucose only in the removal of one of the  $\text{O}_2$  atoms. This analog of glucose is similar enough to glucose that it binds with the enzyme hexokinase catalyzing the first step of glycolysis. However, because of the difference between DG and glucose, the DG cannot proceed down the glycolysis pathway, and the process halts after the DG has been converted to fructose 6-phosphate. The result is that the radioactive label on DG essentially sticks in the tissue. It cannot proceed down the metabolic path, and the clearance of the compound from the tissue is very slow. After a sufficient waiting period to allow clearance of the unmetabolized fraction, the tissue concentration of the label is a direct, quantitative reflection of local CMRGlc.

### Measuring the cerebral metabolic rate for glucose

With the adaptation of the DG method for PET, studies of glucose metabolism were extended to the working human brain. Carbon-14, the radioactive tracer used in the DG autoradiographic method, cannot be used in humans because the electron emitted in the decay of the nucleus has a very short range in tissue, producing a large radiation dose in the subject but virtually no detectable external signal. In PET, the radioactive tracers used are nuclei with an excess ratio of protons to neutrons, and the decay produces a positron. A positron is the antiparticle of an electron, with all the same properties as an electron except for an opposite sign of its charge. Normal matter contains only electrons, so a positron is an exotic particle. Positrons are emitted with substantial kinetic energy, which is dissipated within a few

millimeters of travel through the tissue. When the positron has slowed sufficiently, it will annihilate with an electron. In this process, the positron and the electron cease to exist, and two high-energy photons are created. In this annihilation process, energy and momentum are conserved, with the energy of each photon equal to the rest mass energy of an electron (511 keV), and the photons are emitted in two directions close to 180° apart.

The emitted positron thus annihilates within a few millimeters of its origin, but the two photons travel through the tissue and can be measured with external detectors. Furthermore, because two photons travelling in opposite directions are produced, the detectors can be coordinated to count only *coincidence* detections, the arrival of a photon in each of two detectors within a very narrow window of time. The detection of such a coincidence then determines the origin of the photons – the site of the radioactive nucleus – to lie on a line between the two detectors. The total count of photons along a ray is proportional to the sum of all of the activity concentrations along the ray. By measuring many of these projections of the radioactivity distribution, an image of that distribution can be reconstructed in an analogous way to X-ray computed tomography (CT) images.

Positron-emitting nuclei are particularly useful for human metabolic imaging because the nuclei are biologically interesting (e.g.,  $^{11}\text{C}$ ,  $^{15}\text{O}$ ), the radioactive half-lives are short, and the decay photons readily pass through the body and so can be detected. A short half-life is important because it reduces the radiation dose to the subject, but this also requires that the isotope be prepared shortly before it is used, typically requiring an on-site cyclotron.

The PET version of the DG technique uses [ $^{18}\text{F}$ ]fluorodeoxyglucose (FDG) as the tracer (Phelps and Mazziotta 1985; Reivich *et al.* 1979). Fluorine-18 decays by positron emission with a half-life of approximately 2 h. The tracer is injected in a subject, and after a waiting period of approximately 45 min to allow unmetabolized tracer to clear from the tissue, a PET image of the distribution of the label is made. In fact, PET images can be acquired throughout this period in order to measure the local kinetics of the FDG. Such *time–activity curves* can be analyzed with a kinetic model to extract estimates of individual rate constants for uptake of glucose from the blood and for the first stage of glycolysis. However, the power of the technique is that the distribution of the tracer at a late time point directly reflects the local glucose metabolic rate.

In order to derive a quantitative measure of glucose metabolism with either the DG or FDG technique, two other quantities are required. The first is a record of the concentration of the tracer in arterial blood from injection up to the time of the PET image (or the time of sacrifice of the animal in an autoradiographic study). The integrated arterial time–activity curve describes how much of the agent the brain was exposed to and essentially provides a calibration factor for converting the amount of activity measured in the brain into a measure of the local metabolic rate. The second quantity needed is a correction factor to account for the fact that it is really the metabolic rate of DG, rather than glucose, that is measured. This correction factor is called the *lumped constant*, because it incorporates all of the factors that make the uptake and phosphorylation rate of DG differ from glucose. An important question for the interpretation of FDG-PET studies in disease states is whether the lumped constant remains the same, and this question is still being investigated.

## Increased glucose metabolism is closely associated with functional activity

Since the late 1970s, numerous animal studies have clearly demonstrated a close link between local functional activity in the brain and local CMRGlc (Kennedy *et al.* 1976; Sokoloff 1981).

An early monkey study examining the effects of visual occlusion clearly demonstrated that the striate cortex is organized in alternating ocular dominance columns. This organizational pattern was known from previous, painstaking recordings from many cells, but the autoradiogram showed the full pattern in one experiment. These experiments also demonstrated that CMRGlC decreases in association with a decrease of functional activity. When only one eye was patched, the ocular dominance columns associated with the patched eye appeared lighter (less exposed) on the autoradiogram than the columns corresponding to the open eye. With reduced visual input from the patched eye, CMRGlC was also reduced.

Activation studies, in turn, showed an increase of CMRGlC in the functionally active regions (Schwartz *et al.* 1979). Furthermore, with functional activity of different degrees, the change in CMRGlC also showed a graded response (Kadekaro *et al.* 1985). The connection between functional activity and glucose metabolism through ATP-dependent processes was demonstrated by an experiment in which the activity of the  $\text{Na}^+/\text{K}^+$  pump was blocked by a specific inhibitor, with the result that the increase of glucose metabolism with electrical stimulation was suppressed (Mata *et al.* 1980). In short, animal studies with DG and autoradiography, and human studies with FDG and PET (Phelps and Mazziotta 1985), have found a close correspondence between local neural activity and local CMRGlC.

In the brain, the consumption of glucose is heterogeneous. The metabolic rate in gray matter is three to four times higher than that in white matter. The low metabolic rate in white matter suggests that the energy cost of sending an action potential down an axon is small, most likely because of the efficient propagation along myelinated fibers. Instead, the energy metabolism is more closely associated with the synapses, in keeping with the energy budget estimates described above. Within the layers that make up cortical gray matter, the glucose metabolic rate is highest in layer IV, an area rich in synaptic connections. This area also shows the largest changes in glucose metabolism with activation. High-resolution studies of the precise location of the increased glucose metabolism suggest that it is not the cell body of the neuron but rather these areas of dense synaptic connections which show the largest increase in metabolic rate (Sokoloff 1991).

## Measuring cerebral blood flow and $\text{O}_2$ metabolism

In addition to CMRGlC measurements, other PET techniques provide measurements of CBF and  $\text{CMRO}_2$  as well. The basic idea is similar to FDG studies: a positron-emitting nucleus is attached to a molecule of interest, and from the dynamics of that label as it moves through the tissue, in combination with the measured dynamic curve in arterial blood, a relevant rate is calculated. For DG, the relevant rate is the metabolic rate of glucose. For CBF measurements, the relevant rate is the rate of delivery of arterial blood (discussed in more detail in Ch. 2). The primary isotope used for these studies is  $^{15}\text{O}$ -labeled water in arterial blood.

For  $\text{CMRO}_2$  measurements, the relevant rate is the metabolic rate of  $\text{O}_2$ , and these measurements also use  $^{15}\text{O}$  as the radioactive tracer, but this time labeling  $\text{O}_2$  rather than water. However,  $\text{CMRO}_2$  measurements are significantly more complicated by the fact that the  $^{15}\text{O}$  label switches from labeling  $\text{O}_2$  to labeling water when  $\text{O}_2$  is metabolized. The measured kinetics of the tracer depend on the interplay of delivery and clearance of  $^{15}\text{O}$ . By introducing  $^{15}\text{O}_2$ , the initial delivery of  $^{15}\text{O}$  does measure the delivery of  $\text{O}_2$ , but clearance of  $^{15}\text{O}$  from the tissue could be either from unmetabolized  $^{15}\text{O}_2$  returning to the blood, or from water of metabolism,  $\text{H}_2^{15}\text{O}$ . After a few circulation times, the labeled water builds up in the blood and is re-delivered to the tissue, but now  $^{15}\text{O}$  is being delivered as a label of water rather than molecular  $\text{O}_2$ , so CBF also affects the distribution of the  $^{15}\text{O}$ . In addition, because

much of the  $^{15}\text{O}$  is bound to hemoglobin in the blood, the CBV also affects the distribution of  $^{15}\text{O}$ . To deal with these complications, measurement of  $\text{CMRO}_2$  with PET requires three separate studies: the primary study, introducing  $^{15}\text{O}$ -labeled  $\text{O}_2$ , plus a second study with  $^{15}\text{O}$ -labeled water to assess CBF effects, and a third study with  $^{15}\text{O}$ -labeled carbon monoxide to assess CBV effects (Frackowiak *et al.* 1980; Mintun *et al.* 1984). For this reason,  $\text{CMRO}_2$  studies with PET have been much less common than  $\text{CMRGlC}$  and CBF studies.

## Balance of blood flow, glucose metabolism and $\text{O}_2$ use in the brain at rest and during activation

Based on the discussion above, the ratio of  $\text{CMRO}_2$  to  $\text{CMRGlC}$  should be 6 for complete oxidative metabolism of glucose. This ratio, called the *oxygen/glucose index* (OGI), has been measured in the resting human brain with PET as approximately 5.3 (Raichle *et al.* 1970). The slightly higher rate of glucose metabolism relative to  $\text{O}_2$  metabolism (i.e.,  $\text{OGI} < 6$ ) means that not all of the carbons of glucose are going into  $\text{CO}_2$ . Some could become part of molecular synthesis pathways, and some may appear as a low-level lactate concentration, with the excess flux of glucose into the brain balanced by a continuous clearance of lactate from the brain. Nevertheless, the fact that the OGI is near 6 at rest suggests that the majority of the net glucose metabolic rate is related to oxidative metabolism.

However, neural activation presents a surprisingly different picture. Because  $\text{CMRO}_2$  measurements are difficult, as noted above, CBF and  $\text{CMRGlC}$  measurements have provided the primary windows on brain function. The close correspondence of these two measurements, described above, suggests a straightforward picture of a localized, balanced increase in flow and metabolism with activation. This simple picture was challenged when Fox and Raichle (1986) measured the change in  $\text{CMRO}_2$  associated with brain activation and made a surprising discovery. In a somatosensory stimulation experiment, they found a focal CBF increase of 29% in the appropriate area of the brain, but only a 5% increase in  $\text{CMRO}_2$ . In a later visual stimulation study, they again found a large imbalance in the CBF and  $\text{CMRO}_2$  changes and confirmed that the  $\text{CMRGlC}$  change was indeed large and comparable to the CBF change (Fox *et al.* 1988).

More recent studies have examined the balance of CBF and  $\text{CMRO}_2$  changes with PET and also with MRI methods (described in more detail in later chapters). Most of these studies have found larger changes in  $\text{CMRO}_2$  with activation (as high as 20–30% with a strong activation), but still a weaker  $\text{CMRO}_2$  change compared with the CBF change. Typical values for the ratio of the fractional change in CBF to the fractional change in  $\text{CMRO}_2$  are in the range 2–3. However, these are ratios of CBF changes to  $\text{CMRO}_2$  changes, and not  $\text{CMRGlC}$  changes. Nevertheless, it is often assumed that CBF and  $\text{CMRGlC}$  changes are similar, based on numerous PET studies. In short, with activation the OGI decreases.

The finding that glucose metabolism increases much more than  $\text{O}_2$  metabolism has important implications for the magnitude of the energy metabolism changes during activation. Most of the increase in the metabolic rate of glucose is glycolysis alone, rather than full oxidative metabolism. This means that the actual change in energy metabolism is much less than would have been assumed from the increase in  $\text{CMRGlC}$  alone because glycolysis is much less efficient in generating ATP. The observed imbalance also implies that there should be a substantial production of lactate. This finding was confirmed with direct measurements of lactate accumulation in human subjects measured with spectroscopic nuclear magnetic resonance (NMR) studies (Prichard *et al.* 1991; Sappey-Marinié *et al.* 1992).



### What function is served by the large change in glucose metabolism?

Currently, there is no clear answer to the question of the function of such a large change in glucose metabolism. The additional ATP production associated with glycolysis above and beyond full oxidative metabolism is relatively small. For example, even with a large mismatch of a 30% increase of CMRGlc combined with a 10% increase of CMRO<sub>2</sub>, the increase of ATP production from the excess glycolysis is only approximately 1%. Although the excess glycolysis likely provides only a small component of the total energy costs of neural activity, it may provide needed ATP for particular tasks that cannot be fueled by ATP from oxidative metabolism in the mitochondria. For example, dendritic spines may be too small to allow local mitochondria to be near the synapse, and glycolysis potentially could provide the needed ATP for activity at these synapses.

Another possibility is that the production of ATP in the astrocytes favors glycolysis because it is fast, even though it is highly inefficient, and this may be important for rapid clearance of neurotransmitter from the synaptic cleft (Raichle and Mintun 2006). However, the free energy required for clearance of glutamate is provided by the Na<sup>+</sup> gradient, rather than ATP directly, with uptake of glutamate coupled to Na<sup>+</sup> moving into the astrocyte. The ATP is used to drive the Na<sup>+</sup>/K<sup>+</sup> pump to transport the Na<sup>+</sup> back out of the cell. It is possible that the rapid recovery of the Na<sup>+</sup> gradient within a confined space is important, and that the Na<sup>+</sup>/K<sup>+</sup> pump in the astrocytic processes at the synapse preferentially uses ATP from glycolysis to accomplish this. However, this is unlikely to be a general requirement of the Na<sup>+</sup>/K<sup>+</sup> pump. Because at least 50% of the energy consumed in the brain is thought to be linked to the action of this pump (Ames 2000; Attwell and Laughlin 2001), and glycolysis provides less than 10% of the total ATP production, even during activation, most of the ATP needed for the pump must come from oxidative metabolism.

The excess glucose metabolism, and associated production of lactate, may be associated with the lactate shuttle discussed above. Excess lactate diffuses from the astrocytes to the neurons, and increased lactate production would raise the tissue lactate and increase the lactate gradient, driving the lactate flux into the neurons. Increased tissue lactate would also increase the rate of lactate loss by blood flow, widening the gap between CMRGlc and CMRO<sub>2</sub>. This raises the question of exactly what role is played by the lactate shuttle. If lactate from astrocytes is a critical source of fuel for neurons, in addition to glucose delivered by CBF, then a fall in the OGI and a rise in tissue lactate may be necessary to increase the lactate flux into the neurons. Alternatively, if ATP derived from glycolysis is specifically necessary for recycling neurotransmitter, either because of the speed required or the limitations imposed by the cramped space of a dendritic spine, increased tissue lactate may be an unavoidable consequence. The lactate shuttle then may be a more secondary pathway to avoid wasting the lactate produced.

Based on these considerations, we can speculate that the increase of CMRGlc is driven by pre-synaptic activity, while CMRO<sub>2</sub> reflects the overall energy costs of neural activity. Because most of these energy costs are thought to be on the post-synaptic side, there could be a dissociation of these responses depending on how the input excitatory activity compares with the overall post-synaptic response. A common pattern of neural activity is that as the stimulus intensity systematically increases the neuronal response increases but tapers off. If the overall activity tapers off more quickly than the pre-synaptic activity, then glucose metabolism would increase more than O<sub>2</sub> metabolism as the stimulus intensity increased.

Current thinking about CBF changes also implicates synaptic activity itself in driving acute CBF changes. This could potentially explain why CBF and CMRGlc have similar large changes, while the CMRO<sub>2</sub> change is more modest, because of a difference in the particular aspects of neural activity that drive each response. These questions are considered again in Chapter 2, after a more detailed discussion of CBF.

### Box 1.1. The thermodynamics of neuronal signaling

#### Free energy and biological systems

All cellular processes, including neural signaling, are constrained by the physical laws of thermodynamics: (1) energy is conserved and (2) entropy increases or at best stays the same. Entropy is a subtle concept, but in broad terms it tends to increase if matter or energy are more dispersed. The interplay of these two effects can make it difficult to see which way entropy should change in a particular transformation. For example, consider a reaction in which a compound AB can break up into separate molecules of A and B, or reform as A and B molecules come together. Energy is distributed in the kinetic motion of all of the molecules, but there is also a negative binding energy holding A and B together in the AB molecules. For this reason, on the one hand, energy must be concentrated in the AB molecules in order to overcome the binding energy and break them apart, and this concentration of energy would tend to decrease the entropy. On the other hand, breaking AB into separate A and B molecules is a dispersal of matter, tending to increase entropy. The outcome of these two effects – the actual change in entropy – depends on the temperature. In general, the entropy associated with concentrating energy becomes more dominant at lower temperatures, favoring the condensed form AB. For any given temperature, there is an equilibrium in which the tendency for AB to break into A and B is balanced by the tendency for A and B to recombine to form AB. This equilibrium is characterized by a particular ratio of the reactants to the products,  $K_0(T) = [A][B]/[AB]$ . If the actual ratio differs from  $K_0$ , then the favored direction of the reaction is the one that moves the concentration ratio toward  $K_0$ . Writing this equilibrium ratio as  $K_0(T)$  reminds us that it depends on temperature, but for mammalian cellular activity the temperature normally remains approximately constant.

The concept of *free energy change* (or Gibbs free energy change  $[G]$ ) neatly combines the first and second laws of thermodynamics into a single useful relationship (see Nicholls and Ferguson [2002] for an excellent discussion of free energy in biological systems). For any transformation, such as a chemical reaction or movement of an ion across a membrane, there is an associated free energy change  $\Delta G$ . The free energy is a measure of how far a system is from equilibrium, with a negative value of  $\Delta G$  meaning that the transformation moves the system closer to equilibrium. *Cellular work* refers to processes that have a positive  $\Delta G$ , moving a part of the system away from equilibrium, such as transport of an ion against its electrochemical gradient. A process with a positive  $\Delta G$  can only occur if it is tightly coupled to another process with a more strongly negative  $\Delta G$ , so that the net  $\Delta G$  for the combined transformation is negative. That is, in order to move one system farther from equilibrium, that transformation must be coupled to another system that is moving closer to equilibrium.

For the transformation in which AB breaks into A and B, the free energy can be expressed as:

$$AB \rightarrow A + B: \quad \Delta G = -RT \ln \frac{K_0[AB]}{[A][B]}$$

where  $R$  is the gas constant,  $T$  is the temperature, and  $\ln$  indicates the natural logarithm. Note that if the concentration ratio is equal to the equilibrium ratio ( $1/K_0$ ), the argument of the logarithm is 1 and  $\Delta G = 0$ . That is, a system at equilibrium has no capacity to do cellular work. If the system is moved away from equilibrium owing to an excess of AB compared with A and B, then the break up of AB is associated with a negative  $\Delta G$  and the reaction as written is a downhill reaction in the thermodynamic sense. If the system is shifted away from equilibrium in the other direction, with an excess of A and B, then  $\Delta G$  is positive for the reaction as written, but would be negative if written backwards as  $A+B \rightarrow AB$ . That is, the combination of A and B into AB would be the downhill direction of the reaction.

The importance of considering  $\Delta G$  is that this quantity incorporates both the energy and the entropy changes involved, but this makes it a subtle concept. For example, the dependence of  $\Delta G$  on the ratio of reactant and product concentrations would not be expected if we were dealing just with energy. In a transformation of one molecule of AB to molecules of A and B, the true energy involved would depend just on changing bond energies, and would be the same regardless of the concentrations involved. The dependence on the concentrations comes from entropy considerations, and the condition that  $\Delta G$  must decrease for a transformation to happen is an embodiment of the second law of thermodynamics.

In some systems, the rate at which a transformation happens is directly related to the  $\Delta G$  involved, with the rate increasing as  $\Delta G$  grows more negative. There is a large body of literature devoted to these relationships, typically in systems near equilibrium. However, biological systems have evolved a different mechanism that often allows the rate of a transformation to be completely divorced from the magnitude of  $\Delta G$ . Specific proteins (enzymes) can serve as catalysts to speed up chemical reactions, or as ion channels to change membrane permeability to specific ions. In this role, they strongly affect the rate of the process without affecting the associated  $\Delta G$ . For example, the  $\Delta G$  associated with diffusion of  $\text{Na}^+$  from outside to inside the cell depends on the concentration ratio, but the *rate* of  $\text{Na}^+$  diffusion depends on the number of open channels and on the action of the  $\text{Na}^+/\text{K}^+$  pump.

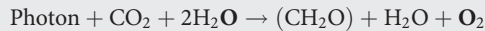
In short, the net  $\Delta G$  tells us which way a particular transformation will go, and the primary use of the magnitude of  $\Delta G$  is to identify systems that are far from equilibrium and which, by moving closer to equilibrium, can drive other processes away from equilibrium and perform useful cellular work. That is,  $\Delta G$  tells us which transformations can happen, but not necessarily how fast they will happen. The ways by which biological sources of  $\Delta G$  are tapped in cellular functions are controlled by specific proteins, and thus by gene expression.

## Free energy for life on Earth

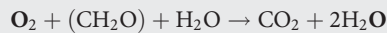
For the brain, the ultimate source of free energy is that the concentrations of glucose,  $\text{O}_2$  and  $\text{CO}_2$  are far from equilibrium inside the cell. And these non-equilibrium concentrations must be maintained by importing glucose and  $\text{O}_2$  into the cell from the environment and clearing  $\text{CO}_2$ . In a broad sense, the supplies of glucose and  $\text{O}_2$  in the environment are maintained by plants, which convert  $\text{CO}_2$  and water into  $\text{O}_2$  and organic compounds, including glucose. The source of free energy for this strongly uphill process is sunlight, and the degradation of sunlight is coupled to these chemical reactions in photosynthesis. The source of the free energy of sunlight is that the photons, which started off in thermodynamic equilibrium when they left the sun, are far from equilibrium when they reach the earth. The energy density and the spectrum of photons in thermal equilibrium are both determined by temperature, with a higher energy density and a spectrum with more high-energy photons at higher temperatures. The distribution of photon energies in the light leaving the sun is set by the sun's surface temperature, approximately 5700 K. As these photons travel away from the sun, they spread out; consequently, the density of photons at the surface of the Earth is much reduced. As a result, the photons arriving at Earth have a

spectrum characteristic of a 5700 K source but an energy density equivalent to thermodynamic equilibrium at a temperature of only approximately 300 K. In other words, the photons arriving at the surface of the Earth can be thought of as a system far from equilibrium, with the energy concentrated in high-energy photons, while thermodynamic equilibrium favors a redistribution of that energy to many more photons each with lower energy. The degradation of these high-energy photons thus releases a tremendous amount of free energy, which plants couple to chemical processes through photosynthesis.

The process of photosynthesis can be thought of as splitting water according to the schematic reaction:



In this scheme  $\text{CH}_2\text{O}$  represents the basic building block of carbohydrates. For example, glucose ( $\text{C}_6\text{H}_{12}\text{O}_6$ ) is composed of six of these blocks. We can think of this transformation as splitting the two water molecules on the left side to form one  $\text{O}_2$  molecule and four H atoms, which then combine with  $\text{CO}_2$  to form a  $\text{CH}_2\text{O}$  unit and an additional water molecule (the bold face for **O** is a reminder that the  $\text{O}_2$  molecule comes from water, not from  $\text{CO}_2$ ). Animals and plants make use of the free energy stored in the separated  $\text{O}_2$  and  $\text{CH}_2\text{O}$  units by reversing this reaction:



Note that the molecular  $\text{O}_2$  is converted back to water, rather than  $\text{CO}_2$ .

Life on Earth thus depends on sunlight to drive chemical synthesis and provide a source of  $\Delta G$  for sustaining biological systems. It is interesting to note that it is not primarily the *heat* of the sunlight that is critical, but rather the *spectrum* of the photons. Just as glucose and  $\text{O}_2$  can combine when burned to produce heat, the energy of the photons from the sun warms the surface of the Earth. The same amount of heating could, in principle, be supplied by a lower temperature source of photons, such as a cooler star closer to the Earth, but these photons would be inadequate to drive photosynthesis. So the existence of life on Earth ultimately depends on the fact that the sun is hot enough to produce high-energy photons, but far enough away that the equilibrium temperature on Earth is much lower.

### Free energy and neuronal signaling

For understanding the thermodynamic basis of neuronal signaling, the two key types of transformation are chemical reactions and diffusion across a membrane. As described in the main text, the ATP/ADP system is the primary source of a strongly negative  $\Delta G$ . For this system, the breakdown of ATP to ADP and inorganic phosphate ( $\text{P}_i$ ) is associated with a free energy change of the form:

$$\text{ATP} \rightarrow \text{ADP} + \text{P}_i : \quad \Delta G_{\text{ATP}} = -RT \ln \frac{K_{\text{ATP}}[\text{ATP}]}{[\text{ADP}][\text{P}_i]}$$

The ratio of the concentrations in this expression is often called the *phosphorylation potential*. Because the in vivo ATP concentration is much higher relative to ADP and  $\text{P}_i$  than it would be at equilibrium,  $\Delta G$  is strongly negative.

Diffusion of ions across the cellular membrane also has an associated  $\Delta G$ . If there is an electrical potential difference  $V$  across the membrane, then the  $\Delta G$  associated with one ion moving across the membrane depends on  $V$  and the extracellular (E) and intracellular (I) concentrations of the ion. For example, for  $\text{Na}^+$ , the  $\Delta G$  for one  $\text{Na}^+$  to move from the extracellular space to the intracellular space is:

$$[\text{Na}^+]_{\text{E}} \rightarrow [\text{Na}^+]_{\text{I}} : \quad \Delta G_{\text{Na}} = -RT \ln \frac{K_{\text{Na}}(V) [\text{Na}^+]_{\text{E}}}{[\text{Na}^+]_{\text{I}}}$$

where the equilibrium constant  $K_{\text{Na}}(V)$  is the ratio of the concentrations (intracellular/extracellular) that would be in equilibrium with the membrane potential  $V$ . If  $V=0$ , there is no longer any interaction with the ion's charge, and at equilibrium the extracellular and intracellular concentrations would be equal ( $K_{\text{Na}}=1$ ). For a typical membrane potential of  $V=-70$  mV, with the inside more negative, the equilibrium for  $\text{Na}^+$  would be a higher concentration inside the cell because the negative potential favors the accumulation of the positive ions, corresponding to  $K_{\text{Na}} \sim 10$ . Because the in vivo distribution is strongly skewed the other way, with a much higher extracellular concentration, there is a strongly negative  $\Delta G$  associated with  $\text{Na}^+$  moving into the cell. Correspondingly, moving  $\text{Na}^+$  out of the cell against its gradient is a strongly uphill process and must be coupled with an even more strongly downhill process, such as the conversion of ATP to ADP.

### Biological batteries

In general, cellular processes often involve an interplay between these two basic sources of  $\Delta G$ : a chemical system in which the reactant/product concentration ratio is far from equilibrium, or an ion distribution across a membrane that is far from equilibrium. In each case, we can think of the system as a biological battery, with the “voltage” of the battery corresponding to how far that system is from equilibrium as measured by the corresponding  $\Delta G$ . Then as one system performs cellular work, with a corresponding degradation of the relevant concentrations and reduction of the equivalent voltage, that system can be “recharged” by coupling it with another system with a higher voltage. The interplay of several systems involved in neuronal signaling discussed in Ch. 1 can be viewed in terms of such biological batteries.

For example, to move  $\text{Na}^+$  back out of the cell in the recovery from signaling, the transport of  $\text{Na}^+$  is coupled to the conversion of ATP to ADP, an example of using a chemical reaction source of negative  $\Delta G$  to recharge an ionic gradient. In the mitochondria, the conversion of ADP and  $\text{P}_i$  back to ATP is coupled to transport of  $\text{H}^+$  across the mitochondrial membrane, an example of an ionic gradient recharging a chemical reaction ratio. The idea of a system far from equilibrium is important for another reason in addition to  $\Delta G$  and energy metabolism: for a chemical messenger to convey a “signal,” it must be part of a system that is far from equilibrium. For example,  $\text{Ca}^{2+}$  is maintained at a much higher concentration outside the cell, and entry of  $\text{Ca}^{2+}$  is a common chemical signal that triggers a chain of events within the cell, such as neurotransmitter release. For  $\text{Ca}^{2+}$  entry to work as a signal, the intracellular concentration must be kept at a low level prior to the signal, despite the high concentration outside the cell. One way the  $\text{Ca}^{2+}$  is removed is by coupling the transport of  $\text{Ca}^{2+}$  out of the cell to  $\text{Na}^+$  transport into the cell, an example of the extracellular/intracellular  $\text{Na}^+$  gradient being used as a source of negative  $\Delta G$  to restore the  $\text{Ca}^{2+}$  signaling system. When a neurotransmitter opens a  $\text{Na}^+$  channel on the post-synaptic neuron, the strong flux of  $\text{Na}^+$  down its gradient is a signaling mechanism.

In short, from a thermodynamic point of view, neuronal signaling involves an interconnected set of biological batteries, systems far from equilibrium that can serve as sources of  $\Delta G$  for either energy metabolism or signaling. These batteries have different equivalent voltages and are linked in a hierarchy in which one can recharge another. They include chemical reaction systems and ionic gradients, coupled through particular enzymes such as the  $\text{Na}^+/\text{K}^+$  pump. Ultimately, the battery with the largest voltage is the system of glucose,  $\text{O}_2$  and  $\text{CO}_2$  within the cell, which is maintained in a state far from equilibrium by continual delivery of glucose and  $\text{O}_2$  and clearance of  $\text{CO}_2$ . The overall conversion of glucose and  $\text{O}_2$  to  $\text{CO}_2$  and water taps the free energy originally stored in carbohydrates when plants coupled photons of sunlight to the splitting of water.

## References

- Ames A, III (2000) CNS energy metabolism as related to function. *Brain Res Brain Res Rev* **34**:42–68
- Attwell D, Iadecola C (2002) The neural basis of functional brain imaging signals. *Trends Neurosci* **25**:621–625
- Attwell D, Laughlin SB (2001) An energy budget for signaling in the grey matter of the brain. *J Cereb Blood Flow Metab* **21**:1133–1145
- Blaustein MP (1988) Calcium transport and buffering in neurons. *Trends Neurosci* **11**:438–443
- Bradford H (1986) *Chemical Neurobiology*. New York: WH Freeman
- Erecinska M, Silver IA (1990) Metabolism and role of glutamate in mammalian brain. *Prog Neurobiol* **35**:245–296
- Erecinska M, Silver IA (1994) Ions and energy in mammalian brain. *Prog Neurobiol* **43**:37–71
- Fox PT, Raichle ME (1986) Focal physiological uncoupling of cerebral blood flow and oxidative metabolism during somatosensory stimulation in human subjects. *Proc Natl Acad Sci USA* **83**:1140–1144
- Fox PT, Raichle ME, Mintun MA, Dence C (1988) Nonoxidative glucose consumption during focal physiologic neural activity. *Science* **241**:462–464
- Frackowiak RSJ, Lenzi GL, Jones T, Heather JD (1980) Quantitative measurement of regional cerebral blood flow and oxygen metabolism in man using  $^{15}\text{O}$  and positron emission tomography: theory, procedure, and normal values. *J Comput Assist Tomogr* **4**:727–736
- Gjedde A (1987) Does deoxyglucose uptake in the brain reflect energy metabolism? *Biochem Pharmacol* **36**:1853–1861
- Gusnard DA, Raichle ME (2001) Searching for a baseline: functional imaging and the resting human brain. *Nat Rev Neurosci* **2**:685–694
- Iadecola C, Nedergaard M (2007) Glial regulation of the cerebral microvasculature. *Nat Neurosci* **10**:1369–1376
- James W (1890) *The Principles of Psychology*. Cambridge, MA: Harvard University Press
- Kadekaro M, Crane AM, Sokoloff L (1985) Differential effects of electrical stimulation of sciatic nerve on metabolic activity in spinal cord and dorsal root ganglion in the rat. *Proc Natl Acad Sci USA* **82**:6010–6013
- Kennedy C, Rosiers MHD, Sakurada O, *et al.* (1976) Metabolic mapping of the primary visual system of the monkey by means of the autoradiographic [ $^{14}\text{C}$ ]deoxyhemoglobin technique. *Proc Natl Acad Sci USA* **73**:4230–4234
- Laughlin SB, Sejnovski TJ (2003) Communication in neural networks. *Science* **301**: 1870–1874
- Logothetis NK (2002) The neural basis of the blood-oxygen-level-dependent functional magnetic resonance imaging signal. *Philos Trans Roy Soc Lond B Biol Sci* **357**:1003–1037
- Mata M, Fink DJ, Gainer H, *et al.* (1980) Activity-dependent energy metabolism in rat posterior pituitary primarily reflects sodium pump activity. *J Neurochem* **34**:213–215
- Mintun MA, Raichle ME, Martin WRW, Herscovitch P (1984) Brain  $\text{O}_2$  utilization measured with  $\text{O-15}$  radiotracers and positron emission tomography. *J Nucl Med* **25**:177–187
- Nicholls DG, Ferguson SJ (2002) *Bioenergetics 3*. London: Academic Press
- Nicholls JG, Martin AR, Wallace BG (1992) *From Neuron to Brain*. Sunderland, MA: Sinauer Associates
- Oldendorf WH (1971) Brain uptake of radiolabeled amino acids, amines, and hexoses after arterial injection. *Am J Physiol* **221**:1629–1639
- Pellerin L, Bouzier-Sore AK, Aubert A, *et al.* (2007) Activity-dependent regulation of energy metabolism by astrocytes: an update. *Glia* **55**:1251–1262
- Phelps ME, Mazziotta JC (1985) Positron emission tomography: human brain function and biochemistry. *Science* **228**: 799–809
- Prichard J, Rothman D, Novotny E *et al.* (1991) Lactate rise detected by  $^1\text{H}$  NMR in human visual cortex during physiologic stimulation. *Proc Natl Acad Sci USA* **88**:5829–5831
- Quistorff B, Secher NH, van Lieshout JJ (2008) Lactate fuels the human brain during exercise. *FASEB J* **22**: 3443–3449
- Raichle ME (1998) Behind the scenes of functional brain imaging: a historical and physiological perspective. *Proc Natl Acad Sci USA* **95**:765–772

- Raichle ME, Mintun MA (2006) Brain work and brain imaging. *Annu Rev Neurosci* **29**:449–476
- Raichle ME, Posner JB, Plum F (1970) Cerebral blood flow during and after hyperventilation. *Arch Neurol* **23**:394–403
- Reivich M, Kuhl D, Wolf A, *et al.* (1979) The [ $^{18}\text{F}$ ]-fluoro-deoxyglucose method for the measurement of local cerebral glucose measurement in man. *Circ Res* **44**:127–137
- Robinson P, Rapoport SI (1986) Glucose transport and metabolism in the brain. *Am J Physiol* **250**: R127–R136
- Sappey-Marinièr D, Calabrese G, Fein G, *et al.* (1992) Effect of photic stimulation on human visual cortex lactate and phosphates using  $^1\text{H}$  and  $^{31}\text{P}$  magnetic resonance spectroscopy. *J Cereb Blood Flow Metab* **12**:584–592
- Schwartz WJ, Smith CB, Davidsen L, *et al.* (1979) Metabolic mapping of functional activity in the hypothalamo-neurohypophysial system of the rat. *Science* **205**:723–725
- Siesjö B (1978) *Brain Energy Metabolism*. New York: John Wiley
- Sokoloff L (1977) Relation between physiological function and energy metabolism in the central nervous system. *J Neurochem* **29**:13–26
- Sokoloff L (1981) The relation between function and energy metabolism: its use in the localization of functional activity in the nervous system. *Neurosci Res Prog Bull* **19**:159–210
- Sokoloff L (1991) Relationship between functional activity and energy metabolism in the nervous system: whether, where and why? In *Brain Work and Mental Activity: Quantitative Studies with Radioactive Tracers*, Lassen NA, Ingvar DH, Raichle ME *et al.*, eds. Copenhagen: Munksgaard, pp. 52–67
- Sokoloff L, Reivich M, Kennedy C, *et al.* (1977) The [ $^{14}\text{C}$ ]deoxyglucose method for the measurement of local cerebral glucose utilization: theory, procedure, and normal values in the conscious and anesthetized albino rat. *J Neurochem* **28**:897–916

# Cerebral blood flow and brain activation

<b>The blood supply of the brain</b>	<i>page</i> 34
The vascular system	34
Tissue perfusion	36
Cerebral blood volume and blood velocity	37
The central volume principle	37
Cerebral blood flow is a measure of delivery of arterial blood	38
<b>Changes in cerebral blood flow and blood volume</b>	39
Blood flow is controlled by changing vascular resistance	39
The relationship between blood volume and blood flow during activation	40
<b>Neural activity and the control of cerebral blood flow</b>	42
The development of ideas about control of cerebral blood flow	42
Smooth muscle relaxation	43
Vasoactive agents	44
The neurovascular unit	48
<b>Measuring cerebral blood flow</b>	49
The microsphere technique	49
The nitrous oxide technique	49
Diffusible versus intravascular tracers	50
The radioactive xenon technique	52
Techniques using PET	52
Techniques using MRI	53
<b>Brain activation</b>	53
Blood flow and glucose metabolism increase with functional activity	53
Oxygen metabolism increases less than blood flow	54
Summary of physiological changes during brain activation	55

## The blood supply of the brain

Cerebral blood flow (CBF) delivers glucose and O<sub>2</sub> to the brain, so it is natural to suppose that local CBF varies with neural activity, as suggested by James (1890) in the second quote at the beginning of Part IA. Although we certainly know more about the changes in CBF with activation and in disease states than was known in James' time, we still lack a full understanding. Nevertheless, the change in CBF with a change in neural activity is the primary signal used for mapping brain activity with functional neuroimaging.

## The vascular system

The vascular system that supplies blood to the brain is organized on spatial scales that span a size range of four orders of magnitude, from the diameter of a capillary (~10 μm) to the



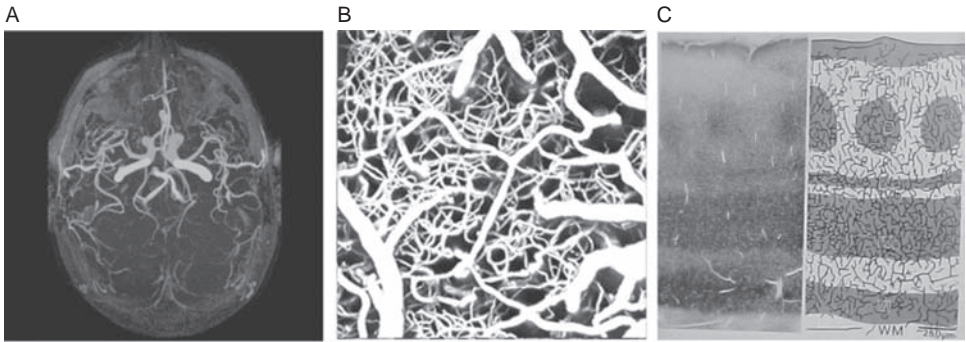


**Fig. 2.1.** The vascular system of the brain. (A) A magnetic resonance angiogram showing the major vessels in the brain. (B) A two-photon microscopy image of the surface vasculature (to a depth of approximately 300  $\mu\text{m}$ ) in the rat somatosensory cortex, showing the multidirectional orientation of the vascular network (image courtesy of A. Devor.) (C) A photomicrograph of a stained section through the lamina of the primary visual cortex of a monkey (Zheng *et al.* 1991). The staining indicates areas with high concentrations of cytochrome oxidase, an enzyme involved in oxidative metabolism, and highlights layers IV and VI and also blobs in layer II. The panel on the right also shows a camera lucida drawing of the vessels in the stained section, showing higher capillary densities in the stained areas. (Figure C reproduced with permission from Zheng *et al.*, *J. Neuroscience* 11:2622–2629, 1991; copyright 1991 by the Society for Neuroscience.)

distribution volume of a major artery ( $\sim 10 \text{ cm}^3$ ). The complexity of the vascular network can be appreciated from Fig. 2.1. Figure 2.1A is a MR angiogram, showing the major arteries delivering blood to the tissue, and the veins carrying it back toward the heart. This angiogram shows vessels down to a few millimeters in diameter. Figure 2.1B is a microscopic view, showing the complex geometry of the smallest vessels, the arterioles, capillaries, and venules. This two-photon microscopic image of the somatosensory cortex of the rat is a maximum intensity projection of a series of 2  $\mu\text{m}$  images extending down to approximately 300  $\mu\text{m}$  in depth. The smallest capillaries have a diameter of approximately 6–8  $\mu\text{m}$ , comparable to the size of a red blood cell. Figure 2.1C shows images illustrating the distribution of capillary density within the layers of the cortex (Zheng *et al.* 1991). The photomicrograph shows a 1 mm wide strip from a cytochrome oxidase-stained section of a slice through the primary visual cortex (area 17) of a squirrel monkey, and the camera lucida tracing shows the blood vessels (mostly capillaries). Cytochrome oxidase is one of the enzymes involved in oxidative metabolism (Ch. 1), and the uneven distribution of the enzyme in the brain suggests a heterogeneous distribution of  $\text{O}_2$  metabolism. In this study, the microvessel density, as measured by the total length of vessels visible in the slice, showed a close correspondence with the cytochrome oxidase-stained areas. The peak density in the cortex was in layer IV, where the density was approximately 1.5–3 times higher than that of white matter.

The study of Zheng *et al.* (1991) also showed how the functional organization of the brain is at least partially reflected in the blood vessel density. The border between the primary and secondary visual cortex (areas 17 and 18) is distinguished by changes in the laminar structure, and the microvessel density correspondingly was found to be approximately 25% higher in the primary visual cortex. On an even smaller scale, in the primary visual cortex of primates, functional units called *blobs* have been identified based on their higher concentration of cytochrome oxidase. The blobs are located in layers II and III of the cortex and are approximately 250  $\mu\text{m}$  in extent in the images in Figure 2.1C. The capillary density in the blobs was approximately 40% higher than that in the interblob regions. In short, the architecture of the vascular tree shows distinct organization on a spatial scale as small as a few hundred micrometers.

## Tissue perfusion

Because many functional imaging techniques, including fMRI, depend on changes in CBF, it is important to understand precisely what CBF is and how it can be measured. The term *perfusion* is used in a general way to describe the process of nutritive delivery of arterial blood to a capillary bed in the tissue. Because functional neuroimaging is potentially sensitive to several aspects of the perfusion state of tissue, it is important to clarify exactly what is meant by several terms. *Cerebral blood flow* is the rate of delivery of arterial blood to the capillary beds of a particular mass of tissue, as illustrated in Figure 2.2. For convenience, a common unit for CBF is milliliters of blood per 100 grams of tissue per minute, and a typical average value in the human brain measured with PET is approximately 50 mL/100 g per min, with gray matter about three times higher than white matter (Ito *et al.* 2004; Rostrup *et al.* 2005). For imaging applications, it often is convenient to express this as flow delivered to a unit volume of tissue rather than a unit mass of tissue, because a signal is measured from a particular volume in the brain, and the actual mass of tissue within that volume is not known. Because the density of brain is close to 1 g/mL, CBF values expressed in these units are similar. Note, however, that the units of CBF are then milliliters per milliliter per minute, which are essentially units of inverse time. For this reason, it is sometimes useful to think of CBF as having the same units as a rate constant (e.g., 60 mL/100 g per min is equivalent to  $0.01 \text{ s}^{-1}$ ).

A useful example of considering CBF as an effective rate constant is a fundamental relationship between CBF and the cerebral metabolic rate of  $\text{O}_2$  ( $\text{CMRO}_2$ ). For a consistent definition of units, CBF can be expressed as milliliters of arterial blood delivered per milliliter of tissue per minute, and  $\text{CMRO}_2$  is then expressed as moles of  $\text{O}_2$  consumed per milliliter of tissue per minute. The rate of delivery of  $\text{O}_2$  to the capillary bed is simply CBF

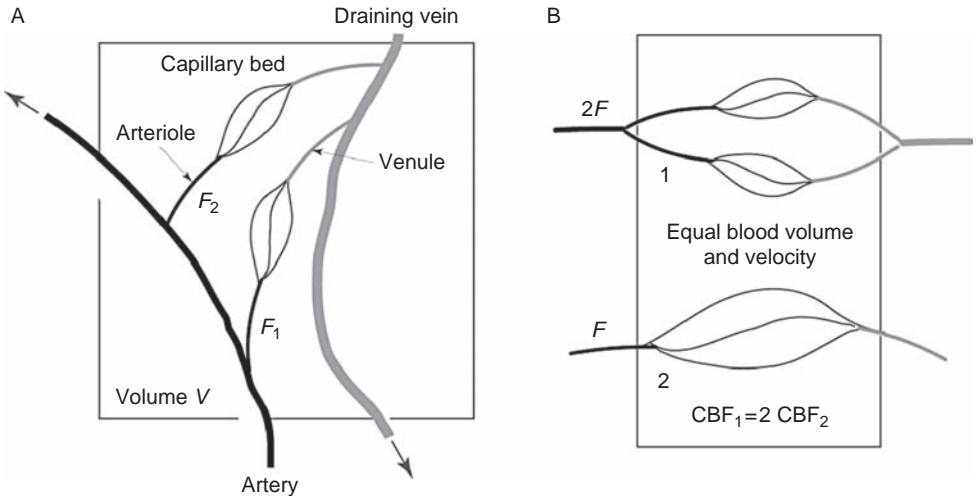


**Fig. 2.2.** The meaning of perfusion. (A) Blood vessels within a small element of tissue. Cerebral blood flow (CBF) is the delivery of arterial blood to the capillary beds ( $F_1 + F_2$ ) and so is not directly related to the local blood volume, which also includes arterial blood destined for a more distal tissue element and venous blood draining more distal tissues. (B) Measurement of blood volume and blood velocity is not sufficient to measure CBF. In the lower capillary bed, the vessels are twice as long as those in the upper capillary bed, so the blood volume and blood velocity are the same, yet the CBF is twice as large in the upper capillary bed. Instead of blood volume and blood velocity determining CBF, it is blood volume and transit time that determine CBF through the *central volume principle*.

times  $[O_2]_a$ , the concentration of  $O_2$  in arterial blood in units of moles of  $O_2$  per milliliter. With these definitions,  $CMRO_2$  can be expressed as

$$CMRO_2 = OEF \cdot CBF \cdot [O_2]_a \quad (2.1)$$

where OEF is the fraction of delivered  $O_2$  that is extracted and metabolized. In this combination, the product of the OEF and CBF acts like a “rate constant” for metabolism of a “substrate” represented by  $[O_2]_a$ . This equation essentially just follows from the definitions of the terms involved, but it is a useful relationship to keep in mind when considering the BOLD effect. If CBF increases more than  $CMRO_2$ , then the OEF must decrease, and this is the essential physiological phenomenon underlying the BOLD response.

## Cerebral blood volume and blood velocity

The cerebral blood volume (CBV) is the fraction of the tissue volume occupied by blood vessels, and a typical value for the brain is approximately 4% ( $CBV = 0.04$ ) (Rostrup *et al.* 2005). The CBV is a dimensionless number (milliliters of blood vessel per milliliter of tissue), and usually refers to the entire vascular volume within the tissue. In some applications, however, it is important to subdivide total CBV into arterial, capillary, and venous volumes. Reliable measurements of the relative sizes of these volumes are scarce, but reported estimates for a sheep brain for vessels smaller than approximately 2 mm in diameter are 20% for arterioles, 50% for capillaries, and 30% for venules (Sharan *et al.* 1998). The blood volume potentially can change in any of these sub-compartments of the vascular system. The dilation of the arterioles that leads to an increase in flow is a volume increase on the arterial side, and a number of studies have shown significant changes in the arterial CBV associated with changes in CBF and neural activity (Devor *et al.* 2007; Hillman *et al.* 2007; Ito *et al.* 2005; Kim *et al.* 2007).

Some early data suggested that only a fraction of the tissue capillaries are open channels at rest and that *capillary recruitment* (i.e., opening the previously collapsed capillaries) is involved in increasing CBF (Frankel *et al.* 1992; Shockley and LaManna 1988; Weiss 1988). However, the accuracy of the techniques used in these early studies has been challenged (Gobel *et al.* 1990), and a number of more recent studies have concluded that capillary recruitment is a small effect, if it occurs at all (Berezcki *et al.* 1993; Gobel *et al.* 1989; Klein *et al.* 1986; Pawlik *et al.* 1981; Vetterlein *et al.* 1990; Villringer *et al.* 1994; Wei *et al.* 1993). Instead, changes of CBF are associated with changes in blood velocity in the capillaries. For example, studies in rats have found increases during hypoxia (Berezcki *et al.* 1993; Krolo and Hudetz 2000) and decreases with pentobarbital (Wei *et al.* 1993). Blood velocity varies from tens of centimeters per second in large arteries to as slow as 1 mm/s in the capillaries. At the capillary level, the pulsatility seen in the arterial vessels is largely damped out. Nevertheless, studies of the passage of red blood cells through individual capillaries have found that the flow is often irregular, rather than a smooth constant velocity (Kleinfeld *et al.* 1998; Villringer *et al.* 1994). This likely reflects the fact that the red cell diameter is about the same as the capillary diameter, and the red cells can clump together to produce transient blockages. In addition, transit of larger white cells can also cause a transient slow down of flow. If one looks just at an individual capillary, flow is an irregular process, and it is only when averaged over thousands of capillaries that CBF takes on a well-defined, stable value.

## The central volume principle

Although CBF, CBV, and blood velocity are all important aspects of the perfusion state of tissue, they are distinct physiological quantities. With the preceding definitions, CBF does

not explicitly depend on either blood volume or the velocity of blood in the vessels. An increase in CBF with brain activation could occur through a number of different changes in blood volume or blood velocity. For example, an increase of blood velocity in a fixed capillary bed or an increase in the number of open capillaries but with blood moving at the same velocity in each capillary would both lead to an increase in CBF. In both cases, more arterial blood flows through the capillary bed. Furthermore, even specifying capillary velocity and capillary volume is not sufficient to determine CBF, as illustrated in Fig. 2.2B. Two idealized capillary beds are shown, one with two sets of shorter capillaries, and one with a single set of capillaries twice as long. In both beds, the blood velocity is the same, and we have constructed them to have the same capillary blood volume. However, the CBF is twice as large in the upper bed with two sets of shorter capillaries because the volume of arterial blood delivered to the bed per minute is twice as great.

Intuitively, it seems that specifying the blood volume and blood velocity ought to determine CBF, but the preceding example shows that it does not. The missing piece that *does* differ between the two scenarios is the capillary transit time. In the capillary bed with the longer capillaries, the capillary transit time is twice as long. And it is transit time, rather than blood velocity, that is directly connected to CBV and CBF. The important relationship, known as the central volume principle, has been recognized for over a century (Stewart 1894):

$$\tau = \text{CBV}/\text{CBF} \quad (2.2)$$

where  $\tau$  is the mean transit time through the volume defined by CBV. For a CBF of 60 mL/100 g per min ( $0.01 \text{ s}^{-1}$ ) and a typical CBV of 4%, the vascular transit time is approximately 4 s from this equation. By restricting the volume to a subset of the entire blood volume, such as the capillary volume, the relation still holds, with  $\tau$  defined as the mean transit time through the capillary volume.

## Cerebral blood flow is a measure of delivery of arterial blood

These considerations indicate that the definition of CBF involves some subtleties important for understanding how CBF is measured, as illustrated in Fig. 2.2. In this idealized tissue vasculature, the flow rates through the two capillary beds are designated  $F_1$  and  $F_2$  (expressed in milliliters per minute), and if these beds feed a volume of tissue  $V$ , then CBF is simply  $(F_1 + F_2)/V$ . However, an element of tissue will also contain arterial blood in larger arteries that is just passing through, destined for a capillary bed in another location. The tissue element may also contain venous blood passing through as it drains another tissue element.

For these reasons, it is difficult to make reliable measurements of CBF by looking at the blood itself within a tissue element, although such techniques are in use. For example, laser Doppler flowmetry measures a frequency shift in light reflected from moving red blood cells (Dirnagl *et al.* 1989; Stern 1975). The proportion of the reflected light that is Doppler shifted is a measure of the number of moving red blood cells, the total blood volume, and the average frequency shift is a measure of the average red blood cell velocity. Taken together, these data provide a measure of blood motion within an element of tissue. This general motion of the blood does not, however, necessarily reflect CBF, the flow of arterial blood into the capillary beds.

For example, an element of tissue could have no change in CBF (e.g.,  $F_1$  and  $F_2$  remain constant in Fig. 2.2) but show increased red blood cell motion if CBF increases in a distal tissue element, with a corresponding increase in speed in the arteries and draining veins that

also happen to pass through the first element. The laser-Doppler flowmetry technique is useful for studies of the microvasculature in animal models, but estimates of CBF with this technique should be interpreted with caution. The central problem is that the defining characteristic of CBF is not blood motion within the tissue element but rather delivery of arterial blood to the capillary bed. For this reason, a more accurate approach for estimating CBF is to measure the rate of delivery of an agent carried to the tissue by flow.

## Changes in cerebral blood flow and blood volume

### Blood flow is controlled by changing vascular resistance

The rate of delivery of arterial blood to a small element of tissue depends on the pressure driving the blood through the vascular tree and the resistance that must be overcome along the way. Specifically, blood flow can be taken to be the ratio of the difference in pressure between the arterial and venous blood ( $\Delta P$ ) to the *cerebrovascular resistance*:  $CBF = \Delta P / CVR$  (this is essentially the definition of cerebrovascular resistance). In the vascular system, the resistance is not uniformly distributed across all of the branches of the network but, instead, is dominated by the arterioles and the capillaries. The arterioles are the smallest of the arterial branches, located just prior to the capillaries. For steady flow through the vascular tree, the net resistance of each stage is reflected in the pressure fall across that stage. Starting with the largest arteries, there is a gradual pressure decrease as the main arteries branch into smaller vessels, a sharper drop across the arterioles and capillary bed, and then again a gradual decrease across the venous branches as the blood collects from the smallest venules into larger veins (Boas *et al.* [2008] give a recent model of the vascular tree). In the healthy brain, *autoregulation* operates to maintain CBF at a nearly constant value despite alterations in arterial pressure over a range from approximately 75 to 175 mmHg (Guyton 1981). As pressure changes, cerebrovascular resistance changes in a compensatory way by dilating or constricting the arterioles.

The arterioles are the seat of control of vascular resistance. A coat of smooth muscle cells surrounds the arterioles, contracting to constrict the vessel and relaxing to dilate it. To maintain control of the arteriolar diameter, and thus resistance, the smooth muscle must be in a chronic state of moderate contraction, described as muscular *tone*, so that resistance can be either increased or decreased (Andresen *et al.* 2006). Control of smooth muscle tension is a complicated process but is closely involved with the intracellular  $Ca^{2+}$  concentration in the smooth muscle cell (Faraci and Sobey 1998). Increased cytosolic  $Ca^{2+}$ , either through opening  $Ca^{2+}$  channels to allow external  $Ca^{2+}$  to enter or through triggered release of internal  $Ca^{2+}$  stores, initiates a contraction. Processes or agents that tend to interfere with these  $Ca^{2+}$  increases or reduce cytosolic  $Ca^{2+}$  lead to relaxation. As discussed in the next section, a large number of factors can affect the arteriolar smooth muscle and alter resistance.

Resistance is likely to be a steep function of arteriolar diameter. For laminar flow of a simple fluid, the resistance is proportional to  $1/r^4$ , where  $r$  is the radius of the vessel. Therefore, to decrease the resistance of the arterioles by 100%, the radius of the arterioles need increase only 19%. Blood is not a simple fluid, and the flow is not likely to be purely laminar; nevertheless, this argument suggests a sensitive mechanism to control blood flow. In principle, dilation of just the arterioles would be sufficient to increase flow through a local capillary bed fed by the arteriole. However, another process occurs that is not fully understood: the dilatation propagates upstream to larger arterial vessels. Several mechanisms have been proposed for this effect, including signaling through gap junctions connecting smooth

muscle cells and nitric oxide (NO) released from the walls of upstream vessels in response to increased shear stress. A recent report indicates that the astrocytes play a direct role in upstream dilatation (Xu *et al.* 2008). Although the mechanisms are unclear, the significance of this effect is that the vessel dilatation associated with increased CBF extends upstream from the initiating arterioles.

A possible function for the upstream dilatation is that this could serve to prevent a phenomenon called *vascular steal*, in which increased flow in one area leads to a decreased flow in other nearby areas. From the point of view of simple flow through a network of pipes, a vascular steal could develop in the following way. Imagine a small artery that branches into two smaller arterioles in parallel. If resistance decreases in one arteriole, the overall resistance of the network decreases and net flow increases. However, if the upstream artery resistance stays the same while the flow through it increases, the pressure drop across the artery will be larger. This means that the pressure where it branches into the arterioles is reduced, and it is this pressure that drives the flow through each of the branches. For the branch that dilated, the resistance has decreased more than the fall in driving pressure, so the flow through that branch increases. However, the branch that did not dilate has the same resistance, but now a lower driving pressure, so the flow is reduced. This steal phenomenon would not happen if the upstream artery also dilated, decreasing its resistance so that flow could increase without reducing the driving pressure for the arterioles. That is, upstream dilatation would serve to further increase CBF in the activated region while preventing a CBF reduction in nearby regions through a vascular steal.

Dilating the arterioles also may increase the pressure in the downstream capillaries and veins, and this may lead to CBV changes as a passive response to the CBF change. Depending on the distensibility of the vessels, this pressure increase could dilate the veins and possibly the capillaries as well. The result is that changes in blood volume are not likely to be evenly distributed along the entire vascular tree, and the dynamics of the change may be different in different vascular compartments. While the arterial CBV changes drive the change in CBF, downstream capillary and venous CBV changes may be a slower, more passive, response to increased pressure.

While the primary control point for CBF is thought to be the arterioles, recent studies suggest that control at the capillary level may also exist. Some capillaries are surrounded by small contractile elements called *pericytes*, which have been shown to constrict and dilate in response to different stimuli in brain slice preparations (Peppiatt *et al.* 2006). Further work is needed to determine whether pericytes represent a significant control point for CBF in the intact brain.

## The relationship between blood volume and blood flow during activation

Based on the arguments above, the relationship between CBF and total CBV is potentially complicated. It is helpful, however, to consider the simple example of laminar flow in a straight cylindrical vessel introduced above. The resistance is proportional to  $1/r^4$ , where  $r$  is the vessel radius, and the volume for a fixed length is proportional to  $r^2$ . Suppose now that the vessel dilates so that the radius doubles to reduce the resistance and increase the flow. For a constant driving pressure, the flow increases by a factor of  $2^4 (= 16)$ , and the volume increases by a factor of 4. More generally, the relationship between the change in blood flow and blood volume for this example is that the volume change is proportional to the square root of the

flow change. If the diameter of every vessel in the vascular tree increased by the same factor, and the resistance to flow follows the  $1/r^4$  law for every vessel, then the changes in CBF and CBV would follow this square root relation.

Motivated by this simplified example, we can treat the relationship between CBV and CBF in a more general way, and characterize it as a power law relation:

$$\frac{V}{V_0} = \left( \frac{F}{F_0} \right)^\alpha \quad (2.3)$$

where  $F_0$  is the resting flow,  $V_0$  is the resting blood volume, and  $\alpha$  is a numerical exponent. For our simple example above,  $\alpha = 0.5$ . In a real vascular tree, we would expect that the volume change necessary to produce a CBF change is much smaller because the cerebrovascular resistance is concentrated in the arterioles. Dilating the arterioles does increase CBV, but because the arterioles are a small fraction of the total blood volume, the net change in CBV is small. For example, suppose that the arterioles account for 20% of the blood volume but 50% of the cerebrovascular resistance at rest. Then, if the diameter of the arterioles increases by 20%, the resistance of the arterioles is reduced by approximately 50%. If there is no change in the rest of the vascular tree, CBF increases by 25% from a change of only 4% in total CBV.

From these arguments, the CBV change *required* to increase CBF may be quite small if it occurs just in the arterioles, but a larger change in CBV could occur through upstream arterial dilatation and downstream passive expansion of capillaries and veins. Note that the magnitude of these additional CBV changes may depend on the extent of the activated area as well. The classic paper of Grubb *et al.* (1974) is still the primary reference for the quantitative relationship between CBF and CBV changes. These investigators altered the inspired partial pressure of  $\text{CO}_2$  ( $p\text{CO}_2$ ) in monkeys and measured global changes in blood flow and blood volume. They then fitted the measured pairs of CBF and CBV values to Eq. (2.3) and found that the data were best described by  $\alpha = 0.38$ . In this experiment, the total CBV was measured, so it was not possible to isolate the contributions of changes in the arterial, capillary, and venous blood volumes. More recent animal studies have used several different approaches, including fluorescent dyes (Vanzetta *et al.* 2004), optical methods (Hillman *et al.* 2007), and MRI methods (Kim *et al.* 2007) to try to distinguish the CBV changes in different vascular compartments. While there is evidence for changes at all levels of the vascular tree, the data indicate that CBV changes are predominantly on the arterial side.

The simple empirical relationship in Eq. (2.3) is widely used, but it is only an approximation for a potentially complex relationship between CBF and CBV changes with activation (Piechnik *et al.* 2008), and this relationship affects the interpretation of the BOLD effect. Although the BOLD effect is primarily driven by changes in oxygenation of the blood, changes in CBV are also thought to play a role. If CBV changes increase the total local deoxyhemoglobin, this will tend to offset the drop in deoxyhemoglobin caused by the decreased OEF. Although there is very little deoxyhemoglobin in the large arteries in a healthy subject with no hypoxia, there is evidence that the arterioles are partly deoxygenated. For this reason, CBV changes at the venous, capillary, and even arteriolar level could modify local deoxyhemoglobin.

In addition, there may be hematocrit changes associated with increased flow that could alter deoxyhemoglobin by a larger factor than the actual vessel volume increase, and thus affect the BOLD signal. Because the red cell diameter is similar to the capillary diameter, a

possible scenario is that some capillaries are perfused at rest with plasma but not red cells, and that with activation a slight dilatation of the capillaries allows the distribution of red cells to become more uniform (Krolo and Hudetz 2000). In this way, the total hemoglobin could potentially increase more than the capillary volume itself. A recent study using optical techniques in a rat model to measure the response to a brief stimulus found that changes in total hemoglobin are dominated by the capillaries, and the dynamics of total hemoglobin in the different compartments are rather different (Hillman *et al.* 2007). For all compartments total hemoglobin increased with the stimulus, but after the stimulus it recovered more quickly in the arterioles and even decreased below the baseline level, while capillary and venous total hemoglobin recovered more slowly. Different dynamics in the vascular compartments may be important for understanding a phenomenon often seen in BOLD imaging called the *post-stimulus undershoot* – a reduction of the BOLD signal below baseline that may persist for tens of seconds (discussed more fully in Ch. 16).

## Neural activity and the control of cerebral blood flow

### The development of ideas about control of cerebral blood flow

Over a century ago, Roy and Sherrington (1890) described the basic principle that, at least in a general sense, motivated much of the early thinking about the local control of CBF:

We conclude then, that the chemical products of cerebral metabolism contained in the lymph which bathes the walls of the arterioles of the brain can cause variations of the calibre of the cerebral vessels: that in this re-action the brain possesses an intrinsic mechanism by which its vascular supply can be varied locally in correspondence with local variations of functional activity.

If we interpret the phrase “chemical products of cerebral metabolism” to mean the products of energy metabolism, then this view presents a relatively simple concept of what happens: neural activity increases the local rate of energy metabolism, and products of energy metabolism, in turn, trigger increased flow to deliver more glucose and O<sub>2</sub>. In this way there is a simple balance between the energy demands of neural activity and the local energy supply, which depends on blood flow.

However, although this simple picture is direct and appealing, recent work is challenging this view. In a recent review, Attwell and Iadecola (2002) concluded:

The view that the haemodynamic response is coupled to signaling processes represents a conceptual shift from the traditional idea that the energy demands of the tissue directly determine the flow increase associated with neural activation. In summary, we suggest that understanding the BOLD response is a signaling problem, not an energy problem.

Specifically, the principle described by Attwell and Iadecola is that the CBF change triggered by increased neural activity is not driven by a depletion of substrates for energy metabolism but rather by the neural activity itself. Instead of a serial chain of events in which neural activity drives energy metabolism which then drives blood flow, the CBF is driven directly by aspects of neural signaling.

A connected and parallel change in thinking relates to the question: What chemical agents mediate a change in CBF? The Roy and Sherrington principle suggests that there are only a few mediators that act on the smooth muscle of the arteries to control blood flow. To some extent, this view carried through to recent times with the discovery of NO as a



candidate for the primary mediator controlling blood flow. However, recent studies have shown that there is not a final common pathway, but rather multiple signaling pathways that alter CBF. Although products of energy metabolism do modify CBF, the observations underlying the second quotation above are that there are numerous pathways directly involving aspects of neural activity. In addition, there has been a profound shift in our understanding regarding the key role played by the astrocytes. Rather than playing a passive role, they appear to be dynamic participants in neuronal signaling, and this has led to the concept of the *neurovascular unit*, a close functional and structural integration of neurons, astrocytes, and blood vessels (Anderson and Nedergaard 2003).

The current view that the CBF changes are not driven by energy metabolism has also raised a basic question: What function is served by the change in CBF? Surprisingly, there is currently no accepted answer to this question. The fact that large CBF changes accompany changes in neural activity is well established, and this appears to serve some function important to the organism, judging from the wide range of mechanisms that have evolved to produce that flow change. Clearly, CBF is necessary to support energy metabolism, but the central question is: If CBF is already high, why does it need to increase so dramatically when neural activity increases? In short, we have a problem in which there are many mechanisms, but these mechanisms do not tell us the underlying functional advantage of having a large CBF change in response to a change in neural activity.

Although the two views expressed in the quotations above appear to be in opposition, they are likely both aspects of a larger synthesis. The key to integrating these ideas may be the time scale involved. A striking aspect of the brain is that the OEF is relatively uniform at rest, despite a several-fold variation across the brain in the local rate of energy metabolism (Gusnard and Raichle 2001). This suggests that during development the CBF to each region adjusts to the basal level of energy metabolism in that region, creating a close coupling of blood flow and energy metabolism such that the same fraction of O<sub>2</sub> (approximately 40%) is removed from the blood across the brain. This long-term basal adjustment of CBF and energy metabolism is in keeping with the Roy and Sherrington principle.

However, for an acute change in neural activity it may be a disadvantage to the organism to wait until substrates for energy metabolism are depleted before increasing blood flow. Instead of such a feedback mechanism, a *feedforward* system in which neural activity drives an increase of CBF in anticipation of a need for increased energy metabolism may be a useful adaptation. In this way, acute CBF changes are closely tied to neuronal signaling, in keeping with the Attwell and Iadecola principle. Note that in this view the function of the CBF change is not directly related to the mechanisms that produce the change. Multiple feedforward mechanisms provide increased CBF, which ultimately supports increased energy metabolism. Along these lines, a possible answer to the question of why CBF increases is that it serves to maintain the O<sub>2</sub> concentration in tissue despite increased energy metabolism. This speculative idea is discussed further in [Box 2.1](#) at the end of this chapter.

Numerous experiments have revealed particular pathways involved in the control of CBF (Girouard and Iadecola 2006; Hamel 2006; Villringer and Dirnagl 1995), but how these pathways function in a coordinated dynamic network is still largely unknown. The following sections describe some of the current ideas.

## Smooth muscle relaxation

As noted above, the relaxation or contraction of smooth muscle surrounding an artery depends on the cytosolic free Ca<sup>2+</sup> concentration in the smooth muscle cell. The Ca<sup>2+</sup> concentration

depends on exchange between the cytosol and  $\text{Ca}^{2+}$  stores within the cell, and on the influx of  $\text{Ca}^{2+}$  from the extracellular space through voltage-sensitive  $\text{Ca}^{2+}$  channels, which tend to open as the cellular membrane depolarizes. For this reason, cytosolic  $\text{Ca}^{2+}$  concentration tends to follow the membrane potential, with a graded depolarization producing a graded increase of  $\text{Ca}^{2+}$  and a corresponding contraction of the smooth muscle. Because of this sensitivity to the membrane potential, a number of agents are thought to exert an effect on the arterial diameter by opening  $\text{K}^+$  channels on the smooth muscle cell. Opening  $\text{K}^+$  channels hyperpolarizes the cell, reducing cytosolic  $\text{Ca}^{2+}$  and relaxing the muscle.

Potassium channels are remarkably diverse, and several distinct types are thought to be involved in smooth muscle action (Faraci and Sobey 1998). *Calcium-activated  $\text{K}^+$  channels* open when cytosolic  $\text{Ca}^{2+}$  rises, and these are thought to be the most abundant on the surface of the smooth muscle cell. These channels may serve as a kind of buffer, or negative feedback system, to limit contraction. If  $\text{Ca}^{2+}$  rises,  $\text{Ca}^{2+}$ -activated  $\text{K}^+$  channels open, hyperpolarizing the cell and reducing cytosolic  $\text{Ca}^{2+}$ . *ATP-sensitive  $\text{K}^+$  channels* are thought to be sensitive to the metabolic state of the cell. Intracellular ATP inhibits these channels, so a reduction of ATP leads to channel opening, membrane depolarization, muscle relaxation, and increased blood flow. Other factors related to metabolism, such as a fall in pH, also open these channels. *Voltage-dependent  $\text{K}^+$  channels* open in response to membrane depolarization. Like the  $\text{Ca}^{2+}$ -activated  $\text{K}^+$  channels, these channels may serve as part of a buffer system to balance contraction, and so may play a role in maintaining muscle tone. *Inward-rectifier  $\text{K}^+$  channels* are characterized by a strong inward rectification, such that they carry inward current more readily than outward current. The action of these channels is rather complex, but the net effect is that these channels open in response to an increase in the  $\text{K}^+$  concentration outside the cell, leading to hyperpolarization (Quayle *et al.* 1997). By this mechanism, extracellular  $\text{K}^+$  itself acts as a vasodilator.

While many agents that affect CBF act through the medium of the smooth muscle membrane potential, by affecting  $\text{K}^+$  channels, other mechanisms interfere with the way cytosolic  $\text{Ca}^{2+}$  couples to the enzymes that control muscle contraction. For example, NO, initiates a chain of events leading to production of cGMP, and the cGMP is thought to affect both  $\text{K}^+$  channels and the sensitivity of the contractile mechanism to  $\text{Ca}^{2+}$ .

## Vasoactive agents

A number of vasoactive agents are now known, including key ions, metabolic factors, and factors related to neural activity. The factors most often considered are discussed below.

### Carbon dioxide and pH

One of the first chemical agents found to have a strong effect on CBF was  $\text{CO}_2$ , which fits in nicely with Roy and Sherrington's original proposal (1890) because  $\text{CO}_2$  is the end product of oxidative glucose metabolism. Raising the arterial  $\text{pCO}_2$  from its normal resting value of approximately 40 mmHg to 60 mmHg by breathing a gas mixture enriched with  $\text{CO}_2$  nearly doubles the global CBF in monkeys (Grubb *et al.* 1974). Carbon dioxide is a gas that readily dissolves in water and also reacts with water to form bicarbonate ions ( $\text{HCO}_3^-$ ) and  $\text{H}^+$ . This has two important consequences. The first is that the high solubility of  $\text{CO}_2$  allows blood to carry it away efficiently from the tissue, with the bulk of it carried as bicarbonate ions. The  $\text{CO}_2$  diffuses down a concentration gradient from tissue to blood, where it is quickly converted to bicarbonate ions through the action of *carbonic anhydrase*, thus maintaining a relatively low concentration of  $\text{CO}_2$  as dissolved gas in blood and a strong gradient of  $\text{CO}_2$  from tissue to

blood. If the conversion of  $\text{CO}_2$  to bicarbonate ions is slowed, as happens when the carbonic anhydrase inhibitor acetazolamide is administered,  $\text{CO}_2$  builds up in the blood and the tissue  $\text{CO}_2$  concentration must increase to maintain the diffusion gradient needed to clear  $\text{CO}_2$ . Thus acetazolamide (Diamox) acts as a vasodilator.

The second important consequence of the conversion of  $\text{CO}_2$  to bicarbonate ions and  $\text{H}^+$  is that the amount of  $\text{CO}_2$  present directly affects the pH. Because  $\text{CO}_2$  passes easily across the blood–brain barrier and cellular membranes (Siesjo 1978), it has a potent effect on the intracellular pH of the brain. In contrast, charged molecules such as bicarbonate ions do not easily cross the barrier. For this reason, increased  $\text{CO}_2$  in the blood has a strong effect on intracellular pH, while a change in the pH of blood at a constant  $\text{CO}_2$  level has little effect on the intracellular pH of brain. For these reasons, clearance of  $\text{CO}_2$  is effectively clearance of acid, and the  $\text{CO}_2$ /bicarbonate system serves as an important pH buffer.

The vasodilating action of  $\text{CO}_2$  is thought to be caused by the pH change at the arterial smooth muscle. Numerous studies have shown that local acidosis causes dilatation and alkalosis constriction of the brain arterioles. Furthermore, animal studies have shown decreases in pH associated with the large flow changes accompanying induced seizures, consistent with the idea that increased  $\text{H}^+$  (decreased pH) produces an increase in CBF (Kuschinsky and Wahl 1979). The brain is evidently very sensitive to pH changes, and the large CBF response may serve to increase the clearance rate of  $\text{CO}_2$  and provide some control over pH.

### Potassium ions

In addition to  $\text{H}^+$ , other positively charged ions (*cations*) exhibit a strong vasodilatory effect. Early studies found that increased  $\text{K}^+$  and decreased  $\text{Ca}^{2+}$  in the fluid space around the cerebral arterioles both produce vessel dilatation. In addition, because neural activity involves an increase of extracellular  $\text{K}^+$  and a decrease of extracellular  $\text{Ca}^{2+}$ , there is a natural mechanism for increasing CBF in response to neural activity, an early idea known as the *cation hypothesis* for CBF regulation (Lassen 1991). Another early idea was that  $\text{K}^+$  taken up by the astrocytes at a high concentration near the synapse could be siphoned to the end-feet near the blood vessels where the concentration is lower, providing a possible mechanism for communicating  $\text{K}^+$  concentration changes to the blood vessels (Paulson and Newman 1987). Although more recent studies argue against this siphoning effect, a more recent model suggests an important role for extracellular  $\text{K}^+$  in the signaling cascade from neurons to blood vessels. This model emphasized the potential role of the astrocytes in integrating neuronal activity signals (Filosa *et al.* 2006) (also see The neurovascular unit, below). In this picture, a  $\text{Ca}^{2+}$  increase in the astrocyte, triggered by neuronal activity, opens  $\text{Ca}^{2+}$ -activated  $\text{K}^+$  channels on the astrocytic end-feet. Potassium flows out of the astrocyte into the restricted space between the end-feet and the blood vessel, increasing extracellular  $\text{K}^+$  and opening inward-rectifier  $\text{K}^+$  channels on the smooth muscle. In this signaling cascade, local neuronal activity is integrated by the cytosolic  $\text{Ca}^{2+}$  increase in the astrocyte and then translated to a  $\text{Ca}^{2+}$  decrease in the smooth muscle cell, with associated vessel dilatation, by intercellular signaling between  $\text{K}^+$  channels.

### Adenosine

Adenosine has intertwined roles in both neural activity and energy metabolism. As discussed in Ch. 1, the primary energy storage molecule is ATP. In addition to its role in energy metabolism, ATP also serves as a neurotransmitter/neuromodulator (Haydon and Carmignoto 2006). In the

extracellular space, ATP is sequentially broken down to produce adenosine, which then has a potent effect by reducing neuronal excitability. Interestingly, ATP also is released by astrocytes (Haydon and Carmignoto 2006). For example, in the retina, ATP released from glial cells is broken down to adenosine, which then opens  $K^+$  channels that hyperpolarize ganglion neurons (Newman 2003). Although details of the mechanism of ATP release from astrocytes are still unclear, this suggests a potentially important mechanism of astrocyte-to-astrocyte and astrocyte-to-neuron signaling. In cell cultures,  $Ca^{2+}$  waves propagate between astrocytes, even when they do not make direct contact with one another, through release of ATP, which then diffuses from the point of release. At the level of the neuronal synapse, adenosine binds to receptors on the pre-synaptic side of the synapse and inhibits transmitter release, potentially providing a basis for regulation of synaptic signaling. Adenosine accumulation is also involved in lateral inhibition, in which activity at one synapse inhibits the activity of nearby synapses.

Adenosine has a strong vasodilatory effect (Dirnagl *et al.* 1994; Villringer and Dirnagl 1995; Winn *et al.* 1991). Caffeine competes for adenosine receptors (Fredholm *et al.* 1999), and a number of studies have shown that caffeine reduces CBF (Perthen *et al.* 2008), consistent with the idea of a reduction of the vasodilatory effect of adenosine.

### Nitric oxide

Since the 1990s, the importance of NO in regulating CBF has been recognized (Iadecola 1993; Watkins 1995). Nitric oxide is a powerful vasodilator. As a signaling molecule, it has the unique property of being a simple gas that easily diffuses across cell membranes; consequently, it can engage directly in intracellular reactions without having to bind to extracellular receptors. It is a reactive molecule, so it is short lived in tissue. Nevertheless, the range of diffusion of NO is thought to be on the order of 200  $\mu\text{m}$ , so NO produced at one site can potentially signal to many nearby cells. As noted above, the action of NO in a target cell is to produce an intracellular second messenger, cGMP, which then triggers subsequent cellular pathways. Nitric oxide is produced by activation of *nitric oxide synthase* (NOS), and there are three forms of the enzyme: endothelial, neuronal and induced. Nitric oxide is produced locally from neurons and astrocytes following glutamate receptor activity, and it has been implicated in modulating the vasodilatory effects of virtually all the potential mediators of CBF control discussed above:  $\text{CO}_2$ ,  $\text{H}^+$ ,  $\text{K}^+$ , and adenosine. Thus, the full picture of the control of CBF may involve complicated interrelationships between NO and other mediators (Lindauer *et al.* 1999).

Current thinking is that NO plays an important role in maintaining vascular tone, with a continuous production of NO in the basal state. The role of NO in triggering acute CBF changes is more complicated, and somewhat less clear. In part, this is because an experimental finding of a reduced CBF response to activation after NOS is blocked could be because basal tone was affected, rather than the CBF response itself. For example, studies in cortex found that the CBF response to activation was reduced when NOS was blocked, but restored when NO was added non-specifically to the tissue, suggesting that the primary effect was on basal tone (Lindauer *et al.* 1999). In contrast, however, a similar experiment in the cerebellum found that blocking NOS reduced the CBF response and that it was not restored by adding NO, suggesting a more fundamental involvement of NO in signaling the CBF change (Akgoren *et al.* 1994).

### Arachidonic acid derivatives

A number of studies have shown that CBF is modulated through an extended metabolic pathway related to arachidonic acid and its derivatives (Girouard and Iadecola 2006; Straub

and Nelson 2007). This is a widespread signaling pathway in human biology, particularly involved in inflammation, fever, and pain associated with injury or disease. A family of locally acting hormones called *eicosanoids* are derived from arachidonic acid through the interaction with specific enzymes. The family name refers to the 20-carbon composition of each (the same origin as *icosahedron*). An important class of eicosanoids, *prostaglandins*, are formed from arachidonic acid by the enzyme cyclooxygenase (COX). Two forms of this enzyme, COX-1 and COX-2, are structurally similar but play different roles in human biology. For example, COX-1 is involved in protecting the stomach lining from acid, while COX-2 is involved in inflammation and pain. Non-steroidal anti-inflammatory drugs (NSAIDs), such as aspirin and ibuprofen, inhibit COX enzymes generally, and so a focus of drug research is on the development of specific COX-2 inhibitors that could address pain without damaging the stomach. In the brain, there is evidence for the involvement of both COX-1 and COX-2 in CBF control. A second pathway involving arachidonic acid products, called the P450 pathway, also is implicated in modulating CBF through the production of epoxyeicosatrienoic acids.

The pathways described above are associated with vasodilation, but the involvement of arachidonic acid and its derivatives appears to be more complicated. Another compound derived from arachidonic acid, 20-hydroxyeicosatetraenoic acid, has a constricting effect on the blood vessel (Koehler *et al.* 2006). For this reason, activation of the arachidonic acid pathway can produce both vasodilation and vasoconstriction, and the potential significance of this complicated behavior is still unclear.

### Neural pathways affecting cerebral blood flow

In addition to the specific agents discussed above, neural pathways also affect CBF (Hamel 2006). The larger arteries receive neural input as part of system-wide control, described as the *extrinsic* sources of innervation. The *sympathetic pathway*, involving release of norepinephrine and neuropeptide Y, produces vasoconstriction. This may serve to protect the brain in the face of a system-wide increase in blood pressure associated with a fight or flight stimulus. The *parasympathetic pathway*, operating through release of vasoactive intestinal peptide, acetylcholine, NO, and other transmitters, produces vasodilation. This system does not appear to have a prominent role in normal physiological regulation but has been implicated in disease processes. Finally, the *trigeminovascular pathway* involves sensory nerves containing calcitonin gene-related peptide and other transmitters and produces vasodilation. This system appears to be involved in restoring vascular tone after vasoconstrictive stimuli, but in addition this system is the focus for studies of migraine headache. This pathway is implicated in an intriguing phenomenon in brain physiology called *cortical spreading depression*, in which a wave of reduced electrical activity and CBF spreads slowly across the cortex at a rate of a few millimeters per minute. This phenomenon is thought to underlie the spreading visual aura that sometimes precedes migraine attacks, and waves of cortical spreading depression also appear to be involved in stroke. Current anti-migraine medications, called triptans, target the trigeminovascular system by blocking release of calcitonin gene-related peptide.

In contrast to the extrinsic innervation of the larger arteries, the smaller arteries receive more local *intrinsic* innervation (Hamel 2006). Cortical neurons receive input from several deeper structures. Projections from the *raphe nuclei* in the brainstem release serotonin. Projections from the *locus coeruleus* in the brainstem, a region associated with responses to stress, release norepinephrine. Projections from the *nucleus basalis* in the basal forebrain, a region that undergoes degeneration in Parkinson's and Alzheimer's diseases, release

acetylcholine. The details of the pathways involved are still unclear but they may also involve the astrocytes and other receptor pathways.

In addition, local *interneurons*, which provide important inhibitory connections in neural networks, have been shown to produce either vasoconstriction or vasodilation. The distinction depends on whether the interneurons are associated with vasoactive intestinal peptide or NOS, eliciting dilation, or somatostatin, eliciting contraction (Cauli *et al.* 2004).

## The neurovascular unit

Research over the last decade has demonstrated a diverse and important role for the glial cells in brain function. These cells account for about half of the cells in the brain and were originally thought to be primarily a structural scaffold. One subtype of glial cell, the astrocyte, has proven to play an important role in neuronal signaling and in energy metabolism (Haydon and Carmignoto 2006; Magistretti 2006). Although relatively quiet in terms of electrophysiology compared with neurons, the astrocytes nevertheless have a sophisticated signaling system based on changes in intracellular  $\text{Ca}^{2+}$ . Astrocytes contain receptors for numerous neurotransmitters, including glutamate, GABA, acetylcholine and adenosine, and activation of these receptors induces changes in cytosolic  $\text{Ca}^{2+}$ . With numerous processes contacting neuronal synapses, the astrocytes are well positioned to play a key role in recycling neurotransmitter, as described in Ch. 1, and also to monitor and integrate local neuronal activity. Additional processes, called end-feet, make contact with blood vessels, so astrocytes create a bridge between neuronal activity and blood flow. This close anatomical arrangement has long suggested an important functional arrangement, and in recent years the mechanisms by which changes in neural activity translate into changes in CBF have become clearer. Because of the close interactions between neurons, astrocytes, and blood vessels, this combination is often referred to as the neurovascular unit (Andresen *et al.* 2006).

The basic picture of the coordinated action of the neurovascular unit is as follows. Neurotransmitter, such as glutamate, released at a synapse binds to the astrocytic process as well as the post-synaptic neuron, initiating a rise in cytosolic  $\text{Ca}^{2+}$  in the astrocyte. This  $\text{Ca}^{2+}$  signal propagates to the end-feet and triggers two processes in parallel: the production of arachidonic acid and the release of  $\text{K}^+$ . Products of the arachidonic acid pathway, probably prostaglandins and epoxyeicosatrienoic acids, are released and open  $\text{K}^+$  channels on the smooth muscle cell, producing vessel dilation. In parallel, the  $\text{Ca}^{2+}$  rise in the astrocyte triggers  $\text{K}^+$  release from the end-feet, opening inward-rectifier  $\text{K}^+$  channels on the smooth muscle. Both of these mechanisms produce vasodilation (Fig. 2.3). However, the full picture may be more complicated, as indicated above. The release of arachidonic acid at the end-feet may lead to production of 20-hydroxyeicosatetraenoic acid in the smooth muscle and vasoconstriction. The effects of astrocyte signaling may thus be complex, involving both relaxation and constriction (Filosa and Blanco 2007).

In summary, there is ample evidence for a direct involvement of astrocytic signaling, through cytosolic  $\text{Ca}^{2+}$  changes and stimulation of arachidonic acid metabolic pathways, in the matching of CBF with neuronal activity. However, the response is complicated, with different studies showing dilatation (Zonta *et al.* 2003) or contraction (Mulligan and MacVicar 2004) when the astrocytes are stimulated. Part of this complexity may be related to the basal state of the vessels in the experiments in brain slice preparations (Blanco *et al.* 2008). When the vessels were pre-constricted, they tended to dilate, and when they were pre-expanded they tended to contract in response to the stimulus. The basal state of the system is an important factor for understanding the specific results of stimulating particular pathways.

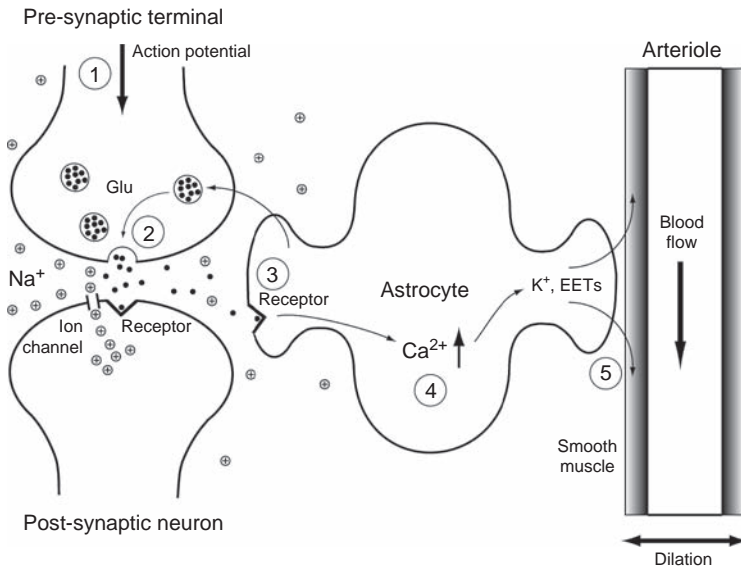


**Fig. 2.3.** Astrocyte signaling to the blood vessels. Arrival of an action potential at a glutamatergic synapse (1) triggers glutamate (Glu) release (2), which binds to receptors on the astrocyte as well as the post-synaptic neuron (3), initiating an increase of intracellular  $Ca^{2+}$  (4), triggering release of  $K^+$  and arachadonic acid products (EET, epoxyeicosatrienoic acids) from the astrocyte end-feet (5) to relax the smooth muscle and dilate the arteriole.

## Measuring cerebral blood flow

### The microsphere technique

The most direct way to measure CBF is to inject labeled microspheres into the arterial system. If these microspheres are carefully designed to be small enough to pass through the arterioles but large enough that they will not fit through the capillaries, then they will be trapped in the capillary bed. After injection in a large artery, the bolus of microspheres will be delivered to each of the tissue elements served by that artery in proportion to their respective local CBF. The number of microspheres lodged in an element of tissue is then a direct measure of the local CBF. Typically, this method uses radioactive microspheres, sectioning of the tissue, and then counting the radioactivity in each sample. For measurements at multiple time points, microspheres labeled with different radioactive nuclei can be used and then distinguished later based on differences in the energies of the radioactive decay photons (Yang and Krasny 1995). More recently, colored microspheres have been used with photometric measurement of the concentrations of different colored spheres in tissue samples. Although widely regarded as the gold standard for perfusion measurements, microspheres are not appropriate for human subjects. However, a number of the techniques we will discuss are closely related, to the extent that they use a tracer that stays in the tissue during the experiment, like a microsphere, and can be measured externally and non-invasively.

### The nitrous oxide technique

A milestone in the development of techniques for measuring CBF in humans was the nitrous oxide ( $N_2O$ ) technique (Kety and Schmidt 1948). This was the first technique capable of

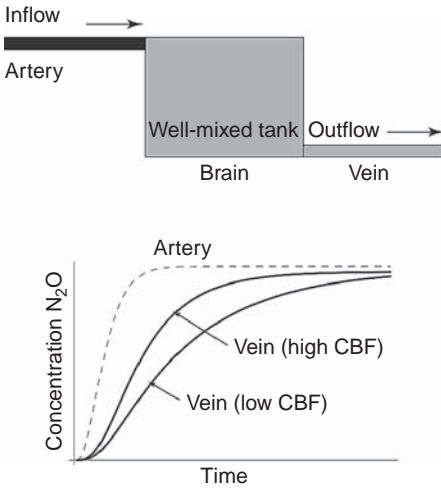


**Fig. 2.4.** The nitrous oxide ( $N_2O$ ) technique for measuring global cerebral blood flow. A subject breathes  $N_2O$  continuously while the blood concentration of the agent is sampled in the carotid artery and jugular vein. Over time, the  $N_2O$  will distribute throughout the brain, like a well-mixed tank being filled with fluid containing a dye, and the venous concentration will approach the arterial concentration. The time constant for reaching this equilibrium is inversely proportional to the global cerebral blood flow (CBF).

producing quantitative measurements of global CBF in humans, and it was quickly applied to investigate perfusion changes in a number of conditions. In this technique, the subject breathes  $N_2O$  continuously for several minutes. During this time, the arterial and venous concentrations of  $N_2O$  are sampled frequently (e.g., from the carotid artery and jugular vein) (Fig. 2.4). The  $N_2O$  diffuses freely from blood into tissue, and if the arterial concentration remains elevated for a sufficiently long time, the arterial, venous, and tissue concentrations of  $N_2O$  will come into equilibrium. In this equilibrium state, the concentrations in tissue, arterial blood, and venous blood are equal, and so this equilibrium condition carries no information about the flow. But the time required to reach this equilibrium is strongly sensitive to flow.

As an analogy, consider a large, well-mixed tank of water (the tissue) fed by an inlet pipe (arterial flow) and drained by an outlet pipe (venous flow), as illustrated in Fig. 2.4. If dye is now introduced into the inlet side at a constant concentration, the concentration of dye in the tank will gradually increase until it comes into equilibrium with the inlet concentration. If the tank is well mixed at all times, the outlet concentration will approach the inlet concentration in an exponential fashion. The larger the rate of inflow, the more quickly the concentration in the tank will reach equilibrium. By observing only the inlet and outlet concentrations, the time constant  $\tau$  for the outlet concentration to equilibrate with the inlet concentration can be measured. This time constant is  $\tau = V/F$ , where  $F$  is the flow rate into the tank (mL/min) and  $V$  is the volume of the tank (mL). To generalize this idea to brain studies with an exogenous agent, the volume  $V$  is more precisely defined as the *volume of distribution* of the agent, the volume to which the agent has access and will eventually fill over time. Nitrous oxide freely diffuses throughout the brain, and so the volume of distribution is approximately the volume of the brain itself.

### Diffusible versus intravascular tracers

The concept of volume of distribution is important for understanding the kinetics of a tracer. Nitrous oxide freely diffuses out of the capillary bed and fills the entire tissue space, so its volume of distribution is essentially the whole brain volume. In contrast, an agent that



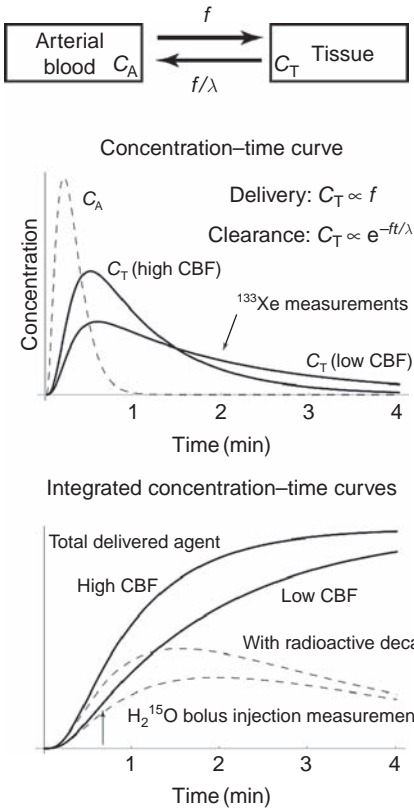


**Fig. 2.5.** Measurement of cerebral blood flow (CBF) with diffusible radioactive tracers. The tissue concentration  $C_T(t)$  of the agent is modeled in terms of the arterial concentration  $C_A(t)$ , the driving function of the system, and the local flow  $f$  and volume of distribution  $\lambda$  using the compartmental model shown at the top. Local flow affects both delivery and clearance of the agent. With the  $^{133}\text{Xe}$  method, flow is estimated from the time constant for clearance, and with the PET  $\text{H}_2^{15}\text{O}$  bolus injection method flow is estimated from the integrated activity delivered during the first 40 s.

remains in the blood has a volume of distribution that is much smaller, only approximately 4% of the total brain volume. A useful definition of volume of distribution derives from a simple experiment. Imagine that an agent is administered in the blood, and that we can measure the concentration in arterial blood and the concentration in a small tissue element (say, with PET). The volume of distribution  $\lambda$  is defined as the ratio of the tissue to blood concentrations after they have come into equilibrium. For this reason, it is sometimes described as the *partition coefficient* for the agent.

Brain studies use a number of different tracers, but most of them fall into one of two basic classes: *diffusible* tracers, with  $\lambda \sim 1$ ; or *intravascular* tracers, with  $\lambda \sim \text{CBV}$ . The significance of  $\lambda$  is that it strongly affects the kinetics of an agent, through the central volume principle introduced above (Fig. 2.5). The basic time constant defining the kinetics of the tracer as it passes through a tissue element is simply  $\lambda/\text{CBF}$ . In other words, the volume of distribution of an intravascular agent is quickly filled because the blood volume is only a small fraction of the total tissue volume.

This difference in the equilibration times directly affects what can be measured with diffusible and intravascular tracers. Imagine that an agent is injected into the blood, and the tissue concentration of the agent is measured over time. After the agent has equilibrated within its volume of distribution, the tissue concentration of the agent is independent of flow but provides a robust measure of the volume of distribution. Just as with  $\text{N}_2\text{O}$ , flow affects the

kinetics of the agent only during its approach to this equilibrium. So an intravascular agent, on the one hand, provides a robust measurement of CBV because that is its volume of distribution, but a poor measurement of flow because it equilibrates so quickly. On the other hand, a diffusible tracer provides a robust measurement of flow because the flow-dependent part of the tissue concentration curve is much longer. With these basic ideas in mind, we can consider the development of techniques to measure local CBF with diffusible tracers.

## The radioactive xenon technique

The N<sub>2</sub>O technique made possible a measurement of global blood flow from measurements of the arterial and venous concentrations of the agent over time. However, this technique provides no way to determine local blood flow to a particular region of the brain. In principle, the flow to a smaller subregion of the brain could be determined by collecting the venous samples from a smaller vein that only drains that subregion, but this is not practical in human studies. An alternative approach measures the local tissue concentration of the agent itself. From the preceding arguments, each local element of tissue should come into equilibrium with the arterial concentration with a local time constant that depends directly on the local blood flow and volume of distribution of the agent. This type of measurement became possible with the introduction of radioactive tracers and external detectors for measuring regional concentrations of the agents. The use of diffusible radioactive tracers to measure CBF is described in more detail in [Ch. 12](#).

In the 1960s, regional measurements of CBF in humans became possible with the introduction of radioactive inert gases (Ingvar and Lassen 1963), most notably the xenon-133 technique (Obrist *et al.* 1967). Xenon is an inert gas that freely diffuses throughout the brain. The radioactive isotope <sup>133</sup>Xe decays with the emission of a photon, which can be captured by an external detector near the surface of the head. The agent typically is administered by inhalation, entering the bloodstream in the lungs and traveling throughout the body in the arterial flow. After allowing sufficient time for the xenon to equilibrate in the brain, the supply of xenon is cut off, and the clearance of the agent from the brain is monitored. An array of detectors is arranged around the head, with each detector most sensitive to the nearest regions of the brain. Each detector then measures a regional level of radioactivity, which decreases over time. Clearance is accomplished by CBF, so the larger the CBF the faster the radioactive xenon clears from the tissue. The time constant for clearance is  $\lambda/f$ , where  $\lambda$ , the volume of distribution of xenon, is approximately 1 because xenon is a diffusible tracer ([Fig. 2.5](#)).

## Techniques using PET

Radioactive xenon studies only allow measurement of regional flows because of the limited spatial selectivity of the detectors. But with PET, an image of the concentration of radioactivity in a brain section can be measured with a spatial resolution of approximately 1 cm<sup>3</sup>. With dynamic measurements, the concentration is measured as a function of time, referred to as a tissue *time–activity curve*. (Note that *activity* here refers to radioactivity, the number of measured radioactive decays per second, and not to neural activity in the brain.) The ability to measure the distribution of a radioactive tracer tomographically with spatial resolution on the order of 1 cm<sup>3</sup> made possible a much more detailed study of local CBF changes.

For blood flow studies with PET, the most common agent used is water labeled with <sup>15</sup>O, which has a radioactive half-life of approximately 2 min (Frackowiak *et al.* 1980; Raichle 1983). Water is a diffusible tracer with  $\lambda$  near 1. There are two standard methods for measuring CBF with

$\text{H}_2^{15}\text{O}$ . In the first, the labeled water is injected and image data are acquired for the first 40 s after injection. Such a measurement is thus an integration over 40 s of the tissue concentration–time curve during the early phase as the tracer is delivered to the brain. The second method takes advantage of the short half-life of  $^{15}\text{O}$ . Because the label is decaying away, there is another way for the agent to “clear” from the voxel in addition to venous flow. The water itself does not clear any faster, but the radioactive tracer marking the water disappears by radioactive decay, so for practical purposes the agent can be cleared from the tissue by two mechanisms. If the  $^{15}\text{O}$  is delivered continuously from the arterial flow, a steady state will be reached in which delivery by flow and clearance by flow plus radioactive decay are balanced. At this steady state, the tissue concentration provides a measurement of CBF, with a higher concentration when the flow is higher. Continuous delivery of the tracer is accomplished by having the subject breath  $\text{C}^{15}\text{O}_2$ . When the labeled  $\text{CO}_2$  enters the blood through the lungs, the  $^{15}\text{O}$  quickly exchanges with the  $\text{O}_2$  of water to produce  $\text{H}_2^{15}\text{O}$ .

## Techniques using MRI

Two MRI methods are based on similar principles to those developed for the radioactive tracer methods described above. The first is *bolus tracking*, or dynamic contrast-enhanced imaging, in which an injected agent is carried by blood flow to the brain where it alters the MR signal as it passes through the capillary bed (Calamante *et al.* 2002). With rapid dynamic imaging, a time–activity curve equivalent to those measured with radioactive tracers can be derived as the agent passes through the tissue. Because the agent remains in the blood in the brain, it acts as an intravascular tracer and so provides a good measurement of CBV. This technique is described in more detail in Ch. 12.

A second technique, called *arterial spin labeling*, measures CBF and is conceptually similar to PET measurements using  $\text{H}_2^{15}\text{O}$  (Buxton *et al.* 1998; Detre *et al.* 1992). In this case, the water of arterial blood is labeled magnetically in the MRI scanner, and CBF is measured from how the labeled blood is distributed within the brain. Unlike the PET methods or the MRI method based on bolus tracking, arterial spin labeling methods do not require any injection of agents and are completely non-invasive. These methods are described in more detail in Ch. 13.

## Brain activation

### Blood flow and glucose metabolism increase with functional activity

In the second quote from William James (1890) that opened Part IA, he speculated that “Blood very likely may rush to each region of the cortex according as it is most active.” With the development of tomographic techniques for measuring local CBF and the cerebral metabolic rate for glucose (CMRGlc), we now know that he was right. This rush of blood to activated areas is the physiological basis for most of the modern techniques of functional neuroimaging. Comparisons of CBF and CMRGlc changes have consistently found good agreement in the locations of the activation (Fox *et al.* 1988; Ginsberg *et al.* 1987, 1988; Yarowsky and Ingvar 1981). In addition, the flow change is a graded response in the sense that the magnitude of the flow change varies with the strength of the stimulus. For example, the flow response in the visual cortex to a flashing checkerboard pattern increases as the flicker rate is increased up to approximately 8 Hz and then slowly declines (Fox and Raichle 1991), and in the auditory cortex the flow response increases with stimulus rate (Binder *et al.* 1994). Experimental results such as these support the idea that CBF change reflects not just

the location of the activated area but also the degree of activation. Direct comparisons of CBF changes and electrophysiology involve complex experiments, but a number of studies have now shown a close correlation with CBF and BOLD responses, in both activation and deactivation (Devor *et al.* 2007; Logothetis *et al.* 2001; Shmuel *et al.* 2006).

There is ample evidence that both flow and glucose metabolism increase substantially in activated areas of the brain. However, the observed correlation between changes in CBF and CMRGlC does not necessarily imply a causal link between the two. Even though it is tempting to suppose that the flow increases to support the change in glucose metabolism, this is likely not the case. Several lines of evidence suggest that an increase in CBF is not required to increase CMRGlC. The first is the observation that at rest glucose is delivered in excess of what is required (Gjedde 1987). That is, about half of the glucose that crosses the capillary wall is not metabolized and is eventually cleared from the tissue in the venous flow. This means that from the point of view of glucose delivery, CMRGlC could, in principle, increase by about a factor of two with no increase in CBF.

The second piece of evidence suggesting that glucose delivery is relatively independent of flow comes from a study in which the change in CBF with activation was measured at several levels of hypoglycemia (Powers *et al.* 1996). Despite the changes in glucose delivery to the capillary bed, there was no change in the CBF response. These investigators concluded that the CBF change is not regulated to match glucose supply with glucose demand. Finally, a study in an animal model showed that blocking the production of NO in the neurons suppressed the CBF change during activation but did not affect the change in CMRGlC (Cholet *et al.* 1997), demonstrating that CMRGlC can increase without a change in CBF. These arguments taken together suggest that the CBF change is not required to support the CMRGlC change, even though the two physiological changes are closely correlated. Instead of CBF being a prerequisite for increasing CMRGlC, the close correlation of the two responses may be because both of them are being driven in parallel by synaptic activity, as discussed at the end of Ch. 1.

## Oxygen metabolism increases less than blood flow

The key finding that the CMRO<sub>2</sub> increase with activation is smaller than the CMRGlC and CBF increases was introduced in Ch. 1. There the emphasis was placed on the mismatch of CMRGlC and CMRO<sub>2</sub>, and the associated decrease of the oxygen/glucose index with activation. Here we can characterize the imbalance of CBF and CMRO<sub>2</sub> in terms of a different dimensionless number, the OEF. As noted above, at rest OEF is approximately 40% and is remarkably uniform across the brain, despite a several-fold variation of CBF and CMRO<sub>2</sub> (Gusnard and Raichle 2001; Marchal *et al.* 1992). The seminal work of Fox and Raichle (1986), demonstrating a larger change in CBF than CMRO<sub>2</sub>, means that OEF decreases with activation. That is, despite the increase of CMRO<sub>2</sub>, because the CBF increases much more, less O<sub>2</sub> is removed from each milliliter of blood, so the OEF decreases. Or, referring back to Eq. (2.1), if CMRO<sub>2</sub> and CBF both increase, but the CBF increase is larger, the OEF must decrease.

The reduction of the OEF with activation is the physiological foundation of fMRI, because this changes the O<sub>2</sub> saturation of hemoglobin, which then produces a slight change in the MR signal – the BOLD effect. In recent years fMRI has provided ample confirmation that the imbalance of flow and O<sub>2</sub> metabolism changes is not an artifact of the PET techniques but is instead a widespread physiological phenomenon (Prichard and Rosen 1994). Many studies using PET and MRI techniques have confirmed that the CBF

change is larger than the  $\text{CMRO}_2$  change by a factor of two to three (although some larger ratios have been reported as well) (Fox and Raichle 1986; Fox *et al.* 1988; Marrett and Gjedde 1997; Roland *et al.* 1987, 1989; Seitz and Roland 1992; Vafaei *et al.* 1998, 1999).

Despite the importance of this phenomenon for understanding the signals measured with fMRI, we still do not understand the functional significance of the decrease of the OEF with activation. This imbalance initially was described as an uncoupling of flow and  $\text{O}_2$  metabolism during activation, in the sense that the large change in CBF seemed to serve some need other than increased  $\text{O}_2$  metabolism, leaving a fundamental question: Why does flow increase so much with activation? From the arguments made above, the large change in CBF is not required to support the  $\text{CMRGlc}$  change, and the magnitude of the change is out of proportion to the smaller change in  $\text{CMRO}_2$ . Note that this question of the function served is a separate question from that of the mechanisms involved. A number of potential mechanisms for triggering a CBF change were discussed earlier in the chapter, but these mechanisms do not address why the CBF change is so large. A speculative explanation for why the large CBF change is useful is that it could serve to maintain an approximately constant  $\text{O}_2$  level in the tissue despite an increase in  $\text{CMRO}_2$ . This idea is further developed in [Box 2.1](#) at the end of this chapter.

## Summary of physiological changes during brain activation

The physiological picture of what happens during brain activation is still incomplete. The evidence to date suggests the following scenario: CBF increases substantially; CBV increases moderately;  $\text{CMRO}_2$  increases moderately; the OEF falls substantially; and the local blood velocity in the arterioles, capillaries, and venules increases with an accompanying fall in the blood transit time. With these changes in mind, we can begin to explore the ways in which MRI can be made sensitive to these effects so that we can map patterns of brain activation. [Chapters 3–5](#) give an overview of how MRI works and how different fMRI techniques are sensitive to these physiological changes during activation.

### **Box 2.1. Does the large change in CBF with activation serve to preserve the tissue $\text{O}_2$ level?**

The physiological phenomenon at the heart of the BOLD effect is that the fractional increase in CBF with activation is about twice as large as the fractional increase in  $\text{CMRO}_2$ . This leads to a decrease in OEF, and a resulting increase of the MR signal. Why this seeming imbalance of CBF and  $\text{CMRO}_2$  changes occurs is not known, but a possible explanation for the function served by decreasing OEF with activation is that this preserves the  $\text{O}_2$  concentration in the tissue. The following is a development of this idea.

### **Oxygen transport to tissue**

Local cellular metabolism requires constant delivery of  $\text{O}_2$  and constant clearance of  $\text{CO}_2$ , since one  $\text{CO}_2$  is produced for each  $\text{O}_2$  metabolized. To understand the transport of these gases, it is important to look at their concentrations as dissolved gases in blood and tissue. A common way to express the concentration of a dissolved gas in a liquid is in terms of the equivalent *partial pressure*: the pressure of gas in a space above the liquid that would be in equilibrium with the concentration of dissolved gas in the liquid. The partial pressure is usually expressed in torr (very similar to millimeters of mercury [mmHg]) or kilopascals (kPa), with  $1 \text{ kPa} = 7.5 \text{ torr}$ . For example,

standard atmospheric pressure at sea level is 760 torr = 101.3 kPa, and this total pressure is the sum of the partial pressures exerted by each of the gases that make up the air. The partial pressure of O<sub>2</sub> (pO<sub>2</sub>) is about 150 torr, and pCO<sub>2</sub> is about 5 torr. In the alveoli of the lungs, however, the pCO<sub>2</sub> is higher and this reduces the pO<sub>2</sub> to about 100 torr. Blood equilibrates with the O<sub>2</sub> in the gas phase in the alveoli, and so the pO<sub>2</sub> of arterial blood delivered to the brain is also about 100 torr. In the venous blood leaving the resting brain, the pO<sub>2</sub> is about 35 torr. However, while partial pressures are a useful way to characterize equilibration between a gas and the dissolved component, another factor is needed to describe the true concentration of the gas in a liquid: the *solubility*. The concentration in the liquid of a dissolved gas is the partial pressure times the solubility.

The essential problem in transporting O<sub>2</sub> through the body is that it has a low solubility in water (Fig. 2.6). Carbon dioxide, in contrast, readily dissolves by chemically combining with water to form bicarbonate ions. If O<sub>2</sub> and CO<sub>2</sub> as gases are maintained at the same partial pressure above a surface of water, the concentration of dissolved CO<sub>2</sub> in the water is about 30 times higher than that of O<sub>2</sub>. The clearance of CO<sub>2</sub> by blood flow is then relatively simple owing to this high CO<sub>2</sub>-carrying

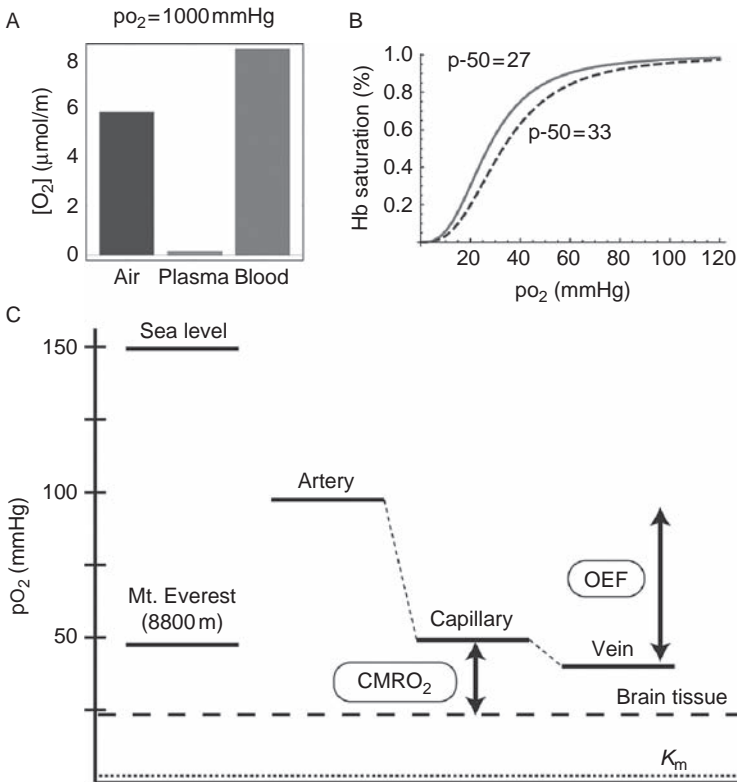


**Fig. 2.6.** Oxygen gradients in the brain. (A) The O<sub>2</sub> concentration in water in equilibrium with a gas phase at a particular partial pressure (pO<sub>2</sub>) is very low because of the low solubility of O<sub>2</sub>. Binding of O<sub>2</sub> to hemoglobin (Hb) greatly increases the effective blood O<sub>2</sub> concentration. (B) The O<sub>2</sub> saturation fraction of Hb depends on pO<sub>2</sub> of the plasma and a parameter p-50, the pO<sub>2</sub> that produces a saturation of 50%. (C) Typical pO<sub>2</sub> values for the atmosphere and blood compartments are illustrated. The O<sub>2</sub> extraction fraction (OEF) is proportional to the difference between arterial and venous values, while the O<sub>2</sub> metabolic rate (CMRO<sub>2</sub>) is proportional to the difference between the mean capillary and tissue values. The observed fall in OEF with activation may serve to raise capillary pO<sub>2</sub> in order to support a larger O<sub>2</sub> gradient between capillary and tissue while preventing the tissue pO<sub>2</sub> from falling.

capacity, and the delivery of  $O_2$  is the difficult task. Nature's solution has been to develop carrier molecules that readily bind  $O_2$  in the lungs and then release it in the capillary. In mammals, this molecule is the hemoglobin contained in the red blood cells, and it increases the  $O_2$ -carrying capacity of blood by a factor of 30–50.

The hemoglobin  $O_2$ -binding curve – the fractional saturation of hemoglobin as a function of the plasma partial pressure of  $O_2$  – has a sigmoidal shape, as illustrated in Fig. 2.6. As long as  $pO_2$  is above approximately 80 mmHg, the arterial hemoglobin is nearly fully loaded with  $O_2$ . The point at which the hemoglobin is half-saturated is called the P-50 of the hemoglobin, approximately 27 torr for human blood. A number of factors, such as pH or temperature, change the P-50 and shift the dissociation curve to the left or right. For example, in the capillary, the increased  $CO_2$  diffusing in from the tissue lowers the blood pH, and the combined effects of the  $CO_2$  and the pH change shifts the  $O_2$ -binding curve to the right. In this way, a given level of saturation is now in equilibrium with a higher  $pO_2$  in the capillary, creating a higher driving head for diffusion of  $O_2$  into the tissue. In the lungs, the release of  $CO_2$  shifts the curve back to the left, so that a given  $pO_2$  is now in equilibrium with a higher  $O_2$  saturation, thus increasing  $O_2$  loading of the hemoglobin as it comes into equilibrium with alveolar  $pO_2$ .

Figure 2.6 also shows typical  $pO_2$  values for sea level, the top of Mt. Everest, and blood compartment and tissue values for a healthy human at sea level to illustrate the gradients involved in  $O_2$  transport. Although the dissolved gas component is relatively unimportant in terms of carriage of  $O_2$  to the capillary bed, it is the key component for the actual transfer of  $O_2$  from blood to tissue. When the blood reaches the capillaries (and to some degree the arterioles as well), the dissolved  $O_2$  diffuses out of the vessel into the tissue. Because the  $O_2$  bound to hemoglobin and the dissolved  $O_2$  are in rapid equilibrium,  $O_2$  is released from the hemoglobin and partly replenishes the dissolved gas in the plasma. As more  $O_2$  leaves the blood, the plasma  $pO_2$  largely follows the  $O_2$  saturation curve. However, as noted above,  $CO_2$  increasing in the blood also leads to a rightward shift of this curve, which somewhat complicates modeling of the gas exchange.

## Cerebral blood flow and tissue $O_2$ content

The significance of the capillary plasma  $pO_2$  is that this provides the driving pressure for diffusion of  $O_2$  into the tissue, where it is consumed by the mitochondria. That is, we can think of  $CMRO_2$  as a net diffusion of  $O_2$  from a high concentration in the capillary to a lower concentration in the mitochondria. For this diffusive transport, the net flux of  $O_2$  is proportional to the  $O_2$  gradient. To simplify this process, consider a system in which  $O_2$  diffuses from an average capillary plasma to an average tissue  $pO_2$  as illustrated in Fig. 2.6. The gradient is then the difference of these two values divided by a characteristic distance between capillaries and mitochondria. We can think of this distance as being controlled by capillary density: as capillary density increases, the diffusion distance decreases. The  $CMRO_2$  is proportional to this gradient, so for  $CMRO_2$  to increase this gradient must increase.

We can imagine three distinct ways in which this could happen: increased capillary density, increased capillary  $pO_2$ , or decreased tissue  $pO_2$ . Although older studies indicated some degree of capillary recruitment with activation, which would increase capillary density, current studies indicate that capillary recruitment does not occur in the brain to any significant degree with activation. A possibility noted in the main text is that hematocrit in the smallest capillaries could increase with activation, and this could effectively shorten the diffusion distance between the red cells and the mitochondria, but more work is needed to determine if this is a significant effect. However, capillary density may well change on a slower time scale (weeks to years) to reflect chronic changes in local metabolism, possibly as a result of disease or chronic conditions such as mild hypoxia when living at high altitudes.

However, if the capillary distances are relatively fixed, for acute changes in  $CMRO_2$  the only way to increase the  $O_2$  gradient is to raise the average capillary  $pO_2$  or lower the average tissue  $pO_2$

(or some combination of the two). The average capillary  $pO_2$  lies between the arterial  $pO_2$  and the venous  $pO_2$ , weighted toward the venous side. Because the arterial  $pO_2$  is fixed by the lungs, the local venous  $pO_2$  must be raised in order to increase the local capillary  $pO_2$ , and to raise the venous  $pO_2$  the OEF must be reduced. Alternatively, if the OEF stays the same but  $CMRO_2$  increases, then capillary  $pO_2$  would remain constant and so tissue  $pO_2$  would need to fall to increase the diffusion gradient.

This suggests a different way of thinking about the larger increase of CBF compared with  $CMRO_2$  observed with activation. Beyond simply delivering  $O_2$  to the capillary bed, CBF provides a way to modulate the diffusion gradient by raising or lowering the capillary  $pO_2$  by changing the OEF. The capillary  $pO_2$  combined with the  $O_2$  metabolic rate then determines what the tissue  $pO_2$  must be to provide the necessary gradient for  $CMRO_2$ , so we can think of CBF as a mechanism for regulating tissue  $pO_2$ . This prompts the question: For a given  $CMRO_2$  change, how much larger does the CBF change need to be to maintain the tissue  $pO_2$  at a constant level? Mathematical models, framed along the lines described above, suggest that the CBF change needs to be about twice as large as the  $CMRO_2$  change in order to maintain tissue  $pO_2$  at a constant level. The idea that the capillary  $pO_2$  must be raised to increase the driving pressure into the tissue was suggested as part of an earlier model attempting to explain the large change in CBF (Buxton and Frank 1997). The difference with the current description is that we are considering tissue  $pO_2$  to be relatively high but maintained during activation, while the earlier model assumed tissue  $pO_2$  was zero.

Several groups have reported dynamic tissue  $pO_2$  measurements in response to brief stimuli (Ances *et al.* 2001; Offenhauser *et al.* 2005; Thompson *et al.* 2003, 2005). The responses show interesting wiggles and transient features, but overall the magnitude of the changes in  $pO_2$  are small, less than 10% for all but the strongest stimuli. In short, a physiological consequence of the drop in the OEF with activation is that tissue  $pO_2$  remains approximately constant.

## Why is maintaining constant tissue $O_2$ partial pressure important?

If the useful function served by the large increase in CBF with activation is to maintain a constant  $pO_2$ , how does this provide an advantage for the organism? Interestingly, it does not appear to be necessary to support the kinetics of  $O_2$  metabolism. In brain tissue, recent studies have found  $pO_2$  values in the rough range 20–30 torr. However, studies in mitochondrial preparations have shown that the  $O_2$  metabolic rate does not become compromised by low  $pO_2$  until  $pO_2$  is well below 1 torr (the characteristic concentration is sometimes called  $K_m$ , and is shown as a dashed line near zero in Fig. 2.6C). For this reason, tissue  $pO_2$  appears to be quite a bit higher than it needs to be. Instead of raising capillary  $pO_2$  to increase  $CMRO_2$ , one could imagine letting tissue  $pO_2$  drop to increase the gradient, and this appears to be what happens in hypoxia. Yet with healthy activation the brain raises capillary  $pO_2$  instead.

One possible advantage of maintaining high  $pO_2$  in the tissue is that this could reduce effects of highly variable flow in individual capillaries. If tissue  $pO_2$  is very low, then a mitochondrion will be dependent on the nearest capillary for its  $O_2$ , and with irregular capillary flow this could create transient hypoxia. By maintaining a higher average  $pO_2$ ,  $O_2$  can diffuse farther before being consumed, and transient flow reductions in individual capillaries will not create dangerous local dips of  $pO_2$ .

A speculative possibility is that the importance of maintaining a high tissue  $pO_2$  relates to the thermodynamics of oxidative metabolism (see Box 1.1). A low tissue  $pO_2$  potentially can limit oxidative metabolism in two distinct ways. The first is a *kinetic* limitation, as described above: if the  $O_2$  concentration is too low, the  $O_2$  metabolic rate can be limited. The second potential limitation is *thermodynamic*: as the  $O_2$  concentration falls, the free energy change  $\Delta G$  available from oxidative metabolism also falls because it depends on the  $O_2$  concentration. Ultimately, the continued conversion of ADP to ATP, with an associated strong positive  $\Delta G$  for the relative concentrations



in brain, must be coupled with the more strongly negative  $\Delta G$  associated with oxidative metabolism. If the  $\Delta G$  available from oxidative metabolism falls too much, it will not be sufficient to provide the  $\Delta G$  required. However, if the ATP/ADP ratio degrades, the required  $\Delta G$  is smaller, and the process can continue despite the reduction of the  $\Delta G$  available from oxidative metabolism. Then as the  $O_2$  concentration declines, the  $O_2$  metabolic rate can be maintained, but the ATP phosphorylation potential also steadily declines. Some experimental support for this speculative scenario comes from an early experimental finding that the ATP/ADP ratio fell with decreasing  $O_2$  concentration even at relatively high  $O_2$  concentrations (Wilson *et al.* 1977).

In Box 1.1, the analogy of biological batteries was introduced, with equivalent voltages related to the  $\Delta G$  associated with different systems such as the ATP/ADP system and the extracellular/intracellular  $Na^+$  gradient. As different biological batteries are used for cellular work or signaling, they are recharged by other batteries with a higher voltage. For example, transport of glutamate into the astrocyte is driven by the  $Na^+$  gradient, and the  $Na^+$  gradient is then “recharged” from the ATP/ADP battery by the  $Na^+/K^+$  pump, which consumes ATP to pump  $Na^+$  against its gradient. In this hierarchy of biological batteries, the one with the highest voltage is the one associated with oxidative metabolism of pyruvate. For this reason, if the voltage available from this battery is degraded, the effect could propagate down through all of the other batteries as well. Perhaps the important function of the large CBF increase with activation is to maintain tissue  $pO_2$  and preserve the  $\Delta G$  available from oxidative metabolism.

## References

- Akgoren N, Fabricius M, Lauritzen M (1994) Importance of nitric oxide for local increases of blood flow in rat cerebellar cortex during electrical stimulation. *Proc Natl Acad Sci USA* **91**:5903–5907
- Ances BM, Wilson DF, Greenberg JH, Detre JA (2001) Dynamic changes in cerebral blood flow,  $O_2$  tension, and calculated cerebral metabolic rate of  $O_2$  during functional activation using oxygen phosphorescence quenching. *J Cereb Blood Flow Metab* **21**:511–516
- Anderson CM, Nedergaard M (2003) Astrocyte-mediated control of cerebral microcirculation. *Trends Neurosci* **26**:340–344; author reply 344–345
- Andresen J, Shafi NI, Bryan RM, Jr. (2006) Endothelial influences on cerebrovascular tone. *J Appl Physiol* **100**:318–327
- Attwell D, Iadecola C (2002) The neural basis of functional brain imaging signals. *Trends Neurosci* **25**:621–625
- Berezcki D, Wei L, Otsuka T, *et al.* (1993) Hypoxia increases velocity of blood flow through parenchymal microvascular systems in rat brain. *J Cereb Blood Flow Metab* **13**:475–486
- Binder JR, Rao SM, Hammeke TA, *et al.* (1994) Effects of stimulus rate on signal response during functional magnetic resonance imaging of auditory cortex. *Cogn Brain Res* **2**:31–38
- Blanco VM, Stern JE, Filosa JA (2008) Tone-dependent vascular responses to astrocyte-derived signals. *Am J Physiol Heart Circ Physiol* **294**: H2855–H2863
- Boas DA, Jones SR, Devor A, Huppert TJ, Dale AM (2008) A vascular anatomical network model of the spatio-temporal response to brain activation. *Neuroimage* **40**:1116–1129
- Buxton RB, Frank LR (1997) A model for the coupling between cerebral blood flow and oxygen metabolism during neural stimulation. *J Cereb Blood Flow Metab* **17**:64–72
- Buxton RB, Frank LR, Wong EC, *et al.* (1998) A general kinetic model for quantitative perfusion imaging with arterial spin labeling. *Magn Reson Med* **40**:383–396
- Calamante F, Gadian DG, Connelly A (2002) Quantification of perfusion using bolus tracking magnetic resonance imaging in stroke: assumptions, limitations, and potential implications for clinical use. *Stroke* **33**:1146–1151
- Cauli B, Tong XK, Rancillac A, *et al.* (2004) Cortical GABA interneurons in neurovascular coupling: relays for

- subcortical vasoactive pathways. *J Neurosci* **24**:8940–8949
- Cholet N, Seylaz J, Lacombe P, Bonvento G (1997) Local uncoupling of the cerebrovascular and metabolic responses to somatosensory stimulation after neuronal nitric oxide synthase inhibition. *J Cereb Blood Flow Metab* **17**:1191–1201
- Detre JA, Leigh JS, Williams DS, Koretsky AP (1992) Perfusion imaging. *Magn Reson Med* **23**:37–45
- Devor A, Tian P, Nishimura N, et al. (2007) Suppressed neuronal activity and concurrent arteriolar vasoconstriction may explain negative blood oxygenation level-dependent signal. *J Neurosci* **27**:4452–4459
- Dirnagl U, Kaplan B, Jacewicz M, Pulsinelli W. (1989) Continuous measurement of cerebral cortical blood flow by laser-Doppler flowmetry in a rat stroke model. *J Cereb Blood Flow Metab* **9**:589–596
- Dirnagl U, Niwa K, Lindauer U, Villringer A (1994) Coupling of cerebral blood flow to neuronal activation: role of adenosine and nitric oxide. *Am J Physiol* **267**:H296–H301
- Faraci FM, Sobey CG (1998) Role of potassium channels in regulation of cerebral vascular tone. *J Cereb Blood Flow Metab* **18**:1047–1063
- Filosa JA, Blanco VM (2007) Neurovascular coupling in the mammalian brain. *Exp Physiol* **92**:641–646
- Filosa JA, Bonev AD, Straub SV, et al. (2006) Local potassium signaling couples neuronal activity to vasodilation in the brain. *Nat Neurosci* **9**: 1397–1403
- Fox PT, Raichle ME (1986) Focal physiological uncoupling of cerebral blood flow and oxidative metabolism during somatosensory stimulation in human subjects. *Proc Natl Acad Sci USA* **83**:1140–1144
- Fox PT, Raichle ME (1991) Stimulus rate dependence of regional cerebral blood flow in human striate cortex, demonstrated by positron emission tomography. *J Neurophysiol* **51**:1109–1120
- Fox PT, Raichle ME, Mintun MA, Dence C (1988) Nonoxidative glucose consumption during focal physiologic neural activity. *Science* **241**:462–464
- Frackowiak RSJ, Lenzi GL, Jones T, Heather JD (1980) Quantitative measurement of regional cerebral blood flow and oxygen metabolism in man using  $^{15}\text{O}$  and positron emission tomography: theory, procedure, and normal values. *J Comput Assist Tomogr* **4**:727–736
- Frankel HM, Garcia E, Malik F, Weiss JK, Weiss HR (1992) Effect of acetazolamide on cerebral blood flow and capillary patency. *J Appl Physiol* **73**:1756–1761
- Fredholm BB, Battig K, Holmen J, Nehlig A, Zvartau EE (1999) Actions of caffeine in the brain with special reference to factors that contribute to its widespread use. *Pharmacol Rev* **51**:83–133
- Ginsberg MD, Dietrich WD, Busto R (1987) Coupled forebrain increases of local cerebral glucose utilization and blood flow during physiologic stimulation of a somatosensory pathway in the rat. *Neurology* **37**:11–19
- Ginsberg MD, Chang JY, Kelly RE, et al. (1988) Increases in both cerebral glucose utilization and blood flow during execution of a somatosensory task. *Ann Neurol* **23**:152–160
- Girouard H, Iadecola C (2006) Neurovascular coupling in the normal brain and in hypertension, stroke, and Alzheimer disease. *J Appl Physiol* **100**:328–335
- Gjedde A (1987) Does deoxyglucose uptake in the brain reflect energy metabolism? *Biochem Pharmacol* **36**:1853–1861
- Gobel U, Klein B, Schrock H, Kuschinsky W (1989) Lack of capillary recruitment in the brains of awake rats during hypercapnia. *J Cereb Blood Flow Metab* **9**:491–499
- Gobel U, Theilen H, Kuschinsky W (1990) Congruence of total and perfused capillary network in rat brains. *Circ Res* **66**:271–281
- Grubb RL, Raichle ME, Eichling JO, Ter-Pogossian MM (1974) The effects of changes in  $\text{Paco}_2$  on cerebral blood volume, blood flow, and vascular mean transit time. *Stroke* **5**:630–639
- Gusnard DA, Raichle ME (2001) Searching for a baseline: functional imaging and the resting human brain. *Nat Rev Neurosci* **2**:685–694
- Guyton AC (1981) *Textbook of Medical Physiology*. Philadelphia, PA: WB Saunders
- Hamel E (2006) Perivascular nerves and the regulation of cerebrovascular tone. *J Appl Physiol* **100**:1059–1064
- Haydon PG, Carmignoto G (2006) Astrocyte control of synaptic transmission and neurovascular coupling. *Physiol Rev* **86**:1009–1031

- Hillman EM, Devor A, Bouchard MB, *et al.* (2007) Depth-resolved optical imaging and microscopy of vascular compartment dynamics during somatosensory stimulation. *Neuroimage* **35**:89–104
- Iadecola C (1993) Regulation of cerebral microcirculation during neural activity: is nitric oxide the missing link? *Trend Neurosci* **16**:206–214
- Ingvar DH, Lassen NH (1963) Regional blood flow of the cerebral cortex determined by 85-krypton. *Acta Physiol Scand* **54**:325–338
- Ito H, Kanno I, Kato C, *et al.* (2004) Database of normal human cerebral blood flow, cerebral blood volume, cerebral oxygen extraction fraction and cerebral metabolic rate of oxygen measured by positron emission tomography with <sup>15</sup>O-labelled carbon dioxide or water, carbon monoxide and oxygen: a multicentre study in Japan. *Eur J Nucl Med Mol Imaging* **31**:635–643
- Ito H, Ibaraki M, Kanno I, Fukuda H, Miura S (2005) Changes in the arterial fraction of human cerebral blood volume during hypercapnia and hypocapnia measured by positron emission tomography. *J Cereb Blood Flow Metab* **25**:852–857
- James W (1890) *The Principles of Psychology*. Cambridge, MA: Harvard University Press
- Kety SS, Schmidt CF (1948) Nitrous oxide method for quantitative determination of cerebral blood flow in man: theory, procedure and normal values. *J Clin Invest* **27**:475–483
- Kim T, Hendrich KS, Masamoto K, Kim SG (2007) Arterial versus total blood volume changes during neural activity-induced cerebral blood flow change: implication for BOLD fMRI. *J Cereb Blood Flow Metab* **27**:1235–1247
- Klein B, Kuschinsky W, Schrock H, Vetterlein F (1986) Interdependency of local capillary density, blood flow, and metabolism in rat brains. *Am J Physiol* **251**:H1330–H1340
- Kleinfeld D, Mitra PP, Helmchen F, Denk W (1998) Fluctuations and stimulus induced changes in blood flow observed in individual capillaries in layers 2 through 4 of rat neocortex. *Proc Natl Acad Sci USA* **95**:15741–15746
- Koehler RC, Gebremedhin D, Harder DR (2006) Role of astrocytes in cerebrovascular regulation. *J Appl Physiol* **100**:307–317
- Krolo I, Hudetz AG (2000) Hypoxemia alters erythrocyte perfusion pattern in the cerebral capillary network. *Microvasc Res* **59**:72–79
- Kuschinsky W, Wahl M (1979) Perivascular pH and pial arterial diameter during bicuculline induced seizures in cats. *Pflugers Arch* **382**:81–85
- Lassen NA (1991) Cations as mediators of functional hyperemia in the brain. In *Brain Work and Mental Activity: Quantitative Studies with Radioactive Tracers*, Lassen NA, Ingvar DH, Raichle ME *et al.*, eds. Copenhagen: Munksgaard, pp. 68–77
- Lindauer U, Megow D, Matsuda H, Dirnagl U (1999) Nitric oxide: a modulator, but not a mediator, of neurovascular coupling in rat somatosensory cortex. *Am J Physiol* **277**:H799–H811
- Logothetis NK, Pauls J, Augath M, Trinath T, Oeltermann A (2001) Neurophysiological investigation of the basis of the fMRI signal. *Nature* **412**:150–157
- Magistretti PJ (2006) Neuron-glia metabolic coupling and plasticity. *J Exp Biol* **209**:2304–2311
- Marchal G, Rioux P, Petit-Taboué M-C, *et al.* (1992) Regional cerebral oxygen consumption, blood flow, and blood volume in healthy human aging. *Arch Neurol* **49**:1013–1020
- Marrett S, Gjedde A (1997) Changes of blood flow and oxygen consumption in visual cortex of living humans. *Adv Exp Med Biol* **413**:205–208
- Mulligan SJ, MacVicar BA (2004) Calcium transients in astrocyte endfeet cause cerebrovascular constrictions. *Nature* **431**:195–199
- Newman EA (2003) Glial cells inhibition of neurons by release of ATP. *J Neurosci* **23**:1659–1666
- Obrist WD, Thompson HK, King CH, Wang HS (1967) Determination of regional cerebral blood flow by inhalation of 133-xenon. *Circ Res* **20**:124–135
- Offenhauser N, Thomsen K, Caesar K, Lauritzen M (2005) Activity-induced tissue oxygenation changes in rat cerebellar cortex: interplay of postsynaptic activation and blood flow. *J Physiol* **565**:279–294
- Paulson OB, Newman EA (1987) Does the release of potassium from astrocyte endfeet regulate cerebral blood flow? *Science* **237**:896–898

- Pawlik G, Rackl A, Bing RJ (1981) Quantitative capillary topography and blood flow in the cerebral cortex of cats: an in vivo microscopic study. *Brain Res* **208**:35–58
- Peppiatt CM, Howarth C, Mobbs P, Attwell D (2006) Bidirectional control of CNS capillary diameter by pericytes. *Nature* **443**:700–704
- Perthen JE, Lansing AE, Liao J, Liu TT, Buxton RB (2008) Caffeine-induced uncoupling of cerebral blood flow and oxygen metabolism: a calibrated BOLD fMRI study. *Neuroimage* **40**:237–247
- Piechnik SK, Chiarelli PA, Jezzard P (2008) Modelling vascular reactivity to investigate the basis of the relationship between cerebral blood volume and flow under CO<sub>2</sub> manipulation. *Neuroimage* **39**:107–118
- Powers WJ, Hirsch IB, Cryer PE (1996) Hypoglycemia. *Am J Physiol* **270**:H554–H559
- Prichard JW, Rosen BR (1994) Functional study of the brain by NMR. *J Cereb Blood Flow Metab* **14**:365–372
- Quayle JM, Nelson MT, Standen NB (1997) ATP-sensitive and inwardly rectifying potassium channels in smooth muscle. *Physiol Rev* **77**:1165–1232
- Raichle ME (1983) Brain blood flow measured with intravenous H<sub>2</sub>O-15: implementation and validation. *J Nucl Med* **24**:790–798
- Roland PE, Eriksson L, Stone-Elander S, Widen L (1987) Does mental activity change the oxidative metabolism of the brain? *J Neurosci*. **7**:2373–2389
- Roland PE, Eriksson L, Widen L, Stone-Elander S (1989) Changes in regional cerebral oxidative metabolism induced by tactile learning and recognition in man. *Eur J Neurosci* **1**:3–18
- Rostrup E, Knudsen GM, Law I, et al. (2005) The relationship between cerebral blood flow and volume in humans. *Neuroimage* **24**:1–11
- Roy CS, Sherrington CS (1890) On the regulation of the blood-supply of the brain. *J Physiol* **11**:85–108
- Seitz RJ, Roland PE (1992) Vibratory stimulation increases and decreases the regional cerebral blood flow and oxidative metabolism: a positron emission tomography (PET) study. *Acta Neurol Scand* **86**:60–67
- Sharan M, Popel AS, Hudak ML, et al. (1998) An analysis of hypoxia in sheep brain using a mathematical model. *Ann Biomed Eng* **26**:48–59
- Shmuel A, Augath M, Oeltermann A, Logothetis NK (2006) Negative functional MRI response correlates with decreases in neuronal activity in monkey visual area V1. *Nat Neurosci* **9**:569–577
- Shockley RP, LaManna JC (1988) Determination of rat cerebral cortical blood volume changes by capillary mean transit time analysis during hypoxia, hypercapnia and hyperventilation. *Brain Res* **454**:170–178
- Siesjo B. (1978) *Brain Energy Metabolism*. New York: John Wiley
- Stern MD (1975) In vivo evaluation of microcirculation by coherent light scattering. *Nature* **254**:56–58
- Stewart GN (1894) Researches on the circulation time in organs and on the influences which affect it, Parts I–III. *J Physiol (Lond)* **15**: 1–30
- Straub SV, Nelson MT (2007) Astrocytic Ca<sup>2+</sup> signaling: the information currency coupling neuronal activity to the cerebral microcirculation. *Trends Cardiovasc Med* **17**:183–190
- Thompson JK, Peterson MR, Freeman RD (2003) Single-neuron activity and tissue oxygenation in the cerebral cortex. *Science* **299**:1070–1072
- Thompson JK, Peterson MR, Freeman RD (2005) Separate spatial scales determine neural activity-dependent changes in tissue oxygen within central visual pathways. *J Neurosci* **25**:9046–9058
- Vafae M, Marrett S, Meyer E, Evans A, Gjedde A (1998) Increased oxygen consumption in human visual cortex: response to visual stimulation. *Acta Neurol Scand* **98**:85–89
- Vafae MS, Meyer E, Marrett S, et al. (1999) Frequency-dependent changes in cerebral metabolic rate of oxygen during activation of human visual cortex. *J Cereb Blood Flow Metab* **19**:272–277
- Vanzetta I, Slovín H, Omer DB, Grinvald A (2004) Columnar resolution of blood volume and oximetry functional maps in the behaving monkey; implications for fMRI. *Neuron* **42**:843–854
- Vetterlein F, Demmerle B, Bardosi A, Gobel U, Schmidt G (1990) Determination of capillary perfusion pattern in rat brain by timed plasma labeling. *Am J Physiol* **258**:H80–H84
- Villringer A, Dirnagl U (1995) Coupling of brain activity and cerebral blood flow: basis of

- functional neuroimaging. *Cerebrovasc Brain Metab Rev* 7:240–276
- Villringer A, Thiem A, Lindauer U, Einhaupl K, Dirnagl U (1994) Capillary perfusion of the rat brain cortex: an in vivo confocal microscopy study. *Circ Res* 75:55–62
- Watkins LD (1995) Nitric oxide and cerebral blood flow: an update. *Cerebrovasc Brain Metab Rev* 7:324–337
- Wei L, Otsuka T, Acuff V, et al. (1993) The velocities of red cell and plasma flows through parenchymal microvessels of rat brain are decreased by pentobarbital. *J Cereb Blood Flow Metab* 13:487–497
- Weiss HR (1988) Measurement of cerebral capillary perfusion with a fluorescent label. *Microvasc Res* 36:172–180
- Wilson DF, Erecinska M, Drown C, Silver IA (1977) Effect of oxygen tension on cellular energetics. *Am J Physiol* 233:C135–C140
- Winn HR, Ngai AC, Ko KR (1991) Role of adenosine in regulating microvascular CBF in activated sensory cortex. In *Brain Work and Mental Activity: Quantitative Studies with Radioactive Tracers* Lassen NA, Ingvar DH, Raichle ME, et al., eds. Copenhagen: Munksgaard pp. 80–91
- Xu HL, Mao L, Ye S, et al. (2008) Astrocytes are a key conduit for upstream signaling of vasodilation during cerebral cortical neuronal activation in vivo. *Am J Physiol Heart Circ Physiol* 294:H622–H632
- Yang SP, Krasny JA (1995) Cerebral blood flow and metabolic responses to sustained hypercapnia in awake sheep. *J Cereb Blood Flow Metab* 15:115–123
- Yarowsky PJ, Ingvar DH (1981) Neuronal activity and energy metabolism. *Fed Proc* 40:2353–2362
- Zheng D, LaMantia AS, Purves D (1991) Specialized vascularization of the primate visual cortex. *J Neurosci* 11:2622–2629
- Zonta M, Angulo MC, Gobbo S, et al. (2003) Neuron-to-astrocyte signaling is central to the dynamic control of brain microcirculation. *Nat Neurosci* 6:43–50



Part

IB

# Introduction to functional magnetic resonance imaging

Commonplace as such [NMR] experiments have become in our laboratories, I have not yet lost a feeling of wonder, and of delight, that this delicate motion should reside in all the ordinary things around us, revealing itself only to him who looks for it. I remember, in the winter of our first experiments, just seven years ago, looking on snow with new eyes. There the snow lay around my doorstep – great heaps of protons quietly precessing in the earth's magnetic field. To see the world for a moment as something rich and strange is the private reward of many a discovery.

*Edward M. Purcell (1953) Nobel Lecture*





# Nuclear magnetic resonance

<b>Introduction</b>	page 67
<b>The NMR signal</b>	70
The basic NMR experiment	70
Precession	71
Relaxation	73
Equilibrium magnetization	73
The radiofrequency pulse	74
The free induction decay signal	75
The basic NMR experiment again	77
<b>Basic pulse sequences</b>	78
Pulse sequence parameters and image contrast	78
Gradient echo pulse sequence	79
The decay $T_2^*$	80
Spin echoes	81
Spin echo pulse sequence	82
Inversion recovery pulse sequence	83

## Introduction

The field of NMR began in 1946 with the independent and simultaneous work of two physics groups led by Edward Purcell and Felix Bloch (Bloch *et al.* 1946; Purcell *et al.* 1946). Building on earlier work in nuclear magnetism, these groups performed the first successful experiments demonstrating the phenomenon of NMR. Certain nuclei (including hydrogen) possess an intrinsic magnetic moment, and when placed in a magnetic field, they rotate with a frequency proportional to the field. This “delicate motion” first detected by Purcell and Bloch has proved to have far-reaching applications in fields they could hardly have imagined (see [Box 3.1](#)). In this chapter and the next, the basic concepts and techniques of MRI are described. In [Chapter 5](#), the different approaches to fMRI are described, including contrast agent and arterial spin labeling techniques in addition to the intrinsic blood oxygenation level dependent (BOLD) signal changes introduced in earlier chapters. Because these techniques depend on subtle properties of the NMR signal, it is necessary to understand in some detail how MRI works.

Magnetic resonance imaging has become an indispensable tool in diagnostic radiology. It reveals fine details of anatomy, and yet is non-invasive and does not require ionizing radiation such as X-rays. It is a highly flexible technique so that contrast between one tissue and another in an image can be varied simply by varying the way the image is made. [Figure 3.1](#) shows three MR images of the same anatomical section, exhibiting radically different patterns of contrast. These three images are described as  $T_1$  weighted, density

**Box 3.1. The historical development of NMR and MRI****A new tool for physics**

In the early part of the twentieth century, it became clear that classical physics could not account for the world of atoms and subatomic particles. Experiments showed that the light emitted from excited atoms consisted of discrete frequencies, suggesting that only certain energy states could exist rather than a continuum of states. To explain subtle but distinct splittings of some of these spectral lines, called the hyperfine structure, Pauli proposed in 1924 that atomic nuclei possess an intrinsic angular momentum (*spin*) and an associated magnetic moment. The interaction of the electrons in the atom with the magnetic field of the nucleus creates a slight shift in the energy levels and a splitting of the spectral lines. The significance of these small effects is that they provide a window to investigate the basic properties of matter. From the magnitude of this hyperfine structure, one could estimate the magnitude of the nuclear magnetic moment, but the precision of these experiments was poor. In the 1930s, new techniques were developed based on the deflection of molecular beams in an inhomogeneous magnetic field (Bloch 1953), but these techniques were still inadequate for precision measurements.

The Second World War brought a stop to all basic physics research and perhaps explains the burst in creative activity just after the war that led to the seminal work of Purcell and Bloch. During the war, Purcell worked at the Massachusetts Institute of Technology on radar development and Bloch worked at Harvard on radar countermeasures, and their experience with RF techniques and measurements may have contributed to the success of their NMR studies (Vleck 1970). In fact, the experiments performed by Purcell and Bloch were rather different, but it was quickly realized that they were looking at two different aspects of the same phenomenon: in a magnetic field nuclei precess at a rate proportional to the field, with the spin axis rotating at a characteristic frequency. Purcell showed that electromagnetic energy is absorbed by a material at this resonant frequency, and Bloch showed that the precessing nuclei induce a detectable oscillating signal in a nearby detector coil. In both experiments, magnetic properties of the nucleus are manifested in terms of a frequency of electromagnetic oscillations, which can be measured with very high precision. In the next few years, NMR became a key tool for investigating atomic and nuclear properties based on these small effects of nuclear magnetization. In 1952, Purcell and Bloch were awarded the Nobel Prize in Physics for the development of NMR techniques and the contributions to basic physics made possible by NMR.

**A new tool for chemistry**

In Purcell's Nobel award lecture, quoted at the beginning of the chapter, he eloquently describes the feelings of a basic scientist who has discovered a previously unappreciated aspect of the world (Purcell 1953). At this time, NMR was valued as a tool for fundamental physics research, but the remarkable applications of NMR in other fields were still unimagined. In fact, much of the subsequent development of the field of NMR can be viewed as turning artifacts in the original techniques into powerful tools for measuring other properties of matter. The original application of NMR was to measure magnetic moments of nuclei based on their resonant frequencies. However, as experimenters moved up the periodic table to heavier atoms, it became clear that additional corrections were necessary to take into account shielding of the nucleus by atomic electrons. Electron orbitals create magnetic fields that alter the field felt by the nucleus, and the result is that the resonant frequency is shifted slightly depending on the chemical form of the nucleus.

In time, this chemical shift artifact in the nuclear magnetic moment measurements became the basis for applications of NMR in analytical chemistry, and NMR spectroscopy has now become an enormously powerful tool for chemical analysis. For example, the  $^1\text{H}$  NMR spectrum of a sample of tissue from the brain is split into numerous lines corresponding to the different chemical forms of hydrogen. By far the most dominant line is from water, but if this strong signal is suppressed, many

other lines appear. Although the frequency differences are small, only a few parts per million, they are nevertheless readily measurable. The relative intensities of the different lines directly reflect the proportion of the corresponding chemical in the sample. A key development in the methodology used in these chemistry applications was the introduction by Richard Ernst of Fourier methods for acquiring and analyzing the signal. Rather than sweeping the magnetic field to excite each spectral line in turn, all of the nuclei are excited at once and the spectrum is sorted out from the combined signals using the Fourier transform. This same basic methodology has carried through to current MRI methods. In 1991, Ernst received the Nobel Prize in Chemistry for his work in applications of NMR to basic chemistry studies.

### A new tool for medicine

Because the resonant frequency of a nucleus is directly proportional to the magnetic field, any inhomogeneities of the magnet translate into an unwanted broadening of the spectral lines. In 1973, Paul Lauterbur proposed that NMR techniques could also be used for imaging by deliberately altering the magnetic field homogeneity in a controlled way. By applying a linear gradient field to a sample, the NMR signals from different locations are spread out in frequency, analogous to the way that the signals from different chemical forms of the nucleus are spread in frequency. Measuring the distribution of frequencies in the presence of a field gradient then provides a direct measure of the distribution of signals within the sample: an image. Peter Mansfield (1977) showed how rapid switching of gradients makes possible fast imaging with a technique called echo-planar imaging (EPI). The first commercial MR imagers were built in the early 1980s, and MRI is now an essential part of clinical radiology. In 2003, Lauterbur and Mansfield were awarded the Nobel Prize in Physiology or Medicine for their contributions to the development of MRI.

### A new tool for mapping brain activity

Even with a perfectly homogeneous magnet, the heterogeneity of the human body itself leads to local variations in the magnetic field. These field inhomogeneities first appeared in images as artifacts, either a distortion of the image or a reduction of the local signal because nuclear spins precessing at different rates become out of phase with each other, reducing the net signal. In the early 1990s, it was demonstrated that the oxygenation state of hemoglobin has a measurable effect on the signal measured with MRI (Ogawa *et al.* 1990), and this soon led to the capability of mapping brain activity based on blood oxygenation changes accompanying neural activation (Kwong *et al.* 1992). This technique of fMRI has become a standard tool for functional neuroimaging and is now widely used for mapping the working human brain.

weighted, and  $T_2$  weighted (the meaning of these technical terms will be made clear shortly). The source of the flexibility of MRI lies in the fact that the measured signal depends on several properties of the tissue, as suggested by these descriptions. This is distinctly different from other types of radiological imaging. For example, in computed tomography (CT) the image is a map of one local property of the tissue: the X-ray absorption coefficient. Similarly, with nuclear medicine studies, the image is a map of the radioactive tracer concentration. But with MRI, the image is a map of *the local transverse magnetization of the hydrogen nuclei*. This transverse magnetization, in turn, depends on several intrinsic properties of the tissue. In fact, the transverse magnetization is a transient phenomenon; it does not exist until we start the MRI process.

The fact that the MR signal depends on a number of tissue properties is the source of its flexibility, but it is also a source of difficulty in developing a solid grasp of MRI. To

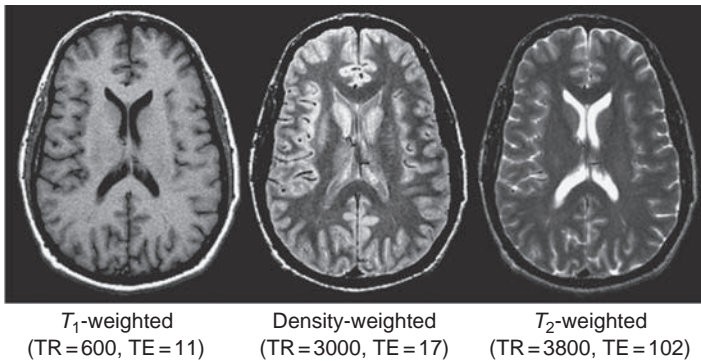


**Fig. 3.1.** Magnetic resonance images of the same anatomical section showing a range of tissue contrasts. In the first image, cerebrospinal fluid is black, whereas in the last image it is bright. Contrast is manipulated during image acquisition by adjusting several parameters, such as the repetition time TR and the echo time TE (times given in milliseconds), which control the sensitivity of the signal to the local tissue relaxation times  $T_1$  and  $T_2$  and the local proton density.

understand the full range of MRI applications, it is necessary to understand the basic physics of NMR and how the MR signal can be manipulated experimentally.

## The NMR signal

### The basic NMR experiment

The phenomenon of NMR is not part of everyday experience, so it is helpful to set the stage by considering a purely empirical description of the basic experiment. Every time an MR image is made, it is a variation on this basic experiment. For the moment we are only concerned with how the MR signal is generated; how that signal is mapped to create an image is taken up in [Chapter 4](#). The basic experimental setup is illustrated in [Fig. 3.2](#). A sample is placed in a large magnetic field, and a coil of wire is placed near the sample oriented such that the axis of the coil is perpendicular to the magnetic field. The coil is used as both a transmitter and a receiver. During the *transmit* phase of the experiment, an oscillating current is applied to the coil for a brief time (a few milliseconds), which produces an oscillating magnetic field in the sample. The oscillations are in the radiofrequency (RF) range, so the coil is often referred to as an *RF coil*, and the brief oscillating magnetic field is referred to as an *RF pulse*. For example, for clinical imaging systems with a magnetic field of 1.5 tesla (1.5 T; about 30 000 times stronger than the natural magnetic field at the surface of the earth), the oscillating field has a magnitude of only a few microtesla, and the oscillations are at a frequency of 64 MHz. During the receive phase of the experiment, the coil is connected to a detector circuit that senses small oscillating currents in the coil.

The basic experiment consists of applying a brief RF pulse to the sample and then monitoring the current in the coil to see if there is a signal returned from the sample. If one were to try this experiment naively, with an arbitrary RF frequency, the result would usually be that there is no returned signal. However, for a few specific frequencies there would be a weak, transient oscillating current detected in the coil. This current, oscillating at the same frequency as the RF pulse, is the NMR signal. The particular frequencies where it occurs are the resonant frequencies of particular nuclei. At its resonant frequency a nucleus is able to absorb electromagnetic energy from the RF pulse during the transmit phase and return a small portion of that energy back to the coil during the receive phase. Only particular

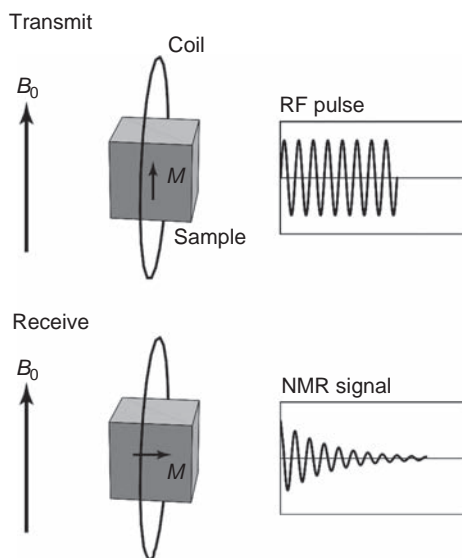


**Fig. 3.2.** The basic NMR experiment. A sample is placed in a large magnetic field  $B_0$ , and hydrogen nuclei partially align with the field creating a net magnetization  $M$ . In the transmit part of the experiment, an oscillating current in a nearby coil creates an oscillating radiofrequency (RF) magnetic field in the sample, which causes  $M$  to tip over and precess around  $B_0$ . In the receive part of the experiment, the precessing magnetization creates a transient oscillating current (the NMR signal) in the coil.

nuclei, those with an odd number of either neutrons or protons, exhibit NMR. For example, carbon-12 ( $^{12}\text{C}$ ) with six protons and six neutrons does not show the NMR effect, whereas carbon-13 ( $^{13}\text{C}$ ) with seven neutrons does have a resonance. In MRI studies, the nucleus of interest is almost always hydrogen.

As an analogy to the NMR experiment, imagine that we are sitting in a quiet room and have a tuning fork with a precise resonant frequency. Our “coil” is a speaker/microphone that can be used either for broadcasting a pure tone into the room or listening for a weak tone coming back from the room. For most frequencies broadcast into the room, there will be no return signal because the tuning fork is unaffected. But when the broadcast frequency matches the resonant frequency of the tuning fork, the fork will begin to vibrate, absorbing acoustic energy. Afterward, the microphone will pick up a weak sound coming back from the vibrating tuning fork.

## Precession

The source of the resonance in an NMR experiment is that the protons and neutrons that make up a nucleus possess an intrinsic angular momentum called *spin*. The word spin immediately brings to mind examples of our classical concept of angular momentum: spinning tops, the spin of a curving baseball, and planets spinning on their axes. However, the physical concept of nuclear spin is a purely quantum mechanical phenomenon and is fundamentally different from these classical examples. For a spinning top, the “spin” is not an intrinsic feature of the top. The top can be spun faster or slower or stopped altogether. But for a proton, angular momentum is an intrinsic part of being a proton. All protons, neutrons, and electrons have the same magnitude of angular momentum, and it cannot be increased or decreased. The only feature that can change is the *axis of spin*, the direction of the angular momentum. When protons combine to form a nucleus, they combine in pairs with oppositely oriented spins, and neutrons behave similarly. The result is that nuclei with an even number of protons and an even number of neutrons, such as  $^{12}\text{C}$ , have no net spin, whereas nuclei with an odd number, such as  $^{13}\text{C}$ , do have a net spin. Hydrogen, with only a single

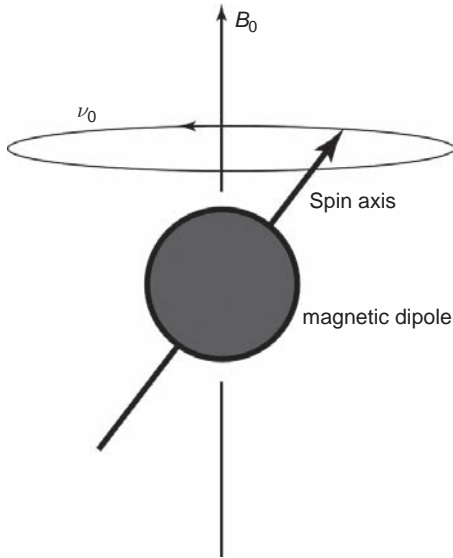


**Fig. 3.3.** Precession of a magnetic dipole in a magnetic field. The magnetic field  $B_0$  exerts a torque on a nuclear magnetic dipole that would tend to make it align with  $B_0$ . However, because the nucleus also has angular momentum (spin), it instead precesses like a spinning top at an angle to the gravitational field. The precession frequency  $\nu_0$  is proportional to the magnetic field and is the resonant frequency of NMR.

proton as its nucleus, has a net spin, and because it is far more abundant in the body than any other nucleus, it is the primary focus of MRI.

Associated with the spin of the proton is a *magnetic dipole moment*. That is, the H nucleus behaves like a tiny magnet, with the north–south axis parallel to the spin axis. Now consider a proton placed in a magnetic field. Because of its magnetic dipole moment, the magnetic field exerts a torque on the proton that, in the absence of other effects, would rotate the dipole into alignment with the field, like a compass needle in the earth’s magnetic field. But because the proton also possesses angular momentum, this alignment does not happen immediately. Instead, the spin axis of the proton *precesses* around the field axis rather than aligning with it (Fig. 3.3). This is an example of the peculiar nature of angular momentum: if one tries to twist a spinning object, the change in the spin axis is at right angles to both the original spin axis and the twisting axis. For example, the wheel of a moving bicycle has an angular momentum around a horizontal axis perpendicular to the bike. If the bike starts to tip to the left it can be righted by twisting the handle bars to the left. That is, applying a torque around a vertical axis (twisting the handle bars) causes the wheel to rotate around a horizontal axis along the length of the bike.

A more direct analogy is a spinning top whose axis is tilted from the vertical. Gravity applies a torque that would tend to make the top fall over. But instead the top precesses around the vertical, maintaining a constant tip angle. In thinking about this process, we must be clear about the distinction between the direction of the field and the axis of the torque the field creates. The gravitational field is vertical, but the torque it creates is around a horizontal axis because it would tend to rotate the top away from vertical, pivoting around the point of contact with the table.

Thus, when placed in a magnetic field, a proton with its magnetic dipole moment precesses around the field axis. The frequency of this precession,  $\nu_0$ , is the resonant frequency of NMR, and is often called the Larmor frequency after the nineteenth century physicist who investigated the classical physics of precession in a magnetic field. The precession frequency is

**Table 3.1.** The gyromagnetic ratio for selected nuclei

Nucleus	Gyromagnetic ratio (MHz/T)
$^1\text{H}$	42.58
$^{13}\text{C}$	10.71
$^{19}\text{F}$	40.08
$^{23}\text{Na}$	11.27
$^{31}\text{P}$	17.25

directly proportional to the strength of the magnetic field because the torque applied to the dipole is proportional to the field. The fundamental equation of magnetic resonance is then

$$\nu_0 = \gamma B_0 \quad (3.1)$$

where  $B_0$  is the main magnetic field strength and  $\gamma$  is a constant called the gyromagnetic ratio. The factor  $\gamma$  is different for each nucleus and is usually expressed in units of megahertz per tesla (Table 3.1). Equation (3.1) is the fundamental basis of MRI, which uses subtle manipulations of the resonant frequency to map the location of the signal.

## Relaxation

The second important process that affects the orientation of the proton's spin in addition to precession is *relaxation*. If we place a proton in a large magnetic field, the precession rate is very fast:  $\nu_0 = 64$  MHz in a 1.5 T field. If we could observe the angle of the dipole axis for a few rotations, we would see no change; it would appear as a pure precession with no apparent tendency for the dipole to align with the field. But if we observed the precession for millions of cycles, we would see that the dipole gradually tends to align with the magnetic field. The time constant for this relaxation process is called  $T_1$ , and after a time several times longer than  $T_1$  the dipole is essentially aligned with  $B_0$ .

Relaxation is an example of energy equilibration. A dipole in a magnetic field is at its lowest energy when it is aligned with the field and at its highest energy when it is aligned opposite to the field. As the dipole changes orientation from its initial angle to alignment with the field, this orientational magnetic energy must be converted into other forms of energy, such as the random thermal motions of the molecules. In other words, the initial orientational magnetic energy must be dissipated as heat. The time required for this energy equilibration depends on how tightly coupled the random thermal motions are to the orientation of the dipole. For H nuclei in water molecules, this coupling is very weak, so  $T_1$  is long. A typical value for  $T_1$  in the human body is approximately 1 s, eight orders of magnitude longer than the precession period in a 1.5 T magnet.

## Equilibrium magnetization

Now consider a collection of magnetic dipoles, a sample of water, in a magnetic field. Each H nucleus is a magnetic dipole; the oxygen nucleus ( $^{16}\text{O}$ ) contains an even number of protons and neutrons and so has no net angular momentum nor a net magnetic moment. The spin axes of the individual H nuclei precess around the field, and over time they tend to align with the field. However, this alignment is far from complete. Exchanges of energy between the orientation of the dipole and thermal motions prevent the dipoles from settling into their

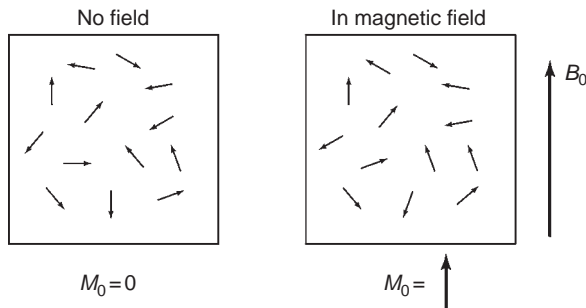


**Fig. 3.4.** Formation of an equilibrium magnetization ( $M_0$ ) as a result of partial alignment of nuclear magnetic dipoles. In the absence of a magnetic field, the spins are randomly oriented, and there is no net magnetization. When placed in a magnetic field  $B_0$ , the spins partly align with the field, a relaxation process with a time constant  $T_1$  of approximately 1 s, creating a net local magnetization.

lowest energy state. In fact, the energy difference between an H nucleus aligned with the field and one opposed to the field at 1.5 T is only approximately 1% of the random thermal energy of the water molecule. The result is that at equilibrium the difference between the number of spins aligned with the field and the number opposed to the field is only approximately 1 part in  $10^5$ . Nevertheless, this creates a weak *equilibrium magnetization*  $M_0$  aligned with the field (Fig. 3.4). The term  $M_0$  is the net dipole moment per cubic centimeter, and one can think of it loosely as a weak, but macroscopic, local magnetic field that is the net result of summing up the magnetic fields of each of the H nuclei. That is, each cubic centimeter of a uniformly magnetized sample carries a net dipole moment  $M_0$ . The magnitude of  $M_0$  is directly proportional to the local *proton density* (or *spin density*).

## The radiofrequency pulse

The local value of  $M_0$  is the net difference between dipoles aligned with the field and opposite to the field, but it is not directly observable because it is many orders of magnitude weaker than  $B_0$ . However, if all the dipoles that contribute to  $M_0$  could be tipped  $90^\circ$ , they would all precess around the field at the same rate. Thus,  $M_0$  would also tip  $90^\circ$  and begin to precess around the main field. Tipping over the magnetization produces a measurable, transient signal, and the tipping is accomplished by the RF pulse. During the transmit part of the basic NMR experiment, the oscillating RF current in the coil creates in the sample an oscillating magnetic field  $B_1$  perpendicular to  $B_0$ . The field  $B_1$  is in general several orders of magnitude smaller than  $B_0$ . Nevertheless, this causes the net magnetic field, the vector sum of  $B_1$  and  $B_0$ , to wobble slightly around the  $B_0$  direction. Initially  $M_0$  is aligned with  $B_0$ , but when the net field is tipped slightly away from  $B_0$ ,  $M_0$  begins to precess around the new net field. If the oscillation frequency of  $B_1$  is different from the precession frequency  $\nu_0$ , not much happens to  $M_0$  except a little wobbling around  $B_0$ . But if the RF frequency matches the precession frequency, a resonance phenomenon occurs. As the net magnetic field wobbles back and forth, the magnetization precesses around it in synchrony. The effect is that with each precessional rotation  $M_0$  tips farther away from  $B_0$ , tracing out a growing spiral (Fig. 3.5). After a time, the RF field is turned off, and  $M_0$  then continues to precess around  $B_0$ . The net effect of the RF pulse is thus to tip  $M_0$  away from  $B_0$ , and such pulses are usually described by the *flip angle* they produce (e.g., a  $90^\circ$  pulse or a  $30^\circ$  pulse). The flip angle can be increased either by increasing the amplitude of  $B_1$  or by leaving  $B_1$  on for a longer time.

It is remarkable that a magnetic field as weak as  $B_1$  can produce arbitrarily large flip angles. From an energetic point of view, tipping the net magnetization away from  $B_0$  increases the orientational energy of the dipoles: the nuclei absorb energy from the RF



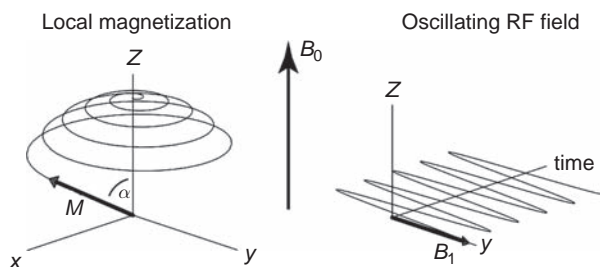


**Fig. 3.5.** Tipping over the magnetization with excitation by a radiofrequency (RF) pulse. The RF pulse is a small oscillating field  $B_1$  perpendicular to  $B_0$  that causes the net magnetic field to wobble slightly around the  $z$ -axis. As the magnetization  $M$  precesses around the net field, it traces out a widening spiral. It is tipped away from the longitudinal axis, and the final tip angle (or flip angle)  $\alpha$  is controlled by the strength and duration of the RF pulse.

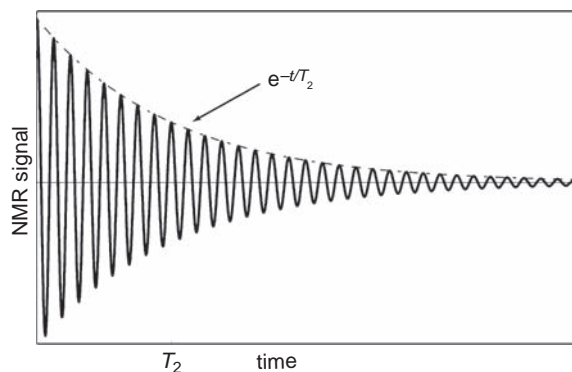


**Fig. 3.6.** Free induction decay. After a  $90^\circ$  radiofrequency pulse tips the longitudinal magnetization into the transverse plane, a detector coil measures an oscillating signal, which decays in amplitude with a time constant  $T_2$  in a perfectly homogeneous magnetic field. (In an inhomogeneous field, the signal decays more quickly, with a time constant  $T_2^* < T_2$ .) The plot is not to scale; typically the signal will oscillate more than a million times during the interval  $T_2$ .

pulse. This transfer of energy is possible even with small  $B_0$  fields because  $B_0$  oscillates at the resonant frequency of the nuclei, the precession frequency. This is much like pushing a child on a swing. The swing has a natural resonant frequency, and giving very small pushes at that frequency produces a large amplitude of motion. That is, the swing efficiently absorbs the energy provided by the pusher when it is applied at the resonant frequency.

## The free induction decay signal

A precessing macroscopic magnetization produces a magnetic field that is changing with time. This will induce a current in a nearby coil, creating a measurable NMR signal that is proportional to the magnitude of the precessing magnetization. This detected signal is called a *free induction decay* (FID) and is illustrated in Fig. 3.6. *Free* refers to free precession of the nuclei; *induction* is the electromagnetic process by which a changing magnetic field induces a current in the coil, and *decay* describes the fact that the signal is transient. The signal decays away because the precessing component of the magnetization itself decays away. The reason for this is that the individual dipoles that sum to produce the magnetization are not precessing at precisely the same rate. As a water molecule tumbles from thermal motions, each H nucleus feels a small, randomly varying magnetic field in addition to  $B_0$  primarily from the other H nucleus in the molecule. When the random field adds to  $B_0$ , the dipole precesses a little faster, and when it subtracts from  $B_0$ , it precesses a little slower. For each nucleus, the pattern of random fields is different, so as time goes on the dipoles get progressively more out of phase with one another, and as a result no longer add coherently. The net precessing magnetization then decays away exponentially, and the time constant for this decay is called  $T_2$ .

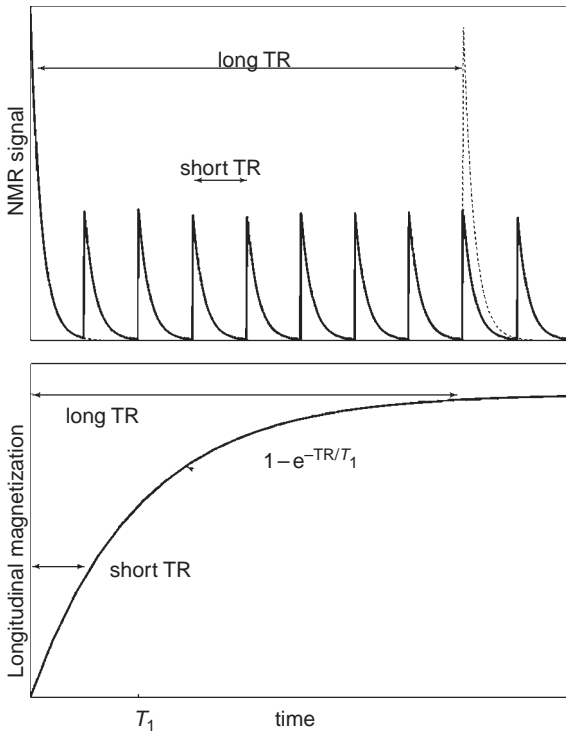


**Fig. 3.7.** Effect of repetition time (TR). Repeated radiofrequency (RF) pulses generate repeated free induction decay (FID) signals, but if TR is short, each repeated signal will be weaker than the first (top). The magnitude of the signal with a  $90^\circ$  RF pulse, is proportional to the magnitude of the longitudinal magnetization just prior to the RF pulse. After a  $90^\circ$  RF pulse, the longitudinal magnetization recovers toward equilibrium with a relaxation time  $T_1$  (bottom). If this recovery is incomplete because  $TR < T_1$ , the next FID signal is reduced.

For the human brain at a magnetic field strength of 1.5 T, some approximate characteristic values for  $T_2$  are 70 ms for white matter, 90 ms for gray matter, and 400 ms for cerebrospinal fluid (CSF). From this we can begin to see how tissue contrast can be produced in an MR image. By delaying measurement of the signal for 100 ms or so, the CSF signal will be much larger than the brain parenchyma signal, and an image of the signal distribution at that time will show CSF as bright and the rest of the brain as dark. The image on the right in Fig. 3.1 is an example of such a  $T_2$ -weighted image.

Now imagine repeating the experiment, after the signal has decayed away, to generate a new signal. How does this new signal compare with the first? The answer depends on the time between RF pulses, called the *repetition time* (TR). When TR is very long (say 20 s), the signal generated by the second RF pulse is equal in magnitude to that generated by the first RF pulse. As TR is shortened, the signal generated by the second RF pulse becomes weaker (Fig. 3.7). To generate a second full-amplitude signal, a recovery time of several times longer than  $T_1$  is required to allow the spins to relax back to equilibrium. The recovery process is also exponential, described by the time constant  $T_1$ . This relaxation time also varies among tissues: at a magnetic field of 1.5 T,  $T_1$  is approximately 700 ms for white matter, 900 ms for gray matter, and 4000 ms for CSF. Here we can see another way to produce contrast between tissues in an MR image. If the repetition time is short (say,  $TR = 600$  ms), the signal from white matter will recover more fully than that of CSF, so white matter will appear bright and CSF dark in an image, as illustrated in the image on the left in Fig. 3.1. This is described as a  $T_1$ -weighted image.

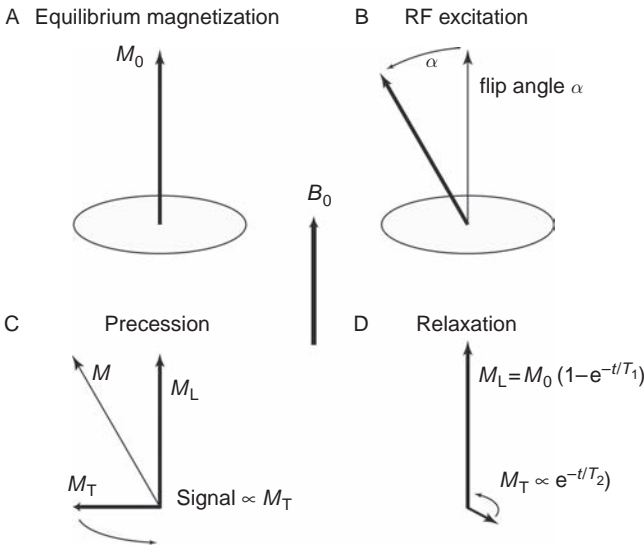


**Fig. 3.8.** The basic physics of the NMR experiment. (A) In a magnetic field  $B_0$ , an equilibrium magnetization  $M_0$  forms from the alignment of nuclear dipoles (B.C). A radiofrequency (RF) pulse tips over  $M_0$  (B), creating a longitudinal component  $M_L$  and a transverse component  $M_T$  (C). Then,  $M_T$  precesses around the direction of  $B_0$ , generating a detectable NMR signal. (D) Over time,  $M_T$  decays to zero with a relaxation time  $T_2$  and  $M_L$  recovers to  $M_0$  with a relaxation time  $T_1$ .

## The basic NMR experiment again

We can now return to the basic NMR experiment and describe it in terms of the basic physics (Fig. 3.8). A sample of water is placed in a magnetic field  $B_0$ . Over an interval of time several times longer than  $T_1$ , the magnetic dipole moments of the H nuclei tend to align with  $B_0$ , creating a local macroscopic  $M_0$  aligned with  $B_0$ . An RF pulse is applied that tips  $M_0$  away from  $B_0$ , creating a transverse magnetization  $M_T$ . The newly created transverse magnetization precesses around  $B_0$ , generating a detectable signal in the coil (the FID) with an amplitude proportional to  $M_T$ . Over time, the precessing magnetization, and, therefore, the signal, decreases exponentially, and after a time several times longer than  $T_2$  the signal is essentially gone. Meanwhile, the longitudinal magnetization along  $B_0$  slowly re-forms, so that after several  $T_1$  times we are back to where we started, with  $M_0$  aligned with  $B_0$ .

However, if another RF pulse is applied before this recovery is complete, the longitudinal magnetization will be less than  $M_0$ . When this partially recovered magnetization is tipped over,  $M_T$  will be smaller, and, therefore, the detected MR signal will also be smaller. Again, the longitudinal magnetization re-grows from zero, and if another RF pulse is applied after the same interval TR, another FID will be created. However, if the RF flip angle is  $90^\circ$ , the amount of recovery during each successive TR period is the same: the longitudinal magnetization is reduced to zero after each  $90^\circ$  pulse and then relaxes for a time TR before the next RF pulse. So the signal generated after each subsequent RF pulse is the same as that after the second pulse. This signal, regenerated with each RF pulse, is described as the steady-state signal.

Nearly all MR imaging applications involve applying a series of RF pulses at a fixed repetition time, so the steady-state signal typically is measured. In fact, the signals from the first few pulses are usually discarded to allow the magnetization to reach a steady state. In this example with  $90^\circ$  pulses, the steady state is reached after one RF pulse, but for other flip angles several pulses are necessary. Thus,  $M_0$  determines the maximum signal that can be generated; however, unless TR is much longer than  $T_1$ , the measured steady-state signal is less than this maximum.

A quantitative description of the MR signal produced by a particular tissue will, therefore, depend on at least three intrinsic tissue parameters: the proton density, which determines  $M_0$ , and the relaxation times  $T_1$  and  $T_2$ . Note that for each of the brain tissues,  $T_1$  is on the order of 10 times larger than  $T_2$ , which is usually the case with biological specimens. This means that the processes that lead to recovery are much slower than those that lead to signal decay.

We have just described a simple *pulse sequence*: an RF pulse is applied to the sample, and after a repetition time TR the same RF pulse is applied again. The signal generated after the second pulse depends on a pulse sequence parameter (TR) but also on properties of the sample (e.g.,  $T_1$ ). This basic theme runs throughout MRI. A particular pulse sequence will involve several parameters that can be adjusted in making the image, and these parameters interact with intrinsic parameters of the tissue to affect the measured signal. This dependence of the signal on multiple parameters gives MRI its unique flexibility.

At this point, it is helpful to review some of the standard terminology used in NMR. We are always dealing with a local three-dimensional magnetization vector  $M$ . This is taken to have a *longitudinal* component parallel to  $B_0$  and a *transverse* component perpendicular to  $B_0$ . The longitudinal axis is usually designated  $z$ , and the transverse plane is then the  $x$ - $y$  plane. The *transverse* component of  $M$  ( $M_{xy}$  or  $M_T$ ) is the part that precesses, so the detected signal is always proportional to the transverse component. The transverse component decays away with a time constant  $T_2$ , called the *transverse relaxation time*. At equilibrium the longitudinal magnetization has the value  $M_0$ , and there is no  $M_T$ . The time constant for the longitudinal magnetization to grow to its equilibrium value is  $T_1$ , the *longitudinal relaxation time*.

## Basic pulse sequences

### Pulse sequence parameters and image contrast

In the preceding sections, we considered how an MR signal is generated in a small volume of tissue. In MRI, the intensity of each pixel in the image is directly proportional to this local MR signal. That is, every MR image is a picture of the local value for  $M_T$  at the time the image data were collected. And because  $M_T$  is intrinsically a transient phenomenon, each MR image is a snapshot of a dynamic process at a particular time. Indeed, before the first excitation pulse there is no  $M_T$  at all, and the RF pulse sequence itself creates the quantity that is imaged. The MR signal depends on several intrinsic properties of the tissue (proton density and tissue relaxation times) and also on particular parameters of the pulse sequence used (e.g., TR). The power and flexibility of MRI derives from the fact that many pulse sequences are possible, and by adjusting pulse sequence parameters such as TR, the sensitivity of the MR signal to different tissue parameters can be adjusted to alter contrast in the image. For example, when TR is longer than any of the tissue  $T_1$  values, each local magnetization recovers completely between RF pulses, so the local magnetization is insensitive to the local  $T_1$ . But if TR is shorter than the tissue  $T_1$  values, recovery is incomplete, and the local magnetization depends strongly on the local  $T_1$ , creating a  $T_1$ -weighted signal.

At first glance, it might appear that the optimal choice of pulse sequence parameters would be those that maximize the signal. The MR signal is intrinsically weak, and noise in the images is the essential limitation on spatial resolution. In fact, maximum signal to noise ratio is not optimal for anatomical imaging as an image at such a ratio would be uniformly gray and not of much use. Instead, the contrast to noise ratio is what determines whether one tissue can be distinguished from another in the image. It is often useful for comparing

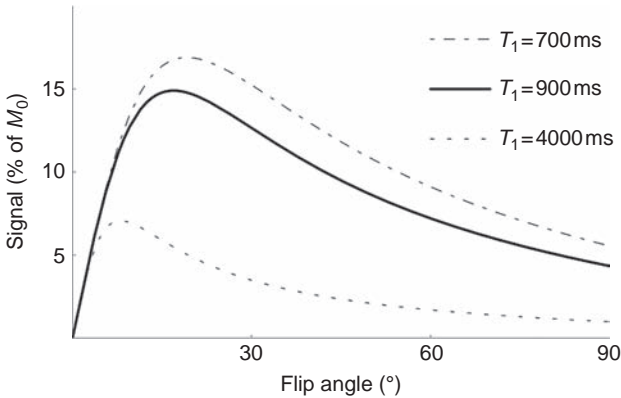


**Fig. 3.9.** Gradient recalled echo (GRE) signal. The dependence of the signal on flip angle for a spoiled GRE pulse sequence is illustrated for three values of  $T_1$ . For small flip angles, the signal is insensitive to  $T_1$  (density weighted), but it is strongly  $T_1$  weighted for larger flip angles. The flip angle for peak signal is substantially smaller than  $90^\circ$  and depends on  $T_1$ .

different pulse sequences to evaluate the contrast to noise ratio between standard tissues such as gray matter, white matter, and CSF. In the following section, we will consider the most commonly used pulse sequences and how they generate image contrast.

## Gradient echo pulse sequence

The simplest pulse sequence is the free induction decay described above: a series of RF pulses creates a precessing  $M_T$  and a measurable signal. When an FID pulse sequence is used for imaging, it is called a *gradient recalled echo (GRE) pulse sequence*, for reasons that will be explained in Ch. 4. In its basic form, the pulse sequence depends on just two parameters: TR and the flip angle  $\alpha$ . The strength of the signal depends on a combination of these adjustable parameters and the intrinsic tissue parameters  $S_0$ , the proton density, and  $T_1$ . (If the signal is measured soon after the RF pulse, there will be little time for the signal to decay away, and so it will not depend strongly on  $T_2$ .) The local MR signal is always proportional to the proton density because the proton density determines  $M_0$  and thus sets the maximum value for  $M_T$  that could be produced. If TR is much longer than  $T_1$ , the longitudinal magnetization will fully recover during TR. Because the signal does not depend on  $T_1$ , but only on the proton density ( $M_0$ ), the contrast with such a pulse sequence is described as density weighted. The fraction of the longitudinal magnetization that is tipped into the transverse plane is  $\sin \alpha$ , so a  $90^\circ$  RF pulse puts all the magnetization into the transverse plane and generates the largest signal. Therefore, for long TR the signal is density weighted and proportional to  $\sin \alpha$ .

However, with shorter TR values, the signal depends on TR,  $T_1$ , and  $\alpha$  in a more interesting way (Fig. 3.9). In fact, the signal and contrast characteristics depend on precisely how the pulse sequence is constructed, which is discussed in Ch. 6. In anticipation of the terminology introduced there, the following discussion applies to a *spoiled GRE pulse sequence*. With  $\alpha = 90^\circ$ , all the longitudinal magnetization is tipped over on each pulse, and there is little time for it to recover before the next pulse if  $\text{TR} < T_1$ . As a result, the steady-state magnetization created after each RF pulse is weak. The degree of recovery during TR depends strongly on  $T_1$ , so the resulting signal is strongly  $T_1$  weighted. Note that the signal is still proportional to  $M_0$ , and so is also density weighted, but the popular terminology is to describe such a pulse sequence as simply  $T_1$  weighted. However, the density weighting is important for determining tissue contrast. For most tissues in the body, a larger proton density is associated with a longer  $T_1$ , and this produces an essential conflict for achieving a good contrast to noise ratio between tissues: the density weighting would tend to

make the tissue with the larger  $T_1$  brighter, but the  $T_1$  weighting would tend to make the same tissue darker because there is less recovery for a longer  $T_1$ . The two sources of contrast thus conflict with each other. Nevertheless,  $T_1$ -weighted imaging is very common because the variability of  $T_1$  between tissues is much greater than the variability of proton density, and so  $T_1$  weighting usually dominates the contrast.

Alternatively, to produce a proton density-weighted image, the sensitivity to  $T_1$  must be reduced. As already discussed, this can be done simply by using a long TR so that tissues with different  $T_1$  values all recover to their equilibrium values. But a long TR is a disadvantage in conventional MRI. To collect sufficient data to reconstruct an image, the pulse sequence usually must be repeated many times, and so the total imaging time is proportional to TR. With a GRE pulse sequence there is another, somewhat surprising, way to reduce the  $T_1$  sensitivity while keeping TR short: the flip angle can be reduced (Buxton *et al.* 1987). At first glance, this would seem to reduce just  $M_T$  (and thus the signal) by tipping only a part of the longitudinal magnetization into the transverse plane. But this also modifies the steady-state amplitude of the longitudinal magnetization in a way that reduces the sensitivity to  $T_1$ . Consider the steady-state signal generated when TR is much smaller than  $T_1$ . For a  $90^\circ$  pulse, the recovery during TR is very small, and so the signal is weak (often described as saturated). If the flip angle is small, however, the longitudinal magnetization is hardly disturbed by the RF pulse. As a result, there is very little relaxation to do; the longitudinal magnetization is already near its equilibrium value. The sensitivity of the resulting signal to differences in  $T_1$  is then greatly reduced. In summary, for short TR, the signal is  $T_1$  weighted for large flip angles but only proton density weighted for small flip angles. [Figure 3.9](#) illustrates how the tissue contrast in an image can be manipulated by adjusting the flip angle.

## The decay $T_2^*$

The simple GRE pulse sequence described above illustrates how pulse sequence parameters and intrinsic tissue parameters interact to produce the MR signal. But one important tissue parameter,  $T_2$ , did not enter into the discussion. The reason  $T_2$  was left out was that we assumed that the signal was measured immediately after the RF pulse. However, the GRE sequence can be modified to insert a delay after the RF pulse before data acquisition begins. During this delay,  $M_T$  and thus the signal, would be expected to decrease exponentially with a time constant  $T_2$  through transverse relaxation. If we performed this experiment, we would indeed find that the signal decreased, but typically by much more than we would expect for a known  $T_2$ . This enhanced decay is described in terms of an *apparent transverse relaxation time*  $T_2^*$  (read as “ $T_2$  star”) that is smaller than  $T_2$ .

The source of this  $T_2^*$  effect is magnetic field inhomogeneity. Because the precession frequency of the local  $M_T$  is proportional to the local magnetic field, any field inhomogeneity will lead to a range of precession rates. Over time, the precessing magnetization vectors will get out of phase with one another so that they no longer add coherently to form the net magnetization. As a result, the net signal is reduced because of this destructive interference. At first glance this seems similar to the argument for  $T_2$  relaxation itself. It was argued above that the net value of  $M_T$  would decrease over time because each spin feels a random fluctuating magnetic field in addition to  $B_0$ . Because each spin feels a different pattern of fluctuating fields, the spins gradually become out of phase with one another (the phase dispersion increases) and net  $M_T$  is reduced. The  $T_2^*$  effect, however, results from constant field offsets rather than fluctuating fields. Because these field offsets are static, there is a clever way to correct for these inhomogeneity effects.

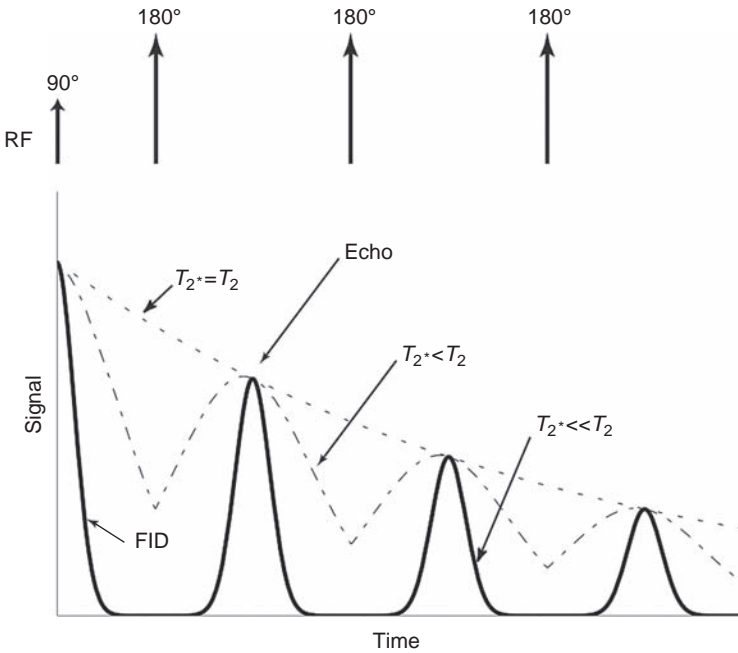


**Fig. 3.10.** Spin echo (SE). In an inhomogeneous field, spins precess at different rates, and the Free induction decay (FID) signal created after a 90° excitation pulse decays with a time constant  $T_2^*$  that is less than  $T_2$ . A 180° radiofrequency (RF) pulse refocuses this signal loss owing to static field offsets and creates a transient SE. The SE signal decays with the true  $T_2$  of the sample. Repeated 180° pulses generate repeated SEs.

## Spin echoes

In 1950, Hahn showed that a remarkable phenomenon occurs when a second RF pulse is applied following a delay after the first RF pulse. After the first RF pulse, an FID signal is generated that decays away quickly because of a short  $T_2^*$ . A second RF pulse applied after a delay  $TE/2$  creates an echo (a *spin echo* [SE]) of the original FID signal at a time  $TE$ , the *echo time*. This effect can be quite dramatic. The original FID signal can be reduced to an undetectable level, but the second pulse will create a strong echo. However, the echo is reduced in intensity from the original full FID by true  $T_2$  decay. As soon as the echo forms, it will again decay quickly through  $T_2^*$  effects, but another RF pulse will create another echo. This can be carried on indefinitely, but each echo is weaker than the last because of  $T_2$  decay (Fig. 3.10).

The phenomenon of echo formation from a second RF pulse is very general and occurs for any flip angle, although for small flip angles the echo is weak. Hahn's original demonstration (1950) used 90° flip angles, but in most applications a 180° pulse is used because it creates the strongest echo. The effect of a 180° pulse is illustrated in Fig. 3.11. After the initial 90° pulse, the individual magnetization vectors corresponding to different parts of the sample are in-phase and so add coherently. Owing to field inhomogeneity, however, each precesses at a slightly different rate. The growing phase dispersion can be visualized by imagining that we ourselves are precessing at the average rate. That is, we plot how these vectors evolve in time in a *rotating reference frame* rotating at the average precession rate. Then a magnetization vector precessing at precisely the average rate appears stationary, whereas vectors precessing faster rotate in one direction and vectors precessing more slowly rotate in the other direction.

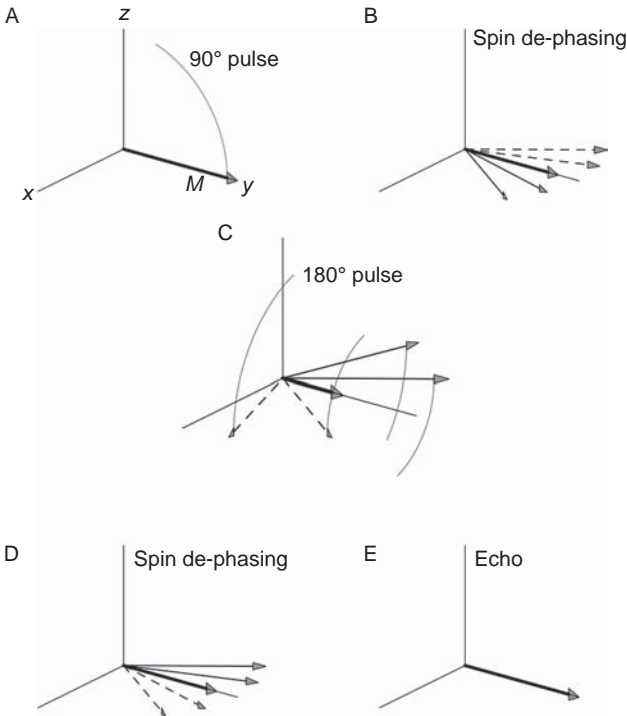


**Fig. 3.11.** Formation of a spin echo. After tipping the magnetization into the transverse plane (A), spins in different fields precess at different rates (B). Individual magnetization vectors begin to fan out, reducing the net signal. The  $180^\circ$  pulse at a time  $TE/2$  flips the transverse plane like a pancake (C), and each magnetization vector continues to precess in the same direction (D), so that they realign to form a spin echo at TE (E). TE, echo time.

Over time, the vectors spread into a fan in the transverse plane, and the net signal is reduced. However, if we now apply a  $180^\circ$  RF pulse, the fan of vectors is rotated through  $180^\circ$ , so that whatever phase was acquired by a particular vector is converted into a negative phase. After the  $180^\circ$  pulse, each vector will again precess at the same rate as before. At TE, each spin will have acquired the same additional phase that it acquired during the interval  $TE/2$  between the  $90^\circ$  and  $180^\circ$  pulses, and the net acquired phase is thus precisely zero. That is, all vectors come back in-phase and create an echo.

This effect works because the phase accumulated by a particular vector is simply proportional to elapsed time, so that the phase acquired during the first half of the echo time is identical to that acquired during the second half. Because the  $180^\circ$  pulse reverses the sign of the phase halfway through, the net phase for each vector is zero at the echo time. Because of this effect, a  $180^\circ$  RF pulse is often called a *refocusing pulse*. However, a  $180^\circ$  pulse does not refocus true  $T_2$  effects because the additional phase acquired from random fluctuations is not the same in the first and second halves of the TE. A multi-echo pulse sequence using a string of  $180^\circ$  pulses thus will create a chain of echoes with the peak of each echo falling on the true  $T_2$  exponential decay curve.

### Spin echo pulse sequence

The *SE pulse sequence* is the workhorse of clinical MRI. Field inhomogeneity is difficult to eliminate, particularly because the head itself is inhomogeneous, and  $T_2^*$  effects lead to signal loss in areas near air–tissue and bone–tissue interfaces (discussed in more detail later in the book). The particular advantage of the SE pulse sequence is that it is insensitive to these inhomogeneities, so the local signal and the tissue contrast reflect only the interaction of the



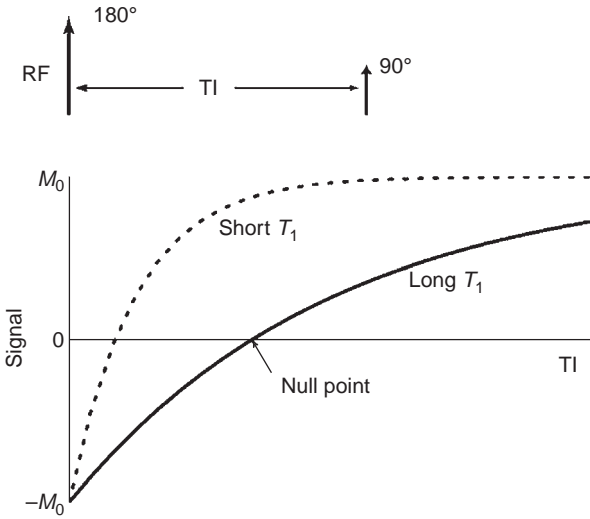


**Fig. 3.12.** Inversion recovery (IR). In an IR pulse sequence, an initial  $180^\circ$  inversion pulse flips the magnetization from  $+z$  to  $-z$ , and it then relaxes back toward equilibrium ( $M_0$ ). After an inversion time  $T_I$ , a  $90^\circ$  excitation pulse tips the current longitudinal magnetization into the transverse plane to generate a signal. The signal is strongly  $T_1$  weighted, and for a particular value of  $T_I$  exhibits a null point where no signal is generated because the longitudinal magnetization is passing through zero.

pulse sequence parameters with the intrinsic tissue parameters. The SE sequence is nearly always used with a  $90^\circ$ – $180^\circ$  combination of RF pulses, so the flip angles usually are not adjusted to control image contrast. That leaves TR and TE as the adjustable pulse sequence parameters, and three tissue parameters affect the signal:  $M_0$ ,  $T_1$ , and  $T_2$ . The dependence of the SE signal on proton density and  $T_1$  is similar to that of the GRE sequence with a  $90^\circ$  pulse. The dependence on  $T_2$  is simply an exponential decrease of the signal with increasing TE. When TE is much shorter than  $T_2$ , there is little decay, so the signal is insensitive to  $T_2$ . For  $TE \gg T_2$ , there is substantial decay and, therefore, very little signal left to measure. When TE is comparable to  $T_2$ , the signal is strongly sensitive to the local  $T_2$ , and the signal is described as  $T_2$  weighted.

In an SE pulse sequence, the signal is measured at the peak of the echo, where the effects of field inhomogeneities are refocused, and this is the standard implementation for clinical imaging. In applications such as fMRI, however, which are based on the BOLD effect, the microscopic field variations induced by changes in blood oxygenation make the MR signal sensitive to brain activation. Some sensitivity to field variations can be retained by shifting the time of data collection away from the echo peak. In such an *asymmetric spin echo pulse sequence*, the data acquisition occurs at a fixed time  $\tau$  after the RF pulse, but the time of the  $180^\circ$  pulse is shifted so that the SE occurs at a time TE different from  $\tau$ . Then, in addition to  $T_2$  decay for a time  $t$ , there will also be an additional decay owing to the phase dispersion resulting from evolution in the inhomogeneous field for a time  $\tau - TE$ .

## Inversion recovery pulse sequence

A third widely used pulse sequence is called *inversion recovery* (IR), illustrated in Fig. 3.12. This sequence begins with a  $180^\circ$  pulse, then after a delay (called the *inversion time* [TI]), a regular SE or GRE pulse sequence is started. The initial  $180^\circ$  pulse is called an inversion pulse and can be thought of as a preparation pulse that affects the longitudinal magnetization before it is tipped over to generate a signal. For the IR sequence, the preparation pulse enhances the  $T_1$  weighting of the signal. The effect of the initial  $180^\circ$  pulse is to invert the longitudinal magnetization so that it points along the  $-z$  axis instead of  $+z$ . Note that this

does not yet create a signal, because there is no  $M_T$ . After the inversion pulse, the longitudinal magnetization begins to re-grow toward its equilibrium value along  $+z$ . After a delay of TI a  $90^\circ$  pulse is applied; this pulse tips whatever longitudinal magnetization exists at that time into the transverse plane. The resulting signal thus reflects the degree of recovery during the time TI.

If TI is much longer than  $T_1$ , the longitudinal magnetization recovers completely, and the inversion has no effect on the resulting signal. But if TI is comparable to  $T_1$ , the recovery is incomplete, and the signal is strongly  $T_1$  weighted. The  $T_1$  weighting is more pronounced than in a typical  $T_1$ -weighted GRE or SE pulse sequence because the longitudinal magnetization is recovering over a wider dynamic range, from  $-M_0$  to  $M_0$  instead of from 0 to  $M_0$ . This is the essential difference between an IR experiment (following a  $180^\circ$  pulse) and a saturation recovery experiment (following a  $90^\circ$  pulse). Indeed, because the longitudinal magnetization in an IR experiment is recovering from a negative value to a positive value, there is a particular value of TI, called the *null point*, when the longitudinal magnetization is zero, and for this TI no signal is generated. A typical set of parameters for  $T_1$ -weighted IR is TI approximately equal to  $T_1$  and TR several times longer than  $T_1$  to allow recovery before the pulse sequence is repeated, beginning with another inversion pulse.

The SE and IR pulse sequences illustrate two different uses of a  $180^\circ$  RF pulse, as reflected in the descriptive terms: it is a “refocusing” pulse in the SE sequence and an “inversion” pulse in the IR sequence. In both cases, it is the same RF pulse. The difference is whether we are concerned with its effect on  $M_T$  or on longitudinal magnetization. A  $180^\circ$  pulse flips  $M_T$  like a pancake, reversing the phase of the  $M_T$  and producing an echo, but the same flip sends the longitudinal magnetization from  $+z$  to  $-z$ . In the SE experiment, the inversion effect of the  $180^\circ$  pulse is small because the longitudinal magnetization was reduced to zero by the initial  $90^\circ$  pulse, so it has only recovered a small amount during the time TE/2 between the  $90^\circ$  and  $180^\circ$  pulses. In the IR experiment, there is no  $M_T$  to refocus at the time of the  $180^\circ$  pulse, and we are interested only in its inversion effect on the longitudinal magnetization.

## References

- Bloch F (1953) The principle of nuclear induction. *Science* **118**:425–430
- Bloch F, Hansen WW, Packard M (1946) Nuclear induction. *Phys Rev* **69**:127
- Buxton RB, Edelman RR, Rosen BR, Wismer GL, Brady TJ (1987) Contrast in rapid MR imaging: T1- and T2-weighted imaging. *J Comput Assist Tomogr* **11**:7–16
- Hahn EL (1950) Spin echoes. *Phys Rev* **80**:580–593
- Kwong KK, Belliveau JW, Chesler DA, et al. (1992) Dynamic magnetic resonance imaging of human brain activity during primary sensory stimulation. *Proc Natl Acad Sci USA* **89**:5675–5679
- Lauterbur PC (1973) Image formation by induced local interactions: examples employing nuclear magnetic resonance. *Nature* **242**:190–191
- Mansfield P (1977) Multi-planar image formation using NMR spin echoes. *J Phys C* **10**:L55–L58
- Ogawa S, Lee TM, Nayak AS, Glynn P (1990) Oxygenation-sensitive contrast in magnetic resonance image of rodent brain at high magnetic fields. *Magn Reson Med* **14**:68–78
- Purcell EM (1953) Research in nuclear magnetism. *Science* **118**:431–436
- Purcell EM, Torrey HC, Pound RV (1946) Resonance absorption by nuclear magnetic moments in a solid. *Phys Rev* **69**: 37
- Vleck JHV (1970) A third of a century of paramagnetic relaxation and resonance. In *International Symposium on Electron and Nuclear Magnetic Resonance*, Coogan CK, Ham NS, Stuart SN et al., eds. Melbourne: Plenum Press, pp. 1–10

<b>Principles of MRI</b>	<i>page</i> 85
Radiofrequency coils	85
Magnetic field gradients and gradient echoes	86
Localization	88
Slice selection	89
Frequency encoding	90
Phase encoding	90
<i>k</i> -Space	91
<b>Techniques in MRI</b>	92
Fast imaging	92
Volume imaging	94
<b>Beyond anatomy</b>	95
Magnetic resonance angiography	95
Diffusion-weighted imaging	97
Magnetic susceptibility effects	98

## Principles of MRI

In [Ch. 3](#) we discussed how the local MR signal is produced as a result of the interaction of the particular pulse sequence parameters with local tissue properties. The pulse sequence produces a transient pattern of transverse magnetization across the brain. How do we map that pattern? It is remarkable that MRI is able to image the distribution of transverse magnetization in the human brain with a spatial resolution of better than 1 mm, even though the coils used for generating the radiofrequency (RF) pulses and detecting the signal are much larger. The heart of MRI can be stated in a beautifully simple way: *the phase of the local signal is manipulated in such a way that the net signal traces out the spatial Fourier transform of the distribution of transverse magnetization*. A full interpretation of what this statement means is developed in [Ch. 9](#), but the basic concepts involved in making an MR image are described here.

## Radiofrequency coils

In an MRI scanner the RF coil used to detect the MR signal is sensitive to a large volume of tissue. For example, in brain imaging studies, the subject is placed in a cylindrical coil that surrounds the head, and typically this coil is used both for the transmit and receive parts of the experiment. When one of the simple pulse sequences described above is applied, the entire head will be exposed to the RF pulses, and the resulting signal produced in the coil will be the sum of the signals from each tissue element in the head. In some studies, the transmit and receive functions are accomplished with separate coils: a large uniform coil to produce

the RF pulses and a smaller receive coil placed near the part of the head of interest. A separate receive coil is referred to as a *surface coil*. The advantage of using a surface coil is that the signal to noise ratio (SNR) is improved because the coil is nearer to the source of the signal to be detected. The cost of this, though, is that the coil is sensitive to only a small volume of tissue rather than to the whole brain. Use of a surface coil thus achieves some degree of volume localization because of its limited spatial sensitivity, but this level of localization is still much coarser than that required for imaging.

In *parallel imaging*, many smaller RF coils arranged in an array each operate as a separate receiver. This takes advantage of the high SNR of a surface coil and overcomes the problem of limited coverage. In addition, different spatial sensitivity of each coil can be exploited to reduce the time required to collect sufficient data to reconstruct an image. Current MRI systems have 8- or 16-channel head coils (or more).

## Magnetic field gradients and gradient echoes

In MRI, spatial localization of the signal is not dependent on the size of the coils used. Instead, localization is based on the fundamental relationship of NMR (Eq. [3.1]): the resonant frequency is directly proportional to the magnetic field at the location of the nucleus. Magnetic resonance imaging is based on manipulations of the local resonant frequency through control of the local magnetic field by applying *magnetic field gradients*. In an MR scanner, there are three gradient coils in addition to the RF coils and the coils of the magnet itself. Each gradient coil produces a magnetic field that varies linearly along a particular axis. For example, a  $z$ -gradient coil produces a magnetic field that is zero at the center of the magnet and becomes more positive moving along the  $+z$  direction and more negative moving along the  $-z$  direction. The three gradient coils are designed to produce field gradients along three orthogonal directions ( $x$ ,  $y$ , and  $z$ ) so that a field gradient along any arbitrary direction can be produced by turning them on in appropriate combinations. The fields produced by the gradient coils add to the main magnetic field  $B_0$  but are much weaker. Nevertheless, these gradients have a pronounced effect on the MR signal.

A key concept in MRI is the phenomenon of a *gradient echo* (Fig. 4.1). The idea of a gradient echo occurs often, and we have already noted that a simple free induction decay (FID) imaging sequence is referred to as a gradient echo pulse sequence. As we will see, this terminology is somewhat unfortunate, but it is now standard usage. To understand what a gradient echo is, consider a simple FID experiment in which a signal is generated, and suppose that a field gradient in  $x$  is then turned on for a few milliseconds (described as a *gradient pulse*). How does this affect the signal? Prior to the field gradient there is a strong coherent signal, as long as  $T_2^*$  is not too short. Each spin precesses at the same rate, so at any instant of time the angle that each magnetization vector makes in the transverse plane (the phase angle) is the same. But with the field gradient on, the magnetization vectors of the spins at different  $x$ -positions precess at different rates. As the magnetization vectors get out of phase with each other, the net signal drops to near zero. The gradient pulse thus acts as a *spoiler* pulse, destroying the coherence of the transverse magnetization.

After the gradient is turned off, the spins again precess at the same rate, but the phase differences induced by the gradient remain locked in. Now suppose that another gradient pulse with the same amplitude is applied, but this time with opposite sign to the first one. By opposite sign, we mean that the gradient runs in the opposite direction. If the first gradient increases the precession rate at positive  $x$ -positions, the second decreases it. If this gradient pulse is left on for the same amount of time as the first, it will precisely unwind the phase

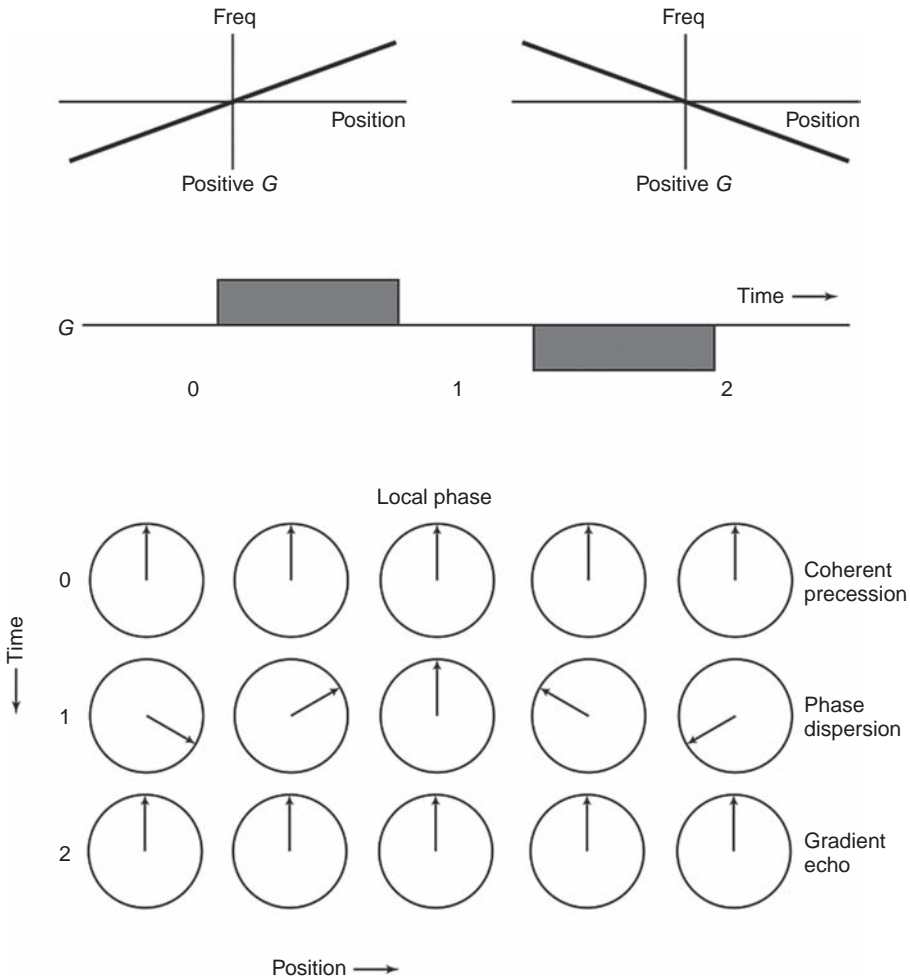


**Fig. 4.1.** Effect of a gradient pulse. In a uniform field, spins precess at the same rate and remain in phase (time point 0). A gradient field produces a linear variation of the precession rate with position (top). At the end of the first gradient pulse (time point 1), the local phase angle varies linearly across the object (phase dispersion). A gradient pulse of opposite sign and equal area reverses these phase offsets and creates a gradient echo when the spins are back in phase (time point 2). freq, frequency.

offsets produced by the first gradient pulse. The result is that the signals arising from different  $x$ -positions come back into phase, creating a gradient echo at the end of the second gradient pulse. For this reason, the second gradient pulse is called a *refocusing* pulse. A gradient echo can occur even when the second pulse has a different amplitude or duration provided that the area under the two pulses is the same. Or, put another way, a gradient echo occurs whenever the net area under the gradient waveform is zero.

A gradient echo can also occur in a spin echo (SE) experiment. Suppose in the experiment above that a  $180^\circ$  RF pulse is inserted after the first gradient pulse. This will change the sign of each of the phases acquired during the first pulse, so now to unwind them the second gradient pulse should have the *same* sign as the first. Again the gradient echo occurs when the spins are back in phase after the second gradient pulse. The rule for an SE pulse sequence is

that a gradient echo occurs when the areas under the gradient pulses are equal on the two sides of the  $180^\circ$  pulse.

The phenomenon of a gradient echo is reminiscent of the process of a SE. The SE refocuses phase offsets caused by static field inhomogeneities, and the gradient echo refocuses phase offsets produced by a gradient pulse. This was the original motivation for calling an FID pulse sequence a gradient recalled echo (GRE) imaging sequence (i.e., that an SE pulse sequence uses an RF echo, and a GRE sequence uses a gradient echo). But this is highly misleading. All imaging pulse sequences, including SE, use gradient echoes as a basic part of the imaging process. In fact, the SE is not directly involved in image formation at all; it simply improves the local signal that is being mapped by refocusing the effects of inhomogeneities. But this terminology is now ubiquitous: any imaging pulse sequence that lacks a  $180^\circ$  refocusing pulse is called a gradient echo pulse sequence.

## Localization

The central task of MRI is to extract information about the spatial distribution of the MR signal. This is a three-dimensional problem: the source of each component of the signal must be isolated to a particular location  $(x, y, z)$ . Any spatial localization method has resolution limits, so the imaging process will lead to some degree of uncertainty about the precise location of the source of the signal. We can express this uncertainty in terms of a volume resolution element (voxel) with dimensions  $(\Delta x, \Delta y, \Delta z)$ . Each of these numbers characterizes the uncertainty of the localization along a particular spatial axis, and the product  $\Delta V = \Delta x \Delta y \Delta z$  is called the voxel volume. It is often convenient to think of a voxel as a rectangular block, but it is important to remember that the localization is never that precise. The quantitative meaning of resolution will be discussed in greater detail in [Ch. 9](#).

In MRI, localization is done in three ways corresponding to the three spatial directions: *slice selection*, *frequency encoding*, and *phase encoding*. The gradient pulses used to accomplish this encoding are shown in [Fig. 4.2](#). The usual terminology is to describe the slice selection axis as  $z$ , the frequency-encoded axis as  $x$ , and the phase-encoded axis

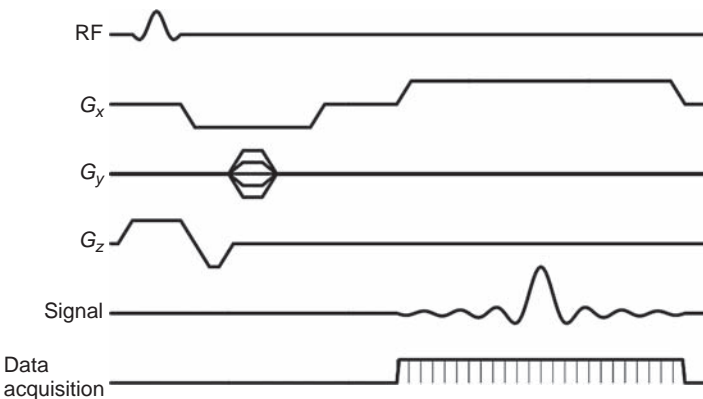


**Fig. 4.2.** A basic imaging pulse sequence. During the radiofrequency (RF) excitation pulse, a gradient in  $z$  is applied (slice selection), and during read-out of the signal a gradient in  $x$  is applied (frequency encoding). Between these gradient pulses, a gradient pulse in  $y$  is applied, and the amplitude of this pulse is stepped through a different value each time the pulse sequence is repeated (phase encoding). Typically 128 or 256 phase-encoding steps (repeats of the pulse sequence) are required to collect sufficient information to reconstruct an image.

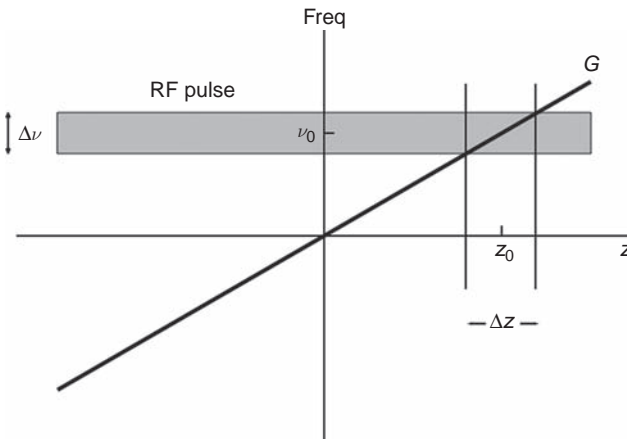


**Fig. 4.3.** Slice selection.

A radiofrequency (RF) excitation pulse with a narrow bandwidth ( $\Delta\nu$ ) is applied in the presence of a  $z$ -gradient. The RF pulse centered on frequency (freq)  $\nu_0$  is on-resonance only for spins within a narrow band of positions  $\Delta z$  centered on  $z_0$  so that only these spins are tipped over.

as  $y$ . However, the actual orientation of this coordinate system in space is arbitrary. In particular, this imaging coordinate system does not have any fixed relationship to the coordinate system used to describe the magnetic field, in which the longitudinal axis along the direction of  $B_0$  was called  $z$  and the transverse plane was called the  $x$ - $y$  plane. The imaging coordinate system can have any orientation relative to the magnetic field, even though both the direction of  $B_0$  and the axis perpendicular to the image plane are usually referred to as the  $z$ -axis. In transverse (or axial) images, the slice selection axis is along the magnetic field direction in most scanners, but in coronal images the two directions are perpendicular.

## Slice selection

With slice selection, the effect of the RF pulse is limited to a single thin slice, typically 1–10 mm thick (Fig. 4.3). This is accomplished by turning on a gradient field along the slice selection axis ( $z$ , perpendicular to the desired slice) while the RF pulse is applied. While the gradient field is on, the resonant frequency will vary linearly along the  $z$ -axis. The RF pulse is tailored so that it contains only a narrow range of frequencies, centered on a frequency  $\nu_0$ . Then because of the presence of the gradient field, only a narrow spatial band in the body will have a resonant frequency within the bandwidth of the RF pulse. On one side of the slice, the local resonant frequency will be too high, and on the other side too low. When the frequency of the RF pulse differs from the local resonant frequency, the pulse has little effect on the local longitudinal magnetization. As a result, the effect of a slice selective RF pulse is to tip over the magnetization only in a restricted slice.

The location of the slice can be varied by changing the center frequency  $\nu_0$  of the RF pulse, and the spatial thickness of the excited slice depends on the ratio of the frequency width of the RF pulse to the strength of the field gradient. If the gradient is increased, the resonant frequency becomes a steeper function of position along the  $z$ -axis, and so the same RF band corresponds to a thinner slice. Similarly, reducing the bandwidth of the RF pulse with the same gradient strength excites a thinner slice. In practice, the slice width typically is adjusted by changing the gradient strength, and on most MR imagers the maximum available gradient strength limits the thinness of selected slices to 1–2 mm.

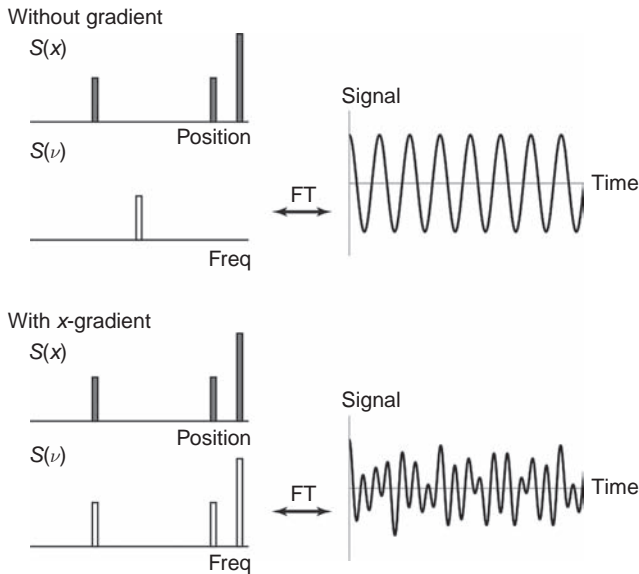


**Fig. 4.4.** Frequency encoding. Three small signal sources ( $S$ ) are shown at different locations on the  $x$ -axis. During data collection, with no field gradient, all spins precess at the same rate, but with a gradient field in  $x$  the frequencies of the three sources are spread out, and this is reflected in the interference of these signals in the net signal. From the net signal, the frequency (freq) spectrum is calculated with the Fourier transform (FT), and the spectrum provides a direct measure of the spatial distribution of the signal along  $x$ .

## Frequency encoding

Slice selection limits the effects of the RF excitation pulse so that transverse magnetization is created only in one slice. However, the net signal still reflects the sum of all the signals generated across the slice, and the remaining localization in the  $x$ - $y$  plane is done with frequency encoding and phase encoding. These two methods are closely related, and both have the remarkable effect of encoding information about the spatial location of the signal into the signal itself. For frequency encoding, a negative field gradient pulse along the  $x$ -axis is turned on after the excitation RF pulse. Following this pulse, a positive  $x$ -gradient is turned on so that a gradient echo occurs halfway through the second gradient pulse. The data collection window is typically centered on this gradient echo (Fig. 4.2). Because the gradient is turned on during data collection, the precession frequency of the local magnetization varies linearly along the  $x$ -axis. The net signal is thus transformed from a sum of signals all at the same frequency to a sum of signals covering a range of frequencies (Fig. 4.4), and the signals corresponding to each frequency can be readily separated. Any signal measured as a series of amplitudes over time can be converted to a series of amplitudes corresponding to different frequencies ( $\nu$ ) by calculating the Fourier transform. Thus, the measured signal  $S(t)$  is mathematically transformed to  $S(\nu)$  and because of the field gradient, frequency corresponds directly with spatial position along the  $x$ -axis.

## Phase encoding

Slice selection limits the signal generated to one slice, and frequency encoding separates the signals arising from different positions along the  $x$ -axis. But each of these separated signals is still a sum of all the signals arising from different  $y$ -positions at a single  $x$ -position. That is, frequency encoding measures a one-dimensional projection of the image on to the  $x$ -axis. This suggests a way to make a full two-dimensional image that is directly analogous to that in computed tomography. The pulse sequence is repeated, exciting a new signal pattern across the slice, but the  $x$ -axis is rotated slightly so that a new projection of the two-dimensional image



is acquired. By continuing to repeat the pulse sequence, each time measuring a different projection, sufficient information can be gathered to reconstruct the two-dimensional image. (This typically requires 128 or more different projection angles.) The rotation of the gradient axis is accomplished by turning on two of the gradient coils at once, varying the relative current applied to each one. The first demonstration of MR imaging by Lauterbur (1973) used this *projection reconstruction* technique. Such techniques are still used in some specialized MRI applications, but conventional MRI uses phase encoding to collect equivalent information.

Phase encoding is a more subtle technique, but it is closely related to frequency encoding. During the interval between the RF pulse and the data acquisition, a gradient field along the  $y$ -axis is applied for a short interval (Fig. 4.2). While the  $y$ -gradient is on, the transverse magnetization at different  $y$ -positions precesses at different rates, so the phase difference between the signals at two positions increases linearly with time. After the gradient is turned off, all spins again precess at the same rate, but with the  $y$ -dependent phase differences locked in. The effect is then that, prior to frequency encoding and data acquisition, each local precessing magnetization is marked with a phase offset proportional to its  $y$ -position. The frequency-encoding process then produces further phase evolution of the signal from a voxel with the rate of change of the phase (i.e., the frequency) proportional to the  $x$ -position. Data acquisition completes one phase-encoding step.

The full image acquisition requires collection of many steps, typically 128 or 256. For each phase-encoding step, the pulse sequence is repeated exactly the same except that the amplitude of the  $y$ -gradient is increased in a regular fashion (typically illustrated as stepped pulses, as in Fig. 4.2). The effect of the increased gradient amplitude is that the  $y$ -dependent phase acquired by the magnetization at a particular  $y$ -position also will increase. Thus, with each repetition the phase of the magnetization at position  $y$  will increase at a rate proportional to  $y$ . But these phase increases with each phase-encoding step are precisely analogous to the phase increases with time during frequency encoding: the rate at which phase increases with time is the definition of frequency.

We can summarize the imaging process as follows. The local transverse magnetization of a small volume of tissue is a precessing vector, so at any point in time it can be described by two numbers: a magnitude, which depends on the local relaxation times and the pulse sequence parameters described above, and a phase angle, which describes how much the magnetization has precessed up to that time. The application of field gradient pulses alters the local phase by speeding up or slowing down the precession in a position-dependent way. Then in MRI an image of the magnitude of the local transverse magnetization is created by encoding the location of the signal in the phase of the magnetization. The  $x$ -position of a local signal is encoded in the rate of change of the phase of the signal with time during each data acquisition window, and the  $y$ -position is encoded in the rate of change of the local phase between one data acquisition window and the next. Although these two processes both manipulate the phase of the signal, they do not interfere with one another.

## $k$ -Space

We can picture this imaging process as measuring a data matrix in which the signals measured for one phase-encoding step constitute one line in the matrix (Fig. 4.5). Stepping through all the phase-encoding steps fills in the data matrix, and the image is calculated by applying the two-dimensional Fourier transform to the data. Just as a time series can be represented as a sum of pure frequencies with different amplitudes, a distribution in space can be represented in terms of amplitudes of different spatial frequencies ( $k$ ). The two-dimensional Fourier

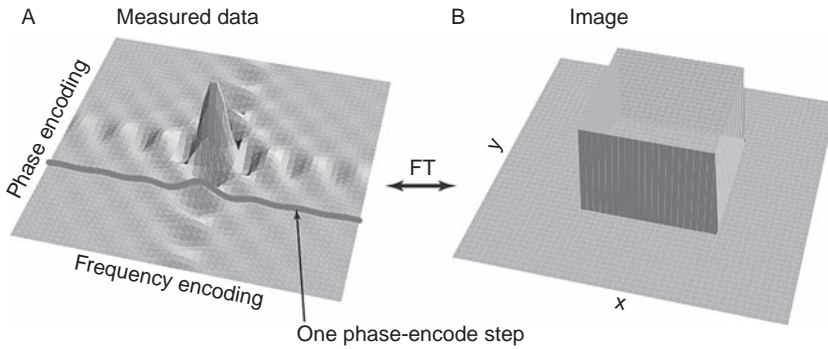


**Fig. 4.5.** Basic Fourier imaging. The measured data is the two-dimensional Fourier transform (FT) of the spatial distribution of transverse magnetization (pictured as a square in B). Each time the pulse sequence in Fig. 4.2 is repeated one line is measured, and the phase-encoding step moves the sampling to a new line. Applying the FT along both directions yields the image. The representation of the image in terms of spatial frequencies (A) is described as  $k$ -space, where  $k$  is a spatial frequency (inverse wavelength). (See plate section for color version.)

transform of the image relates the image to this  $k$ -space representation, and so MRI directly maps  $k$ -space. The spatial resolution of the image depends on the range of  $k$  values measured (i.e., the largest values of  $k$  that are sampled). Resolution in  $x$  can be improved by using a stronger read-out gradient or by extending the data collection time. Resolution in  $y$  can be improved by increasing the strength of the maximum phase-encoding gradient. Viewing the MRI process as a sampling of the  $k$ -space representation of the image is a powerful tool for understanding many aspects of MRI, and this approach is developed in detail in Ch. 9.

## Techniques in MRI

### Fast imaging

In the conventional imaging scheme just described, the data corresponding to one phase-encoding step are acquired each time the pulse sequence is repeated. With each repetition, another excitation pulse is applied, generating a new signal that is then position encoded. The total imaging time depends on the total number of phase-encoding steps and the repetition time (TR). For example, for a resolution of 128 pixels across the field of view in the  $y$ -direction, 128 phase-encoding steps are required. A  $T_1$ -weighted SE image, with a TR of 500 ms, would require approximately 1 min of imaging time. However, a  $T_2$ -weighted SE image, with a TR of 3000 ms, would require approximately 6 min. One approach to faster imaging is to use a GRE pulse sequence and simply reduce the TR, using the flip angle to adjust the contrast. For example, with TR = 7 ms, a  $128 \times 128$  image can be collected in less than 1 s.

Another approach to reducing the imaging time is to collect the data corresponding to more than one phase-encoding step from each excitation, and there are a number of schemes for doing this (Fig. 4.6 shows some examples). In echo planar imaging (EPI), the gradients are oscillated so rapidly that sufficient gradient echoes are created to allow measurement of all the phase-encoding steps required for an image (Mansfield 1977). In this single-shot imaging, the full data for a low-resolution image are acquired from the signal generated by one RF pulse. Echo planar imaging requires strong gradients and puts more demands on the imaging hardware than does conventional imaging. Single-shot images can also be collected with pulse sequences that generate a string of SEs, a technique originally called

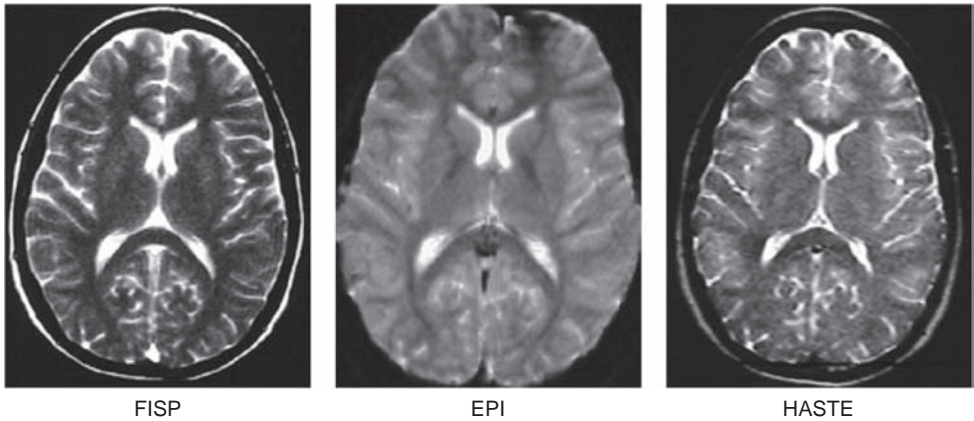


**Fig. 4.6.** Examples of techniques for fast MRI. The fast imaging with steady-state precession (FISP) pulse sequence collects one phase-encoding step after each radiofrequency (RF) excitation, but the repetition time is very short (7 ms), so the total data collection time is approximately 900 ms. The echo planar imaging (EPI) and half Fourier acquisition single-shot turbo spin echo (HASTE) sequences are examples of single-shot imaging, in which all the phase-encoding lines following one RF pulse are collected in fewer than 100 ms with a series of gradient echoes (EPI) or collected in fewer than 300 ms with a series of spin echoes (HASTE). (Images courtesy of D. Atkinson.)

rapid acquisition with relaxation enhancement (RARE) (Hennig *et al.* 1986). A more recent descendent of RARE is HASTE (half Fourier acquisition single-shot turbo spin echo), which is also a single-shot technique, and fast spin echo (FSE), which uses multiple excitations but a train of SEs following each one, with each SE phase encoded differently. For example, if an echo train of eight echoes is used, the imaging time is reduced by a factor of eight from that of a conventional image. This reduction is not as dramatic as with the single-shot techniques, but single-shot images are also low resolution. The FSE techniques are widely used in clinical imaging because they greatly reduce the imaging time for  $T_2$ -weighted imaging without sacrificing resolution or SNR.

Although blood oxygenation level dependent (BOLD) activations have been demonstrated with many different imaging schemes, most fMRI work is done with single-shot EPI. The image matrix is typically  $64 \times 64$ , so the spatial resolution is poorer than with standard MR images, but the temporal resolution is far better. The entire data collection window for the image can be as short as 30 ms. Spatial resolution can be improved by using multishot EPI, in which a few RF pulses are used to collect data for more phase-encoding steps, but at the expense of more imaging time. One of the key advantages of single-shot imaging is that the data collection is so short that the images are insensitive to motions that would create artifacts in standard images, such as pulsatile flow, swallowing, and other patient motions.

Finally, as noted above, parallel imaging techniques can further reduce the imaging time (de Zwart *et al.* 2006; Wiesinger *et al.* 2006). An array of coils provides some spatial sensitivity, because each coil is most sensitive to the closest parts of the head. Effectively, this known spatial sensitivity provides some of the information that sampling  $k$ -space provides, and this makes it possible to reconstruct a full image from a reduced set of  $k$ -space data. By reducing  $k$ -space sampling, the acquisition time typically can be reduced by a factor of two or more.

## Volume imaging

The techniques just described are all examples of two-dimensional planar imaging. Only one slice is acquired at a time by selectively exciting just that one slice. With these techniques, a volume can be imaged by simply imaging many slices in succession. For example, with EPI, as soon as the acquisition is completed on one slice, another slice can be excited and imaged. With more conventional imaging, requiring many RF pulses, the multiple slices can be interleaved in an efficient way. A *multislice interleaved* acquisition takes advantage of the fact that the data acquisition on one slice requires only a small fraction of TR because the TR is chosen to produce a desired tissue contrast. For example, with a  $T_1$ -weighted SE sequence (TR = 500 ms; echo time [TE] = 20 ms), the pulse sequence has completely played out after approximately 25 ms. During the long dead time between repetitions, data for other slices are acquired sequentially until it is time to return to the original slice after a delay TR and acquire data for another phase-encoding step. In this interleaved multislice acquisition, there is no time cost for imaging multiple slices; the scanner is simply acquiring data more efficiently by using the dead time. For EPI, however, multiple slices are acquired sequentially, so the time required to cover a volume is directly proportional to the number of slices needed. On most scanners equipped with EPI, the maximum image acquisition rate is in the range of 15 to 20 images per second.

The methods described so far are all intrinsically two-dimensional methods, but true three-dimensional imaging also can be done. The slice selective pulse is eliminated so that the whole volume of tissue within the RF coil is excited, or reduced so that only a thick slab is excited. Spatial information in the third ( $z$ ) dimension is then encoded by phase encoding that axis in addition to the  $y$ -axis. This means that data must be collected for every possible pairing of phase-encoding steps in  $y$  and  $z$ . That is, for each of the phase-encoding steps in  $y$ , the full range of phase-encoding steps in  $z$  must be measured. Compared with a single slice acquisition, the total imaging time is then increased by a factor equal to the number of phase-encoding steps in  $z$ . This makes for a prohibitively long acquisition time unless the TR is very short. But with GRE acquisitions, the TR can be shorter than 10 ms, so volume acquisitions with high spatial resolution are possible in a few minutes.

The advantage of a three-dimensional acquisition is a large improvement in the SNR. The SNR in an image depends on two factors: the voxel volume, which determines the raw signal contributing to each voxel, and the number of times the signal from a voxel is measured, which helps to beat down the noise. For the same TR and TE, the SNR is then proportional to  $\Delta V\sqrt{n}$ , where  $\Delta V$  is the voxel volume (the product of the resolution in each direction:  $\Delta x\Delta y\Delta z$ ) and  $n$  is the total number of measurements made of the signal from a voxel. For a standard two-dimensional acquisition, with  $n_x$  samples collected during frequency encoding on each of  $n_y$  phase-encoding steps,  $n = n_x n_y$ . If each phase-encoding step is averaged  $n_{av}$  times,  $n = n_{av} n_x n_y$ . For a multislice interleaved acquisition, the data collected on subsequent slices does not contribute to the SNR of a voxel in the first slice. In a three-dimensional acquisition, however, the signal from each voxel contributes to every measurement, so  $n = n_{av} n_x n_y n_z$ . With this boost in SNR, it is possible to reduce the voxel volume and acquire high-resolution images with a voxel volume of  $< 1 \text{ mm}^3$  while maintaining reasonable SNR. The factors that affect image SNR are discussed more fully in Ch. 9.

A commonly used volume-imaging sequence is MP-RAGE (magnetization prepared rapid gradient echo), which combines a periodic inversion pulse to enhance the  $T_1$  weighting in the image with a rapid GRE acquisition to produce images of high spatial resolution with good contrast between gray matter and white matter (Fig. 4.7).

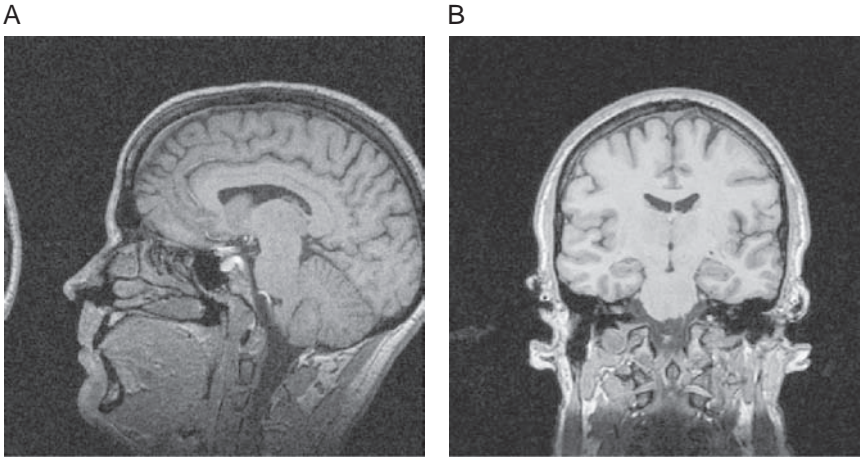


**Fig. 4.7.** Images of high spatial resolution collected with a volume-imaging pulse sequence. (A) Sagittal section 1 mm thick from a volume collected in approximately 8 min. (B) Coronal section 3 mm thick from a volume collected in approximately 12 min. Note the improved signal to noise ratio in the image on the right with the larger voxel and longer acquisition time.

## Beyond anatomy

In MRI, as described above, contrast in an image results from the interplay of a few adjustable pulse sequence parameters (e.g., TR and TE) and physical properties of the local tissue (e.g., proton density,  $T_1$ , and  $T_2$ ). Because these physical quantities vary between tissues, the resulting images provide a sensitive map of anatomy. However, MRI is such a flexible technique that it is possible to make the MR signal sensitive to several other physiological parameters, and this can carry MRI beyond anatomical imaging. These techniques open the door to fMRI and the mapping of physiological activity as well as anatomy. It is interesting to note that the physical effects that underlie these fMRI techniques first appeared as artifacts in conventional anatomical MRI: sensitivity to motion and magnetic field inhomogeneities.

## Magnetic resonance angiography

Sensitivity of MRI to bulk motion makes possible direct imaging of blood flowing in large vessels and the construction of MR angiograms for visualizing the vascular tree (Anderson *et al.* 1993; Schellinger *et al.* 2007). These MR angiography (MRA) techniques are non-invasive and do not require administration of a contrast agent; the intrinsic motion of the blood distinguishes it from the surrounding tissue.

Two effects of motion on the MR signal underlie MRA techniques. The *time-of-flight* (TOF) effect results from refreshment of blood in the imaging slice by flow. Imagine an image plane cutting through a blood vessel with fast flow. In the imaging process, the pulse sequence is repeated at TR. For a static tissue, if TR is shorter than  $T_1$ , the longitudinal magnetization will not fully recover, so the steady-state magnetization will be reduced or partly saturated. With a short TR gradient echo pulse sequence with a large flip angle, the tissue signal is usually substantially reduced by this saturation. If, however, the flow in the blood vessel is fast enough, the blood in the imaging plane will be replaced by fresh blood carrying a fully relaxed magnetization during each TR interval. As a result, the

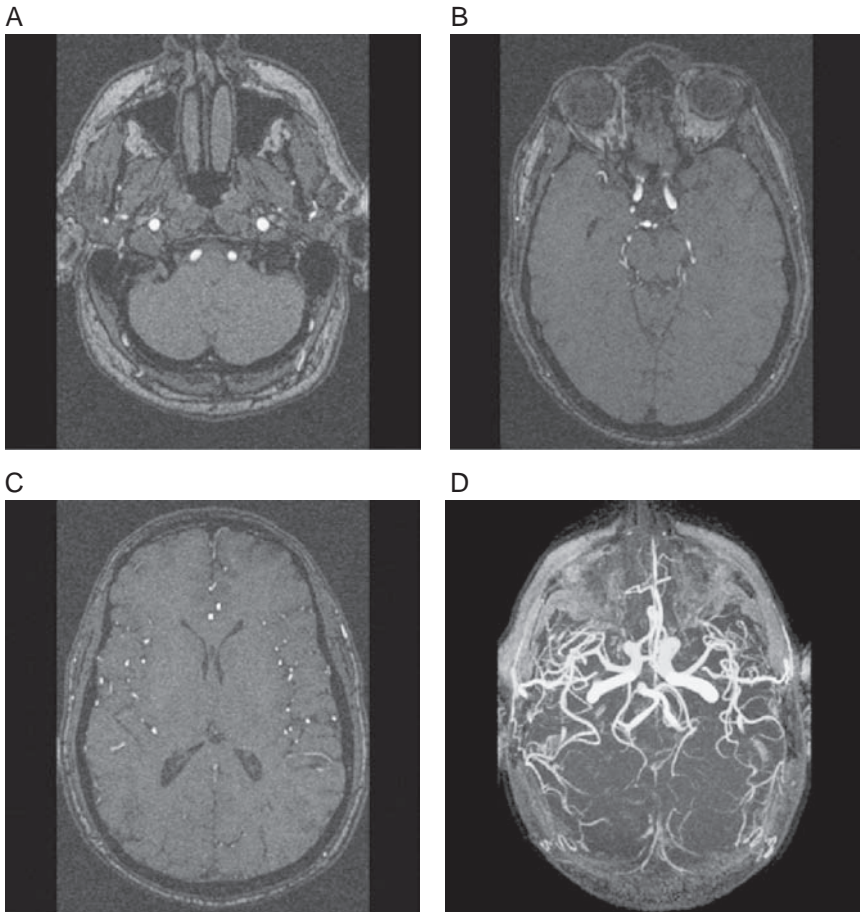


**Fig. 4.8.** Time-of-flight MR angiography. In these thin-section (1 mm) volume acquisitions, the signal of flowing blood is refreshed, but the signal of static tissue is saturated, creating strong contrast between blood and tissue in the images. Data were collected as six slabs, with a saturation pulse applied above each slab to reduce the refreshment effect for veins, so the visible vessels are primarily arteries. The sections shown illustrate cuts through carotid and vertebral arteries in the neck (A), major cerebral arteries near the circle of Willis (B), and smaller arteries (C). The maximum intensity projection through the full stack of 135 images (D) reveals the arterial vascular tree.

blood signal when this magnetization is tipped over will be much stronger than the signal of the surrounding tissue, creating strong image contrast. Because of this *inflow effect*, the MR image shows bright focal spots where the image plane cuts through blood vessels (Fig. 4.8).

A common way to view these data, which brings out the structure of the vascular tree, is to take a stack of such images and view them with a *maximum intensity projection* (MIP). The projection image is constructed by viewing the three-dimensional data set along a chosen axis, and taking the maximum intensity encountered along the ray for each ray through the data as the intensity in the projection image (Fig. 4.8). Typically a series of projections from different angles are calculated and viewed as a cine loop.

The second effect of motion on the MR signal is a phase effect, and this is the basis of the *phase contrast MRA techniques*. The phase of the local MR signal is altered whenever

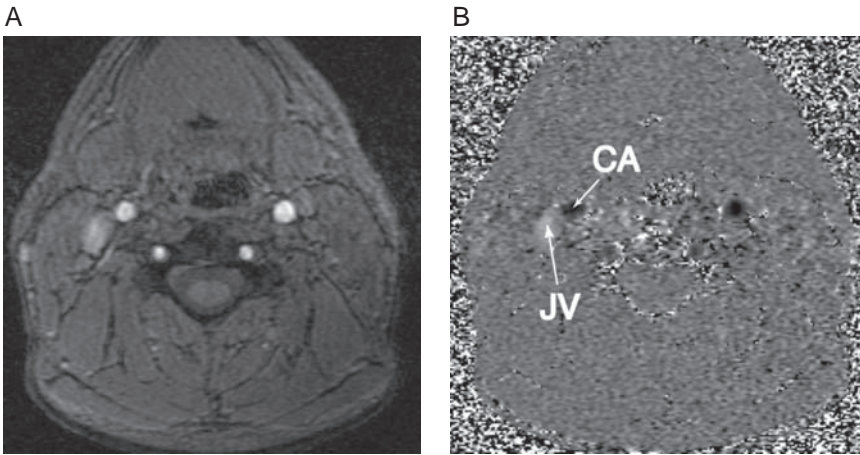


**Fig. 4.9.** Phase contrast MR angiography. This differs from time-of-flight (TOF) acquisitions by the addition of bipolar gradient pulses along one of the spatial axes, and both the magnitude image (A) and the phase image (B) now carry information on flow. The result is that the phase of the local signal (B) is proportional to the velocity along the axis of the bipolar gradient. The magnitude image (A) shows some TOF contrast enhancement in both the carotid artery (CA) and the jugular vein (JV), indicating flow refreshment in both vessels, but the phase image (B) also reveals the magnitude and direction of the flow (note the opposite phase offsets in the artery and vein, indicated by arrows).

a bipolar gradient pulse is applied in the presence of motion. A bipolar pulse consists of a gradient pulse followed by another of opposite sign and forms the basis of the idea of a gradient echo (Fig. 4.1). For static spins, the first lobe of the gradient pulse creates a phase offset that depends on the spins' position. The second lobe with opposite sign reverses that phase offset and brings all the spins back in phase. If, however, the spin moves along the gradient axis during the interval between the two lobes, then the phase acquired during the second lobe will not be precisely the opposite of the phase acquired during the first lobe. The signal from moving spins will thus acquire a phase offset. This offset is proportional to the distance moved and so is proportional to the spins' velocity. This has two important results. First, this effect provides a way to measure quantitatively the velocity of flowing blood by measuring the phase of the local signal. Second, any dispersion of velocities within an imaging voxel will lead to a range of phase angles and attenuation of the net signal. Consequently, in areas where the flow pattern is reasonably uniform on the scale of a voxel, the phase effect can be used to map flow velocity, but in areas of complex flow the signal may be destroyed by phase dispersion. Figure 4.9 shows an example of phase contrast MRA.

## Diffusion-weighted imaging

Sensitivity to motion also can be pushed to the microscopic scale with *diffusion-weighted imaging* (DWI), which is sensitive to the intrinsic random thermal motions of water molecules (Le Bihan 1991). Clinical applications of diffusion imaging have shown that the local diffusion of water is altered in stroke and that this alteration is detectable before there are changes in the MR relaxation times (Baird and Warach 1998; Schaefer *et al.* 2006). In addition, diffusion is not always isotropic. In white matter, water diffuses more readily along the fiber tracts, and this effect can be used to map fiber orientations (Jellison *et al.* 2004; Moseley *et al.* 1990).

Diffusion-weighted imaging methods also are based on the effect of motion on the phase of the MR signal. Because of their intrinsic thermal energy, water molecules are in constant random motion and so over time each molecule tends to drift away from its starting location. As a result of this self-diffusion, a molecule moves only approximately  $20\ \mu\text{m}$  during a 100 ms interval, but this small displacement is sufficient to have a measurable effect on the MR signal with appropriate pulse sequences. With a sufficiently strong bipolar gradient pulse, even these small displacements can create significant phase offsets, and because the motions are random a range of phase offsets is produced. The net signal from the voxel is attenuated by the phase dispersion, and the degree of attenuation depends on the magnitude of the diffusional motions. In tissues, the diffusional motion of water is often restricted by the presence of membranes and large protein molecules; as a result, the magnitude of the diffusion varies among tissues and sometimes along different directions within one tissue, such as white matter. Diffusion effects on the MR signal are considered in more detail in [Ch. 8](#).

## Magnetic susceptibility effects

When a body is placed in a magnetic field  $B_0$  created by the magnet, the local field at a particular location is not just  $B_0$ . All materials become partly magnetized as magnetic moments within the body tend to align with the field, and the net field at any location is then  $B_0$  plus the field generated by the magnetized body itself. Magnetic susceptibility is a measure of the degree to which a material becomes magnetized when placed in a magnetic field. Whenever dissimilar materials are in close proximity, there are likely to be magnetic field distortions because of different magnetic susceptibilities. This is often seen at interfaces of air, bone, and other tissues, as illustrated in [Fig. 4.10](#). This figure shows the magnitude and phase of a coronal GRE image of the brain. Because each local spin precesses at a rate proportional to the local field, an image of the phase of the signal is a map of the field offset. The phase of a GRE image is thus a useful way to map the distortions of the magnetic field.

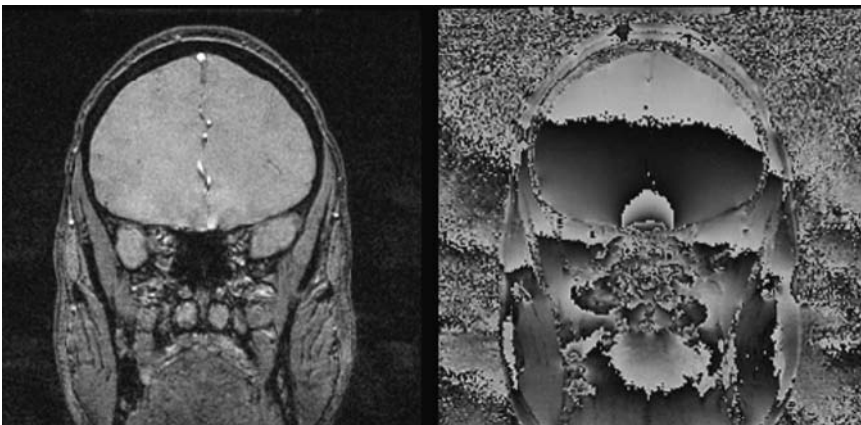


**Fig. 4.10.** Mapping the local magnetic field with gradient echo phase images. The local precession frequency is proportional to the local magnetic field offset, so the local phase of the signal at the time of data collection is proportional to the field offset. The abrupt changes from black to white in the phase image (right) are the result of the cyclic nature of the phase angle and can be interpreted as contour lines of the magnetic field. The field offset resembles a dipole field centered on the sinus cavity.



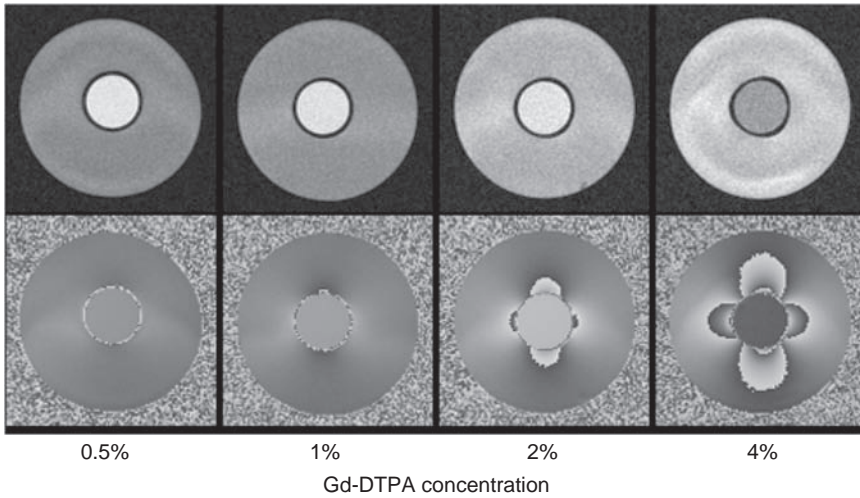


**Fig. 4.11.** Field distortions around a magnetized cylinder. Cylinders filled with different concentrations of gadolinium diethylenetriaminepentaacetic acid (Gd-DTPA), a common MR contrast agent, were imaged with a gradient recalled echo pulse sequence. These phantoms consist of concentric cylinders with the Gd-DTPA in the inner cylinder and water in the outer cylinder. The top row of magnitude images illustrates the *relaxivity* effect of gadolinium: in low concentrations the signal is increased on these  $T_1$ -weighted images because  $T_1$  is reduced, and with a high concentration the shortening of  $T_2$  becomes important and the signal is reduced. The phase images (bottom) show the dipole field distortion caused by the magnetic susceptibility effect of gadolinium, creating field gradients around the cylinder. Similar field distortions occur around magnetized blood vessels containing deoxyhemoglobin.

Because the phase angle is cyclic, the phase image shows abrupt transitions from black to white as the phase changes from  $359^\circ$  to  $0^\circ$ . These transitions are, therefore, artifacts of the display but can be thought of as contours of equal field offset. [Figure 4.10](#) shows substantial field variation caused, in large part, by the susceptibility difference between the sinus cavities and the brain tissue.

Furthermore, the pattern of field distortion depends strongly on the geometry of the tissues. A very simple field distortion is illustrated in [Fig. 4.11](#). Each image shows a cross-section through two concentric cylinders. Both cylinders contain water, but the inner cylinder was doped with gadolinium-linked diethylenetriaminepentaacetic acid (Gd-DTPA), a commonly used MR contrast agent, which has the effect of altering the magnetic susceptibility. (Gadolinium also alters the relaxation times, but that is not the effect we are after here.) Gradient echo MRI was used to map the field offsets. The field offset pattern is a *dipole field*, and it becomes more pronounced as the susceptibility difference between the inner cylinder and the surrounding medium is increased by increasing the concentration of Gd-DTPA. The field distortion around a magnetized cylinder is a useful model for thinking about field distortions around blood vessels. Susceptibility differences between blood and the surrounding tissue, either caused by injected contrast agents or by intrinsic changes in blood oxygenation, are at the heart of most fMRI techniques.

The MR signal is sensitive to magnetic field variations within a voxel produced by magnetic susceptibility variations. Spins precess at a rate determined by the local magnetic field, so with a gradient echo sequence the individual signals that make up the net voxel signal become steadily more and more out of phase, and the signal is strongly attenuated. One remedy for this  $T_2^*$  effect is to use an SE sequence to refocus the phase dispersion; this will

restore signal dropouts caused by large-scale field variations such as those produced by the sinus cavities. But when the spatial scale of the field variations is much smaller, comparable to the distance a water molecule diffuses during TE, an SE is less effective at refocusing because of the motions created by diffusion. An SE works only if the phase acquired by a spin during the first half of the echo is the same as that acquired during the second half, and motion through spatially varying magnetic fields will change this. The effect is analogous to that of a bipolar gradient pulse described above, except that now the effect is caused by intrinsic field variations within the tissue rather than applied gradients.

## References

- Anderson CM, Edelman RR, Turski PA (1993) *Clinical Magnetic Resonance Angiography*. New York: Raven Press
- Baird AE, Warach S (1998) Magnetic resonance imaging of acute stroke. *J Cereb Blood Flow Metab* **18**:583–609
- de Zwart, JA van Gelderen P, Duyn JH (2006) Receive coil arrays and parallel imaging for functional magnetic resonance imaging of the human brain. *Conf Proc IEEE Eng Med Biol Soc* **1**:17–20
- Hennig J, Nauerth A, Friedburg H (1986) RARE imaging: a fast imaging method for clinical MR. *Magn Reson Med* **3**:823–833
- Jellison BJ, Field AS, Medow J, *et al.* (2004) Diffusion tensor imaging of cerebral white matter: a pictorial review of physics, fiber tract anatomy, and tumor imaging patterns. *Am J Neuroradiol* **25**:356–369
- Lauterbur PC (1973) Image formation by induced local interactions: examples employing nuclear magnetic resonance. *Nature* **242**:190–191
- Le Bihan D (1991) Molecular diffusion nuclear magnetic resonance imaging. *Magn Reson Q* **7**:1–30
- Mansfield P (1977) Multi-planar image formation using NMR spin echoes. *J Phys C* **10**:L55–L58
- Moseley ME, Cohen T, Kucharczyk J (1990) Diffusion weighted MR imaging of anisotropic water diffusion in cat central nervous system. *Radiology* **176**:439–446
- Schaefer PW, Copen WA, Lev MH, Gonzalez RG (2006) Diffusion-weighted imaging in acute stroke. *Magn Reson Imaging Clin N Am* **14**:141–168
- Schellinger PD, Richter G, Kohrmann M, Dorfler A (2007) Noninvasive angiography (magnetic resonance and computed tomography) in the diagnosis of ischemic cerebrovascular disease. Techniques and clinical applications. *Cerebrovasc Dis* **24** (Suppl 1): 16–23
- Wiesinger F, van de Moortele PF, Adriany G, *et al.* (2006) Potential and feasibility of parallel MRI at high field. *NMR Biomed* **19**:368–378

<b>Magnetic resonance effects of brain activation</b>	<i>page</i> 101
Blood velocity effects	101
Intravascular contrast agents	102
Deoxyhemoglobin effects	102
Cerebral blood flow measurement	103
Functional neuroimaging	104
<b>Contrast agent methods</b>	104
Alteration of local relaxation times	104
Signal fall with contrast agent in the vasculature	105
Brain activation measured with contrast agents	107
<b>Arterial spin labeling</b>	107
Imaging cerebral blood flow	107
Principles of arterial spin labeling	108
<b>Imaging using BOLD-fMRI</b>	110
Blood susceptibility depends on deoxyhemoglobin content	110
Mapping brain activation	111

## Magnetic resonance effects of brain activation

In [Ch 2](#), the basic physiological changes accompanying brain activation were described. Cerebral blood flow (CBF) increases dramatically, and the metabolic rate of  $O_2$  consumption ( $CMRO_2$ ) increases by a smaller amount. As a result, the  $O_2$  content of the capillary and venous blood is increased. In addition, the blood volume (CBV) and blood velocity increase. With this picture of brain activation in mind, what are the possible observable effects these physiological changes might have on the MR signal that could form the basis for measuring activation with MRI?

### Blood velocity effects

The first potential effect is from increased velocity of the blood. By applying bipolar gradient pulses, the intrinsic flow sensitivity of the MR signal can be exploited. Individual capillaries cannot be resolved, so the flow effect is more analogous to diffusion imaging than to MR angiography. An early conceptual model for functional imaging is to imagine that a capillary bed consists of randomly oriented cylinders. Then the uniform motion of the blood, but in random directions, is similar to the random walk of freely diffusing water molecules (Le Bihan *et al.* 1988). The effect on the MR signal of this *intravoxel incoherent motion* (IVIM) is qualitatively similar to the effect of diffusion: when a bipolar gradient is applied, the signal is reduced because the spins move during the interval between the two lobes of the gradient pulse so that refocusing is incomplete. Quantitatively, the IVIM effect is much

larger than diffusion because the spins are carried farther by capillary flow than by true random motions.

If the bipolar gradient pulse is sufficiently strong that the signal from moving blood is completely destroyed, rather than just attenuated, the blood volume can be measured by subtracting the signals measured with and without diffusion weighting. However, this approach involves some complications. The total signal is viewed as the sum of the signals from two pools: the intravascular spins and the extravascular spins. Ideally, we would manipulate only the intravascular signal by applying the bipolar gradient pulse, so that the extravascular signal would subtract out leaving just a measure of the intrinsic intravascular signal. But the extravascular signal is also affected by the gradient pulse because of true diffusion of the spins in the tissue. The attenuation of the extravascular signal by diffusion is much less than the attenuation of the blood signal by flow, but the absolute signal change associated with the two effects is similar because the intravascular signal is such a small fraction of the total signal. For example, the net signal change resulting from a gradient pulse that attenuates the tissue signal by 5% by diffusion is comparable to complete attenuation of a blood signal that makes up 4% of the total signal. This approach, consequently, requires accurate measurements of small signal changes, and careful corrections for confounding effects such as diffusion attenuation of the tissue signal.

## Intravascular contrast agents

An alternative approach to measuring blood volume is to use intravascular contrast agents, such as gadolinium-linked diethylenetriaminepentaacetic acid (Gd-DTPA) (Rosen *et al.* 1989; Villringer *et al.* 1988). As described in Ch. 4, gadolinium has a large magnetic moment and so alters the magnetic susceptibility of the blood. The altered susceptibility in turn creates field gradients within and around the vessels, leading to attenuation of the MR signal. Although the agent is confined to the intravascular space, the total MR signal is affected because the microscopic field gradients penetrate into the extravascular space. As a result, the signal changes can be quite large (30–50%), much larger than the small changes associated with the IVIM effect. Following a bolus injection of the agent, the local MR signal in the brain drops transiently as the agent passes through the vasculature. This effect lasts only a brief time (10 s or so) and fast dynamic imaging is required to measure it. For the same bolus, the signal dip will be more pronounced in areas with a larger blood volume.

## Deoxyhemoglobin effects

With contrast agents, a susceptibility difference between the intravascular and extravascular space is induced by the experimenter. There is, however, also a natural physiological mechanism for producing a susceptibility difference: deoxyhemoglobin is paramagnetic, but oxyhemoglobin is not. As a result, the magnetic susceptibility of the blood is altered depending on the blood concentration of deoxyhemoglobin (Ogawa *et al.* 1990a). At rest, arterial blood arrives at the brain fully oxygenated, and approximately 40% of the O<sub>2</sub> is extracted in passing through the capillary bed. The venous blood, and to a lesser extent the capillary blood, will, therefore, contain a significant concentration of deoxyhemoglobin. The susceptibility change resulting from this amount of deoxyhemoglobin is about an order of magnitude smaller than that caused by a concentrated bolus of gadolinium, so the signal attenuation is weaker. In the resting brain the gradient recalled echo (GRE) signal attenuation is estimated to be approximately 8% at a field strength of 1.5 T compared with what the signal would be if the blood remained fully oxygenated (i.e., no O<sub>2</sub> metabolism) (Davis *et al.* 1998).

This signal attenuation is called the blood oxygenation level dependent (BOLD) effect (Ogawa *et al.* 1990b).

However, the existence of a BOLD effect on the MR signal does not necessarily lead to a way of measuring brain activation. If blood flow and  $O_2$  metabolism increase in a matched way (e.g., a 20% increase in both), then the blood oxygenation remains the same and the signal attenuation caused by the BOLD effect would also remain the same. However, the nature of brain activation is that CBF increases much more than  $CMRO_2$  (Chs. 1 and 2), leading to increased venous blood oxygenation and a reduced concentration of deoxyhemoglobin. As a result, the degree of attenuation from the BOLD effect is reduced, and the MR signal increases. In a typical study to map patterns of brain activation based on the BOLD effect, a series of dynamic images is acquired while the subject alternates between periods of performing a task and periods of rest. The time series of images is then analyzed to identify individual pixel time courses that show a significant correlation with the stimulus pattern (i.e., a signal increase during performance of the task) (Bandettini *et al.* 1993). These pixels are then colored to produce a map of the pattern of brain activation and overlaid on a gray-scale image of the anatomy.

## Cerebral blood flow measurement

The MR methods described so far all yield information about the perfusion state of the brain, but none of them provides a direct measure of the perfusion itself: CBF. One approach to measurement of CBF is to look more closely at the dynamic signal change curves measured with contrast agents such as Gd-DTPA (Østergaard *et al.* 1996a,b). With such curves the magnitude of the transient signal change is determined by the blood volume, and these data yield a robust measurement of CBV, as described above. But the *duration* of the signal dip depends on the vascular transit time, which, in turn, depends on CBF. The lower CBF, the longer the transit time. However, pulling out a quantitative measurement of CBF from such data is difficult because CBF is not the only factor that affects the width of the signal dip. The dominant contribution to the width is the width of the bolus itself. The agent is injected into a vein and so must pass through the heart before being delivered to the brain in arterial blood. As a result, even if the injected bolus is sharply defined in time, the delivered bolus to the brain is substantially broadened. To derive a measurement of CBF from contrast agent data, an estimate of the intrinsic width of the bolus in the arterial blood arriving at the brain tissue is required, and this usually involves imaging of the blood signal in a large artery (Duhamel *et al.* 2006). The calculation of CBF is then more involved mathematically than computing a map of CBV and is likely more prone to error.

An alternative approach to measuring CBF directly is related to the idea of the time-of-flight effects that are the basis of the MR angiography techniques described in Ch. 4. In arterial spin labeling (ASL) techniques, the magnetization of the arterial blood is manipulated before it reaches the slice of interest (Detre *et al.* 1992). In a typical ASL experiment, the arterial blood is tagged by inverting the magnetization, and after a delay this tagged blood arrives at the image plane and an image is acquired. A control measurement is then made without tagging the arterial blood. If the tag and control images are carefully adjusted so that the signal from the static spins is the same in both, then the difference signal will be proportional to the amount of arterial blood delivered, and thus proportional to CBF.

Like other fMRI techniques, the signal change associated with tagging the blood is small. A rough estimate can be made by considering how much tagged water can enter the brain during the experiment. The essential limitation on this is the short longitudinal relaxation

time, which is of the order of 1 s. One can think of this as analogous to dealing with a tracer with a very short half-life. The arterial inversion creates labeled water that can be measured, but after a few seconds the label has disappeared. The amount of label that can be delivered into a tissue voxel is then of the order of  $fT_1$ , where  $f$  is the local CBF and  $T_1$  is the longitudinal relaxation time. For the human brain  $f$  is around  $0.01\text{ s}^{-1}$ , and  $T_1$  is approximately 1 s, so the fractional change in the total signal from arterial tagging is only around 1%. Nevertheless, these small signal changes can be measured reliably, and ASL techniques can produce quantitative maps of perfusion with high temporal and spatial resolution.

At first glance, the IVIM and ASL methods sound somewhat similar. In both cases, the MR signal of blood is selectively manipulated so that a difference image isolates the signal of blood from the net MR signal. Yet the IVIM method yields a measurement of blood volume, and the ASL method yields a measurement of blood flow, a very different quantity. The key difference between these methods is which pool of blood is manipulated. With the IVIM method, all the blood in the voxel is affected, and so the method provides a measure of how much blood is there. But this tells us nothing about how fast that blood is being replaced by fresh arterial blood. In contrast, with the ASL methods, only the arterial blood is manipulated before it arrives in the voxel. This gives a direct measure of how much blood is delivered during the experiment and is independent of how much blood is within the voxel.

## Functional neuroimaging

These changes in the MR signal induced by changes in blood velocity, volume, flow, and oxygenation are the basis for all the functional imaging methods to follow. Historically, the IVIM methods were the first MR methods for examining the perfusion state of tissue, but they have largely been superseded by the other methods. The first demonstration of brain activation used two bolus injections of Gd-DTPA, with and without a visual stimulus (Belliveau *et al.* 1991). However, because of the requirement for multiple injections, contrast agent methods are not routinely used for brain activation studies. Such techniques have become an important clinical tool for evaluating brain pathology associated with altered blood volume, such as tumors and stroke. (Such studies are often described as “perfusion” studies, even though blood volume, rather than blood flow, is usually measured.)

The discovery of the BOLD effect significantly broadened the field of functional neuroimaging (Bandettini *et al.* 1992; Frahm *et al.* 1992; Kwong *et al.* 1992; Ogawa *et al.* 1992). Virtually all the fMRI studies performed to map patterns of brain activation are based on the BOLD effect. However, the BOLD effect has an important drawback for clinical applications: all that can be measured is a change in the perfusion state. That is, BOLD studies tell us nothing about the resting perfusion, only which areas change when the subject performs a different task. For clinical applications involving chronic changes in CBF, such as stroke, the important measurement is the resting CBF. For this reason, clinical fMRI studies are likely to require ASL techniques (Wolf and Detre 2007). The various fMRI techniques are described in more detail in the following sections and in later chapters.

## Contrast agent methods

### Alteration of local relaxation times

Most MRI is done completely non-invasively, in the sense that nothing is injected into the subject. Detailed anatomic images can be created based solely on intrinsic properties of the

tissues. The use of a contrast agent, however, can further enhance the contrast in an image. The most commonly used contrast agent in clinical studies is Gd-DTPA. The gadolinium is the active part of the agent, and the DTPA is a chelating agent that prevents the gadolinium from being toxic. Gadolinium has several unpaired electrons, and the interaction of the large magnetic dipole moments of these electrons with the water molecules leads to a decrease in the local relaxation times. In describing the effects of a contrast agent, it is convenient to talk of the effect on the relaxation *rate constant* ( $R$ ), the inverse of the relaxation time. In brain tissues, the transverse relaxation rate  $R_2 (= 1/T_2)$  is approximately 10 times larger than the longitudinal relaxation rate  $R_1 (= 1/T_1)$ . The effect of gadolinium is to add to each of these rates a change  $\Delta R$  that is proportional to the concentration of gadolinium. But because  $R_2$  is much larger than  $R_1$ , for moderate concentrations of gadolinium the effect is a large change in  $R_1$ , but only a minor change in  $R_2$ . For this reason, gadolinium acts primarily as a  $T_1$ -agent, altering the  $T_1$  of spins that come into contact with it.

The relaxivity effect of gadolinium is exploited in clinical studies to enhance the signal of particular tissues in  $T_1$ -weighted images, with the primary application being in brain tumor imaging. An important criterion for evaluating brain masses is whether they have an intact blood-brain barrier, and this can be directly assessed with Gd-DTPA. The relaxivity effect of gadolinium only operates when the water comes into contact with the agent. With an intact blood-brain barrier, the gadolinium cannot cross into the extravascular space and so remains confined in the blood. The relaxation time of the blood is reduced, but because the blood contributes only a few percent of the net signal, there is little enhancement in a  $T_1$ -weighted image. In contrast, if the blood-brain barrier is leaky, the gadolinium enters the tissue and reduces  $T_1$ . The result is a significant enhancement of the tumor in a  $T_1$ -weighted image.

More recently, Gd-DTPA-enhanced angiography has become a useful tool for visualizing the large blood vessels. After a rapid injection of the agent, dynamic imaging is used to capture the passage of the agent through the major vessels. Because the  $T_1$  of the blood is greatly reduced, the blood signal relaxes quickly and so produces a strong signal and high contrast between the vessels and the surrounding tissues.

## Signal fall with contrast agent in the vasculature

The possibility of using Gd-DTPA to assess aspects of microvascular flow in the brain began with the observation that a bolus of Gd-DTPA creates a transient *drop* in the MR signal as it passes through the brain ((Villringer *et al.* 1988) (Fig. 5.1). This clearly suggested that dynamic measurement of the kinetics of Gd-DTPA could provide information on the perfusion state of the tissue. However, the observed effect was rather surprising given the discussion above because Gd-DTPA is commonly used to enhance the MR signal by reducing  $T_1$ . In a normal brain with an intact blood-brain barrier, the gadolinium remains confined to the vascular space, so there should be no effect on the  $T_1$  of tissue. This, combined with the fact that the signal change is in the wrong direction for a  $T_1$  shortening effect, indicates that the observed signal drop is caused by an effect of gadolinium that differs from its effect on the longitudinal relaxation.

As described above, gadolinium possesses an additional physical property with magnetic effects: a large magnetic dipole moment. The large magnetic moment of gadolinium alters the magnetic susceptibility of the blood, creating a large susceptibility difference between the vessels and the extravascular space. Field gradients are produced throughout the tissue, and these field gradients lead to signal loss. Note that this susceptibility effect occurs for precisely

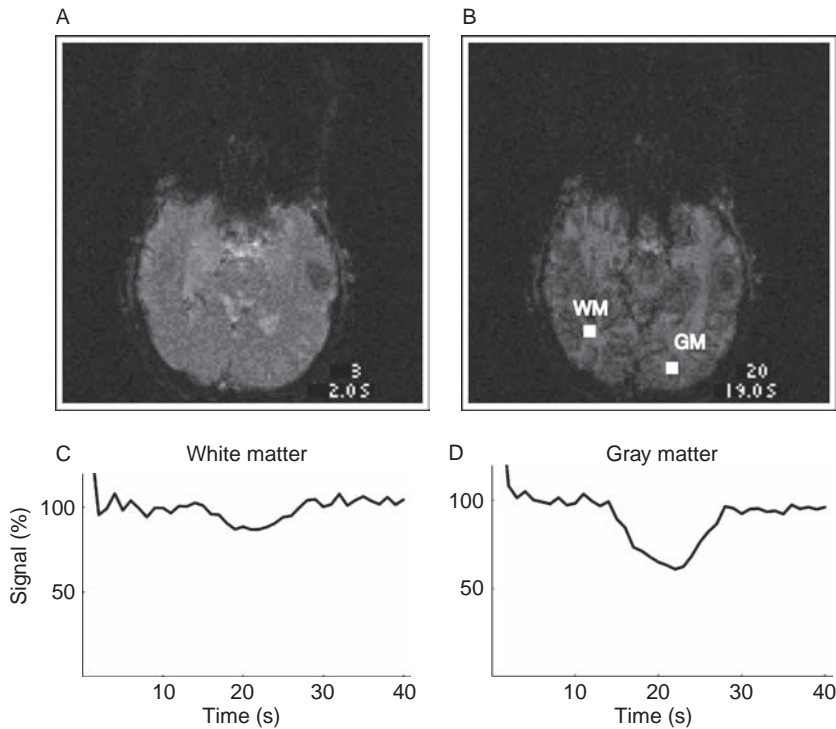


**Fig. 5.1.** Dynamic imaging of the passage of contrast agent through the vasculature. Echo planar single-shot images are collected every second for 40 s following injection of the contrast agent gadolinium-diethylenetriaminepentaacetic acid (Gd-DTPA). Gadolinium alters the magnetic susceptibility of the blood, creating field gradients around the vessels and a transient drop in the signal. The magnitude of the signal drop reflects the local blood volume. The third image in the series (A) shows little contrast between gray matter (GM) and white matter (WM), whereas the image at 20 s (B) shows a deeper signal reduction in gray matter owing to the larger blood volume. The signal variations over time are plotted for a region of white matter (C) and gray matter (D). (Data courtesy of B. Georgi.)

the same reason that the relaxivity effects of gadolinium are minor: the agent is confined to the vascular space. If, instead, the gadolinium freely diffused into the extravascular space, the intra- and extravascular concentrations would be about the same, and there would be no susceptibility difference and no signal loss. The fact that there is a strong susceptibility effect has been demonstrated by using a different contrast agent, dysprosium. Dysprosium also has a large magnetic moment, even larger than gadolinium, but has essentially no effect on relaxivity. Experiments with dysprosium show an even larger signal drop for the same dose, as would be expected for a larger change in magnetic susceptibility (Villringer *et al.* 1988).

The signal fall as gadolinium passes through the microvasculature is transient but it can be measured with fast imaging techniques such as echo planar imaging (EPI). In qualitative terms, we expect that the larger the amount of the agent within the voxel, the larger the signal dip will be. Because the agent is confined to the blood vessels, the total amount present is directly proportional to the local CBV. A full quantitative analysis of the kinetic curves of Gd-DTPA is somewhat more involved and is discussed in Ch. 12, but the basic idea is that the magnitude of the signal fall reflects local blood volume.



## Brain activation measured with contrast agents

The first measurement of brain activation with MRI used this basic analysis to measure CBV in two states (Belliveau *et al.* 1991). In the resting state, the subject was lying quietly in the dark. In the active state, the subject viewed a flashing grid of red lights through a goggle system. In each state, Gd-DTPA was injected, and the kinetic curves were measured in a slice through the visual cortex along the calcarine fissure. The dynamic curve for each voxel was analyzed to produce a map of CBV, and image voxels showing a significant change in CBV were highlighted. The results were that CBV increased on average by 24% in the visual cortex.

For studies of brain activation, contrast agent techniques are technically demanding. A separate injection is required for each measurement of CBV. The gadolinium quickly spreads to other parts of the body, so it is present in the blood in sufficient concentration to produce the desired susceptibility effect only in its first pass through the vasculature. Because multiple injections are required, only a few states of activation can be examined in one subject. Also, the dose and rate of injection must be carefully controlled to ensure that each injection is identical. The administered dose, and even the rate of injection, directly affect the shape of the tissue curve, so any difference in the injections could produce an artifactual difference in the CBV measured in two states. Furthermore, the gadolinium bolus injection technique cannot measure the dynamics of a changing CBV. In each measurement, it is assumed that the CBV is constant, and the changing MR signal then reflects the changing concentration of gadolinium as it passes through this fixed volume.

These technical problems could be alleviated if the susceptibility agent remained in the blood for a sufficiently long time that the blood concentration remains constant during a study. For a fixed CBV, the signal would be offset from the signal without the agent but would be constant once the agent had equilibrated in the blood. Dynamic changes in the signal then would reflect changes in CBV. Experimental paradigms like those used for BOLD studies could be used, and because the signal changes produced by contrast agents can be substantially larger than BOLD signal changes based on oxygenation changes, these techniques could be quite sensitive to subtle brain activations. Such agents have been developed for animal studies and used to measure dynamic CBV changes during activation (Mandeville *et al.* 1998). If such agents are approved for human studies, they will provide a powerful tool for investigating brain activation. For now, though, contrast agent methods for fMRI have been superseded for activation studies in humans by the methods based on intrinsic blood oxygenation changes. However, blood volume measurements with Gd-DTPA have become a standard clinical tool for the evaluation of stroke and other brain lesions.

## Arterial spin labeling

### Imaging cerebral blood flow

The goal with ASL is to map CBF directly. The contrast agent methods described above are primarily sensitive to CBV, and it is difficult to extract a CBF measurement from observations of the kinetics of an intravascular tracer. The BOLD methods are sensitive to changes in blood oxygenation, which depends on the combined effect of changes in CBF, CBV, and  $CMRO_2$ . Even though the BOLD effect correlates strongly with changes in CBF, it does not provide a direct quantitative measurement of CBF alone.

In nuclear medicine studies, CBF is measured with a diffusible tracer that readily leaves the capillary and diffuses throughout the tissue volume. The tracer is delivered to different brain areas in proportion to the local CBF, and so the amount delivered to a tissue element directly reflects the perfusion of that element. Over time, the tracer will clear from the tissue element, and the rate of clearance is also proportional to local CBF. Blood flow can be found by measuring the tissue concentration over time, monitoring either the delivery or the clearance of the tracer. In PET studies with  $\text{H}_2^{15}\text{O}$ , the tissue concentration of  $^{15}\text{O}$  is imaged to determine the rate of delivery of the tracer to each image voxel, and in  $^{133}\text{Xe}$  studies, the rate of clearance of the tracer from different brain regions is monitored with external detectors (see [Chapter 2](#)).

In recent years, several MRI techniques have been developed that are similar in principle to these nuclear medicine techniques (Detre *et al.* 1992; Edelman *et al.* 1994; Kim 1995; Wong *et al.* 1998). With these ASL techniques, the water of arterial blood is labeled before it is delivered to the imaging plane, and so these methods are similar in many respects to tracer studies with  $\text{H}_2^{15}\text{O}$ . Although the basic principles and approach to quantifying CBF carry over from nuclear medicine techniques to MRI, a crucial difference between ASL methods and radioactive tracer methods is that in ASL no tracer is injected. Instead, the arterial blood is tagged magnetically with MR techniques, and the delivery of this tagged water to each image voxel is measured. Because these techniques are completely non-invasive, the tagging can be repeated many times for averaging to produce perfusion maps with a high SNR. In addition, the ability to repeat the measurement every few seconds makes possible dynamic imaging of blood flow, and for this reason ASL has the potential to produce maps of perfusion in the human brain with higher spatial and temporal resolution than any other existing technique.

## Principles of arterial spin labeling

Arterial spin labeling is based on a simple idea, but in practice using this idea to create quantitative perfusion maps requires careful attention to several sources of systematic error. For this reason, dealing with these technical difficulties is a critical aspect of ASL methods, and the implementation of these methods involves some subtle, but important, features. To begin with, though, we will ignore these difficulties to clarify the basic idea behind the method. The practical problems are discussed in [Ch. 13](#).

Suppose that the goal is to measure the perfusion in each voxel of a transverse slice through the brain. The ASL experiment involves making two images of this slice, referred to as the tag and control images. For the tag image, the magnetization of the water in the arterial blood is inverted before it reaches the slice. For example, a  $180^\circ$  RF pulse applied in a slice-selective fashion to a thick slab below the imaging slice will invert all the spins, including those of arterial blood that will eventually be delivered to the slice of interest. After a delay inversion time (TI; typically 1–1.5 s) to allow inverted blood to flow into the slice, an image of the slice itself is collected, creating the tag image. The control image is acquired in exactly the same way but with one exception: the arterial magnetization is not inverted. If this is done carefully, any difference in the signal of a voxel between the tag and control images should result only from the difference in the signal of arterial blood delivered during the interval TI. Specifically, in each image the voxel signal is proportional to the longitudinal magnetization of the voxel at the time of the image. If no arterial blood is delivered, the signals measured in the tag and control images should be the same, and so the difference image should be zero. However, if arterial blood is

delivered to a voxel, it will carry an inverted magnetization in the tag image but a fully relaxed magnetization in the control image, and so the signals of blood will not cancel in the subtraction image.

The ASL difference image is then proportional to how much arterial blood has entered the slice during the interval  $TI$ . Extending the argument from above, if the local CBF is denoted by  $f$  (milliliters of blood per milliliter of tissue per second), and the volume of a voxel is  $V$  (mL), then the total rate of arterial flow (mL/s) into the voxel is  $fV$ , and the volume of arterial blood delivered during  $TI$  is  $fV \times TI$ . Or, more simply, the fraction of the voxel volume that is replaced with incoming arterial blood during the interval  $TI$  is  $fTI$ . For example, for a typical CBF in the human brain,  $f = 0.01$  s, and so for a typical delay of  $TI = 1$  s, the delivered volume of arterial water is only 1% of the volume of the voxel. If CBF increases by 50%, the amount of arterial water delivered will also increase by 50%, so the ASL difference signal is directly proportional to CBF.

In practice, to make a quantitatively accurate measurement, several confounding factors must be taken into account. Probably the most important correction that must be included accounts for the fact that the blood requires some time to travel from the inversion band to the imaging voxel (Alsop and Detre 1996; Buxton *et al.* 1998). This transit delay not only varies across the brain but also changes in the same brain region with activation. If the transit delay effect is not taken into account, the ASL image is only a semiquantitative map of perfusion because the measured signal will reflect the transit delay as well. Another problem is that some of the tagged arterial blood present in the slice when the image is acquired may be in large vessels and destined to perfuse a more distal capillary bed, rather than the capillary bed of the voxel in which it appears. This can lead to an overestimate of local perfusion.

The magnetization of the tagged blood decays in the time between the inversion pulse and the measurement, reducing the ASL signal. This decay is analogous to radioactive decay of a tracer, and a correction must be made to account for it. This is complicated, however, because the decay rate initially is governed by the  $T_1$  of arterial blood, but after the water molecule has left the capillary and entered the extravascular space, the decay is governed by the  $T_1$  of tissue. This correction, depends therefore, on the time of exchange of water from the blood to the tissue. Finally, an absolute calibration of the ASL difference signal in terms of CBF units requires information about the equilibrium magnetization of blood. All these factors must be taken into account to produce a quantitative map of CBF, and much of the current research in this area focuses on how to deal with these problems. When these effects are carefully controlled, ASL can produce accurate maps of CBF.

There are several versions of ASL techniques, differing in how the tagging is done, the nature of the control image, whether they are compatible with multislice imaging, and sensitivity to the various confounding factors that complicate the determination of a quantitative CBF map. These techniques are discussed in detail in Ch. 13. Here, we can illustrate the potential of ASL imaging of perfusion with a set of images made with a technique called QUIPSS II (quantitative imaging of perfusion with a single subtraction, version II; Wong *et al.* 1998). The images in Fig. 5.2 show five slices with the  $T_1$ -weighted anatomical images on the bottom and the ASL perfusion images on the top. The perfusion images were acquired in a total imaging time of 3 min by alternating between tag and control images every 2 s and constructing the average difference map. Because the ASL signal change is so small, averaging is necessary to improve the SNR. The areas of highest perfusion closely follow the gray matter.

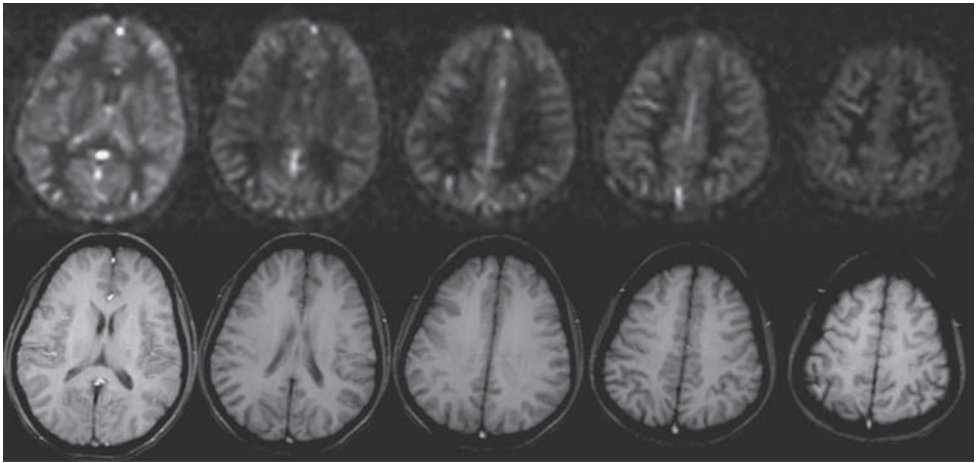


**Fig. 5.2.** Arterial spin labeling (ASL) images of cerebral blood flow. The top row shows five contiguous 8 mm sections through the brain collected with the QUIPSS II pulse sequence (see text), and the bottom row shows conventional anatomical images for comparison. Note that cerebral blood flow is highest in gray matter, as would be expected. Averaging for the ASL images required 3 min of data acquisition. (Data courtesy of E. Wong.)

## Imaging using BOLD-fMRI

### Blood susceptibility depends on deoxyhemoglobin content

In studies using contrast agents, the susceptibility of the blood is manipulated by the experimenter. But nature has also provided an intrinsic physiological agent that alters blood susceptibility: deoxyhemoglobin. Fully oxygenated blood has about the same susceptibility as other brain tissues, but deoxyhemoglobin is paramagnetic and changes the susceptibility of the blood. As capillary and venous blood become more deoxygenated, field distortions around the vessels are increased, and the local signal decreases. In a complementary fashion, if blood oxygenation increases, the local MR signal also increases. This BOLD contrast is the basis of most of the fMRI studies of brain activation performed today.

The phenomenon of changes in blood oxygenation producing a measurable effect on MR images was first observed by Ogawa and co-workers (1990a). In this pioneering study, they imaged the brain of a mouse breathing different levels of  $O_2$ , using a 7 T system with strong gradients to produce a voxel resolution of  $65 \mu\text{m}$  in plane and a slice thickness of  $700 \mu\text{m}$ . They found that when the mouse breathed 100%  $O_2$ , the brain image was rather uniform and featureless. But when the animal breathed only 20%  $O_2$ , there was a dramatic change. Many dark lines appeared, outlining the major structures in the brain. The dark lines corresponded to the locations of blood vessels, and when the oxygenation of the blood was increased back to 100%, the lines reversibly disappeared. These investigators also noted that the signal loss around the vessels was greater with increased echo time, and that the width of some of the lines grew larger as the echo time was increased, suggesting that the presence of the deoxygenated blood in the vessels affected the transverse relaxation outside as well as within the vessels. The observed signal loss was interpreted to be a result of the change in the magnetic susceptibility of the blood vessel compared with its surroundings owing to an increase in deoxyhemoglobin.

The fact that deoxyhemoglobin is paramagnetic, and that this creates magnetic field gradients inside and around the red blood cells, was well known (Thulborn *et al.* 1982), but

this was the first demonstration that this phenomenon could produce a measurable effect in an MR image following a physiological manipulation. Subsequent studies in a cat model at 4 T using EPI further demonstrated that changes in brain oxygenation following respiratory challenges could be followed with GRE imaging (Turner *et al.* 1991).

These animal studies in which blood oxygenation was manipulated by the experimenter suggested that natural physiological processes that alter the oxygenation of blood also might be detectable with MRI. Kwong and co-workers (1992) reported a demonstration of mapping activation in the human brain using GRE MR imaging during visual stimulation and a simple motor task. In these experiments a 1 min stimulus period alternated with a 1 min rest period, and EPI images were collected throughout several periods of stimulus and rest. The GRE signal in the visual cortex increased by approximately 3–4% during the photic stimulation, and a similar increase was observed in the hand motor area during a hand-squeezing task. This report, and several others published shortly afterward (Bandettini *et al.* 1993; Frahm *et al.* 1992; Ogawa *et al.* 1992), marked the beginning of functional human brain mapping based on the BOLD effect.

At first glance, the observation of a signal increase during activation seems somewhat surprising because it implies that the blood is more oxygenated in areas of focal brain activation. Ogawa and colleagues in their earlier paper (1990a) had speculated that the deoxyhemoglobin effect could be used to monitor regional  $O_2$  usage, suggesting that more active regions would appear darker because of increased deoxyhemoglobin resulting from higher  $O_2$  consumption. However, this plausible prediction turned out to be wrong because of the nature of the physiological changes that occur during brain activation. As discussed in Chs. 1 and 2, earlier PET studies by Fox and co-workers (Fox and Raichle 1986; Fox *et al.* 1988) had found a pronounced mismatch between the increases in blood flow and  $O_2$  metabolism during brain activation: CBF increases much more than  $CMRO_2$ . As a result, the delivery of  $O_2$  to the capillary bed is substantially increased, but less is removed from the blood, so the blood is more oxygenated.

Our picture of the BOLD effect is then as follows. In the normal awake human brain, approximately 40% of the  $O_2$  delivered to the capillary bed in arterial blood is extracted and metabolized. There is consequently a substantial amount of deoxyhemoglobin in the venous vessels, and so the MR signal is attenuated from what it would be if there were no deoxyhemoglobin. When the brain is activated, the local flow increases substantially, but  $O_2$  metabolism increases only by a small amount. As a result, the  $O_2$  extraction is reduced, and the venous blood is more oxygenated. The fall in deoxyhemoglobin concentration leads to a signal increase. At 1.5 T, the increase is typically small (a few percent or less). Nevertheless, with careful statistical analysis such small changes can be reliably detected. At higher fields, such as 7 T, the signal changes can be several times larger because the field distortions from magnetic susceptibility effects are proportional to the main magnetic field, so that the same amount of deoxyhemoglobin causes a larger signal reduction.

## Mapping brain activation

Since the discovery that brain activation creates small changes in the local MR signal through the BOLD effect, a number of imaging approaches have been used to measure it. The prototype brain mapping experiment consists of alternating periods of a stimulus task and a control task (Bandettini *et al.* 1993). For example, in one of the most often repeated experiments, a subject rapidly taps the fingers of one hand against the thumb for a short period (e.g., 30 s) and then rests for the same period. This cycle is repeated several times. Throughout these stimulus–control cycles dynamic EPIs are collected covering all or part of the brain. For a

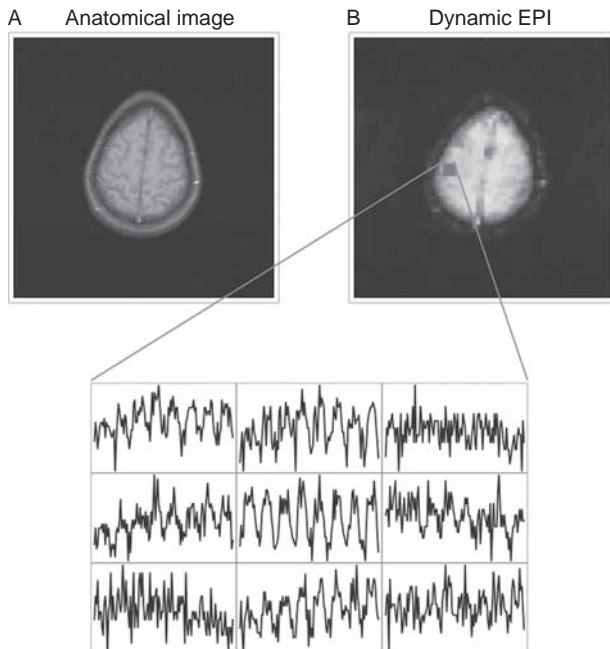


**Fig. 5.3.** Signal changes in a BOLD study. (A) High-resolution anatomical image ( $256 \times 256$  matrix) cutting through the central sulci and the hand motor and sensory areas. (B) One image from a series of 128 low-resolution dynamic images ( $64 \times 64$  matrix) collected every 2 s with EPI. The signal time courses for a  $3 \times 3$  block of pixels are shown below. During the data acquisition, the subject performed eight cycles of a bilateral finger tapping task, with one cycle consisting of 16 s of tapping followed by 16 s of rest. Several pixels show clear patterns of signal variation that correlate with the task. (See plate section for color version.) (Data courtesy of L. Frank.)

typical implementation, the images are acquired rapidly in a single-shot mode, requiring 100 ms or less for each image acquisition, and the spatial resolution is low compared with conventional MR images (e.g.,  $3 \text{ mm} \times 3 \text{ mm} \times 5 \text{ mm}$ ). In this multislice dynamic imaging, images of each of the chosen slices are acquired in rapid succession, and after a repetition time (TR) this set of images is acquired again. The image acquisition is repeated at regular intervals of TR throughout the experiment, while the subject alternates between stimulus and control tasks.

This set of images can be thought of as a four-dimensional data set: three spatial dimensions plus time. For example, Fig. 5.3 shows a single slice through the motor area from such a study in which eight cycles of 16 s of finger tapping were alternated with 16 s of rest. With  $\text{TR} = 2 \text{ s}$ , 128 images were collected covering the eight cycles. The figure shows a high-resolution anatomical image and one image from the dynamic EPI series. The signal time courses for a block of  $3 \times 3$  pixels of the dynamic images are also shown.

These data are analyzed to identify areas of activation by examining the signal time course for each individual pixel with the goal of identifying pixels in which the signal shows a significant change between the stimulus and control periods. In Fig. 5.3, the eight-cycle pattern is clearly evident in a few pixels, but often changes that are not apparent to the eye are nevertheless statistically significant. Because the signal changes from the BOLD effect are small (only a small percentage change at 1.5 T), this statistical analysis is a critical aspect of interpreting BOLD data. It is described in more detail in Ch. 15. The end result of the statistical analysis is a decision for each voxel of whether or not there was a significantly detectable activation, based on whether a calculated statistic, such as the  $t$ -statistic or the correlation coefficient, passed a chosen threshold.

An important factor to include in the statistical analysis of BOLD data is that the metabolic activity producing the change in blood oxygenation and the BOLD effect lag behind the stimulus itself. That is, one must assume some model for the hemodynamic

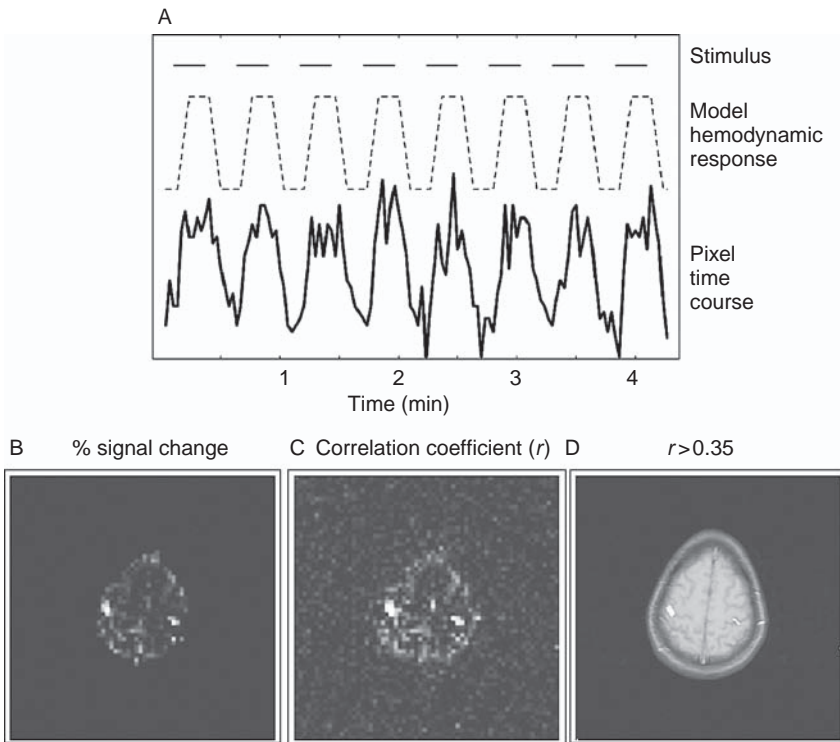


**Fig. 5.4.** Correlation analysis of dynamic echo planar imaging data to identify pixels showing evidence of activity. (A) The hemodynamic response is modeled as a trapezoid, with 6 s ramps and a delay of 2 s from the beginning of the stimulus. (B,C) By correlating the model function with a pixel time course, the signal change (B) and the correlation coefficient  $r$  (C) can be calculated. (D) The pixels passing a threshold of  $r > 0.35$  are highlighted on the anatomical image. For this final display, the  $64 \times 64$  calculated image of  $r$  was interpolated up to  $256 \times 256$  to match the high-resolution image (See plate section for color version.)

response to stimulation, and a typical assumed form is a smoothed and delayed trapezoid. Figure 5.4 illustrates a correlation analysis of the dynamic BOLD data in Fig. 5.3. The hemodynamic response (i.e., the BOLD signal change) is modeled as a trapezoid with 6 s ramps and a delay of 2 s after the start of the stimulus, and the correlation of this model function with the measured pixel time course is calculated for each pixel. Those pixels that show a correlation coefficient greater than a chosen threshold value are designated as activated pixels and are then displayed in color overlaid on a gray scale image of the underlying anatomy. The gray scale image could be one of the EPI images from the dynamic time series or a higher-resolution structural image acquired separately, such as a volume acquisition. Only the pixels that pass the chosen statistical threshold are colored, and for these pixels the color used typically reflects either the value of the statistic (e.g., the correlation coefficient) or a measure of the degree of signal change (e.g., percentage signal change) (Bandettini *et al.* 1993).

This basic paradigm is widely used, but there are many variations. Single-shot EPI is the most commonly used image acquisition technique because it has desirable features of rapid data acquisition and a high SNR. But multishot EPI and conventional two- and three-dimensional GRE imaging are also used. Both GRE and SE images exhibit BOLD effects,

although the GRE signal is more sensitive because the signal changes produced by activation are larger. However, at higher magnetic fields, the SE signal changes are larger, and because they are more likely to reflect microvascular changes, they may give a more precise spatial map of the areas of activation (Yacoub *et al.* 2003). In addition, ASE is sometimes used because the ASE signal is intermediate between the GRE and SE signals in terms of both overall sensitivity and sensitivity to the microvasculature. The basic block design of stimulus trials is often used, but single-trial (Dale and Buckner 1997) and continuously varying (Serenio *et al.* 1995) stimulus paradigms also have been developed.

## References

- Alsop DC, Detre JA (1996) Reduced transit-time sensitivity in non-invasive magnetic resonance imaging of human cerebral blood flow. *J Cereb Blood Flow Metab* **16**: 1236–1249
- Bandettini PA, Wong EC, Hinks RS, Tikofsky RS, Hyde JS (1992) Time course EPI of human brain function during task activation. *Magn Reson Med* **25**: 390–397
- Bandettini PA, Jesmanowicz A, Wong EC, Hyde JS (1993) Processing strategies for time-course data sets in functional MRI of the human brain. *Magn Reson Med* **30**: 161–173
- Belliveau JW, Kennedy DN, McKinstry RC, *et al.* (1991) Functional mapping of the human visual cortex by magnetic resonance imaging. *Science* **254**: 716–719
- Buxton RB, Frank LR, Wong EC, *et al.* (1998) A general kinetic model for quantitative perfusion imaging with arterial spin labeling. *Magn Reson Med* **40**: 383–396
- Dale AM, Buckner RL (1997) Selective averaging of rapidly presented individual trials using fMRI. *Hum Brain Mapping* **5**: 329–340
- Davis TL, Kwong KK, Weisskoff RM, Rosen BR (1998) Calibrated functional MRI: mapping the dynamics of oxidative metabolism. *Proc Natl Acad Sci USA* **95**: 1834–1839
- Detre JA, Leigh JS, Williams DS, Koretsky AP (1992) Perfusion imaging. *Magn Reson Med* **23**: 37–45
- Duhamel G, Schlaug G, Alsop DC (2006) Measurement of arterial input functions for dynamic susceptibility contrast magnetic resonance imaging using echoplanar images: comparison of physical simulations with in vivo results. *Magn Reson Med* **55**: 514–523
- Edelman RR, Siewert B, Darby DG, *et al.* (1994) Qualitative mapping of cerebral blood flow and functional localization with echo-planar MR imaging and signal targeting with alternating radiofrequency (STAR) sequences: applications to MR angiography. *Radiology* **192**: 513–520
- Fox PT, Raichle ME (1986) Focal physiological uncoupling of cerebral blood flow and oxidative metabolism during somatosensory stimulation in human subjects. *Proc Natl Acad Sci USA* **83**: 1140–1144
- Fox PT, Raichle ME, Mintun MA, Dence C (1988) Nonoxidative glucose consumption during focal physiologic neural activity. *Science* **241**: 462–464
- Frahm J, Bruhn H, Merboldt K-D, Hanicke W, Math D (1992) Dynamic MR imaging of human brain oxygenation during rest and photic stimulation. *J Magn Reson Imaging* **2**: 501–505
- Kim S-G (1995) Quantification of regional cerebral blood flow change by flow-sensitive alternating inversion recovery (FAIR) technique: application to functional mapping. *Magn Reson Med* **34**: 293–301
- Kwong KK, Belliveau JW, Chesler DA, *et al.* (1992) Dynamic magnetic resonance imaging of human brain activity during primary sensory stimulation. *Proc Natl Acad Sci USA* **89**: 5675–5679.
- Le Bihan D, Breton E, Lallemand D, *et al.* (1988) Separation of diffusion and perfusion in intravoxel incoherent motion MR imaging. *Radiology* **168**: 497–505
- Mandeville JB, Marota JJA, Kosofsky BE, *et al.* (1998) Dynamic functional imaging of relative cerebral blood volume during rat forepaw stimulation. *Magn Reson Med* **39**: 615–624
- Ogawa S, Lee TM, Nayak AS, Glynn P (1990a) Oxygenation-sensitive contrast in magnetic resonance image of rodent brain at high magnetic fields. *Magn Reson Med* **14**: 68–78
- Ogawa S, Lee TM, Kay AR, Tank DW (1990b) Brain magnetic resonance imaging with



- contrast dependent on blood oxygenation. *Proc Natl Acad Sci USA* **87**: 9868–9872
- Ogawa S, Tank DW, Menon R, *et al.* (1992) Intrinsic signal changes accompanying sensory stimulation: functional brain mapping with magnetic resonance imaging. *Proc Natl Acad Sci USA*. **89**: 5951–5955
- Østergaard L, Sorensen AG, Kwong KK, *et al.* (1996a) High resolution measurement of cerebral blood flow using intravascular tracer bolus passages. Part II: experimental comparison and preliminary results. *Magn Reson Med* **36**: 726–736
- Østergaard L, Weisskoff RM, Chesler DA, Gyldensted C, Rosen BR (1996b) High resolution measurement of cerebral blood flow using intravascular tracer bolus passages. Part I: mathematical approach and statistical analysis. *Magn Reson Med* **36**: 715–725
- Rosen BR, Belliveau JW, Chien D (1989) Perfusion imaging by nuclear magnetic resonance. *Magn Reson Quart* **5**: 263–281
- Sereno MI, Dale AM, Reppas JB, *et al.* (1995) Borders of multiple visual areas in humans revealed by functional magnetic resonance imaging. *Science* **268**: 889–893
- Thulborn KR, Waterton JC, Matthews PM, Radda GK (1982) Oxygenation dependence of the transverse relaxation time of water protons in whole blood at high field. *Biochim Biophys Acta* **714**: 265–270
- Turner R, LeBihan D, Moonen CTW, Despres D, Frank J (1991) Echo-planar time course MRI of cat brain oxygenation changes. *Magn Reson Med* **27**: 159–166
- Villringer A, Rosen BR, Belliveau JW, *et al.* (1988) Dynamic imaging with lanthanide chelates in normal brain: contrast due to magnetic susceptibility effects. *Magn Reson Med* **6**: 164–174.
- Wolf RL, Detre JA (2007) Clinical neuroimaging using arterial spin-labeled perfusion magnetic resonance imaging. *Neurotherapeutics* **4**: 346–359
- Wong EC, Buxton RB, Frank LR (1998) Quantitative imaging of perfusion using a single subtraction (QUIPSS and QUIPSS II). *Magn Reson Med* **39**: 702–708
- Yacoub E, Duong TQ, van de Moortele PF, *et al.* (2003) Spin-echo fMRI in humans using high spatial resolutions and high magnetic fields. *Magn Reson Med* **49**: 655–664



**Part**

**I**

# Principles of magnetic resonance imaging

## **Part IIA** The nature of the magnetic resonance signal

- 6 Basic physics of magnetism and NMR
- 7 Relaxation and contrast in MRI
- 8 Diffusion and the MR signal

## **Part IIB** Magnetic resonance imaging

- 9 Mapping the MR signal
- 10 Techniques in MRI
- 11 Noise and artifacts in MR images





# The nature of the magnetic resonance signal



# Basic physics of magnetism and NMR

<b>Introduction</b>	<i>page</i> 121
<b>Electromagnetic fields</b>	122
The field concept	122
Magnetic fields	123
Induction and NMR signal detection	125
Gradient and radiofrequency coils	128
<b>Dynamics of nuclear magnetization</b>	130
Interaction of a magnetic dipole with a magnetic field	130
Precession	131
Relaxation	131
Radiofrequency excitation	134
Frequency selective radiofrequency pulses: slice selection	136
Adiabatic radiofrequency pulses	139
<b>Magnetic properties of matter</b>	140
Paramagnetism, diamagnetism, and ferromagnetism	140
Magnetic susceptibility	142
Field distortions in the head	144

## Introduction

In [Ch. 3](#) the basic features of the NMR experiment were introduced, and in this chapter the basic physics underlying NMR is presented in more detail. We begin with a review of the basic physics of magnetic fields, including how coils are used to detect the NMR signal and how gradient fields are produced for imaging. The dynamics of a magnetic dipole in a magnetic field, which is the central physics underlying NMR, is considered next in terms of the two important physical processes of *precession* and *relaxation*. Precession and relaxation have quite different characteristics; precession is a rotation of the magnetization without changing its magnitude, whereas relaxation creates and destroys magnetization. The interplay of these two processes leads to a rich variety of dynamic behavior of the magnetization. In the [final section](#) of the chapter, the magnetic properties of matter are considered in terms of how the partial alignment of dipoles with the magnetic field creates additional fields in the body. These field variations caused by magnetic susceptibility differences between tissues lead to unwanted distortions in MR images, but such effects are also the basis for most of the fMRI techniques.

In trying to understand how NMR works, it is helpful to have an easily visualized model for the process. The physical picture presented here is a classical physics view, and yet the physics of a proton in a magnetic field is correctly described only by quantum mechanics. The source of the NMR phenomenon is that the proton possesses *spin*, and spin is intrinsically

a quantum mechanical property. Despite the familiar sounding name, spin is fundamentally different from the angular momentum of more familiar terrestrial scale objects. For example, a spinning baseball possesses angular momentum, and yet we can easily imagine changing that angular momentum by spinning it faster or stopping it altogether. In other words, the spin is not an intrinsic part of the baseball. But for a proton, the spin is an intrinsic part of being a proton. It never speeds up and never slows down, and the only aspect of the spin that can be changed is the orientation of the spin axis. Neutrons also possess spin, and protons and neutrons combine to form a nucleus such that their spins mutually cancel (opposite spin axes), so that the nucleus has no net spin unless there are an odd number of protons or neutrons. As a result, the nuclei of  $^1\text{H}$  (one proton) and  $^{13}\text{C}$  (six protons and seven neutrons) have a net spin, but  $^{12}\text{C}$  does not.

Furthermore, the quantum view is still stranger, with only certain states allowed, and even the definition of a state is rather different from the classical view. At first glance, the quantum view seems to simplify the picture of the NMR phenomenon. The centerpiece of the quantum view is that any measurement of one component of the spin of a proton will yield only one of two possible values of the spin orientation: spin up or spin down. It seems as if this two-state system ought to be easier to think about than magnetic moment vectors that can point in any direction. However, this sort of partial introduction of quantum ideas into the description of NMR often leads to confusion. After all, if the spin can only be up or down in a magnetic field, how do we ever get transverse magnetization, precession, and the NMR signal? In short, the quantum view is correct, but it is difficult to think about the wide range of phenomena involved in NMR from a purely quantum viewpoint. Fortunately, however, the classical view, although totally incorrect in its description of the behavior of a single proton, nevertheless gives the correct physics for the *average* behavior of many protons, and accurately describes most of the physics encountered in MRI. For this reason, we will develop a physical picture of NMR based on a classical view, and the only feature from quantum mechanics that is essential is the existence of spin itself. For the interested reader, the Appendix contains a sketch of the quantum mechanical view of NMR.

## Electromagnetic fields

### The field concept

Nearly every aspect of the world around us is the result of the interactions of charged particles. Electrons in an atom are bound to the nucleus by the electric force between the charges, and light, and other forms of electromagnetic radiation, can be understood as the cooperative interplay among changing electric and magnetic fields. The phenomenon of NMR is, of course, deeply connected to magnetic field interactions, in particular the behavior of a magnetic dipole in a magnetic field. In addition, a recurring theme in MRI is the geometrical shape of the magnetic field, which underlies the design of coils for MRI, distortions in fast MRI, and the microscopic field variations that are the basis for the blood oxygenation level dependent (BOLD) signal changes measured during brain activation. To begin with, we consider the nature of magnetic fields. (Excellent introductions to electromagnetic fields are given by Purcell (1965) and Feynman *et al.* (1965).)

The concept of a field is a useful way of visualizing physical interactions, and the simplest example is a gravitational field. In comparison with the complex interactions of charged particles, the gravitational interaction of two massive bodies is relatively simple. The two bodies attract each other with a force that is proportional to the product of their masses and



inversely proportional to the square of the distance between them. We describe this interaction in terms of a field by saying that the second body interacts with the gravitational field created by the first body. The field extends through all of space, and the strength of the field at any point is proportional to the mass of the body and falls off with distance from the body with an inverse square law.

The gravitational field is a vector field in which each point in space has a vector arrow attached that describes the local strength and direction of the field. For visualizing a field, the most direct way is to imagine such arrows at every point in space, but this is difficult to draw. Instead, the usual way to show fields is to draw continuous *field lines*. A field line is an imagined line running through space such that the direction of the local field at any point on the line is tangent to the line. Each point in space has a field line running through it, but the field pattern can be graphically depicted by showing only selected field lines. Field lines naturally show the local field direction, but the magnitude of the local field is shown in a more subtle way. The stronger the field, the more closely spaced the field lines. Therefore, for the gravitational field around a spherical body, the field is drawn as radial lines pointed inward, with the spread of the field lines indicating the weakening of the field with increasing distance.

The electric field is in some ways analogous to the gravitational field, with electric charge playing the role of mass. The electric force between two charged bodies is proportional to the product of their charges and falls off with the square of the distance between them. However, there are two important differences between the electric field and the gravitational field: (1) the electric force between two like charges is repulsive, rather than attractive; and (2) charges can be either positive or negative, and the force between opposite charges is attractive. Because mass is always positive, gravity is always attractive and tends to pull matter into large massive bodies such as stars and planets. Because charges can be positive or negative, the electric force tends to group matter into smaller stable structures with no net charge, such as atoms and molecules.

The electric field can be represented graphically in the same way as the gravitational field, with the local vector arrows indicating the direction of the force on a positively charged particle (a negatively charged particle would feel a force in the opposite direction). For example, Fig. 6.1A shows the electric field around a positive charge, a *monopole field*. The field lines are radial and point outward, indicating that the force on another positive charge is repulsive. If the central charge were negative, the field lines would point inward like a gravitational field. However, because there are both positive and negative charges, there are electric field configurations that have no counterpart in a gravitational field. For example, Fig. 6.1B shows the field around two nearby charges with equal magnitude but opposite sign, a pattern known as an *electric dipole field*. There is no corresponding dipole gravitational field.

## Magnetic fields

The existence of both positive and negative charges introduces some complexities into the interaction of charged particles, but the electric field is only a part of the picture. In addition to the electric interactions, there are additional forces generated by the motions of the charges. When a charged particle moves through a region where a magnetic field is present, the particle will feel a force in addition to that of any electric field that may be present. For example, consider two parallel wires carrying currents in the same direction. The positive and negative charges in each wire are balanced, so there is no electric force between the two wires. Yet experiments show that with parallel currents there is an attractive force between

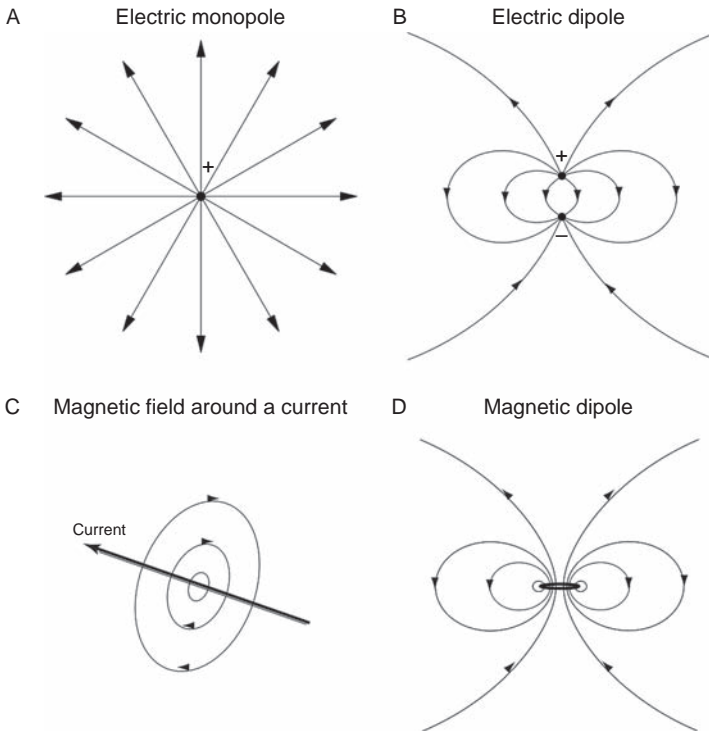


**Fig. 6.1.** Basic electric and magnetic field patterns. The simplest electric fields are the monopole field produced by a single charge (A) and the dipole field produced by two opposite and slightly displaced charges (B). There are no magnetic monopoles, and the simplest source of a magnetic field is a straight wire carrying a current (C). If the wire is bent into a small loop of current, the field is a magnetic dipole field (D). The electric and magnetic dipole fields are identical far from the source but are quite different near the source.

the two wires. If the current in one wire is reversed, the force becomes repulsive, and if the current in one wire is reduced to zero, the force disappears. This additional force is a result of the interaction of the moving charges in one wire interacting with the magnetic field created by the current in the other wire.

The force on a wire carrying a current in a magnetic field is the basis for a loudspeaker system, making possible the conversion of electrical signals into mechanical vibrations. It is also the source of the loud acoustic noise in an MR scanner. Imaging depends on applying pulsed gradient fields to the sample, which means that strong current pulses are applied to the gradient coils. These wires carry substantial current and are in a large magnetic field, so there are large forces produced, creating a sharp tapping sound when the gradients are pulsed. The sound can be quite loud, particularly when strong gradients are used, and subjects to be scanned must wear ear protection.

Magnetic fields are produced whenever there is a flow of electric charge creating a current. Figure 6.1C shows the magnetic field around a long straight wire. The field lines for this simple current are concentric circles in the plane perpendicular to the wire and centered on the wire. The direction of the field lines depends on the direction of the current, following a right-hand rule: with your right thumb pointing along the direction of the current, your fingers curl in the direction of the magnetic field. The magnetic field strength diminishes as the distance from the wire increases.

If a wire carrying a current is bent into a small circular loop, the magnetic field is distorted, as shown in Fig. 6.1D. Near the wire, the concentric field lines are similar to the straight wire. That is, if one is close enough to the current loop so that the curvature is not apparent, the magnetic field is similar to that of a straight wire. However, far from the source this

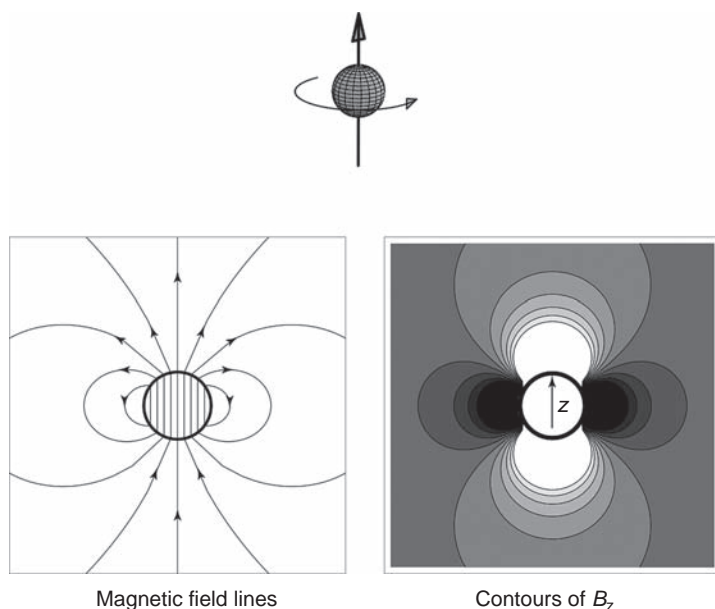


**Fig. 6.2.** The dipole field of a spinning charged sphere. A charged sphere rotating around the  $z$ -axis produces a magnetic dipole field outside. The field lines themselves are shown ( $B_z$ ) but usually just the  $z$ -component of the field is of interest. Contours of equal  $B_z$  are shown on the right.

magnetic field pattern is identical to the electric dipole field, and, correspondingly, this pattern is called a *magnetic dipole field*. In general, the term *dipole field* refers to the pattern far from the source, and so two fields can be quite different near the source but still be described as dipole fields. For the electric dipole field, all the field lines end on one or the other of the two charges that make up the dipole. In contrast, the magnetic dipole field is composed of continuous loops that pass through the ring of current. This is a general and important difference in the geometry of electric and magnetic fields: magnetic field lines always form closed loops.

A small ring of current is the prototype of a magnetic dipole, but another classical example of a magnetic dipole is a spinning, charged sphere (Fig. 6.2). This is the basic picture of an atomic nucleus (e.g., the proton, the nucleus of hydrogen) often used for visualizing NMR. For simplicity, assume that the charge is uniformly distributed over the surface of the sphere. This rotating sphere can be viewed as a stack of current loops, with the largest loop area and highest current at the equator of the sphere. When these loops are summed, the net magnetic dipole moment of the sphere turns out to be identical to that of a single current loop at the center of the sphere. Figure 6.2 illustrates the magnetic dipole field by plotting both the field lines and a contour map of just the  $z$ -component of the magnetic field ( $B_z$ ). (For most NMR applications, the  $z$ -component of additional fields are important because this is what adds to the main magnetic field [ $B_0$ ] to create field variations.)

## Induction and NMR signal detection

Our picture of electromagnetic fields so far is that charges create electric fields, and charges in motion (currents) create magnetic fields. In the first half of the nineteenth century, Faraday unraveled an additional feature: *changing* magnetic fields create electric fields. This phenomenon, called *electromagnetic induction*, is at the heart of many examples of electrical technology. For example, induction makes possible the generation of electricity from a mechanical

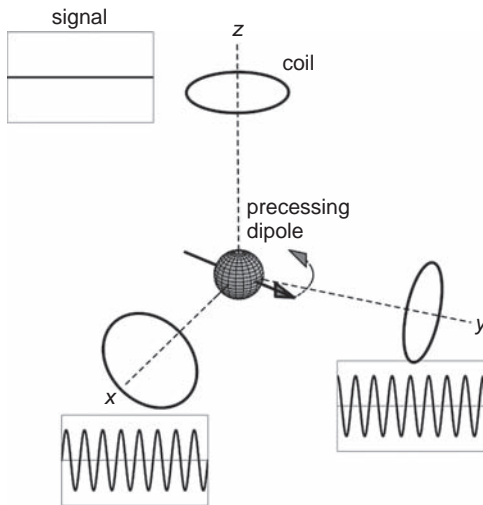


**Fig. 6.3.** Induction signals in coils near a precessing magnetic dipole. For a dipole rotating in the  $x$ - $y$  plane, coils along the  $x$ - and  $y$ -axis show oscillating signals with a relative phase shift of  $90^\circ$  as the magnetic flux of the dipole sweeps across the coils. For the coil along the  $z$ -axis, the flux is constant, and so no current is induced.

energy source, such as hydroelectric power, and the conversion of acoustic signals into electrical signals in a microphone.

In NMR, induction is the process that generates a measurable signal in a detector coil. Imagine a small dipole moment, a spinning charged sphere, rotating around an axis perpendicular to its spin axis. The spinning sphere creates a dipole magnetic field in its vicinity, and as the magnet rotates the dipole field sweeps around as well. As a result, at any fixed point in space near the magnetic dipole, the magnetic field changes cyclically with time. If we now place a loop of wire, a detector coil, near the spinning dipole, the changing magnetic field will create a current in the wire through the process of induction (Fig. 6.3).

The strength of the induced current in the coil depends on both the proximity and the orientation of the coil with respect to the magnetic dipole. The quantitative relation is that the induced current is proportional to the rate of change of the *flux* of the magnetic field through the coil. For example, consider a circular coil and imagine the surface enclosed by the wire. The net flux of the magnetic field is calculated by adding up the perpendicular components of the magnetic field lines at each point on this surface. Or, more qualitatively, the flux is proportional to the number of field lines enclosed by the coil.

The somewhat abstract concept of magnetic flux suggests a flow of something through the coil, but the thing “flowing” is the magnetic field. The source of the terminology is a close analogy between magnetic fields and velocity fields in a fluid. Velocity is also a vector, and the velocity field within a fluid can be plotted as a field with the same conventions that we use for the magnetic field. Velocity field lines in an incompressible fluid also form closed loops, like magnetic field lines. Placing our coil in the fluid, the calculated flux is simply the volume flow rate through the coil. When the coil is perpendicular to the local flow direction, the flux is high; if the coil is placed so that the flow passes over it rather than through it, the flux is zero.

Figure 6.3 illustrates a spinning magnetic dipole inducing currents in several nearby coils. Note that when the coil is oriented such that the axis of the coil is the same as the axis of rotation of the dipole, the flux is constant so there is no induced current. For other orientations though, a cyclic signal is generated in the coil with the same frequency as the

frequency of rotation of the dipole. The maximum signal is produced when the axis of the coil is perpendicular to the axis of rotation of the dipole, because this orientation creates the largest change in flux as the dipole field sweeps past the coil. When the coil is moved farther from the source, the flux is diminished, and so the change in flux also is diminished, and the signal created in the coil is weaker.

The two coils oriented  $90^\circ$  from each other, but with the axis of each coil perpendicular to the rotation axis, show the same strength of induced current, but the signals are shifted in time. This time shift of the signal is described as a *phase shift*, and in this case it is a phase shift of  $90^\circ$ . For any periodic signal with a period  $T$ , a shift in time can be described as an angular phase shift in analogy with circular motion. A phase shift of one full period  $T$  corresponds to one complete cycle, while a phase shift of  $360^\circ$ , and a time shift of  $T/4$  corresponds to a phase shift of  $90^\circ$ . Sometimes phase shifts are expressed in radians rather than degrees, where  $360^\circ = 2\pi$  radians.

The concept of phase recurs often in MRI. In particular, the concept of *phase dispersion* and a resulting loss in signal is important in virtually all MRI techniques. Imagine a coil detecting the signal from several rotating dipoles. If the dipoles are all rotating in phase with one another, so that at any instant they are all pointing in the same direction, then the signals induced by each in the coil add coherently and create a strong net signal. However, if there is phase dispersion, so that at any instant the dipoles are not aligned, then there is destructive interference when the signals from each dipole are added together in the coil, and the net signal is reduced.

The configuration of two coils perpendicular to each other is an example of a *quadrature detector*. Each coil is sensitive to the component of the magnetization perpendicular to the coil because that is the component that creates a changing flux through the coil. Because of their orientation, the signal measured in the second coil is phase-shifted  $90^\circ$  from the signal in the first coil. By electronically delaying the second signal for one quarter of a cycle, the two signals are brought back in phase and can be averaged to improve the signal to noise ratio (SNR) before being sent to the amplifier. Noise comes about primarily from fluctuating stray currents in the sample, which create random currents in the detector coil. Because the two coils of a quadrature detector are oriented perpendicular to each other, the fluctuating fields that cause noise in one coil have no effect on the other coil. If the fluctuating fields along these two directions are statistically independent, the noise signals measured in the two coils will also be independent. Then when the signals from the two coils are combined, the incoherent averaging of the noise improves the SNR by  $\sqrt{2}$  compared with a single-coil measurement.

In a *phased array* coil arrangement, two or more coils send signals to separate amplifiers, with the result that the detected signals are analyzed individually. Phased array coils are useful for imaging as a way of improving the SNR beyond what can be achieved by quadrature detection alone (Grant *et al.* 1998). The noise picked up by a coil is proportional to its sensitive volume, which is linked to the size of the coil. Therefore, a small coil has a higher SNR, but the drawback of a small coil is that only a small region can be imaged. With a phased array system, several small coils can be used to achieve the coverage of a large coil but with the SNR of a small coil. Each coil is sensitive to a different location and so provides a high SNR for the signal from that location. Note that this requires separate amplifier channels for each coil. If the signals from the different coils were combined before being sent to a single amplifier, the noise from each coil would contaminate the signals from the other coils, destroying the SNR advantage.

## Gradient and radiofrequency coils

Any configuration of wires carrying a current creates a magnetic field in the vicinity of the wires. We will refer to any such arrangement as a coil, even if it is not a simple loop or helical configuration. In MRI, coils are used for generating the main magnetic field for generating gradient fields used for imaging, for generating the oscillating radiofrequency (RF) field used to tip over the local magnetization, and for detecting the NMR signal. A surface coil for detecting the signal may be as simple as a single loop of wire, but the designs of more complex RF and gradient coils are much more sophisticated. Nevertheless, we can appreciate how different field patterns can be created by considering two prototype coil configurations produced by combining two circular coils carrying a current. The field of each coil separately was shown in Fig. 6.1, and the net fields for two coil arrangements are illustrated in Fig. 6.4. Each set consists of two circular coils oriented on a common axis, with the currents parallel in the first set (Fig. 6.4A) and opposite in the second set (Fig. 6.4B).

The first arrangement, called a Maxwell pair, produces a rather uniform field between the two coils, with the field diverging and weakening at the two ends. If many such coils are stacked together, the result is a solenoid with a very uniform field inside. This is the basic coil

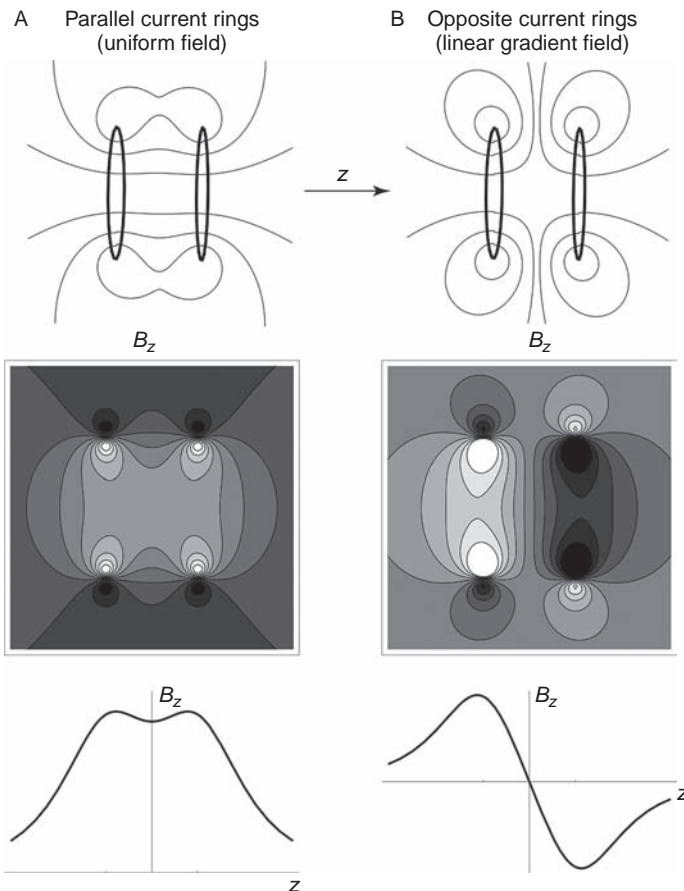


**Fig. 6.4.** Two simple coil configurations suggest how the geometry of magnetic fields can be manipulated. (A) Two circular coils with parallel currents, called a Maxwell pair, create a roughly uniform field between them, a prototype for the solenoid current arrangement that generates a uniform main magnetic field  $B_0$ . (B) Two circular coils with opposite currents, called a Helmholtz pair, generate a linear gradient field in the region between them, a prototype for the gradient coils used for imaging. The top row shows the field lines, the middle row shows contour plots of the  $z$ -component of the magnetic field ( $B_z$ ), and the bottom row shows plots of  $B_z$  versus  $z$  along the axis of the coils.

design used for creating  $B_0$  in an MRI system, and in a commercial scanner the field variation over a central region of approximately 20 cm is less than a few tenths of a part per million. The field strength depends on the total current flowing through the coil, and large, uniform magnetic fields can be created when superconducting (zero resistance) coils are used.

The arrangement of two coils with currents running in opposite directions is known as a Helmholtz pair. The effect of this arrangement is that the fields created by the two loops tend to cancel in the region halfway between them. Moving off-center along the coil axis, the field increases in one direction and decreases in the other direction. This type of field is called a *gradient field*, and gradient fields are a critical part of MRI. In an MR imager, the gradient coils produce additional fields, which add to  $B_0$ . The direction of  $B_0$  is usually defined as the  $z$ -axis, and the goal with a gradient coil is to produce an additional field along  $z$  such that  $B_z$  varies linearly along one axis. In practice, the designs for linear imaging gradients are more sophisticated than this simple Helmholtz pair to improve the linearity and homogeneity of the field. That is, for an ideal linear gradient coil the field component  $B_z$  varies linearly moving along the coil axis but is uniform moving perpendicular to the coil axis.

In imaging applications, we are interested in just the  $z$ -component of the field offset because that is the only component that will make a significant change in the net field amplitude and so affect the resonant frequency. A weak field component, of the order of a few parts per million, perpendicular to  $B_0$  will produce a change in the total field magnitude of the order of  $10^{-12}$ , a negligible amount. But an offset in  $B_z$  itself of a few parts per million will directly alter the total field strength, and thus the resonant frequency, by a few parts per million. Offsets of this magnitude are comparable to the field offsets between one voxel and its neighbor during frequency encoding in MRI. The important effect of gradient fields for imaging is that they modify the  $z$ -component, producing a gradient of  $B_z$ .

The preceding discussion suggests how different coil configurations can be used to generate different patterns of magnetic field. However, when a coil is used for signal *detection*, the physics at first glance seems to be rather different. As described in the [previous section](#) of this chapter, the current induced in a coil by a local precessing magnetization is proportional to the changing magnetic flux through the coil. Fortunately, it turns out that there is a simple relation between the magnetic field *produced* by a coil when a current is run through it and the current *induced* in the coil by an external changing magnetic field. For any coil used as a detector, an associated *sensitivity* pattern describes the strength of the signal produced in the coil by sources at different locations in space. One could calculate the sensitivity map by placing rotating dipoles at many positions relative to the coil and using the changing magnetic flux rule to determine the induced current. However, this sensitivity pattern also can be calculated from a useful rule called the *principle of reciprocity*: the sensitivity of any coil to a rotating magnetic dipole at any point in space is directly proportional to the magnetic field that would be produced at that point in space by running a current through the coil. Specifically, imagine a precessing magnetic dipole  $M$  sitting near a coil, and consider the magnetic field vector  $\mathbf{b}$  that would be produced at the location of the dipole by running a unit current through the coil. The signal produced in the coil by the dipole depends directly on the vector  $\mathbf{b}$ : the signal is proportional to the product of the magnitude of  $\mathbf{b}$  and the component of  $M$  that lies along  $\mathbf{b}$  (i.e., the scalar product of  $\mathbf{b}$  and  $M$ ). For example, if the arrangement of the coil is such that  $\mathbf{b}$  is perpendicular to  $M$  (such as a circular coil with its axis along  $z$ ), no signal is generated. For any orientation, the magnitude of  $\mathbf{b}$  is small far from the coil, so the sensitivity of the coil is weak. Therefore, an RF coil can be thought of

as having two roles: a producer of magnetic fields and a detector of changing magnetic fields. The geometrical pattern associated with each is the same.

## Dynamics of nuclear magnetization

### Interaction of a magnetic dipole with a magnetic field

In the previous discussion, we focused on the magnetic field created by a magnetic dipole. In NMR, the fundamental interaction is between the magnetic dipole moment of the atomic nucleus and the local external magnetic field, which is characterized by two basic effects. The first is that the field exerts a torque on the dipole that tends to twist it into alignment with the field, and the second is that in a non-uniform field there is a force on the dipole pulling it toward the region of stronger field. These effects are most easily understood by considering an electric dipole in an electric field. A magnetic dipole in a magnetic field behaves in the same way as the electric dipole, but the physical arguments that demonstrate this are more subtle (details are given in the Appendix).

An electric dipole can be thought of as two opposite charges attached to a rod of fixed length, with the direction of the dipole vector running from the negative to the positive charge. When the dipole is placed at an angle to a uniform electric field (Fig. 6.5), there is a moment arm between the points where the two forces are applied, and the result is a torque on the dipole. One end is pulled up, the other is pushed down, and the dipole pivots around the center. The only stable configuration for the dipole is when it is aligned with the field. When the dipole is placed in a non-uniform electric field, again the field will produce a torque that will align the dipole with the field. However, because the field is not uniform, the forces on the positive and negative charges do not balance even when the dipole is aligned with the field; the force down on the lower charge is stronger than the force up on the positive charge in Fig. 6.5. The result is that there is a net force downward on the dipole, pulling the dipole toward the region of stronger field. If the dipole is aligned opposite to the field, the force also is opposite, pushing the dipole toward the region of weaker field. However, such an alignment would be unstable for an electric dipole: the torque would twist it 180°, and it would be pulled toward the region with a stronger field.

Both of these effects can be described in an equivalent way in terms of the energy of a dipole in a field. The dipole has the lowest energy when it is aligned with the field, and the energy progressively increases as the dipole is tipped away from the field. The highest energy configuration is when the dipole is aligned opposite to the field. Similarly, the energy of the

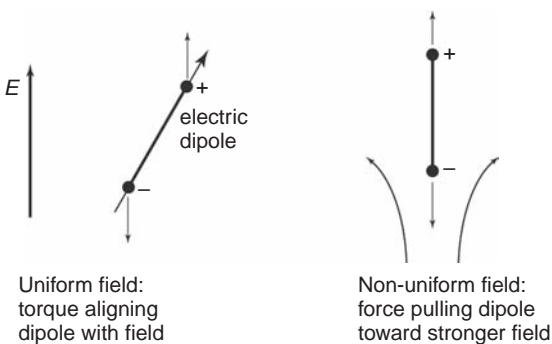


**Fig. 6.5.** Dipole interactions with a field. The nature of the forces is most easily illustrated by an electric dipole placed in an electric field  $E$ . An electric dipole consists of two opposite charges separated by a short distance, and an external field exerts a torque acting to align the dipole with the field and a force drawing the aligned dipole into regions of stronger field. (Forces are shown as thin arrows.)



dipole is lower when it is in a stronger field, so it is drawn toward regions with a larger field. Both alignment with the field and moving toward stronger fields are then examples of the system seeking a lower energy state.

## Precession

A magnetic dipole placed in a magnetic field experiences the same two effects: a torque tending to align the dipole with the field and a force drawing it toward regions of stronger field. However, for a nuclear magnetic dipole the intrinsic angular momentum of the nucleus changes the dynamics in a critical way. Viewing a magnetic dipole as a rotating charged sphere brings out the close connection between the magnetic moment and the angular momentum. Both the angular momentum and the magnetic dipole moment are proportional to the rate of spin of the sphere. Faster rotation increases the angular momentum as well as the current produced by the charges on the surface, and so also increases the magnetic moment. Because of this intimate link between angular momentum and the magnetic dipole moment, the ratio of the two is a constant called the *gyromagnetic ratio* ( $\gamma$ ). Each nucleus that exhibits NMR has a unique value of  $\gamma$ .

The presence of angular momentum makes the dynamics of a magnetic dipole in a magnetic field distinctly different from the dynamics of an electric dipole in an electric field. As already described, the effect of the field is to exert on the dipole a torque that would tend to twist it into alignment. Physically, torque is the rate of change of angular momentum, analogous to Newton's first law that force is the rate of change of momentum. Precession comes about because the torque axis is perpendicular to the existing angular momentum around the spin axis. The *change* in angular momentum then is along the direction of the torque and so is always perpendicular to the existing angular momentum. In other words, the change in angular momentum produced by the torque is a change in the *direction* of spin, not the magnitude. Thus, the angular momentum (and the spin axis) precesses around the field. (A more mathematical derivation of precession is given in the Appendix.)

This is an example of the peculiar nature of angular momentum and is exactly analogous to the behavior of a spinning top or bicycle wheel. A spinning top tipped at an angle to the vertical would be in a lower energy state if it simply fell over; instead, the rotation axis precesses around a vertical line. For a nucleus in a magnetic field, the frequency of precession, called the *Larmor frequency* ( $\omega_0$ ), is  $\gamma B_0$ ; the stronger the field, the stronger the torque on the dipole and the faster the precession. We will use the convention that when frequency is represented by  $\omega$ , it is expressed as angular frequency (radians per second), and when it is represented by  $\nu$ , it is expressed as cycles per second (Hz), with the relation  $\omega = 2\pi \nu$ . The equation for the Larmor frequency holds regardless of whether we are using angular frequency or cycles per second, with a suitable adjustment in the magnitude of  $\gamma$ . The precession frequency  $\omega_0 = \gamma B_0$  is the resonant frequency of NMR.

## Relaxation

The foregoing considerations apply to a single nucleus in a magnetic field. From the precession arguments alone, one might conclude that a proton would never align with the main field, despite the fact that the energy is lower. However, in a real sample,  $B_0$  is not the only source of magnetic field. The magnetic moments of other nuclei produce additional, fluctuating magnetic fields. For example, in a water molecule, an H nucleus feels the field produced by the other H nuclei in the molecule. Because the molecules are rapidly tumbling in their thermal motions, the total field felt by a particular nucleus fluctuates around the mean field  $B_0$ . These

fluctuations alter both the magnitude of the total magnetic field and the direction felt by that nucleus. As a result, the proton's precession is more irregular, and the axis of precession fluctuates. Over time, the protons gradually tend to align more with  $B_0$ , through the process called *relaxation*. Note, though, that relaxation is a much slower process than precession: relaxation times on the order of 1 s are approximately  $10^8$  times longer than the precession period with a typical MRI magnet.

Because the energy associated with the orientation of the magnetic dipole moment of an H nucleus in a magnetic field is small compared with the thermal energy of a water molecule, the average degree of alignment with the field is small, corresponding to a difference of only approximately 1 part in  $10^5$  between those nuclei aligned with the field and those opposite. However, this is sufficient to produce a slight net equilibrium magnetization ( $M_0$ ) of the water. The creation of  $M_0$  can be understood as a relaxation toward thermal equilibrium. When a sample is first placed in a magnetic field, the magnetic dipoles are randomly oriented so that the net magnetization is zero. This means that the dipoles possess a higher energy based on their orientation than they would if they were partly aligned with the field. (The lowest possible energy would correspond to complete alignment.) As the system relaxes, this excess energy is dissipated as heat; the dipoles align more with the field, and the longitudinal magnetization  $M$  grows toward its equilibrium value  $M_0$ .

In a pure water sample, the main source of a fluctuating magnetic field that produces relaxation is the field produced by the other H nucleus in the same water molecule. But the presence of other molecules in the liquid (e.g., protein) can alter the relaxation rate by changing either the magnitude or the frequency of the fluctuating fields. A large molecule will tumble more slowly than a water molecule and, as a result, a water molecule that transiently binds to the large molecule will experience more slowly fluctuating fields. The magnitude of the fluctuating fields can be increased significantly in the presence of paramagnetic compounds. Paramagnetic compounds have unpaired electrons, and electrons have magnetic moments more than a thousand times larger than a proton. This is the basis for the use of paramagnetic contrast agents, such as gadolinium-labeled diethylenetriaminepentaacetic acid (Gd-DTPA), as a way of reducing the local relaxation time. The physical sources of the relaxation times are discussed more fully in Ch. 7.

The time constant for relaxation along the magnetic field, creating the net magnetization  $M_0$ , is  $T_1$  and varies from approximately 0.2 to 4.0 s in the body. The fact that  $T_1$  varies by an order of magnitude between different tissues is important because this is the source of most of the contrast differences between tissues in MR images. The  $T_1$  variations result from differences in the local environment (e.g., chemical composition or biological structures). In general, the higher the water content of a tissue, the longer the  $T_1$ . The strong dependence of the relaxation time on the local environment is exactly analogous to everyday experiences of relaxation phenomena. A cup of hot coffee sitting in a cool room is not in thermal equilibrium. Over time, the coffee will cool to room temperature (thermal equilibrium), but the time constant for this relaxation depends strongly on the local environment. If the coffee is in a thin-walled open cup, it may cool in a few minutes, whereas if it is in a covered, insulated vessel, it may take hours to cool. Regardless of how long it takes to get there, the final equilibrium state (cold coffee) is the same. Similarly with NMR relaxation, the value of  $M_0$  depends on the density of dipoles and the magnetic field, but the value of  $T_1$  required to reach this equilibrium depends on the environment of the spins.

The relaxation time  $T_1$  is called the *longitudinal* relaxation time because it describes the relaxation of the component of the magnetization that lies along the direction of  $B_0$ . Two

other relaxation times,  $T_2$  and  $T_2^*$ , describe the decay of the *transverse* component of the magnetization. At equilibrium, the magnetization is aligned with  $B_0$ , so there is no transverse component. Application of a  $90^\circ$  RF pulse tips the magnetization into the transverse plane, where it precesses and generates a signal in a detector coil by induction. In a homogeneous field, the transverse component, and therefore also the NMR signal, decays away with a time constant  $T_2$ , and this process often is abbreviated as transverse relaxation. In the human body at field strengths typical of MR imagers,  $T_1$  is approximately 8–10 times larger than  $T_2$ .

In practice, one finds experimentally that the NMR signal often decays more quickly than would be expected for the  $T_2$  of the sample. This is qualitatively described by saying that the decay time is  $T_2^*$ , with  $T_2^*$  less than  $T_2$ . The reason for this is simply inhomogeneity of the magnetic field. If two regions of the sample feel different magnetic fields, the precession rates will differ, the local transverse magnetization vectors will quickly get out of phase with each other, and the net magnetization will decrease through phase dispersion. However, this signal decay results from constant field offsets within the sample and not the fluctuating fields that produce  $T_2$  decay. Because of this, the additional decay caused by inhomogeneity is reversible with a spin echo, introduced in Ch. 3 and discussed in more detail in Ch. 7.

The combined processes of precession and relaxation are mathematically described by the *Bloch equations*, a set of differential equations for the three components of the magnetization (Box 6.1). These are the basic dynamic equations of NMR and are used frequently to describe the behavior of the magnetization.

### Box 6.1. The Bloch equations

Early in the development of NMR, Bloch proposed a set of differential equations to model the dynamics of the magnetization produced by nuclear magnetic dipoles in a magnetic field. The equations include precession, as derived above, and also exponential relaxation with relaxation times  $T_1$  and  $T_2$ . The representation of relaxation is essentially empirical, designed to reproduce the experimentally observed exponential dynamics. The Bloch equations are still the basic equations used to understand the magnitude of the NMR signal. The equations are written separately for the three components of the magnetization,  $M_x$ ,  $M_y$ , and  $M_z$  in a magnetic field  $B_0$  along the  $z$ -axis:

$$\frac{dM_x}{dt} = \gamma B_0 M_y - \frac{M_x}{T_2}$$

$$\frac{dM_y}{dt} = -\gamma B_0 M_x - \frac{M_y}{T_2}$$

$$\frac{dM_z}{dt} = -\frac{M_z - M_0}{T_1}$$

Precession is incorporated into the equations in the way that the rates of change of the two transverse components,  $M_x$  and  $M_y$ , depend on the current values because precession rotates  $M_x$  partly into  $M_y$ , and vice versa. Relaxation is described by a steady decrease of the transverse component by the transverse relaxation rate,  $1/T_2$ , and relaxation with a rate  $1/T_1$  of the  $M_z$  component toward the equilibrium magnetization  $M_0$ . If we start with an arbitrary magnetization

vector, with a transverse component  $M_{xy}(0)$  and a longitudinal component  $M_z(0)$ , the magnitudes of these components at later times given by the solution of the Bloch equations are:

$$M_{xy} = M_{xy}(0) e^{-t/T_2}$$

$$M_z = M_0 - [M_0 - M_z(0)] e^{-t/T_1}$$

In addition to these magnitude changes, the full solution also includes precession of the transverse component with frequency  $\gamma B_0$ .

The transverse component decays exponentially with time constant  $T_2$ . The relaxation of the longitudinal component can be described as an exponential decay with time constant  $T_1$  of the difference between the starting value  $M_z(0)$  and the equilibrium value  $M_0$ . In fact, we could describe both decay processes as an exponential decay of the *difference* between the initial state and the equilibrium state, and the equilibrium state is  $M_0$  along  $M_z$  and a transverse component of zero.

The preceding equations describe relaxation and free precession when the only magnetic field acting on the magnetization is  $B_0$ . To describe what happens during the RF pulse, we must also include the effects of an oscillating field  $B_1$ . This is most easily represented in a frame of reference rotating at the frequency of  $B_1$  oscillations,  $\omega$ . This transformation essentially takes out the basic precession and simplifies the equations. In this rotating frame,  $B_1$  appears to be constant, and we can take it to lie along the  $x$ -axis. Also, the apparent precession rate of  $M$  caused by  $B_0$  in this rotating frame is reduced to  $\omega_{\text{rot}} = \omega_0 - \omega$ , and so it appears as if the magnetic field in the  $z$ -direction has been reduced to  $B_z = B_0 - \omega_1/\gamma$ . The effective magnetic field ( $B_{\text{eff}}$ ) in the rotating frame then has two components,  $B_1$  along the  $x$ -axis and  $B_z$  along the  $z$ -axis, and the dynamics of  $M$  is then precession around  $B_{\text{eff}}$  plus relaxation. If we represent the amplitude of  $B_1$  as an equivalent precession frequency  $\omega_1 = \gamma B_1$  (the rate at which  $M$  would precess around  $B_1$ ), the Bloch equations in the rotating frame take the form:

$$\frac{dM_x}{dt} = \omega_{\text{rot}} M_y - \frac{M_x}{T_2}$$

$$\frac{dM_y}{dt} = -\omega_{\text{rot}} M_x - \frac{M_y}{T_2} + \omega_1 M_z$$

$$\frac{dM_z}{dt} = -\frac{M_z - M_0}{T_1} - \omega_1 M_y$$

This form of the equations clearly shows how the dynamics of the magnetization depends on four distinct rate constants: the off-resonance frequency of  $B_1$ ,  $\omega_{\text{rot}}$ ; the amplitude of  $B_1$  expressed as a precession frequency,  $\omega_1$ ; and the two relaxation rates,  $1/T_2$ , and  $1/T_1$ . Different proportions of these parameters produce a wide range of dynamics. Furthermore, in a tailored RF pulse, the amplitude of  $B_1$  is a function of time, and in an adiabatic pulse the off-resonance frequency is also a function of time.

## Radiofrequency excitation

Nuclear magnetic resonance is a transient phenomenon. The fact that the magnetic dipole moments of protons tend to align with the field, producing a net magnetization  $M_0$ , does not lead to any measurable signal (a constant magnetic field produces no currents). However, if

$M_0$  is tipped away from the direction of  $B_0$ , it will precess; all the nuclear dipoles will precess together if they are tipped over, so  $M_0$  also will precess at the same frequency. The transverse component of  $M_0$  then produces a changing magnetic field and will generate a transient NMR signal in a nearby detector coil by induction.

The tipping of the magnetization is accomplished by the RF pulse, an oscillating magnetic field  $B_1$  perpendicular to  $B_0$  and oscillating at the proton precession frequency. It is simplest to picture  $B_1$  as a small magnetic field with constant amplitude in the transverse plane that rotates at a rate matched to the proton precession rate. Such a field is described as a *circularly polarized* oscillating field. When  $B_1$  is turned on, the net field, the vector sum of  $B_0$  and  $B_1$ , is tipped slightly away from the  $z$ -axis and rotates over time. Because  $M_0$  along the  $z$ -axis is no longer aligned with the net magnetic field, it begins to precess around the net field even as that field itself rotates. In other words, the basic physical process involved with the RF pulse is still just precession of  $M_0$  around a magnetic field, but it is now more difficult to picture because the magnetic field itself is also rotating as the magnetization tries to precess around it. To understand the complexity of this process, a useful conceptual tool is the *rotating frame of reference*.

To introduce the rotating frame, forget  $B_1$  for the moment and picture a magnetization vector  $M$  tipped away from the  $z$ -axis (Fig. 6.6). We know that in the laboratory frame of reference, the magnetization will simply precess around the field  $B_0$  lying along the  $z$ -axis. We will ignore relaxation effects for now as well and assume that we are watching the magnetization for a short enough time that relaxation effects are negligible. Because the time scale for precession is so much shorter than that for relaxation, we could observe the precession for thousands of cycles with no detectable effects from relaxation. Now imagine that we observe this precession from a frame of reference that is itself rotating at the Larmor frequency ( $\omega_0 = \gamma B_0$ ). In this frame, we are carried around at the same rate as the precession, as though we were riding on a turntable, and so in the rotating frame the magnetization appears to be stationary. Because there appears to be no precession in the rotating frame, it appears as if there is no magnetic field (i.e., as if  $B_0$  is zero). Now suppose that we are in a rotating frame rotating with an arbitrary angular frequency  $\omega$ . In this new rotating frame, the magnetization precesses around the  $z$ -axis, but with an effective angular frequency  $\omega_0 - \omega$ .

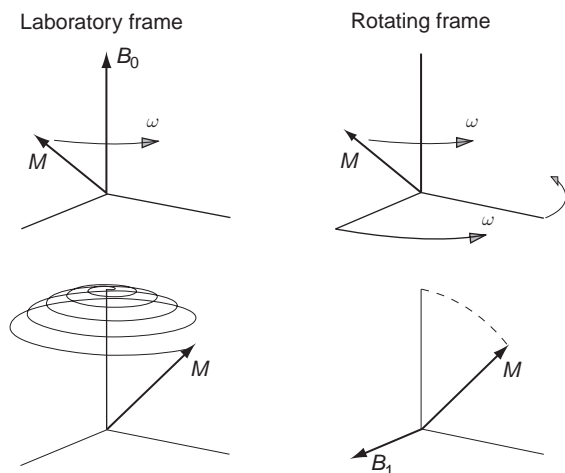


**Fig. 6.6.** The rotating frame of reference. In the laboratory frame of reference, the magnetization ( $M$ ) precesses around the magnetic field ( $B_0$ ) with a frequency  $\omega$ . In a frame of reference rotating at the same rate, the magnetization appears to be stationary, so in this frame there appears to be no magnetic field. A radiofrequency (RF) field  $B_1$  rotating at the resonant frequency appears stationary in the rotating frame, and RF excitation is then a simple precession of  $M$  around  $B_1$  in the rotating frame. In the laboratory frame, this motion is a slowly widening spiral.

In other words, the magnetization behaves in this rotating frame exactly as it would in a stationary frame if the magnetic field were reduced from  $B_0$  to  $B_0 - \omega/\gamma$ . This is the power of the rotating frame as a conceptual tool: the physics of precession is the same in a rotating frame as in a stationary frame, but the apparent magnetic field in the rotating frame is changed.

We can now return to the RF pulse and look at  $B_1$  in the frame rotating with angular velocity  $\omega$ , the oscillation frequency of  $B_1$ . To begin with, we will assume that  $B_1$  is oscillating on-resonance with the protons ( $\omega = \omega_0$ ), and we will return to consider off-resonance effects later. In the rotating frame,  $B_1$  is constant, and we will call its direction the  $x$ -axis of the rotating frame. When  $B_1$  is on-resonance, the apparent field along the  $z$ -axis is zero in the rotating frame. This means that from this perspective there is only the field  $B_1$  along  $x$ , so  $M_0$  begins to precess around the  $x$ -axis in the rotating frame. The RF field  $B_1$  is much weaker than  $B_0$ , so the rate of precession around  $B_1$  is correspondingly slower. But if we wait long enough (perhaps a few milliseconds for the RF pulses used in imaging), the magnetization will rotate around  $B_1$ , tipping away from the  $z$ -axis and toward the  $y$ -axis of the rotating frame. If  $B_1$  is left on long enough to tip  $M_0$  fully on to the  $y$ -axis, the RF pulse is called a  $90^\circ$  pulse. If left on longer, or if the amplitude of  $B_1$  is increased, the flip angle can be increased to  $180^\circ$  or even  $360^\circ$ , which would leave  $M_0$  where it started along the  $z$ -axis. Thus, the complex picture of precession around a time-varying magnetic field in the laboratory frame is reduced to a simple precession around  $B_1$  in the rotating frame. To picture the full dynamics of the magnetization as it would appear in the laboratory frame, this slow precession around  $B_1$  must be added to a rapid precession of the rotating frame itself around the  $z$ -axis. The net result in the laboratory frame is a tight spiral that slowly increases the angle between  $M_0$  and  $B_0$  (Fig. 6.6).

After  $B_1$  is turned off,  $M_0$  continues to precess around  $B_0$  and generates a signal in the detector coil. The signal is called a *free induction decay* (FID), where *free* relates to free precession, *induction* is the physical process described above in which a varying magnetic field (the precessing magnetization) produces a current in a coil, and *decay* indicates that the signal eventually dies out. Over time,  $M_0$  will relax until it is again aligned with  $B_0$ . Because the action of an RF pulse is to tip  $M_0$  away from  $B_0$ , such pulses usually are described by the *flip angle* (or *tip angle*) they produce (e.g., a  $90^\circ$  RF pulse or a  $180^\circ$  RF pulse). The flip angle is adjusted by changing either the duration or the amplitude of  $B_1$ .

From the thermodynamic point of view, the process of tipping  $M_0$  can be interpreted as the system of magnetic dipoles absorbing energy from the RF field because the alignment of  $M_0$  is changing and then dissipating this energy over time as heat as the system relaxes back to equilibrium. For this reason, the RF pulse is often described as an *excitation pulse* because it raises the system to an excited (higher energy) state.

## Frequency selective radiofrequency pulses: slice selection

In the previous description of the RF pulse, we assumed that  $B_1$  was oscillating at precisely the resonant frequency of the protons,  $\omega_0$ . What happens if the RF pulse is off-resonance? This is an important question for imaging applications because the process of *slice selection*, which limits the effects of the excitation pulse to just a thin slice through the body, is based on the idea that an RF pulse far off-resonance should have a negligible effect on the magnetization. Slice selection is accomplished by turning on a magnetic field gradient during the RF pulse so that the resonant frequency of spins above the desired slice will be higher, and that of spins below the slice will be lower, than the frequency of the RF pulse. The RF pulse

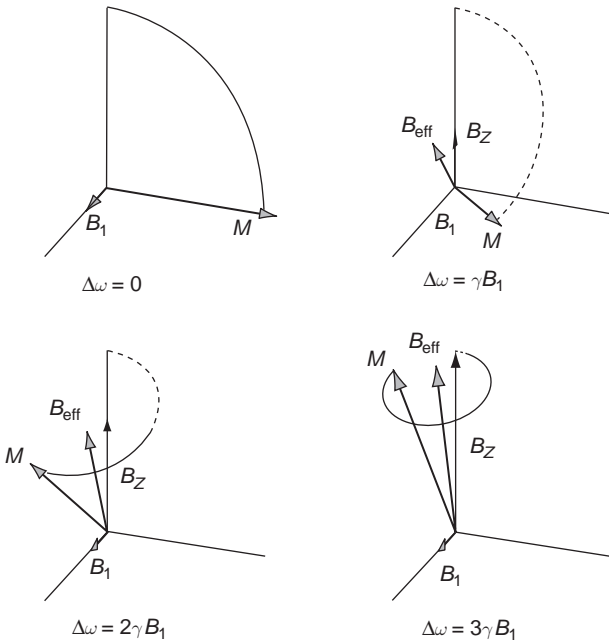


**Fig. 6.7.** Off-resonance excitation. The effect of an off-resonance radiofrequency (RF) pulse ( $B_1$ ) can be understood as precession around the effective field in the rotating frame. Because the rotation of the frame differs from the precession frequency of the magnetization ( $M$ ), the precession of  $M$  in the rotating frame is equivalent to precession in a magnetic field  $B_z$ . The vector sum of  $B_1$  and  $B_z$  is the effective field  $B_{\text{eff}}$ . When  $B_1$  is on-resonance (top left), the effect is a simple  $90^\circ$  flip of  $M$ , but as the off-resonance frequency  $\Delta\omega$  is increased, the RF pulse is less effective in tipping over  $M$ .

will then be on-resonance for the spins at the center of the slice, and only these will be tipped over. However, for spins slightly removed from the central slice plane, the RF pulse will only be a little off-resonance, so we would expect that these spins will be partly flipped, but not as much as those at the center. The slice profile, the response of spins through the thickness of the slice, will then depend on the degree of tipping produced by a slightly off-resonance RF pulse. The most desirable slice profile is a perfect rectangle because this means that the slice has a well-defined slice thickness and a sharp edge. In practice, this cannot be achieved, but with carefully tailored RF pulses the slice profile approaches a rectangle.

We can understand the physics of off-resonance excitation by returning to the frame of reference rotating at the oscillation frequency  $\omega$  of  $B_1$ , and we will now relax our earlier assumption that  $\omega$  is equal to  $\omega_0$  (Fig. 6.7). If  $\omega$  and  $\omega_0$  are different, then in the rotating frame the magnetization behaves as though there were an apparent field along the  $z$ -axis of  $B_z = B_0 - \omega/\gamma$ . In other words, in the absence of  $B_1$ , the magnetization would precess in the rotating frame around the  $z$ -axis with an angular frequency  $\omega_0 - \omega$ . When  $B_1$  is turned on along the  $x$ -axis in the rotating frame, the effective field  $B_{\text{eff}}$  is the vector sum of  $B_z$  and  $B_1$ , and so is a vector lying somewhere in the  $x$ - $z$  plane. If  $B_1$  is nearly on-resonance, then  $\omega_0 - \omega$  is small and  $B_z$  is small, so  $B_{\text{eff}}$  points only slightly away from the  $x$ -axis. But if the frequency of  $B_1$  is far off-resonance,  $B_{\text{eff}}$  points nearly along the  $z$ -axis. The effective field is constant in the rotating frame, so the motion of  $M_0$  is simply a precession around  $B_{\text{eff}}$  with angular frequency  $\gamma B_{\text{eff}}$  for the duration of the  $B_1$  pulse.

Qualitatively, then, we can see why a far off-resonance pulse does little tipping of the magnetization because, with  $B_{\text{eff}}$  nearly aligned with the  $z$ -axis, the precession around  $B_{\text{eff}}$  leaves  $M_0$  very near to its original orientation along the  $z$ -axis (Fig. 6.7). More quantitatively, this picture can be used to calculate the effects of off-resonance excitation, and thus the slice

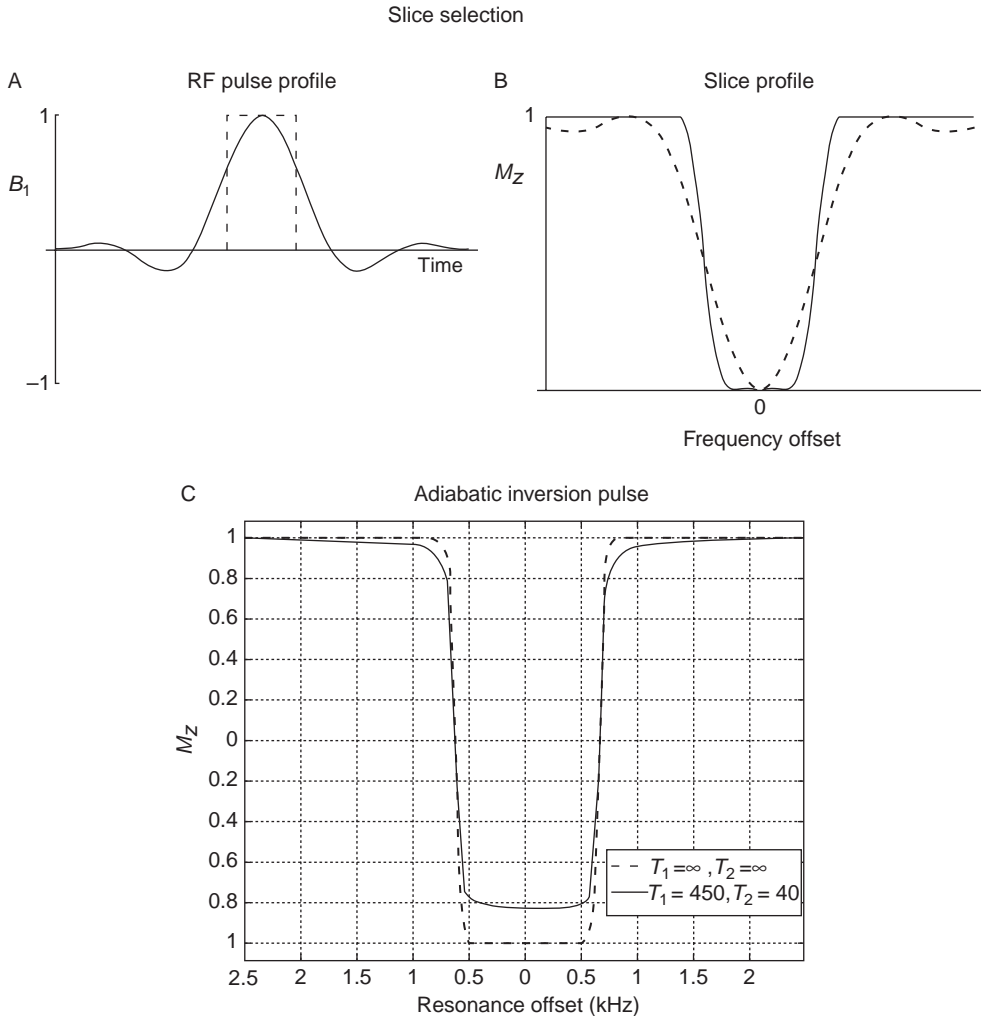


**Fig. 6.8.** Slice selection with frequency-selective radiofrequency (RF) pulses. Slice selection in MRI uses RF pulses with a narrow bandwidth in combination with a magnetic field gradient to tip over spins within a narrow range of positions. For two RF pulse shapes (A) the resulting slice profiles are shown by plotting the remaining  $z$ -magnetization ( $M_z$ ) after the pulse (B). A simple rectangular RF pulse produces a poor slice profile, but a longer, shaped RF pulse produces a profile closer to a rectangle. With even longer, adiabatic pulses, the profile is even better, as illustrated by the inversion profile (C). With the adiabatic pulse the duration is long enough for relaxation to begin to have an effect. (Adiabatic inversion plot courtesy of L. Frank)

profile in an imaging experiment. **Figure 6.8A** shows  $M_z$  after an RF pulse with an amplitude and duration matched to give a  $90^\circ$  flip angle on-resonance. Two curves are shown, one for a constant amplitude  $B_1$  throughout the RF pulse and one for a tailored RF pulse in which the amplitude of  $B_1$  is modulated. By modulating the amplitude of  $B_1$ , the frequency selectivity of the pulse, and thus the slice profile, can be improved considerably. The cost of using a shaped pulse, however, is that the duration of the RF pulse is increased. The on-resonance flip angle is proportional to the area under the RF pulse profile, so a constant amplitude pulse is the most compact in time. To create a shaped RF pulse profile with the same



duration and flip angle, the peak amplitude of  $B_1$  would have to be significantly increased, but hardware limitations set the maximum peak amplitude. So it is usually necessary to extend the duration of the RF pulse to produce a cleaner slice profile.

## Adiabatic radiofrequency pulses

The slice profile can be further improved by allowing  $B_1$  to vary in frequency as well as amplitude. An *adiabatic RF pulse* is an example that produces a particularly clean slice profile (Frank *et al.* 1997; Silver *et al.* 1985). In an adiabatic pulse, the magnetization is not so much precessing around the effective field as following it as it slowly rotates. To see how this works, imagine starting  $B_1$  far off-resonance. Then  $B_{\text{eff}}$  is nearly along the  $z$ -axis, and the magnetization will precess around it, while remaining nearly parallel to  $B_{\text{eff}}$ . If we now slowly change the frequency of  $B_1$ , moving it closer to resonance, the effective field will slowly tip toward the  $x$ -axis. If this is done slowly enough, so that the magnetization precesses many times around  $B_{\text{eff}}$  during the process, then  $M_0$  will follow  $B_{\text{eff}}$ , precessing in a tight cone around it, as  $B_{\text{eff}}$  slowly tips toward the  $x$ -axis. As soon as the frequency of  $B_1$  reaches  $\omega_0$ , the effective field and  $M_0$  will lie along the  $x$ -axis, and the net effect will be a  $90^\circ$  pulse. If the pulse is continued, moving beyond the resonance condition until  $M_0$  is rotated on to the negative  $z$ -axis, the net effect is a  $180^\circ$  inversion pulse. As shown in Fig. 6.8C, the slice profile can be quite good. The cost of this, however, is that such RF pulses take a long time to play out because of the need to sweep slowly through frequency. In imaging applications, a standard slice selection pulse may take 3 ms, whereas a good adiabatic pulse may require 20 ms or more.

Finally, an ingenious application of the idea of an adiabatic pulse is the selective inversion of flowing blood using a continuous RF pulse. Calling something a continuous pulse sounds like an oxymoron, but it is actually fairly descriptive: no RF field lasts forever, so really any applied RF field is a pulse, and *continuous* just indicates that it is on for a much longer time (e.g., several seconds) than is typical for a standard excitation pulse. Such pulses are often used in arterial spin labeling (ASL) methods for measuring cerebral blood flow (Alsop and Detre 1996). The goal in such experiments is to invert the magnetization of arterial blood (i.e., flip it  $180^\circ$ ) before the blood reaches the tissue of interest and then subtract this tagged image from a control image in which the blood was not inverted. This ASL difference signal is then directly proportional to the amount of blood delivered to the tissue. Continuous inversion works on the same principle as an adiabatic RF pulse, except that  $B_1$  is constant; it is the resonant frequency of the moving spins that is varied. This is accomplished by turning on a gradient in the superior/inferior direction so that as an element of blood moves up the artery toward the head its resonant frequency changes because its position in the gradient field changes. The frequency of the RF pulse is set to correspond to the resonant frequency in a particular transverse plane in the neck or head. When an element of blood is far from this zero plane,  $B_1$  is off-resonance, and so the effective field is nearly along the  $z$ -axis. As the blood approaches the zero plane, the  $z$ -component of the effective field diminishes as the resonant frequency approaches the RF frequency. When the blood crosses the zero plane,  $B_{\text{eff}}$  is entirely along  $x$ , and as the blood continues, moving off-resonance in the other direction,  $B_{\text{eff}}$  tips down toward the negative  $z$ -axis. If this sweep of  $B_{\text{eff}}$  is slow enough, the magnetization will follow  $B_{\text{eff}}$  and end up inverted. This continuous labeling technique produces a steady stream of inverted blood as long as the RF is turned on. Chapter 13 discusses ASL techniques in greater detail.

## Magnetic properties of matter

### Paramagnetism, diamagnetism, and ferromagnetism

Matter contains several components that possess magnetic dipole moments, and the nuclear spins that give rise to NMR are actually among the weakest. Far more important in determining the magnetic properties of materials are the magnetic dipole moments of unpaired electrons. The dipole moment of an electron is three orders of magnitude larger than that of a proton, and so the alignment of electron magnetic moments in a magnetic field leads to much larger effects. Based on our preceding arguments about the interactions of a magnetic dipole with a magnetic field, we would expect that when a sample is placed in a magnetic field  $B_0$ , the dipole moments in the sample would tend to align with the field, creating a net dipole moment parallel to the field. If the magnetic field is non-uniform, we would expect there to be a net force on the sample drawing it toward the region of higher field.

To test this prediction, that materials should feel a force in a non-uniform field, we could perform an experiment using a standard MR imager. The magnet is typically oriented horizontally, with a uniform magnetic field in the center but a diverging and weakening field near the ends of the bore. Then we would expect that, as a sample of a particular material is brought near to the bore, it would feel a force pulling it into the magnet. Because the magnetization associated with the intrinsic magnetic dipoles is weak, the force on most materials should also be weak, so a sensitive measuring system is required. When this experiment is performed on a variety of materials, some, such as aluminum, are pulled toward the bore with a force on the order of 1% of the weight of the sample, and these materials are described as *paramagnetic*. However, many other materials, such as water, are weakly repulsed by the magnetic field and pushed away from the bore with weaker forces, and these materials are described as *diamagnetic*. Finally, a third class of materials, including iron and magnetite, are strongly attracted toward the magnet, with forces orders of magnitude larger than those of paramagnetic materials. These materials are described as *ferromagnetic*.

From our foregoing arguments about the forces on dipoles in a field, paramagnetism is easily understood and expected. Paramagnetism arises primarily from the effects of unpaired electrons aligning with the magnetic field, with a small additional component from the alignment of nuclear dipoles (Fig. 6.9). But the existence of diamagnetism is unexpected because a repulsive force indicates a net dipole moment aligned opposite to the field. Diamagnetism results from the effects of the magnetic field on the orbital motions of the electrons. An electron orbiting an atom or molecule is effectively a current, and so there is a magnetic dipole moment associated with the orbital state, as well as the spin state, of the electron. The curious feature of these induced orbital dipole moments, however, is that the net dipole moment is oriented opposite to the external magnetic field.

Diamagnetism can be understood in a rough classical physics way by looking at the oversimplified picture of two atoms with electrons orbiting the nucleus in different directions (Fig. 6.9). The orbital magnetic dipole moment is opposite for the two different orbital directions, and both directions of rotation are equally likely. With no magnetic field, the net magnetization is zero. The stability of the electron orbit results from the balance between the inward electrical force and the outward centrifugal force from the electron's velocity. When a magnetic field is added, the additional magnetic force on the electron is inward for one sense of orbital motion and outward for the other. If the velocities of the electrons adjust to

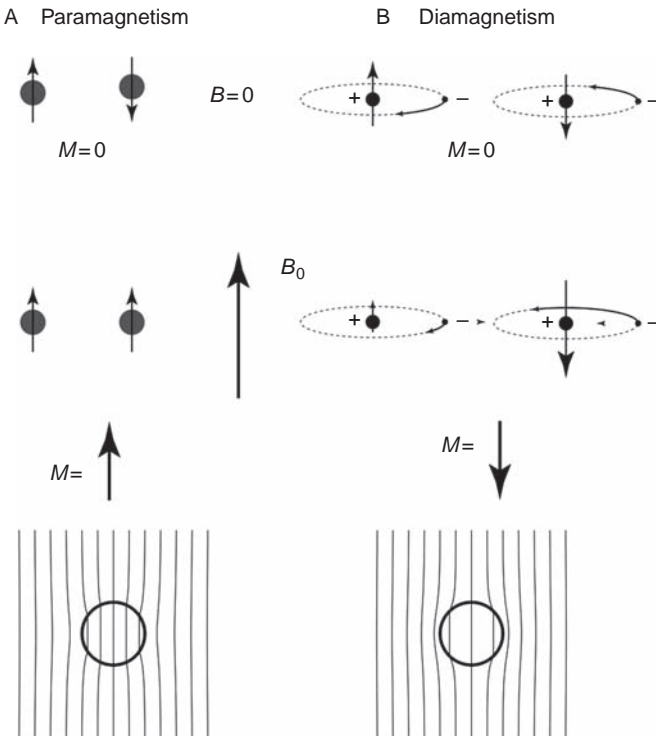


**Fig. 6.9.** Paramagnetism and diamagnetism. (A) Magnetic dipole moments (unpaired electrons and nuclei) align with the magnetic field to produce a magnetization ( $M$ ) aligned with the main magnetic field  $B_0$  (paramagnetism). (B) The magnetic dipole moments resulting from the orbital motions of electrons are altered to produce a net magnetization aligned opposite to the field (diamagnetism). For diamagnetism, the diagrams suggest how the added force from the magnetic field either adds to or subtracts from the centrifugal force on the electron; consequently, the electron velocity for stability increases or decreases depending on the direction of motion. The bottom row shows distortions of uniform magnetic field lines by a magnetized sphere.

rebalance the forces, one is sped up and the other slowed down, increasing the magnetic dipole moment aligned opposite to the field and decreasing the other. The net magnetization is then opposite to the field.

All materials have diamagnetic effects as a result of orbital electron motions that create a magnetization aligned opposite to the field, and some materials in addition have paramagnetic effects from the spins of unpaired electrons, which create a magnetization aligned with the field. The net magnetization that results reflects the balance between diamagnetic and paramagnetic effects, and the classification of materials as diamagnetic or paramagnetic reflects the outcome of this balance. But both diamagnetism and paramagnetism are relatively weak effects, in that the magnetic forces on such materials, even in a magnetic field as high as those used for imaging, are still only approximately 1% of the force of gravity.

A striking exception to this discussion of materials that interact weakly with a magnetic field is a ferromagnetic material, which can be strongly magnetized when placed in a magnetic field and can retain that magnetization when the field is removed. The very large magnetization induced in such materials corresponds to the coordinated alignment of many electron spins, although the magnetic interactions of the spins are not responsible for the coordination. In ferromagnetic materials such as iron, unpaired electrons are in a lower

energy state when they are aligned with each other, for reasons related to the quantum nature of the spins. The unpaired electron spins of nearby atoms in a crystal of iron then tend to become aligned with each other, forming a small volume of material with a uniform orientation, called a *domain*. A large block of material consists of many domains, with a random direction of orientation within each domain. Each domain is still microscopic but nevertheless contains billions of atoms, and so the magnetic field associated with the aligned electrons is quite large. In the absence of an external magnetic field, there is no net magnetization because of the random orientation of the domains. When the iron is placed in a magnetic field, the domains aligned with the field are energetically favored, and they begin to grow at the expense of the other domains. That is, the electrons in a neighboring domain switch their orientation to join the favored domains. The result is the creation of a very large magnetization, and even after the external field is turned off the rearranged domain structure tends to persist, leaving a permanent magnetization.

Ferromagnetic materials are always excluded from the vicinity of an MRI system. Small fragments of ferromagnetic material can severely distort MR images. Even a sample as small as a staple can produce a large area of signal dropout in an image. More seriously, the inadvertent use of ferromagnetic tools in the vicinity of a large magnet is a severe safety risk. In the field of a 1.5 T magnet, the magnetic force on a 2 lb (1 kg) iron wrench is more than 50 lb (23 kg), and the wrench will fly toward the scanner. Care should always be taken to check carefully any equipment brought into the MR scan room to ensure that no ferromagnetic components can become dangerous projectiles. In addition, subjects must be carefully screened to ensure that they have no ferromagnetic materials in their body, such as metal plates, old surgical clips, or even small metal fragments from sheet metal work. From here on we will focus only on materials that are weakly magnetized.

## Magnetic susceptibility

In addition to the magnetic forces discussed above, a second effect of placing a sample of a material in a magnetic field is that the local magnetic field is distorted by the interaction of the internal dipole moments with the field. Each cubic millimeter of the material contains many magnetic dipole moments, and each of these dipoles creates its own dipole field. In a magnetic field, the dipole moments tend to align with the field if the material is paramagnetic, or opposite to the field if it is diamagnetic, and the sum of the moments of each of these dipoles is the net magnetization of the material. The net magnetization is the equivalent dipole density in the material and so depends on both the intrinsic dipole density and the degree of alignment of the dipoles.

The creation of a net magnetization has two important effects for MR imaging. The first is that the part associated with the alignment of nuclear dipoles is the magnetization that can be manipulated to generate the NMR signal. The second effect is that other dipole moments, such as unpaired electrons, contribute a much larger net magnetization, and this creates an additional, non-uniform magnetic field that adds to the main field  $B_0$ . For example, the effect on the total magnetic field of placing a sphere of diamagnetic or paramagnetic material in a uniform field is illustrated in the bottom row of Fig. 6.9. In the absence of the sphere, the field lines are vertical and parallel. For a paramagnetic sphere, the field lines are pulled in and concentrated within the sphere, and for the diamagnetic sphere the lines are pushed out from the sphere. These field inhomogeneities produce distortions and signal loss in MR images, but they also are the basis for functional imaging exploiting the BOLD effect or using injected contrast agents.

The degree to which a material becomes magnetized is measured by the *magnetic susceptibility*,  $\chi$ , of the material: the local magnetization  $M$  is  $\chi B_0$ . As  $M$  has the same dimensions as  $B_0$ ,

$\chi$  is dimensionless. This can be a bit confusing because  $M$  is the equivalent density of magnetic dipoles, rather than a magnetic field, despite the fact that they have the same units. The magnetic fields produced in the neighborhood of a magnetized body are of the same order as  $M$ , but they also depend on the geometrical shape of the body. For most materials, the value of  $\chi$  is of the order of a few parts per million, so the additional weak field that results from the alignment of intrinsic magnetic dipoles in matter is typically only a few parts per million of  $B_0$ . The susceptibility  $\chi$  may be positive (paramagnetic) or negative (diamagnetic), depending on whether the component of magnetization resulting from the unpaired electrons or the component from the orbital motions is dominant. Exogenous contrast agents used in MRI are paramagnetic.

It is important to maintain a clear distinction between the local magnetization of a magnetized body and the magnetic field created by that magnetized body. Whenever a body with a uniform composition is placed in a uniform magnetic field, it becomes uniformly magnetized. This means that in any small volume of the body, the partial alignment of the magnetic dipoles of the body is the same, so they add up to a uniform magnetization throughout. All this is independent of the shape of the body; it is a direct effect of the interaction of each of the dipoles with the magnetic field, leading to partial alignment. A collection of partially aligned dipoles, in turn, creates its own magnetic field through all of space, and this field adds to  $B_0$ . This additional field depends strongly on the geometry of the body.

However, if the local magnetization of a body depends on the partial alignment of the dipoles with the local field, and the local field is then altered by the additional field produced by the magnetized body, would this feed back on the local magnetization itself and alter it? The presence of the magnetized body does alter the local field, and indeed this does alter the local magnetization, but by a negligibly small amount. The field distortions in the human head are only approximately 1 ppm of  $B_0$ , so the variations in the local magnetization from this additional field are only 1 ppm of 1 ppm, and so are negligibly small. For practical purposes then, we can assume that a body of arbitrary shape but uniform composition, when placed in a uniform magnetic field  $B_0$ , becomes uniformly magnetized with a dipole moment density  $M = \chi B_0$ .

The field distortions around a magnetized body depend on the shape of the body. Figure 6.10 shows the pattern of field offsets around a uniformly magnetized sphere. For this simple spherical geometry, field distortion is again a dipole field pattern. That is, adding up the contributions from each of the individual dipoles produces a field that is equivalent to one big dipole at the center of the sphere. However, this is only true for the perfect symmetry of a sphere; a body with a more complex shape would produce a more complex field distortion. Another simple geometrical shape that is relevant for fMRI is a long cylinder oriented perpendicular to the magnetic field (Fig. 6.10). The field distortion is qualitatively similar to the distortion around a sphere, although the radial dependence is different: the field offset falls off as  $1/r^3$  for the sphere, but  $1/r^2$  for the cylinder ( $r$  is the radial distance). At the surface of the cylinder, the maximum field offset  $\Delta B$  is  $2\pi\Delta\chi B_0$ , where  $\Delta\chi$  is the susceptibility difference between the inside and the outside of the cylinder, and this maximum offset is independent of the radius of the cylinder. A magnetized cylinder is a useful model for thinking about blood vessels magnetized by the presence of deoxyhemoglobin and the resulting BOLD effect.

In the preceding discussion we have focused on the field distortions outside a magnetized body, but for most shapes the field inside is distorted as well. The sphere and the infinitely long cylinder are special cases in that they produce a uniform field offset inside. A short cylinder produces an external field intermediate between that of a sphere and a long cylinder, and the internal field is also distorted.

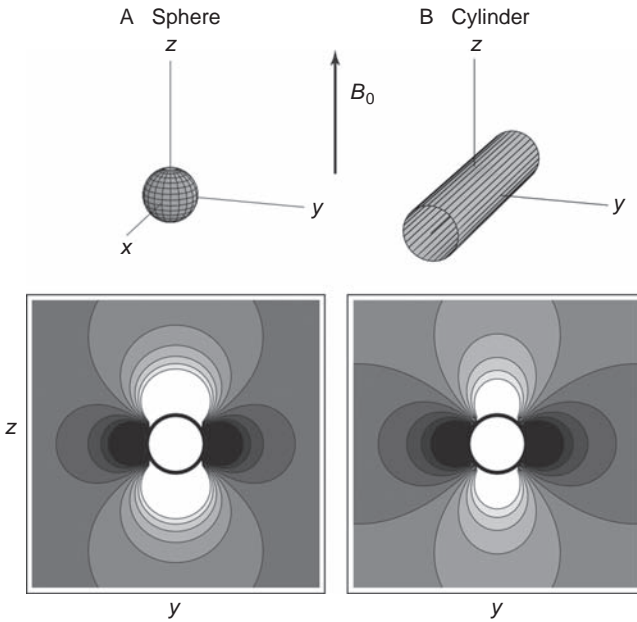


**Fig. 6.10.** Magnetic field distortions around magnetized objects. Contour plots of the offset of the  $z$ -component of the field,  $B_z$ , in a plane cutting through a uniformly magnetized sphere (A) and cylinder (B). Both patterns have a dipole-like shape.

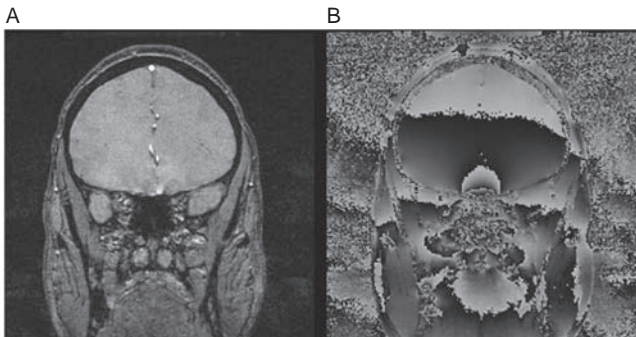


**Fig. 6.11.** Magnetic field distortions in the head. A coronal gradient echo image, showing magnitude (A) and phase (B). The phase map shows magnetic field distortions owing to the heterogeneity of the brain. Distortions include a dipole-like field near the sinus cavity and a superior–inferior gradient.

## Field distortions in the head

The significance of these magnetic susceptibility effects is that whenever a body is placed in a uniform, external magnetic field  $B_0$ , the net field is distorted both outside and inside the body. This happens even if the body has a perfectly uniform composition and depends strongly on the shape of the body. Furthermore, if the body is heterogeneous, composed of materials with different magnetic susceptibilities, the field distortion is even worse. Figure 6.11 (shown also as Fig. 4.10) shows the field distortion within a human head when it is placed in a uniform magnetic field. To a first approximation, the head consists of three types of material: water, bone, and air. Field distortions are evident in the vicinity of interfaces between these materials. The large sinus cavities produce a local field distortion rather like a dipole field, which extends through several centimeters of the brain, and also there is a broad field gradient in the superior–inferior direction caused by the presence

of the rest of the body. In general, the size of the field distortion in terms of the volume affected is comparable to the size of the heterogeneity. The largest field offsets result from the air–water interface near the sinus cavities. Detailed modeling of the air spaces of the head predict field offsets of a few parts per million, in good agreement with what is measured (Li *et al.* 1995).

In MRI such field distortions within the body are a nuisance. A central assumption of MRI is that the magnetic field is uniform so that any field offsets measured when the field gradients are applied are entirely a result of the location of the source of the signal, and not caused by intrinsic field non-uniformity. Field distortions caused by magnetic susceptibility variations between tissues thus lead to distortions in the MR images, and for some imaging techniques (e.g., EPI) these distortions can be severe. For this reason, MR scanners are equipped with additional coils called *shim coils*, which can be used to flatten the magnetic field. This process is called shimming the magnetic field, and it is important to remember that this involves correcting for the intrinsic inhomogeneities of the human body as well as for non-uniformities of the magnet itself.

The macroscopic field distortions shown in Fig. 6.11 are an unwanted byproduct of tissue heterogeneity. However, *microscopic* field distortions around small blood vessels are the basis for both contrast agent studies of blood volume and BOLD-fMRI. A gadolinium-based contrast agent alters the susceptibility of the blood, creating field offsets in the space around the vessels (Villringer *et al.* 1988). At the peak of the passage of a bolus of Gd-DTPA through the vasculature, the susceptibility change of the blood is approximately 0.1 ppm (Boxerman *et al.* 1995), and if we model the vessels as long cylinders, this produces maximum field offsets of approximately 0.6 ppm. The BOLD effect is based on the fact that during brain activation the O<sub>2</sub> content of the venous blood is increased, which in turn alters the blood susceptibility relative to the surrounding tissue water. The susceptibility change owing to increased oxygenation of the blood in the activated state is on the order of 0.01 ppm (Weisskoff and Kiihne 1992), so the maximum field offsets are approximately 0.06 ppm. Because the susceptibility difference between the blood and the surrounding water is reduced when the blood is more oxygenated, the signal increases slightly. Magnetic susceptibility effects relevant to fMRI thus span nearly two orders of magnitude, from the large-scale heterogeneity of the brain that produces field variations of a few parts per million and image artifacts, to BOLD microscopic susceptibility differences of a few hundredths of a part per million, which reveal areas of functional activity.

## References

- Alsop DC, Detre JA (1996) Reduced transit-time sensitivity in non-invasive magnetic resonance imaging of human cerebral blood flow. *J Cereb Blood Flow Metab* **16**: 1236–1249
- Boxerman JL, Hamberg LM, Rosen BR, Weisskoff RM (1995) MR contrast due to intravascular magnetic susceptibility perturbations. *Magn Reson Med* **34**: 555–566
- Feynman RP, Leighton RB, Sands M (1965) *The Feynman Lectures on Physics*. New York: Addison-Wesley
- Frank LR, Wong EC, Buxton RB (1997) Slice profile effects in adiabatic inversion: application to multislice perfusion imaging. *Magn Reson Med* **38**: 558–564
- Grant PE, Vigneron DB, Barkovich AJ (1998) High resolution imaging of the brain. *MRI Clin N Am* **6**: 139–154

- Li S, Williams GD, Frisk TA, Arnold BW, Smith MB (1995) A computer simulation of the static magnetic field distribution in the human head. *Magn Reson Med* **34**: 268–275
- Purcell EM (1965) *Electricity and Magnetism*. New York: McGraw-Hill
- Silver MS, Joseph RI, Hoult DI (1985) Selective spin inversion in nuclear magnetic resonance and coherent optics through an exact solution of the Bloch–Riccati equation. *Phys Rev A* **31**: 2753–2755
- Villringer A, Rosen BR, Belliveau JW, *et al.* (1988) Dynamic imaging with lanthanide chelates in normal brain: contrast due to magnetic susceptibility effects. *Magn Reson Med* **6**: 164–174
- Weisskoff RM, Kiihne S (1992) MRI susceptometry: image-based measurement of absolute susceptibility of MR contrast agents and human blood. *Magn Reson Med* **24**: 375–383



<b>Introduction</b>	page 147
<b>The spin echo signal</b>	148
Spin echoes	148
Spin echo signal intensity	150
Image contrast	150
Generalized echoes	156
Stimulated echoes	156
Multiple echo pathways from a string of radiofrequency pulses	158
<b>The gradient echo signal</b>	159
Gradient echoes	159
Decay constant $T_2^*$ and chemical shift effects	160
Controlling $T_1$ weighting with the flip angle	162
Steady-state free precession	163
The varieties of gradient echo pulse sequences	165
<b>Sources of relaxation</b>	166
Fluctuating fields	166
A simple model for transverse relaxation	167
The difference between longitudinal and transverse relaxation rates	168
Contrast agents	170

## Introduction

The contrast between one tissue and another in an MR image varies over a wide range depending just on the pulse sequence used for imaging. This dramatic soft-tissue contrast makes MRI sensitive to subtle differences in anatomy. In this chapter, we will consider the basic factors that affect the MR signal and determine the contrast characteristics of an image. How this signal is mapped to produce an MR image is taken up in [Ch. 9](#), but it is helpful to remember that an MR image is essentially a snapshot of the distribution of the MR signal, and we will illustrate some of the signal characteristics with images.

The flexibility of MRI comes about largely because the MR signal depends on a number of tissue properties. The utility of MRI for clinical studies stems from the variability of the relaxation times between one tissue type and another and between healthy and diseased tissue. The important questions for clinical imaging then tend to focus around issues of static signal contrast, and pulse sequences for best emphasizing the tissue differences (Hendrick *et al.* 1984). For functional imaging, however, physiological changes such as altered blood oxygenation have more subtle effects on the MR signal, and the goal is to detect dynamic changes in the signal over time. In the following sections, the sources of contrast in an MR image are discussed in terms of how the intrinsic NMR properties of the tissue,

such as the relaxation times and the proton density, interact with different pulse sequence parameters to affect the signal intensity. We then examine the physical factors and conditions that determine these NMR properties.

## The spin echo signal

### Spin echoes

In a simple free induction decay (FID) experiment, the generated signal decays away faster than it should as a result of  $T_2$  decay alone because of magnetic field inhomogeneity. Spins sitting in different magnetic fields precess at different rates, and the resulting phase dispersion reduces the net signal. The apparent relaxation time  $T_2^*$  then is less than  $T_2$ . We can separate the decay of the net signal from a sample into two processes: the intrinsic decay of the local signal from a small, uniform region, which is governed by  $T_2$ , and the mutual cancellation of signals from different nearby locations from the phase dispersion caused by field inhomogeneities. The net decay is described by  $T_2^*$ , but it is sometimes useful to isolate the decay caused by inhomogeneities from that resulting from  $T_2$  (Hoppel *et al.* 1993). This additional decay caused by inhomogeneities alone has been called  $T_2'$  decay. The assumed relationship between these three quantities is:  $1/T_2^* = 1/T_2 + 1/T_2'$ . The inverse of a relaxation time is a relaxation *rate constant*, and it is the rates that add to give the net relaxation effects. But it is important to remember that this relationship is really only qualitative. It would be a correct quantitative description if inhomogeneities always create a monoexponential decay, but that is rarely the case. Nevertheless, it is useful to think of signal decay in these terms.

As introduced in Ch. 3, signal loss as a result of field inhomogeneity can be reversed by applying a second radiofrequency (RF) pulse that causes the magnetization vectors to come back into phase and create an echo of the original FID signal (a *spin echo*, SE) at a time (the *echo time*, TE) after the original excitation pulse. To review how this remarkable effect comes about, imagine two small magnetized regions sitting in slightly different magnetic fields. After a  $90^\circ$  excitation pulse, the magnetization vectors are tipped into the transverse plane. As they begin to precess at slightly different frequencies, the phase difference between them grows larger. After waiting a time TE/2, a  $180^\circ$  RF pulse is applied along the  $y$ -axis in the rotating frame. The action of the  $180^\circ$  pulse is to flip the transverse plane like a pancake, reversing the *sign* of the phase of each magnetization vector. In other words, the phase  $\phi_1$  of the first magnetization is changed to  $-\phi_1$ , and the phase  $\phi_2$  of the second group is changed to  $-\phi_2$ . After the RF pulse, the phase of each magnetization continues to evolve, just as before, so that after another time delay TE/2 the first group again acquires an additional phase  $\phi_1$ , and the second group again acquires an additional phase  $\phi_2$ . At this point, the net phase of each group is then zero, meaning that they are back in phase and add coherently to form a strong net signal (the echo) at time TE.

In fact, the echoing process is quite general, and any RF pulse will create an echo, although with flip angles other than  $180^\circ$ , the refocusing is not complete. In particular, repeated RF pulses generate a rich pattern of echoes, and we will consider this phenomenon in more detail later in the chapter. To understand the formation of echoes, it is helpful to examine how a  $180^\circ$  RF pulse rotating spin vectors around the same axis as the original  $90^\circ$  pulse (the  $x$ -axis of the rotating frame), also produces an echo. Figure 7.1 illustrates the formation of an echo by a  $180^\circ$  pulse by following the fate of four representative spin vectors. After a  $90^\circ$  pulse around  $x$  tips the spin vectors into the transverse plane, they each begin to precess at a different rate owing to field inhomogeneity. In Fig. 7.1, spin vector 1 has the

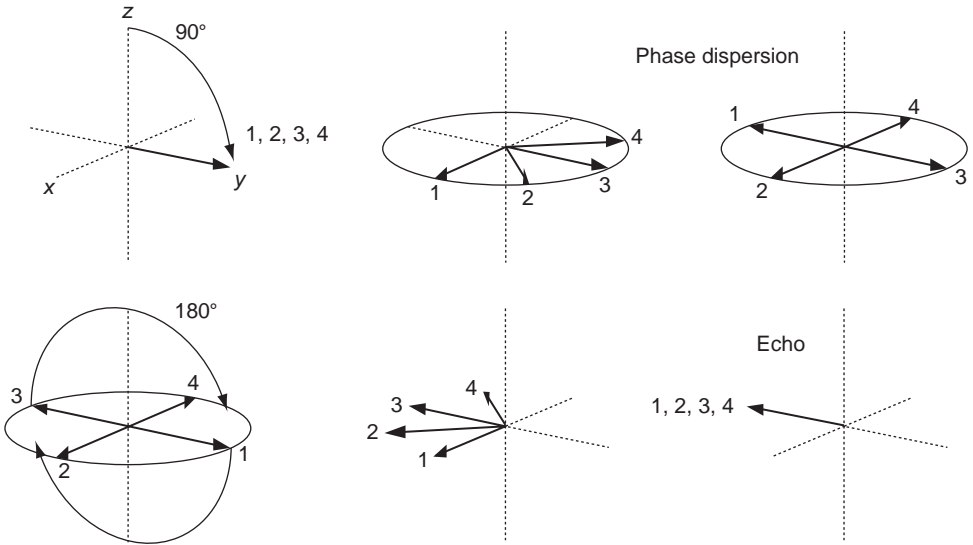


**Fig. 7.1.** Formation of a spin echo. The separate fates of four representative spin vectors are depicted during a spin echo pulse sequence. After being tipped into the transverse plane by a  $90^\circ$  pulse around the  $x$ -axis in the rotating frame, the spins precess at different rates because of field inhomogeneities, spreading into a disk in the transverse plane (top). A  $180^\circ$  pulse around  $x$  flips the disk, and the continued precession of each spin causes an echo to form along the  $-y$ -axis.

highest offset of the precession frequency, vector 3 is on-resonance and so appears to be stationary in the rotating frame, and vectors 2 and 4 have plus and minus precession frequency offsets half as large as that for vector 1. After a time sufficient for vector 1 to accumulate a phase offset of  $180^\circ$  from vector 3, the vectors have spread evenly in the transverse plane.

The  $180^\circ$  RF pulse then flips this plane around the  $x$ -axis, reversing the positions of vectors 1 and 3 and leaving vectors 2 and 4 unchanged. Each vector then continues to precess, and after an equal elapsed time they are all in phase along the  $-y$ -axis, creating an echo. The distinction between this example and the first example is that the  $180^\circ$  pulse is applied along the  $x$ -axis rather than the  $y$ -axis. In the first example, the echo formed along the  $+y$ -axis, and in the second example (with the RF along the  $x$ -axis) the echo formed along the  $-y$ -axis, but in both cases all of the spin vectors come back into phase to form a strong echo. In short, a  $180^\circ$  RF pulse applied along any axis will create a strong echo, but the orientation of this echo depends on the axis of the RF pulse.

Note that although a  $180^\circ$  pulse will correct for field inhomogeneities, it will not refocus true  $T_2$  decay. The reason an echo forms is that the phase acquired during the interval before the  $180^\circ$  pulse is exactly the same as the phase acquired during the interval after the pulse. But the phase variations associated with  $T_2$  decay are caused by fluctuating fields, and the pattern of fluctuations is not repeated before and after the RF pulse. In short, an SE reverses the de-phasing effects of static fields but not fluctuating fields. As a result, the echo signal intensity is weaker than the initial FID signal due to  $T_2$  decay during the interval TE. After the echo, the signal again decays because of  $T_2^*$  effects, but another  $180^\circ$  RF pulse will create another echo. This can be continued indefinitely, but each echo will be weaker than the last because of  $T_2$  decay.

The basic SE pulse sequence can be summarized as:

90° pulse – wait TE/2 – 180° pulse – wait TE/2 – measure

Typically, this pulse sequence is repeated at a regular interval called the repetition time (TR). In a conventional MRI setting, it is necessary to repeat the pulse sequence many times to collect all the data needed to reconstruct the image. The contrast between one tissue and another in the image will depend on the magnitude of the SE signal generated at each location.

## Spin echo signal intensity

The mathematical expression for the SE signal is derived in [Box 7.1](#). The signal is always proportional to the local proton density but also depends on the relaxation times. There are two pulse sequence parameters that are operator controlled: TR and TE ([Fig. 7.2](#)). These parameters control how strongly the local tissue relaxation times,  $T_1$  and  $T_2$ , affect the signal. The TE is the time when the SE occurs as a result of the refocusing effects of the 180° pulse and is typically the time when the MR signal is measured. By lengthening TE (i.e., waiting a longer time after the excitation pulse before applying the 180° refocusing pulse), there is more time for transverse ( $T_2$ ) decay. The repetition time, by comparison, controls how much longitudinal relaxation is allowed to happen before the magnetization is tipped over again when the pulse sequence is repeated. During the period TR, a sample with  $T_2$  much shorter than TR will relax nearly completely, and so the longitudinal magnetization just before the next 90° pulse is large. But a sample with  $T_1$  longer than TR will be only partly relaxed, and the longitudinal magnetization will be smaller. After the next 90° pulse, this longitudinal magnetization becomes the transverse magnetization and generates a signal, so the sample with the short  $T_1$  will produce a stronger signal.

The SE signal can be viewed as having some degree of proton density weighting,  $T_1$  weighting, and  $T_2$  weighting in the sense that all these parameters contribute to the signal, and different tissues can be distinguished in an image based on how their differences in equilibrium magnetization ( $M_0$ ),  $T_1$ , and  $T_2$  modify the local signal intensity. The SE sequence is always proton density weighted because  $M_0$  is proportional to the proton density, and the maximum signal that can be generated is proportional to  $M_0$ . But this maximum signal is only achieved when TR is much longer than  $T_1$  so that the longitudinal magnetization fully recovers between repetitions, and when TE is much smaller than  $T_2$  so that the signal decay during TE is negligible. For other pulse sequence parameters, there will be some degree of  $T_1$  weighting and  $T_2$  weighting in the local signal. The sensitivity of the signal to  $T_1$  is controlled by TR, with longer TR decreasing the  $T_1$  weighting of the signal, and the sensitivity to  $T_2$  is controlled by TE, with shorter TE decreasing  $T_2$  weighting.

## Image contrast

It seems plausible that we could maximize the contrast between two tissues by maximizing the sensitivity to both  $T_1$  and  $T_2$  differences. However, this turns out to be a bad idea. In the body, proton density,  $T_1$ , and  $T_2$  are positively correlated, so that more watery tissues (e.g., cerebrospinal fluid [CSF]) tend to have larger proton density and longer  $T_1$  and  $T_2$ , and this leads to conflicting contrast effects.  $T_1$  weighting produces a stronger signal from tissues with short relaxation times, whereas  $T_2$  weighting tends to produce a stronger signal from the tissues with long relaxation times ([Fig. 7.2](#)). If the signal is sensitive to both  $T_1$  and

**Box 7.1. The magnetic resonance signal equations**

From the Bloch equations (Box 6.1), the expected signal intensity for any pulse sequence can be derived. From such signal equations, expressing the dependence on  $M_0$ ,  $T_1$ ,  $T_2$ , and the pulse sequence parameters, the expected image contrast between tissues can be calculated. We can illustrate the procedure by deriving the signal intensity for an SE pulse sequence, a  $90^\circ$  RF pulse followed by a  $180^\circ$  pulse after a delay  $TE/2$ , and with the pulse sequence repeated after  $TR$ . The pulse sequence can be described in a compact way as

$$90^\circ \text{ pulse} - \text{wait } TE/2 - 180^\circ \text{ pulse} - \text{wait } TE/2 - \text{measure} - \text{wait } (TR - TE)$$

Note that  $TR$  is the interval between the initial  $90^\circ$  pulse and the next repeat of the  $90^\circ$  pulse, the sum of each of the waiting intervals in this notation. If  $TR$  is not much longer than  $T_1$ , then the magnetization will not have fully recovered during the  $TR$  interval. After the pulse sequence is repeated a few times, a steady state will develop such that the magnetization just before each  $90^\circ$  RF pulse is the same, and the signal generated is then described as the steady-state signal for that pulse sequence.

Our goal is to calculate this steady-state signal. If  $M_z(0)$  is the longitudinal magnetization just before the  $90^\circ$  pulse, the initial magnitude of the transverse magnetization after the pulse will also be  $M_z(0)$ . The signal is measured at  $TE$ , and so the SE signal is  $M_z(0)e^{-TE/T_2}$ . The question then is what is  $M_z(0)$ ?

We can calculate the steady-state longitudinal magnetization by following through the pulse sequence, rotating the components of the magnetization as required by the RF pulses, incorporating relaxation in the intervals between RF pulses as dictated by the Bloch equations, and then applying the steady-state condition that the resulting magnetization at time  $TR$  must be the same as that we started with at time zero. Mathematically, the growth of  $z$ -magnetization can be described as an exponential decay of the difference between the current value of  $M_z$  and the equilibrium value  $M_0$ , so that if the  $z$ -magnetization starts at  $M_{z1}$  and relaxes for a time  $t$ , the final magnetization is

$$M_z = M_0 - (M_0 - M_{z1}) e^{-t/T_1}.$$

This rule is applied twice to calculate how the  $z$ -magnetization evolves. The progressive changes in the  $z$ -component of the magnetization are as follows. The  $90^\circ$  pulse tips  $M_z(0)$  into the transverse plane, and the longitudinal component then begins to grow from zero, reaching a value of

$$M_z = M_0 - [M_0 - M_z(0)] e^{-TE/2T_1}$$

by time  $TE/2$ . The  $180^\circ$  pulse flips the regrown component from  $+z$  to  $-z$ , and it then begins to regrow from this negative value. After relaxing for a time  $TR - TE/2$ , the longitudinal magnetization is back to the starting point, just before the  $90^\circ$  pulse, and so this magnetization is again  $M_z(0)$  in the steady state. Applying the same relaxation rule for the period after the  $180^\circ$  pulse to the expression for  $M_z$  directly gives an expression for  $M_z(0)$ . The full SE signal intensity is then

$$S_{SE} = M_0 e^{-TE/T_2} (1 - 2 e^{-(TR-TE/2)/T_1} + e^{-TR/T_1}) \quad (B7.1)$$

Note that if  $TE$  is very short, the signal is approximately

$$S_{SE} \approx M_0 e^{-TE/T_2} (1 - e^{-TR/T_1}) \quad (B7.2)$$

We can apply the same type of reasoning to other pulse sequences to derive appropriate expressions for the NMR signal. For the inversion recovery (IR) pulse sequence with an SE acquisition, the form of the pulse sequence is

180° pulse – wait TI – 90° pulse – wait TE/2 – 180° pulse – wait TE/2  
 – measure – wait (TR – TI – TE),

where TI is the inversion time.

The initial 180° pulse acts as a preparation pulse, modifying the longitudinal magnetization, and the transverse magnetization is not created until the 90° pulse is applied after TI. The second 180° pulse creates an SE of this transverse magnetization. The resulting signal intensity is

$$S_{\text{IR}} = M_0 e^{-\text{TE}/T_2} (1 - 2e^{-\text{TI}/T_1} + 2e^{-(\text{TR}-\text{TE}/2)/T_1} - e^{-\text{TR}/T_1}) \quad (\text{B7.3})$$

If  $\text{TR} \gg \text{TI}$ , the IR signal is approximately

$$S_{\text{IR}} \approx M_0 e^{-\text{TE}/T_2} (1 - 2e^{-\text{TI}/T_1}) \quad (\text{B7.4})$$

The IR signal differs from the SE signal in two ways. First, the signal is more  $T_1$  weighted because of the factor 2 in Eq. (B7.4) compared with Eq. (B7.2). This expresses the fact that the IR signal is recovering over a range twice as large ( $-M_0$  to  $M_0$ ) as the range of the SE signal (0 to  $M_0$ ). The second unique feature of the IR signal is that there is a null point when the longitudinal magnetization, relaxing from a negative value, passes through  $M_z = 0$ . A 90° pulse applied at this time will generate no signal because the longitudinal magnetization is zero. The null point occurs when  $\text{TI} = T_1 \ln 2 = 0.693 T_1$  so that the expression in parentheses in Eq. (B7.4) is zero. This effect is used in imaging to suppress the signal from particular tissues. For example, fat has a short  $T_1$ , and so the fat signal is nulled when TI is approximately 150 ms. This is described as a *short TI inversion recovery* (STIR) pulse sequence.

The preceding calculations of signal intensities are relatively simple because of an implicit assumption that TR is much greater than  $T_2$  and so the transverse magnetization has completely decayed away before the pulse sequence is repeated. However, for GRE pulse sequences this is often not true. The calculation of signal intensity is then quite a bit more complicated because all three components of the magnetization must be considered (Buxton *et al.* 1989; Gyngell 1988). Another way of stating the complexity of this problem is that when TR is shorter than  $T_2$ , each RF pulse creates echoes of the previous transverse magnetization, and these echoes add to form the net signal. However, with a spoiled GRE pulse sequence, the formation of these echoes is prevented (the echoes are spoiled), and for this case the signal can be calculated in the same manner as for the SE and IR signals (Buxton *et al.*, 1987). The pulse sequence is then very simple:

$\alpha$  – wait TE – measure – wait (TR – TE).

The flip angle is now taken to be an arbitrary angle  $\alpha$ , and the effect of this is that the longitudinal magnetization is not reduced to zero with each excitation pulse. Taking this into account, the resulting signal intensity is

$$S_{\text{GRE}} = M_0 e^{-\text{TE}/T_2^*} \sin \alpha \frac{1 - e^{-\text{TR}/T_1}}{1 - \cos \alpha e^{-\text{TR}/T_1}} \quad (\text{B7.5})$$

Note that the transverse decay now depends on  $T_2^*$ , rather than  $T_2$ , because there is no SE to refocus the effects of magnetic field inhomogeneity. This expression for the signal exhibits some interesting properties that differ from the SE and IR cases. When TR is long, the maximum signal is produced with a flip angle of 90°, as one would expect. But as TR becomes shorter, the flip angle that produces the maximum signal is reduced. This flip angle for maximum signal is the Ernst angle  $\alpha_E$  (Ernst and Anderson 1966) and is given by

$$\cos \alpha_E = e^{-\text{TR}/T_1} \quad (\text{B7.6})$$

For example, with  $TR = 30$  ms and  $T_1 = 1000$  ms, the maximum signal is achieved with  $\alpha_E = 25^\circ$ .

Furthermore, when  $\alpha$  is smaller than  $\alpha_E$  the signal is relatively independent of the value of  $T_1$ . In the limit of small flip angle, so  $\cos \alpha$  is close to one, Eq. (B7.5) reduces to

$$S_{GRE} \approx M_0 e^{-TE/T_2^*} \sin \alpha \quad (\text{B8.7})$$

and the signal is independent of  $T_1$ . Consequently, the flip angle is an important parameter for manipulating contrast in GRE images. With large flip angles, the signal is strongly  $T_1$  weighted, but with small flip angles the  $T_1$  sensitivity is suppressed, and the signal is just density and  $T_2^*$  weighted.

$T_2$ , these effects tend to cancel one another and produce poor tissue contrast. This means that if one wants to produce a signal with strong  $T_1$  weighting, the sensitivity to  $T_2$  must be suppressed. A  $T_1$ -weighted SE sequence, therefore, uses short TR to increase  $T_1$  weighting and short TE to minimize  $T_2$  weighting. Similarly, a  $T_2$ -weighted SE sequence, uses long TR to minimize  $T_1$  weighting and long TE (approximately equal to  $T_2$ ) to maximize  $T_2$  weighting. Finally, a purely density-weighted sequence uses long TR to suppress  $T_1$  weighting and short TE to suppress  $T_2$  weighting.

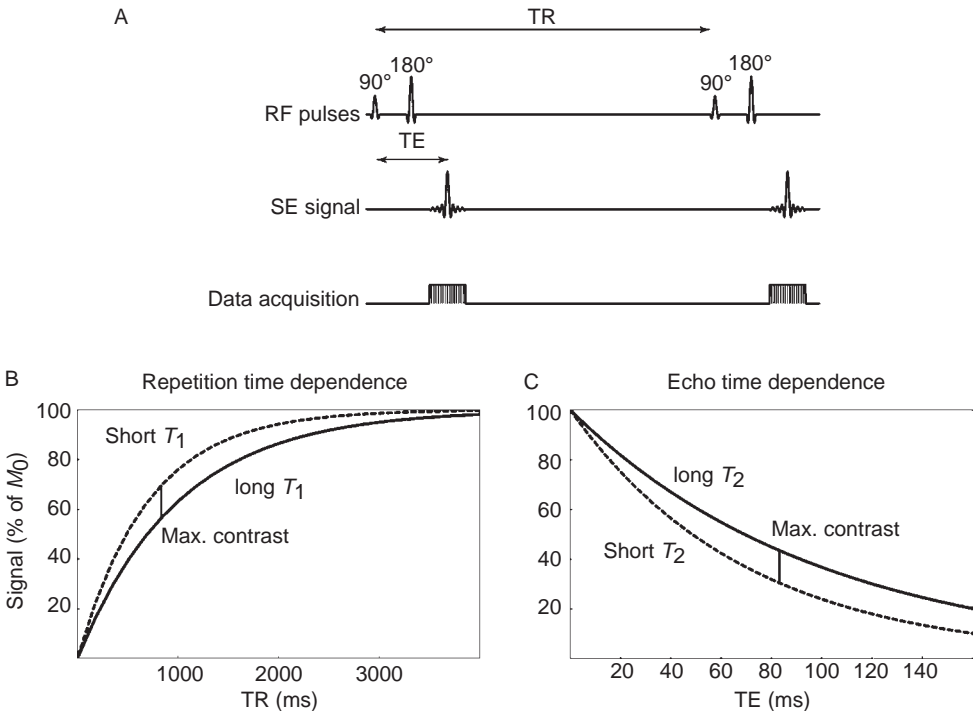
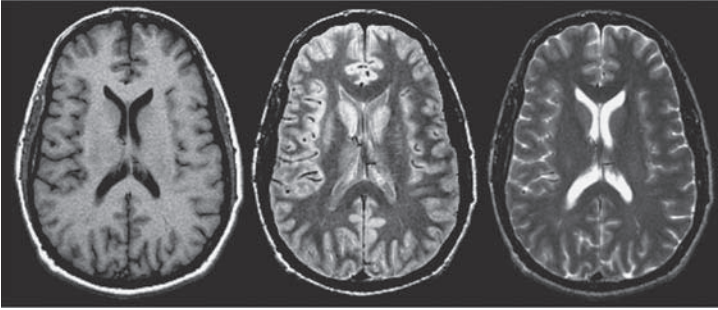


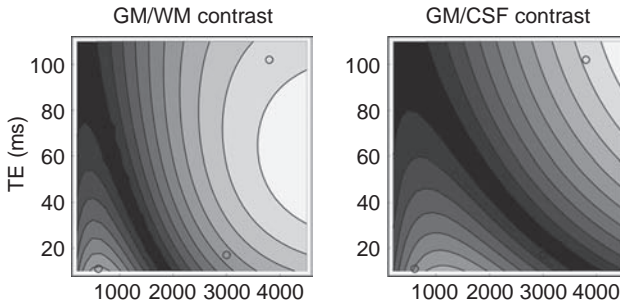
**Fig. 7.2.** Spin echo (SE) signal. (A) The SE pulse sequence is defined by two operator-controlled parameters, the repetition time (TR) and the echo time (TE). The SE signal increases with longer TR in a way that depends on  $T_1$  (B) and decreases with increasing TE in a way that depends on  $T_2$  (C). Maximum  $T_1$ -weighted contrast between tissues occurs when TR is about equal to  $T_1$ , and maximum  $T_2$ -weighted contrast occurs when TE is about equal to  $T_2$ .

A



$T_1$  weighted (TR = 600, TE = 11)      Density weighted (TR = 3000, TE = 17)       $T_2$  weighted (TR = 3800, TE = 102)

B Raw contrast



C Contrast per unit time

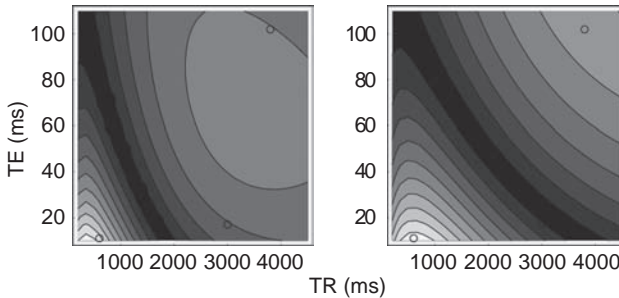


**Fig. 7.3.** Spin echo contrast. (A) Examples of  $T_1$ -weighted, density-weighted, and  $T_2$ -weighted contrast (timing parameters echo time [TE] and repetition time [TR] given in milliseconds). (B,C) Contour plots show contrast in the TR/TE plane for two tissue pairs: gray matter (GM) and white matter (WM) and GM and cerebrospinal fluid (CSF). (B) Raw signal difference between tissues. (C) Contrast to noise ratio per unit time.

The contrast characteristics of the SE pulse sequence applied to brain imaging are illustrated in Fig. 7.3. In the examples of  $T_1$ -weighted, density-weighted, and  $T_2$ -weighted images (Fig. 7.3A), the contrasts between gray matter (GM), white matter (WM), and CSF are radically different. White matter is brightest and CSF is darkest in the  $T_1$ -weighted image, and this pattern is reversed in the  $T_2$ -weighted image. In the so-called density-weighted image, GM is brightest despite the fact that CSF has the highest proton density. The reason for this is that the  $T_1$  of CSF is so long that for TR = 3 s the CSF signal is still substantially  $T_1$  weighted. In comparing these images, it is important to keep in mind that we have



**Table 7.1.** Typical NMR parameters in the brain at 1.5 T

Tissue	$M_0$ (arbitrary units)	$T_1$ (ms)	$T_2$ (ms)
Gray matter	85	950	95
White	80	700	80
Cerebrospinal fluid	100	2500	250

followed the common practice of adjusting the window and level of each image individually to best bring out the intrinsic tissue contrast. In other words, the gray scale is different for each image so that even though it looks as though CSF is brighter on the  $T_2$ -weighted image than on the density-weighted image, the absolute signal is not. It is just that the CSF signal has decayed much less than GM or WM with their long TE values so relative to these tissues it is much brighter.

To see in a more continuous way how the contrasts change when the pulse sequence parameters TR and TE are varied, we can calculate the contrast for a pair of tissues from the SE signal intensity equation in [Box 7.1](#) and assumed values for the NMR parameters for particular tissues. These parameters are somewhat variable, but typical numbers are given in [Table 7.1](#). The contour plots in [Fig. 7.3B, C](#) show absolute values of the contrast between GM and WM and between GM and CSF in the TR/TE plane. [Figure 7.3B](#) shows the raw contrast calculated for one repetition of the pulse sequence. For GM/WM contrast there are two islands of high contrast, corresponding to  $T_1$ -weighted and  $T_2$ -weighted images, with a diagonal trough of poor contrast running between them. For GM/CSF contrast, there are also two islands, but slightly shifted. Both contrasts are maximized using a  $T_2$ -weighted sequence with a very long TR and a moderately long TE.

However, this comparison of the raw signal differences between tissues does not address a critical factor: the noise in the image. In most applications, the ability to distinguish one tissue from another in an image depends not just on the raw contrast but rather on the contrast to noise ratio (CNR) ([Hendrick \*et al.\* 1984](#); [Wehrli \*et al.\* 1984](#)). The image noise is independent of TR and TE, so for one repetition of the pulse sequence the noise will be approximately the same for any TR or TE. But the total time required for a pulse sequence to play out is TR, so a sequence with a short TR can be repeated several times and averaged in the same time it takes a long TR sequence to play out once, and averaging reduces the noise in proportion to the square root of the number of averages. For example, for the same total imaging time a sequence with TR = 500 ms can be repeated four times as many times as a sequence with TR = 2000 ms, so the noise is cut in half in the short TR sequence.

A figure of merit for comparing different pulse sequences that takes this into account is the CNR per unit time, which is just proportional to the CNR divided by  $\sqrt{TR}$ . [Figure 7.3C](#) shows the CNR per unit time for GM/WM contrast and GM/CSF contrast. In this example, both contrasts are largest for the  $T_1$ -weighted pulse sequence because the long TR required for a  $T_2$ -weighted sequence is inefficient. A substantial amount of clinical MR research is directed toward identifying optimal pulse sequence parameters for different applications. Other criteria in addition to CNR affect these decisions. For example, pathological tissue is more readily detected when it is brighter than normal tissue, and so because many types of lesion involve lengthening of the relaxation times,  $T_2$ -weighted images are often used. In practice, clinical imaging usually includes a mixture of  $T_1$ -weighted,  $T_2$ -weighted, and proton density-weighted images.

The terminology of density weighted and  $T_1$  weighted is widely used but somewhat misleading, as shown in Fig. 7.3. The MR signal is always proportional to the proton density, and so to be precise all signals are density weighted. The important difference between the long TR signal and the short TR signal is that with long TR there is only density weighting, whereas with short TR there is  $T_1$  weighting as well. From Table 7.1,  $T_2$  weighting and density weighting are mutually supportive, in the sense that both tend to make the signal with long  $T_2$  and high spin density larger. However, with short TR, the  $T_1$  weighting is in direct conflict with density weighting and  $T_2$  weighting. For example, the proton density difference between GM and CSF would tend to make the CSF signal stronger, whereas the  $T_1$  difference tends to make the GM signal stronger, and the trough in the contour plots reflects the region where these conflicting effects reduce the contrast. The terminology is also potentially misleading because a particular TR may be longer than  $T_1$  for some tissues but comparable to  $T_1$  for others. As noted above, with  $TR = 3$  s, the  $T_1$  sensitivity is suppressed for GM and WM but is strong for CSF. The descriptive terms  $T_1$  weighted,  $T_2$  weighted, and density weighted are used frequently, but bear in mind that this terminology is imprecise.

## Generalized echoes

The process of SE formation was described above in terms of the action of a  $180^\circ$  RF pulse. In fact, the echoing process is much more general, and any RF pulse can create an echo of previous transverse magnetization. To see how this comes about, consider two  $90^\circ$  pulses applied in succession with a delay  $T$  between them, and assume that the RF pulse is applied along the  $x$ -direction in the rotating frame. The original demonstration of spin echoes used such  $90^\circ$  pulses, rather than  $180^\circ$  pulses (Hahn 1950). The first RF pulse rotates the longitudinal magnetization from the  $z$ -axis to the  $y$ -axis in the rotating frame, where it begins to precess (Fig. 7.4). During the period  $T$ , the individual spin vectors precess at different rates owing to field inhomogeneities. In the rotating frame precessing at the mean precession rate, the spin vectors will spread into a fan and eventually a disk covering the plane and so the net magnetization is reduced to zero. The second  $90^\circ$  pulse then rotates this disk around the  $x$ -axis, putting some of the magnetization along the  $z$ -axis, but preserving some of the magnetization in the transverse plane. To simplify the picture, the fates of four representative spin vectors are plotted in Fig. 7.4, in a similar fashion to those in Fig. 7.1. By the time of the second  $90^\circ$  pulse, these vectors have spread evenly in the transverse plane, lying along axes  $+x$ ,  $-x$ ,  $+y$ , and  $-y$ . After the second  $90^\circ$  pulse, the  $x$ -axis vectors are unaffected, but the  $+y$ -vector is rotated to  $-z$ , and the  $-y$ -vector is rotated to the  $+z$ -axis. After a second evolution period  $T$ , each of the  $x$ -vectors will acquire the same phase offset as during the first  $T$  interval,  $+90^\circ$  for one and  $-90^\circ$  for the other. They are then back in phase along the  $-y$ -axis, creating a spin echo. But this SE is weaker than the echo created by a  $180^\circ$  pulse because some of the original transverse magnetization is now stored along the  $z$ -axis and so does not contribute to the echo. In general, the smaller the flip angle of the refocusing pulse, the weaker the echo. Over time, the transverse components decay away.

## Stimulated echoes

What happens to the magnetization that was “parked” along the  $z$ -axis in the experiment in Fig. 7.4? Over time it also will relax back toward equilibrium, but with a time constant  $T_1$  instead of  $T_2$ . However, if instead it is tipped back down to the transverse plane before it has fully relaxed, another echo will be formed, called a *stimulated echo*. A third  $90^\circ$  pulse around  $x$  returns this magnetization to the transverse plane, putting the original  $+y$ -vector along  $-y$ , and the original  $-y$ -vector along  $+y$ . Now that these vectors are back in the transverse plane,

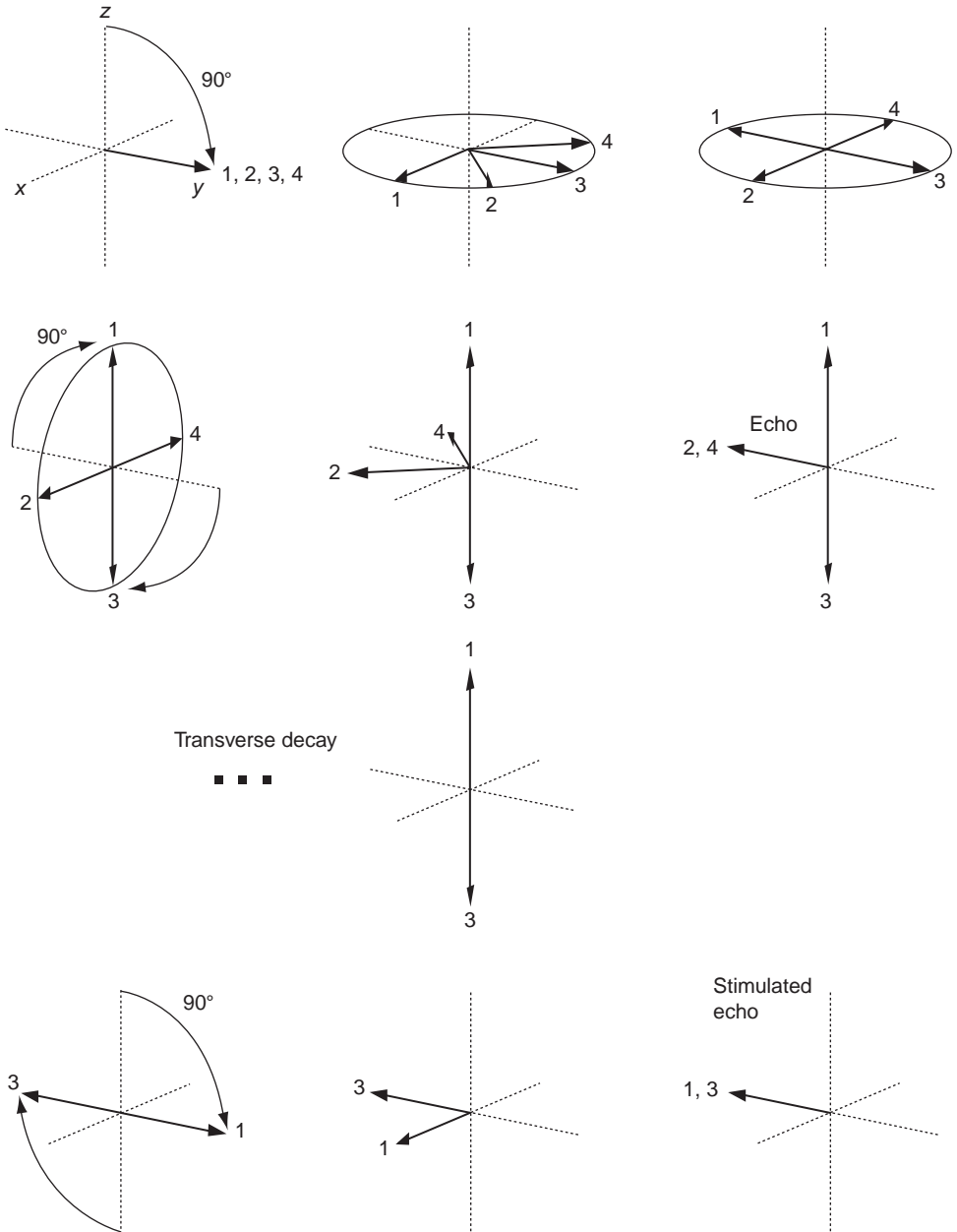


**Fig. 7.4.** Formation of echoes with  $90^\circ$  pulses. The fate of four spin vectors is shown during application of three  $90^\circ$  pulses, presented as in Fig. 7.1. The first  $90^\circ$  pulse tips the spin vectors into the transverse plane, where they precess at different rates and spread into a disk. The second  $90^\circ$  pulse tips the disk so that vectors 1 and 3 lie on the  $z$ -axis. Spin vectors 2 and 4 continue to precess and form an echo along the  $-y$ -axis. Over time, the transverse components decay away with time constant  $T_2$ , but spin vectors 1 and 3 decay more slowly, with time constant  $T_1$ . A third  $90^\circ$  pulse tips these spin vectors back to the transverse plane, and resumed precession produces another echo, called a *stimulated echo*.

they will begin to precess again at the same rate as before. After another interval  $T$ , the vector that had originally precessed  $180^\circ$  to end up on the  $-y$ -axis will precess another  $180^\circ$  and return to the  $-y$ -axis, where it adds to the vector that stays along the  $-y$ -axis to form the stimulated echo. Like the direct SE that formed after the second RF pulse, the stimulated echo is weaker than the full echo of a  $180^\circ$  pulse because only a part of the transverse magnetization is refocused.

## Multiple echo pathways from a string of radiofrequency pulses

A series of RF pulses can thus generate both direct and stimulated echoes. An example that suggests just how complicated this can become is illustrated in Fig. 7.5, which shows the echo pattern formed by an initial  $90^\circ$  pulse followed by two  $\alpha$ -degree pulses. To emphasize that echo formation results simply from free precession, interrupted by occasional RF pulses, the curves in Fig. 7.5 were calculated without including any relaxation effects. In these simulations, spin vectors with a random distribution of precession frequencies freely precess, and the net signal is the average  $y$ -component of the ensemble of spins. When  $\alpha = 180^\circ$ , the situation is the standard SE pulse sequence (Fig. 7.5A): the initial pulse generates an FID, and each  $180^\circ$  pulse creates a full echo of the original transverse magnetization, for a total of two echoes. The first echo is along the  $-y$ -axis and so appears negative in the plot, and the second echo, being an echo of the first echo, is positive. In other words, with repeated  $180^\circ$  RF pulses along the  $x$ -axis, the successive echoes alternate sign.

However, if  $\alpha$  is reduced to  $135^\circ$  (Fig. 7.5B), the echo pattern develops an interesting complexity. The original two echoes are reduced in amplitude, as we might expect, but in addition two new echoes appear, both with a negative sign. The weak echo occurring before the second of the original echoes is the stimulated echo described in Fig. 7.4. The second new echo, occurring later than the original two echoes, is an echo of the original signal resulting from the initial  $90^\circ$  pulse refocused by the second  $\alpha$ -pulse. As the flip angle is reduced, the original two echoes grow progressively weaker, with the second echo decreasing in amplitude more quickly than the first. The reason for this is that this second echo is really an echo of an echo, so if each echoing process is only partial, it will depend more strongly on the flip angle, and in this example it is not detectable if the flip angle is reduced to as low as  $45^\circ$  (Fig. 7.5D). In contrast, the stimulated echo increases as the flip angle is reduced, peaking at  $90^\circ$  but remaining as the strongest echo for lower flip angles. Finally, the fourth echo also increases in amplitude with decreasing flip angle, peaking at  $90^\circ$ . One can think of this echo (a bit loosely) as formed from spin vectors that were not completely refocused by the first RF pulse but are then refocused by the second RF pulse. This echo does not occur for a  $180^\circ$  pulse because all the spin vectors do refocus after the first RF pulse, so the second RF pulse only creates an echo of the echo.

This example illustrates that the echo pattern formed by a string of RF pulses can be quite complex. It also shows that a  $180^\circ$  pulse is in some sense an exception, in that the echo pattern is fairly simple. This can present practical problems in a multi-echo pulse sequence because real  $180^\circ$  pulses are never perfect. In imaging applications, the flip angle can vary through the thickness of the slice, so in reality we must deal with refocusing pulses with a range of flip angles. The resulting unwanted echoes can cause artifacts in the images if they are not carefully controlled.

Furthermore, the foregoing example was simplified by ignoring relaxation effects. By starting with a  $90^\circ$  pulse so that the longitudinal magnetization was reduced to zero and by neglecting any regrowth of that magnetization, the role of each RF pulse as a refocusing pulse was emphasized. In reality, each pulse (except for the special case of a perfect  $180^\circ$  pulse)

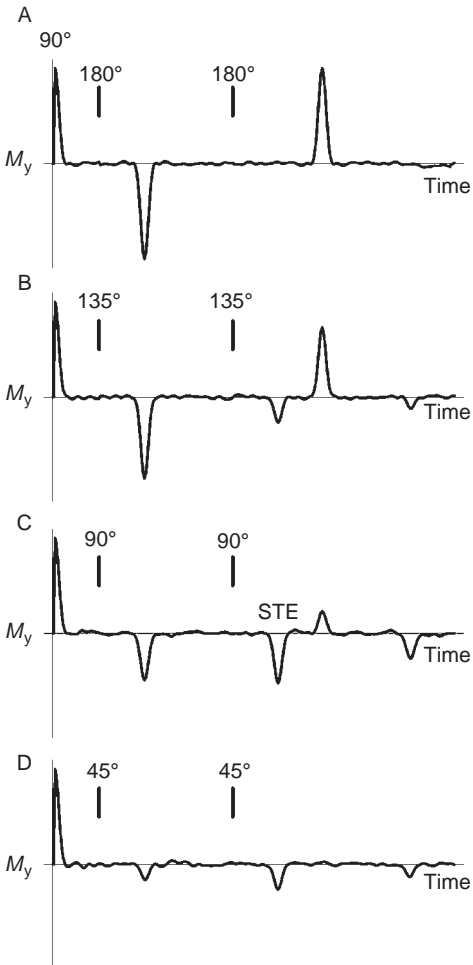


**Fig. 7.5.** Echo patterns from three radio frequency pulses. Each row shows the echoes formed by two successive  $\alpha$ -degree pulses, with  $\alpha = 180^\circ$  (A),  $135^\circ$  (B),  $90^\circ$  (C), and  $45^\circ$  (D). Each time course begins with a  $90^\circ$  pulse and the resulting free induction decay. The curves show a simulation of  $T_2^*$  losses and echo refocusing by plotting the average value of the  $y$ -component of the magnetization ( $M_y$ ) for 2000 spins, each precessing at its own constant rate, but with small random differences of the precession frequency among the spins. The simple double-echo pattern results from  $180^\circ$  pulses (A), but with smaller RF pulses more echoes appear (B–D), including a stimulated echo (STE).

would also produce new coherent transverse magnetization. This illustrates a basic feature of RF pulses that is important for understanding the fast gradient echo imaging sequences discussed below. Whenever a series of RF pulses is applied, each RF pulse does two things: it produces a new FID itself, but it also contributes to creating an echo of previous FIDs. Furthermore, if the RF pulses are equally spaced, the echoes occurring by different routes occur at the same time, such as a direct echo from the previous FID and a stimulated echo of the FID produced by the pulse two back. In fast imaging with short TR values, these echoes can build up and strongly affect the measured signal, adding an interesting complexity to the signal measured with gradient echoes and short TR.

## The gradient echo signal

### Gradient echoes

The simplest pulse sequence consists of a single RF pulse with arbitrary flip angle applied repeatedly at TR, and with the signal measured at TE after each RF pulse. The prototype of such a pulse sequence is FLASH (fast low-angle shot) (Haase *et al.* 1986). In an imaging

setting, such a pulse sequence is described as a gradient recalled echo (GRE) or simply a gradient echo. The terminology refers to the fact that the gradient pulses used for imaging are usually constructed with an initial negative lobe so that a gradient echo forms at the center of data collection when the effects of the positive frequency-encoding gradient just balance the effects of the initial gradient lobe. In other words, at the gradient echo the net effect of the gradients applied up to that time is zero.

The term *gradient echo imaging* is somewhat unfortunate because it suggests that this method uses gradient echoes *instead* of RF echoes. There is indeed no  $180^\circ$  RF pulse in GRE imaging, but as described in the [section](#) above on generalized echoes, a series of closely spaced RF pulses of any flip angle can also create echoes that affect the steady-state signal. Furthermore, gradient echoes are an integral part of both SE and GRE imaging. The distinction between the two is really just that GRE pulse sequences do not contain a  $180^\circ$  refocusing pulse. We will adopt this standard terminology even though we will not be considering the effects of imaging gradients until [Ch. 9](#). For now we will simply explore the signal and contrast properties of the GRE pulse sequence. Even though there is no  $180^\circ$  refocusing pulse involved, and thus no explicit echo at the time when the signal is measured, we still refer to the data collection time as TE for consistency with the SE pulse sequence.

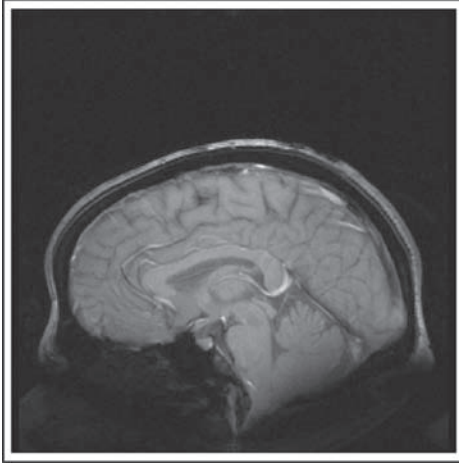
## Decay constant $T_2^*$ and chemical shift effects

There are two important differences in the signal characteristics of the GRE and SE signals. The first is a direct result of the fact that there is no  $180^\circ$  refocusing pulse in a GRE pulse sequence. As a consequence, the dephasing effects of field inhomogeneities are not reversed, and so the signal decays exponentially with increasing TE with a decay constant  $T_2^*$ , rather than  $T_2$ . Because the head itself is inhomogeneous, a GRE image with a long TE usually shows areas with reduced signal where the local  $T_2^*$  is shortened by the inhomogeneous fields ([Fig. 7.6](#)). This can be an asset in studies of brain iron ([Wisner \*et al.\* 1988](#)) or in studies of hemorrhage, where the evolution and breakdown of blood products leads to measurable variations in the GRE signal ([Thulborn and Brady 1989](#)). However, the sensitivity to field inhomogeneities also leads to artifactual signal dropouts simply because of the non-uniformity of the head (e.g., near sinus cavities). Furthermore, the  $T_2^*$  of an imaging voxel may depend on the size of the voxel, because a larger voxel may contain a larger spread of precession frequencies causing the signal to decay more quickly (see the example in [Fig. 7.6](#)). For this reason, the TE is usually kept short in GRE imaging, often as small as a few milliseconds.

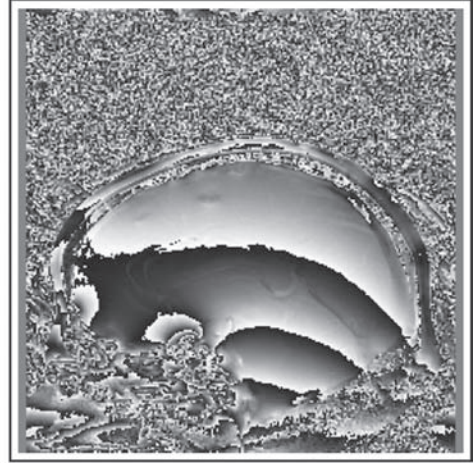
An exception to this is fMRI based on the blood oxygenation level dependent (BOLD) effect, where the goal is to detect small local changes in  $T_2^*$  caused by microscopic field variations between the intravascular and extravascular spaces, and within the blood itself, arising from changes in blood oxygenation. For BOLD studies, TE is usually in the moderate range 30–50 ms, as in the example in [Fig. 7.6](#). Thus, there is always an essential conflict involved in BOLD imaging based on  $T_2^*$  effects. A somewhat long TE is required so that the signal will be sensitive to the  $T_2^*$  changes produced by the BOLD effect, but this brings in added sensitivity to signal dropouts resulting from the non-uniformity of the head. For this reason, shimming the magnet to try to flatten out the broad field inhomogeneities is an important part of fMRI studies.

Gradient echo imaging also exhibits a chemical shift effect because the resonant frequencies of the hydrogen nuclei in fat and water differ by approximately 3.5 ppm ([Wehrli \*et al.\* 1987](#)). Because there is no  $180^\circ$  RF pulse to refocus the phase differences that develop

## A Magnetic field mapping

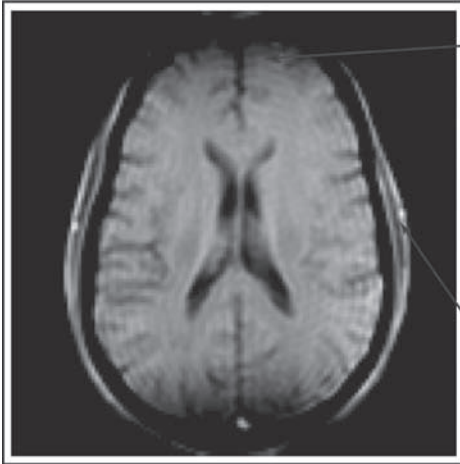
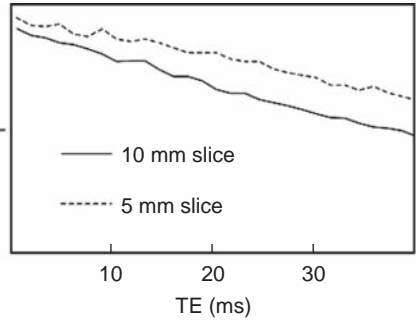


Magnitude



Phase

## B EPI-GRE Image

 $T_2^*$  decay

Chemical shift effect

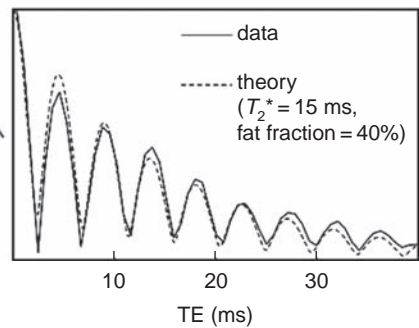


**Fig. 7.6.** Echo time (TE) effects on the gradient recall echo (GRE) signal. (A) With no  $180^\circ$  radiofrequency refocusing pulse, the phase of the local GRE signal at the time of measurement (TE) is proportional to the local magnetic field offset, as illustrated by the magnitude and phase images. (B) When the signals contributing to the net signal of an imaging voxel have different resonant frequencies, phase dispersion leads to signal loss ( $T_2^*$  effect). When the voxel contains both fat and water, the dependence of the signal on TE contains an oscillation as the fat and water signals come in and out of phase (chemical effect). EPI, echo planar imaging.

between the fat and water signals, the net signal from a voxel containing both fat and water shows oscillations in intensity with increasing TE as the fat and water signals come in and out of phase. Fig. 7.6 shows an example of this chemical shift effect in a voxel in the scalp. Note that the troughs of the signal, when fat and water are out of phase, are sharper than the peaks, as illustrated in Figure 7.6 with both an experimental curve and a theoretical curve. At 1.5 T, the cycle time for water to precess a full cycle relative to fat is only approximately 4.4 ms (2.2 s at 3 T), and so this is the period of the oscillations in the signal decay curve. The interference of the fat and water signals can be used to estimate the fat content of tissues or partly to suppress the signal from tissues containing fat by choosing TE to be at a point where the fat and water signals are out of phase. For example, in MR angiography applications in which the goal is to achieve good contrast between blood and surrounding tissue, an out-of-phase TE of 2.2 or 6.6 ms is often used partly to suppress the tissue signal. In the healthy brain, a fat signal is seen only in the scalp and skull marrow. The lipids that make up the myelin sheath of nerves are highly structured and so have a very short  $T_2$  and are not observed in standard MRI.

## Controlling $T_1$ weighting with the flip angle

The second important difference between the GRE and SE signals arises because the TRs used with GRE pulse sequences are usually much shorter than those used with SE pulse sequences. The use of short TRs is made possible in part because there is no  $180^\circ$  RF pulse. The essential limitation on how short TR can be is set by government guidelines limiting RF exposure to the subject. Each time an RF pulse is applied, heat is deposited in the body. The amount of deposited energy is proportional to the square of the flip angle, so one repetition of an SE pulse sequence with a  $90^\circ$  and a  $180^\circ$  RF pulse deposits 45 times as much energy as one repetition of a GRE pulse sequence with a single  $30^\circ$  RF pulse. For this reason, TR can be drastically shortened while keeping the rate of energy deposition (the specific absorption rate) below the guidelines. In practice, the TR for a GRE pulse sequence can be as short as 2 ms, and with a total imaging time as short as 1 s; motion artifacts caused by respiration can be significantly reduced by collecting the entire image during one breath-hold. Alternatively, three-dimensional volume acquisitions with high spatial resolution can be collected in a few minutes.

An essential useful feature of GRE pulse sequences is thus the ability to use very short TRs. Before tackling the more complex problem of understanding the signal with short TR, we begin with the long TR case. When TR is much greater than  $T_2$ , so any transverse magnetization generated by one of the RF pulses has decayed away by the time of the next pulse, the contrast characteristics are similar to those of the SE pulse sequence. If the flip angle is  $90^\circ$ , all the longitudinal magnetization is flipped into the transverse plane. This is often described as a *saturation recovery pulse sequence*, and the  $90^\circ$  pulse is called a saturation pulse because it reduces the longitudinal magnetization to zero. If TR is much longer than  $T_1$ , the magnetization fully recovers between RF pulses, producing a proton-density-weighted signal such that CSF is brightest and WM is darkest. As TR is reduced, the signal becomes more  $T_1$  weighted, just as it does with an SE pulse sequence. If TR were the only way to influence the degree of  $T_1$  weighting, the contrast characteristics of the GRE and SE pulse sequences would be similar. But an additional parameter to vary in a GRE pulse sequence is the flip angle.

Figure 7.7 shows the effect on the contrast of reducing the flip angle for short TR, when TR is shorter than  $T_1$  but longer than  $T_2$  (curves were calculated from the equation derived in Box 7.1). The plot shows signal curves for two tissues with the same proton density but with



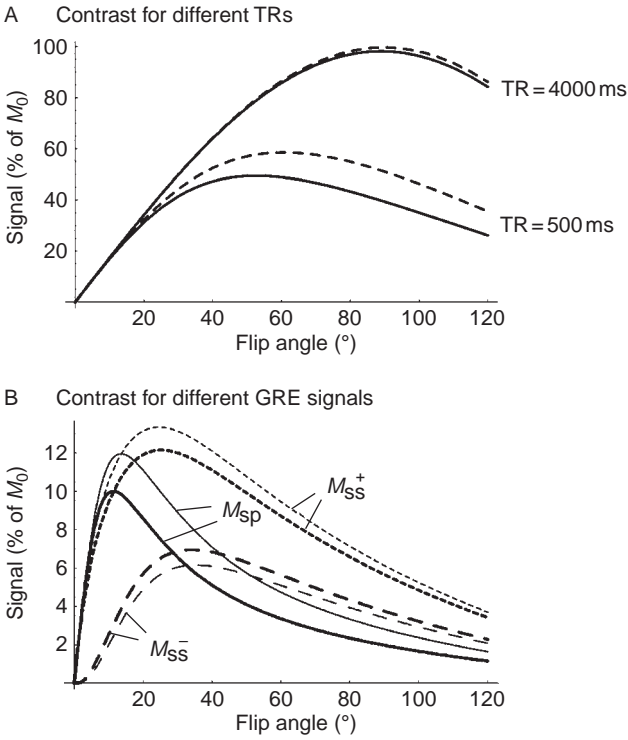


**Fig. 7.7.** Effect of flip angle on gradient recalled echo (GRE) signals. (A) Curves are plotted for two tissues with a 30% difference in both relaxation times (solid line:  $T_1 = 1000$  ms and  $T_2 = 100$  ms; dashed line:  $T_1 = 700$  ms and  $T_2 = 70$  ms). The  $T_1$  weighting can be minimized with either a long repetition time (TR) or with a small flip angle. (B) Curves show the contrast between the same two tissues for very short TR (20 ms) for the three types of GRE signal (see Fig. 7.8) (in each pair the bold lines are for the tissue with longer relaxation times).  $M_0$ , equilibrium magnetization;  $M_{sp}$ , coherent spoiled magnetization;  $M_{ss}^-$  and  $M_{ss}^+$ , coherent magnetization before and after each pulse, respectively.

$T_1$  values of 1000 and 700 ms, calculated for TR = 4000 and 500 ms. As expected, for long TR there is little  $T_1$  weighting, and the signals of the two tissues are nearly equal for all flip angles. With shorter TR and a flip angle near  $90^\circ$ , the signal is strongly  $T_1$  weighted as described above, with the tissue with a shorter  $T_1$  creating a larger signal.

However, as the flip angle is reduced, the signal becomes less and less  $T_1$  weighted until for a small flip angle it is essentially just density weighted. For the calculated curves in Fig. 7.7, the proton densities were assumed to be equal, so all the signal curves are the same for small flip angles. That is, even though TR is smaller than  $T_1$ , so that there is little time for recovery of the longitudinal magnetization, the signal nevertheless can be made insensitive to  $T_1$  by using a small flip angle (Buxton *et al.* 1987). The source of this useful effect is that tipping the magnetization by a small angle leaves most of the longitudinal magnetization intact near the equilibrium value, so  $T_1$  relaxation makes a negligible change in the longitudinal component and the resulting signal is then insensitive to  $T_1$ . In short, the MR signal can be made insensitive to  $T_1$  either by increasing TR or by decreasing the flip angle with short TR.

## Steady-state free precession

When TR is much greater than  $T_2$ , the transverse magnetization decays away before the next RF pulse. As a result, the measured signal is entirely the result of the FID generated by the most recent RF pulse. But when TR is less than  $T_2$ , this situation is changed in an interesting way. Each pulse still produces new transverse magnetization, but the transverse magnetization from previous RF pulses will not have decayed away completely. Different components of this previous transverse magnetization will have acquired different phases through

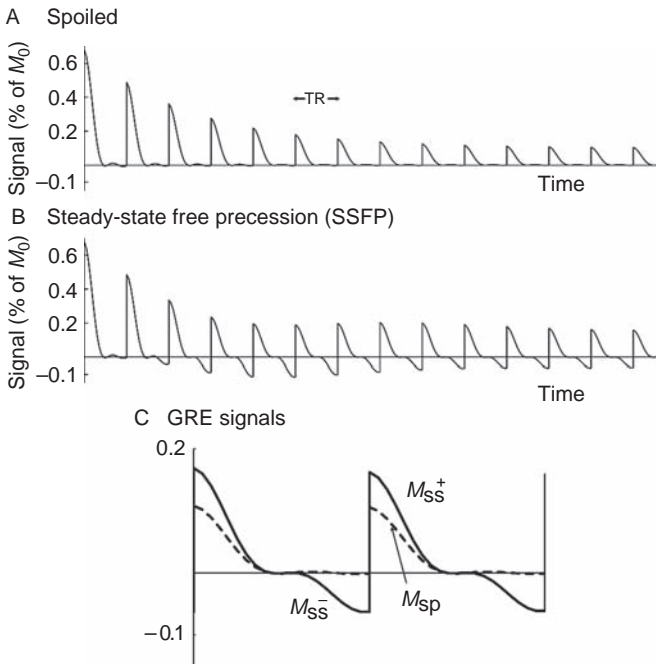


**Fig. 7.8.** The gradient recalled echo (GRE) signal. When a radio frequency (RF) pulse is applied repeatedly at a set flip angle and with a repetition time ( $TR < T_2$ ), a steady state develops after several pulses. (A) If the echoes are spoiled, a coherent magnetization ( $M_{sp}$ ) is created after each RF pulse. (B) If the echoes are not spoiled, a coherent magnetization forms both before ( $M_{ss}^-$ ) and after ( $M_{ss}^+$ ) each pulse. (C) There are thus three distinct signals that could be measured with a GRE pulse sequence.

local field offsets (e.g., applied gradients or main field inhomogeneity) so that this old transverse magnetization may be incoherent. However, if these field offsets are the same during each TR period, the RF pulses will create echoes of the previous transverse magnetization at multiples of TR. These echoes will add to the new transverse magnetization from the most recent RF pulse, creating a strong coherent signal immediately before and after each RF pulse (Fig. 7.8). After a number of RF pulses are applied, the magnetization will approach a steady state in which the signal pattern is repeated in the same way during each TR period. In this condition of *steady-state free precession* (SSFP), the coherent magnetization signal just after the RF pulse,  $M_{ss}^+$ , and the signal just before the RF pulse,  $M_{ss}^-$ , are both constant (Gyngell 1988; Patz 1989).

The value of  $M_{ss}^-$  is the net result of the echoes of all the FIDs generated by the previous RF pulses. The next RF pulse then partly flips this coherent transverse magnetization and also adds to it a new FID signal to create  $M_{ss}^+$ . So for an SSFP pulse sequence such as this, there are two possible signals to measure, and both  $M_{ss}^+$  and  $M_{ss}^-$  depend on the echoing process resulting from many closely spaced RF pulses. However, in addition to these two signals, a third possible signal is the *spoiled* signal that results when the echoes are suppressed. The echoes occur because whatever phase precession occurs during one TR interval is exactly repeated in the next. The echo formation can be blocked by inserting random gradient pulses into each TR interval after data collection to produce a random additional precessional phase before the next RF pulse (*gradient spoiling*). Alternatively, the echoes can be spoiled by varying the flip axis of the RF pulse (*RF spoiling*), which also adds a variable phase angle to the precession during each TR interval. With the echoes spoiled, there is no coherent magnetization before each RF pulse ( $M_{ss}^- = 0$ ), and the signal just after the RF pulse,  $M_{sp}$ , consists only of the FID generated by that pulse with no echo component. Note that if the TR is very

long so that the echoes are naturally attenuated by  $T_2$  decay, the magnetization  $M_{ss}^+$  is the same as the spoiled magnetization  $M_{sp}$ , and  $M_{ss}^-$  is zero.

## The varieties of gradient echo pulse sequences

For imaging with short TR, different GRE pulse sequences are used depending on which of the signals  $M_{ss}^+$ ,  $M_{ss}^-$ , or  $M_{sp}$  is to be measured. Unfortunately, each manufacturer of MR imagers has given a different name to these pulse sequences, and this can lead to confusion. Each of these names is an acronym, but the full names generally do not make the matter any clearer. Although there are many variations of GRE pulse sequences, they can all be grouped according to which of these three signals is being measured. Some common GRE pulse sequence acronyms, and the associated signal being imaged, are:

- $M_{sp}$ : FLASH, SPGR
- $M_{ss}^+$ : GRASS, FISP, FAST
- $M_{ss}^-$ : SSFP, PSIF, CE-FAST.

Figure 7.7B shows plots of the three signals  $M_{ss}^+$ ,  $M_{ss}^-$ , and  $M_{sp}$  as a function of flip angle for a short TR for relaxation times similar to GM and WM. These curves illustrate several interesting properties of the GRE signal. For small flip angles, the echoes are weak, and so  $M_{ss}^-$ , which consists solely of echoes, is weak. Also,  $M_{ss}^+$  is similar to  $M_{sp}$ , again because the echoes are weak. But notice that what small contribution there is from echoes actually decreases the steady-state signal slightly compared with the spoiled signal ( $M_{sp}$ ). As the flip angle increases, the  $M_{ss}^-$  signal increases, and the contrast between two tissues is essentially  $T_2$  weighted and so the tissue with the longer  $T_2$ , and thus the stronger echoes, is brighter.

Both the  $M_{ss}^+$  and the  $M_{sp}$  signals increase rapidly with increasing flip angle up to a critical angle called the *Ernst angle*,  $\alpha_E$  (Box 7.1). The Ernst angle is the flip angle that produces the maximum signal with a spoiled pulse sequence, and it is also the flip angle where the steady-state and spoiled signals have equal intensities (the crossing point in Fig. 7.7B). For flip angles greater than  $\alpha_E$ , the steady-state signal  $M_{ss}^+$  is larger than  $M_{sp}$  because of the coherent addition of the echo signals. But notice that the contrast between two tissues often is greater for  $M_{sp}$  despite the fact that the signal itself is intrinsically weaker. This is another example of the conflict between  $T_1$ -weighted and  $T_2$ -weighted signals that we encountered when considering SE contrast. In this case, a long  $T_1$  tends to reduce the magnitude of each FID because there is less longitudinal recovery during TR, but a long  $T_2$  tends to increase the signal because the echoes are stronger. The result is reduced contrast between tissues with the steady-state signal.

The fact that a moderate flip angle (e.g.,  $30^\circ$ ) produces a larger spoiled signal than a  $90^\circ$  pulse may at first seem somewhat surprising. After all, a  $90^\circ$  pulse flips all the longitudinal magnetization into the transverse plane, whereas a  $30^\circ$  pulse flips only a fraction of it. Indeed, if only one RF pulse were applied, the  $90^\circ$  pulse *would* create a larger signal. Here, however, we are interested in the *steady-state* signal that develops when many RF pulses are applied in succession. The signal still depends on how much of the longitudinal magnetization is flipped into the transverse plane, but it also depends on how large that longitudinal magnetization is, and that also depends on the flip angle. For a small flip angle, the longitudinal magnetization is only slightly disturbed, whereas for a  $90^\circ$  flip angle it is destroyed completely, and so the longitudinal magnetization that regrows during TR will be quite small. Consequently, for large flip angles, the signal is a large part of a small magnetization, and for small flip angles it

is a small part of a larger magnetization. The optimal balance that produces the largest signal is an intermediate flip angle,  $\alpha_E$ , which depends on the ratio  $TR/T_1$ .

## Sources of relaxation

### Fluctuating fields

In the discussion of the physics of NMR in Ch. 6, the phenomenon of relaxation was attributed to the effects of fluctuating fields. These fluctuations determine the relaxation times  $T_1$  and  $T_2$  and the previous sections of this chapter have discussed how the SE and GRE signals depend on these tissue parameters. In particular, by manipulating pulse sequence parameters such as TR, TE, and the flip angle, the sensitivity of the MR signal to these relaxation times can be controlled. Pulse sequences can be optimized to detect subtle differences between one tissue and another, as in anatomical imaging, or changes over time, as in functional imaging. In this section, we will focus on the physical origins of these relaxation times. Note that in this discussion we interchangeably refer to the relaxation times ( $T_1$ ,  $T_2$ ) and the corresponding relaxation rates ( $1/T_1$ ,  $1/T_2$ ).

Our goal is to understand, at least in part, why the observed relaxation times are what they are. However, this is not a simple task, and despite the importance of relaxation effects for medical imaging, a full understanding of NMR relaxation in the body is still lacking. In the NMR literature, a considerable body of work has developed around the theory of relaxation in NMR (Bloembergen 1957; Bloembergen *et al.* 1948; Solomon 1955). However, the sources of relaxation in biological systems are an active area of research, and in this section we will only brush the surface by introducing a few key concepts.

A natural first question when thinking about  $T_1$  and  $T_2$  is why are they so long? The most basic time constant associated with NMR is the period of the precessional motion. Yet, broadly speaking, the relaxation times are of the order of 1 s, nearly eight orders of magnitude longer than the precession period in a 1.5 T magnetic field. If this were not so, MRI would be extremely difficult. Frequency encoding depends on reliably measuring frequency differences of the order of 1 ppm. This is only possible if the signal oscillates millions of times before it decays to undetectable levels. There are two related questions. Why is  $T_1$  longer than  $T_2$ ? Why do the relaxation times differ from one tissue to another? If the relaxation times of all tissues were the same, the contrast in MR images would result just from differences in proton density, which varies over a much more limited range than the relaxation times. The sensitivity of MRI for detecting subtle pathological anatomy or functional activation would be greatly reduced.

To address these questions, we can examine the physical sources of relaxation. Relaxation results from the effects of fluctuating magnetic fields, and the ultimate source of fluctuating fields is the random thermal motions of the molecules. Each water molecule is in constant motion, colliding with other molecules, rotating, vibrating, and tumbling randomly. The basic conceptual model for understanding the effects of such fluctuations is the random walk. We will use it both to understand how fluctuating fields lead to phase dispersion and signal loss through relaxation, and also in Ch. 8 to understand how the MR signal is affected by random motions of molecules through spatially varying magnetic fields. As a water molecule tumbles, each hydrogen nucleus feels a fluctuating magnetic field. In a pure water sample, the primary source of this fluctuating field is the dipole field of the other hydrogen nucleus in the same water molecule. As the molecule rotates to a new position, the relative orientation of the two nuclei changes, and because the dipole field produced by the proton has a strong directional dependence, the magnetic field felt by a nucleus fluctuates randomly.

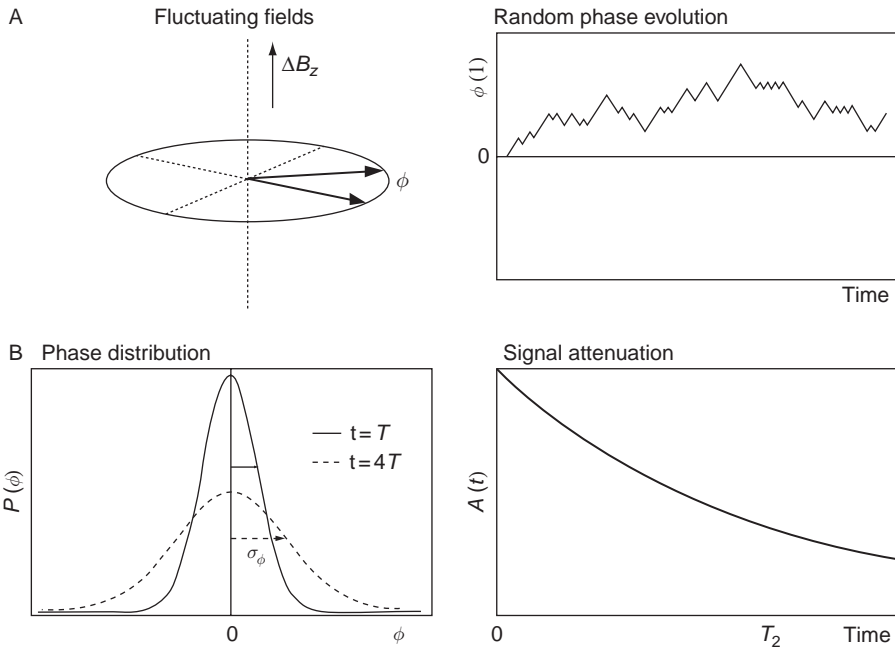


**Fig. 7.9.** Effect of fluctuating magnetic fields on the net signal. (A) Each spin feels a randomly fluctuating component of the magnetic field,  $B_z$ , producing a random phase angle  $\phi$ , which grows over time in a random walk fashion. (B) For a collection of spins, each undergoing an independent random walk, the width of the phase distribution ( $P$ ) grows in proportion to the square root of time, which creates an attenuation of the signal ( $A$ ) that is exponential in time.

## A simple model for transverse relaxation

To illustrate how these field fluctuations lead to relaxation, we can look at how  $T_2$  decay arises. Suppose that we examine a sample of pure water after applying a  $90^\circ$  RF pulse that generates a coherent transverse magnetization. We can picture this magnetization as being the result of a set of identical dipoles, starting out in alignment and precessing together in phase. However, in addition to the primary magnetic field  $B_0$ , each dipole also feels a fluctuating field from the magnetic moments of other nuclei. The  $z$ -component of this field adds to (or subtracts from)  $B_0$  and so briefly alters the precession rate. Then for each nucleus, the full precessional motion is a combination of a uniform precession from  $B_0$ , plus a weaker, jerky precession added in.

It is easiest to think about this by imagining that we are in a rotating frame of reference rotating at the average precession rate  $\omega_0 = \gamma B_0$ . Then the additional precessional motions appear as a slow, irregular fanning out of the dipole vectors because the pattern of random fields felt by each dipole is different. We can describe this phase dispersion by plotting the distribution of the phase angle  $\phi$  for the set of dipoles, as in Fig. 7.9. Because the net phase angle is the accumulation of many small random steps, we expect that this distribution will be Gaussian. We can call the standard deviation of the phase distribution  $\sigma_\phi(t)$ , and over time  $\sigma_\phi$  will grow as the phase dispersion increases. The net signal is then the sum of many dipole vectors with this distribution of phases, and because of the phase dispersion, the net signal is attenuated from the value it would have if all the spin vectors added coherently. We can

calculate an expression for this attenuation factor ( $A$ ) by integrating  $\cos \phi$  over a Gaussian distribution of phases, which gives:

$$A(t) = e^{-\sigma_\phi^2/2} \quad (7.1)$$

The time dependence of the signal decay then depends on how  $\sigma_\phi(t)$  increases with time.

To understand the time dependence of the phase dispersion, we can simplify the physics with a random walk model. Imagine that the water molecule stays in one position for a time  $\tau$ , called the *correlation time*, and then randomly rotates to a new position. During each interval  $\tau$ , a nucleus feels a constant magnetic field  $B$  added to the main field  $B_0$ . During the first  $\tau$  interval, the magnitude of the random field is  $B_1$ , during the second interval it is  $B_2$ , and so on. Then during the  $n$ th interval the dipole acquires a phase offset  $\gamma B_n \tau$ , where  $\gamma$  is the gyromagnetic ratio, and the net phase offset after a total time  $t$  is the sum of all of these random phase offsets.

Because each phase increment is directly proportional to  $B_n$ , the net phase is proportional to the sum of all the  $B$  values. To calculate this sum, we can further simplify the physics and assume that each value of  $B_n$  has the same magnitude  $B_{av}$ , but the sign switches randomly between positive and negative. (This may sound like a gross oversimplification, but in fact it is identical to letting the field take on a range of values if  $B_{av}^2$  is the average squared magnitude.) The pattern of fluctuating fields can then be viewed as a random walk with step size  $B_{av}$ . After  $N$  steps, the sum of the  $B$  values will be different for each nucleus, and the standard deviation of the accumulated phase will be proportional to the standard deviation of the sum of the  $B_n$ . For a random walk the standard deviation of the sum of the  $B_n$  is  $B_{av} \sqrt{N}$ . We can relate the number of steps and the total time by  $N = t/\tau$ , and putting all these arguments together the variance of the phase is:

$$\sigma_\phi^2(t) = \gamma^2 B_{av}^2 \tau t \quad (7.2)$$

The key result of this equation is that the phase dispersion grows with the square root of time (or the variance grows in proportion to time). When Eq. (7.2) is substituted into Eq. (7.1),  $A(t)$  is a monoexponential decay, and we can identify the decay constant as:

$$\frac{1}{T_2} = \frac{1}{2} \gamma^2 B_{av}^2 \tau \quad (7.3)$$

Although this is only a rough and somewhat simplified calculation, it nevertheless illustrates the factors that give rise to  $T_2$ . The transverse relaxation rate ( $1/T_2$ ) increases whenever the magnitude of the fluctuating fields or the correlation time increases. For a hydrogen nucleus in a sample of pure water, the primary source of fluctuating magnetic fields is the dipole moment of the other hydrogen nucleus in the water molecule. In a more complex biological fluid, the relaxation of hydrogen nuclei also is influenced by additional fluctuating dipole fields from other nuclei and unpaired electrons. Furthermore, in this simple argument, we only considered the slow fluctuations of the magnetic field. With a rapidly varying field, there are also fluctuations at the Larmor frequency that contribute to relaxation, and these fluctuations are critical for understanding  $T_1$  relaxation.

## The difference between longitudinal and transverse relaxation rates

As previously noted, in a pure water sample  $T_1$  and  $T_2$  are similar and long. Why is  $T_1$  so much longer than  $T_2$  in the body? To understand the difference between the two, we need to

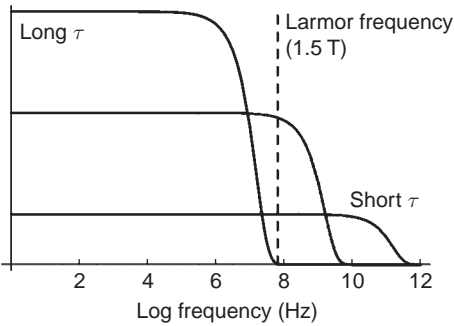


**Fig. 7.10.** Sources of relaxation. Schematic plots of the frequency spectrum of fluctuating fields suggest how the amplitudes at different frequencies depend on the correlation time  $\tau$  of the fluctuations. For shorter  $\tau$ , the energy of the fluctuations is spread over a wider frequency range, and the amplitude at zero frequency is reduced. Roughly speaking,  $1/T_2$  is proportional to the amplitude at zero frequency, and  $1/T_1$  is proportional to the amplitude at the Larmor frequency. Fluctuations with a long  $\tau$  promote transverse relaxation, making  $T_2$  short, but have little effect on  $T_1$ .

consider the magnitude of the fluctuating fields at different frequencies. In the previous arguments, we only considered the average of the fluctuating fields over time, and this is essentially just the field fluctuations at zero frequency. The key difference between  $T_1$  and  $T_2$  is that  $T_2$  depends on these zero-frequency fluctuations, but  $T_1$  does not. To produce  $T_1$  relaxation, the fluctuations must occur at the Larmor frequency. To see this, consider what is required to cause transverse and longitudinal relaxation. Fluctuations in the  $z$ -component of the magnetic field cause  $T_2$  relaxation, as already described because they produce added random precession around the  $z$ -axis. But precession around the  $z$ -axis does not alter the  $z$ -component of the magnetization and so does not contribute to  $T_1$  relaxation. To change the  $z$ -component, the fluctuating field must act like an excitation RF pulse, producing a slight tipping of the magnetization. But just as with the RF pulses applied in the NMR experiment, this requires a magnetic field along the  $x$ - or  $y$ -axis fluctuating at the Larmor frequency. Then in the rotating frame, the fluctuating field looks like a non-zero average field in the transverse plane, and the magnetization will precess slightly around this field, changing the  $z$ -component. Fluctuations at the Larmor frequency also affect  $T_2$ , and so the fundamental reason why  $T_1$  is longer than  $T_2$  is that transverse relaxation is promoted by fluctuations at both zero frequency and the Larmor frequency, while longitudinal relaxation is unaffected by the zero-frequency fluctuations.

In our earlier simplified analysis of  $T_2$ , we effectively only considered the zero-frequency fluctuations. A more complete theory, even for simple dipole-dipole interactions, must include contributions at the Larmor frequency and also at twice the Larmor frequency. Nevertheless, Eq. (7.3) captures the essential dependence of relaxation on the magnitude and correlation time of the fluctuating fields. By comparing the intensity of the fluctuations at zero frequency and at the Larmor frequency, we can see in a rough way why  $T_1$  and  $T_2$  are different.

A useful way to characterize the frequency spectrum of the fluctuations is in terms of the correlation time  $\tau$ . Figure 7.10 suggests how the energy in different frequency components for the same magnitude of fluctuating fields changes with different values of  $\tau$ . The spectrum is relatively flat up to frequencies around  $1/\tau$  and then rolls off to zero. The amplitude of the initial plateau decreases as  $\tau$  becomes shorter and the energy of the fluctuations is spread over a wider range of frequencies.

From this plot we can get a rough idea of how the relaxation times vary by assuming that  $1/T_2$  is proportional to the amplitude of the spectrum at zero frequency, and  $1/T_1$  is proportional to the amplitude at the Larmor frequency. For very long  $\tau$ , the amplitude at

zero frequency is large, so  $T_2$  is short. But the Larmor frequency is past the roll-off frequency of the spectrum, so fluctuations are ineffective in promoting longitudinal relaxation and  $T_1$  is long. As  $\tau$  decreases, the amplitude at zero frequency, on the one hand, steadily decreases, lengthening  $T_2$ . On the other hand, the amplitude at the Larmor frequency increases, so  $T_1$  becomes shorter. However, there is a minimum of  $T_1$  when  $1/\tau$  is approximately equal to the Larmor frequency. For shorter  $\tau$ , the amplitude at the Larmor frequency begins to decline again, lengthening  $T_1$ . If  $1/\tau$  is much larger than the Larmor frequency, both  $T_1$  and  $T_2$  are long. The fact that the two relaxation times are comparable in a room temperature sample of pure water indicates that the correlation time is very short. The fact that  $T_1$  is approximately 10 times longer than  $T_2$  in the body indicates that the more complex composition of tissue, with slowly tumbling macromolecules and biological structures, produces fluctuating fields with longer correlation times and so  $T_2$  is affected more than  $T_1$ .

Considerations of the frequency spectrum of the fluctuating fields also help to explain how the relaxation times change with different values of  $B_0$ . Changing  $B_0$  changes the Larmor frequency and so shifts the point on the frequency spectrum that controls  $T_1$  relaxation. Because the amplitude of the fluctuating fields tends to decrease at higher frequencies, the  $T_1$  at higher magnetic fields tends to increase. However, the  $T_2$  is primarily determined by the fluctuations at zero frequency and so is relatively independent of field strength. For example, in going from 1.5 to 4 T, the  $T_1$  of gray matter increases from approximately 1000 ms to approximately 1250 ms (Barfuss *et al.* 1988; Breger *et al.* 1989).

In short, the tissue relaxation times are determined by the magnitude and correlation times of the local fluctuating magnetic fields, and these, in turn, depend on the local environment of the water molecules. In general, for a more structured environment the correlation times are long; as a result, field fluctuations are concentrated in the low frequencies, and the result is that  $T_2$  is shorter than  $T_1$ . In the brain, for example, the more structured environments of GM and WM have shorter relaxation times than the more fluid CSF. Lesions in the brain of various kinds tend to have longer relaxation times. In very highly organized structures, such as bone or the myelin sheath around nerves, the correlation times are quite long. These longer correlation times drastically shorten  $T_2$  and lengthen  $T_1$ . For example, bone mineral contains calcium phosphate compounds, which potentially can be imaged with  $^{31}\text{P}$ -NMR (Ackerman *et al.* 1992). But the challenge for imaging is that the  $T_2$  may be as short as a few hundred microseconds, whereas the  $T_1$  may be as long as 60 s.

## Contrast agents

In clinical MRI studies, contrast agents are often used to enhance the contrast between different tissues by altering the local relaxation times. These agents affect the magnitude and correlation times of the fluctuating fields, and the basics of how these agents work can be understood from the preceding arguments. The most commonly used contrast agents are gadolinium compounds (Young *et al.* 1981; Yuh *et al.* 1992). There are different forms, but each is essentially a gadolinium atom attached to a chelating agent, such as diethylenetriaminepentaacetic acid (DTPA), which binds the agent, which is toxic on its own, into a non-toxic form. Gadolinium alters the relaxation time because it contains unpaired electrons, and the water molecules can approach near enough for the magnetic moment of the electrons to have an effect on the relaxation of the protons. The magnetic field produced by an electron is three orders of magnitude stronger than the field of the proton, so the magnitude of the fluctuating fields is greatly increased. The correlation time is short, so gadolinium affects both  $T_1$  and  $T_2$ . In fact, the absolute change in the two relaxation rates is the same, but because the



initial transverse relaxation rate is typically 10 times larger than the longitudinal relaxation rate, the fractional change in  $T_1$  is much larger than the fractional change in  $T_2$ . For example, if the initial transverse relaxation rate is  $10 \text{ s}^{-1}$  ( $T_2 = 100 \text{ ms}$ ), and the longitudinal relaxation rate is  $1 \text{ s}^{-1}$  ( $T_1 = 1000 \text{ ms}$ ), and if gadolinium produces a change of  $1 \text{ s}^{-1}$  in each of the relaxation rates, then this will be a 50% change in  $T_1$  (1000 to 500 ms) but only a 10% change in  $T_2$  (100 to approximately 90 ms). For this reason, agents such as this are described as  $T_1$ -agents.

A second class of contrast agents effectively reduces  $T_2$  more than  $T_1$  by producing large spatial variations in the magnetic field. These agents possess a large magnetic moment, and if they remain in the blood, they alter the blood magnetic susceptibility relative to the surrounding tissue, creating field gradients through the tissue. This has a direct effect on  $T_2^*$  because the heterogeneity of the field leads to signal decay from just the static field offsets. However,  $T_2$  itself is also affected because diffusion of the water molecules leads to random displacements of the dipoles, and as they move through the inhomogeneous field, they precess at different rates and phase dispersion develops. Technically speaking, this is a diffusion effect caused by the heterogeneity of the tissue, rather than a true alteration of  $T_2$ , but for classification purposes we can describe this as a  $T_2$  effect because it produces large signal changes on a  $T_2$ -weighted image. Such diffusion effects will be taken up in Ch. 8.

The primary agent in clinical use that behaves in this fashion is in fact Gd-DTPA (Villringer *et al.*, 1988). That is, in addition to its relaxivity effect, which primarily alters the local  $T_1$ , gadolinium also creates a susceptibility effect when it is confined to the vasculature, and this affects  $T_2$  and  $T_2^*$ . The effects of gadolinium on the signal intensity can, therefore, be rather complex. Imagine that a bolus of Gd-DTPA is injected into a patient, and a series of rapid images of the brain is acquired. In the healthy portions of the brain, the blood–brain barrier prevents the gadolinium from leaving the vasculature. As the bolus passes through the blood volume, the  $T_2^*$  and to a lesser extent the  $T_2$  are reduced, and the signal intensity drops transiently as the bolus passes. This is the basis for using Gd-DTPA to measure blood volume because the dip is accentuated when the cerebral blood volume is larger (this is discussed more fully in Ch. 13). But now consider what happens if there is a brain tumor with a leaky blood–brain barrier. The gadolinium then enters the tissue and reduces the local  $T_1$ , which increases the signal from the tumor in a  $T_1$ -weighted image. This enhancement of tumors is the primary diagnostic use of gadolinium.

Other agents lack the relaxivity effects of gadolinium but possess a similar large magnetic moment and so produce only the  $T_2^*$  and  $T_2$  effects. For example, dysprosium (Dys) has a larger magnetic moment than gadolinium, and Dys-DTPA produces a larger change in transverse relaxation without a change in  $T_1$  (Villringer *et al.* 1988). Other compounds exploit the magnetic properties of iron (Chambon *et al.* 1993; Kent *et al.* 1990; Majumdar *et al.* 1988). Superparamagnetic particles carry a large magnetic moment and so strongly affect transverse relaxation. Finally, a natural physiological agent is deoxyhemoglobin. Deoxyhemoglobin is paramagnetic, but oxyhemoglobin is diamagnetic. As a result, if the concentration of deoxyhemoglobin changes, the susceptibility of the blood changes, and this produces weak field gradients through the tissue. As introduced in Ch. 5, this effect is the basis for most of the fMRI studies done today to map patterns of brain activation, because blood oxygenation changes with activation. The susceptibility differences produced naturally by deoxyhemoglobin alterations during activation are approximately an order of magnitude smaller than those produced by a typical bolus of gadolinium. As a result, the extravascular signal change is only a small percentage.

## References

- Ackerman JL, Raleigh DP, Glimcher MJ (1992) Phosphorous-31 magnetic resonance imaging of hydroxyapatite: a model for bone imaging. *Magn Reson Med* **25**: 1–11
- Barfuss H, Fischer A, Hentschel D, Ladebeck R, Vetter J (1988) Whole-body MR imaging and spectroscopy with a 4 T system. *Radiology* **169**: 811–816
- Bloembergen N (1957) Proton relaxation times in paramagnetic solutions. *J Chem Phys* **27**: 572–573
- Bloembergen N, Purcell EM, Pound RV (1948) Relaxation effects in nuclear magnetic resonance absorption. *Phys Rev* **73**, 679–712
- Breger RK, Rimm AA, Fischer ME (1989) T1 and T2 measurements on a 1.5 T commercial imager. *Radiology* **71**: 273–276
- Buxton RB, Edelman RR, Rosen BR, Wismer GL, Brady TJ (1987) Contrast in rapid MR imaging: T1- and T2-weighted imaging. *J Comput Assist Tomogr* **11**: 7–16
- Buxton RB, Fisel CR, Chien D, Brady TJ (1989) Signal intensity in fast NMR imaging with short repetition times. *J Magn Reson* **83**: 576–585
- Chambon C, Clement O, Blanche AL, Schouman-Claeys E, Frija G (1993) Superparamagnetic iron oxides as positive MR contrast agents: in vitro and in vivo evidence. *Magn Reson Imaging* **11**: 509–519
- Ernst RR, Anderson WA (1966) Application of Fourier transform spectroscopy to magnetic resonance. *Rev Sci Instrum* **37**: 93–102
- Gyngell ML (1988) The application of steady-state free precession in rapid 2DFT NMR imaging. *Magn Reson Imaging* **6**: 415–419
- Haase A, Frahm J, Matthaei D, Haenicke W, Ferboldt K-D (1986) Flash imaging: rapid NMR imaging using low flip-angle pulses. *J Magn Reson* **67**: 258–266
- Hahn EL (1950) Spin echoes. *Phys Rev* **80**: 580–593
- Hendrick RE, Nelson TR, Hendee WR (1984) Optimizing tissue differentiation in magnetic resonance imaging. *Magn Reson Imaging* **2**: 193–204
- Hoppel BE, Weisskoff RM, Thulborn KR, *et al.* (1993) Measurement of regional blood oxygenation and cerebral hemodynamics. *Magn Reson Med* **30**: 715–723
- Kent T, Quast M, Kaplan B, Lifsey RS, Eisenberg HM (1990) Assessment of a superparamagnetic iron oxide (AMI-25) as a brain contrast agent. *Magn Reson Med* **13**: 434–443
- Majumdar S, Zoghbi SS, Gore JC (1988) Regional differences in rat brain displayed by fast MRI with superparamagnetic contrast agents. *Magn Reson Imaging* **6**: 611–615
- Patz S (1989) Steady-state free precession: an overview of basic concepts and applications. *Adv Magn Reson Imaging* **1**: 73–102
- Solomon I (1955) Relaxation processes in a system of two spins. *Phys Rev* **99**: 559
- Thulborn KR, Brady TJ (1989) Iron in magnetic resonance imaging of cerebral hemorrhage. *Magn Reson Quart* **5**: 23–38
- Villringer A, Rosen BR, Belliveau JW, *et al.* (1988) Dynamic imaging with lanthanide chelates in normal brain: contrast due to magnetic susceptibility effects. *Magn Reson Med* **6**: 164–174
- Wehrli FW, MacFall JR, Glover GH, *et al.* (1984) The dependence of nuclear magnetic resonance (NMR) image contrast on intrinsic and pulse sequence timing parameters. *J Magn Reson Imaging* **2**: 3–16
- Wehrli FW, Perkins TG, Shimakawa A, Roberts F (1987) Chemical shift induced amplitude modulations in images obtained with gradient refocusing. *Magn Reson Imaging* **5**: 157–158
- Wisner GL, Buxton RB, Rosen BR, *et al.* (1988) Susceptibility induced MR line broadening: applications to brain iron mapping. *J Comput Assist Tomogr* **12**: 259–265
- Young I, Clarke G, Bailes D, *et al.* (1981) Enhancement of relaxation rate with paramagnetic contrast agents in NMR imaging. *J Comput Assist Tomogr* **5**: 543–547
- Yuh W, Engelen J, Muhonen M, *et al.* (1992) Experience with high-dose gadolinium MR imaging in the evaluation of brain metastases. *Am J Neuroradiol* **13**: 335–345

# Diffusion and the MR signal

<b>Introduction</b>	<i>page</i> 173
<b>Diffusion imaging</b>	174
The nature of diffusion	174
Diffusion in a linear field gradient	175
Techniques for diffusion imaging	179
<b>Diffusion mechanisms in biological systems</b>	180
Multicompartment diffusion	180
Restricted diffusion	182
Diffusion imaging in stroke	183
<b>Diffusion tensor imaging</b>	184
Anisotropic diffusion	184
The diffusion tensor	188
Measuring the trace of the diffusion tensor	189
Fiber tract mapping	192
Limitations of the diffusion tensor model	193
Beyond the diffusion tensor model	194
<b>Diffusion effects in functional imaging</b>	196
Diffusion around field perturbations	196
Motional narrowing	198

## Introduction

Water molecules in the body are in constant motion. In [Ch. 7](#), we considered how these thermal motions lead to random rotations of the water molecule, producing fluctuations of the local magnetic field felt by the hydrogen nucleus. These fluctuating fields lead to relaxation; in particular, the low-frequency fields alter relaxation rates, reducing  $T_2$  without affecting  $T_1$ . However, in addition to random rotations of the molecule, thermal motions also produce random displacements, the process of *diffusion*. In a non-uniform magnetic field, as a spin moves randomly to another position, there are corresponding random changes in its precession rate, and thus an additional dephasing of the spins and greater signal loss. This additional signal decay caused by diffusion through inhomogeneous fields is exploited in three ways in MRI. First, by applying a strong linear field gradient and measuring the additional signal attenuation, the local diffusion coefficient  $D$  can be measured. This is the basis of diffusion imaging, and one of the primary applications of diffusion imaging is in early assessment of injury in stroke (Baird and Warach 1998). Conventional MRI does not reveal the affected area in stroke until several hours after the event, when  $T_2$  changes become apparent. As the apparent  $D$  is reduced very early in the development of a stroke, maps of altered  $D$  in the acute phase correlate well with the  $T_2$  maps of the affected area made several hours later.

Second, the ability to measure the local value of  $D$  provides a potentially powerful tool for mapping the connections between brain regions (Jones 2008). In white matter fiber bundles, the diffusion of water is *anisotropic*, with  $D$  approximately 10 times larger along the fibers than across the fibers. Mapping the diffusion anisotropy with *diffusion tensor imaging* (DTI), therefore, provides a way to map white matter fiber tracts. These methods provide a new structural approach to the investigation of the functional organization of the brain that complements fMRI studies of dynamic patterns of activation.

Finally, the third way in which diffusion effects enter MRI is that injected contrast agents or intrinsic effects in the blood such as changes in deoxyhemoglobin, create microscopic field perturbations around the small blood vessels leading to changes in  $T_2^*$  or  $T_2$ . The random motions of water molecules through these field gradients affect both relaxation rates (Weisskoff *et al.* 1994). In fact, if the water molecules did not diffuse, such microscopic, static field offsets would affect only  $T_2^*$ , and not  $T_2$ . With diffusion, the spins move in a random way through these field perturbations, and so the effects are not fully refocused with a spin echo (SE) experiment. Spin echo fMRI methods based on these diffusion effects are potentially more accurate in localizing the site of neuronal activity than the more commonly used gradient recalled echo (GRE) fMRI techniques (Lee *et al.* 1999; Yacoub *et al.* 2003).

## Diffusion imaging

### The nature of diffusion

Water is a highly dynamic medium, with water molecules continuously tumbling and colliding with one another and with other molecules. With each collision, a water molecule is both rotated to a new angle and deflected to a new position. These effects are random, in the sense that the small deflection or rotation in one collision is unrelated to the effects of the last collision. Both of these effects are important in understanding the NMR signal. As a molecule rotates, the relative orientation of a hydrogen nucleus in the magnetic field produced by the other hydrogen nucleus in the molecule changes, and so each nucleus feels a randomly fluctuating magnetic field. These fluctuations lead to relaxation, as described in Ch. 7. The fact that each molecule also undergoes random displacements of position means that a group of molecules that are initially close together will eventually disperse, like a drop of ink in water (Fig. 8.1). This self-diffusion of water produces only small displacements of the spins, but these displacements are nevertheless measurable with NMR.

The essential nature of diffusion is that a group of molecules that start at the same location will spread out over time, with each molecule suffering a series of random displacements. For free diffusion, after a time  $T$  the spread of positions along a spatial axis  $x$  has a Gaussian shape with a variance of

$$\sigma_x^2 = 2DT \quad (8.1)$$

where  $D$ , the diffusion coefficient, is a constant characteristic of the medium. (Box 8.1 contains a more complete discussion of this equation.) In other words, during the time interval  $T$ , any particular molecule moves a distance on the order of  $\sigma_x$ , but it is equally likely to move in either direction.

Furthermore, the typical displacement of a particle grows only as the square root of time. This is fundamentally different from motion at a constant velocity, where displacement is proportional to time. For example, compare the average displacement of a water molecule diffusing with  $D = 0.001 \text{ mm}^2/\text{s}$  (a typical number for brain) and a water molecule being

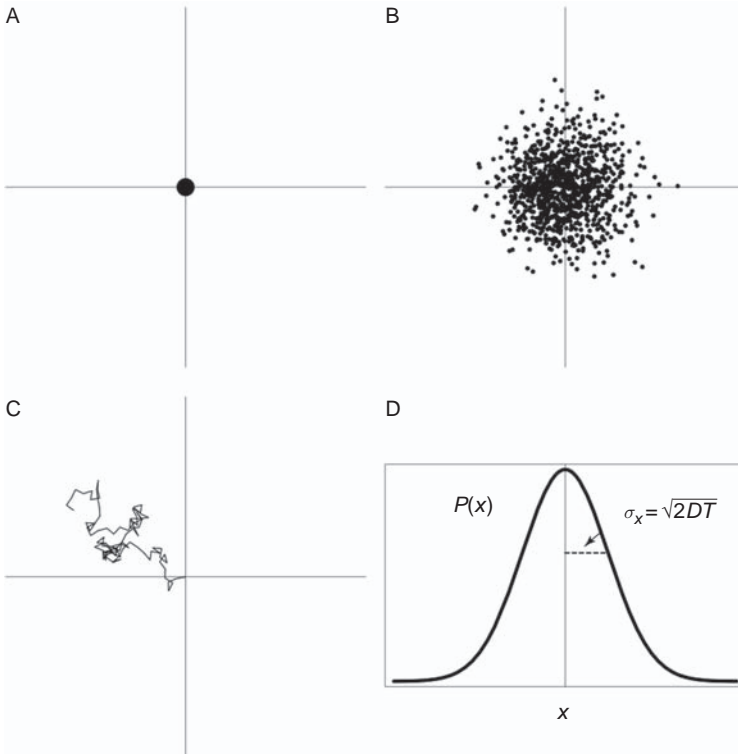


**Fig. 8.1.** Diffusion. Water molecules that start from the same location (A) over time spread out (B), like a drop of ink in a clear fluid. Each molecule undergoes a random walk (C) in which each step is in a random direction. (D) The mean displacement of many molecules that start at the same location is zero, but the standard deviation of the spread of their positions increases in proportion to the square root of  $DT$ , where  $D$  is the diffusion coefficient and  $T$  is the elapsed time.  $\sigma_x$ , variance along the  $x$ -axis.

carried along in the blood of a capillary with a speed of 1 mm/s. In 2 ms each will move approximately 2 mm, but while the time for the flowing molecule to move 20 mm is only 20 ms, the time for the diffusing molecule to move the same distance is 200 ms. Diffusion is, therefore, reasonably efficient for moving molecules short distances, but it is highly inefficient for transport over large distances. It is a remarkable fact that such small displacements as these (tens of micrometers) can have a measurable effect on the MR signal.

## Diffusion in a linear field gradient

Diffusion imaging is built around the effects of diffusion through a linear field gradient (Box 8.1). The MR signal is made sensitive to diffusion by adding a pair of strong bipolar gradient pulses to the pulse sequence (Fig. 8.2) (Stejskal and Tanner 1965). The two gradient pulses are balanced so that their net effect would be zero for a spin that does not move, but each spin that moves during the interval between pulses acquires a phase offset proportional to how far it has moved. The result is a phase dispersion that is proportional to the dispersion of positions, producing an attenuation (A) of the net signal by a factor that depends on the value of  $D$ . For free diffusion, with a Gaussian distribution of spin phases, A for the signal is a simple exponential decay (Le Bihan 1991):

$$A(D) = e^{-bD} \quad (8.2)$$

**Box 8.1. The physics of diffusion and the magnetic resonance signal**

The effects of diffusion can be understood with a simple random walk model, such that in each time interval  $\tau$  a molecule moves a distance  $s$  in a random direction. This view of diffusion as a random walk may seem to have little to do with the classical concept of diffusion as a flux of particles down a concentration gradient as described by Fick's law:

$$J = -D \frac{dC}{dx} \quad (\text{B8.1})$$

where  $J$  is the particle flux (number of particles passing through a unit area per second),  $dC/dx$  is the gradient of the particle concentration, and  $D$  is the diffusion coefficient. Based on this equation, it is sometimes said that diffusion is "driven" by a concentration gradient. This seems inconsistent with the random walk model in which each step is random regardless of the concentration. However, Eq. (B8.1) is the natural result of random motions: there is a net flux from high to low concentrations simply because more particles start out from the region of high concentration.

To relate the parameters of a random walk ( $s$  and  $\tau$ ) to  $D$ , consider a one-dimensional random walk and the net flux past a particular point  $x$ . The local density of particles along the line is  $C(x)$ . Additionally, for one time step, we need only look at the particles within a distance  $s$  of  $x$  to calculate the flux because these are the only particles that can cross  $x$  in one step. Let  $C_L = C(x - s/2)$  be the mean concentration on the left and  $C_R = C_L + s dC/dx$  is then the mean concentration on the right of  $x$ . In a time interval  $\tau$  (one step), on average half of the particles within a distance  $s$  to the left of  $x$  will move to the right past  $x$ , so the number of particles crossing  $x$  from the left is  $sC_L/2$ , giving a positive flux (particles per unit time) of  $J^+ = sC_L/2\tau$ . Similarly, half of the particles within a distance  $s$  to the right will move left to form a negative flux  $J^- = sC_R/2\tau$ . The net flux  $J = J^+ - J^-$  is then

$$J = -\frac{s^2}{2\tau} \frac{dC}{dx} \quad (\text{B8.2})$$

The classical  $D$  is related to the parameters of a random walk as

$$D = \frac{s^2}{2\tau} \quad (\text{B8.3})$$

For a one-dimensional random walk of  $N$  steps, the mean final displacement is zero because each step is equally likely to be to the left or the right. But the variance of the final positions is  $\sigma^2 = Ns^2$ . That is, the width of the spread of final positions grows in proportion to the square root of the number of steps. Noting that the total time  $T$  is simply the number of steps  $N$  multiplied by the step interval  $\tau$  of the random walk, we can complete the connection between  $D$  and the random walk:

$$\sigma^2 = 2DT \quad (\text{B8.4})$$

Diffusion imaging is built around the effects of diffusion through a linear field gradient. A basic diffusion pulse sequence is shown in Fig. 8.2. After a  $90^\circ$  excitation pulse, a strong gradient pulse is applied with amplitude  $G$  and duration  $\delta t$ . At a time  $T$  after the beginning of the first pulse, a second pulse is applied with equal amplitude but opposite sign. If the spins did not diffuse, the second pulse would exactly balance the effects of the first pulse, creating a gradient echo. The net effect would be as if the gradient pulses were not applied at all. (If the experiment is done as a spin echo [SE], with a  $180^\circ$  refocusing pulse between the two gradient pulses, then the second gradient pulse also should be positive to balance the first pulse.) But with diffusion, each spin is likely to be in a different location when the second pulse is applied than it was when the first pulse was applied. The result is that the effects of the two gradient pulses will not balance, leaving each spin with a

small random phase offset that depends on how far it moved between the two pulses. The net signal is then reduced because of these random phase offsets.

To quantify this diffusion effect on the MR signal, we can simplify the experiment so that  $\delta t$  is very short. Then we do not have to worry about how diffusion during the gradient pulse affects the signal. Instead, we can focus just on how far a spin has moved between the first pulse and the second. That is, we can consider that the effect of each gradient pulse is to mark the current position of a spin by its phase. The field offset at position  $x$  as a result of the gradient  $G$  is  $Gx$ , and the corresponding frequency offset is  $\gamma Gx$ , where  $\gamma$  is the gyromagnetic ratio. Then a spin at position  $x$  will acquire a phase  $\phi = \gamma Gx\delta t$  during the first gradient pulse, and the second gradient pulse will add a phase  $-\phi$  if the spin does not move, unwinding the effect of the first pulse. If the spin has moved a distance  $\Delta x$  by diffusion during the interval  $T$ , then the net effect of the two gradient pulses will be a phase offset  $\Delta\phi$ , given by

$$\Delta\phi = \gamma G\delta t\Delta x \quad (\text{B8.5})$$

For simple free diffusion, the distribution of  $\Delta x$  is Gaussian with a variance given by Eq. (B8.4), so the distribution of phase offsets is then also Gaussian with a variance  $\sigma_\phi^2$  proportional to the variance of the displacements:

$$\sigma_\phi^2 = 2(\gamma G\delta t)^2 DT \quad (\text{B8.6})$$

As noted in Ch. 7, a Gaussian distribution of phases produces an exponential attenuation ( $A$ ) of the signal. The result is that the additional attenuation caused by diffusion can be written as

$$A(D) = e^{-bD} \quad (\text{B8.7})$$

where the factor  $b$  incorporates all the amplitude and timing parameters of the gradient pulses. From the preceding argument,  $b$  would be  $(\gamma G\delta t)^2 T$ . A more careful analysis, taking account of the diffusion effects during the application of the gradient pulse, yields (Stejskal and Tanner 1965)

$$b = (\gamma G\delta t)^2 (T - \delta t/3) \quad (\text{B8.8})$$

By measuring the MR signal with no gradient pulses and by comparing that with the signal for a reasonably large  $b$ ,  $A(D)$  can be calculated. From the measured value of  $A$ ,  $D$  can be calculated. By incorporating such diffusion weighting into an imaging pulse sequence, the local value of  $D$  can be mapped.

The arguments that led to Eq. (B8.6) and subsequent equations assumed that the distribution of displacements  $\Delta x$  during the diffusion time  $T$  was Gaussian, which is the case for free diffusion. However, in biological structures, the diffusion of water is often restricted by membranes and large molecules. For example, if water is confined to a small space by impermeable membranes, then as  $T$  grows larger the displacement of a molecule does not continue to grow as it would in free diffusion because the molecule would be blocked by the membranes. With restricted diffusion, the actual distribution of displacements will depend on the local structure, and so it is useful to be able to determine that distribution. The technique to do that is called *q-space* imaging, also called *diffusion spectrum imaging* (Callaghan 1991; Cory and Garroway 1990).

To see how this works, we return to Eq. (B8.5). The action of the two gradient pulses is to create a phase offset  $\Delta\phi$  for each spin that depends on the displacement  $\Delta x$ . If we define  $q$  as the product of the factors multiplying  $\Delta x$  ( $q = \gamma G\delta t$ ), the acquired phase is simply  $\Delta\phi = q\Delta x$ . The net signal is derived by adding spin vectors with these phase offsets, weighted by the distribution of displacements. To simplify the notation, we use  $x$  for the displacement  $\Delta x$ , and call the unknown distribution of those displacements  $p(x)$ . By describing each vector as a complex exponential with phase  $\Delta\phi$  and the same magnitude, the net signal is

$$S(q) = \int e^{i\Delta\phi(x)} p(x) dx = \int e^{iqx} p(x) dx \quad (\text{B8.9})$$

This is the mathematical form of the Fourier transform so if either  $S(q)$  or  $p(x)$  are known, the other can be calculated by applying the appropriate Fourier transform. By stepping through many values of  $q$  and measuring  $S(q)$ , the distribution of displacements  $p(x)$  can be determined. Although somewhat time consuming because of the need to measure  $A$  for many  $q$  values, this is a powerful tool for exploring the complexities of restricted diffusion in biological structures.

The factor  $b$  is an experimental parameter that depends only on the amplitude and timing parameters of the applied gradient pulses (Box 8.1). The local tissue  $D$  can be calculated by measuring the signal with no gradients applied ( $b=0$ ) and again with a large value of  $b$ . The ratio of the two signals is the attenuation factor  $A(D)$ . Note that in these two measurements the echo time (TE) must be kept the same, so that the effects of  $T_2$  decay are identical. In practice, there are two ways of displaying diffusion-sensitive images (Fig. 8.3). The first is to calculate pixel by pixel the value of  $D$  and then to create an image of  $D$ . Such an image is usually called a map of the *apparent diffusion coefficient* (ADC), and in these images the tissues with the largest  $D$  values are brightest. An alternative is to display the diffusion-weighted image (DWI) itself (i.e., the image made with a large  $b$ -value), and in such an image the tissues with the largest  $D$  values tend to be the darkest because they suffer the most attenuation. Note, however, that a DWI will have other contrast characteristics as well (e.g., some degree of  $T_2$  weighting) and so is not a pure reflection of diffusion effects, in contrast to an ADC map.

A typical value of  $D$  in the brain is  $0.001 \text{ mm}^2/\text{s}$ . To measure  $D$ ,  $b$  must be sufficiently large to produce a measurable value of  $A$ . For example, a  $b$ -value of  $1000 \text{ s}/\text{mm}^2$  would attenuate the signal by a factor of  $e$ , but  $b = 100 \text{ s}/\text{mm}^2$  would only attenuate it by 10%. The  $b$ -factor depends on both the gradient strength and the duration, and so in principle a large value of  $b$  can be created with weak gradients if they are on for a long enough time. However, the time during which diffusion can act is limited by  $T_2$ , the lifetime of the signal, so strong

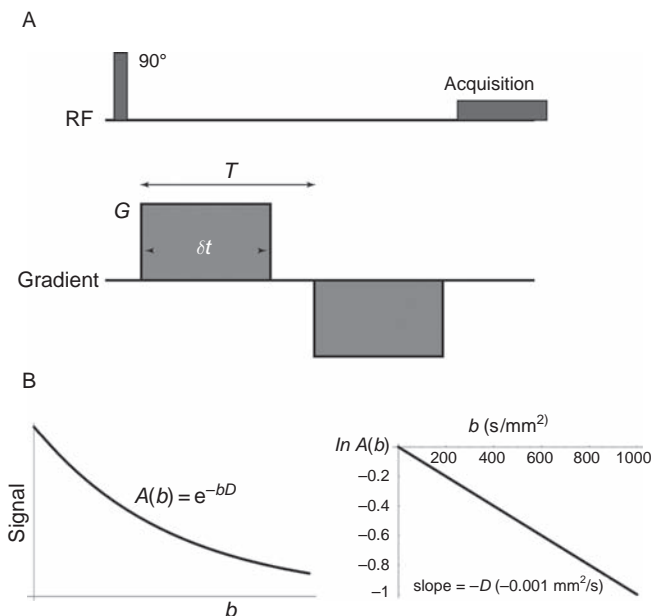


**Fig. 8.2.** Measuring the diffusion coefficient with NMR. (A) The NMR signal is made sensitive to diffusion by applying a bipolar gradient pulse between signal excitation and signal detection. If spins were stationary, the additional position-dependent phase acquired by precession during the first gradient pulse would be precisely unwound by the second gradient pulse, and there would be no effect on the net measured signal. (B) With diffusion, the random displacements of water molecules between the two gradient pulses produce random phase offsets and signal attenuation (A). The attenuation is exponential in the term  $bD$ , where  $b$  is an experimental parameter that depends on the gradient strength and duration, and  $D$  is the local diffusion coefficient.



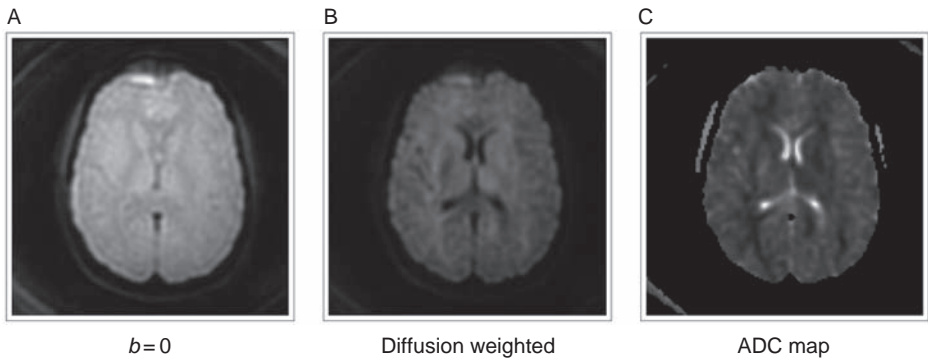


**Fig. 8.3.** Diffusion-weighted imaging. (A) An image without diffusion weighting ( $b=0$ ) from a healthy human brain. (B) When bipolar gradients are added to the imaging pulse sequence, each local signal is diffusion weighted. Cerebrospinal fluid, with the largest apparent diffusion coefficient (ADC), is the most attenuated. (C) From two images made with different  $b$ -values, a map of the ADC can be calculated on a voxel-by-voxel basis. Images were made with a spiral acquisition. (Data courtesy of L. Frank.)

gradients are essential for creating large values of  $b$ . Example numbers for an MRI system are a gradient amplitude of 20 mT/m, with each pulse lasting 27 ms and a diffusion time between the start of the first pulse and the start of the second pulse of 57 ms (i.e., two 27 ms pulses with a 30 ms gap between them), which produces  $b = 1000 \text{ s/mm}^2$  (Shimony *et al.* 1999). Note that it takes a substantial amount of time to play out the gradient pulses to achieve sufficient diffusion sensitivity. For this example, TE was 121 ms.

The basic procedure for calculating  $D$  is to measure the signals with a range of  $b$ -values, including  $b = 0$ . The value of  $A$  is calculated by dividing the signal for a particular  $b$  by the signal with  $b = 0$ , and then a plot of the natural logarithm of  $A$  ( $\ln A$ ) versus  $b$  will yield a straight line with a slope of  $-D$  (Fig. 8.2). The minimum data required are just two measurements, one with  $b = 0$  and one with  $b$  sufficiently large to produce a measurable attenuation. For a two-point measurement, the optimum choice of  $b$  to maximize the signal to noise ratio (SNR) is  $1/D$ , where  $D$  is the diffusion coefficient of the tissue being measured.

## Techniques for diffusion imaging

Diffusion sensitivity can be added to any imaging pulse sequence by inserting a bipolar gradient pulse after the excitation pulse and before the signal read-out. For example, the gradient pulses shown in Fig. 8.2 could be directly inserted into a GRE pulse sequence. Note that the axis of the diffusion-sensitizing gradient is arbitrary and can be adjusted by the experimenter. For an SE pulse sequence, the two gradient pulses are usually put on opposite sides of the  $180^\circ$  radiofrequency (RF) refocusing pulse. In this case, the two gradient pulses have the same sign, such that the  $180^\circ$  pulse would create a full echo of the signal if there were no motion. That is, the local phase change induced by the first gradient pulse would be reversed by the  $180^\circ$  pulse, and the second gradient pulse would then unwind the local phase offset.

One of the limitations of diffusion imaging is the need to have long TEs in order to apply the diffusion-sensitizing gradient pulses. In other words, the *diffusion* time, the time available for spins to diffuse apart, is limited by TE and so ultimately is limited by the  $T_2$  of the tissue. This makes it very difficult to study tissues with short  $T_2$  and small  $D$ . Stimulated echo (STE) techniques offer a way to solve this problem (Merboldt *et al.* 1985; Tanner 1970). This approach was introduced in Ch. 7. The simplest STE pulse sequence for diffusion imaging

uses three sequential  $90^\circ$  RF pulses, with gradient pulses after the first and third. Then the first gradient pulse produces a transverse magnetization, and the gradient pulse changes the local phase in proportion to the spins' locations. The second  $90^\circ$  pulse tips a part of the transverse magnetization back on to the longitudinal axis, and the part remaining in the transverse plane decays away with time constant  $T_2$ . But the components parked along the longitudinal axis decay much more slowly, with a time constant  $T_1$ . The third  $90^\circ$  pulse then returns this magnetization to the transverse plane, and the second gradient pulse then refocuses the signal to create the STE. The power of the STE method is that the diffusion time, the time between the second and third  $90^\circ$  pulses, can be made quite long because the magnetization decays only with  $T_1$  rather than  $T_2$ .

Finally, diffusion imaging also can be done using steady-state free precession (SSFP) pulse sequences (Le Bihan 1988). As described in Ch. 7, SSFP occurs in a string of closely spaced RF pulses when TR is smaller than  $T_2$ , so a steady-state signal forms both before and after each pulse. Each of these signals has a strong contribution of echoes, with each RF pulse forming a partial echo of the signals generated by the previous RF pulses. In particular, the signal that forms just before each RF pulse ( $M_{ss}^-$  in the notation of Ch. 7) is composed entirely of echoes. These echoes are a combination of direct SEs and STEs, and so the SSFP signal is strongly sensitive to diffusion when diffusion-weighting gradients are added (Buxton 1993). In fact, for the same  $b$ -value, the SSFP sequence is much more sensitive to diffusion than either the straight SE or the STE pulse sequences, and this sensitivity is improved with smaller flip angles, which will maximize the STE component of the echoes. However, quantification of  $D$  is not straightforward with an SSFP pulse sequence because the dependence of the attenuation on  $D$  is more complicated than Eq. (8.2) and involves the local relaxation times as well. Nevertheless, recent work suggests that SSFP can provide a sensitive measure of the directional dependence of diffusion (*anisotropy*, discussed below) with high spatial resolution (McNab and Miller 2008).

In practice, diffusion imaging in the living human brain suffers from several potential artifacts. The purpose of adding the bipolar gradient pulses is to sensitize the MR signal to the small motions of diffusion. However, this also makes the signal sensitive to other motions, such as blood flow in vessels and brain pulsations from arterial pressure waves. The potential sensitivity of diffusion measurements to blood flow led to one of the earliest approaches to measuring perfusion with MRI, the intravoxel incoherent motion method (Le Bihan 1988; Le Bihan *et al.* 1988). This method has been superseded by newer approaches, described in Chs. 12–13, but the technique was an important milestone in the development of MRI. Because of the very high motion sensitivity of a DWI, brain motions from arterial pulsations can severely degrade the images. Often diffusion imaging is done with the TR gated to the cardiac cycle to minimize the effects of motions resulting from arterial pulsatility. Single-shot echo planar imaging (EPI) avoids these motion artifacts, although EPI images can be distorted when using strong gradient pulses by eddy current effects (Haselgrove and Moore 1996; Jezzard *et al.* 1998).

## Diffusion mechanisms in biological systems

### Multicompartment diffusion

The linear decrease in  $\ln A$  with increasing  $b$  (Eq. (8.2) and Fig. 8.2) describes the diffusion behavior of a simple substance such as pure water. Brain tissues, however, are complex structures, and this leads to a rich variety of diffusion effects that alter this basic picture. The

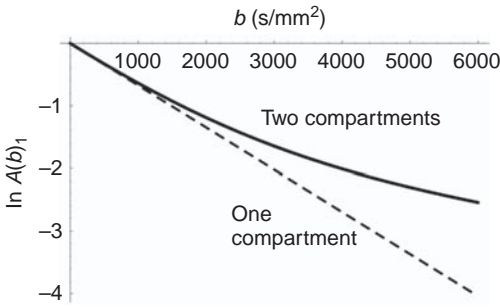


**Fig. 8.4.** Diffusion in more complex systems. With multiple compartments of diffusing water, the diffusion attenuation ( $A$ ) curve depends on how rapidly the water molecules exchange between compartments. With rapid exchange, the system behaves like a single-compartment, and the decay curve is a single exponential. With slow exchange, the decay curve is similar to the single-compartment decay curve for low  $b$ -values, but for higher  $b$ -values the curve bends upward as the signal from the compartment with the higher diffusion coefficient is more attenuated.

first effect is the heterogeneity of the tissue, with potentially multiple pools of water within a resolution element of our imaging experiment (e.g., an image voxel of a few cubic millimeters). For example, a prominent hypothesis is that  $D$  for intracellular water is significantly smaller than  $D$  for extracellular water. What type of diffusion decay curve would we expect to measure for such a two-compartment system? The answer depends on two factors: (1) the rate of exchange of water between the two compartments and (2) the range of  $b$ -values used. If a typical water molecule moves back and forth between the two compartments multiple times during the experiment, the system is described as being in the *fast exchange* state. In this case, all the water molecules have similar histories, in the sense that each one spends approximately the same amount of time in each compartment. As a result, the system behaves like a uniform system with a  $D$  value equal to the volume-weighted average of the  $D$  values of the two compartments (a and b):

$$D_{\text{av}} = v_a D_a + v_b D_b \quad (8.3)$$

where  $v_a$  and  $v_b$  are the volume fractions of the two compartments (e.g., 0.2 for the extracellular space and 0.8 for the intracellular space), and  $D_a$  and  $D_b$  are the respective diffusion coefficients. In this fast exchange limit, the diffusion attenuation curve is linear with a slope equal to  $-D_{\text{av}}$ .

However, if the exchange of water is slow, so the two compartments are effectively isolated during the experiment, the attenuation takes on a biexponential form (Fig. 8.4):

$$A = v_a e^{-bD_a} + v_b e^{-bD_b} \quad (8.4)$$

For small  $b$ -value, this biexponential curve is well approximated by a single exponential with  $D = D_{\text{av}}$ , and so initially the slope of  $\ln A$  is just  $-D_{\text{av}}$ . But for larger  $b$ -value, this approximation breaks down, and the compartment with the larger  $D$  is more attenuated and so contributes less to the signal. The result is that the slope of  $\ln A$  approaches a value corresponding to the smaller  $D$ , so there is an upward curvature of the diffusion attenuation curve (Fig. 8.4).

In short, this curve deviates from a straight line when two conditions are satisfied: (1) there are multiple isolated or slowly exchanging water compartments with different values for  $D$  and (2) large  $b$ -values are used. To probe multicompartment diffusion in a tissue, one must make measurements with many  $b$ -values to characterize this curvature. Or, put another way, with a two-point measurement of  $D$  in a multicompartment, slow-exchange system, the value measured will vary depending on what  $b$ -value is used. The measured value will lie somewhere between the true average,  $D_{\text{av}}$ , values and the smaller of the two  $D$  values. By using a small  $b$ -value, one can ensure that the measured value is close to the true average, but the cost of such a measurement is reduced SNR.

A number of studies have found diffusion curves that look like those in Fig. 8.4, and such curves can be fit to a pair of exponentials as in Eq. (8.4) to determine “compartmental” volumes and  $D$  values. For example, in one early study in the brain, two diffusing components were identified, with  $D$  differing by about a factor of five between the two components (Niendorf *et al.* 1996). However, the volume fraction associated with the faster diffusing component was approximately 70%, much larger than the expected extracellular water fraction of around 20%. Instead of interpreting multi-exponential diffusion as resulting from two compartments, several other studies suggest that the biexponential behavior can occur within the intracellular compartment alone (Schwarcz *et al.* 2004; Sehy *et al.* 2002), and that the intravascular and extravascular  $D$  values are similar (Duong *et al.* 2001). However, measurements of intravascular and extravascular  $D$  values are difficult and often rather indirect, so this remains a controversial issue.

In short, diffusion decay in brain tissue often is not monoexponential, as in Eq. (8.2). Often this is described as biexponential, but these terms should not be taken too literally to imply the existence of two compartments, even if the fits are quite good.

## Restricted diffusion

There is another effect, common in measurements of  $D$  in biological tissues, that also affects the diffusion attenuation curve. In biological structures, the motion of water molecules is restricted by natural barriers such as cell membranes, an effect called *restricted diffusion* (Cooper *et al.* 1974). The cause of this restricted diffusion effect is the heterogeneous structure of tissue. With large macromolecules and numerous membranes and other barriers, water is not freely diffusing. To understand the implications of restricted diffusion, the key is to focus on the final distribution of displacements after a specific diffusion time. For example, imagine water molecules compartmentalized in a small box with impermeable walls. For short diffusion times, the water molecules do not move far, and most of them do not reach the edge of the box, so the barriers have little effect on how far a molecule diffuses. But for longer diffusion times, more molecules reach the walls of the box and are bounced back rather than diffusing past. The result is that, for the same diffusion time, the spread of displacements is not as large as it would be if the water were freely diffusing, and so  $D$  appears to be smaller with longer diffusion times. In addition, the presence of the restriction also can change the shape of the distribution of displacements so that it is no longer Gaussian. The simple monoexponential behavior described by Eq. (8.2) arises only for a Gaussian distribution of displacements.

The distribution of displacements in complex tissues as a result of restricted diffusion – a narrowing and change of shape of the distribution – can be probed with several methods. The first is to note that in the construction of a diffusion attenuation curve, such as those in Fig. 8.4, the parameter  $b$  can be changed in two distinct ways. As described above and in Box 8.1,  $b$  can be increased either by increasing the gradient strength or by increasing the diffusion time. For this reason, separate attenuation decay curves can be constructed for different diffusion times by holding fixed the diffusion time while varying the gradient amplitude. Suppose that two of these curves are constructed, for a shorter and a longer diffusion time. For free diffusion, the curves will be identical, because from Eq. (8.2) the value of  $A$  depends only on the magnitude of  $b$ , not on how it is varied. However, with restriction, the curves will not be the same. For the short diffusion time, the curve may be reasonably linear if the diffusion distances are sufficiently short that restriction is not yet having much of an effect. But for the longer diffusion time, the reduced width of the distribution curve will

produce a shallower slope (a smaller apparent  $D$ ) and curvature because of the non-Gaussian shape of the distribution. Diffusion in complex tissues can be complicated, and sorting out restriction and multicompartment effects is challenging.

Another approach, called *diffusion spectrum imaging*, is described in [Box 8.1](#). With this approach, the distribution of displacements caused by diffusion is measured with an elegant mathematical formalism that relates the signal attenuation measured with different gradient strengths to the Fourier transform of the distribution of displacements (Callaghan 1991; Cory and Garroway 1990; Wedeen *et al.* 2005). However, collecting sufficient data for a full evaluation of the local diffusion characteristics, with many  $b$ -values at each of many diffusion axis angles, is quite time consuming.

Short of a full characterization of the distribution of displacements resulting from diffusion, measurements with a limited number of  $b$ -values can provide quantitative estimates of how the distribution differs from a Gaussian. *Diffusional kurtosis imaging* estimates the degree of kurtosis of the distribution (Jensen *et al.* 2005). Kurtosis is a measure of how the fourth moment of a distribution compares with the second moment (the variance), and is defined such that it is zero for a Gaussian distribution. If the distribution is more sharply peaked than a Gaussian, the kurtosis is negative, and if it is more rounded than a Gaussian, the kurtosis is positive. Early reports suggest that kurtosis may provide a useful way to characterize neural tissue in both health and disease (Hui *et al.* 2008).

## Diffusion imaging in stroke

One of the primary applications of diffusion imaging in clinical studies is in the early assessment of stroke (Baird and Warach 1998; Moustafa and Baron 2007). A stroke begins with a sudden interruption of blood flow to a region of the brain, starting a cascade of destructive events that ultimately leads to ischemic injury and infarction. The therapeutic window for delivering drugs to break up the embolus, and restore flow before irreversible damage has occurred, is the first few hours after onset (Brott *et al.* 1992; Neumann-Haefelin and Steinmetz 2007). In the acute stages of stroke, conventional MRI, such as  $T_1$ -weighted,  $T_2$ -weighted, or density-weighted images, and computed tomography all appear normal. These conventional techniques show the area of the stroke only several hours after the event. However, diffusion-weighted imaging (DWI) shows a fall in the ADC within minutes of the interruption of blood flow (Kucharczyk *et al.* 1991). In human studies, the size of the lesion measured acutely with DWI correlated strongly with the neurologic deficit assessed 24 h after the stroke onset (Tong *et al.* 1998). Other disorders such as status epilepticus (Zhong *et al.* 1993) and spreading depression (Takano *et al.* 1996) also exhibit early changes in the ADC value. For this reason, DWI is widely used clinically for the early assessment of stroke and other disorders and is also a standard technique for animal studies investigating the pathophysiological changes involved in stroke.

The reason for the abrupt decrease of the ADC in stroke is not understood. Early ideas were based on the hypothesis noted above, that the  $D$  for intracellular water is substantially lower than the  $D$  for extracellular water, so that the measured ADC is a weighted average of these two different values. The change in the ADC with stroke then could be a result of cytotoxic edema, with a water shift from the extracellular to the intracellular space, which would move the average ADC toward the intracellular value (Benveniste *et al.* 1992; Moseley *et al.* 1990). Other investigators have argued, on the basis of an observed biexponential behavior, that a simple averaging of  $D$  values is not adequate to understand the ADC changes fully (Niendorf *et al.* 1996). An alternative theory is that the intracellular swelling increases

the tortuosity of the diffusion paths in the extracellular space, decreasing the extracellular ADC (Norris *et al.* 1994). Other data, though, indicate that  $D$  is reduced in both the intracellular and the extracellular compartment (Goodman *et al.* 2008; Schwarcz *et al.* 2004). An intriguing alternative idea is that a part of the ADC of the intracellular water results from active cytoplasmic motions driven by ATP-dependent mechanisms, and that early in stroke these driven motions stop, leading to a reduced intracellular ADC (Duong *et al.* 1998). All of these mechanisms may play a role in reducing the measured brain ADC, but a quantitative understanding of the phenomenon is lacking.

## Diffusion tensor imaging

### Anisotropic diffusion

From the arguments above, we can expect that the ADC will vary between tissues, depending on the structure of the tissues. Furthermore, in addition to being heterogeneous, tissues are often *anisotropic*. That is, there are oriented structures, such as nerve fibers in white matter, and this means that diffusion within a tissue also depends on the direction along which diffusion is measured. Figure 8.5 shows DWI of a healthy brain. In the two images, the diffusion-sensitizing gradients were perpendicular to each other. For many tissues,  $A$  is approximately the same, indicating that the diffusion is reasonably isotropic. However, for white matter, the diffusion attenuation depends strongly on the orientation. This diffusion anisotropy can be both a problem and a useful tool. For stroke studies, where the goal is to identify regions with low  $D$ , the natural anisotropy of white matter can produce false identifications of affected areas. But the anisotropy also makes possible mapping of the orientation of the fiber tracts.

The question, then, is how to measure anisotropic diffusion. Naively, we might imagine that measurements of  $D$  along three perpendicular axes (e.g.,  $x$ ,  $y$ , and  $z$ ) would completely describe the diffusion at a point in the brain. However, diffusion is more subtle than this, and three measurements are not sufficient to characterize diffusion fully. In fact, six

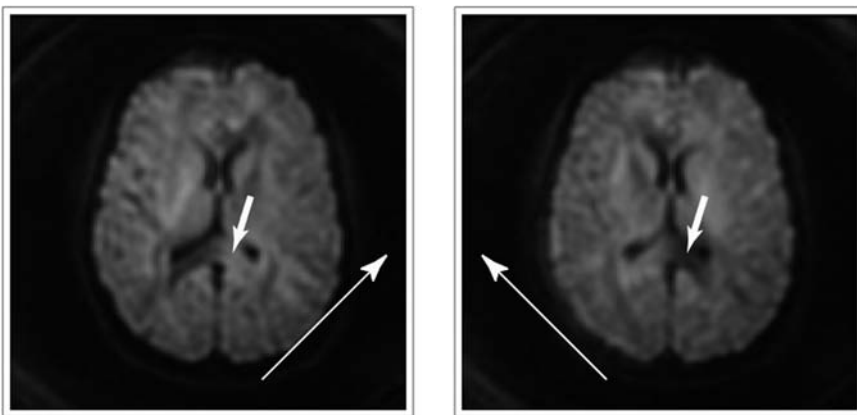


**Fig. 8.5.** Anisotropic diffusion. In some tissues, the magnitude of the signal reduction with diffusion weighting depends on the orientation of the diffusion-sensitizing gradient (anisotropic diffusion). This is pronounced in white matter, with the diffusion coefficient along the fiber direction as much as 10 times larger than that for the perpendicular direction. Note the dramatic change (thick arrows) when the gradient direction (thin arrows) is changed by  $90^\circ$ . (Data courtesy of L. Frank)

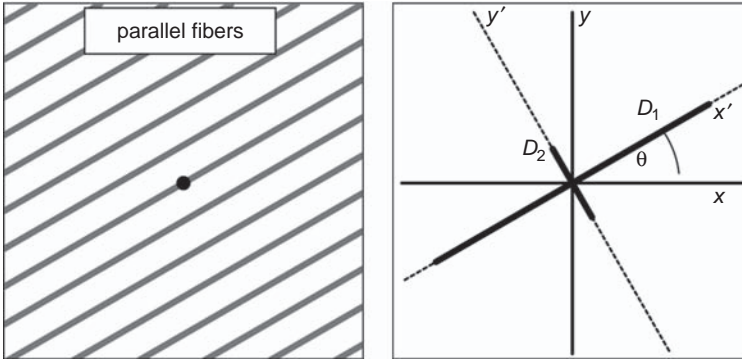


**Fig. 8.6.** Diffusion in white matter fiber tracts. In a system with parallel fibers, the diffusion along the fibers is greater than diffusion perpendicular to the fibers ( $D_1 > D_2$ ). In this example, the fibers are oriented at an unknown angle  $\theta$  with respect to the  $x$ - and  $y$ -axes of the imager coordinate system. The coordinates aligned with the fibers,  $x'$  and  $y'$ , are the principal axes. To characterize local diffusion for this two-dimensional example, three measurements of diffusion along different axes are required because there are three quantities to be measured ( $D_1$ ,  $D_2$ , and  $\theta$ ).

measurements are required, each along a different axis (Basser and Pierpaoli 1998). To see why this is so, it is helpful to simplify the problem to just two dimensions,  $x$  and  $y$ , and imagine that diffusion takes place only in these two dimensions. For this case, three measurements are required to characterize diffusion (instead of two). To illustrate this, imagine that we are measuring a sample of white matter in which the fibers are oriented along an axis at an angle  $\theta$  to the  $x$ -direction (Fig. 8.6). We will call this axis  $x'$ , and the perpendicular axis  $y'$ . These are the natural axes of symmetry of the diffusion process, called the *principal axes*. The  $D$  value along the fibers ( $x'$ ) is  $D_1$ , and perpendicular to the fibers ( $y'$ ) it is  $D_2$ , a smaller value. Now suppose that we measure  $D$  with a gradient oriented along the  $x$ -axis. What value of  $D$  will we measure? Both  $D_1$  and  $D_2$  should contribute because diffusion both along the fibers and perpendicular to the fibers contributes to the displacement of spins along the gradient direction ( $x$ ).

We can think of any one molecule as undergoing two random and independent displacements, one along  $x'$  and one along  $y'$ , and the projection of each of these on to the  $x$ -axis is the contribution to the net displacement of that molecule along  $x$ . The displacements along  $x$  as a result of diffusion along  $x'$  are characterized by a standard deviation  $\sigma_1 = (2D_1T)^{1/2} \cos \theta$ , and the displacements along the  $x$ -direction as a result of diffusion along  $y'$  have a standard deviation  $\sigma_2 = (2D_2T)^{1/2} \sin \theta$ . These two displacements are both random with zero mean, and so the net standard deviation when two independent random variables are added together is given by  $\sigma^2 = \sigma_1^2 + \sigma_2^2$ . From Eq. (8.1), this variance is equivalent to an effective  $D_x$  along the  $x$ -axis of

$$D_x = D_1 \cos^2 \theta + D_2 \sin^2 \theta \quad (8.5)$$

Consequently, the effective  $D$  will lie between  $D_1$  and  $D_2$  and depend on the angle  $\theta$  that defines the orientation of the fibers. Equation (8.5) also demonstrates a somewhat surprising property of these diffusion measurements. Suppose that  $D$  is measured along two arbitrary but perpendicular axes. For example, in addition to the  $D$  measured along  $x$ , we also measure  $D$  along the perpendicular axis  $y$ . Taking the projections of displacements along  $x'$  and  $y'$  onto the  $y$ -axis, the measured  $D$  is

$$D_y = D_1 \sin^2 \theta + D_2 \cos^2 \theta \quad (8.6)$$

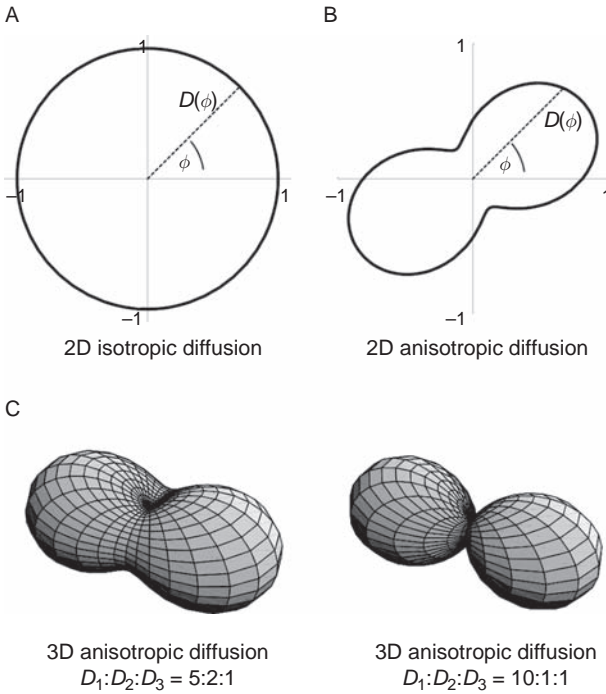


**Fig. 8.7.** Anisotropic diffusion. In anisotropic diffusion, the measured value of the diffusion coefficient  $D$  is different for different directions. We can visualize this by plotting a curve (in two dimensions) such that the distance to the curve along an angle  $\phi$  is proportional to the value of  $D$  that would be measured along that direction. (A) For isotropic diffusion, this curve is a circle. (B) For anisotropic diffusion, it takes on a dumbbell shape. (C) In three dimensions, the equivalent curve is a peanut-shaped surface, for two sets of ratios of the principal diffusivities. (See plate section for color version.)

If we add these two measurements together, we find  $D_x + D_y = D_1 + D_2$  (because  $\sin^2 \theta + \cos^2 \theta = 1$  for any  $\theta$ ). That is, regardless of the orientation of the fibers, the sum of the  $D$  values measured along orthogonal axes is always the same. This fact is very useful for measuring an ADC, averaged over different directions to remove anisotropy effects. In mathematical terms, the sum of the  $D$  values along orthogonal directions is the *trace* of the diffusion tensor (we will return to this mathematical formalism in the next section).

We can generalize the previous arguments with an expression for  $D$  measured along an arbitrary axis at an angle  $\phi$  to the  $x$ -axis:

$$D(\phi) = D_1 \cos^2(\theta - \phi) + D_2 \sin^2(\theta - \phi) \quad (8.7)$$

Then  $\phi = 0$  corresponds to the  $D$  measured with a gradient along the  $x$ -axis, and  $\phi = 90^\circ$  corresponds to the  $D$  measured with a gradient along the  $y$ -axis. We can illustrate this angular dependence by plotting a curve such that the distance from the origin to the curve along an axis at angle  $\phi$  is proportional to the value of  $D$  along that axis, as in Fig. 8.7. For isotropic diffusion with  $D_1 = D_2$ , the curve is a circle, but when  $D_1$  and  $D_2$  are distinctly different it takes on more of a dumbbell (or peanut) shape.

From these arguments, we can see why three measurements of  $D$  along different axes are necessary to characterize two-dimensional diffusion. There are three unknown quantities ( $\theta$ ,  $D_1$ , and  $D_2$ ) that characterize the underlying diffusion and must be determined, so at least three different measurements of diffusion will be required. If only two measurements are made, for example along  $x$  and  $y$ , the two measured points will be consistent with many diffusion curves, as illustrated in Fig. 8.8. An additional measurement (e.g., at an angle of  $45^\circ$ ) is necessary to identify the correct curve. Note that a diffusion curve such as this characterizes



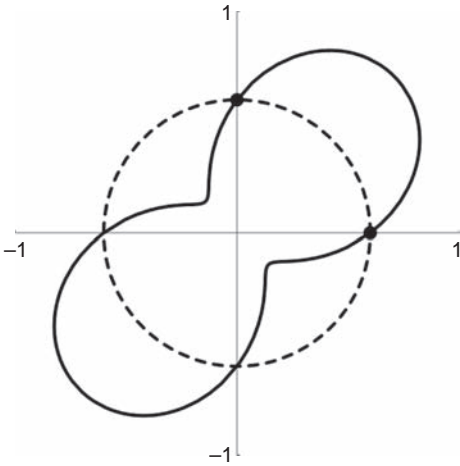


**Fig. 8.8.** Ambiguities of diffusion measurements. In two dimensions, measurements of the diffusion coefficient  $D$  along two axes (indicated by dots) are consistent with a family of different diffusion curves (in this case an isotropic diffusion curve and a highly anisotropic diffusion curve). An additional measurement of diffusion along an axis at  $45^\circ$  would resolve the ambiguity.

diffusion measurements made at one point in the brain. With imaging, many spatial points can be measured at the same time, and each imaging voxel will have its own diffusion curve that must be calculated from the image data.

The same ideas apply to three-dimensional anisotropic diffusion. The diffusion properties at one point in the tissue can be described by three principal diffusion coefficients ( $D_1$ ,  $D_2$ , and  $D_3$ ) along three perpendicular (but unknown) principal axes, as illustrated in Fig. 8.7. If we now measure diffusion along an arbitrary direction, the projections of each of the independent distributions of displacements along each of the principal axes will add to form the net displacement along the gradient axis, and the net variance is the sum of each of the projected variances (Hsu and Mori 1995). The measured  $D$  is then

$$D = D_1 \cos^2 \theta_1 + D_2 \cos^2 \theta_2 + D_3 \cos^2 \theta_3 \quad (8.8)$$

where each  $\theta_i$  is the angle between the  $i$ th principal axis and the measured axis. For the general case of three-dimensional anisotropic diffusion, the measured diffusion along an arbitrary axis depends on six quantities: three  $D$  values along the principal axes and three angles that specify how these principal axes are oriented with respect to the measurement axis. The three-dimensional curve of  $D$  as a function of orientation then looks like the peanut in Fig. 8.7.

In practice, the calculation of the local diffusion characteristics does not use Eqs. (8.6) or (8.8) directly. Instead, the calculations are framed in terms of the *diffusion tensor*, which is mathematically equivalent. Before turning to the diffusion tensor formalism, we should clarify a subtle point that can be misleading in the literature. In most papers on DTI, the geometrical shape of the diffusion tensor is described as an ellipse, and yet the fundamental geometry we have described is closer to that of a peanut, distinctly different from an ellipse (e.g., Fig. 8.7). The diffusion curves in Fig. 8.7 describe the variance of the displacements of the water molecules along an arbitrary axis, and by Eq. (8.1) this variance is interpreted as an effective  $D$  along a particular axis. However, this is not the same as the spatial distribution of final positions of diffusing particles. That is, if the diffusion process leads to independent displacements along three principal axes, the distribution of *final positions* is elliptical, and the widths of the distribution along each of the principal axes are proportional to the square root of the principal diffusivity along that axis. The diffusion tensor describes the variance of

the *total* distribution along one direction, however, not just those points that happen to end up lying along that particular axis. In other words, what the diffusion tensor tells us is the variance of the *projection* of the final positions of all the particles on to a particular axis. So if we imagine projecting that elliptical distribution on to axes at different angles and then calculating the variance of each projection, the resulting curve of  $D$  looks like our peanut-shaped curve. In short, it is reasonable to think of anisotropic diffusion producing an elliptical spread of particle positions, but it is important to remember that the quantity we measure, the apparent diffusion attenuation along a particular axis  $D(\phi)$ , has a more complex shape.

## The diffusion tensor

In mathematical terms, the added complexity of anisotropic diffusion is that  $D$  must be considered to be a tensor, rather than a scalar. That is, instead of being characterized by a single number, it is described by a  $3 \times 3$  matrix of numbers. In a diffusion imaging experiment, diffusion is measured along a  $D$  particular axis, which we can indicate by a unit vector  $\mathbf{u}$ . For example, if the diffusion-sensitizing gradient pulses are applied along the  $x$ -axis,  $\mathbf{u} = (1, 0, 0)$ , or if the measurement axis is at an angle  $\theta$  to the  $x$ -axis and lies in the  $x$ - $y$  plane,  $\mathbf{u} = (\cos \theta, \sin \theta, 0)$ . Then the measured value of  $D$  along any axis  $\mathbf{u}$  is given by (Hsu and Mori 1995):

$$D = \begin{pmatrix} u_x & u_y & u_z \end{pmatrix} \begin{pmatrix} D_{xx} & D_{xy} & D_{xz} \\ D_{yx} & D_{yy} & D_{yz} \\ D_{zx} & D_{zy} & D_{zz} \end{pmatrix} \begin{pmatrix} u_x \\ u_y \\ u_z \end{pmatrix} \quad (8.9)$$

With a more compact notation, we can use the symbol  $\mathbf{D}$  to distinguish the diffusion matrix from a particular value of  $D$  and the superscript T to indicate the transpose and write

$$D = \mathbf{u}^T \mathbf{D} \mathbf{u} \quad (8.10)$$

The diffusion tensor is symmetric, with  $D_{ik} = D_{ki}$ , so there are six unknown quantities: the elements down the diagonal, and the three elements in one corner. Measuring all six components is described as measuring the full diffusion tensor. The values of these tensor components depend on the coordinate system used (i.e., measurements are carried out in the coordinate system defined by the imager gradients). In one special coordinate system, called the *principal axes*, the diffusion tensor is diagonal (all the off-diagonal components are zero), and the three values along the diagonal are called the *principal diffusivities*. The diffusion tensor in this principal axis coordinate system then has the form

$$D_{\text{pa}} = \begin{pmatrix} D_1 & 0 & 0 \\ 0 & D_2 & 0 \\ 0 & 0 & D_3 \end{pmatrix} \quad (8.11)$$

where  $D_1$ ,  $D_2$ , and  $D_3$  are the principal diffusivities.

The diffusion tensor in any other coordinate system is directly related to the principal axis form of the tensor and the rotation matrix  $\mathbf{R}$  that converts coordinates in the principal axis system into the coordinate frame in which the measurements are performed (i.e., the coordinate system defined by the imager gradients) such that

$$\mathbf{D} = \mathbf{R} \mathbf{D}_{\text{pa}} \mathbf{R}^{-1} \quad (8.12)$$

where  $\mathbf{R}^{-1}$  is the matrix inverse of  $\mathbf{R}$ . In practice, this procedure is done in reverse. The diffusion tensor is measured in a particular coordinate system, and one must then find the coordinate transformation that produces a diagonal matrix and thus identifies the principal axes. In other words, the six measured components of the diffusion tensor are used to calculate the three rotation angles that define the transformation to the principal axes system and the three principal diffusivities. These computations are equivalent to solving for the six unknown quantities in Eq. (8.8). Calculations are done pixel by pixel in an imaging experiment.

In practice, these calculations are done with a generalized version of Eq. (8.2), in which the diffusion sensitivity of the pulse sequence is characterized by a matrix  $b_{ik}$  (called the *b*-matrix) instead of a single scalar  $b$  (Mattiello *et al.* 1997). Then in the expression for the decay of the signal,  $bD$  is replaced by a sum of terms in which each  $b_{ik}$  is multiplied by the corresponding term  $D_{ik}$  in the diffusion tensor. The accuracy of the diffusion tensor measurements can be improved by including in the *b*-matrix the diffusion effects of the imaging gradients themselves in addition to the gradients applied specifically for diffusion weighting.

A common approach to measuring  $\mathbf{D}$  is to acquire one image with  $b = 0$  and six images with  $b$  approximately equal to  $1000 \text{ s/mm}^2$  but with the gradient pulses applied along six different directions (Basser and Pierpaoli 1998), and an example is shown in Fig. 8.9. From these data, the local value of each of the six independent values of the diffusion tensor are calculated for each voxel. Two useful combinations of these tensor components are the *trace* and the *fractional anisotropy index*. The trace is simply the average  $D_{\text{av}} = (D_1 + D_2 + D_3)/3$  of the principal diffusivities and represents the isotropic part of the diffusion tensor. Several measures have been proposed to capture the degree of anisotropy of a diffusion tensor in a single number, and the fractional anisotropy is the most commonly used (Conturo *et al.* 1996; Pierpaoli and Basser 1996; Shrager and Basser 1998). The fractional anisotropy (FA) is defined roughly as the ratio of the standard deviation of the three principal diffusivities to a measure of the overall magnitude of diffusion (Basser and Pierpaoli 1998):

$$FA = \frac{\sqrt{3} \sqrt{[(D_1 - D_{\text{av}})^2 + (D_2 - D_{\text{av}})^2 + (D_3 - D_{\text{av}})^2]}}{\sqrt{D_1^2 + D_2^2 + D_3^2}} \quad (8.13)$$

The normalization is such that the fractional anisotropy varies from zero, when there is no anisotropy because the three principal diffusivities are equal, to one when one principal diffusivity is much larger than the other two. Describing the full nature of the anisotropy, including the directions of the principal axes, requires the full diffusion tensor, but the advantage of reducing this to a single measure is that it is easy to construct and display maps of fractional anisotropy.

## Measuring the trace of the diffusion tensor

The sum of the three components along the diagonal of the matrix is the trace of the diffusion tensor, and the trace is the same regardless of the coordinate system used to represent the tensor. In particular, in the principal axis coordinate system, the trace is the sum of the principal diffusivities. Because the trace is independent of the coordinate system used to measure  $\mathbf{D}$ , it can be calculated from just three measurements of  $D$  along any set of orthogonal axes. That is, measuring  $D$  along the  $x$ -,  $y$ -, and  $z$ -directions will yield the same sum regardless of the orientation of the principal axes. This is a very useful way to derive an isotropic, average value for  $D$ .

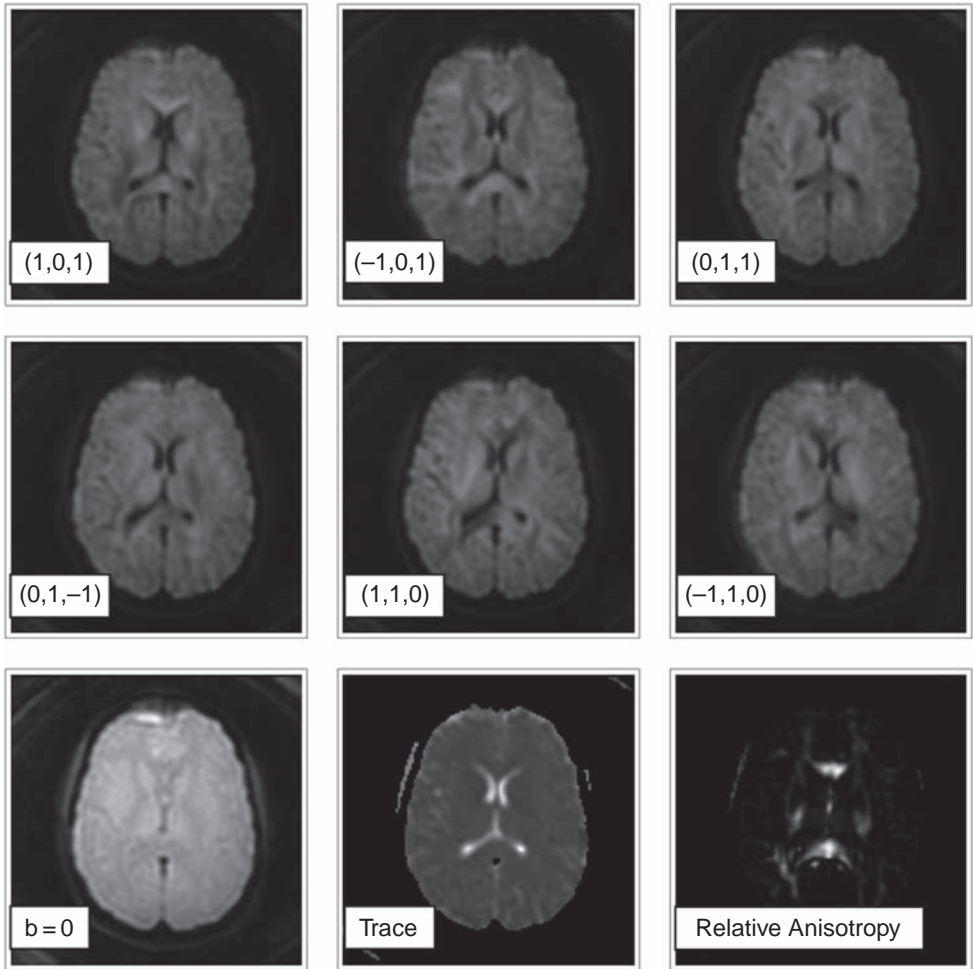


**Fig. 8.9.** Diffusion tensor imaging. To measure the full three-dimensional diffusion tensor, a total of seven images are required, six measured with a large  $b$ -value with the gradient along different axes (top two rows) and one with  $b=0$ . Labels indicate the  $(x, y, z)$  direction of the gradient. From these data, the six elements of the diffusion tensor are calculated, and maps of the local values of these elements can be displayed as an image. The trace is the isotropic part of the diffusion tensor, the average of the three principal diffusivities. The relative anisotropy index is a measure of how different the three principal diffusivities are from one another. (Data courtesy of L. Frank)

The trace can be measured with a single pulse sequence by successively applying bipolar gradient pulses along separate axes. For example, for the simple two-dimensional case discussed in the previous section, we could apply a pair of bipolar  $x$ -gradient pulses followed by a pair of  $y$ -gradient pulses, as shown in Fig. 8.10. The first pair will attenuate the signal by a factor  $e^{-bD_x}$ , and the second pair will further attenuate the signal by a factor  $e^{-bD_y}$ . The logarithm of the net attenuation is then  $-b(D_x + D_y)$ , giving a direct measurement of the trace. In measuring the trace, it is tempting to save time and apply the two pairs of gradient pulses at the same time, as in Fig. 8.10. Intuitively, it seems that this ought to produce the same amount of diffusion attenuation, but in fact the measured  $D$  with such a pulse sequence is not simply  $D_x + D_y$ . When two equal gradient pulses are applied simultaneously along two orthogonal axes, this creates a

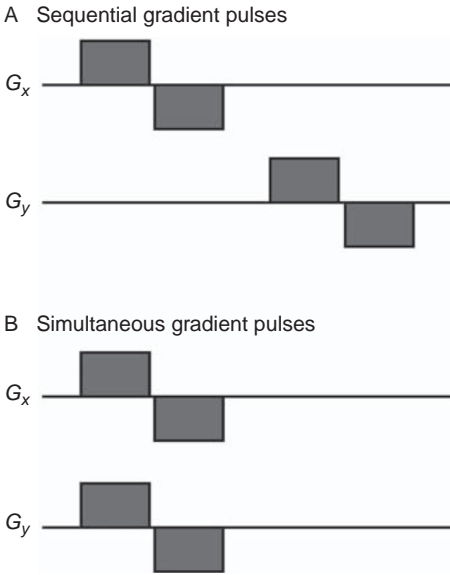


**Fig. 8.10.** Measuring the trace of the diffusion tensor. The trace of the diffusion tensor is the sum of the diagonal elements (the principal diffusivities) and reflects the average diffusion coefficient in an anisotropic medium. The plots illustrate gradient patterns for two-dimensional diffusion imaging. (A) Sequential bipolar gradients along different axes produce a net signal attenuation that depends on the trace. (B) Applying the same gradient pulses simultaneously is not sensitive to the trace but instead is sensitive to diffusion along a single axis at an angle of  $45^\circ$  to  $x$  and  $y$ .

gradient along an axis at  $45^\circ$  to the other two. This pulse sequence is, thus, sensitive to one set of net displacements along this diagonal axis, whereas the original pulse sequence is sensitive to two separate, sequential sets of displacements along  $x$  and  $y$ .

The reason the two measurements are different is that with anisotropic diffusion the displacements along  $x$  and  $y$  during the same time interval are not statistically independent of each other. If there were no correlation between the random displacements  $\Delta x$  and  $\Delta y$ , then the aligned gradient scheme sensitive to one set of displacements would work because the separate attenuations produced by the  $x$ - and  $y$ -gradients are independent processes. But the problem is that, in general, the displacements along  $x$  and  $y$  are correlated. We can calculate this correlation for our two-dimensional example with principal axes  $x'$  and  $y'$ , with  $x'$  tilted at an angle  $\theta$  with respect to the  $x$ -axis (as in Fig. 8.6). The displacements along the principal axes,  $\Delta x'$  and  $\Delta y'$ , are uncorrelated, but the measured displacements  $\Delta x$  and  $\Delta y$  have contributions from both:

$$\begin{aligned}\Delta x &= \Delta x' \cos \theta - \Delta y' \sin \theta \\ \Delta y &= \Delta x' \sin \theta + \Delta y' \cos \theta\end{aligned}\quad (8.14)$$

Each  $\Delta x'$  is drawn from a distribution with standard deviation  $\sigma_1$ , and each  $\Delta y'$  is drawn from a distribution with standard deviation  $\sigma_2$ . With this in mind, we can examine the correlation between  $\Delta x$  and  $\Delta y$  by calculating the expected value of the product  $\Delta x \Delta y$ :

$$\begin{aligned}\Delta x \Delta y &= (\Delta y'^2 - \Delta x'^2) \sin \theta \cos \theta + \Delta x' \Delta y' (\cos^2 \theta - \sin^2 \theta) \\ \langle \Delta x \Delta y \rangle &= (\sigma_2^2 - \sigma_1^2) \sin \theta \cos \theta\end{aligned}\quad (8.15)$$

The term in  $\Delta x' \Delta y'$  is zero on average because these variables are truly uncorrelated, but the remaining terms produce a non-zero average unless either  $\sigma_1 = \sigma_2$  or the angle  $\theta$  is zero or a multiple of  $90^\circ$ . In other words, displacements along  $x$  and  $y$  are correlated unless the diffusion is isotropic or our measurement axes happen to line up with the principal axes.

To avoid the effect of these correlations, a measurement of the trace must look at separate displacements along orthogonal axes, such as the sequential measurement in Fig. 8.10A. This pattern of gradients works but is not the most time efficient, and cleverer sets of gradient pulses have been designed to pack the gradients in tightly while avoiding correlations in the measured displacements (Chun *et al.* 1998; Wong *et al.* 1995).

## Fiber tract mapping

One of the most promising applications of DTI in basic studies of the brain is mapping white matter fiber tracts (Mori and Zhang 2006). In regions of oriented fibers, the local diffusion is anisotropic, with a larger  $D$  along the fiber direction than perpendicular to it. Measurements in monkeys found that in structures with a regular, parallel arrangement of fibers the average value of  $D$  along the fibers was nearly a factor of 10 times larger than the  $D$  measured perpendicular to the fibers (Pierpaoli and Basser 1996). Local fiber orientation can be mapped by measuring the full diffusion tensor and identifying the first principal axis, the one with the largest  $D$ . That is, DTI provides a vector at each image voxel that indicates the dominant orientation (the first principal axis) of the local white matter fibers. Starting at a particular seed point and connecting these vectors produces paths of apparent connectivity between the seed point and other parts of the brain.

Since the mid 1990s, fiber tract mapping has grown into a very active area of research. The resulting images of white matter connections are striking and often reproduce known pathways (Fig. 8.11). The simple description above hides a number of real technical challenges that affect the accuracy of the fiber tract maps (Assaf and Pasternak 2008; Jones 2008).

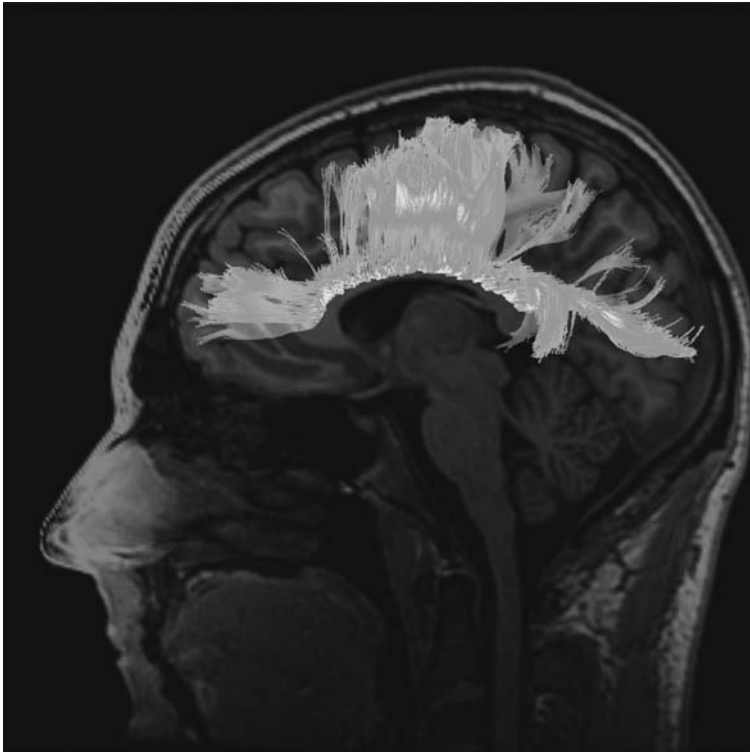


**Fig. 8.11.** White matter fiber tract mapping. Fiber tracts calculated from diffusion tensor images with seeds in the central region of the corpus callosum. (Data courtesy of L. Frank.) (See plate section for color version.)

There are two principal challenges. How should the local fiber orientations be estimated from diffusion imaging data? How should these individual local measurements be connected up to make pathways? The first question relates to the problem of crossing fibers within a voxel, a problem that ultimately derives from the limited spatial resolution of the imaging data. This problem is taken up in the next section. For constructing pathways, two general approaches are used: deterministic or probabilistic. In a deterministic method, rules are adopted for starting with a seed point and moving to the next point based on the local fiber orientation, usually working with subvoxel step sizes. Probabilistic methods are more sophisticated in that they try to deal with the inherent uncertainties in making decisions about how a pathway deflects or branches (Behrens *et al.* 2007). There is not yet a consensus on the best approach for constructing pathways.

The critical question is whether the reconstructed fiber tract maps are accurate. Often they reproduce known tracts in exquisite detail, although there are examples of known tracts that are not found with the diffusion data (Behrens *et al.* 2007; Jones 2008). Direct comparisons of tracts derived from diffusion data with tract mapping based on invasive methods in the same brain are still relatively rare, although a recent study found a generally good correspondence (Lawes *et al.* 2008). Nevertheless, mapping fiber tracts with DTI represents an exciting approach to investigating connectivity in the brain, and this anatomical approach is nicely complementary to the functional approach of fMRI.

## Limitations of the diffusion tensor model

A critical problem in mapping fiber tracts with DTI is that the local geometry is not always the simple one of parallel fibers. An imaging voxel may contain several sets of overlapping fibers, and the interpretation of diffusion tensor measurements then becomes more complicated. The classical diffusion tensor is closely tied in with the idea of a Gaussian distribution of displacements along an axis. Then the variance of this distribution is directly proportional to  $D$  through (Eq. 8.1). However, if the distribution of displacements is not Gaussian, as it is with multiple fiber orientations, how does this affect the measurements? Specifically, if we think of the diffusion tensor as essentially describing the variance of displacements along an axis, does this still capture what we see as attenuation of the MR signal even if the distribution is not Gaussian? The answer is that the MR signal changes depend on more than just the variance of the displacements resulting from diffusion, and this provides a sensitivity to diffusion beyond what is described by the diffusion tensor.

As an example, suppose that a voxel contains equal proportions of two sets of parallel fibers oriented at an angle of  $90^\circ$  to each other. In each set, the value of  $D$  along the fibers is  $D_1$  and perpendicular to the fibers it is  $D_2$ . We will compare diffusion in this mixed system with the case of isotropic diffusion with the average diffusion coefficient,  $D = (D_1 + D_2)/2$ , and for simplicity we treat this example as two-dimensional diffusion. The crossed fiber arrangement is highly symmetric, but the diffusion characteristics are nevertheless quite distinct from the case of isotropic diffusion. Fig. 8.12 illustrates the diffusion pattern that would be found in each of these two examples: isotropic diffusion leads to a spherical spread of displacements, and the crossed fibers produce a cross-shaped diffusion pattern. However, despite the fact that the diffusion patterns are distinct, the diffusion tensors are identical. That is, if we were to measure  $D$  along any axis, the measured  $D$  would be constant for both systems. To see this, suppose we calculate  $D$  along an axis at an angle  $\phi$  to the first principal axis of one set of fibers, which means that it is also at an angle  $\phi$  to the second principal axis of the other set of fibers. The net variance of displacements along the axis is then

$$D(\phi) = \frac{1}{2}(D_1 \cos^2 \phi + D_2 \sin^2 \phi) + \frac{1}{2}(D_1 \sin^2 \phi + D_2 \cos^2 \phi)$$

$$D(\phi) = \frac{D_1 + D_2}{2} \quad (8.16)$$

In other words, no matter which axis is chosen, the displacements along the principal axes of both sets of fibers combine to produce the same net variance. Despite the underlying structure, the apparent  $D$  along every axis, if we take  $D$  as simply proportional to the variance of the displacements according to Eq. (8.1), is the same.

## Beyond the diffusion tensor model

This example shows that the diffusion tensor does not fully describe the diffusion characteristics of a medium. It *does* describe the net variance of displacements along any direction, but different diffusion patterns can create the same net variance. This brings us to the question of precisely what is measured in MR diffusion imaging. If MRI is only sensitive to the mean squared displacement along an axis, then diffusion imaging data is fully described by the diffusion tensor. If this were the case, the example shown in Fig. 8.12 would be an insurmountable problem: the symmetric crossed fibers would be indistinguishable from isotropic diffusion. Fortunately, however, MR measurements are potentially sensitive to aspects of diffusion beyond what is described by the conventional diffusion tensor (Tuch *et al.* 1999).

In fact, we have already encountered this aspect of diffusion imaging in the earlier context of multicompartment diffusion. If two compartments with different  $D$  values are both present within an imaging voxel, then for small values of  $b$  the ADC is the true average of the  $D$  values for the two compartments. For larger values of  $b$ , the decay becomes biexponential (as in Eq. (8.4)). The key result of this effect is that the MR signal attenuation does not depend just on the net variance of the displacements but instead depends on the separate

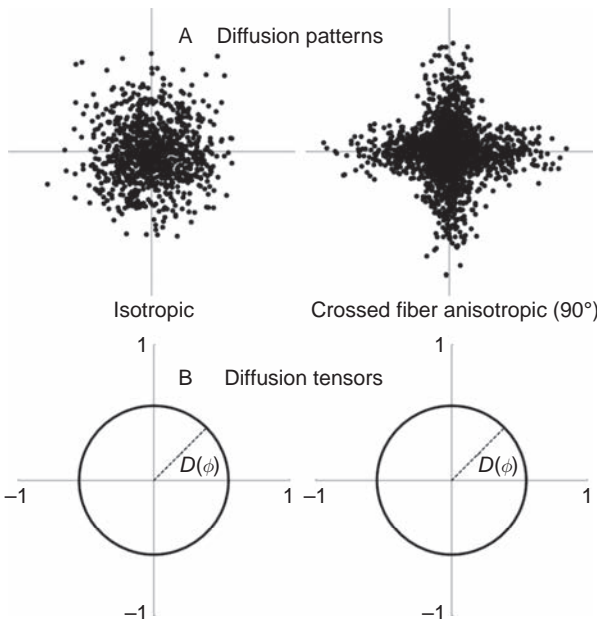


**Fig. 8.12.** Ambiguities of the diffusion tensor. Isotropic diffusion (A) and crossed-fiber anisotropic diffusion create different patterns of displacements, yet the net variance along any axis (and the equivalent diffusion coefficient  $D$  from Eq. (8.1)) is the same. (B) The diffusion tensor describes diffusion along different directions at an angle  $\phi$  ( $D(\phi)$ ), and this is proportional to the variance of the projection of the distribution shown at the top on to the axis at angle  $\phi$ . For both examples, these projections are symmetric.



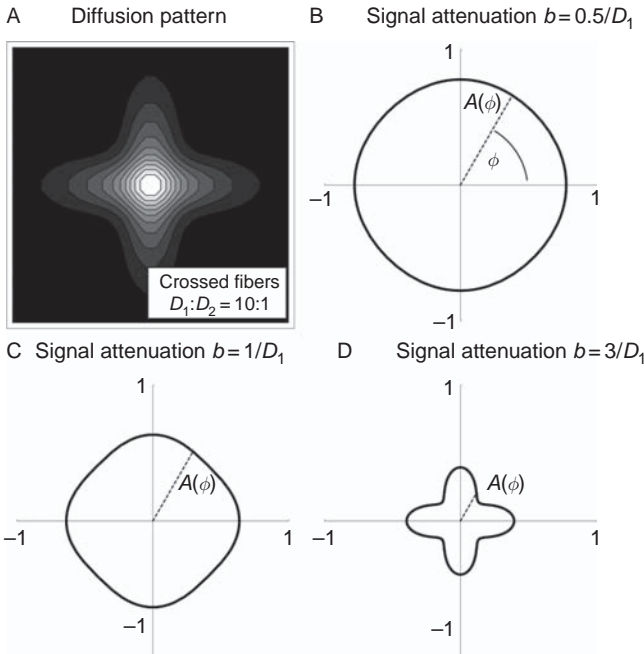
variances in the two compartments. This effect carries directly over to DTI. With large  $b$ -values, the MR signal is no longer sensitive just to the net variance of displacements, which is what the diffusion tensor describes, but depends on the separate variances of the different compartments. For example, if the voxel contains equal fractions of two identical sets of fibers at right angles to each other, the signal attenuation measured with diffusion sensitivity  $b$  along an axis at an angle  $\phi$  is

$$A(\phi) = \frac{1}{2} e^{-b(D_1 \cos^2 \phi + D_2 \sin^2 \phi)} + \frac{1}{2} e^{-b(D_1 \sin^2 \phi + D_2 \cos^2 \phi)} \quad (8.17)$$

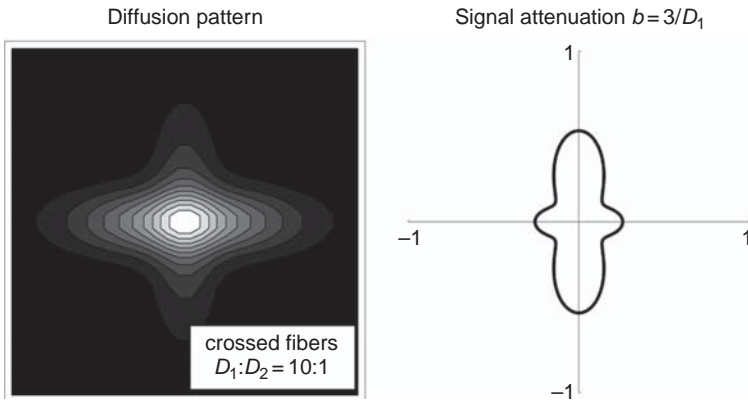
For small  $b$ -values, this expression is equivalent to Eq. (8.16), and the diffusion attenuation is sensitive only to the average  $D$ . However, with large  $b$ -values, the non-linear form of Eq. (8.17) becomes important.

Fig. 8.13 illustrates this effect for two-dimensional diffusion by plotting the MR signal attenuation as a function of angle,  $A(\phi)$ , for the example of crossed fibers. (These plots are analogous to the plots of  $D(\phi)$ : the distance to the curve is proportional to  $A$ , the ratio of the signal measured with  $b > 0$  to the signal with  $b = 0$ .) For a small  $b$ -value, the diffusion tensor does approximately describe the diffusion effects, and the attenuation pattern is essentially isotropic. However, as  $b$  is increased, the shape of  $A(\phi)$  begins to change, and with very large values of  $b$  (e.g., 3000 s/mm<sup>2</sup>)  $A(\phi)$  reveals the true diffusion pattern.

High angular resolution diffusion imaging (HARDI) methods are the three-dimensional implementation of this idea (Frank 2002; Tuch *et al.* 1999). By measuring diffusion attenuation along many axes, with a relatively large  $b$ -value, the surface equivalent of  $A(\phi)$  can be measured. In their original implementation of this idea, Tuch and co-workers (1999) measured  $A$  along 126 different directions and used these data to plot the diffusion surface



**Fig. 8.13.** Angular dependence of the magnetic resonance signal attenuation. (A) For the two-dimensional example of crossed fibers, the diffusion pattern has the shape of a blurred cross. (B–D) The other plots show the attenuation ( $A$ ) of the MR signal measured with different values of  $b$  as a function of the angle  $\phi$  of the diffusion-encoding axis. For weak values of  $b$ , the shape of  $A(\phi)$  is governed by the diffusion tensor, and so  $A(\phi)$  is reasonably symmetric. For larger values of  $b$ , the pattern of  $A(\phi)$  begins to reveal the true diffusion pattern.



**Fig. 8.14.** Signal attenuation in MR with unequal proportions of crossed fibers. The interpretation of the angular dependence of the signal attenuation  $A(\phi)$  shown in Fig. 8.12 involves some subtleties. When the proportions of the two sets of fibers are not equal, the asymmetry of the diffusion pattern is opposite to the asymmetry of  $A(\phi)$ .

for each point in the brain. Moving beyond the diffusion tensor description of diffusion is thus a potentially powerful approach for resolving ambiguities resulting from crossed fibers and for fully exploiting the diffusion sensitivity of MRI. Frank (2002) showed that the diffusion surface can be modeled in terms of spherical harmonic functions, similar to atomic orbitals. Simple diffusion appears in the lowest harmonic, while complex tissues such as crossing fibers have higher-order components.

However, the interpretation of  $A(\phi)$  involves some subtleties. Fig. 8.14 shows the diffusion pattern when the proportions of the two sets of crossed fibers are not equal. In this example, 70% of the voxel volume is occupied by fibers running left–right, so the cross-shaped diffusion pattern is elongated in this direction. However, the corresponding plot of  $A(\phi)$  is elongated along the vertical axis. The reason for this is that this direction is dominated by the short axis of the left–right fibers, and so this direction shows the least attenuation (i.e.,  $A$  is largest). In short,  $A(\phi)$  is sensitive to the more complex diffusion pattern of crossed fibers, but the pattern must be interpreted carefully to identify the dominate fiber direction. Tuch (2004) introduced a method for dealing with this problem, a model-independent way to identify the direction of maximum diffusion, called Q-ball imaging.

Finally, another promising approach to dealing with diffusion in complex tissues is to develop more detailed biophysical models for the diffusion process that take into account key aspects of the microscopic structure. For example, Assaf and Basser (2005) introduced a composite hindered and restricted model of diffusion (CHARMED) for white matter. In this model, a pool of water outside the fibers is considered to be hindered by having to diffuse around the fibers, but still exhibits a Gaussian distribution of displacements. A second pool is restricted with a non-Gaussian distribution of displacements. More recently, Peled (2007) described a model that included water in the intracellular and extracellular spaces plus the myelin sheath. In general, these models treat the tissue as being composed of multiple diffusion tensors.

## Diffusion effects in functional imaging

### Diffusion around field perturbations

The preceding sections dealt with the effects on the MR signal of diffusion in a linear magnetic field gradient. Random motions lead to a degree of signal attenuation that is directly related to the strength of the gradient and the local value of  $D$ . In diffusion imaging, the field gradient is applied by the experimenter and so is controllable in magnitude and orientation. However,

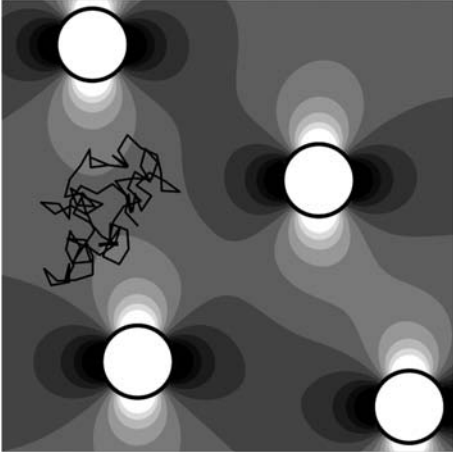


**Fig. 8.15.** Diffusion around magnetized capillaries. Small blood vessels containing paramagnetic contrast agent or deoxyhemoglobin create dipole-like magnetic field distortions in their vicinity, shown as a contour plot of the field. A diffusing water molecule undergoes a random walk (jagged line), carrying the precessing nuclei through different magnetic fields. The random phase changes resulting from the varying field lead to attenuation of the net signal.

there are a number of important situations in which the field variations are intrinsic to the tissue, and these local field variations are generally non-linear. These might arise from the intrinsic heterogeneity of the tissue or from the presence of contrast agents.

The primary effect of this type related to fMRI occurs when the susceptibility of the blood differs from the surrounding tissue space, either because of an intrinsic change in deoxyhemoglobin or because of the presence of a contrast agent (Fisel *et al.* 1991; Hardy and Henkleman 1991; Majumdar and Gore 1988; Ogawa *et al.* 1993; Weisskoff *et al.* 1994; Yablonsky and Haacke 1994). Field gradients then develop around the vessels, and as the water molecules diffuse around the vessels they move through different magnetic fields. This physical picture is more complex than the simple case of diffusion in a linear field gradient discussed above and is better described as diffusion through field perturbations. Because of the complexity of this process, the discussion is necessarily more qualitative than the linear gradient case described above.

The physical picture of this process is that the blood vessels are scattered randomly throughout the medium, with each one creating a local field distortion in its vicinity (Fig. 8.15). Without diffusion, spins near a vessel would precess at a different rate than spins far away. For a simple GRE pulse sequence, this would produce a shortening of  $T_2^*$  because the spins would dephase more quickly. However, for an SE pulse sequence, the  $180^\circ$  RF pulse refocuses the effects of field offsets and so the signals from the near and far spins come back into phase and create the SE. Without diffusion, the SE signal would be unaffected by the presence of field perturbations.

With diffusion, though, both the SE and the GRE signals are affected. However, the nature of the diffusion effect is quite different from the effects in a linear gradient, and, in fact, the effects on SE and GRE signals can even be in opposite directions. It is helpful to describe these effects as an effective change in the transverse relaxation rate. Normal  $T_2$  decay is a simple exponential with a decay rate  $R_2 = 1/T_2$ , and for a GRE experiment the decay rate is  $R_2^* = 1/T_2^*$ . We can keep this form and describe the additional signal attenuation as a result of the field perturbations by the term  $\Delta R_2$ . So for a decay time  $t$ , the additional attenuation is

$$\begin{aligned} A_{\text{SE}}(t) &= e^{-\Delta R_2 t} \\ A_{\text{GRE}}(t) &= e^{-\Delta R_2^* t} \end{aligned} \quad (8.18)$$

The changes in the relaxation rates ( $\Delta R_2$  and  $\Delta R_2^*$ ) capture the effects of the field perturbations, and it is these changes that we want to understand. Characterizing these effects in this manner is useful, even if the additional attenuation is not strictly monoexponential. In this case, the changes would be functions of time (i.e., functions of TE). For example, for SE measurements in a linear field gradient, we can use the results from [Box 8.1](#), where the decay is of the form  $e^{-bD}$ . For a continuous gradient, both the diffusion time  $T$  and the duration of the pulse  $\delta t$  are proportional to  $t$ , so  $b \propto t^3$ . Then in the form of [Eq. \(8.18\)](#), we would write this as  $\Delta R_2 \propto t^2$ . Because  $\Delta R_2$  usually does depend on time, we can simplify things by looking at a fixed time corresponding to a typical TE (e.g., 40 ms), and then see how  $\Delta R_2$  and  $\Delta R_2^*$  depend on  $D$ .

Describing the attenuation in terms of relaxation rates also ties in directly with the line width measured in spectroscopy. Because of the decay of the signal, the proton spectral line from a sample is not infinitely thin. The faster the signal decays, the broader the spectral line will be. The frequency width of the line is directly proportional to  $R_2$  or  $R_2^*$ , depending on the type of experiment. So, for example, the effect of field perturbations in a SE experiment can be described in three equivalent ways: (1) an additive change in the transverse relaxation rate,  $\Delta R_2$ , (2) a decrease in the signal measured at a particular TE, or (3) a broadening of the spectral line. All three descriptions are used in the literature.

## Motional narrowing

Suppose that we perform a thought experiment in which we start with a fixed collection of field perturbations (e.g., a network of magnetized capillaries) and vary the water diffusion coefficient in the surrounding medium, beginning with no diffusion ( $D=0$ ) and then increasing  $D$ , repeating our SE and GRE experiments as we go. Each experiment is done with the same fixed TE, so true  $T_2$  effects are the same, and variations in the signals are then

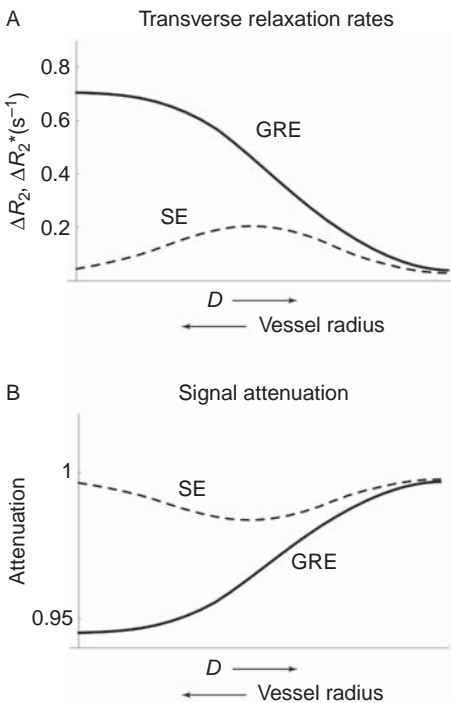


**Fig. 8.16.** Effects of diffusion through random fields on the MR signal. Diffusion through random field perturbations caused by magnetized blood vessels produces changes in the transverse relaxation rates  $\Delta R_2$  and  $\Delta R_2^*$  (A) and results in signal attenuation (B). The effect of diffusion depends on how the typical diffusion distance compares with the vessel radius, so these curves can be viewed as showing the effects of increased diffusion coefficient  $D$  moving to the right or increased vessel radius moving to the left. The maximum spin echo (SE) attenuation occurs at approximately the capillary radius, and the maximum gradient echo (GRE) effect occurs for the largest vessels.

due to  $\Delta R_2$  and  $\Delta R_2^*$ . Fig. 8.16 illustrates the effects of changing  $D$  by plotting the change in the relaxation rates and the resulting signal attenuation as functions of  $D$ . The attenuation plots show just the additional attenuation from  $\Delta R_2$  and  $\Delta R_2^*$  so that  $A = 1$  corresponds to the signal that would be measured without field perturbations.

Starting with  $D = 0$  on the left side of the plots, there is substantial additional attenuation of the signal in the GRE experiment and no signal loss in the SE experiment because the SE refocuses the effects of the field perturbations. From the preceding discussion of diffusion in linear field gradients, we might naively expect that as  $D$  increases we will have more signal loss (increased  $\Delta R_2$ ), and initially we do see the SE signal decrease. However, the GRE signal *increases* with increasing  $D$  (i.e.,  $\Delta R_2^*$  decreases). As we continue to increase  $D$ , the GRE signal continues to increase, but the SE signal exhibits a more complex behavior. As  $D$  increases, the SE signal first decreases but then begins to plateau, and finally, when  $D$  is large enough, the SE signal begins to increase. In this situation, the SE and GRE signals are nearly the same.

The effect that leads to this behavior is called *motional narrowing*, referring to the narrowing of the spectral line (reduction of  $\Delta R_2^*$  or  $\Delta R_2$ ) when  $D$  is large. It occurs when the typical distance moved by a spin as a result of diffusion during the experiment is much larger than the size of the local field perturbation, and, consequently, each spin samples a range of field offsets. The key physical difference between diffusion through an array of magnetized cylinders and diffusion in a linear field gradient is that with the cylinders the range of fields a spin can experience is limited. The field offset is maximum at the surface of the cylinder and diminishes with increasing distance. In a linear field gradient, the farther a spin moves, the larger the field offset, and spins that tend to diffuse in different directions will acquire large phase differences. If the cylinders are small enough (or  $D$  is high enough), it is possible for a spin to diffuse past many cylinders and thus sample the full range of field distortions. If all the diffusing spins also sample all the field variations, the net phase acquired by each is about the same, corresponding to precession in the average field. With relatively little phase dispersion present, the signal is only slightly decreased. If  $D$  increases (or the cylinder diameter decreases), the averaging will be even more effective and there will be less attenuation.

This argument addresses the question of why  $\Delta R_2^*$  for the GRE experiment steadily decreases as  $D$  increases. In the SE experiment, however,  $\Delta R_2$  exhibits a more complicated pattern, initially increasing as  $D$  increases, but decreasing again after reaching a peak. We can think of this peak in  $\Delta R_2$  as a cross-over point for two processes affecting the SE signal. The intrinsic signal that could potentially be recovered by the  $180^\circ$  RF pulse is the GRE signal decrease, and we have already seen how the GRE signal loss improves with increasing  $D$  caused by motional narrowing. In addition, the ability of the SE to refocus the remaining phase offsets *decreases* with increasing  $D$ . This decrease occurs because when spins are moving through variable fields, the pattern of field fluctuations felt before the  $180^\circ$  pulse will have increasingly less relation to the fields felt after the  $180^\circ$  pulse as  $D$  increases. The result is that the SE is less effective in refocusing the phase offsets. In other words, the SE signal is not attenuated at either extreme of  $D$  values. When  $D$  is small, the field offsets are refocused by the  $180^\circ$  pulse. When  $D$  is large, there is little spread in the phase offsets because each spin samples all the field offsets, so there is no need for refocusing. It is only when the motional narrowing effect is not complete, but  $D$  is large enough to disrupt the refocusing effect, that the SE signal is attenuated. This peak of the SE attenuation occurs when the average distance a water molecule moves by diffusion during the experiment is

approximately the same size as the spatial scale of the field perturbations (i.e., neither much larger nor much smaller).

This specificity of the SE diffusion effect is potentially useful in localizing signal changes in the microvasculature rather than those in larger vessels. In the preceding arguments, we imagined changing  $D$  for a fixed set of magnetized blood vessels. But the same arguments apply when considering one value of diffusion but a range of vessel sizes (Kennan *et al.* 1994). For any magnetized blood vessel, the spatial scale of the magnetic field perturbations is on the scale of the vessel diameter. Then for a fixed  $D$ , the effects around large vessels would correspond to the left side of the plots in Fig. 8.16, and decreasing vessel size corresponds to moving right on the plots. During the course of the experiment, a water molecule will move a distance  $\Delta x$  on the order of  $\Delta x^2 = 2DTE$ , and for  $TE = 40$  ms and  $D = 0.001$  mm<sup>2</sup>/s (1  $\mu$ m<sup>2</sup>/s), this is approximately 9  $\mu$ m. This distance is close to the diameter of a capillary (5–8  $\mu$ m), and so we would expect that an SE experiment would only show an appreciable attenuation from magnetized vessels of capillary size, whereas a GRE experiment would be more sensitive to larger vessels (Lee *et al.* 1999; Yacoub *et al.* 2003). We will return to this difference in the discussion of the blood oxygenation level dependent (BOLD) effect in Ch. 15.

## References

- Assaf Y, Basser PJ (2005) Composite hindered and restricted model of diffusion (CHARMED) MR imaging of the human brain. *Neuroimage* 27:48–58
- Assaf Y, Pasternak O (2008) Diffusion tensor imaging (DTI)-based white matter mapping in brain research: a review. *J Mol Neurosci* 34:51–61
- Baird AE, Warach S (1998) Magnetic resonance imaging of acute stroke. *J Cereb Blood Flow Metab* 18:583–609
- Basser PJ, Pierpaoli C (1998) A simplified method to measure the diffusion tensor from seven MR images. *Magn Reson Med* 39:928–934
- Behrens TE, Berg HJ, Jbabdi S, Rushworth MF, Woolrich MW (2007) Probabilistic diffusion tractography with multiple fibre orientations: what can we gain? *Neuroimage* 34:144–155
- Benveniste H, Hedlund LW, Johnson GA (1992) Mechanism of detection of acute cerebral ischemia in rats by diffusion-weighted magnetic resonance microscopy. *Stroke* 23:746–754
- Brott TG, Haley EC, Levy DE, *et al.* (1992) Urgent therapy for stroke I: pilot study of tissue plasminogen activator administered within 90 minutes. *Stroke* 23:632–640
- Buxton RB (1993) The diffusion sensitivity of fast steady-state free precession imaging. *Magn Reson Med* 29:235–243
- Callaghan PT (1991) *Principles of Magnetic Resonance Microscopy*. New York: Oxford University Press
- Chun T, Ulug AM, van Zijl PCM (1998) Single-shot diffusion-weighted trace imaging on a clinical scanner. *Magn Reson Med* 40:622–628
- Conturo TE, McKinsty RC, Akbudak E, Robinson BH (1996) Encoding of anisotropic diffusion with tetrahedral gradients: a general mathematical diffusion formalism and experimental results. *Magn Reson Med* 35:399–412
- Cooper RL, Chang DB, Young AC, Martin CJ, Ancker-Johnson D (1974) Restricted diffusion in biophysical systems. Experiment. *Biophys J* 14:161–177
- Cory DG, Garroway AN (1990) Measurement of translational displacement probabilities by NMR: an indicator of compartmentation. *Magn Reson Med* 14:435–444
- Duong TQ, Ackerman JJH, Ying HS, Neil JJ (1998) Evaluation of extra- and intracellular apparent diffusion in normal and globally ischemic rat brain via <sup>19</sup>F NMR. *Magn Reson Med* 40:1–13
- Duong TQ, Sehy JV, Yablonskiy DA, *et al.* (2001) Extracellular apparent diffusion in rat brain. *Magn Reson Med* 45:801–810
- Fisel CR, Ackerman JL, Buxton RB, *et al.* (1991) MR contrast due to microscopically

- heterogeneous magnetic susceptibility: numerical simulations and applications to cerebral physiology. *Magn Reson Med* 17:336–347
- Frank LR (2002) Characterization of anisotropy in high angular resolution diffusion-weighted MRI. *Magn Reson Med* 47:1083–1099
- Goodman JA, Ackerman JJ, Neil JJ (2008) Cs + ADC in rat brain decreases markedly at death. *Magn Reson Med* 59:65–72
- Hardy PA, Henkleman RM (1991) On the transverse relaxation rate enhancement induced by diffusion of spins through inhomogeneous fields. *Magn Reson Med* 17:348–356
- Haselgrove JC, Moore JR (1996) Correction for distortion of echo-planar images used to calculate the apparent diffusion coefficient. *Magn Reson Med* 36:960–964
- Hsu EW, Mori S (1995) Analytical expressions for the NMR apparent diffusion coefficients in an anisotropic system and a simplified method for determining fiber orientation. *Magn Reson Med* 34:194–200
- Hui ES, Cheung MM, Qi L, Wu EX (2008) Towards better MR characterization of neural tissues using directional diffusion kurtosis analysis. *Neuroimage* 42:122–134
- Jensen JH, Helpert JA, Ramani A, Lu H, Kaczynski K (2005) Diffusional kurtosis imaging: the quantification of non-Gaussian water diffusion by means of magnetic resonance imaging. *Magn Reson Med* 53:1432–1440
- Jezzard P, Barnett AS, Pierpaoli C (1998) Characterization of and correction for eddy current artifacts in echo planar diffusion imaging. *Magn Reson Med* 39:801–812
- Jones DK (2008) Studying connections in the living human brain with diffusion MRI. *Cortex* 44:936–952
- Kennan RP, Zhong J, Gore JC (1994) Intravascular susceptibility contrast mechanisms in tissues. *Magn Reson Med* 31:9–21
- Kucharczyk J, Mintorovich J, Asgari HS, Moseley M (1991) Diffusion/perfusion MR imaging of acute cerebral ischemia. *Magn Reson Med* 19:311–315
- Lawes IN, Barrick TR, Murugam V, *et al.* (2008) Atlas-based segmentation of white matter tracts of the human brain using diffusion tensor tractography and comparison with classical dissection. *Neuroimage* 39:62–79
- Le Bihan D (1988) Intravoxel incoherent motion imaging using steady-state free precession. *Magn Reson Med* 7:346–351
- Le Bihan D (1991) Molecular diffusion nuclear magnetic resonance imaging. *Magn Reson Quart* 7:1–30
- Le Bihan D, Breton E, Lallemand D, *et al.* (1988) Separation of diffusion and perfusion in intravoxel incoherent motion MR imaging. *Radiology* 168:497–505
- Lee SP, Silva AC, Ugurbil K, Kim SG (1999) Diffusion-weighted spin-echo fMRI at 9.4 T: microvascular/tissue contribution to BOLD signal changes. *Magn Reson Med* 42:919–928
- Majumdar S, Gore JC (1988) Studies of diffusion in random fields produced by variations in susceptibility. *J Magn Reson* 78:41–55
- Mattiello J, Basser PJ, Bihan DL (1997) The *b* matrix in diffusion tensor echo-planar imaging. *Magn Reson Med* 37:292–300
- McNab JA, Miller KL (2008) Sensitivity of diffusion weighted steady state free precession to anisotropic diffusion. *Magn Reson Med* 60:405–413
- Merboldt KD, Hanicke W, Frahm J (1985) Self-diffusion NMR imaging using stimulated echoes. *J Magn Reson* 64:479–486
- Mori S, Zhang J (2006) Principles of diffusion tensor imaging and its applications to basic neuroscience research. *Neuron* 51:527–539
- Moseley ME, Cohen Y, Mintorovich J, *et al.* (1990) Early detection of regional cerebral ischemia in cats: comparison of diffusion- and T<sub>2</sub>-weighted MRI and spectroscopy. *Magn Reson Med* 14:330–346
- Moustafa RR, Baron JC (2007) Clinical review: imaging in ischaemic stroke – implications for acute management. *Crit Care* 11:227
- Neumann-Haefelin T, Steinmetz H (2007) Time is brain: is MRI the clock? *Curr Opin Neurol* 20:410–416
- Niendorf T, Dijkhuizen RM, Norris DG, van Lookeren Campagne M, Nicolay K (1996) Biexponential diffusion attenuation in various states of brain tissue: implications for diffusion-weighted imaging. *Magn Reson Med* 36:847–857
- Norris DG, Niendorf T, Leibfritz D (1994) Healthy and infarcted brain tissues studied at short diffusion times: the origins of apparent

- restriction and the reduction in apparent diffusion coefficient. *NMR Biomed* 7:304–310
- Ogawa S, Menon RS, Tank DW, *et al.* (1993) Functional brain mapping by blood oxygenation level-dependent contrast magnetic resonance imaging: a comparison of signal characteristics with a biophysical model. *Biophys J* 64:803–812
- Peled S (2007) New perspectives on the sources of white matter DTI signal. *IEEE Trans Med Imaging* 26:1448–1455
- Pierpaoli C, Basser PJ (1996) Toward a quantitative assessment of diffusion anisotropy. *Magn Reson Med* 36:893–906
- Schwarz A, Bogner P, Meric P, *et al.* (2004) The existence of biexponential signal decay in magnetic resonance diffusion-weighted imaging appears to be independent of compartmentalization. *Magn Reson Med* 51:278–285
- Sehy JV, Ackerman JJ, Neil JJ (2002) Evidence that both fast and slow water ADC components arise from intracellular space. *Magn Reson Med* 48:765–770
- Shimony JS, McKinstry RC, Akbudak E, *et al.* (1999) Quantitative diffusion-tensor anisotropy brain MR imaging: normative human data and anatomic analysis. *Radiology* 212:770–784
- Shrager RI, Basser PJ (1998) Anisotropically weighted MRI. *Magn Reson Med* 40:160–165
- Stejskal EO, Tanner JE (1965) Spin-diffusion measurements: spin echoes in the presence of a time-dependent field gradient. *J Chem Phys* 42:288–292
- Takano K, Latour LL, Formato JE, *et al.* (1996) The role of spreading depression in focal ischemia evaluated by diffusion mapping. *Ann Neurol* 39:308–318
- Tanner JE (1970) Use of stimulated echo in NMR diffusion studies. *J Chem Phys* 52:2523–2526
- Tong DC, Yenari MA, Albers GW, *et al.* (1998) Correlation of perfusion- and diffusion-weighted MRI with NIHSS score in acute (< 6.5 hour) ischemic stroke. *Neurology* 50:864–870
- Tuch DS (2004) Q-ball imaging. *Magn Reson Med* 52:1358–1372
- Tuch DS, Weisskoff RM, Belliveau JW, Wedeen VJ (1999) High angular resolution diffusion imaging of the human brain. In *Seventh Meeting of the International Society for Magnetic Resonance in Medicine*, Philadelphia, p. 321
- Wedeen VJ, Hagmann P, Tseng WY, Reese TG, Weisskoff RM (2005) Mapping complex tissue architecture with diffusion spectrum magnetic resonance imaging. *Magn Reson Med* 54:1377–1386
- Weisskoff RM, Zuo CS, Boxerman JL, Rosen BR (1994) Microscopic susceptibility variation and transverse relaxation: theory and experiment. *Magn Reson Med* 31:601–610
- Wong EC, Cox RW, Song AW (1995) Optimized isotropic diffusion weighting. *Magn Reson Med* 34:139–143
- Yablonsky DA, Haacke EM (1994) Theory of NMR signal behavior in magnetically inhomogeneous tissues: the static dephasing regime. *Magn Reson Med* 32:749–763
- Yacoub E, Duong TQ, van de Moortele PF, *et al.* (2003) Spin-echo fMRI in humans using high spatial resolutions and high magnetic fields. *Magn Reson Med* 49:655–664
- Zhong J, Petroff OAC, Prichard JW, Gore JC (1993) Changes in water diffusion and relaxation properties of rat cerebrum during status epilepticus. *Magn Reson Med* 30:241–246



**Part**

**IIB**

# **Magnetic resonance imaging**



# Mapping the MR signal

<b>Introduction</b>	<i>page</i> 205
<b>Basics of imaging</b>	207
Magnetic field gradients	207
Slice selection	208
Gradient echoes	208
<b>Fourier imaging</b>	209
The Fourier transform and $k$ -space	209
The net MR signal traces out the Fourier transform of the image	211
Imaging as a snapshot of the transverse magnetization	212
Phase encoding	214
Mapping $k$ -space	216
<b>Properties of MR images</b>	219
Image field of view	219
Image resolution	220
Pixels, voxels, and resolution elements	222
The point spread function	223
A more general definition of resolution	226
Gibbs artifact	229

## Introduction

There are many techniques for producing an MR image, and new ones are continuously being developed as the technology improves and the range of applications grows. The variety of techniques available is in part an illustration of the intrinsic flexibility of MRI. The MR signal can be manipulated in many ways: radiofrequency (RF) pulses as excitation pulses to tip magnetization from the longitudinal axis to the transverse plane to generate a detectable MR signal and as refocusing pulses to create echoes of previous signals; gradient pulses to eliminate unwanted signals when used as spoilers and, in their most important role, to serve to encode information about the spatial distribution of the signal for imaging. By manipulating the RF and gradient pulses, many pulse sequences can be constructed.

The large variety of available pulse sequences for imaging also reflects the variety of goals of imaging in different applications. In most clinical imaging applications, the goal is to be able to identify pathological anatomy, and this requires a combination of sufficient spatial resolution to resolve small structures and sufficient signal contrast between pathological and healthy tissue to make the identification. Because the MR signal depends on several properties of the tissue, and the influence of these properties can be manipulated by adjusting the timing parameters of the pulse sequence, MR images can be produced with strong signal contrast between healthy and diseased tissue. For example, in [Ch. 3](#), MRI was introduced with an illustration ([Fig. 3.1](#)) of

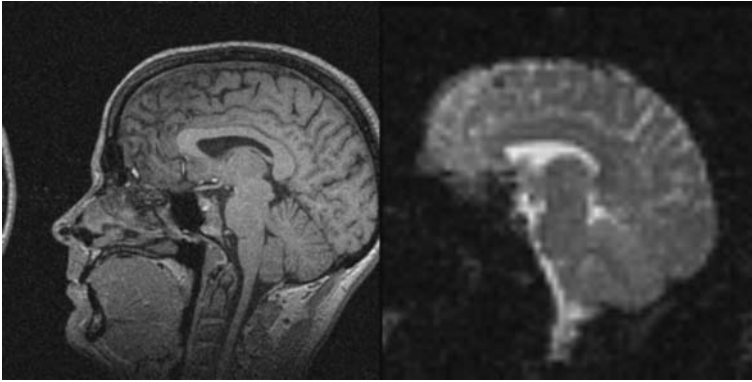


**Fig. 9.1.** Spatial and temporal resolution in MRI. On the left is a high-spatial-resolution image collected with a magnetization prepared rapid acquisition gradient echo (MP-RAGE) pulse sequence in approximately 6 min, with a voxel volume of  $1 \text{ mm}^3$ . On the right is a rapid, but low-spatial-resolution, image collected with an echo planar imaging pulse sequence in approximately 60 ms, with a voxel volume of  $45 \text{ mm}^3$ .

the range of tissue contrast that results simply from manipulating the repetition time (TR) and the echo time (TE) of a spin echo (SE) pulse sequence.

In other applications, the speed of imaging is critically important to be able to follow a dynamic process or simply to minimize artifacts from subject motion. On modern scanners, an image can be acquired in as little as 30 ms, and images can be collected continuously at rates exceeding 20 images/s. **Figure 9.1** shows an image collected with an echo planar imaging (EPI) pulse sequence in only 60 ms. In morphometric mapping to measure the volumes of brain structures with high precision, spatial resolution rather than imaging speed is the primary concern. With volume imaging, the resolved volume element (*voxel*) can be smaller than  $1 \text{ mm}^3$ , although the time required to collect such high-resolution images of the whole brain is 5–10 min. **Figure 9.1** also shows one slice from a magnetization prepared rapid acquisition gradient echo (MP-RAGE) volume acquisition with a voxel volume of  $1 \text{ mm}^3$ , requiring 6 min to acquire a full 140 slice data set covering the head. For comparison, the EPI image of the same slice in **Fig. 9.1** has a voxel volume of  $45 \text{ mm}^3$ .

An ideal imaging technique would have rapid acquisition of data to provide good temporal resolution, high spatial resolution to be able to resolve fine details of anatomy, and a high signal to noise ratio (SNR) to distinguish tissues of interest by differences in the MR signal they generate. Yet these goals directly conflict with one another. As spatial resolution is improved, the smaller image voxel generates a weaker signal relative to the noise. A very-high-resolution image, with voxel volumes much less than  $1 \text{ mm}^3$ , could be acquired with standard equipment, but the SNR would be so degraded that the anatomical information would be lost. In addition, as the voxel size decreases, the total number of voxels in the image increases, requiring a longer imaging time to collect the necessary information. In some applications, the goal of achieving a particular tissue contrast also requires a long imaging time. For example, with conventional imaging,  $T_2$ -weighted contrast requires a long TR, and, therefore, a long total imaging time. With newer techniques for fast imaging, there is much more flexibility in dealing with the trade-offs of image contrast and imaging time, but the essential conflicts involved in simultaneously

achieving high SNR, high spatial resolution, and high temporal resolution still remain. The different imaging pulse sequences reflect different approaches to balancing these conflicting goals.

The central concept in understanding how MRI works is the idea of  $k$ -space, the spatial Fourier transform of the image. This, rather than the image itself, is directly measured in MRI. Different imaging techniques are distinguished by two features: (1) how they sample  $k$ -space to collect sufficient data to reconstruct an image of the transverse magnetization at one time point, and (2) what the magnitude of the local magnetization is at that time point. The  $k$ -space sampling determines the basic parameters of the image, such as field of view (FoV), spatial resolution, and speed of acquisition. The second feature, the magnitude of the local MR signal, determines whether an image will show useful contrast between one tissue and another. The two features of imaging, how  $k$ -space is sampled and the nature of the local signal, can be considered independently. In Ch. 7, the focus was on the signal itself, and this chapter focuses on how an image of that signal distribution is created.

A brief word about the naming of pulse sequences is in order. Sometimes the naming is based on the nature of the signal (e.g., SE), sometimes it is based on the acquisition technique (e.g., EPI), and sometimes it is both to specify precisely the imaging (e.g., SE-EPI). Acronyms are ubiquitous in MRI, and the sheer number of named pulse sequences is often daunting to the novice trying to get a handle on how MRI works. Sometimes the acronyms are helpfully descriptive, but usually they simply serve to distinguish one pulse sequence from another, and this author, at least, can rarely remember exactly what the acronyms stand for. To add to the confusion, the same pulse sequence sometimes has different names depending on the manufacturer of the scanner (e.g., GRASS, FISP, and FAST). The goal of this chapter is to clarify the basic principles on which MRI is based rather than to provide a comprehensive survey of existing imaging techniques. Nevertheless, a number of imaging pulse sequences are described along the way.

## Basics of imaging

### Magnetic field gradients

The MRI technique exploits the physical fact that the resonant frequency is directly proportional to the magnetic field. By altering the magnetic field in a controlled way so that it varies linearly along a particular axis, the resonant frequency also will vary linearly with position along that axis. Such a linearly varying field is called a *gradient field* and is produced by additional coils in the scanner. An MR imager is equipped with three orthogonal sets of gradient coils so that a field gradient can be produced along any axis. Because these gradient fields usually are turned on for only a few milliseconds at a time, they are referred to as *pulsed gradients*.

Compared with the main magnetic field  $B_0$ , the field variations produced by the gradients are small. Typical gradient strengths used for imaging are a few millitesla per meter (mT/m), and conventional MR imagers usually have maximum strengths of 10–40 mT/m. At maximum strength, the magnetic field variation across a 30 cm object is 3 mT with a 10 mT/m gradient, only 0.2% of a typical  $B_0$  of 1.5 T. For the following discussion of spatial encoding, it is convenient to express field gradients in units of the resonant frequency change they produce per centimeter (Hz/cm): 10 mT/m = 4258 Hz/cm for protons.

## Slice selection

In most applications, the first step in image acquisition is the application of a slice-selective RF pulse that tips over the magnetization in only a particular desired slice. To do this, the RF pulse is shaped so that it contains only a relatively narrow band of frequencies centered on a particular frequency  $\omega_0$ . While the RF pulse is applied, a magnetic field gradient along the slice-selection axis ( $z$ ) is applied, so that the resonant frequency at the center of the desired slice is  $\omega_0$ . (We will call the slice-selection axis  $z$ , but the actual orientation is arbitrary.) In the presence of the field gradient, the resonant frequency varies with position along the  $z$ -axis, so the RF pulse is on-resonance for only a small range of  $z$ . Then only those spins within a narrow range centered on the desired slice are excited by the RF pulse. The process of slice selection was described in more detail in [Ch. 6](#).

The process of slice selection produces a precessing transverse magnetization at each point of the selected plane. The rest of this chapter deals with how we make an image of the spatial distribution of that magnetization. An MR image is essentially a snapshot of the local amplitude of the transverse magnetization at a particular time point. The central task of MRI then is to encode information about the  $x$ - and  $y$ -positions of each signal in such a way that an image of the signal distribution in the  $x$ - $y$  plane can be reconstructed. A remarkable aspect of MRI is that this spatial information is encoded into the signal itself.

## Gradient echoes

A central concept in MRI is the process of formation of a gradient echo. If a gradient pulse is applied after an RF excitation pulse, spins at different positions along the gradient axis will precess at different rates. The effect of the gradient pulse is, therefore, to produce a large dispersion of phase angles, which grows while the gradient is on, and the net signal is severely reduced (*spoiled*). In [Fig. 9.2](#) this is illustrated by drawing curves of the phase differences over time of spins with different  $x$ -positions. Initially the spins are in-phase, but when the gradient is turned on, they begin to dephase, and once the gradient is turned off, the phase dispersion remains but no longer grows. However, if an opposite gradient pulse is then applied for the same duration, each spin will acquire a phase angle opposite to the phase it acquired during the first pulse. The phase dispersion diminishes until all the spins are back in-phase, and all spins add coherently to produce a strong signal called a *gradient recalled echo* (GRE), or just a gradient echo. If a  $180^\circ$  RF pulse is placed between the two gradient pulses, the two gradients must have the same sign for a gradient echo to occur. The  $180^\circ$  RF pulse will reverse the phase of each spin group, and the second gradient pulse will then bring them back into phase ([Fig. 9.2](#)).

The simplest MR measurement is the generation of a free induction decay (FID), described in previous chapters. A  $90^\circ$  RF pulse tips over the longitudinal magnetization to generate a signal, and the signal decays over time with a time constant  $T_2^*$ . The simple FID pulse sequence, when used for imaging, is called a GRE pulse sequence. This terminology, although in standard use, can be confusing. Gradient echoes are an important part of the imaging process, but they are involved in every type of imaging, not just imaging an FID signal. The situation is further confused because sometimes a distinction is drawn between an SE pulse sequence and a GRE pulse sequence, based on the type of echoing process involved: RF echoes for the SE, and gradient echoes for the GRE. However, gradient echoes are ubiquitous in imaging; both SE and GRE imaging use gradient echoes. The difference between these two pulse sequences is that SE *also* includes an RF refocusing pulse to generate

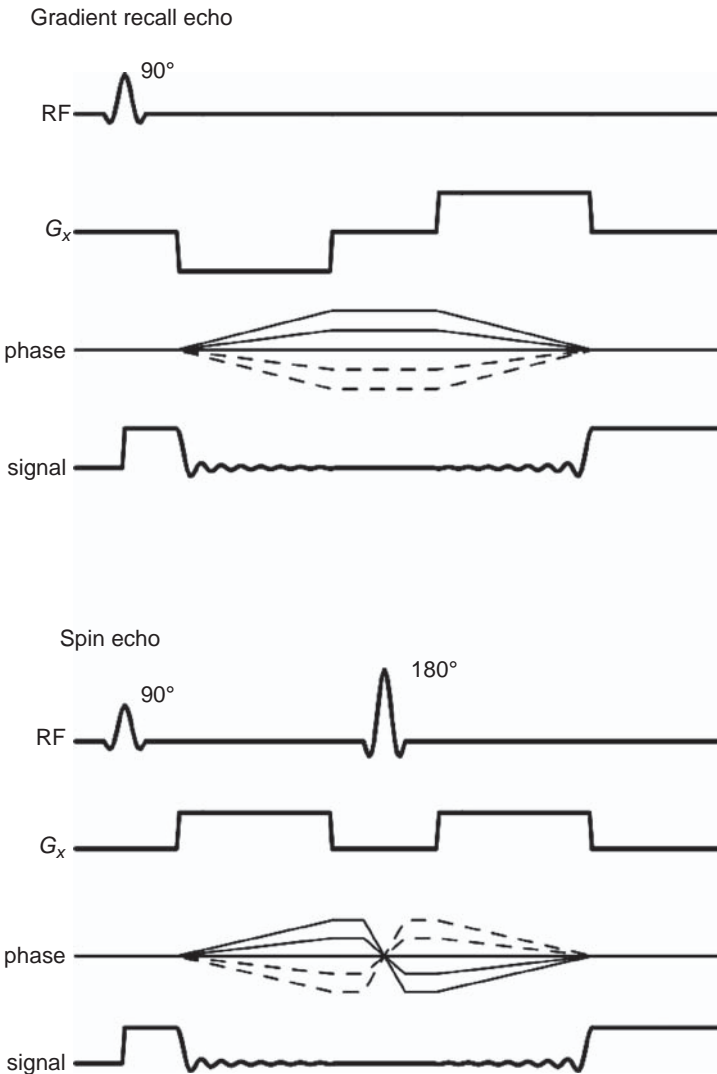


**Fig. 9.2.** Gradient echoes. After a signal is generated by a  $90^\circ$  radiofrequency (RF) pulse, a gradient pulse will cause spins at different positions to precess at different rates, producing phase variations and a reduction of the net signal (spoiling). A second gradient pulse with opposite sign (or the same sign if a  $180^\circ$  RF refocusing pulse is applied first) will refocus the phase offsets, creating a gradient echo when the areas under the two gradient pulses are matched.

a SE, but GRE does not. The convention is that a pulse sequence which does not explicitly contain a  $180^\circ$  refocusing pulse is called a GRE pulse sequence.

## Fourier imaging

### The Fourier transform and $k$ -space

Taking just the simple GRE pulse sequence, how can we separate and map the signals from different locations? Imaging is done by exploiting the basic relationship of NMR: that the local precession frequency is proportional to the local magnetic field and so can be manipulated by applying gradient fields. When a gradient field is turned on, the total signal is

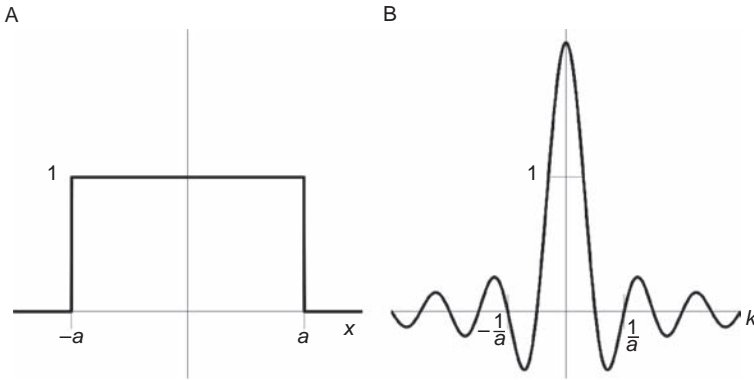


**Fig. 9.3.** The Fourier transform. Any function of position, such as a profile through an image  $I(x)$  (A), can also be described as a function of spatial frequencies  $S(k)$  (B) where  $k$  is the inverse of the spatial wavelength. The functions  $I(x)$  and  $S(k)$  are related by the Fourier transform so that given one representation the other can be calculated.

spread out over a range of frequencies, and the precession frequency then varies linearly with position along the gradient direction. This basic picture of frequency encoding was introduced qualitatively in Ch. 4, and the following is a more quantitative development in terms of the Fourier transform and the important concept of  $k$ -space.

To begin with, consider the simple example of an object with a rectangular profile, as illustrated in Fig. 9.3. We can think of this as a one-dimensional image  $I(x)$ , with  $I(x)$  representing the density of transverse magnetization at position  $x$ . That is, the net signal produced by spins located within a small range  $dx$  centered on  $x$  is  $I(x)dx$ . By the Fourier transform theorem, any function of position  $x$  can also be expressed as a sum of sine and cosine waves of different wavelengths and amplitudes that spread across all of  $x$ . The different spatial frequencies of these waves are denoted by  $k$ , the inverse of the wavelength, so that small  $k$ -values correspond to low spatial frequencies and long wavelengths. Then, the profile  $I(x)$  can be expressed as  $S(k)$ , where  $S(k)$  is the amplitude of the wave with spatial frequency  $k$ . The two representations  $I(x)$  and  $S(k)$  are equivalent, in the sense that both carry the same information about the profile, just expressed in a different way. The importance of this  $k$ -space representation for imaging is that  $S(k)$  is what is actually measured, and  $I(x)$  is reconstructed from the raw data by calculating the Fourier transform.

The mathematical relationship between these two representations given by the Fourier transform is (Bracewell 1965)

$$S(k) = \int_{-\infty}^{\infty} I(x) e^{i2\pi kx} dx \quad (9.1a)$$

$$I(x) = \int_{-\infty}^{\infty} S(k) e^{-i2\pi kx} dk \quad (9.1b)$$

The simplicity of the form of Eq. (9.1) is in part a result of using complex numbers. The Fourier transform could also be written in terms of real sines and cosines, but in a more



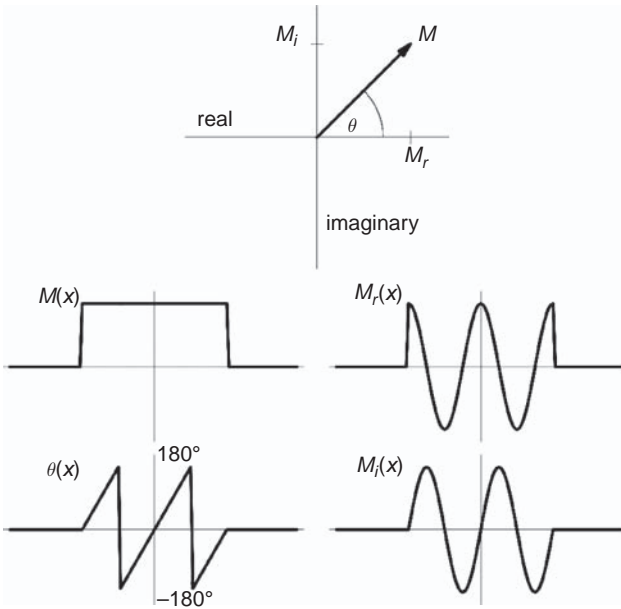


**Fig. 9.4.** Complex numbers. In MR applications, it is useful to describe the local magnetization and the Fourier transform in terms of complex numbers. In the Fourier transform, the representations  $I(x)$  and  $S(k)$  each consist of two numbers, which can be taken as the magnitude and phase (left) or the real and imaginary parts (right) of a complex number. In this example, the magnitude profile  $M(x)$  is rectangular, and the phase varies linearly across the object. Physically, the magnitude of  $M(x)$  is the net magnitude of the local precessing magnetization vector at  $x$ , and the phase is the phase angle of this vector at the center of data acquisition.

cumbersome way. Furthermore, the complex notation is convenient for describing the MR signal produced by a precessing magnetization vector. The precessing transverse magnetization can be expressed as a complex number whose magnitude is the amplitude of the transverse magnetization and whose phase is the precessional phase angle. Mathematically, the magnetization is written as  $Me^{i\theta}$ , where  $M$  is the magnitude of the vector and  $\theta$  is the phase angle in the transverse plane (Fig. 9.4). Alternatively, an equivalent representation is the projection of the vector on to two perpendicular axes in the transverse plane, with the two projections treated as the real and imaginary parts of a complex number. If the two axes are labeled  $r$  and  $i$  for the real and imaginary components, then the complex magnetization is written as  $M_r + iM_i$ , where  $i$  is the square root of  $-1$ . Both components are, of course, real physical quantities, and the term “imaginary” just means that it is the term multiplied by  $i$ . With this in mind, we can treat  $I(x)$ , representing both the magnitude and phase of the local magnetization, as a complex number at each position  $x$ .

## The net MR signal traces out the Fourier transform of the image

Figure 9.4 shows magnitude/phase and real/imaginary representations for a rectangular distribution of magnetization magnitude with a phase that varies linearly with  $x$  and so wraps around each time phase increase by  $360^\circ$ . A snapshot of the distribution of transverse magnetization along  $x$  can be represented in complex form as  $M(x) = \rho(x)e^{i\theta(x)}$ , where  $\rho(x)$  is the density of magnetization along  $x$ , and  $\theta(x)$  is the local phase angle at  $x$ . In general, both  $\rho$  and  $\theta$  are also functions of time:  $\rho$  typically decreases as a result of relaxation, and  $\theta$  steadily increases through precession. For now, however, we are only interested in mapping the distributions of  $\rho$  and  $\theta$  at one particular time, a snapshot of the distributions. The measured MR signal is the net signal from the entire object, which is calculated by integrating over the profile  $M(x)$ . The signal contributed from a small region between  $x$  and  $x + dx$  is  $M(x)dx$ , so the net signal  $S$  is

$$S = \int_{-\infty}^{\infty} M(x) dx \quad (9.2)$$

All we can measure is this net MR signal from the object. Imaging is accomplished by turning on a gradient field and measuring the evolution of this net signal for a short time centered on our snapshot time. A gradient field has no effect on the center of the field of view ( $x = 0$ ) but causes the total field to vary linearly with  $x$ , adding to  $B_0$  for positive  $x$  and subtracting from  $B_0$  for negative  $x$ . The magnitude  $G$  of the gradient is conveniently expressed in units of hertz per centimeter and the resonant frequency offset of spins at position  $x$  is  $Gx$ . After precessing for a time  $t$  in this gradient field, the magnetization of a spin at position  $x$  will acquire an additional phase  $\theta = 2\pi Gxt$ . Because we are expressing the magnetization as a complex number consisting of a magnitude and a phase, the mathematical equivalent of adding a phase twist  $\theta$  is a multiplication by  $e^{i\theta}$ . The gradient field thus modifies the local phase of the magnetization in a position-dependent way, and the net signal at time  $t$  becomes

$$S(t) = \int_{-\infty}^{\infty} M(x) e^{i2\pi Gxt} dx \quad (9.3)$$

If we identify  $k = Gt$ , this is precisely the form of the Fourier transform in Eq. (9.1). That is, while the gradient is on, the net signal over time traces out the spatial Fourier transform of the object so that  $S(t)$  is a direct measure of  $S(k)$ . After  $S(t)$  has been measured, the image  $I(x)$  can be reconstructed by applying the inverse Fourier transform to the data. This remarkable relationship lies at the heart of all of MRI and provides a powerful way of thinking about different ways of doing imaging (Twieg 1983).

## Imaging as a snapshot of the transverse magnetization

There are some subtleties involved in Fourier imaging. First of all, we described this imaging procedure as taking a snapshot of the distribution of transverse magnetization at one time point, yet it takes some time to collect the data. There must be sufficient time for phase evolution under the influence of the gradient field to measure  $S(k)$ . But during this data acquisition period, the intrinsic transverse magnetization (i.e., the transverse magnetization without the effects of the gradient) is not constant. The phase angle continues to increase by precession, and the amplitude decreases by relaxation. Precession at the primary resonant frequency as a result of  $B_0$  is not a problem; the receiver accounts for this known precession. However, if the intrinsic resonant frequency is altered from the nominal value, by chemical shift or field inhomogeneities, the result will be artifacts in the image. The essential assumption of imaging is that, prior to turning on the gradient, all spins precess at precisely the same frequency. They are not necessarily in-phase with one another, but these phase offsets are assumed to be constant. The result when this ideal assumption does not hold is that spins with intrinsic resonant frequency offsets are mapped to the wrong location. These off-resonance effects, and the decay of the signal by relaxation during data acquisition, are sources of artifacts in imaging.

In short, MRI is built on an idealization that, during the data acquisition period, the intrinsic local MR signals are constant in amplitude and oscillating at frequency  $f_0$  and, as a result, any changes observed in the net signal are caused entirely by the effects of the applied gradient. That is, the evolution of the signal over time is interpreted as being a result of the

distribution of magnetization in space interacting with the applied gradient, and not as an intrinsic change in the local signal. Because this idealization is never true, artifacts will result, and the magnitude of the artifacts will increase as the duration of data acquisition increases. In conventional MRI, the data acquisition window is relatively short (approximately 8 ms), and these artifacts do not seriously degrade the image. With fast imaging techniques, however, the data acquisition window typically is much longer (up to 100 ms); consequently, these artifacts are more of a problem. Artifacts are discussed in more detail in [Ch. 10](#).

The expression for the Fourier transform involves another somewhat subtle feature. Note that [Eq. \(9.1b\)](#), the expression for the inverse Fourier transform used to reconstruct the image from the measured data, requires adding up the contributions from both positive and negative values of  $k$ . A negative spatial frequency may seem like a strange concept, but mathematically it is perfectly straightforward. The sign of  $k$  simply describes whether the phase increases or decreases with increasing  $x$ . The necessity of measuring negative as well as positive spatial frequencies makes the data acquisition slightly more complicated. In the simplest approach, a gradient is turned on and maintained at a constant value, and data are collected during this read-out gradient. But remembering that  $k = Gt$ , this only measures the positive spatial frequencies, and to measure the negative  $k$ -values requires that either  $G$  or  $t$  must be negative. The negative frequencies could be measured by repeating the experiment and reversing the sign of the gradient, but this would then require two shots to measure the data from one profile.

Instead, both positive and negative  $k$ -values can be measured by creating a *gradient echo* at the center of the data acquisition window ([Fig. 9.5](#)). Prior to applying the read-out gradient, a gradient pulse with opposite sign and half the duration is applied, sometimes called a *compensation* pulse. The physical effect of this is to wind up the phase with the

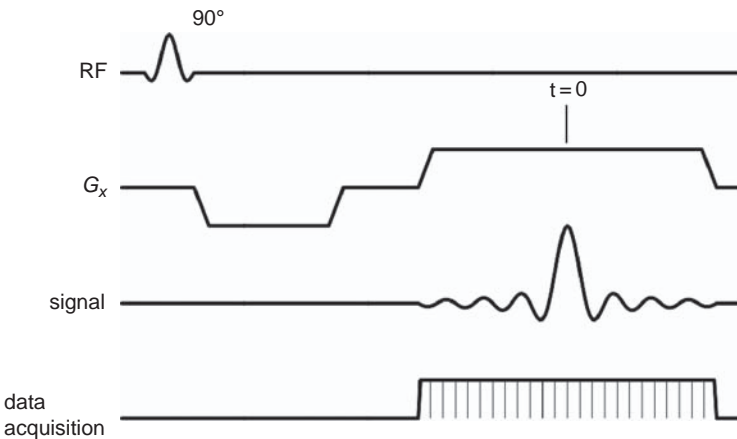


**Fig. 9.5.** Frequency encoding. Pulse sequence diagram illustrating frequency encoding of position along the  $x$ -axis. By applying a field gradient along  $x$  during data acquisition, the signals from different positions along  $x$  are spread over different frequencies, with a one-to-one correspondence between position and temporal frequency. The measured quantity is the net signal over time,  $S(t)$ . The distribution of temporal frequencies is just the Fourier transform of this signal, which is then directly proportional to  $I(x)$ . In other words, the signal  $S(t)$  directly maps out the spatial Fourier transform of the object,  $S(k)$ , with the correspondence between time ( $t$ ) and spatial frequency ( $k$ ) given by  $k = Gxt$ , where  $G$  is gradient. Both positive and negative spatial frequencies are measured by preceding the data acquisition with a negative gradient pulse so that the point where all spins are in-phase, corresponding to  $t=0$  (and thus  $k=0$ ), is moved to the center of the data acquisition window.

compensation pulse prior to applying the read-out gradient so that during the first half of data acquisition the phases unwind, with the effect of the compensation pulse neatly canceled at the center of the data acquisition window, creating a gradient echo when all spins are back in phase. In the second half of data acquisition, the local phases continue to increase. The mathematical effect of this is that the first half of the data acquisition samples the negative  $k$ -values, and the second half samples the positive  $k$ -values. Effectively, the zero of time, corresponding to  $k=0$  when all the spins are back in phase, has been moved from the beginning of the read-out window to the middle. If we think of MRI as a snapshot of the distribution of transverse magnetization at a particular time point, that time point is the time when the  $k=0$  sample is measured.

## Phase encoding

The gradient echo is the basic tool of MRI. During data acquisition, the total signal maps out  $k$ -space, the spatial Fourier transform of the distribution of transverse magnetization at one instant of time. The time of this snapshot is when the data sample corresponding to  $k=0$  is measured. Everything discussed up to this point has described one-dimensional imaging. Frequency encoding alone measures a one-dimensional projection of a two-dimensional image on to the  $x$ -axis. That is, all the signals with a given  $x$ -coordinate, regardless of their  $y$ -position, contribute to the net signal corresponding to position  $x$ . How do we sort out the  $y$  distribution of the signals to make a two-dimensional image? There are several ways, but the most common is to use *phase encoding* for the second dimension (Edelstein *et al.* 1980; Kumar *et al.* 1975). In fact, phase encoding is accomplishing the same thing as frequency encoding, but in a more discrete way.

To see how phase encoding works, it is helpful to examine how frequency encoding works in more detail. From the preceding discussion about the correspondence between temporal frequency and position during the read-out gradient, one might conclude that the key feature is the precession rate when a data sample is measured. This is not quite right; the key feature is the accumulated phase differences between spins at the time of each sample. Imagine breaking the read-out gradient used in frequency encoding into a series of short pulses, with a data sample between each pulse (Fig. 9.6). The resulting data are identical to the original data measured with the continuous gradient; relative phase changes between spins at different locations grow only when the gradients are on because the spins precess at the same rate in

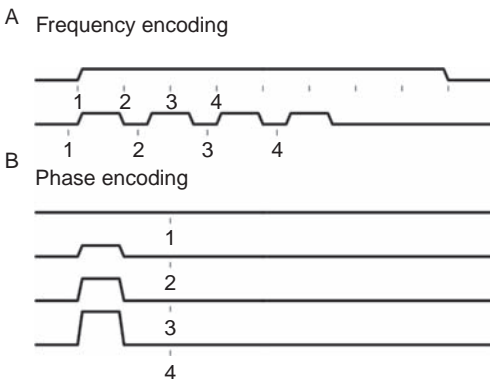


**Fig. 9.6.** Equivalence of frequency encoding and phase encoding. (A) Frequency encoding employs a constant gradient, but a series of short gradient pulses interleaved with data samples would produce identical measurements at times 1, 2, 3, and so on because each sample measures the cumulative effects of all the previous gradient pulses. (B), In phase encoding the signal is measured after a single gradient pulse, and the magnitude of the gradient pulse is increased with each new excitation. The phase twists produced by a gradient pulse depend only on the area under the gradient pulse, so the numbered samples would be identical to those measured with frequency encoding. The primary difference is that with frequency encoding the samples are measured rapidly after one excitation pulse, whereas with phase encoding they are measured one at a time with separate excitations.

the gaps. So inserting the gaps has no effect on the cumulative phase offsets produced at the time of each of the data samples, and indeed a sample could be collected at any time within the gap. In other words, it is not necessary that a gradient is on when a data sample is measured because the signal depends on the cumulative phase changes produced by previous gradient pulses, which remain locked in after the gradient is turned off.

From the point of view of sampling in  $k$ -space, the sampling point moves when the gradient pulses are on and then pauses during the gaps. Each of these data samples simply records the cumulative effects of all the previous gradient pulses, and the net effect of a string of gradient pulses is identical to that of a single gradient pulse with the same amplitude and total duration. However, the phase effects of a gradient pulse are the same for any gradient pulse that has the same *area* (the product of the gradient amplitude and duration) because the phase produced at a point is proportional to  $Gt$ . The same sampling in  $k$ -space could then be done one point at a time by applying gradient pulses of different amplitude followed by a data sample, as shown in Fig. 9.6, and this process is called phase encoding. In short, the identical data samples measured in frequency encoding could be measured with phase encoding by repeating the pulse sequence to generate a new MR signal, applying a single gradient pulse whose amplitude is incremented each time the pulse sequence is repeated, and measuring one data sample for each generated MR signal.

Two-dimensional imaging is done by frequency encoding the  $x$ -axis and phase encoding the  $y$ -axis, and it is a remarkable fact that these two processes do not interfere with one another. Figure 9.7 shows the full pulse sequence diagram for a simple imaging sequence. Slice selection is done by applying a frequency-selective RF pulse in conjunction with a gradient in  $z$ . The selected  $z$ -plane is then mapped by frequency encoding and phase encoding, with the pulse sequence repeated for each new phase-encoding step. From the Fourier transform view, the measured data traces out the two-dimensional Fourier transform of the image in a two-dimensional  $k$ -space ( $k_x, k_y$ ). Each time the pulse sequence is repeated, one line in  $k_x$  at a fixed  $k_y$  is measured with a gradient echo in  $x$ . Each phase-encoding pulse in  $y$  moves the  $k$ -space

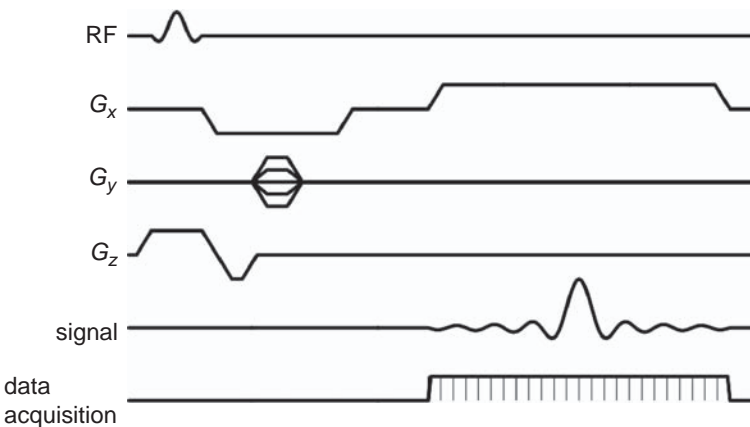


**Fig. 9.7.** Gradient echo imaging pulse sequence. Each line shows the time sequence for different events. The radiofrequency (RF) pulse sequence begins with slice selection along the  $z$ -axis, followed by phase encoding along  $y$  and frequency encoding along  $x$ . The phase-encoding gradient ( $G$ ) is incremented each time the pulse sequence is repeated, and each repetition measures one line in  $k$ -space. After sufficient repetitions (e.g., 128 or 256), the image is calculated as the Fourier transform of the  $k$ -space matrix.

sampling to a new line at a new value of  $k_y$ . The data collection fills in a block of samples in  $k$ -space, and then the image is reconstructed by applying the Fourier transform to the data.

At first glance, phase encoding seems very inefficient compared with frequency encoding. With frequency encoding, for each RF excitation pulse to generate a signal, the full distribution in one direction is collected; however, with phase encoding, only one sample is collected for each RF pulse. Why is it not possible to simply rotate the read-out gradient and use frequency encoding again along the  $y$ -axis? This would yield a projection of the image on to the  $y$ -axis. However, projections of an image on to two axes are not sufficient data to reconstruct the image. Projections on to many axes, with only a small angle of rotation between them, are required. This method is called *projection reconstruction* and is analogous to the technique used in X-ray computed tomography and positron emission tomography. The first MR images were made with a projection reconstruction technique (Lauterbur 1973). This technique is still in use for specialized applications, but most MRI now uses some form of phase encoding.

## Mapping $k$ -space

With the preceding ideas, we can now formalize the idea of  $k$ -space and how it relates to the local magnetization. Any image is a distribution of intensities in the  $x$ - $y$  plane, represented by  $I(x,y)$ . In MRI, the physical quantity imaged is the local transverse magnetization. Consequently, at each point  $(x,y)$ , there are, in fact, two numbers needed to specify the local signal: the magnitude of the local magnetization vector and its phase angle. The local magnetization is precessing, so the phase angle is constantly changing, but we can think of an MR image as a snapshot of the transverse magnetization at one instant of time. Then the local phase angle may differ from one location to the next, if, for example, the main magnetic field is different at the two locations so that the magnetization vectors precess at different rates. This is a useful way to map the magnetic field distribution in the head by simply imaging the relative phase angle distribution, as illustrated in Fig. 9.8. Note that the map of phase angle

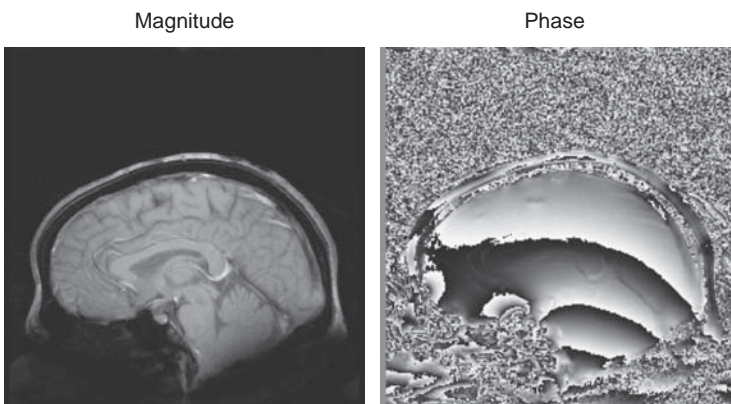


**Fig. 9.8.** Magnitude and phase images. An MR image reflects the local transverse magnetization at the center of data acquisition (when the  $k=0$  data sample is measured). The local magnetization is described by a magnitude and a phase angle. Magnetic field variations across the brain create different precession rates, resulting in different phase angles at the time of imaging with a gradient recalled echo pulse sequence (a spin echo pulse sequence refocuses these phase offsets). The sharp transitions of the phase image are an artifact of the display caused by the cyclic nature of phase, but they effectively serve as contour lines of the magnetic field distribution.

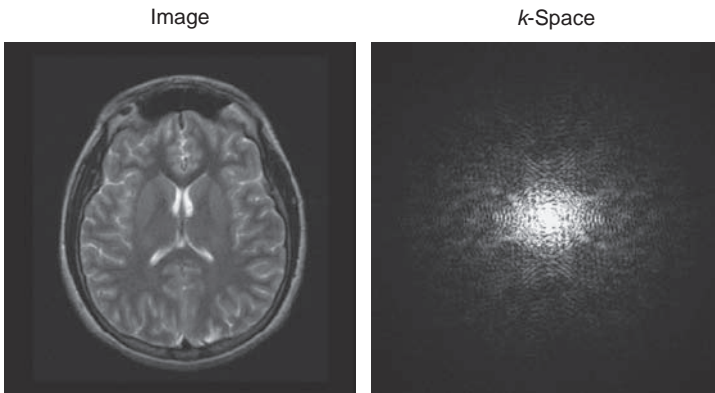


**Fig. 9.9.** Image space and  $k$ -space. Any magnetic resonance image can be equivalently represented as a matrix of intensities  $I(x,y)$  or a matrix of spatial frequency amplitudes  $S(k_x,k_y)$ . The central portion of  $k$ -space describes the low-spatial-frequency components, and the outer edges describe the high frequencies, which determine image resolution. (Only the magnitude images are shown, and there is a corresponding phase map in each space.)

shows abrupt transitions between white and black, which simply result from the fact that the phase is cyclic, so that moving from  $359^\circ$  to  $0^\circ$  is a smooth phase change, but the number describing the phase jumps. One can think of the bands of black and white as contour levels of phase, marking  $360^\circ$  phase changes.

With this in mind, we can treat  $I(x,y)$ , representing both the magnitude and phase of the local magnetization, as a complex number at each point of the  $x$ - $y$  plane. Any distribution  $I(x,y)$  can also be described as a function of spatial frequencies,  $S(k_x,k_y)$ , in a  $k$ -space with axes  $(k_x,k_y)$  (Fig. 9.9). At each point in  $k$ -space, there is also a complex number, with a magnitude and a phase, and this number describes the amplitude and phase of a simple sine wave extending across the entire image plane, as illustrated in Fig. 9.10. Each value of  $k$  is associated with a distinct wave, with the wavelength equal to the inverse of the magnitude of  $k$ , and the direction given by the location of the point in the  $k_x$ - $k_y$  plane. Therefore, small values of  $k$  correspond to long wavelengths, and large values of  $k$  correspond to short wavelengths. The amplitude  $S(k_x,k_y)$  at each point in  $k$ -space describes the amplitude of the wave with spatial frequencies  $(k_x,k_y)$ , and the phase describes how that wave pattern is shifted in the  $x$ - $y$  plane. Figures 9.9 and 9.10 illustrate the basic relationships between image space and  $k$ -space. The low spatial frequencies usually have the largest amplitude and so contribute most to the image intensity, but the high spatial frequencies provide spatial resolution in the image. Given either distribution,  $I(x,y)$  or  $S(k_x,k_y)$ , the other can be calculated with the Fourier transform, using the two-dimensional form of Eq. (9.1).

The power of thinking about imaging from the perspective of  $k$ -space is that  $k$ -space is actually measured in the imaging process, and image reconstruction just requires applying the Fourier transform to the raw data. The relationship at the heart of MRI is that, by applying magnetic field gradients, the net MR signal from the entire slice is itself a direct measure of  $k$ -space. During data acquisition, as the local phase changes induced by the gradient field continue to evolve, the net signal sweeps out a trajectory in  $k$ -space. Each measured sample of the net signal is then a measured sample in  $k$ -space, and the task of imaging is to measure sufficient samples in  $k$ -space to allow reconstruction of an image.

Earlier,  $k$ -space sampling was introduced by discussing frequency encoding and gradient echoes, and we can now look at this as a  $k$ -space trajectory controlled by the applied

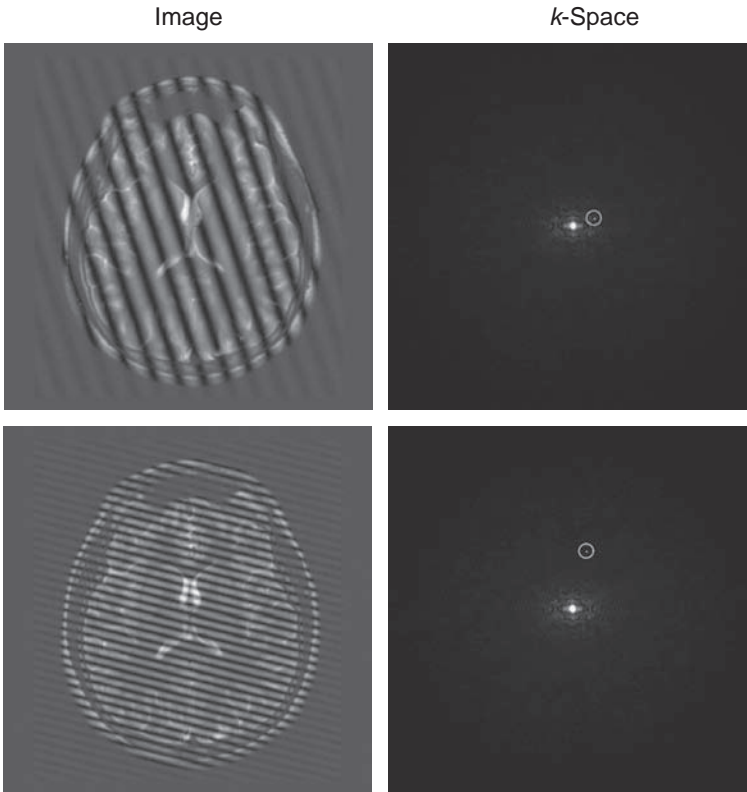


**Fig. 9.10.** Effect on the image of individual  $k$ -space values. Each point in  $k$ -space represents a sine wave pattern across the image plane (illustrated for the two circled points), and the  $k$ -space amplitude is the amplitude of that wave in the image. The wavelength gets shorter moving away from the center of  $k$ -space, and the angle of the point in  $k$ -space determines the angle of the wave pattern in image space.

gradients. Each time a gradient echo is acquired, a line through  $k$ -space is measured. For an  $x$ -gradient echo, the first sample starts at a large  $-k_x$  value, moves through  $k_x = 0$  at the peak of the gradient echo, and continues on to large  $+k_x$  values at the end of data sampling. The phase-encoding steps in  $y$  prior to each sampled gradient echo serve to bump the sampling trajectory to a new  $k_y$  line in  $k$ -space. Then by stepping through many phase-encoding steps in  $y$ , and for each step acquiring a gradient echo with a frequency-encoding gradient turned on in  $x$ ,  $k$ -space is measured one line at a time with a raster scanning type of trajectory. This is the basic sampling pattern in conventional MRI.

We can generalize this by defining  $\mathbf{k}(t)$  as a vector in  $k$ -space defining the location that is being sampled at time  $t$ . Then if  $\mathbf{G}(t)$  is the total field gradient vector applied at time  $t$ , including both  $x$ - and  $y$ -gradient components, the general expression for  $\mathbf{k}(t)$  is

$$\mathbf{k}(t) = \int_0^t \mathbf{G}(t) dt \quad (9.4)$$

The sampled point in  $k$ -space at time  $t$  depends on the full history of the gradients that have been applied after the transverse magnetization was created at  $t = 0$ . When the gradients



along each axis are balanced (at the time of a gradient echo), the  $\mathbf{k} = 0$  point is sampled. In this equation,  $G$  is expressed in hertz per centimeter. The more familiar units for a magnetic field, gauss or tesla, are converted to an equivalent precession frequency by multiplying by the gyromagnetic ratio. This conversion of units emphasizes that the important role of a magnetic field gradient is to create a gradient of resonant frequency, so it is natural to express a field strength in terms of the resonant frequency it produces.

This is the basic imaging equation for MRI. At each time point  $t$ , the net signal from the entire slice measures the amplitude and phase at the point in  $k$ -space described by  $\mathbf{k}(t)$ . A prescribed pulse sequence defines how the gradients are applied and so defines  $G(t)$  and the trajectory through  $k$ -space. This equation is defined in two dimensions but is equally valid in three dimensions. The intensity at each point in a volume of space can be described by  $I(x, y, z)$  and in the corresponding  $k$ -space,  $S(k_x, k_y, k_z)$ . Field gradients along all three spatial axes can be prescribed to create a three-dimensional trajectory in  $k$ -space.

## Properties of MR images

### Image field of view

Basic properties of the MR image, such as the FOV and resolution, are determined by how  $k$ -space is sampled in the image acquisition process. To see how this comes about, we begin with the FOV, the spatial extent of the image from one edge to the opposite edge. In photography, the FOV is determined by a lens that restricts light entering the aperture so that only light rays originating within a narrow cone reach the film to produce the image. Light originating from outside the FOV is not a problem because it never reaches the film plane. But in MRI, there is no lens to restrict which signals reach the detector coil. A small surface coil is only sensitive to a small volume of tissue in its vicinity and so acts somewhat to restrict the FOV. But uniform imaging of the brain requires a head coil that is sensitive to signals generated anywhere within the head. The FOV of an MR image is not determined by the geometry of the detector coil but, instead, by how  $k$ -space is sampled. Specifically, the FOV is determined by the spacing  $\Delta k$  of measured samples in  $k$ -space.

To see how the  $k$ -space sampling interval determines the FOV, consider frequency encoding along the  $x$ -direction and the phase changes that develop between one measured sample of the signal and the next. Because of the gradient, spins at different  $x$ -positions precess at different rates and acquire a phase offset proportional to  $G\Delta t$ , where  $\Delta t$  is the time between data samples. [Figure 9.11](#) shows several combinations of gradient strengths and sampling rates and plots of the phase difference acquired between one sample and the next as a function of position. The slope of this phase versus  $x$  curve depends just on the area under the gradient between two successive samples, so the slope is twice as great in [Fig. 9.11A](#) it is in [Fig. 9.11B](#). As we move away from the center toward positive  $x$ , the phase difference grows until it reaches  $180^\circ$ ; then, it falls to  $-180^\circ$  and continues to increase from there.

Because of this cycling of the phase angle, there is a characteristic separation distance that produces a  $360^\circ$  phase difference between two points. This distance is the FOV. The cycling of the phase means that the signal from any position  $x$  will be exactly in-phase with the signal from  $x + \text{FOV}$ ,  $x + 2\text{FOV}$ , and so on. During the interval before the next sample of the net signal, the local signal at  $x + \text{FOV}$  will again acquire a  $360^\circ$  phase offset relative to the signal at  $x$ , and so on for all the measured samples. But a  $360^\circ$  phase change is indistinguishable from a  $0^\circ$  phase change; consequently, throughout the data acquisition, the signal at  $x + \text{FOV}$  behaves precisely like the signal from  $x$ , so the two signals are indistinguishable in the data.

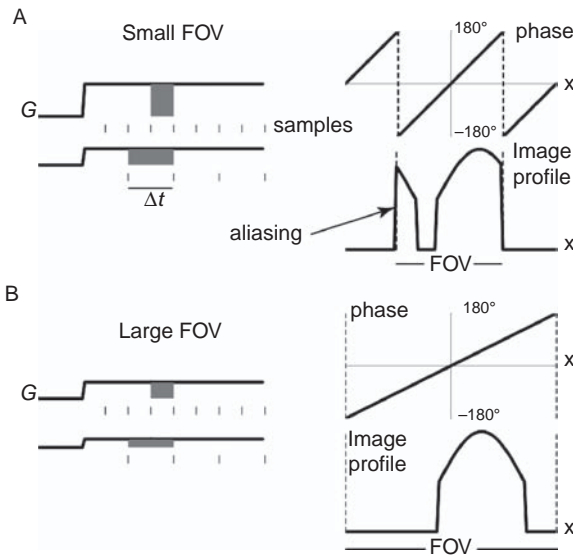


**Fig. 9.11.** Image field of view (FOV). The FOV of an image is set by the area under the frequency-encoding gradient ( $G$ ) between one data sample and the next, and this area is simply the sampling interval ( $\Delta t$ ) in  $k$ -space:  $\Delta k = G\Delta t$ . (A) Two combinations of gradient strength and sampling time that produce the same small FOV (B) Two combinations that produce a larger FOV. The phase offset acquired between one time sample and the next is plotted as a function of position on the right for each FOV. Two positions that acquire phase offsets between time samples which differ by  $360^\circ$  are indistinguishable in the data and so are mapped to the same image point. This creates a wraparound of signals outside the FOV to the other side of the image. The FOV can be increased by decreasing either  $G$  or  $\Delta t$ .

The result is that the signal from  $x + \text{FOV}$  (and  $x + 2\text{FOV}$  etc.) is mapped to the same location as the signal from  $x$  in the reconstructed image. The effect in the image is *wraparound*, in which the signal arising outside the FOV on one side appears to be added in to the signal from the other side. In signal processing, this phenomenon is called *aliasing*. The MP-RAGE image in Fig. 9.1 shows an example of wraparound, with the back of the head appearing in front of the nose.

The FOV is inversely proportional to the area under the gradient during the interval between samples ( $G\Delta t$ , the shaded areas in Fig. 9.11). To enlarge the FOV, the gradient area must be decreased. This can be done either by decreasing the gradient strength  $G$  or the sampling interval  $\Delta t$ , as shown in Fig. 9.11. Returning to the  $k$ -space view and Eq. 9.4, this area is just the sampling interval  $\Delta k$  in  $k$ -space. The wavelength corresponding to  $\Delta k$  is the FOV, and because  $k$  is reciprocally related to wavelength, the FOV increases as  $\Delta k$  is reduced. The same argument applies to all directions in  $k$ -space. An image with a rectangular FOV can be acquired by sampling with different intervals  $\Delta k_x$  and  $\Delta k_y$ . For example, an image in which  $\text{FOV}_x$  is half of  $\text{FOV}_y$  would be created if  $\Delta k_x$  is twice  $\Delta k_y$ .

In short, the FOV is determined by the sampling interval in  $k$ -space. If the object being imaged extends farther than the FOV, the parts outside the FOV are wrapped around to the other side.

## Image resolution

The spatial resolution of an image determines how well two signals can be distinguished when they originate close together in space and, in MRI, resolution is determined by the largest values of  $k$  that are sampled. Consider again frequency encoding along the  $x$ -axis. To distinguish between the signal arising at  $x$  and the signal from a short distance away  $\Delta x$ , there must be some data sample collected where the signals from  $x$  and  $x + \Delta x$  have a significantly different phase. At the center of the gradient echo, these two signals are in-phase; as time continues, their relative phase will change through the effect of the gradient. But because these two points are close together, the field difference between the two points caused by the

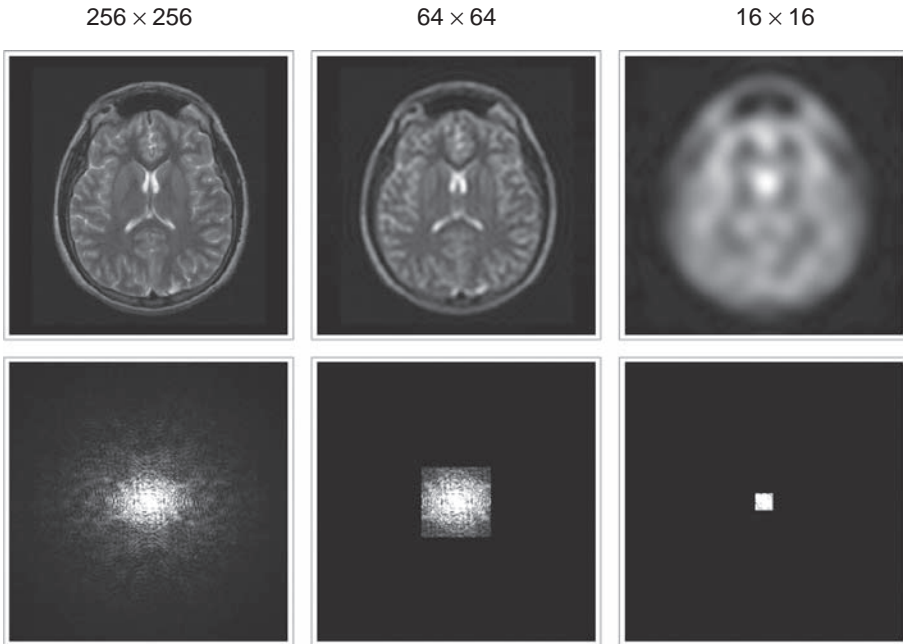


**Fig. 9.12.** Image resolution. Resolution is determined by the highest spatial frequencies that are measured, the outer points in  $k$ -space. The image is progressively blurred (top) as the extent of sampling in  $k$ -space is reduced (bottom).

gradient is small, and so the phase evolution is slow. The maximum relative phase difference will occur in the last measured data sample, where the cumulative effect of the gradient is maximum. The resolution is defined as the distance  $\Delta x$  such that, for two signals separated by  $\Delta x$ , the phase difference in the last data sample is  $180^\circ$ .

In  $k$ -space, the last data sample is a measurement at the highest sampled value of  $k_x$ , which we can call  $k_{\max}$ . High spatial resolution requires sampling out to large values of  $k_{\max}$ , as illustrated in Fig. 9.12. Note that the wavelength associated with  $k_{\max}$  is not  $\Delta x$  but rather  $2\Delta x$  because two points separated by a distance  $\Delta x$  differ in phase by  $180^\circ$ , not  $360^\circ$ . For example, for a resolution of 1 mm,  $k_{\max}$  must be 5 cycles/cm. As  $k_{\max}$  increases,  $\Delta x$  becomes smaller, and resolution improves. As with the FOV, the spatial resolution need not be the same in all directions. If  $k_{\max}$  in the  $k_y$ -direction is smaller than  $k_{\max}$  in the  $k_x$ -direction, the resolution in the  $y$ -direction will be worse. That is, a rectangular sampling pattern in  $k$ -space will create an image with different spatial resolution in  $x$  and  $y$ . This relationship is symmetrical with that for FOV. There, a rectangular array in image space was associated with different separations in  $k$ -space, which is just the  $k$ -space “resolution.” In general, the Fourier transform relationship is completely symmetrical: the resolution in one domain is determined by the FOV in the other domain (Fig. 9.13).

In summary, MRI consists of sampling in  $k$ -space. The spacing of the samples determines the image FOV ( $1/\Delta k$ ), and the largest  $k$ -value sampled determines the resolution ( $\Delta x = 1/(2k_{\max})$ ). Because both  $-k$  and  $+k$  locations are sampled, the total number of data samples along one axis in  $k$ -space is  $N = 2k_{\max}/\Delta k = \text{FOV}/\Delta x$ . In other words, for  $N$  measured samples in  $k$ -space, equally spaced along a line, the image FOV is divided into  $N$  resolution elements.

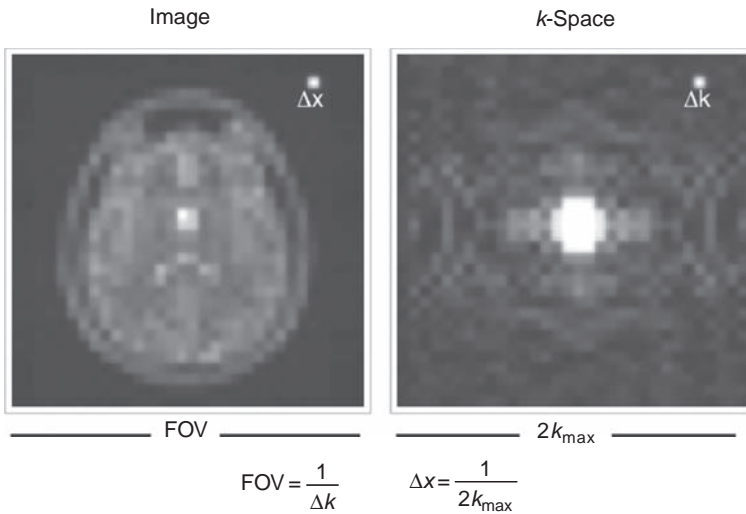


**Fig. 9.13.** The symmetry between image space and  $k$ -space. The resolution in one domain is inversely proportional to the FOV in the other domain, and vice versa.

## Pixels, voxels, and resolution elements

When an image is reconstructed from the  $k$ -space data, it is presented as a matrix of signal values. Each point in this matrix is called a pixel (from “picture element”), and on a display screen each pixel is shown as a small square with uniform intensity. Because the imaging process collects data from a certain slice thickness, there is a volume associated with each pixel, called a *voxel* (loosely from “volume element”). In practice, from an  $N \times N$  matrix of measured signal values in  $k$ -space, an  $N \times N$  matrix of image intensities is reconstructed using an algorithm called the fast Fourier transform (FFT), which dramatically speeds up the calculation of the Fourier transform (Brigham, 1974). For the FFT, it is most convenient to work with matrices whose dimensions are a power of two, so it is common to deal with matrices with dimensions of  $64 \times 64$ ,  $256 \times 256$ , and so on. The availability of the FFT has had a huge impact on many areas of technology, and it is difficult to overestimate its importance. If the FFT did not exist, it is hard to imagine that MRI could have developed into the powerful tool it is today.

Because the FFT naturally converts an  $N \times N$  matrix of points in  $k$ -space into an  $N \times N$  matrix of points in image space, the image pixel size typically is the same as the resolution element. But it is important to note that there is nothing fundamental about this, and that in some applications it may be useful to reconstruct the image with the pixel size smaller than the true resolution element. In other words, it is tempting to think that because the FFT algorithm takes the  $N \times N$   $k$ -space data and calculates a specific grid of  $N \times N$  points in the image plane, there is something special about those particular points, and that our imaging process has somehow produced measured samples of the image intensity at those particular pixel locations. In fact, each measured point in  $k$ -space describes a continuous wave covering every point in the image plane, so the data can be used to calculate the intensity at any point, not just the pixel centers that naturally emerge from the FFT. The simplest way to reconstruct the image with reduced pixel size is to place the measured,  $N \times N$   $k$ -space matrix in the center of a larger matrix, such as  $4N \times 4N$ , put zeroes in all of the locations where data were not measured (called *zero padding*), and apply the FFT to produce a  $4N \times 4N$  matrix of pixels in

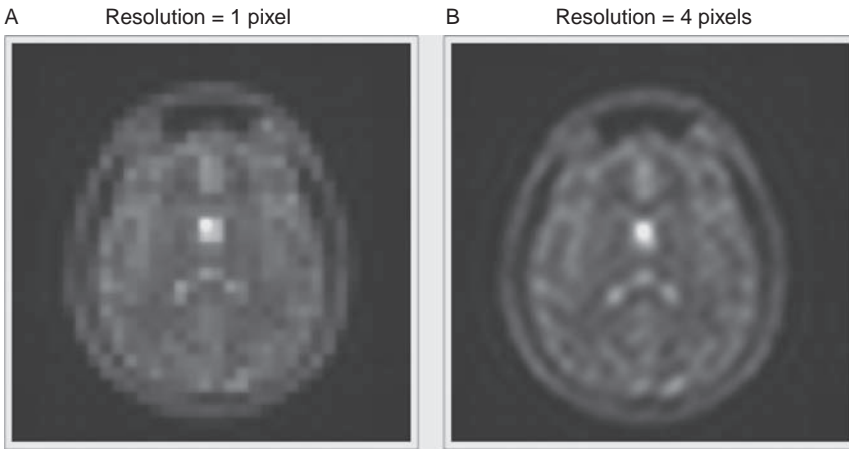


**Fig. 9.14.** Pixels and resolution elements. (A) The pixel size in an image display is often matched to the resolution, but the “tiled” look is entirely artificial. (B) When the same image is displayed with a smaller pixel size, the intrinsic blurring caused by finite resolution is better visualized.

the image plane (Fig. 9.14 illustrates this with a low resolution  $32 \times 32$  image). The spacing of samples in the  $k$ -space matrix has not changed, so the FOV of the larger image matrix is the same. Similarly, the true spatial resolution set by the sampling of  $k$ -space also has not changed, but now that resolution size is four pixels instead of one in the reconstructed image.

The effect of finite spatial resolution is to produce an image that is a blurred version of the true distribution of intensities. The process of zero padding the data to create a smaller pixel size does not add any information to that contained in the measured data; it simply makes the blurring associated with the true resolution easier to see. The nature of this blurring is described more fully in the next section. For now, it is important simply to note that any MR image, although based on only a finite amount of  $k$ -space data, can be reconstructed with any number of pixels that is desired. The imaging process creates a continuous, blurred image of the true distribution, and the pixel size is simply a choice of how to sample that blurred image for display. A pixel size that is matched to the true resolution can at times be a poor representation of the data, in the sense that the image described by the  $k$ -space data is nothing like a patchwork of square tiles. That is, the sharp jumps in intensity at the borders of pixels are entirely an artifact of the display; the MRI process creates a smoothed version of the true distribution rather than a sampled version. A good rule of thumb is that the pixel size should be reduced if the individual pixels of the display are readily apparent to the eye.

## The point spread function

Spatial resolution in the image was defined above in terms of the  $k$ -space sampling done in acquiring the image data. But how, precisely, does the blurring in the reconstructed image depend on the  $k$ -space sampling? Consider imaging a single, small point source, and imagine reconstructing an image with the pixel size much smaller than the true resolution  $\Delta x$  so the blurring can be easily seen. Ideally, we would find only a single pixel lit up, no matter how small we make the pixels in the reconstruction, because that is the true distribution. Instead, what we find is that the point source is spread out over many pixels in the image, and the shape that describes this is called, logically enough, the *point spread function* (PSF).

To see how the PSF comes about, it is helpful to use an important property of the Fourier transform called the convolution theorem (Bracewell 1965). The most familiar example of the mathematical process of convolution is smoothing. A function  $f(x)$  can be smoothed in  $x$  by replacing the value at each location  $x$  with an average of the values in the vicinity of  $x$ . The set of weights used for constructing the average can be described by a function  $w(x)$ , such that  $f(x)$  is smoothed with  $w(x)$  by sliding  $w(x)$  along the  $x$ -axis until it is centered on a point  $x$ , multiplying the two functions together, integrating to calculate the average, and then sliding  $w(x)$  to a new location in  $x$  and repeating the calculation. Then if  $h(x)$  is the resulting smoothed function, we write  $h(x) = w(x) * f(x)$ ;  $h(x)$  is the *convolution* of  $w(x)$  and  $f(x)$ . The convolution theorem says that the Fourier transform of the convolution of two functions is the product of the Fourier transforms of the two functions:  $H(k) = W(k)F(k)$ , where the capital letters denote the Fourier transform of the corresponding Function (i.e.  $H(k)$  is the Fourier transform of  $h(x)$ ). This is often a useful way to calculate convolutions, but for our purposes here it provides a powerful way of thinking about how processes in  $k$ -space, where MR data is measured, translate into effects on the reconstructed image.

To begin with, consider again the sampling in  $k$ -space during data acquisition. An ideal, true image of a continuous distribution of magnetization would specify an intensity value for every point in the plane, and the  $k$ -space representation of this distribution would similarly be continuous and extend to infinitely large values of  $k$  (top row of Fig. 9.15). We can then look at the imaging process and the sampling in  $k$ -space as modifying this true  $k$ -space distribution to create a  $k$ -space representation of a different image, but one that approximates the ideal image. There are two modifications in  $k$ -space: a discrete sampling with a spacing  $\Delta k$  and a windowing created by the finite extent of sampling, described by  $k_{\max}$ . The discrete sampling leads to the wraparound problem:  $\Delta k$  defines the FOV, and if the extent of the object is larger than the FOV, the signal wraps around. But as long as the FOV is sufficiently large to avoid wraparound, a regularly sampled  $k$ -space, with samples extending out to infinite values of  $k$ , would still represent the full resolution of the ideal image. Then the fact that  $k$ -space is only measured out to a maximum of  $k_{\max}$ , instead of infinite  $k$ , is equivalent to multiplying the full  $k$ -space distribution by a rectangular windowing function that has the value 1 between  $-k_{\max}$  and  $+k_{\max}$  and zero everywhere else (middle row of Fig. 9.15). Because windowing (multiplication) in one domain is equivalent to convolution in the other domain, multiplying the  $k$ -space distribution by this rectangular window is equivalent to convolving the true image with the Fourier transform of the windowing function. That is, the resulting reconstructed image is a smoothed version of the true image (bottom row of Fig. 9.15), and the PSF that describes the smoothing is the Fourier transform of the windowing function.

The resulting PSF, the Fourier transform of a rectangular window in  $k$ -space with an amplitude of one and a width of  $2k_{\max}$  is

$$\text{PSF}(x) = \frac{\sin(2\pi k_{\max} x)}{\pi x} \quad (9.5)$$

This form is called a *sinc* function, and Fig. 9.3 shows the shape of this function (with  $a = 2k_{\max}$ ). It takes on both positive and negative values, with oscillating lobes that diminish in intensity moving away from the center. Sampling farther out in  $k$ -space reduces the width of the PSF, while preserving the same shape. The central value is  $2k_{\max}$ , and the net area under  $\text{PSF}(x)$  is one. The first zero-crossing occurs at  $\Delta x = 1/2k_{\max}$ , the resolution of the

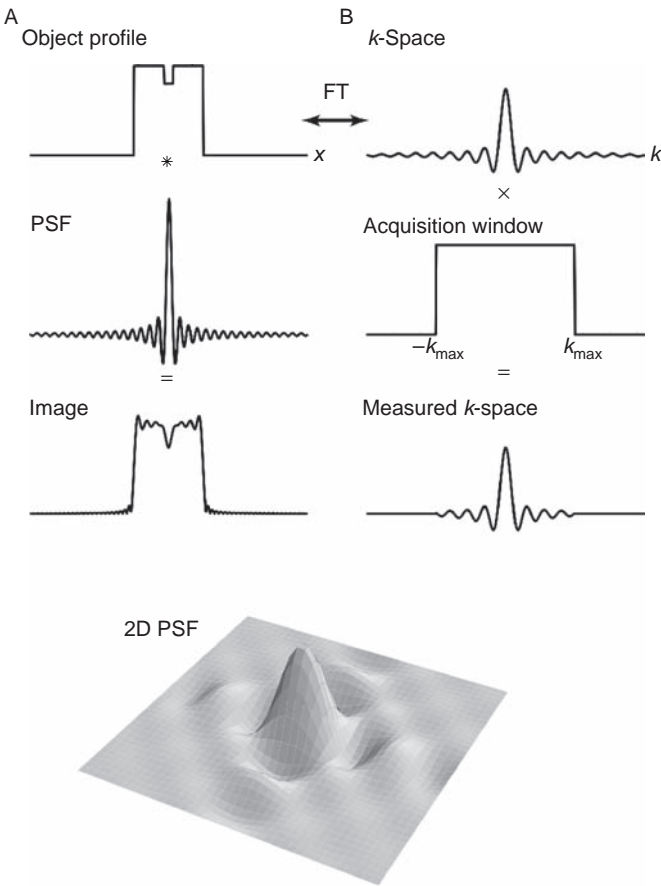


**Fig. 9.15.** The point spread function. The production of a blurred image is shown as equivalent operations in the image domain (A) and in  $k$ -space (B). The limited extent of sampling in  $k$ -space is described by multiplying the full  $k$ -space distribution by a windowing function that cuts out the high spatial frequencies. The resulting image is the convolution of the true image with the Fourier transform (FT) of the windowing function, the point spread function  $PSF(x)$ . The full two-dimensional (2D) version of the PSF is shown at the bottom. (See plate section for color version.)

image, and subsequent zero-crossings occur at integer multiples of  $\Delta x$ . The resulting image is then a convolution of the true image with  $PSF(x)$ . That is, the intensity at each point is a weighted average of the true intensities in the vicinity of the point, with the weighting factors defined by  $PSF(x)$ . This is equivalent to replacing the intensity of each point in the true image with a spread-out version of that intensity given by  $PSF(x)$ , and then adding up each of these blurred points to produce the final image. In other words,  $PSF(x)$  describes not just how a point is spread out but also how much the signal at different locations contributes to the reconstructed signal at one point. For example, the net signal measured at  $x=0$  comes mostly from signals arising between  $-\Delta x$  and  $+\Delta x$ , which add coherently. But there are also negative signal contributions from  $-1.5\Delta x$  and  $+1.5\Delta x$ . Finally, for display of this continuous, blurred version of the true image, samples are selected at discrete points defined by the pixel size. If the pixel is chosen to match the resolution so that the separation between pixels is  $\Delta x$ , then for each pixel all the other pixel locations fall on the zero-crossings of  $PSF(x)$ . This has important consequences for the statistical correlations of the noise in the reconstructed pixels and is considered in more detail in later sections.

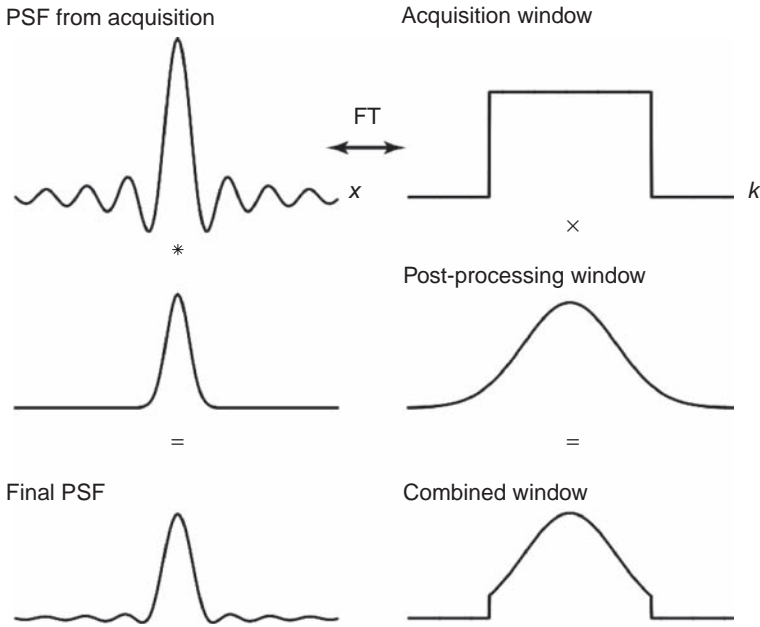


**Fig. 9.16.** Effect of image smoothing on the point spread function (PSF). The PSF is modified by additional image smoothing in post-processing, illustrated here with a Gaussian smoothing. Convolution of the image with a Gaussian smoothing is equivalent to multiplying the  $k$ -space acquisition window by a Gaussian (the Fourier transform of a Gaussian is another Gaussian) to create a combined windowing function. The final PSF is the Fourier transform of the combined window.

## A more general definition of resolution

The imaging process itself produces a blurred version of the image, but in practice the image sometimes is further smoothed during reconstruction or in post-processing. In smoothing, the image is convolved with a smoothing function, so this is equivalent to multiplying by another window in  $k$ -space, as illustrated in Fig. 9.16. The rectangular block of data is multiplied by a function that is 1 at the center but rolls off smoothly in the vicinity of  $k_{\max}$ . Again, the PSF is simply the Fourier transform of the windowing function, but because the sharp edges of the intrinsic rectangular window produced by the  $k$ -space sampling have been smoothed off, the sidelobes of the PSF are greatly reduced. The cost of this, however, is that the central lobe of the PSF is reduced and broadened, so the resolution is somewhat coarser because the high spatial frequencies are attenuated.

By altering the windowing function (i.e., filtering the  $k$ -space data), the shape of the PSF is altered, so the question of how to define the spatial resolution becomes subtle. A full description of the blurring of the image depends on the full shape of the PSF, but we would like to be able to characterize the resolution by a single number in a meaningful way. A useful approach is to think about the intensity distribution in the reconstructed image of a point source. Imagine imaging a one-dimensional distribution of magnetization density  $M(x)$  in which all the spins contributing to the signal are tightly clustered around the position  $x = 0$ . If the total magnetization of these spins is  $m$ , and they are confined within an interval  $\delta x$ , then the magnetization density is  $M(0) = m/\delta x$ . We can then imagine making  $\delta x$  smaller until it is



much less than any resolution distance  $\Delta x$  we will consider, so that  $M(x)$  is very large at  $x = 0$  (approaching infinity as  $\delta x$  approaches zero) and zero everywhere else.

The imaging process then produces a smoothed version of  $M(x)$ . For a resolution  $\Delta x$ ,  $m$  from the point source is effectively spread out over the range  $\Delta x$ , and so the signal density in the image is  $I(0) = m/\Delta x$  in the pixel containing the point source. As the resolution distance increases, the same net signal is further diluted in a larger  $\Delta x$ , and so the image intensity is reduced. This brings up a somewhat subtle point: it is tempting to think of the image intensity at a point in an MR image as the total signal arising from the voxel, but this is not really correct. Instead, the image intensity is the apparent *density* of magnetization, averaged over that voxel. In our example, the net signal  $m$  in the voxel at  $x = 0$  is constant no matter how the imaging is done, but because  $I(0)$  represents magnetization *density*, the pixel intensity will depend on the resolution. Multiplying the image intensity by the resolution will convert each density measurement into a measurement of the total signal from the voxel, which for a single image just rescales all the intensity numbers. Therefore, for considering just one resolution,  $I(x)$  can be taken as a measure of the net signal from each voxel. But when comparing images with different resolutions, it is important to remember that  $I(x)$  is really apparent magnetization density.

The result of the foregoing argument is that the image intensity in a pixel containing a point source is inversely proportional to the resolution. We can now reverse this argument and use it to *define* the characteristic resolution for any shape of the PSF. If the effect of an altered PSF is to cut the image intensity of a point source in half, then the characteristic resolution distance has doubled. We can also relate the image intensity of a point source directly to the central value of the PSF. The true image, with a point source of net signal  $m$  at  $x = 0$ , is convolved with  $\text{PSF}(x)$  to produce  $I(x)$ . Because  $M(x)$  is a point source, the image value at  $x = 0$  is simply  $m\text{PSF}(0)$ . That is,  $\text{PSF}(x)$  describes the contribution of  $M(x)$  to the net signal at  $x = 0$ , and since all the spins *are* at  $x = 0$ , the total contribution to  $I(0)$  is  $m$  weighted with  $\text{PSF}(0)$ . So if  $I(0) = m/\Delta x$  from the original argument, and  $I(0) = m\text{PSF}(0)$  from the viewpoint of the PSF, the central value of the PSF is directly related to the resolution:  $\text{PSF}(0) = 1/\Delta x$ .

To summarize, the effect of filtering in  $k$ -space on resolution can be characterized in a quantitative way by how the filtering affects the image intensity of a point source, and this is described by the magnitude of the central value of the PSF. We can take this one step farther and ask how the peak value of the PSF is related to the shape of the window in  $k$ -space. A basic property of the Fourier transform is that, in either domain, the central value is equal to the integral of the function in the other domain. So, the area under the window function,  $A_w$ , is the central value of the PSF. For example, the image acquisition effectively multiplies the  $k$ -space distribution of the true image by a window that has an amplitude of 1 and a width of  $2k_{\text{max}}$ . The area under the window  $A_w$  is then  $2k_{\text{max}}$ , and so the resolution is  $\Delta x = 1/A_w = 1/2k_{\text{max}}$ , in agreement with our original definition of resolution.

If another windowing function is applied to the data, such as a smoothing in post-processing, the resolution changes in proportion to the change in area,  $A_w$ . Specifically, the ratio of the area under the new windowing function to the original area is the same as the ratio of the old resolution to the new resolution. For example, if the area under the window is reduced by a factor of two, the characteristic resolution distance is increased by a factor of two. This definition of the resolution can be stated in another way, as the width of an equivalent rectangle that has the same area as the actual PSF and the same amplitude as the central point. Because the area under the PSF is 1, the equivalent width must be the reciprocal

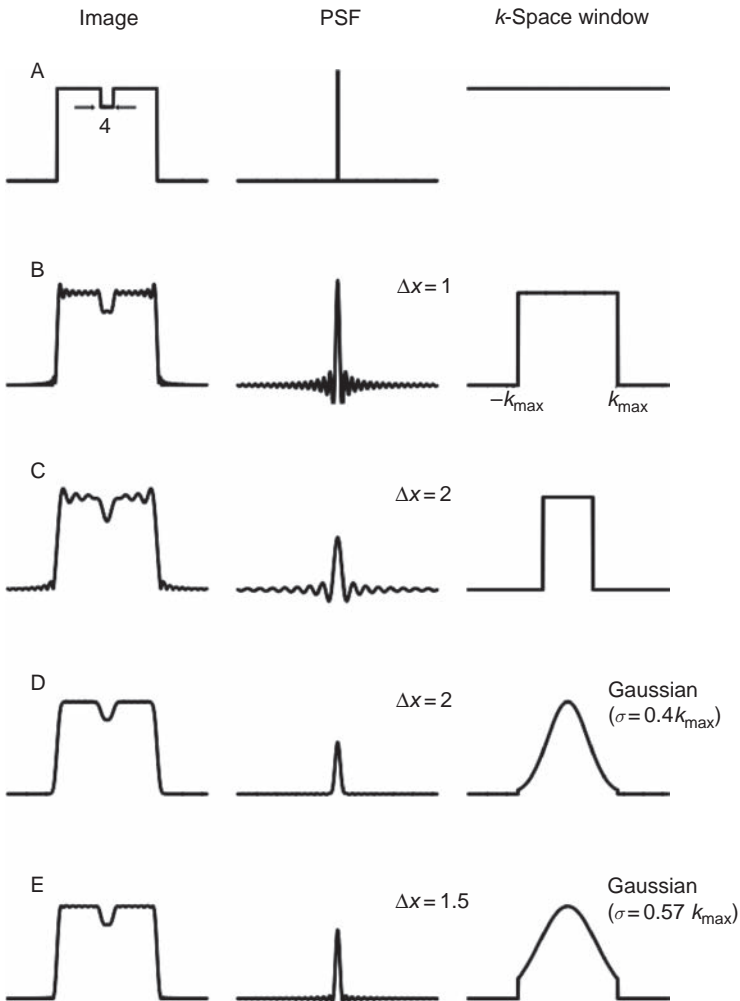


**Fig. 9.17.** Effect of smoothing on image resolution. Examples of the effects of different combined  $k$ -space point spread function (PSF) windowing functions (right column) on the PSF (middle column) and the resulting image (left column) of an ideal image profile. (A) The ideal image profile is a rectangle with an intensity depression that is 4 mm wide in the middle. (B) High-resolution acquisition with no post-processing. (C) Low-resolution acquisition with no post-processing. (D, E) Examples of the high-resolution acquisition with two degrees of Gaussian smoothing. The resolution  $\Delta x$ , as defined by the reduction in signal of a point source, is the reciprocal of the area under the combined windowing function. The sharp edges of the acquisition window create significant ripples in the PSF and in the resulting image, and the Gaussian smoothing damps them out.

of  $\text{PSF}(0)$ . For the PSF given by Eq. (9.5), the equivalent width is the distance from the center to the first zero-crossing (i.e., half the full width of the central lobe).

Fig. 9.17 illustrates this principle with different window functions. Figure 9.17A shows the true profile through the object, represented by a full  $k$ -space distribution. The object is a rectangle 32 mm wide, with a small area of reduced intensity in the middle that is 4 mm wide. Figure 9.17B shows the image that results when the acquisition covers  $k$ -space out to  $k_{\max} = 5 \text{ cm}^{-1}$ , giving a resolution of 1 mm. Note that the sidelobes of the PSF create a ringing pattern in the image near the edges (discussed in the next section). Figure 9.17C–E shows examples

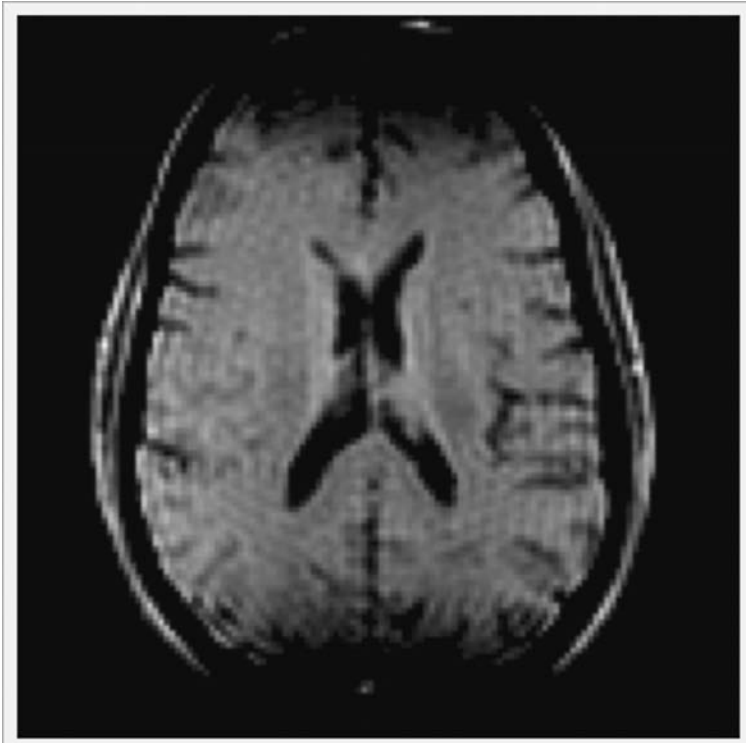


**Fig. 9.18.** Gibbs artifact (or truncation artifact). The ringing pattern illustrated in this brain image occurs because of the ripples of the point spread function in low-resolution images.

of post-processing windows to smooth the data: Fig. 9.17C uses a narrower rectangular window, whereas Fig. 9.17D,E show the effect of Gaussian smoothing. In each case, the resolution is defined by the amplitude of  $\text{PSF}(0)$ , but clearly the resolution itself does not fully describe the effect on the reconstructed image, as can be seen by comparing Fig. 9.17C and 9.17D. Both have a resolution of 2 mm, but the sidelobes of the PSF and the ringing in the image are suppressed by the Gaussian smoothing. We will return to the question of image smoothing in the context of noise reduction in Ch. 10. But first we consider the source of the ringing artifact in more detail.

## Gibbs artifact

The filtering described above to reduce the sidelobes of the PSF illustrates a fundamental property of the Fourier transform: a sharp edge in one domain requires many components to represent it accurately in the other domain. In the filtering example, a sharp boundary to the sampling in  $k$ -space produces an extended PSF with many sidelobes in image space. When this PSF is convolved with a sharp edge in image space, such as the edge of the brain, the resulting image of that edge is both blurred and shows a “ringing” pattern that looks like small waves emanating from the edge into the brain (Fig. 9.18). Mathematically, this pattern simply results from the lobes of the PSF. But another way of describing the problem is that a sharp edge requires an infinite range of spatial frequencies, and with the finite  $k$ -space sampling the highest frequencies are not measured.

We can then look at the process of building up a sharp edge by successively adding the spatial frequencies up to a given cut-off frequency (Fig. 9.19). As more spatial frequencies are

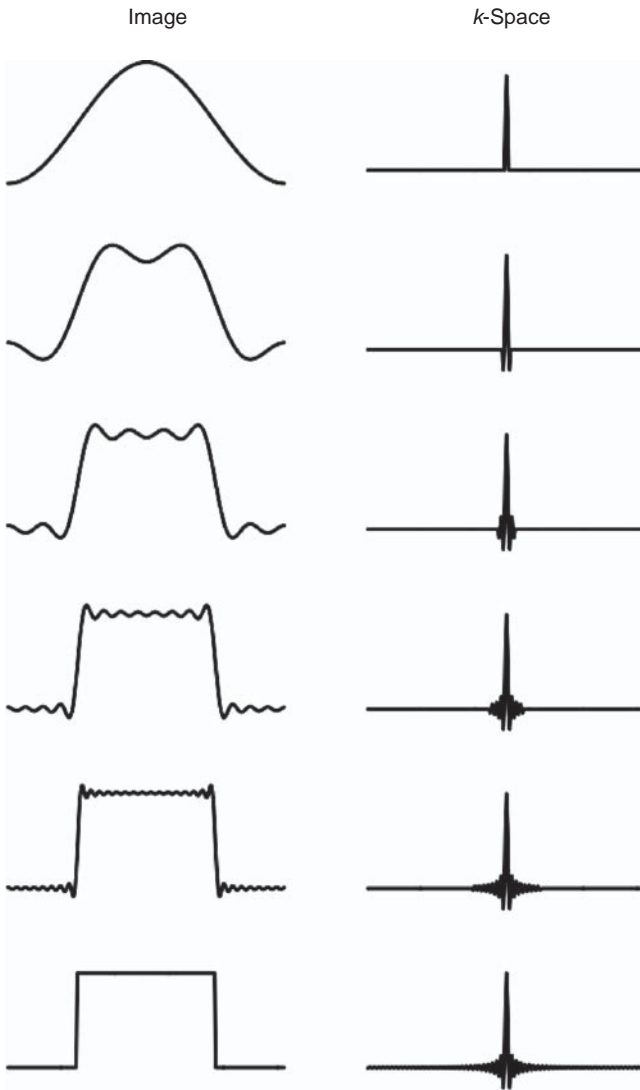


**Fig. 9.19.** Gibbs phenomenon. Effect of representing a sharp edge (bottom row) with a finite range of  $k$ -space values. Because a sharp edge requires an infinite range of frequencies for an accurate description, any finite set of  $k$ -space samples creates ripples. Remarkably, the magnitude of the overshoot at the edge does not decrease with more samples, although the wavelength of the ripples becomes shorter.

added, the resulting curve approaches closer to the sharp step function, with the slope of the blurred edge continuously increasing toward a vertical line. But there is a fascinating way in which the resulting shape still differs from a clean step function. The wavelength of the ripples on both sides of the edge decreases as more frequencies are added in, but the *amplitude* of the ripples stays the same. Specifically, the overshoot at the top and the undershoot at the bottom are always approximately 9% of the amplitude of the step. This curious effect of the Fourier transform was studied by the physicist Willard Gibbs around the turn of the nineteenth century and is usually called Gibbs phenomenon (Bracewell 1965). The ringing artifact near sharp edges in an MR image is usually referred to as a Gibbs artifact, or *truncation* artifact, because it results from the truncation of sampling in  $k$ -space.

To look more closely at how the Gibbs artifact comes about, consider a non-ideal step in which the transition from one intensity level to another is described by a linear change over a distance  $\delta x$ . Such an edge is described by spatial frequencies up to approximately  $1/\delta x$ . If the cut-off of  $k$ -space sampling is much smaller than this frequency, there will be a Gibbs artifact owing to the missing spatial frequencies. If the  $k$ -space sampling extends out far enough to include  $k = 1/\delta x$ , the edge is reproduced with reasonable fidelity. For a true step function, the required values of  $k$  extend to infinity. In practice, edges of tissues in an MR image are not perfectly sharp. The finite thickness of the imaged slice generally leads to some slight angling of tissue boundaries, so the transition is broadened. As a result, Gibbs artifact can usually be eliminated, or reduced to an acceptable level, by increasing spatial resolution. For dynamic imaging, such as EPI for blood oxygenation level dependent (BOLD) fMRI studies, the spatial resolution is coarse, and Gibbs artifact can be quite pronounced.

An interesting variation of the Gibbs artifact occurs when imaging a thin band embedded in a background with a different intensity. When the width of the band is large, the Gibbs artifact appears at both edges, but the center is reasonably flat. When the width begins to approach the intrinsic resolution, the Gibbs artifacts from the two sides begin to overlap. When the width is four resolution elements, the ripples reinforce each other, creating a striking thin dark line down the middle of the band. This artifact can give a pronounced, but false, impression of a trilaminar structure. Such an artifact is sometimes seen in imaging of the spinal cord and articular cartilage (Frank *et al.* 1997).

## References

- Bracewell RN (1965) *The Fourier Transform and its Applications*. New York: McGraw-Hill
- Brigham EO (1974) *The Fast Fourier Transform*. Englewood Cliffs, NJ: Prentice-Hall
- Edelstein WA, Hutchison JMS, Johnson G, Redpath T (1980) Spin warp NMR imaging and applications to human whole body imaging. *Phys Med Biol* **25**: 751–756
- Frank LR, Brossman J, Buxton RB, Resnick D (1997) MR imaging truncation artifacts can create a false laminar appearance in cartilage. *AM J Roentgenol* **168**: 547–554
- Kumar A, Welte D, Ernst RR (1975) NMR Fourier zeugmatography. *J Magn Reson* **18**: 69–83
- Lauterbur PC (1973) Image formation by induced local interactions: examples employing nuclear magnetic resonance *Nature* **242**: 190–191
- Twieg DB (1983) The k-trajectory formulation of the NMR imaging process with applications in analysis and synthesis of imaging methods. *Med Phys* **10**: 610–621

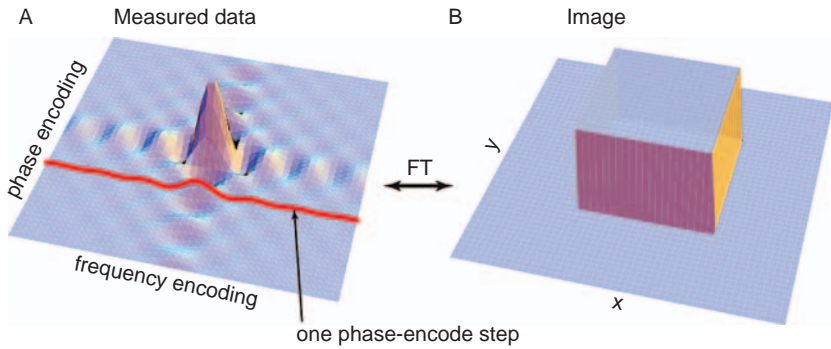


**Plate 1 (Fig. 4.5).** Basic Fourier imaging. The measured data is the two-dimensional Fourier transform (FT) of the spatial distribution of transverse magnetization (pictured as a square in B). Each time the pulse sequence in Fig. 4.2 is repeated one line is measured, and the phase-encoding step moves the sampling to a new line. Applying the FT along both directions yields the image. The representation of the image in terms of spatial frequencies (A) is described as  $k$ -space, where  $k$  is a spatial frequency (inverse wavelength).

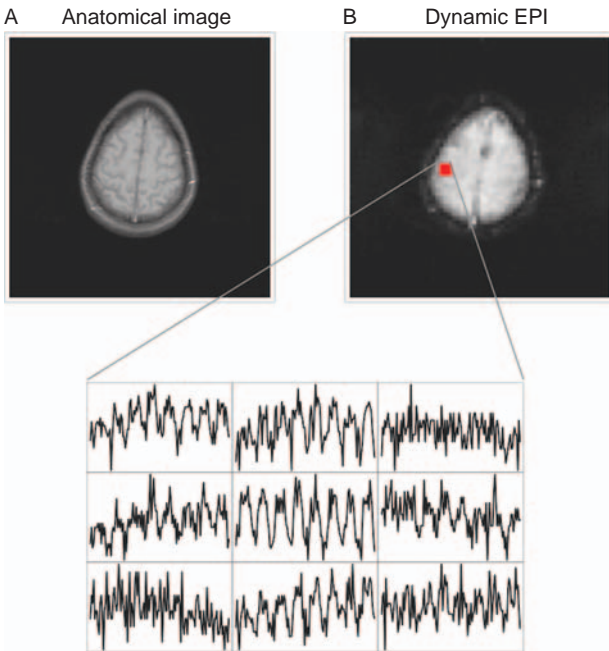


**Plate 2 (Fig. 5.3).** Signal changes in a BOLD, study. (A) High-resolution anatomical image ( $256 \times 256$  matrix) cutting through the central sulci and the hand motor and sensory areas. (B) One image from a series of 128 low-resolution dynamic images ( $64 \times 64$  matrix) collected every 2 s with EPI. The signal time courses from echo planar imaging (EPI) for a  $3 \times 3$  block of pixels are shown below. During the data acquisition, the subject performed eight cycles of a bilateral finger tapping task, with one cycle consisting of 16 s of tapping followed by 16 s of rest. Several pixels show clear patterns of signal variation that correlate with the task. (Data courtesy of L. Frank.)

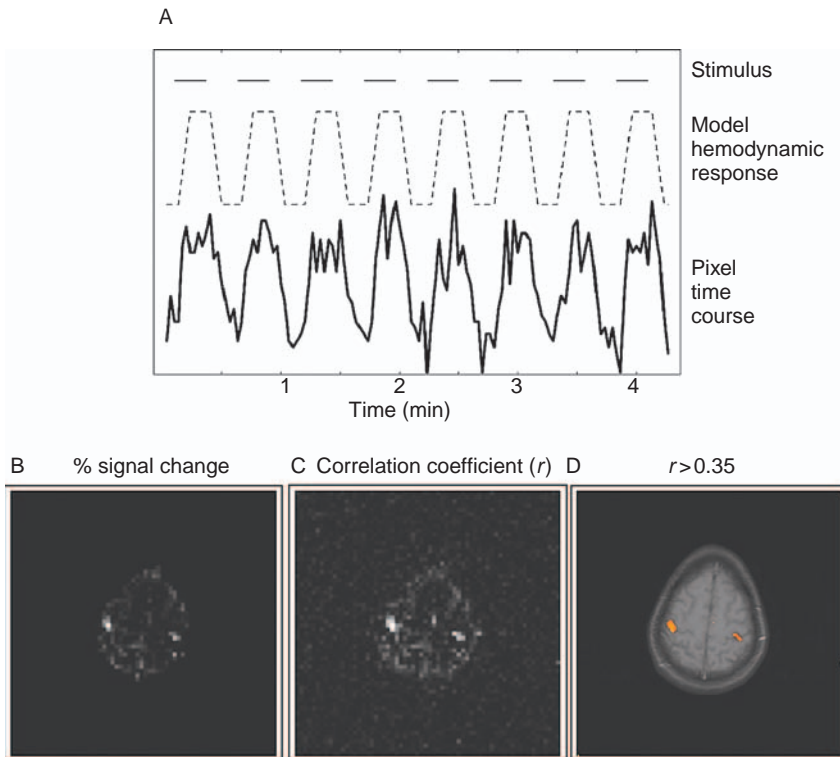


**Plate 3 (Fig. 5.4).** Correlation analysis of dynamic echo planar imaging data to identify pixels showing evidence of activity. (A) The hemodynamic response is modeled as a trapezoid, with 6 s ramps and a delay of 2 s from the beginning of the stimulus. (B,C) By correlating the model function with a pixel time course, the signal change (B) and the correlation coefficient  $r$  (C) can be calculated. (D) The pixels passing a threshold of  $r > 0.35$  are highlighted on the anatomical image. For this final display the  $64 \times 64$  calculated image of  $r$  was interpolated up to  $256 \times 256$  to match the high-resolution image.

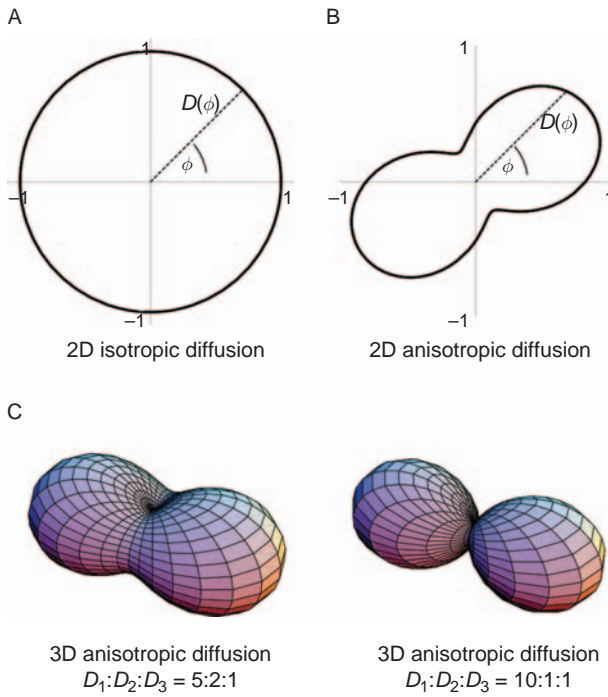


**Plate 4 (Fig. 8.7).** Anisotropic diffusion. In anisotropic diffusion, the measured value of the diffusion coefficient  $D$  is different for different directions. We can visualize this by plotting a curve (in two dimensions) such that the distance to the curve along an angle  $\phi$  is proportional to the value of  $D$  that would be measured along that direction. (A) For isotropic diffusion, this curve is a circle. (B) For anisotropic diffusion, it takes on a dumbbell shape. (C) In three dimensions, the equivalent curve is a peanut-shaped surface, for two sets of ratios of the principal diffusivities.



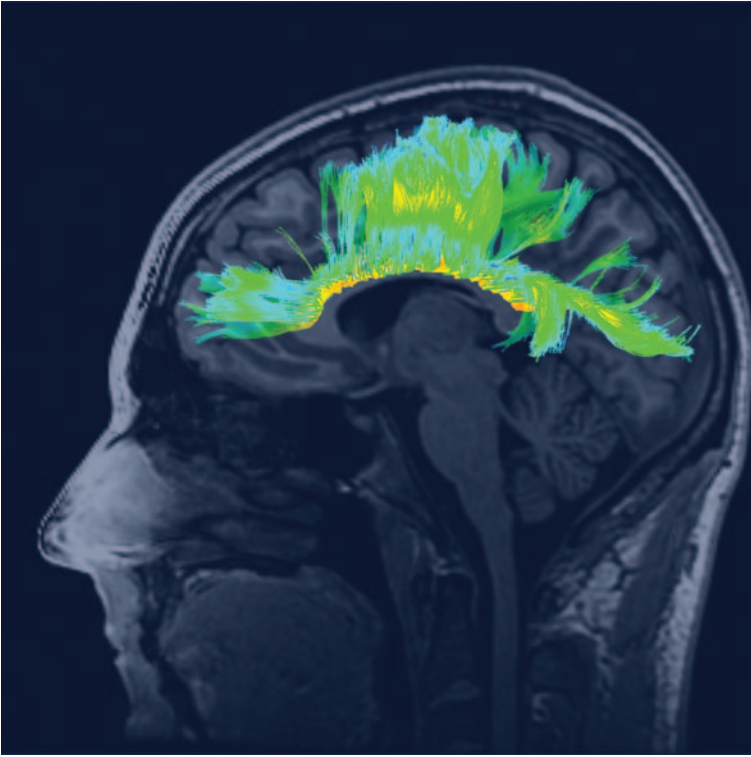


**Plate 5 (Fig. 8.11).** White matter fiber tract mapping. Fiber tracts calculated from diffusion tensor images with seeds in the central region of the corpus callosum. (Data courtesy of L. Frank)

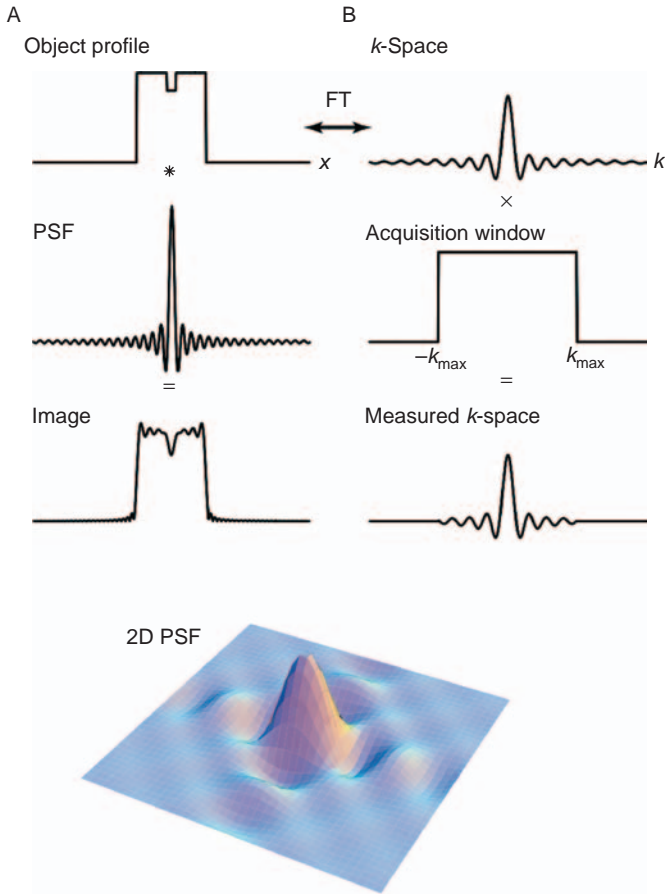
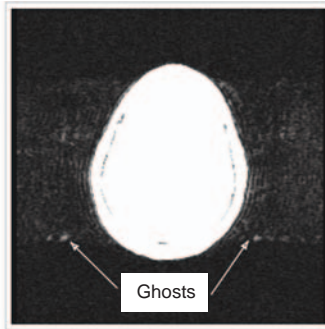


**Plate 6 (Fig. 9.15).** The point spread function. The production of a blurred image is shown as equivalent operations in the image domain (A) and in  $k$ -space (B). The limited extent of sampling in  $k$ -space is described by multiplying the full  $k$ -space distribution by a windowing function that cuts out the high spatial frequencies. The resulting image is the convolution of the true image with the Fourier transform (FT) of the windowing function, the point spread function  $PSF(x)$ . The full two-dimensional (2D) version of the PSF is shown at the bottom.

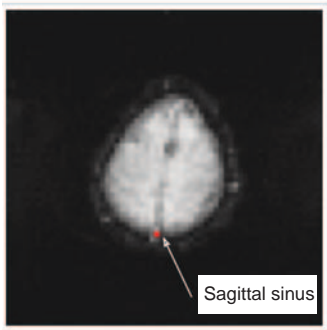
FLASH



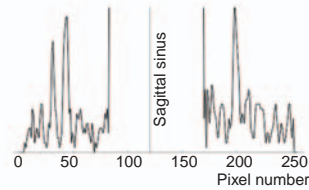
FLASH (windowed)



EPI



FLASH image profile



EPI time series spectrum

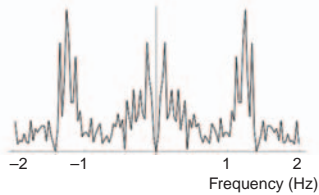


**Plate 7 (Fig. 11.10).**

Physiological motion artifacts. Pulsatile flow in the sagittal sinus creates ghost images of the vessel in a conventional fast low-angle shot (FLASH) image acquired in 32 s with a repetition time of 250 ms, 128 phase-encoding steps (along a left/right axis), and reconstructed as a 256 matrix (so one resolution element is 2 pixels). The spectrum of a dynamic time series of echo planar imaging (EPI) images of the same section acquired with the same repetition time for an equal period of time show strong cardiac components at approximately 1.2 Hz. The ghosting pattern in the FLASH image is directly related to the spectrum of the fluctuations graphs.

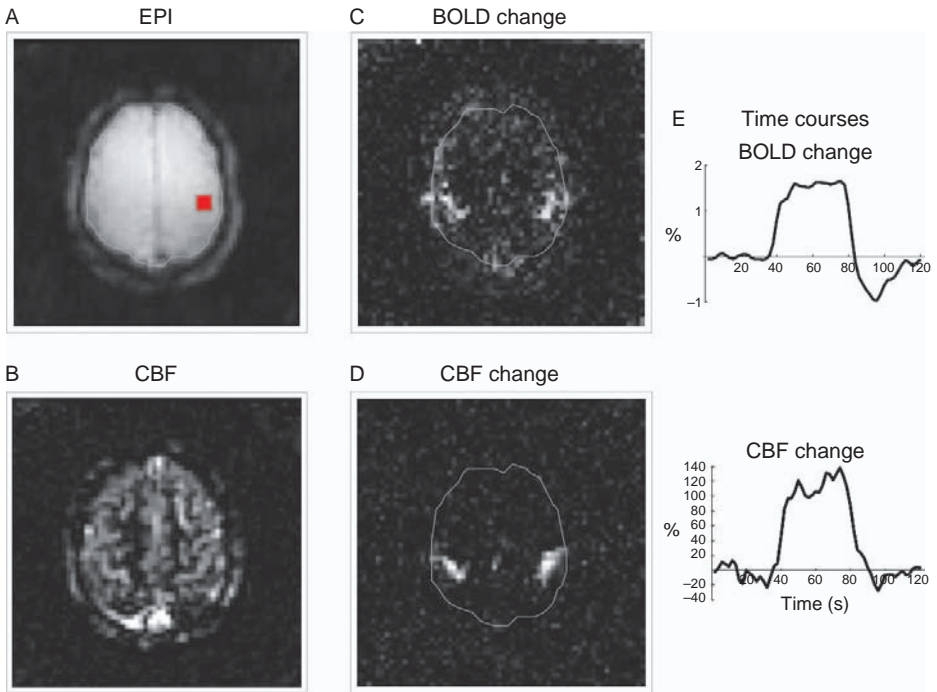


**Plate 8 (Fig. 13.14).** Simultaneous measurements of flow and BOLD changes with activation. Data from a combined flow and BOLD finger-tapping study at 1.5T acquired with a spiral dual-echo acquisition are shown. The arterial spin label pulse sequence was PICORE–QUIPSS II, with the flow time series calculated from the first echo ( $TE = 3$  ms) and the BOLD time series calculated from the second echo ( $TE = 30$  ms). (A) The echo planar image shows a  $3 \times 3$  region of interest (ROI), and the average time courses for the ROI are on the right (average of 16 cycles, 40 s of tapping alternated with 80 s of rest). (B) The average cerebral blood flow (CBF) image is on the lower left. (C, D) Maps of fractional signal change with activation measured for BOLD (C) and CBF (D). The activation maps are similar but not identical. (E) The flow and BOLD time courses are distinctly different, with the BOLD signal showing a distinct post stimulus undershoot. (Data courtesy of T. Liu)

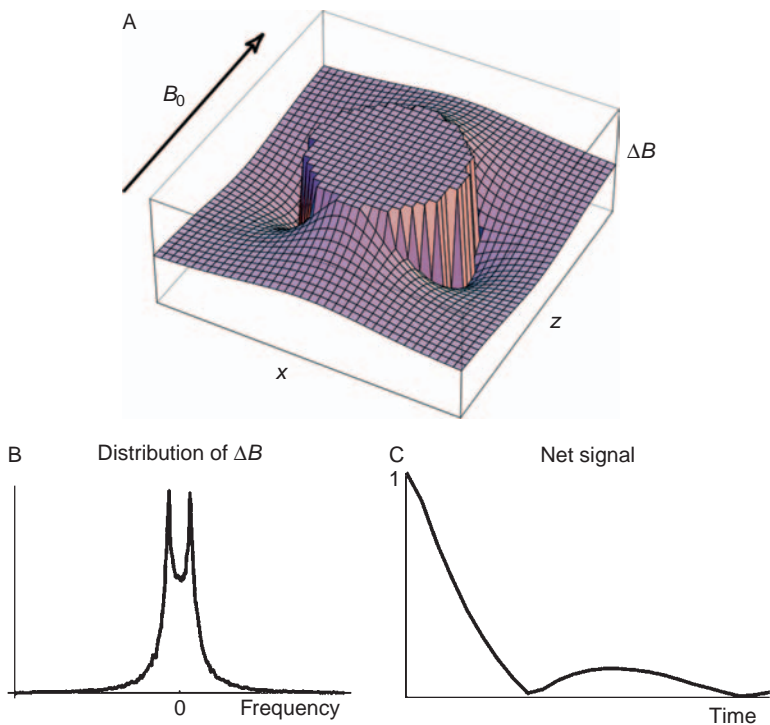


**Plate 9 (Fig. 14.2).** Field distortions around a magnetized blood vessel. (A) A single magnetized cylinder oriented perpendicularly to the magnetic field  $B_0$  creates field offsets ( $\Delta B$ ) in the surrounding space, with the field increased along the main field axis and decreased along a perpendicular axis. (B) The distribution of fields creates a resonant frequency spectrum with two peaks. (C) The Fourier transform of the frequency spectrum shows how the net signal evolves in time.

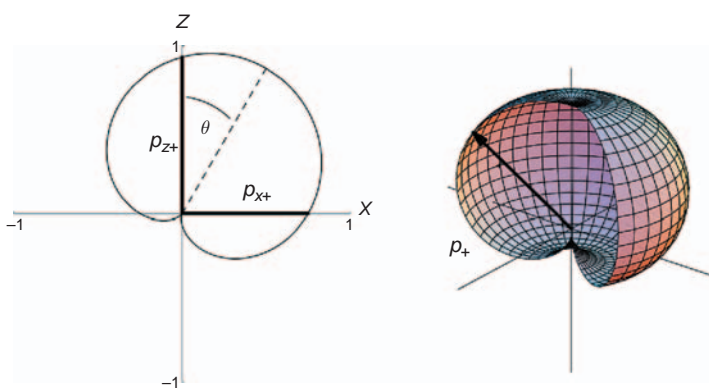


**Plate 10 (Fig. A.4).** The spin state of the proton. The spin state of the proton describes the probability that a measurement of the spin component along a particular axis will yield spin up or spin down, the only two possible results allowed by quantum theory. This state can be visualized by plotting the surface shown on the right, such that the distance from the origin to the surface along a particular direction is the probability for measuring spin up along that axis. A two-dimensional cut through this surface is shown on the left. The spin state is described by angles  $\theta$  and  $\phi$ , which are  $30^\circ$  and  $0^\circ$  in this example. The time evolution of the spin state is a steady precession of this surface such that  $\phi = \phi_0 + \omega_0 t$ , where  $\omega_0$  is the classical Larmor frequency.

<b>Introduction</b>	page 232
<b>Conventional imaging techniques</b>	233
Spin echo	233
Asymmetric spin echo	234
Gradient echo	236
Echo-shifted pulse sequences	238
Volume imaging	240
Exploiting symmetries of $k$ -space	241
<b>Fast imaging techniques</b>	242
$k$ -Space sampling trajectories for fast imaging	242
Echo planar imaging	243
<b>Safety issues</b>	249

## Introduction

Chapters 6–8 described the enormous flexibility of the MR signal, how it depends on several tissue properties such as relaxation times and diffusion, and how it can be manipulated to emphasize these different properties by adjusting pulse sequence parameters. The sensitivity to the relaxation times is controlled by adjusting timing parameters such as the repetition time (TR) or the echo time (TE), and the MR signal becomes sensitive to the self-diffusion of water by adding additional field gradient pulses. Chapter 9 described how images are made by using gradient fields and exploiting the fact that the NMR precession frequency is directly proportional to the local magnetic field. The central idea of MRI is that the application of field gradients makes the net signal over time trace out a trajectory in  $k$ -space, the spatial Fourier transform of the distribution of the MR signal. The image is reconstructed by applying the Fourier transform to the measured data. Because the gradients are under very flexible control, many trajectories through  $k$ -space are possible.

In this chapter, we bring together these ideas from the previous chapters to describe several techniques for imaging in terms of how they produce useful contrast and how they scan through  $k$ -space. This review is selective, focusing on techniques that illustrate basic concepts of imaging or that are commonly used for fMRI. Most fMRI work is done with single-shot echo planar imaging (EPI), so this technique is presented in more detail.

A central idea running throughout MRI is that the signal is a transient phenomenon: it does not exist until we start the experiment, and it quickly decays away. When we make an image of that signal, we can think of it as a snapshot of the signal at a particular time. This is necessarily an approximation because the imaging process requires some time for the signal to evolve under the influence of the imaging gradients and trace out a trajectory in  $k$ -space. However, the contrast in an image is primarily determined by the magnitude of the MR

signal when the sampling trajectory measures the  $k=0$  sample. This is the sample that directly reflects the raw signal, and all the other samples serve to encode the spatial distribution of the signal. So we can think of an MR image as a snapshot of the transient distribution of magnetization at the time the  $k=0$  sample is measured.

As described in earlier chapters, two broad classes of imaging techniques are spin echo (SE) and gradient recalled echo (GRE). An SE technique includes a  $180^\circ$  radiofrequency (RF) refocusing pulse that corrects for signal loss caused by magnetic field inhomogeneities. After an excitation pulse, the SE signal decays exponentially with a time constant  $T_2$ , and for a GRE pulse sequence the signal decays through a combination of  $T_2$  and local field inhomogeneity effects, described as  $T_2^*$  decay. For a particular TE, the SE signal is attenuated by a factor  $e^{-TE/T_2}$ , and the attenuation of the GRE signal is attenuated by a factor  $e^{-TE/T_2^*}$ . Whenever we refer to the TE of an imaging pulse sequence, we mean the time when the  $k=0$  sample is measured. In fact,  $T_2^*$  decay is a rather complicated process, depending on intrinsic properties of the tissue, chemical shift, and even the voxel size of the image. These complications will be considered in [Ch. 11](#), and for now we can assume that the GRE signal simply decays exponentially with time constant  $T_2^*$  and consider the basic pulse sequences for SE and GRE imaging.

## Conventional imaging techniques

### Spin echo

A helpful graphical tool in understanding how imaging pulse sequences work is the pulse sequence diagram, showing how RF and gradient pulses are played out over time (e.g., [Fig. 10.1](#)). A pulse sequence diagram shows a separate time line for each of the different events that occur. This includes lines for RF pulses, gradient pulses along each of the three spatial axes, and a data sampling line indicating when samples are measured. The full pulse sequence diagram for a conventional two-dimensional SE pulse sequence is shown in [Fig. 10.1](#). During the application of the  $90^\circ$  and  $180^\circ$  RF pulses, a slice selection gradient is applied along the  $z$ -axis. After the  $90^\circ$  excitation pulse, the phase-encoding gradient in  $y$  is applied, and the stepped pattern in the diagram indicates that the amplitude of this gradient is incremented each time the pulse sequence is repeated. The data acquisition is centered on

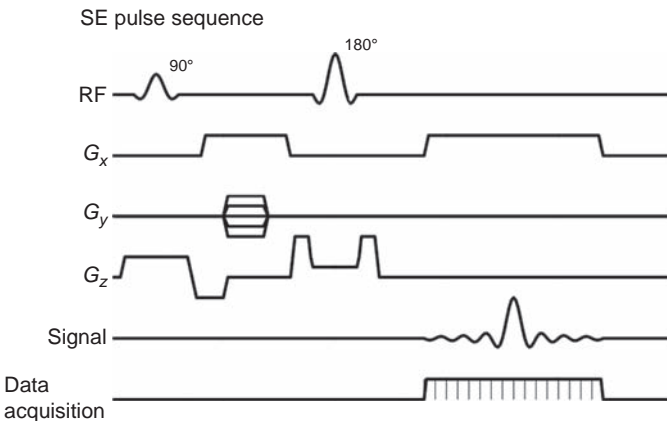


**Fig. 10.1.** Pulse sequence diagram for a spin echo (SE) image acquisition. Each line shows how one component of the pulse sequence plays out over time. The radiofrequency (RF) pulses excite a signal, and the spatial information (gradient pulses [ $G$ ]) is encoded with slice selection along  $z$ , frequency encoding along  $x$ , and phase encoding along  $y$ .

the SE and is collected with a read-out gradient turned on in the  $x$ -direction. The sampling trajectory in  $k$ -space is then a raster pattern, with one line in  $k_x$  measured after each excitation pulse.

In addition to these primary gradient pulses for slice selection along  $z$ , phase encoding along  $y$ , and frequency encoding along  $x$ , there are a few other gradient pulses shown in Fig. 10.1 that are necessary to make high-quality images. After the slice selection pulse in  $z$ , a shorter, negative  $z$ -gradient pulse is applied. The purpose of this  $z$ -compensation gradient is to refocus phase dispersion created by the slice selection gradient. The slice selection RF pulse takes some time to play out, typically 3 ms or more, so as the transverse magnetization begins to form during this excitation pulse, it also precesses at the frequency set by the slice selection gradient. The spins at different  $z$ -positions within the selected slice will begin to get out of phase with one another, and if this phase dispersion through the slice thickness is not corrected, the image signal will be severely reduced. The negative  $z$ -gradient pulse performs the refocusing, effectively creating a gradient echo with spins at all  $z$ -levels back in phase at the end of the  $z$ -gradient pulse. For the gradient pulse during the slice selection  $180^\circ$  RF pulse, the phase dispersion effects of the gradient are naturally balanced because of the symmetrical placement of the gradient pulse around the  $180^\circ$  pulse. In other words, whatever phase changes are produced by the first half of the gradient pulse are reversed by the  $180^\circ$  pulse, and the second half of the gradient pulse then cancels these phase changes.

Prior to the positive read-out gradient pulse along  $x$ , a negative  $x$ -gradient pulse, called the  $x$ -compensation pulse, is applied. As described in Ch. 9, this gradient pulse combination produces a gradient echo at the center of the data acquisition window so that Fourier components corresponding to both positive and negative values of  $k$  can be measured. The center of each line in  $k$ -space ( $k_x = 0$ ) is sampled at the time of the gradient echo, and so this defines the time of our snapshot of the distribution of transverse magnetization. There are, therefore, two echoing processes occurring during data collection in an SE pulse sequence: the gradient echo produced by the  $x$ -gradient pulses and the RF echo produced by the  $180^\circ$  pulse. In a standard SE sequence, these two echoes are aligned so that they occur at the same time. In this way, any dephasing of the spins caused by field inhomogeneities is refocused when the center of  $k$ -space is measured, so the resulting image intensities depend only on  $T_2$  decay, and not on  $T_2^*$ .

## Asymmetric spin echo

In the standard SE acquisition the gradient echo and SE are aligned, but another possibility is to deliberately misalign them. In an *asymmetric spin echo* (ASE) pulse sequence, the relative timings of the gradient and RF pulses are offset so that the SE is shifted by a time  $\tau$  from the center of acquisition, the time when the  $k_x = 0$  sample is measured (Fig. 10.2). As a result, the imaged signal is partly dephased by the effects of inhomogeneities. By making repeated measurements and varying  $\tau$  but holding TE fixed, one could plot out a signal decay curve  $S(\tau)$  (Hoppel *et al.* 1993). However, the time constant for decay of this curve is neither  $T_2$  nor  $T_2^*$ . The decay with increasing  $\tau$  has no  $T_2$  component because TE is fixed, and signal decay results just from the dephasing effects of field inhomogeneities. To describe this additional decay in an ASE sequence in a semiquantitative way, we need to introduce an additional decay time,  $T_2'$ , with the relationship:

$$\frac{1}{T_2'} = \frac{1}{T_2^*} - \frac{1}{T_2} \quad (10.1)$$



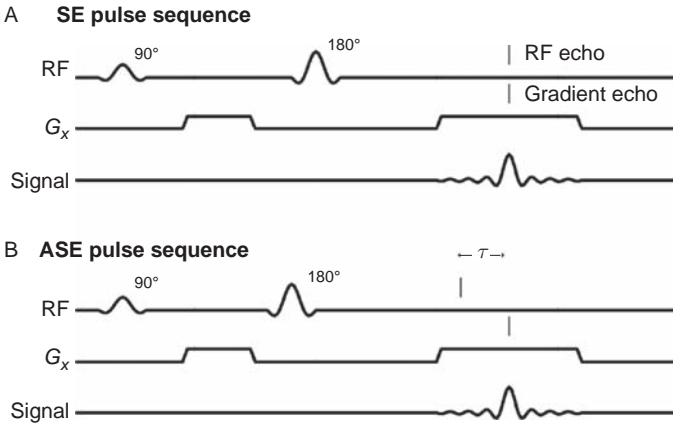


**Fig. 10.2.** Asymmetric spin echo (SE) pulse sequence. In an SE imaging sequence, there are two echoing processes at work: a radiofrequency (RF) echo from the 180° RF pulse and a gradient echo from the read-out gradient pulses. (A) In a standard SE, these two echoes occur at the same time. (B) However, if the 180° pulse is shifted by a time  $\tau/2$ , the time of the RF echo is shifted by a time  $\tau$  relative to the gradient echo. The time of the gradient echo marks the time when the  $k=0$  sample is measured, so this is the time that determines contrast in the image. Because the RF echo is displaced in this asymmetric (ASE) pulse sequence, the local phase evolves owing to field inhomogeneities for a time  $\tau$ , giving the ASE sequence a greater sensitivity to microscopic magnetic susceptibility effects.

In other words,  $T_2'$  describes the part of the full unrefocused relaxation rate described by  $T_2^*$  that results only from field inhomogeneities, and not from  $T_2$  decay itself. The reason this is a semiquantitative relation is that the effects of field inhomogeneities often do not produce a pure monoexponential decay. Nevertheless, this relation is useful in thinking about the different signal characteristics of SE, ASE and GRE pulse sequences. In short, the SE signal decays with increasing TE by  $T_2$  effects alone; the GRE signal decays with TE by  $T_2$  and field inhomogeneity effects, and the ASE signal decays with  $\tau$  by the field inhomogeneity effects alone.

The ASE pulse sequence was originally introduced as a way of separating the fat and water signals in an image (Buxton *et al.* 1986; Dixon 1984). Roughly speaking, the protons in lipids precess at a rate 3.5 ppm different from those of water. In fact, there are a number of lipid proton resonances corresponding to different chemical forms of hydrogen, and there is even a resonance near that of water. But the average effect can be approximated as though it were a single resonance shifted from water. In an SE acquisition, these chemical shift effects are refocused so that the fat and water signals are back in phase. (However, the fat signal is displaced in the image because of the resonant frequency shift, as discussed in Ch. 11.) With an ASE sequence, the fat and water signals precess relative to each other at a rate determined by the resonant frequency shift. At 1.5 T, fat and water complete a full 360° relative phase rotation every 4.4 ms. Then for a voxel containing both fat and water, the ASE signal will oscillate as  $\tau$  is increased: when  $\tau = 2.2$  ms, the two signals are out of phase, and so subtract from each other, but at  $\tau = 4.4$  ms, they add coherently again. A GRE sequence also shows this oscillation but it is superimposed on an overall decay from  $T_2$  (e.g., Fig. 7.6).

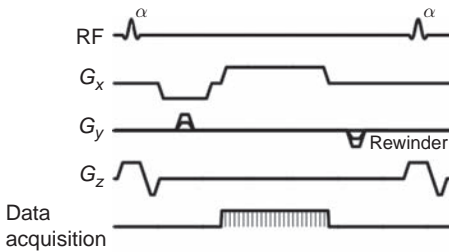
In fMRI studies based on the blood oxygenation level dependent (BOLD) effect, the goal is to measure small changes in the MR signal produced by microscopic field inhomogeneities caused by the presence of deoxyhemoglobin. The SE pulse sequence is the least sensitive to these effects. In fact, if the spins generating the MR signal were perfectly static, the SE would

perfectly refocus the phase changes produced by these field offsets, and the SE signal would be insensitive to the BOLD effect. The reason that the SE sequence is sensitive to the BOLD effect at all is that the spins move around through diffusion, wandering through regions of variable field and accumulating phase offsets that are not completely refocused by the SE (Ch. 8). The GRE sequence is the most sensitive to the BOLD effect because the phase offsets from field inhomogeneities grow during the full TE. The ASE sequence is intermediate in sensitivity between SE and GRE, and because the time for field offset effects to accumulate depends on  $\tau$ , rather than TE, there is somewhat more flexibility in tuning the sensitivity of the pulse sequence.

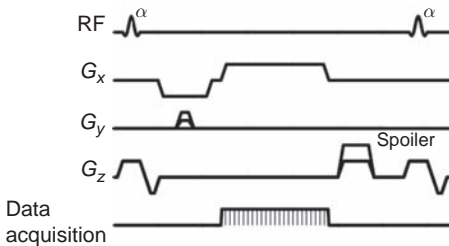
## Gradient echo

The diagrams for three different types of GRE imaging pulse sequences are shown in Fig. 10.3. The defining characteristic of a GRE pulse sequence is the absence of a  $180^\circ$  RF refocusing pulse. A gradient echo is still required at the center of data acquisition (TE), so the

### A Steady-state sequence



### B Spoiled sequence



### C SSFP (PSIF)

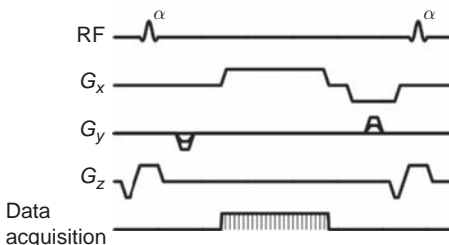


**Fig. 10.3.** Three types of gradient recalled echo (GRE) imaging. In GRE imaging with short repetition time, each radiofrequency (RF) pulse generates both a new free induction decay (FID) and echoes of previous FIDs. (A) With a steady-state sequence (e. g., GRASS, FISP), both the new FID and the echoes contribute to the signal. (B) With a spoiled sequence (e. g., FLASH, SPGR), the echo component is destroyed. (C) With a steady-state free precession (SSFP or PSIF) sequence, only the echoes contribute to the signal. See text for details of the specific techniques.

sign of the initial  $x$ -compensation gradient is reversed from the SE sequence. Other than this change, the rest of the pulse sequence is similar to the standard SE sequence, and the sampling trajectory in  $k$ -space is the same: one line in  $k_x$  is measured for each RF excitation pulse. However, a critical practical difference between the conventional SE and GRE acquisitions is that TR can be made much shorter with a GRE sequence (Wehrli 1990). The limiting factor on the TR of the SE sequence is the rate of deposition of RF energy in the subject. The RF energy increases with the square of the flip angle, so a  $90^\circ$ – $180^\circ$  combination in an SE sequence deposits 45 times as much energy as a single  $30^\circ$  RF pulse! So with a GRE sequence with a reduced flip angle, the TR can be reduced to a very short time ( $< 10$  ms) without exceeding regulations on RF heating of the subject. With a TR of 10 ms, acquisition of an image with 128 phase-encode steps requires only approximately 1.25 s. The prototype GRE fast imaging sequence is called FLASH (fast low-angle shot) (Haase *et al.* 1986), but many variations have now been developed.

In Ch. 7, the characteristics of the MR signal when TR is shorter than  $T_2$  were discussed. With very short TR, there is a general echoing process such that each RF pulse both creates a new free induction decay (FID) and generates echoes of the previous FIDs. When this process reaches a steady state, the net signal after each RF pulse contains two components: the FID from the most recent RF pulse plus echoes of the previous FIDs. The magnitudes of both components depend strongly on the flip angle as well as TR. Furthermore, the contributions of these two components to the imaged signal can be manipulated by applying appropriate spoiler pulses. There are then three types of signal that one could choose to image with a short-TR GRE sequence: both components, the FID component alone, or the echo component alone. Fig. 10.3A shows the pulse sequence for imaging the FID and echo components together, the net steady-state signal. This pulse sequence is usually called GRASS (gradient recalled acquisition in the steady state) or FISP (fast imaging with steady-state precession), depending on the manufacturer of the MR imager. The key element for preserving the echo component is a rewinder gradient pulse along the  $y$ -axis that reverses each of the phase-encoding gradients before the next RF pulse. For the echoes to form, the phase evolution during each of the TR periods must be the same. An unbalanced phase-encoding gradient pulse that varied with each TR would act as a spoiler, destroying the echoes.

Fig. 10.3B shows a spoiled-GRE sequence designed to image only the FID component of the signal. By inserting a spoiler gradient pulse on the  $z$ -axis after the data collection and by varying the strength of the pulse with each repetition of the pulse sequence, the echoes do not form because the net phase accumulation in different TR periods is randomized. The FID component is generated before the spoiler pulse is applied and so is not affected. On current scanners, the spoiling is often done by varying the RF pulse so that the magnetization is tipped on to a different axis with each TR. The flip angle stays the same, so the magnitude of the transverse magnetization is the same. However, by varying the axis of rotation, the phase in the transverse plane is altered with each phase-encode step, preventing the echoes from forming. In its current form, FLASH is a spoiled sequence, and this pulse sequence is also called SPGR (spoiled GRASS). Note that leaving the phase-encoding gradient unbalanced would also produce some spoiling, but in a non-uniform way. Near  $y = 0$  in the image, the phase-encoding gradient has little effect on the local precession, so the spoiling would be ineffective in this part of the image.

Finally, to image only the echoes, the odd-looking pulse sequence in Fig. 10.3C is used. Note that the pattern of gradient pulses looks like a time-reversed version of the GRASS sequence. The reason for this is that we do not want the FID from the most recent RF pulse to

contribute to the signal, but we do want the echoes of all the previous FIDs to contribute. So the gradients after the RF pulse are left unbalanced, to spoil the FID component, but after the next RF pulse the same gradients are applied again to create an echo during the data collection window. This pulse sequence usually is called SSFP (steady-state free precession) or PSIF (FISP spelled backwards).

Another way of looking at these different GRE signals is to consider that the steady state that forms when a long string of RF pulses is applied produces a coherent magnetization  $M^-$  just before each RF pulse and  $M^+$  just after each RF pulse. Then a data collection window between two RF pulses could potentially contain contributions from both  $M^-$  and  $M^+$ . Whether these signals contribute depends on whether the gradient pulses are balanced during the interval between the time when the coherent signals form and when the center of data acquisition is measured. This is the data sample corresponding to  $k=0$ , and so for a signal to contribute to the image the net area under the  $x$ - and  $z$ -gradients must be zero at this time. For example, in the steady-state GRASS sequence, the gradients between  $M^+$  and the center of data acquisition sum to zero, but those between  $M^-$  and the  $k=0$  sample do not. The result is that only the  $M^+$  signal contributes. Similarly, in the echo-only SSFP sequence, the gradients between the center of data acquisition and  $M^-$ , but not  $M^+$ , are balanced.

The contrast between tissues in these three types of imaging was discussed in Ch. 7. In brief, for small flip angles, the steady-state GRE signal and the spoiled GRE signal are both primarily density weighted, and there is little difference between the two because the echo component is weak with small flip angles. For larger flip angles, the steady-state GRE signal is much larger than the spoiled GRE signal because the echo component is larger, but contrast between tissues is better with the spoiled signal. The reason for this is that the spoiled signal is strongly  $T_1$  weighted, whereas the steady-state signal also contains  $T_2$  weighting from the echoes, and this tends to conflict with the  $T_1$  contrast. As  $T_1$  and  $T_2$  become longer, the FID component decreases, but the echo component increases, so the net steady-state signal has poor contrast.

In SSFP, the echo-only signal is strongly  $T_2$  weighted. To emphasize this, the pulse sequence is often described as one in which TE is longer than TR. The rationale for this is that the FID generated by an RF pulse will not contribute to the measured signal until the next TR interval when it returns as an echo. For example, if TR is 30 ms and the data acquisition is at the center of the TR interval, then the TE would be called 45 ms because that is the time interval between the echo and the FID from two RF pulses back, the most recent FID that contributes to the echo. But unfortunately, this terminology can be misleading. The echo signal that is imaged contains contributions from the echoes of all previous FIDs (except the most recent one) in addition, and each of these echoes has a different TE. Furthermore, if one is concerned about the effects of field inhomogeneities, the relevant time for  $T_2^*$  effects to develop is not the stated TE, but rather the time interval between the center of data collection and the next RF pulse (15 ms in this example).

## Echo-shifted pulse sequences

Conventional gradient echo pulse sequences are useful in many applications because fast acquisitions are possible with short TR. However, for applications such as fMRI and bolus tracking of a contrast agent, there is a basic conflict between the need for a short TR to provide high temporal resolution for dynamic imaging and a reasonably long TE to make the image sensitive to magnetic susceptibility effects. As noted earlier, the TE in an SSFP sequence is often described as being longer than TR, but this is not true for  $T_2^*$  effects.

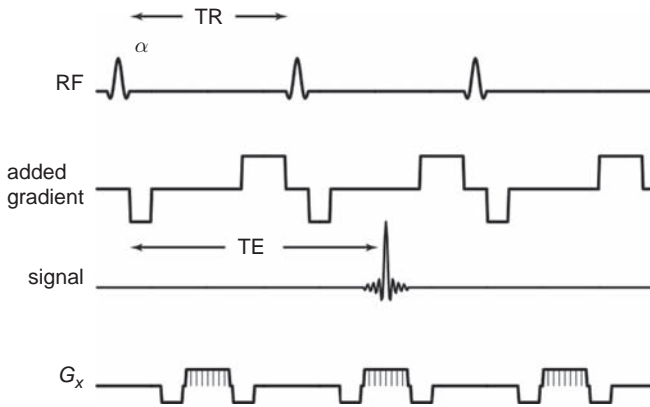


**Fig. 10.4.** Echo-shifted pulse sequences. In fMRI applications of conventional gradient recalled echo imaging, there is a conflict between the need for a short repetition time (TR) to provide high temporal resolution and the need for a sufficiently long echo time (TE) to provide sensitivity to magnetic susceptibility ( $T_2^*$ ) effects. Echo shifting makes possible a TE longer than TR by adding additional gradient pulses ( $G_x$ ) so that the signal generated from one RF pulse is dephased during the read-out period in that TR frame but refocused in the next TR read-out period.

Echo-shifted sequences were introduced as a way to truly produce a TE for phase evolution that is longer than the TR (Chung and Duerk 1999; Duyn *et al.* 1994; Liu *et al.* 1993a; Moonen *et al.* 1992).

The basic idea of an echo-shifted pulse sequence is that additional gradient pulses are added so that the transverse component produced by an RF pulse is dephased during the read-out period right after it is generated, but rephased during the read-out in the next TR period. Fig. 10.4 illustrates this idea with a stripped-down pulse sequence showing just the gradient pulses used to shift the echo and the read-out gradient. The other imaging gradients have been left out for simplicity, and the read-out gradient simply shows when data acquisition occurs. The echo-shifting effect results entirely from the additional gradient pulses. The FID generated by the first RF pulse is quickly spoiled by the first gradient pulse, so it does not contribute to the signal in the first read-out window. However, as this magnetization continues to precess in the transverse plane, the subsequent gradient pulses create a gradient echo at the time of the second read-out window. That is, between the initial RF pulse and the second read-out window, the gradient pulses are balanced so that the net area under the gradients is zero. For all subsequent read-out windows, the net area is non-zero, so the signal generated by the first RF appears only in the next TR period. The TE in this example is then equal to 1.5 TR.

The preceding argument ignored the effect of the second RF pulse on the transverse magnetization. We simply imagined the transverse magnetization to carry through subsequent RF pulses and focused just on the effects of the gradient pulses. But each RF pulse does have an effect on the transverse magnetization. Imagine an imaging voxel containing spins precessing at the same rate. In the absence of any gradient pulses, these spins would remain coherent as they precess, generating a strong signal. When a strong gradient pulse is applied, spins at different locations within the voxel along the gradient axis precess at different rates; if the gradient is strong enough, these spin vectors will fan out into a disk in the transverse plane. The next RF pulse will tip this disk, reducing the amplitude of the vectors that remain in the transverse plane. For example, if the RF pulse rotates the disk around  $x$  by an angle  $\alpha$ , then the  $y$ -component of each spin vector is reduced by a factor  $\cos \alpha$ . When the spin vectors are refocused by the next gradient pulse, the amplitude of the net vector will be reduced. However, if the flip angle of the RF pulse is small, this reduction in amplitude is relatively

minor. Most importantly, the phase of the refocused vector corresponds to precession for the full time between the first RF pulse and the second read-out window. In other words, the second RF pulse slightly reduces the amplitude of the echo but does not affect the phase. Because of this, the effective TE for the development of magnetic susceptibility effects is longer than TR.

Variations on this idea have been used to develop pulse sequences in which the echo can be shifted by any number of TR periods (Liu *et al.* 1993a). The echo-shifted technique has been adapted for fMRI studies in a version called PRESTO (principles of echo shifting with a train of observations) (Duyn *et al.* 1994; Liu *et al.* 1993b) and also applied to bolus tracking studies of contrast agent dynamics (Moonen *et al.* 1994).

## Volume imaging

Volume acquisitions require trajectories that cover a three-dimensional  $k$ -space. Any two-dimensional imaging trajectory can, of course, be used to acquire images of a volume by acquiring separate images of the individual planes that make up the volume. In multislice acquisitions, the data for multiple slices can be acquired in an interleaved fashion to improve the time efficiency. However, true three-dimensional volume acquisitions in which the scanning trajectory moves throughout a three-dimensional  $k$ -space are possible. The most important difference between two- and three-dimensional approaches to measuring a volume of data is the signal to noise ratio (SNR). With the two-dimensional approach, signal is collected from a particular voxel only when the slice containing that voxel is excited. The acquisition of data from other slices does nothing to improve the SNR of that voxel. In contrast, with a three-dimensional acquisition, each measured signal contains contributions from every voxel in the volume, and so each contributes to the SNR of that voxel. The SNR in an image is discussed more fully in Ch. 11, but for now the important point is that three-dimensional acquisitions offer an SNR advantage over two-dimensional acquisitions, and this SNR can be traded against resolution to acquire high-resolution images with very small voxels.

The most commonly used trajectory in three-dimensional imaging is a rectilinear scanning with a gradient echo along  $x$ , with phase-encoding pulses along  $y$  and  $z$  to move the scanning line to a new  $k_y$  and  $k_z$  position. A popular pulse sequence for acquiring high-resolution anatomical images is SPGR, which provides good  $T_1$ -weighted contrast between white matter and gray matter and so is useful for segmenting brain images into tissue types. With this type of acquisition, the typical scanning trajectory is to cover a  $k_x$ - $k_y$  plane at one value of  $k_z$  and then to move to a new plane at a new  $k_z$ . With each excitation RF pulse, one line in  $k_x$  is acquired at fixed  $k_y$  and  $k_z$ . From this  $k$ -space data, the images are usually reconstructed and stored as a set of two-dimensional images in  $(x,y)$  corresponding to different  $z$ -locations. If the data were acquired with the same resolution along each axis (isotropic voxels), the three-dimensional block can be resliced in any orientation to create a new set of slices. In doing this, the voxels that make up the image are often treated as small blocks that are rearranged to form new slices, but it is important to remember the earlier discussion in Ch. 9 of the point spread function. With this type of acquisition, the point spread function is a sinc function along each axis (see Fig. 9.15).

Another popular pulse sequence for acquiring high-resolution structural images is magnetization prepared rapid gradient echo (MP-RAGE) (Mugler and Brookeman 1990). In MP-RAGE, the trajectory in  $k$ -space is again a rectilinear sampling, but RF inversion pulses are added periodically to improve the  $T_1$ -weighted contrast. After each sampling of a

plane at fixed  $k_z$ , an inversion pulse is added, so the longitudinal magnetization then follows an inversion recovery curve during acquisition. The excitation pulses use small flip angles that do not strongly disturb the longitudinal magnetization. As a result, during the acquisition of one plane in  $k_x$ - $k_y$ , the signal is slowly varying owing to the relaxation of the longitudinal component as the  $k$ -space sampling proceeds. The primary effect of the inversion pulses is to improve contrast by sampling the center of  $k$ -space at the part of the inversion recovery curve that is most sensitive to  $T_1$ . But a secondary effect is that the changing intrinsic signal affects the measured net signal and so affects the sampling in  $k$ -space. Such relaxation effects create an additional blurring in the image and are discussed in more detail later in the chapter. Despite the complexities introduced by imaging a signal that varies during image acquisition, the MP-RAGE pulse sequence produces high-resolution images with superior contrast between gray matter and white matter.

## Exploiting symmetries of $k$ -space

In the preceding discussion of conventional SE and GRE imaging, the importance of reducing TR in speeding up data acquisition was emphasized. With these conventional techniques, the basic  $k$ -space sampling trajectory is unchanged: one line of  $k$ -space is sampled following each RF excitation pulse, and with GRE imaging, this is simply done faster with a shorter TR. A more general approach to performing fast imaging is to consider different  $k$ -space trajectories, and in particular to develop trajectories that collect more than one  $k$ -line for each RF pulse. However, before considering some of these ultrafast techniques, there are ways to decrease acquisition time even with a conventional trajectory by exploiting some symmetries of  $k$ -space.

In conventional imaging, one line of  $k$ -space is collected each time a signal is excited. For a total of  $N$  lines of data, the total imaging time is  $N \times \text{TR}$ . One approach to reducing the data acquisition time is a *partial  $k$ -space* acquisition, which exploits a symmetry of  $k$ -space that sometimes occurs (Feinberg *et al.* 1986; Haacke *et al.* 1990). If the intrinsic distribution of transverse magnetization is all in-phase, as for example at the peak of an SE, then the negative half of  $k$ -space is redundant. The value at  $-k$  is the same as that at  $+k$ , but with opposite phase, so it is only necessary to measure half of  $k$ -space. The division of  $k$ -space into two parts can be along either  $k_x$  or  $k_y$ . When only a part of the full  $k_x$  range is measured, it is described as a *partial echo* acquisition. By reducing the  $x$ -compensation gradient, the time TE of the gradient echo, where the  $k_x = 0$  sample is measured, is moved closer to the beginning of data sampling. When only half of the  $k_y$  range is sampled, it is referred to as a *half-NEX* or *half-Fourier* acquisition, where NEX is a common abbreviation for the number of excitations used for each phase-encoding step (i.e., the number of averages). Because the signal from each excitation is used to collect two lines in  $k$ -space, one measured directly and the other inferred from the first, the number of excitations per line in  $k$ -space is only 1/2.

However, with a pure gradient echo acquisition, with no refocusing SE, the spins in different locations continue to precess at different rates because of field inhomogeneities. Nevertheless, the phase variations across the image plane are often relatively smooth, and the central points in  $k$ -space can be used effectively to reconstruct a low-resolution image of the phase distribution and to use this image to correct the full data. To do this, some data must also be collected in the second half of  $k$ -space, but often collecting 60 or 70% of the total  $k$ -space data is sufficient. The cost of partial  $k$ -space acquisition is a reduced SNR because fewer measurements go into the reconstructed image (Hurst *et al.* 1992). But there are advantages as well. A half-NEX acquisition reduces the total imaging time by a factor of

two. A partial echo acquisition does not shorten the imaging time because the same number of phase-encoding steps are collected, but it does make possible a shorter TE, which can improve the SNR. Short TE is especially important in angiography applications, where the motion of the flowing spins through the applied gradient fields leads to a rapid phase dispersion and a resulting loss in signal.

## Fast imaging techniques

### *k*-Space sampling trajectories for fast imaging

Partial *k*-space acquisitions can reduce the minimum imaging time by up to a factor of two. Much larger reductions can be realized by acquiring more than one line in *k*-space from each excited signal, and there are now a number of ways of doing this (Fig. 10.5). In *fast spin echo* (FSE, also called turbo SE [TSE]), multiple 180° pulses are used to create a train of echoes, and each echo is phase encoded differently to measure a different line in *k*-space (Atlas *et al.* 1993). For example, an echo train of eight echoes will reduce the minimum imaging time by a factor of eight. This makes it possible to acquire  $T_2$ -weighted images, which require a long TR, in less than 1 min. By increasing the number of SEs, a low-resolution image can be acquired in a single-shot mode by acquiring 64 echoes of one excited signal, a technique called RARE (rapid acquisition with relaxation enhancement) (Hennig and Friedburg 1988; Hennig *et al.* 1986). The RARE technique was the original version of a pulse sequence that used multiple SEs to encode different lines in *k*-space, and FSE is essentially a multishot version of RARE. Another version of this technique is HASTE (half-Fourier acquisition with a single-shot turbo spin echo), which combines the idea of multiple SEs with a half-Fourier acquisition, to take advantage of the symmetry of *k*-space to produce single-shot images (Kiefer *et al.* 1994).

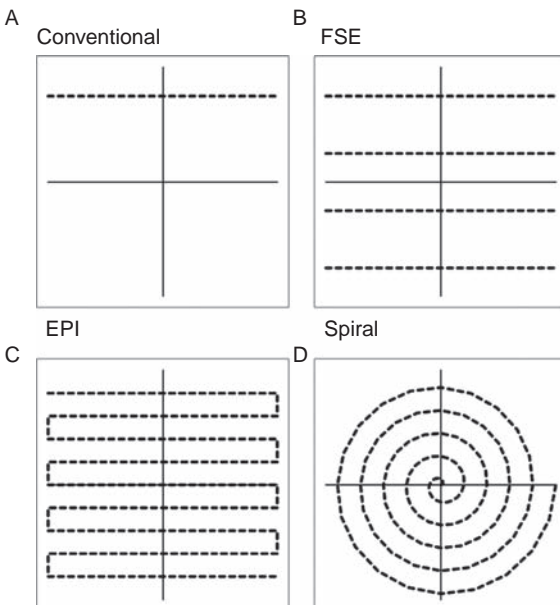


**Fig. 10.5.** *k*-space sampling trajectories. (A) In conventional MRI one line in *k*-space is measured with each excited signal. Each time the pulse sequence is repeated the phase-encoding gradient shifts the sampling to a new line in *k*-space. (B) In fast spin echo imaging, multiple echoes are generated for each excited signal, and each echo is separately phase encoded to measure several lines in *k*-space with each shot. (C) In echo planar imaging (EPI), the gradients are rapidly switched so that with a single shot the *k*-space trajectory scans back and forth across the full range of *k*-space required for an image. (D) Spiral trajectories use sinusoidally varying gradients to create a trajectory that spirals out from the center. Both EPI and spiral trajectories can be used in either single-shot mode for the highest temporal resolution or in a multishot mode for higher spatial resolution.



In EPI, a rapid series of gradient echoes is generated to cover  $k$ -space in a back and forth scanning pattern (Schmitt *et al.* 1998a). In single-shot EPI, a block of  $k$ -space equivalent to a low-resolution image can be measured from one excitation pulse. To improve spatial resolution, multishot EPI can be used to cover more of  $k$ -space. Combined SE and gradient echo acquisition (GRASE) is achieved by generating a series of SEs and then generating several gradient echoes under the envelope of each SE, with each gradient echo measuring a new line in  $k$ -space (Feinberg and Oshio 1992). This pulse sequence is less sensitive to  $T_2^*$  effects than a standard EPI acquisition.

The scanning trajectories for the foregoing pulse sequences are essentially a raster scanning type. Each gradient echo samples one straight line across  $k$ -space, a new phase-encoding pulse moves the sampling to a new line, and a new straight line is sampled. However, many scanning patterns are possible. By turning on gradients in  $x$  and  $y$  simultaneously, but varying the proportions, a radial pattern of sampling is produced. Each line passes through the center of  $k$ -space, but at a different angle. This technique is called *projection reconstruction* imaging (Glover and Lee 1995) and is analogous to X-ray computed tomography. With projection reconstruction imaging, it is possible to collect each ray one half at a time, using two excitation pulses with sampling starting in the center of  $k$ -space. Each sampled line is then a ray starting out from zero. This is not very fast imaging, but it makes possible an extremely short TE because the center of  $k$ -space is sampled right after the excitation pulse. Such pulse sequences are useful when there are very short  $T_2$  or  $T_2^*$  components in the signal that would be gone by the time of more standard image acquisitions. This type of pulse sequence is becoming available on standard imagers but is primarily used in specialized research applications.

A useful strategy is spiral imaging, in which the sampling trajectory spirals out from the center of  $k$ -space. This can be done in a single-shot fashion, or higher-resolution images can be acquired with multiple spirals interleaved. Spiral imaging efficiently uses the available gradient strength because the  $k$ -space trajectory is smoothly varying, and it is relatively insensitive to motion (Glover and Lee 1995; Noll 1995). Spiral imaging is not widely available on MR imagers, but a few institutions are using spiral imaging for fMRI studies with great success (Cohen *et al.* 1994; Engel *et al.* 1994; Gabrieli *et al.* 1997; Noll *et al.* 1995). Another novel approach to fast imaging is burst imaging, described in Box 10.1. and illustrated in Fig. 10.6. This is much quieter than other imaging techniques but suffers from a poor SNR.

## Echo planar imaging

The previous section suggests the diversity and flexibility of pulse sequences for MRI. Virtually every type of imaging has been used in some form of functional MRI experiment. But the most common imaging technique for fMRI is single-shot EPI, and so it is worth looking more closely at how EPI works. The idea of EPI was proposed early in the history of MRI (Mansfield 1977), but it is only since the mid 1990s that this technique has become widely available. A comprehensive history and survey of current applications of EPI can be found in Schmitt *et al.* (1998a). Fig. 10.7 shows a simplified pulse sequence diagram for a single-shot (EPI) pulse sequence, and Fig. 10.8 shows how the basic gradient switching moves the sampling point through  $k$ -space. Because of the rapid gradient reversals, it is not possible to show the full diagram, and the small boxed region in Fig. 10.7 is repeated  $N/2$  times, where  $N$  is the total number of lines measured in  $k$ -space. Not shown in this diagram is the preparation module to saturate fat that is almost always used in EPI. The initial negative gradient pulses in  $x$  and  $y$  move the location of  $k$ -space sampling to  $-k_{\max}$  on both the  $k_x$ - and

**Box 10.1. Quiet imaging with burst techniques**

One of the most surprising features of MRI when one is first exposed to a scanner is the loud acoustic noise associated with the image acquisition. The gradient coils used for imaging carry large currents and are sitting in a large magnetic field, and so are subject to large forces. When the current is pulsed in the coil, a sharp pulsed force is applied, and the acoustic noise results from the flexing of the coils under this force. The gradient coil thus acts like a large loudspeaker system. This can be a significant complicating factor in fMRI experiments. With EPI, the sound can reach levels of 130 dB, with the energy centered on the fundamental switching frequency of the EPI acquisition (approximately 1000 Hz) (Savoy *et al.* 1999). This poses problems for any auditory fMRI study and makes studies of sleep very difficult.

The acoustic noise is directly related to the fast gradient switching that makes possible fast imaging with EPI. A single read-out period during an EPI acquisition is on the order of 1 ms, so the read-out gradient is switched from a large negative amplitude to a large positive amplitude roughly every millisecond during acquisition. This rapid switching drives the sampling trajectory in  $k$ -space. With a constant gradient, the sampling trajectory is a straight line in  $k$ -space, and so to scan back and forth and cover a plane in  $k$ -space the trajectory must bend. But bending the trajectory requires switched gradients, so the loud acoustic noise is tightly connected to the ability to do single-shot imaging. And indeed, from this argument, it is difficult to see how the acoustic noise could be eliminated. Both the amplitude of the sound and the fundamental frequency can be reduced by using weaker gradients and slower rise times, which then extends the image acquisition time. Even though such an approach can reduce the noise, it cannot eliminate it. Remarkably, however, there is a pulse sequence that is virtually silent and acquires an image in less than 50 ms. The technique is called burst imaging (Hennig and Hodapp 1993; Jakob *et al.* 1998; Lowe and Wysong 1993), and it has recently been applied to fMRI studies of sleep (Jakob *et al.* 1998; Lovblad *et al.* 1999).

A simple pulse sequence for burst imaging is shown in Fig. 10.6. A series of RF pulses with low flip angle  $\alpha$  is applied in the presence of a constant  $x$ -gradient. A  $180^\circ$  RF pulse is then applied, and afterwards the same  $x$ -gradient is turned on again as a read-out gradient. During this read-out, the FIDs produced by each of the original  $\alpha$ -RF pulses create a string of echoes. Each of these echoes is a frequency-encoded signal and, in the absence of any other gradient, would simply scan across the same line in  $k$ -space. By turning on a  $y$ -gradient as well during the read-out period, each successive echo is shifted to a different line in  $k$ -space. Each scanned line is at an angle because the  $y$ -gradient is also on during acquisition, but this tipped  $k$ -space sampling nevertheless covers the plane.

Burst imaging thus produces a rapid image with hardly any gradient switching. The reason it is able to do this is that, unlike EPI, burst imaging does not generate one signal and then use that signal to map a continuous trajectory through  $k$ -space. Instead, burst generates many signals and then moves each one on a straight line through  $k$ -space. For example, consider the signal generated by the first  $\alpha$ -pulse. The remainder of the first  $x$ -gradient pulse moves this signal far out in  $k_x$ , way past the maximum of the image. The second  $x$ -gradient then reverses the trajectory, moving back toward  $k = 0$ . When the  $y$ -gradient is turned on, the trajectory tips up slightly, and it is then this straight but slightly angled line that passes through the region of  $k$ -space that will be used for imaging. But this trajectory is never turned around to make another pass through. Instead, the next line is measured with the second generated signal, and so on.

Burst imaging can, therefore, be viewed as a technique that generates a number of signals, and each one provides a single line through  $k$ -space. However, this description brings out the problem with burst imaging: the SNR is poor. We can think of the initial local longitudinal magnetization as the available signal we have for imaging. With an EPI acquisition with a  $90^\circ$  RF pulse, all of this signal is generated at once and then moved through  $k$ -space to generate the image. But with burst imaging, this signal is broken into many small parts, with each one moved through  $k$ -space on a

single line. For a rapid acquisition such as this, there is no time for any significant longitudinal relaxation, so the flip angle  $\alpha$  must be small so that the longitudinal magnetization is not completely destroyed. Each generated signal is then smaller than the full available signal by at least a factor of  $\sin \alpha$  (after each  $\alpha$ -pulse the longitudinal magnetization is slightly reduced, so after the first pulse the generated transverse magnetization is even less). Then for any line in  $k$ -space, the amplitude of the signal used for mapping is much less with burst than with EPI, so the SNR is correspondingly much less.

The signal loss of a full burst sequence compared with EPI is complicated to calculate because each of the  $\alpha$ -pulses has some effect on the transverse magnetization created by the previous pulses. Careful optimization of the phase of each of the RF pulses is necessary to minimize the effects of these interactions (Zha and Lowe 1995). For now we can ignore these complications to try to estimate the highest SNR that could be achieved with this approach even if there were no interactions. Specifically, suppose that each RF pulse generates an MR signal that is then unaffected by subsequent RF pulses, and further suppose that relaxation is negligible during the experiment. Then the amplitude of the signal produced with each pulse directly measures the intrinsic signal amplitude when scanning through  $k$ -space. For EPI, this intrinsic signal is equal to the full longitudinal magnetization because EPI uses a  $90^\circ$  pulse to put all the available magnetization into the transverse plane. But for burst imaging, this signal is reduced by a factor  $\sin \alpha$ , so the key question becomes how large  $\alpha$  can be. The problem is that each  $\alpha$ -pulse reduces the longitudinal magnetization, so the signal generated by the next pulse is weaker. This is undesirable for scanning through  $k$ -space because the idealization of imaging is that the intrinsic signal is constant, so that any changes in the net signal are the result of the spatial distribution of the signal interacting with the imaging gradients. In other words, a variable intrinsic signal while scanning through  $k$ -space leads to distortions and blurring in the image.

We can imagine dealing with this variable signal problem by using progressively larger flip angles in the RF pulse train so that each generates the same magnitude of transverse magnetization. If this string of RF pulses is optimized to use all the available longitudinal magnetization for imaging, then the final RF pulse should be  $90^\circ$  to bring the last bit of magnetization fully into the transverse plane. This optimization of the RF flip angles is not standard in burst imaging, but it is a fruitful way to think about how burst imaging could be optimized for SNR. So the key question then becomes how we can design a string of  $N$  equally spaced RF pulses so that the full longitudinal magnetization  $M$  is broken into  $N$  equal transverse magnetization components  $M_T$ , leaving no longitudinal magnetization at the end. This would divide up the available signal evenly among the individual lines of  $k$ -space, and the SNR of burst relative to EPI will then be  $M_T/M$ . Naively, we might expect that if the longitudinal magnetization is divided into  $N$  transverse components, the intrinsic burst signal would be  $M/N$ . However, this is not right, and it turns out that a longitudinal magnetization  $M$  can produce  $N$  transverse components each with amplitude  $M/\sqrt{N}$ . Clearly, magnetization is not conserved when going from longitudinal to transverse! The SNR of burst is, therefore, reduced from that of EPI by a factor of  $\sqrt{N}$ . Because  $N$  is the number of lines measured in  $k$ -space,  $N$  also is the number of resolved voxels along the  $y$ -axis. In other words, as the resolution of the image improves, the SNR of burst becomes even worse compared with EPI. Even for a low-resolution image matrix of 64 voxels, the SNR of EPI is eight times better. The cost of silent imaging is consequently a very large hit in SNR.

To see how this factor of  $\sqrt{N}$  comes about, we start by imagining that we have a string of optimized RF pulses with flip angle  $\alpha_1, \alpha_2, \dots, \alpha_N$ , each of which produces the same (but unknown) transverse magnetization  $M_T$ . The full longitudinal magnetization  $M$  is consumed in this process, so the last pulse must put all the remaining longitudinal magnetization into the transverse plane ( $\alpha_N = 90^\circ$ ). The first RF pulse produces a transverse magnetization  $M_T = M \sin \alpha_1$ , so the ratio of the SNRs of burst compared with EPI is  $\sin \alpha_1$ . To calculate the optimal flip angles, imagine that we are looking somewhere in the middle of the pulse train. Let the remaining longitudinal magnetization

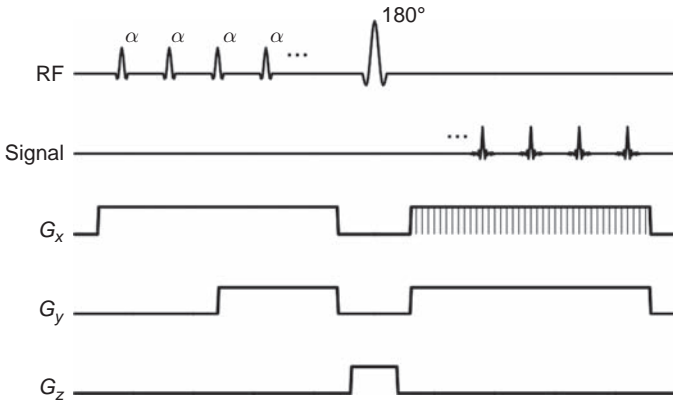


**Fig. 10.6.** Burst imaging. Burst imaging is a nearly silent imaging technique because it eliminates the rapid gradient switching used in techniques such as echo planar imaging (EPI). A series of radiofrequency (RF) pulses of small flip angle is applied in the presence of a constant gradient  $G_x$ . A slice-selective  $180^\circ$  pulse is then applied. With the same  $x$ -gradient turned on again, a series of echoes forms from each of the signals excited by the original string of RF pulses. Each of these echoes samples a single line in  $k$ -space. By collecting the data with a gradient in  $y$  ( $G_y$ ) also turned on, each line is effectively phase encoded differently. (The  $k$ -space trajectory is actually parallel lines but tipped at an angle because of the constant  $G_x$ .) Although burst imaging is virtually silent and very rapid, it suffers from a much lower signal to noise ratio compared with EPI.

just before the  $n$ th RF pulse be  $M_n$ . After the  $n$ th pulse, the transverse magnetization is  $M_T = M_n \sin \alpha_n$ , and the remaining longitudinal magnetization is  $M_n \cos \alpha_n$ . After the next RF pulse, this remaining longitudinal component is tipped over to create a transverse component  $M_T = M_n \cos \alpha_n \sin \alpha_{n+1}$ . Equating these two expressions for  $M_T$ , the relationship between subsequent flip angles is

$$\begin{aligned} \sin \alpha_{n+1} &= \tan \alpha_n \\ \frac{1}{\sin^2 \alpha_{n+1}} &= \frac{1}{\sin^2 \alpha_n} - 1 \end{aligned} \quad (\text{B10.1})$$

where the second form shows the simple relation in terms of the sine of each flip angle. We can now calculate the string of flip angles by starting with the last, which we know must be  $\alpha_N = 90^\circ$ . Moving toward the beginning of the train,  $1/\sin^2 \alpha_n$  is simply one plus the value for  $\alpha_{n+1}$ . So, the initial flip angle that produces the maximum attainable SNR of burst compared with EPI is

$$\sin \alpha_1 = \frac{1}{\sqrt{N}} \quad (\text{B10.2})$$

Consequently, although burst imaging has a number of unique and interesting features, it is not optimal for general fMRI studies because of its intrinsically low SNR. Nevertheless, it is a promising approach for sleep studies or other studies that are incompatible with the loud sounds of EPI.

$k_y$ -axes. After that, the repeated gradient echo module produces a back and forth scanning of  $k$ -space. The small phase-encoding pulses along  $y$  are called *blips*.

Echo planar imaging requires strong gradients and rapid switching capabilities. A central problem in doing single-shot imaging is that the data acquisition window is limited by  $T_2^*$ . If

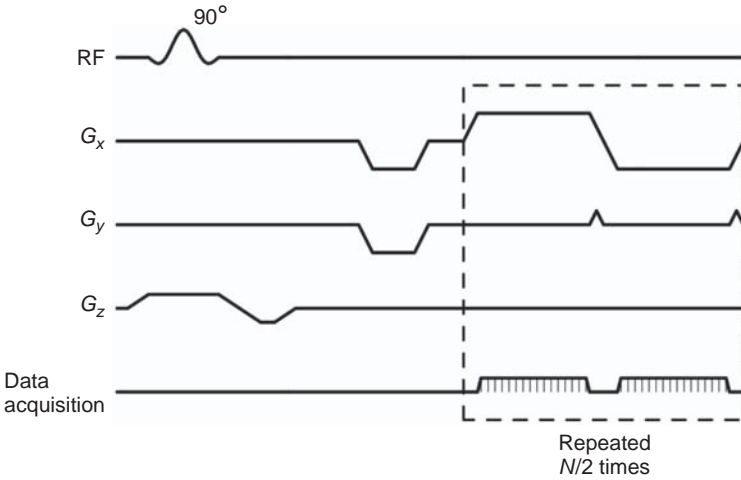


**Fig. 10.7.** Echo planar imaging. The pulse sequence diagram shows the rapidly switched gradient pulses ( $G$ ) used for a back and forth scanning of  $k$ -space. The read-out gradient ( $x$ ) alternates between positive and negative values, creating a gradient echo at the center of each read-out window. During a constant gradient, the scanning trajectory in  $k$ -space is a straight line in  $k_x$ , with the sign of  $G_x$  determining whether the trajectory moves to the left or the right. The small  $y$ -gradient pulses (blips) shift the  $k$ -space sampling to a new  $k_y$  line, so the full trajectory is as shown in Fig. 10.8.

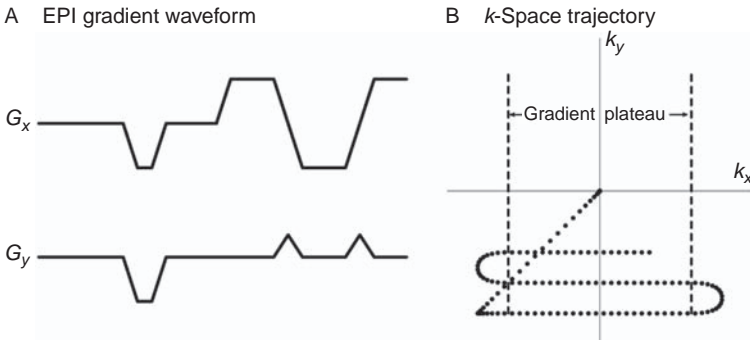


**Fig. 10.8.** The echo planar image (EPI)  $k$ -space trajectory. The correspondence between the timing of gradient pulses (A) and the  $k$ -space trajectory (B) is illustrated for part of an EPI pulse sequence. The dots in  $k$ -space show the location of the sampling point at equal time steps to give a sense of the varying speed of the trajectory through  $k$ -space. The initial gradient pulses in  $x$  and  $y$  move the sampling to the left and down, and then the oscillating gradient  $G_x$  creates the back and forth motion while the periodic blips in  $G_y$  move the sampling to a new  $k_y$ -line. The part of the trajectory corresponding to the plateaus of  $G_x$  are indicated in (B). Note that, during the ramps, the trajectory extends to larger values of  $k_x$ , and these data can also be used if corrections are applied for the different speeds of the  $k$ -space trajectory.

it is much longer than  $T_2^*$ , the intrinsic signal will have significantly decayed during data acquisition. The corresponding  $k$ -space samples will then be reduced because of the intrinsic decay. Since the later samples are often the larger  $k$ -samples describing the high spatial frequencies, this amounts to an additional blurring of the image. Such effects are considered in more detail in Ch. 11, but for now the essential problem is that the acquisition window is limited by  $T_2^*$  effects to approximately 100 ms to sample a block of  $k$ -space sufficient to reconstruct an image.

From Eq. (9.4), the trajectory through  $k$ -space depends on the temporal pattern of the applied gradient fields. Under the influence of the gradients, the evolving net signal is a direct measure of the  $k$ -space distribution of the image. Choosing a desired field of view and resolution for the image defines a grid of points in  $k$ -space that must be sampled. The total imaging time required then depends on how quickly the sampling point can be moved over the grid in  $k$ -space, and this depends on two properties of the gradient coils used for imaging: the maximum gradient strength and how fast the gradient can be changed. The gradient amplitude is usually expressed in units of millitesla per meter (mT/m) or gauss per centimeter (G/cm, with 1 G/cm = 10 mT/m), and the maximum gradient strength on current MR imagers is typically in the range 20–40 mT/m. To put the gradient strength in perspective, consider again frequency encoding in which samples from  $-k_{\max}$  to  $+k_{\max}$  are acquired during a gradient echo. With stronger gradients, this  $k$ -space line can be sampled more quickly, so a natural measure of the maximum gradient strength is the minimum time required to scan over a specified range of  $k_x$ . A convenient range is  $-k_{\max}$  to  $+k_{\max}$ , for the  $k_{\max}$  needed to achieve a resolution of 1 mm. With a gradient strength of 25 mT/m, the time required to scan one line in  $k$ -space equivalent to a resolution of 1 mm is approximately 1 ms. For increased gradient strength, this number is decreased in proportion; for higher spatial resolution, this time is increased in proportion to the improvement of the resolution.

The second factor that affects the speed of scanning is how fast the gradient can be reversed so that the direction of sampling in  $k$ -space can be reversed. There are two common ways of expressing this: the slew rate, which describes the maximum rate of change of the field gradient, usually expressed in tesla per meter per second, and the rise time, which describes the time required to increase the gradient amplitude from zero to its positive maximum value. Typical numbers for a 1.5 T scanner are a slew rate of 80–120 T/(m · s) and a rise time of 200–300  $\mu$ s. These parameters are, of course, related: the maximum gradient strength divided by the rise time is the slew rate. The rise time directly measures how much time must be spent in changing the direction of sampling in  $k$ -space. One can think of sampling in  $k$ -space, as in Fig. 10.8, as analogous to a car racing along a winding track with sharp turns. The time to complete the circuit depends on both how fast the car moves on the straightaway (governed by the gradient strength) and how fast the car can corner (determined by the gradient rise time).

To see more specifically how gradient strength and rise times affect EPI data collection, we can consider the primary gradient waveform used in EPI, the basic oscillating pattern used to collect successive gradient echoes sampling a line in  $k_x$ . Between gradient echoes, phase-encoding blips in  $y$  are applied to shift the  $k$ -space sampling to a new  $k_y$ -line. Ideally, the oscillation of the  $x$ -gradient would be a square wave, but the gradient rise times limit the possible shapes to more rounded forms (Fig. 10.8). For example, if the plateau duration is 1 ms and the rise time is 300  $\mu$ s, a total of 1600  $\mu$ s is required for each gradient echo. For an image matrix size of  $N$  resolution elements,  $N$  gradient echoes are required for a full  $k$ -space acquisition, giving a total data collection time of 102 ms for a 64 × 64 matrix.

In the earlier discussion of sampling in  $k$ -space, the sampling was done during application of a constant read-out gradient. But because the rise times are typically fairly long, waiting for the gradient to reach the plateau means that data are collected during only a fraction of the time (approximately 62% in the previous example). This waiting wastes some of the gradient power that is available. One way to think about this is to note that the resolution in  $x$  is inversely proportional to the area of the gradient pulse. In the previous example, the area under the full trapezoidal gradient is 30% more than the area under the

plateau portion alone. Instead of collecting data only on the gradient plateau, the signal also can be sampled on the ramps to achieve better spatial resolution with the same gradient waveforms. The problem then is that the samples are not uniformly spaced along  $k_x$  (Fig. 10.8). During the ramps, the sampling point moves more slowly through  $k$ -space because the gradient is weaker, so for evenly spaced samples in time, the samples in  $k$ -space are bunched together during the ramps. Before applying the fast Fourier transform to reconstruct the image, the unevenly spaced  $k$ -space samples must be interpolated on to an evenly spaced grid. This can slow down the reconstruction time because of the additional computations required. Alternatively, the sampling in time can be adjusted to match the trajectory through  $k$ -space, with a longer interval between the samples during the ramps so that the measured samples in  $k$ -space are evenly spaced. This scheme requires a longer setup time because the appropriate sampling intervals must be calculated before the sequence is run, but the reconstruction is then faster.

## Safety issues

In conventional MRI, safety concerns related to pulse sequences generally focus on heating the body by the applied RF pulses (Shellock and Kanal 1996). Each RF pulse deposits energy in the body, and the rate of energy deposition measured in watts per kilogram of tissue is called the specific absorption rate (SAR). The US Food and Drug Administration provides guidelines for the maximum SAR, and calculations of SAR are usually done in the pulse sequence code so that the operator is informed if the RF heating of the prescribed sequence is excessive. The limits on SAR are most critical for fast SE acquisitions, which use many  $180^\circ$  refocusing pulses. The energy of an RF pulse depends on the square of the amplitude of the electromagnetic field, so when the flip angle is changed by altering the strength of the RF field with the duration held constant, the SAR depends on the square of the flip angle. Therefore, GRE acquisitions with reduced flip angles deposit much less energy than SE acquisitions. Ultrafast imaging with EPI acquisitions use fewer RF pulses and so are not significantly limited by SAR guidelines.

In fast imaging with EPI, there are two safety concerns related to the fast gradient switching necessary to scan rapidly through  $k$ -space. The first is the very loud acoustic noise associated with fast gradient switching. Magnetic fields exert forces on currents, so when a current is pulsed through the gradient coil, the force flexes the coil and produces a sharp tapping sound. In fact, the gradient coil acts much like a loudspeaker, and the sound level can be as high as 130 dB (Savoy *et al.* 1999). For this reason, subjects must always wear ear protection such as ear plugs or close-fitting headphones.

The second safety concern with EPI is nerve stimulation by the rapid gradient switching, which depends on the gradient strength and the slew rate (Schmitt *et al.* 1998b). Nerve stimulation can occur when the rate of change of the local magnetic field ( $dB/dt$ ) exceeds a threshold value (Reilly 1989). Note that it is not the amplitude of the magnetic field, but rather its rate of change, that causes the problem. A large but constant magnetic field has little effect on the human body, but a changing field induces currents in the body in the same way that a precessing magnetization induces currents in a detector coil. When the current in a gradient coil is reversed, and the gradient strength is ramped quickly between its maximum negative and positive values, the rate of change of the local magnetic field can be quite large.

The value of  $dB/dt$  depends on the slew rate and gradient strength, but it also depends on location within the coil. At the center, the coil produces no additional field, so there is

nothing to change. The largest field changes are at the ends of the coil, at the maximum distance along the gradient direction.

For imaging applications, only the  $z$ -component of the magnetic field matters, and when we refer to a gradient field, we mean the gradient of the  $z$ -component. But for considerations of  $dB/dt$ , we must also consider the fields perpendicular to  $z$  created by the coil. All magnetic field lines must form closed loops, so the field lines running through the coil bend around at the ends of the coil. For example, a transverse  $y$ -gradient coil creates a strong field near the ends of the coil running in the  $y$ -direction, perpendicular to the main field. When the gradient is pulsed, this perpendicular field creates a large  $dB/dt$ . Furthermore, nerve stimulation depends on the electric field created by the changing magnetic field. If we imagine a loop of wire near the end of the coil, the current induced in the loop is proportional to the rate of change of the flux of the magnetic field through the loop and so is proportional to the size of the loop. Thinking of the body as a current loop, the larger the cross-section of the body exposed to the changing magnetic field, the larger the induced currents will be. The largest cross-section is in the coronal plane. Because the  $y$ -gradient produces a magnetic flux change through this plane, the  $y$ -gradient is the most sensitive for generating nerve stimulation. For this reason, the  $y$ -gradient is generally not used for frequency encoding in EPI (e.g., a sagittal image with frequency encoding in the anterior–posterior direction).

Different governments and agencies have set different regulations on the maximum rate of change of the magnetic field, but generally values of  $dB/dt$  below 6 T/m are considered a level of no concern (see Schmitt *et al.* (1998b), for a review of current guidelines). Note that this limit does not directly limit the slew rate because a shorter coil can operate with a larger slew rate while keeping the maximum  $dB/dt$  below threshold (Wong *et al.* 1992). The imaging speed of acquisition techniques such as EPI currently is limited by these concerns about physiological effects rather than hardware performance.

## References

- Atlas SW, Hackney DB, Listernd J (1993) Fast spin-echo imaging of the brain and spine. *Magn Reson Quart* **9**: 61–83
- Buxton RB, Wismer GL, Brady TJ, Rosen BR (1986) Quantitative proton chemical-shift imaging. *Magn Reson Med* **3**: 881–900
- Chung YC, Duerk JL (1999) Signal formation in echo shifted sequences. *Magn Reson Med* **42**: 864–875
- Cohen JD, Forman SD, Braver TS, *et al.* (1994) Activation of the prefrontal cortex in a non-spatial working memory task with functional MRI. *Hum Brain Mapp* **1**: 293–304
- Dixon WT (1984) Simple proton spectroscopic imaging. *Radiology* **153**: 189–194
- Duyn JH, Mattay VS, Sexton RH, (1994) 3-Dimensional functional imaging of human brain using echo-shifted FLASH MRI. *Magn Reson Med* **32**: 150–155
- Engel SA, Rumelhart DE, Wandell BA, *et al.* (1994) fMRI of human visual cortex. *Nature* **369**, 370 [erratum 525, 106]
- Feinberg DA, Oshio K (1992) Gradient-echo shifting in fast MRI techniques (GRASE) for correction of field inhomogeneity errors and chemical shift. *J Magn Reson* **97**: 177–183
- Feinberg DA, Hale JD, Watts JC, Kaufman L, Mark A (1986) Halving MR imaging time by conjugation: demonstration at 3.5 kG. *Radiology* **161**: 527–531
- Gabrieli JD, Brewer JB, Desmond JE, Glover GH (1997) Separate neural bases of two fundamental memory processes in the human medial temporal lobe. *Science* **276**: 264–266
- Glover GH, Lee AT (1995) Motion artifacts in fMRI: comparison of 2DFT with PR and spiral scan methods. *Magn Reson Med* **33**: 624–635
- Haacke EM, Mitchell J, Lee D (1990) Improved contrast using half-Fourier imaging: application to spin-echo and angiographic imaging. *Magn Reson Imaging* **8**: 79–90



- Haase A, Frahm J, Matthaei D, Hänicke W, Merboldt KD (1986) Flash imaging: rapid NMR imaging using low flip-angle pulses. *J Magn Reson* **67**: 258–266
- Hennig J, Friedburg H (1988) Clinical applications and methodological developments of the RARE technique. *Magn Reson Imaging* **6**: 391–395
- Hennig J, Hodapp M (1993) Burst imaging. *MAGMA* **1**: 39–48
- Hennig J, Nauerth A, Friedberg H (1986) RARE imaging: A fast imaging method for clinical MR. *Magn Reson Med* **3**: 823–833
- Hoppel BE, Weisskoff RM, Thulborn KR (1993) Measurement of regional blood oxygenation and cerebral hemodynamics. *Magn Reson Med* **30**: 715–723
- Hurst GC, Hua J, Simonetti OP, Duerk JL (1992) Signal-to-noise, resolution and bias function analysis of asymmetric sampling with zero-padded magnitude FT reconstruction. *Magn Reson Med* **27**: 247–269
- Jakob PM, Schlaug G, Griswold KO (1998) Functional burst imaging. *Magn Reson Med* **40**: 614–621
- Kiefer B, Grassner J, Hausmann R (1994) Image acquisition in a second with half-Fourier acquisition single shot turbo spin echo. *J Magn Reson Imaging* **4**(P): 86
- Liu G, Sobering G, van Gelderen P, Olson AW, Moonen CJW (1993a) Fast echo-shifted gradient-recalled MRI: combining a short repetition time with variable T2\* weighting. *Magn Reson Med* **30**: 68–75
- Liu G, Sobering G, Duyn JH, Moonen CTW (1993b) A functional MRI technique combining principles of echo shifting with a train of observations (PRESTO). *Magn Reson Med* **30**: 764
- Lovblad KO, Thomas R, Jakob PM, et al. (1999) Silent functional magnetic resonance imaging demonstrates focal activation in rapid eye movement sleep. *Neurology* **53**: 2193–2195
- Lowe IJ, Wysong RE (1993) DANTE ultrafast imaging sequence (DUFIS). *J Magn Reson* **101**: 106–109
- Mansfield P (1977) Multi-planar image formation using NMR spin echoes. *J Phys* **C10**: L55–L58
- Moonen CTW, Liu G, van Gelderen P, Sobering G (1992) A fast gradient-recalled MRI technique with increased sensitivity to dynamic susceptibility effects. *Magn Reson Med* **26**: 184–189
- Moonen CTW, Barrios FA, Zigun JZ, et al. (1994) Functional brain MR imaging based on bolus tracking with a fast T2\*-sensitized gradient echo method. *Magn Reson Imaging* **12**: 379–385
- Mugler JP, Brookeman JR (1990) Three dimensional magnetization prepared rapid gradient echo imaging (3D MP-RAGE). *Magn Reson Med* **15**: 152–157
- Noll DC (1995) Methodologic considerations for spiral k-space functional MRI. *Int J Imaging Syst Tech* **6**: 175–183
- Noll DC, Cohen JD, Meyer CH, Schneider W (1995) Spiral k-space MR imaging of cortical activation. *J Magn Reson Imaging* **5**: 49–56
- Reilly J (1989) Peripheral nerve stimulation by induced electric currents: exposure to time varying magnetic fields. *Med Biol Eng Comput* **27**: 101–110
- Savoy RL, Ravicz ME, Gollub R (1999). The psychophysiological laboratory in the magnet: stimulus delivery, response recording, and safety. In *Functional MRI*, Moonen CTW, Bandettini PA, eds. Berlin: Springer, pp. 347–365
- Schmitt F, Stehling MK, Turner R (1998a). *Echo Planar Imaging: Theory, Technique and Application*. Berlin: Springer
- Schmitt F, Irnich W, Fischer H (1998b) Physiological side effects of fast gradient switching. In *Echo Planar Imaging: Theory, Technique and Application*, Schmitt F, Stehling MK, Turner R, eds. Berlin: Springer, pp. 201–252
- Shellock FG, Kanal E (1996) Bioeffects and safety of MR procedures. In *Clinical Magnetic Resonance Imaging*, Edelman RR, Hesselink JR, Zlatkin MB, eds. Philadelphia, PA: Saunders, pp. 391–434
- Wehrli FW (1990) Fast-acan magnetic resonance: principles and applications. *Magn Reson Quart* **6**: 165–236
- Wong EC, Bandettini PA, Hyde JS (1992). Echo-planar imaging of the human brain using a three axis local gradient coil. In *Eleventh Annual Meeting of the Society of Magnetic Resonance in Medicine*, Berlin, p. 105
- Zha L and Lowe IJ (1995) Optimized ultra-fast imaging sequence (OUFIS). *Magn Reson Med* **33**: 377–395.

# Noise and artifacts in MR images

<b>Image noise</b>	<i>page</i> 252
Image signal to noise ratio	252
Noise distribution	255
Spatial smoothing	257
Spatial correlations in noise	258
Smoothing compared with reduced resolution acquisitions	259
<b>Image distortions and artifacts</b>	261
Ghost images in echo planar imaging	261
Effects of $T_2^*$ on image quality	262
Image distortion from off-resonance effects	265
Motion artifacts	270
Physiological noise	273

## Image noise

### Image signal to noise ratio

Chapter 9 described how the local MR signal is mapped with MRI. However, noise enters the imaging process in addition to the desired MR signal, so the signal to noise ratio (SNR) is a critical factor that determines whether an MR image is useful (Hoult and Richards 1979; Macovski 1996; Parker and Gullberg 1990). The signal itself depends on the magnitude of the current created in a detector coil by the local precessing magnetization in the body. The noise comes from all other sources that produce stray currents in the detector coil, such as fluctuating magnetic fields arising from random ionic currents in the body and thermal fluctuations in the detector coil itself.

The nature of the noise in MR images is critical for the interpretation of fMRI data. The signal changes associated with blood oxygenation changes are weak, and the central question that must be addressed when interpreting fMRI data is whether an observed change is real, in the sense of being caused by brain activation, or whether it is a random fluctuation caused by the noise in the images. This remains a difficult problem in fMRI because the noise has several sources and is not well characterized. Noise is a general term that describes any process that causes the measured signal to fluctuate in addition to the intrinsic NMR signal of interest. In MRI, there are two primary sources of noise: *thermal noise* and *physiological noise*. We will begin with the thermal noise because it is better understood and take up physiological noise at the end of the chapter. In many applications, the thermal noise is the primary source of noise, but in dynamic imaging the dominant source of noise often is physiological.

The SNR depends strongly on the radiofrequency (RF) coil used for signal detection. A small surface coil near the source of the signal picks up less stray noise from the rest of the

body, and for focal studies, such as fMRI experiments measuring activation in the visual cortex, the SNR can be improved by using a well-placed small surface coil for RF detection. The limitation of small coils, however, is that they provide only limited coverage of the brain. The trade-off between small coils for better SNR and large coils for better coverage can be overcome by using multiple small coils in a phased array system (Grant *et al.* 1998). This requires a scanner hardware configuration with multiple receiver channels to accommodate the multiple coils, and this is now standard on most MRI systems. The result is the SNR of a small coil but with more extended coverage, although the sensitivity pattern of a phased array system is not as uniform as the pattern of a larger head coil optimized for uniformity.

Once the hardware has been optimized to provide the most sensitive detection of the MR signal, the SNR in an image still depends strongly on the pulse sequence used to acquire the data. Three factors affect this pulse-sequence-dependent SNR. The first is the intrinsic magnitude of the generated transverse magnetization at the time of data acquisition. The flexibility of MR as an imaging modality comes from the ease with which we can manipulate this transverse magnetization so that its magnitude reflects different properties of the tissue, as described in Chs. 6–8. Density-weighted,  $T_1$ -weighted, and  $T_2$ -weighted images all are commonly used, and the transverse magnetization is manipulated to reflect these weightings by adjusting pulse sequence parameters such as the repetition time (TR) and the echo time (TE). The maximum value of the transverse magnetization is  $M_0$ , the local equilibrium magnetization. With higher magnetic field strengths ( $B_0$ ),  $M_0$  increases because of the greater alignment of spins with the field. Because  $M_0$  sets the scale for the magnitude of the transverse magnetization, the SNR improves with increasing  $B_0$ , and this is a primary motivation for the development of high-field MRI systems.

The second factor that affects the SNR is the voxel volume. When more spins contribute to the local signal, we would naturally expect the SNR to be larger. However, from the discussion of the point spread function (PSF) of the image in Ch. 9, the voxel volume may appear to be a somewhat slippery concept. Intuitively, we would like to be able to look at one point in the reconstructed image and interpret the intensity there as an average of the signals over a small volume. In general, however, the reconstructed signal at a point has contributions from the entire image plane, defined by the PSF, although the reconstructed intensity is certainly dominated by the nearby signals. The definition of voxel volume is thus somewhat approximate, describing the volume that contributes most of the signal to the intensity at a point in the image.

A useful definition of voxel volume is to treat it as a rectangular block with dimensions on each side equal to the corresponding resolution on each axis, giving a specific volume  $\Delta V$ . In the same fashion above, we defined the resolution along an axis as the equivalent width of a rectangular PSF with the same central value as the actual PSF. For the standard sinc-shaped PSF from a rectangular window in  $k$ -space (Eq. [9.5]), the resolution is the distance from the center to the first zero-crossing. The voxel volume is then the product of these resolution dimensions along each of the three spatial axes. This view, although only a rough approximation, is useful for manipulating data, such as reslicing a three-dimensional block of data to construct a new plane. But it is important to remember that a rectangular block is only a crude picture of the resolution of an MR image. The true resolved volume has a more complicated appearance described by the PSF in each of the directions.

Finally, the third factor that affects the SNR of a voxel is the total time spent collecting data from that voxel. The total time,  $T$ , depends on the length of the data acquisition window, the number of repetitions of the acquisition required to sample  $k$ -space, and the number of

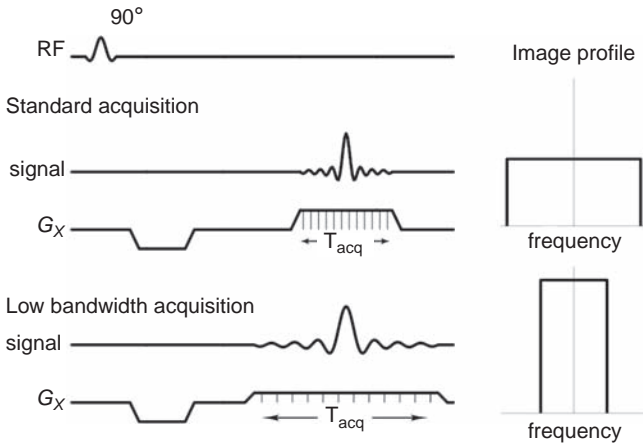


**Fig. 11.1.** Changing the image acquisition time. The diagrams show two forms of the read-out gradient pulses used for frequency encoding that measure the same points in  $k$ -space. In the low-bandwidth version, the gradient amplitude ( $G_x$ ) is reduced, and the time between samples is increased so that the area under the gradient between samples is held constant. With a weaker gradient, the signal from the object being imaged is spread over a narrower range of frequencies. Because noise enters the data uniformly at all frequencies, the signal to noise ratio is improved with the low-bandwidth sequence. RF, radiofrequency;  $T_{acq}$  acquisition time.

averages performed for each of the sampled points in  $k$ -space. Specifically, if the pulse sequence is repeated  $n$  times in collecting data for the image, and the acquisition time on each repetition is  $T_{acq}$ , then  $T = nT_{acq}$ . The SNR is then

$$\text{SNR} \propto M \Delta V \sqrt{T} \quad (11.1)$$

where  $\Delta V$  is the voxel volume and  $M$  the transverse magnetization. This expression is written as a proportionality because the absolute number depends on the coil configuration used. Equation (11.1) is useful for describing how changes in the pulse sequence will affect SNR for the same coil setup. The SNR is directly proportional to the intrinsic signal of the transverse magnetization and the volume of tissue contributing to each voxel, both of which are intuitively clear. The SNR is also proportional to the square root of the time spent collecting data, a dependence that is familiar from averaging data, in which the SNR increases with the square root of the number of averages.

It may seem surprising that the expression for SNR is as simple as this. Imaging pulse sequences use different gradient strengths and data sampling rates, and yet these parameters do not enter directly into the expression for SNR. In fact, these parameters are important, and one can look at SNR from the point of view of the bandwidth associated with each voxel. For example, using a stronger frequency-encoding gradient produces a larger spread of frequencies across the field of view (FOV) and so associates each voxel with a larger bandwidth (Fig. 11.1). Noise enters uniformly at all frequencies, with a net amplitude proportional to the square root of the bandwidth, and so the larger bandwidth means that more noise enters each voxel. But to produce the same voxel size in the image (i.e., the same sampling in  $k$ -space), the signal during the stronger read-out gradient would have to be sampled more rapidly because the relative phases of signals at different locations would be evolving more rapidly, and the total data collection time would be reduced. This is why we can represent the SNR just in terms of the total time spent collecting data. All the manipulations of the gradients and sampling rates that modify the bandwidth per voxel, for the same image resolution, simply translate into a change in the data acquisition time. A pulse sequence that uses a longer read-out time with a reduced gradient amplitude to improve SNR is often called a *low-bandwidth* sequence.

Equation (11.1) explains some features of MRI that are not immediately obvious. An important practical question is whether averaging the  $k$ -space samples for an image with a small FOV gives a better SNR than collecting more  $k$ -space samples to image a larger FOV. Consider two images of the same plane, made with the same resolution. In the first image, the FOV is 20 cm measured with 128 phase-encoding steps, and each phase-encoding step is measured twice to improve the SNR. In the second image, the FOV is 40 cm measured with 256 different phase-encoding steps, with each step measured only once. Then the total time required to collect each image is the same (both acquisitions collect a total of 256 phase-encoding steps), and the resolution is the same. In the second image, the head appears smaller in the frame because the FOV is larger, but it is a 256 matrix compared with the 128 matrix of the first image. The central 128 matrix from the second image is then identical to the first image in imaging time, FOV, and resolution. Which image has the higher SNR? Naively, it seems that in the second image the extra work done by the additional phase-encoding steps was to provide an extensive view of the empty space around the head, data that seem irrelevant to the central image of the brain. The first image seems somehow more tightly focused on imaging the head, and so it seems plausible that averaging this more critical data should provide a better SNR. But in fact, the SNR is identical in the two images, as shown by Eq. (11.1). The voxel volume is the same, and the total time spent collecting the data is the same. In short, using different phase-encoding steps instead of repeating a more limited set for the same resolution exacts no cost in SNR and yet provides an image of a larger FOV.

## Noise distribution

In MRI, each measured signal intensity during data acquisition corresponds to a sample in  $k$ -space, as described in Ch. 9. Our goal now is to understand how random noise in the measured  $k$ -space samples produces noise in the reconstructed image intensities. Each  $k$ -space sample can be thought of as a complex number with a real and an imaginary component, and independent noise is added to each component. To clarify the nature of the noise in a concrete way, consider a simple one-dimensional imaging experiment in which 128 samples are measured in  $k$ -space, with the data reconstructed as a 512-point one-dimensional image. Furthermore, suppose that the intensity profile being imaged is perfectly flat in the middle and somewhat rounded at the edges so that the Gibbs artifact is not important, as illustrated in Fig. 11.2. The ideal, noiseless image is shown as a dashed line, and

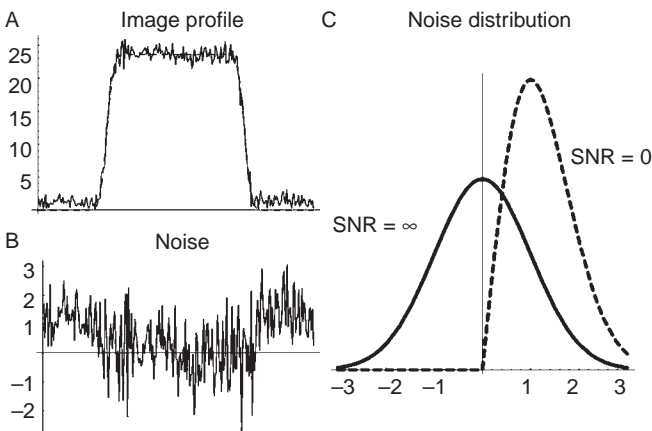


**Fig. 11.2.** Noise in MR images. Noise added to the measured  $k$ -space samples is transformed into noise in the reconstructed images. The one-dimensional profile of a magnitude image illustrates how the noise appears different in regions of high signal to noise ratio (SNR) (A) and in the background air space with no intrinsic signal (B). For normal Gaussian noise in the  $k$ -space data, the noise in a magnitude image is approximately Gaussian for high SNR but distinctly non-Gaussian when the SNR is low (C).

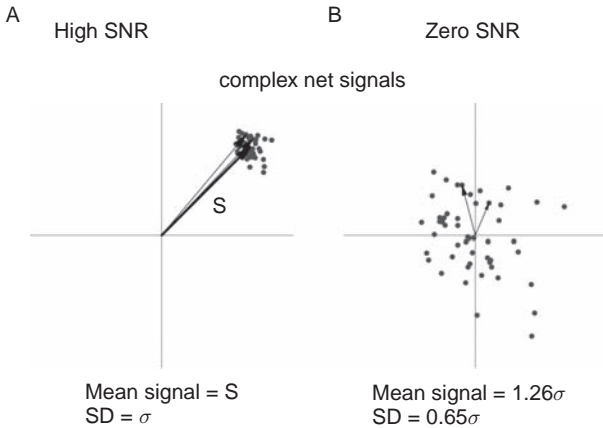


**Fig. 11.3.** Noise in magnitude images. The full net signal reconstructed in each pixel is a complex number, and noise in the measured  $k$ -space samples adds independently to each of the complex components (the variability of the measured vector as a result of noise is shown as dots). In a magnitude image, the pixel intensity is the magnitude of this complex number. (A) For high signal to noise ratio (SNR), only the noise component along the intrinsic signal vector contributes, so the image noise has a mean of zero and a standard deviation  $\sigma$ . (B) However, when there is no intrinsic signal, as in the air space around the head, the mean of the noise is  $1.26\sigma$  instead of zero (because there are no negative magnitudes) and the standard deviation is  $0.65\sigma$  (see distributions in Fig. 11.2).

an image with noise is shown as a solid line. Subtracting the two gives an image of just the noise component, amplified in Fig. 11.2 to make it clearer.

The first effect to notice is that the noise looks different outside the object than it does inside. Inside, the noise has a mean of zero, and the distribution of values around zero has a standard Gaussian shape. But outside the object, the noise distribution is distinctly non-Gaussian, and the mean is not zero. This peculiar behavior results from the fact that we have reconstructed a *magnitude* image. When the image is reconstructed with the Fourier transform, the noise signals in each component of the  $k$ -space signal are transformed into noise in the real and imaginary components of the image. The net signal in a reconstructed voxel is then the sum of the intrinsic MR signal and the complex noise signal, and we can think of this as adding two vectors in the complex plane (Fig. 11.3).

When the SNR is large, a small random noise vector is added to a large signal vector. In this case, only the component of the noise along the direction of the intrinsic signal vector contributes significantly to changing the magnitude of the net vector, and the fluctuations of any one component of the noise are normally distributed with a mean of zero. As a result, the distribution of measured magnitudes is centered on the intrinsic magnitude and normally distributed. But when the SNR is zero, there is no intrinsic signal, just a small randomly oriented noise vector in the complex plane. In the magnitude image, the measured pixel value will be the length of this random vector. However, the distribution of the lengths of a random vector in a plane is very different from a Gaussian. The magnitude can never have a negative amplitude, and the probability that the net vector will have a length near zero is small. If the standard deviation with high SNR is  $\sigma$ , then in the background of the image, where there is no intrinsic signal, the mean is  $1.26\sigma$  and the standard deviation is  $0.65\sigma$ .

In short, the noise distribution in the image is Gaussian only when the SNR is high. In practice, for an  $\text{SNR} > 3$ , the assumption of a Gaussian distribution is a reasonable approximation, although it is good to remember that, strictly speaking, this is only true for infinite SNR. This also illustrates that one must be careful when estimating the amplitude of the noise from measurements in the background air space of the image. The mean of the background is not zero, but this does not mean that an offset has been added to every point in the

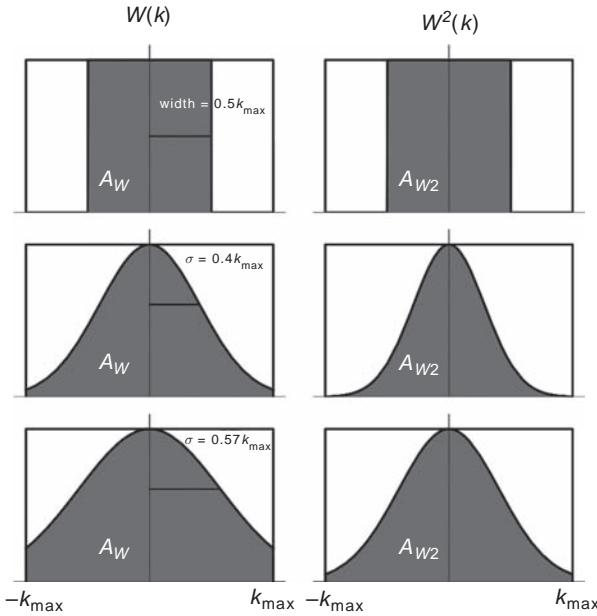
image; when the SNR is high, there is no offset of the mean. Furthermore, either the background mean or the standard deviation can be used to estimate the noise in an image, since both are proportional to  $\sigma$ , but the measured values must be appropriately scaled as described above to measure the value of  $\sigma$  appropriate for the high SNR parts of the image.

## Spatial smoothing

In most imaging applications, the raw SNR is sufficiently high that the alterations of the noise distribution associated with working with a magnitude image are negligible, and we can assume a normal distribution for the noise. The raw SNR is given by Eq. (11.1) and depends on the image voxel size and the time spent collecting data from that voxel. In fMRI applications, the goal is to be able to identify small changes in the signal, so to improve the SNR of each voxel measurement, the images are often further smoothed in post-processing. In Ch. 9, the effect of smoothing in post-processing on spatial resolution was considered. Smoothing with a function  $w(x)$  is equivalent to multiplying the  $k$ -space distribution by a windowing function  $W(k)$ , the Fourier transform of  $w(x)$ . Smoothing worsens the spatial resolution, and the resolution distance is increased in proportion to the reduction in area under  $W(k)$  compared with the original rectangular sampling window in  $k$ -space (see Fig. 9.17). Then, for example, a rectangular sampling window extending out to only  $k_{\max}/2$  or a Gaussian window with  $\sigma = 0.404k_{\max}$  will both reduce the area under the windowing function by a factor of 2, and so double the resolution distance. Both of these smoothings should improve the SNR at a point as well, but by how much?

To answer this question, we need to separate the effects of smoothing on the intrinsic signal itself and on the noise. The effect of smoothing on the intrinsic signal depends on the size and uniformity of the object. So for now we will restrict the question just to the noise component. What is the effect of smoothing on the random noise component added to the signal in a pixel? To further simplify matters, we will continue to consider one-dimensional imaging. Based on our intuitive understanding of averaging, we might naively expect that the noise should be reduced by the square root of the increase in the resolution distance. But the behavior of the noise turns out to be somewhat subtle. The improvement in the noise amplitude does not depend on the area under  $W(k)$ , which governs how the resolution changes with smoothing, but rather on the area under  $W^2(k)$  (Fig. 11.4). For rectangular windows, this distinction does not matter because the amplitude of the rectangle is one: the square of the window function then is the same as the function itself. So, if the image is smoothed by multiplying  $k$ -space by a narrower rectangle (i.e., by simply deleting the samples corresponding to high spatial frequencies), the SNR improves by the square root of the increase in the resolution distance, in agreement with our naive intuition, that doubling the resolution distance decreases the noise by  $\sqrt{2} \cong 1.41$ .

Multiplying  $k$ -space with a rectangular window is equivalent to smoothing the image with a sinc function (Eq. [9.5]). Smoothing with any other function will affect the noise differently. For example, a Gaussian window has a value of 1 at the center of  $k$ -space, but  $< 1$  at all other points (Fig. 11.4). That is, this window modifies the amplitudes in  $k$ -space, rather than eliminating some of them entirely as with the rectangular window. The curve  $W^2(k)$  is then narrower than  $W(k)$ . For the Gaussian with  $\sigma = 0.404k_{\max}$ , the area under  $W(k)$  is reduced by a factor of 2, but the area under  $W^2(k)$  is reduced by a factor of approximately 2.8. Thus, the resolution distance is increased by a factor of 2, but the SNR is increased by  $\sqrt{2.8} \cong 1.67$ . The differential effect of smoothing on resolution and noise comes about because the post-processing smoothing changes the shape of the PSF. If the new PSF were the same shape as



$$\text{Resolution distance} = 1/A_W$$

$$\text{Noise correlation distance} = 1/A_{W2}$$

$$\text{SNR} = \text{SNR}_0 / \sqrt{A_{W2}}$$

**Fig. 11.4.** Effect of image smoothing on resolution, noise correlations, and the signal to noise ratio (SNR). Smoothing an image is equivalent to multiplying the  $k$ -space data by a windowing function  $W(k)$ . In these examples, the original window resulting from  $k$ -space sampling is shown as a rectangle with amplitude one extending from  $-k_{\max}$  to  $k_{\max}$ . With smoothing, the change in the resolution distance is determined by  $A_W$ , the fractional area under  $W(k)$  compared with the area of the original rectangular sampling window. However, the noise correlation distance and the SNR depend on  $A_{W2}$ , the fractional area under  $W^2(k)$ . For a rectangular window,  $A_W = A_{W2}$  (top row), but for a Gaussian window (or any window other than a rectangle), the two are different. The Gaussian window that increases the resolution distance by a factor of 2 (middle) is narrower than the Gaussian window that increases the correlation distance by a factor of 2 (bottom).  $\sigma$ , standard deviation.

the original (i.e., if the new window is a narrower rectangle), the noise change would be inversely proportional to the square root of the resolution change. However, the Gaussian window alters the shape as well as broadening the PSF, and the result is that the benefit of improved SNR is greater than one might naively expect given the cost in loss of resolution.

## Spatial correlations in noise

The preceding arguments considered the noise that appears in one pixel of the reconstructed image. That is, if we repeated the one-dimensional experiment in Fig. 11.2 many times, looking at the noise values at one pixel, we would find SNR-dependent distributions like those shown. In particular, if we look just at the high-SNR plateau, the noise is normally distributed. However, we can reconstruct the image with as many pixels as we like, and clearly the noise in two adjacent pixels cannot be entirely independent. Intuitively, we would expect that  $N$  samples in  $k$ -space, each with an independent noise contribution, could lead to no more than  $N$  independent noise signals in the image. In an image reconstructed with the pixel size smaller than the intrinsic resolution, there will be correlations of the noise in nearby pixels. The practical effect of noise correlations becomes clear when we try to average the data on the plateau. For example, for two independent measurements of the same intrinsic signal, we expect the noise samples to add incoherently, so the net increase in the noise component is only  $\sqrt{2}$  whereas the intrinsic signal doubles. The SNR then improves by  $\sqrt{2}$ . If the noise samples are correlated, they add more coherently, and the improvement in SNR is not as great. In the extreme case of perfectly correlated noise, there is no improvement with averaging at all.



Prior to any smoothing, the thermal noise in the raw image should be uncorrelated between one resolution element and the next. Note, though, that physiological noise, and systematic scanner fluctuations, can produce additional noise that can be highly correlated. For the moment, we just want to consider how smoothing in post-processing alters the spatial noise correlations. We can define an effective correlation distance  $x_{\text{corr}}$  as the distance apart two points must be for there to be no correlation in the noise signals. Then for the original image prior to smoothing,  $x_{\text{corr}} = \Delta x_0$ , the intrinsic resolution of the image. After smoothing with a windowing function  $W(k)$ , the correlation distance and the resolution diverge unless  $W(k)$  is a simple rectangle. This behavior is identical to the SNR itself, which scales with the area under  $W^2(k)$  (see the discussion above).

It is interesting that smoothing the image has different effects on resolution and noise correlation. To summarize the arguments, we can think of three characteristic distances in the image: (1) the intrinsic resolution  $\Delta x_0$ , set by the initial acquisition in  $k$ -space; (2) the final resolution  $\Delta x$  after smoothing with a windowing function  $W(k)$ ; and (3) the noise correlation distance  $x_{\text{corr}}$  resulting from applying  $W(k)$ . These three distances are

$$\begin{aligned}\Delta x_0 &= \frac{1}{2k_{\text{max}}} \\ \Delta x &= \frac{1}{A_w} \\ x_{\text{corr}} &= \frac{1}{A_{w^2}}\end{aligned}\tag{11.2}$$

where  $A_w$  is the area under  $W(k)$  and  $A_{w^2}$  is the area under  $W^2(k)$ . If no post-processing is done, these three distances are the same, and if  $W(k)$  is rectangular in shape, these three distances change by the same amount. If, for example,  $k$ -space is multiplied by a Gaussian window with  $\sigma_w = 0.57k_{\text{max}}$ , then  $\Delta x \cong 1.5\Delta x_0$ , and  $x_{\text{corr}} \cong 2\Delta x_0$ . From the preceding arguments, the reduction in image noise follows the change in correlation length rather than the change in resolution, so SNR is improved by  $\sqrt{2}$  in this example. The changes in the three lengths are different because smoothing with any function  $W(k)$  other than a rectangle changes the shape of the PSF.

## Smoothing compared with reduced resolution acquisitions

These considerations of the effects of smoothing on resolution and noise bring us to an important issue. Spatial smoothing occurs in the imaging process itself because of the finite range of  $k$ -space sampling, but it can also be applied in post-processing. If the goal is to maximize the SNR for a given spatial resolution, what is the most efficient way to collect and process the data?

Consider three strategies for producing a one-dimensional image with a given resolution in a fixed data acquisition time: (1) acquire an image with resolution twice as good as needed, and then smooth the image with a sinc function to increase the resolution distance by a factor of 2; (2) acquire the same image, but smooth with a Gaussian to achieve the same resolution distance; or (3) acquire an image with the desired coarser resolution, and since this only takes half as long as the first two, acquire it again, average to reduce the noise, and do no post-processing. These three strategies produce images with the same resolution in the same total data acquisition time, but which has the best SNR?

To begin with, let the raw SNR in the images acquired with better resolution than is needed be  $\text{SNR}_0$ , and we can then see how each strategy improves it. For strategy 3, there is no

smoothing in post-processing, but the raw voxel size is larger by a factor of 2, so by Eq. (11.1),  $\text{SNR}_3 = 2\text{SNR}_0$ . For strategy 1, smoothing with a sinc function to increase the resolution distance by a factor of 2 increases SNR by  $\sqrt{2}$  so  $\text{SNR}_1 = 1.41\text{SNR}_0$ . In fact, smoothing with a sinc function is equivalent to throwing away the outer  $k$ -space samples (windowing with a narrower rectangle), so the final  $k$ -space sampling locations are identical to those acquired with strategy 3. But whatever time was spent collecting those large  $k$  samples was wasted, and so strategy 3 is more efficient. Finally, strategy 2 produces  $\text{SNR}_2 = 1.67\text{SNR}_0$ , as discussed above and so is intermediate between the other two strategies.

In short, collecting data sufficient to produce a high-resolution image, and then smoothing it to the desired coarser resolution, is an inefficient way to improve SNR. It is better to collect only the data required for the desired resolution and then to use the extra time to average that data. This seems to contradict the argument made above concerning acquisition of extra  $k$ -space data to increase the FOV. There we argued that, for constant resolution, acquiring extra points in  $k$ -space to reconstruct an image with a larger FOV produced the same SNR as an image with a smaller FOV that was averaged for the same total time. The argument was that in both cases the total acquisition time  $T$  in Eq. (11.1) was the same. But here we are arguing the opposite for acquiring extra  $k$ -space samples to reconstruct an image with better spatial resolution: that the SNR of the smoothed image is degraded compared with what it could have been by focusing only on the desired  $k$ -space samples.

The root of this apparent paradox is whether the extra  $k$ -space samples are higher or lower than the desired  $k_{\text{max}}$ . The extra samples that increase the FOV are between the original samples, and so for all these samples,  $k < k_{\text{max}}$ . The samples that improve resolution beyond what is desired are all high spatial frequencies with  $k > k_{\text{max}}$ . All  $k$ -space samples with  $k < k_{\text{max}}$  contribute to the SNR, whereas samples with  $k > k_{\text{max}}$  are wasted. One way to think about this is to imagine that we are imaging a single small cube with the dimensions of the desired voxel (i.e.,  $1/2k_{\text{max}}$ ) and to examine the amplitude of each of the measured samples of the signal by considering the sine wave pattern across that cube corresponding to different values of  $k$ . For low values of  $k$ , the wavelength is longer than the voxel dimension, so all the signals within the voxel add approximately coherently, and the signal is strong. The image reconstruction process then adds up each of these signals, so each contributes to the SNR in a way equivalent to simple averaging. For high values of  $k$ , corresponding to wavelengths smaller than the voxel dimension, there is substantial phase variation within the voxel, and so the net signal is greatly reduced. If we imagine averaging these signals with the others, they do not improve the SNR. They add very little of the intrinsic signal and yet contribute noise to the average.

So, in general, spatial smoothing in post-processing is a poor strategy for improving SNR. Nevertheless, it is often done for practical reasons. For example, the available pulse sequences on the MR scanner may not allow complete control over these parameters. Also, in the preceding example comparing a Gaussian-smoothed high-resolution image with an acquired and averaged low-resolution image, the final resolution distance is the same, but the images are not identical because the PSFs have a different shape. The Gaussian-smoothed image shows much less of a Gibbs artifact (see Fig. 9.17). Furthermore, a Gaussian-smoothed image may be easier to work with when considering the statistical correlations of noise in the image. For example, to improve the sensitivity for detecting small signal changes in fMRI, clustering algorithms that look for several nearby pixels activated together are sometimes used. The rationale for this is that the probability of several adjacent pixels all showing spurious activations from noise is much more unlikely than a single pixel showing the same magnitude of random signal change (Lange 1996; Poline *et al.*

1997). To interpret the significance of clusters of activated pixels, it is necessary to understand how the noise is correlated between one pixel and another. The statistical analysis of Gaussian random fields is well developed, so Gaussian smoothing will put the images closer to a more convenient form (Friston 1996). It is important to remember that choosing such a strategy, of significant smoothing in post-processing, makes a sacrifice in the SNR that could be attained by optimizing the image acquisition instead.

## Image distortions and artifacts

### Ghost images in echo planar imaging

One of the most common image artifacts encountered in fMRI studies with echo planar imaging (EPI) are faint ghost images shifted by half an image (Fig. 11.5). Specifically, the ghost appears as an image of the head shifted in the phase-encoded direction by  $N/2$  pixels, where  $N$  is the number of resolved voxels along this axis (we will refer to the phase-encoded axis as  $y$  even if it is not the vertical axis of the image). The half of the ghost shifted out of the image frame is wrapped around to the other side of the image. A useful way to understand artifacts such as this is look at it from the viewpoint of how the sampling in  $k$ -space has been affected. For the EPI ghost, the problem arises from the way the lines in  $k$ -space are sampled.

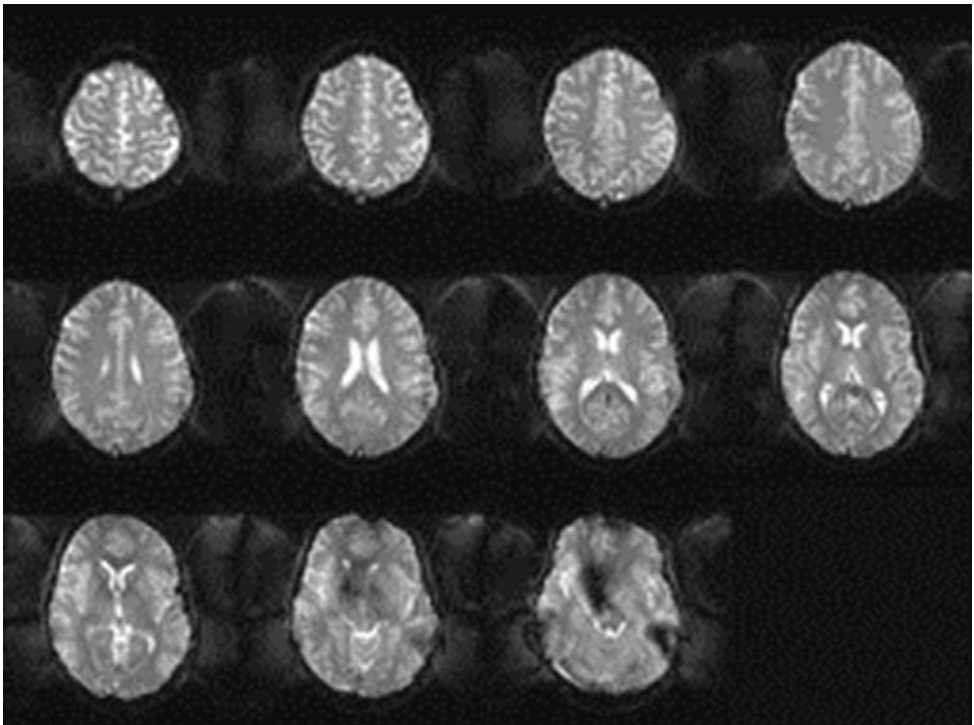


**Fig. 11.5.** Echo planar imaging (EPI) artifacts. Single-shot EPI images of several brain sections are shown with the gray-scale window set to reveal the weak ghosts in the background. Any systematic effect that causes alternate lines in  $k$ -space to differ produces  $N/2$  ghosts, an image of the brain shifted by half an image frame and wrapped around the other side. The inferior images also show signal dropouts from magnetic susceptibility variations and a resulting shortening of  $T_2^*$ . (Data courtesy of E. Wong.)

With EPI, the  $k$ -space trajectory is a back and forth motion, with the  $k$ -space sampling moving to the left for one line and back to the right for the next line. This alternation in scanning direction can lead to a systematic difference between the odd and even lines in  $k$ -space. For example, if the gradients are not precisely balanced, the gradient echo can be displaced from the center of data acquisition in each read-out period. Furthermore, if the gradient echo occurs earlier when the odd  $k_y$ -space lines are collected, it will occur later when the even lines are collected. Alternating lines in  $k_y$  then are consistently different.

We can think about this periodic modulation of the  $k$ -space samples by imagining the full data to consist of a true set of  $k$ -space samples that accurately reflect the true image plus another set that consists of the true  $k$ -space values multiplied by another function  $H(k)$ . That is, the first set are the correct values, and the second set is the error set that will produce an artifact in the image. The Fourier transform used to reconstruct the image is linear, so the image is the sum of the separate images of these two sets of  $k$ -space samples. The true set of samples produces the correct image, but added to this is the artifactual image. Then we can look at the formation of the artifact just as we looked at smoothing (convolution) in the image domain above as a multiplication by a windowing function  $W(k)$ . The resulting artifactual image is the convolution of the true image with the Fourier transform of  $H(k)$ .

For the case of the  $N/2$  ghosts, the effect of multiplying by  $H(k)$  is to produce a modulation in  $k_y$  that alternates with each line. We can see the general form of the Fourier transform of  $H(k)$  just from the nature of the  $k$ -space description and the symmetry of the Fourier transform. If we were to reverse domains, and instead look at a periodic modulation of the image domain, we know that a pattern repeating with every other line in the image is in fact the highest spatial-frequency component in the image, and it is described by a single point at the maximum value of  $k_y$  in the  $k$ -space domain. Then because the Fourier transform is symmetric, the Fourier transform of a pattern that alternates with each line in  $k_y$  is a single point at the maximum value of  $y$  (i.e., at the edge of the image). And the convolution of the true image with a spike (a  $\delta$ -function) at the edge of the image simply moves the image to be centered on the spike. In other words, the artifactual ghost image is shifted by half of the image frame.

Note that this type of ghost could arise from any effect that causes alternate sampled lines in  $k$ -space to vary. The structure of the artifact is directly related to the periodicity in  $k$ -space. In the following, we examine a number of sources of artifacts in terms of how they affect the  $k$ -space data.

## Effects of $T_2^*$ on image quality

Turning back now to the intrinsic SNR from image acquisition itself, Eq. (11.1) suggests that the raw SNR can be improved by lengthening the data acquisition time. Consider again the prototype measurement of a gradient echo to sample one line in  $k$ -space, as illustrated in Fig. 11.1. The data acquisition window can be lengthened, while maintaining the same spatial resolution and FOV, by reducing the gradient strength and sampling the signal more slowly in time. The relative phase changes induced by the weaker gradient evolve more slowly, so the total time needed to sample the same points in  $k$ -space is increased. Halving the read-out gradient and the data sampling rate and doubling the acquisition window would yield the same sampling in  $k$ -space, but with SNR improved by  $\sqrt{2}$  as a result of the longer acquisition time. By the SNR argument alone, using even weaker gradients and longer acquisition times would continue to improve the image SNR. But two other effects become important as the data acquisition window is increased: relaxation effects and off-resonance effects.

As the data acquisition time is increased, we begin to come into direct conflict with one of the basic assumptions of MRI, that the MR image is a snapshot of the distribution of transverse magnetization at one instant of time. This cannot be perfectly true because some time is required to allow the applied field gradients to induce local phase changes, which creates the sampling in  $k$ -space. To be more precise, the basic premise of MRI is that the intrinsic local magnetization has a constant amplitude during data acquisition so that the measured signal changes all result from the controlled interference of these signals induced by the gradients, and not from changes in the intrinsic signals themselves. This is a good approximation if the acquisition time is much less than  $T_2^*$ , the apparent transverse relaxation rate for a voxel. But as the acquisition time is increased, relaxation effects can cause a signal change unrelated to the effects of the gradient pulses. Because the signal measured over time is interpreted as samples in  $k$ -space, relaxation effects alter the  $k$ -space data. In this way, they act like a natural filter, analogous to the applied filter for smoothing discussed above. Relaxation effects, therefore, alter the windowing function in  $k$ -space and so modify the PSF. In the extreme case of using a data acquisition window much longer than  $T_2^*$ , the PSF is dominated by  $T_2^*$  effects rather than the applied gradients. Although large values of  $k_{\max}$  are measured, if the intrinsic signal has decayed away by the time these samples are measured, the associated amplitude in  $k$ -space is near zero. The high spatial frequencies are then suppressed, and the image is blurred. For this reason,  $T_2^*$  sets a practical upper limit for the data acquisition time.

The blurring effect of  $T_2^*$  signal loss during data acquisition is, in fact, somewhat subtle. In most acquisitions, the  $k$ -space trajectory moves from  $-k_{\max}$  to  $+k_{\max}$ , with the  $k = 0$  sample measured in the center of the acquisition window. The high positive  $k$ -values are attenuated relative to the intrinsic signal at the time of the  $k = 0$  sample through  $T_2^*$  decay. The samples for negative  $k$ -values are enhanced relative to the  $k = 0$  sample, however, in the sense that the intrinsic signal has not decayed as much when these samples are measured. The added windowing function in  $k$ -space as a result of  $T_2^*$  decay is, therefore, not symmetric around the  $k = 0$  sample. This effect is illustrated in Fig. 11.6. In effect, the amplified negative large  $k$ -values partly offset the diminished positive large  $k$ -values so that the blurring for when the acquisition time is equal to  $T_2^*$  is not very significant. For an acquisition time of  $3T_2^*$ , the PSF is more severely distorted.

The apparent transverse relaxation rate is a somewhat ill-defined number. The true, intrinsic  $T_2$  is the natural decay time for transverse magnetization, and although it depends on the type of tissue, it does not depend on the size of the imaging voxel. But  $T_2^*$  includes both intrinsic relaxation and effects from field inhomogeneity, and the latter effects can depend on the voxel size. For example, magnetic susceptibility differences between tissues can produce broad field gradients running through the head. A larger voxel lying in this intrinsic field gradient will include a wider range of frequencies; consequently, the spins contributing to the net signal from the voxel will get out of phase with one another more rapidly, producing a shorter  $T_2^*$ . This effect can be seen in the lower images in Fig. 11.5 showing transverse cuts through the brain near the sinus cavity. The susceptibility difference between the sinus (air) and the brain (water) produces broad field gradients. The magnitude of signal dropouts depends on the slice thickness and on the orientation of the frequency and the phase-encoding gradients (Fig. 11.7). With thick slices, there is substantial signal dropout as a result of the short  $T_2^*$ . With thinner slices,  $T_2^*$  is longer, and signal dropout is less of a problem. For gradient recalled echo (GRE) acquisitions, signal dropouts are more severe than with spin echo (SE) acquisitions because the SE refocuses the phase dispersion caused by field

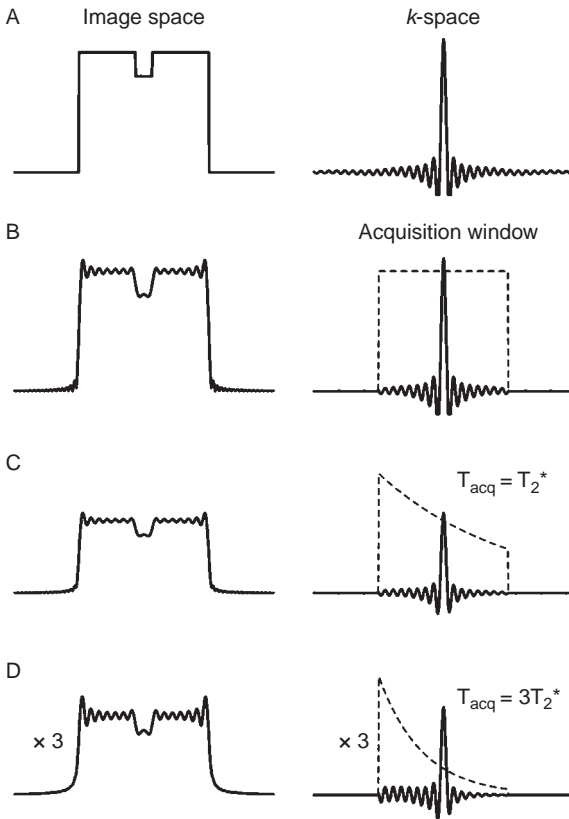
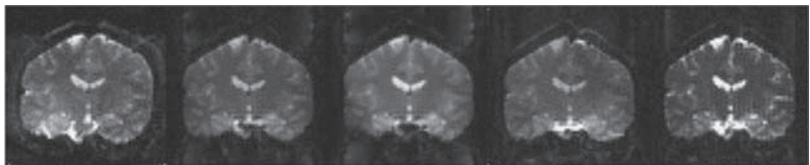


**Fig. 11.6.** Effect of  $T_2^*$  decay during data acquisition. The plots show a one-dimensional image space and the corresponding  $k$ -space. (A, B) The true shape of the imaged object is described by an infinite range of  $k$ -space (A), so the finite rectangular acquisition window introduces some ringing (Gibbs artifact) in the reconstructed image (B). If the intrinsic signal decreases during acquisition by  $T_2^*$  decay, the effect on the image is equivalent to smoothing with an asymmetric window in  $k$ -space. (C) With the acquisition time  $T_{\text{acq}}$  equal to  $T_2^*$  there is little additional effect on the image except for the overall reduction of the amplitude by a factor  $e^{-TE/T_2^*}$ , where TE is the time of the center of acquisition when the  $k=0$  sample is measured. (D) For  $T_{\text{acq}} = 3T_2^*$ , the distortion of the resulting image is more severe.



pulse sequence	GRE	GRE	GRE	ASE	SE
slice thickness	2 mm	2 mm	5 mm	2 mm	2 mm
orientation	S/I	R/L	R/L	R/L	R/L

**Fig. 11.7.** Signal dropouts in echo planar imaging. In regions of susceptibility variation, short  $T_2^*$  can produce signal dropouts, as in the areas near the sinus cavities and the temporal lobes. Examples are shown for gradient recalled echo (GRE), asymmetric spin echo (ASE), and spin echo (SE) acquisitions. The severity of the dropouts depends on slice thickness and the orientation of the frequency-encoding gradient (S, superior; I, inferior; L, left; R, right). (Data courtesy of E. Wong.)

offsets. An asymmetric spin echo (ASE) is intermediate between an SE and a GRE acquisition. Note that the SE acquisition can also contain strong signal fluctuations independent of the  $T_2^*$  effects caused by image distortions (discussed below).

The problem of signal dropouts with thicker slices illustrates the complicated effect of voxel size on the SNR. From Eq. (11.1), the SNR is directly proportional to the voxel volume, so an increase in the voxel size should increase SNR. However, the effective  $T_2^*$  of a voxel

tends to decrease with increasing voxel size as spins with a wider range of precession frequencies are included in the net signal. For example, if the field varies linearly across the voxel, the range of field offsets would double if the voxel size doubled. The shorter  $T_2^*$  with larger voxels tends to decrease the SNR. Because of this conflict, the optimal voxel size for maximizing SNR depends on the part of the brain under examination.

Relaxation effects, consequently, have two separate, though related, effects on the reconstructed image: the local signal mapped to each point is attenuated by  $T_2^*$  decay, but in addition the larger  $k$ -space samples are attenuated by signal decay during data acquisition, leading to blurring in the image. These two effects are somewhat separable: signal dropout depends primarily on TE when the  $k = 0$  sample is measured, whereas the additional blurring caused by  $T_2^*$  depends on the length of the data acquisition time. For example, if the shortest  $T_2^*$  is around 30 ms, then an image made with a 10 ms acquisition window centered on TE = 100 ms will show signal reductions as a result of  $T_2^*$  decay, but minimal blurring from  $T_2^*$ .

However, when the data acquisition time is longer than the  $T_2^*$  values of the tissues, as it often is in EPI, the local  $T_2^*$  affects the local spatial resolution as well. One can visualize the full effect of this by imagining breaking up the full image plane into multiple image planes segregated on the basis of local  $T_2^*$ . For example, as a first approximation, we can imagine a slice through the brain to consist of three separate images of cerebrospinal fluid (CSF), gray matter, and white matter, each characterized by a different  $T_2^*$ , and the full image is the sum of these three images. We could then further subdivide the image based on variations in  $T_2^*$  within a tissue type, such as gray matter or white matter near the sinus cavities with reduced  $T_2^*$ . Then we can look at the effect of  $T_2^*$  on each of these subimages separately. In each case, the relaxation effects modify the  $k$ -space samples and so alter the PSF. Then the imaging process produces a convolution of each of the subimages with its appropriate  $T_2^*$ -dependent PSF, and the net reconstructed image is then the sum of the individually blurred subimages. In general, short local  $T_2^*$  will reduce the later measured samples in  $k$ -space, and because these are large  $k$ -samples for most  $k$ -space sampling trajectories, this produces additional blurring of the image. In areas where  $T_2^*$  is very short, the signal may drop out completely. The result is that the net reconstructed image is blurred in a non-uniform way, with the most blurring in the regions with short  $T_2^*$ , and with signal dropouts in regions with very short  $T_2^*$ .

## Image distortions from off-resonance effects

As the data acquisition time is increased, off-resonance effects, in addition to  $T_2^*$  effects, become important. Like the  $T_2^*$  effects described in the [previous section](#), these artifacts can be viewed as arising because a basic premise of MRI is violated. In this case, the assumption is that all spins precess at the same rate in the absence of the applied gradients. Then any relative phase changes that develop during data acquisition are entirely the effects of the gradient fields and so are directly related to the location of the signals. Any intrinsic resonant frequency offset thus leads to errors in localizing the signal.

The primary example of a resonance offset in the body is the 3.5 ppm resonant frequency difference of H nuclei (protons) in fat and water. This is a chemical shift effect, resulting from the partial shielding of the nucleus by electronic molecular orbitals, so, when placed in the same magnetic field  $B_0$ , the H nuclei in lipids feel a slightly different magnetic field and so precess at a slightly different rate than do the H nuclei in water. Although the frequency difference is only a few parts per million, this is sufficient to produce large errors in the

localization of fat relative to water. In brain imaging, there is usually no detectable fat signal from the brain itself. Although myelin consists of lipids, the highly structured environment of the myelin creates a very short  $T_2$  for the lipid protons, so any signal generated in an imaging experiment has decayed away by the time the imaging data are measured. So, in imaging of the head, the measurable fat signal arises from the skull marrow and the scalp.

The artifact that results can be understood by again considering the basic gradient echo measurement of one line in  $k$ -space (Fig. 11.1). Position along the axis of the gradient is frequency encoded, so any intrinsic frequency offset will appear as a location offset. The image of fat is, therefore, shifted along the frequency-encoded axis relative to water. In a conventional image, the shift typically is about two resolution elements because the frequency offset between fat and water is approximately twice the bandwidth per resolution element. This chemical shift artifact can be reduced by increasing the bandwidth per resolution element sufficiently that the shift is less than the resolution, but this damages the SNR. In practice, for conventional clinical imaging, the radiologist simply learns to recognize the chemical shift artifact and, in some cases, even to make use of it. The appearance of the artifact tends to highlight the boundaries between fatty tissues and tissues composed mostly of water. At a fat-water boundary, this can appear as a dark edge if the fatty tissue is moved away from the water, or as a bright edge if the fat signal from one tissue is moved on top of the water signal from the adjacent tissue so that the fat and water signals add.

However, in EPI, off-resonance artifacts are much more of a problem. In EPI, successive lines in  $k$ -space are sampled in the  $k_x$ -direction with successive gradient echoes, with a phase-encoding pulse along the  $y$ -direction inserted between the gradient echoes to shift the sampling to a new value of  $k_y$ . The gradient amplitude for the  $x$ -gradient echoes is usually quite large, so the displacement of fat along the  $x$ -direction is much less than the resolution and so is not apparent. Instead, there is a large shift of fat along the phase-encoded  $y$ -direction. The nature of off-resonance effects in EPI at first glance seems puzzling. The off-resonance of fat in a conventional image is a small displacement of the image of fat along the frequency-encoded direction, but in EPI the effect is a large displacement of fat along the phase-encoded direction. To understand how this comes about, we need to look at off-resonance effects in a slightly different way.

In conventional MRI, the intrinsic MR signal is created fresh for each phase-encoding step. Spins that are off-resonance acquire additional phase offsets as time evolves, but this unwanted phase evolution is reset before each new phase-encoding step because a fresh signal is generated with each new excitation pulse. There is no phase evolution across phase-encoding steps; whatever phase offsets are present when the signal is measured after the first phase-encoding step are the same for all the steps. And a constant phase offset simply appears in the phase of the reconstructed image and has no effect on the magnitude image. Conventional phase encoding is, therefore, insensitive to errors from off-resonance effects, and the chemical shift artifact appears as a pure shift in the frequency-encoded direction alone.

However, in single-shot EPI, all  $k$ -space is sampled after one intrinsic MR signal is generated. The phase offsets from off-resonance effects are not reset before each phase-encoding pulse, and because the phase-encoding blips are spread throughout the data acquisition period, there is time for substantial unwanted phase offsets to accumulate. Think of the blipped phase encoding done in EPI as equivalent to frequency encoding using a very weak gradient during the entire acquisition time with widely spaced samples. That is, the series of sharp gradient pulses, with a data sample after each pulse, is equivalent to



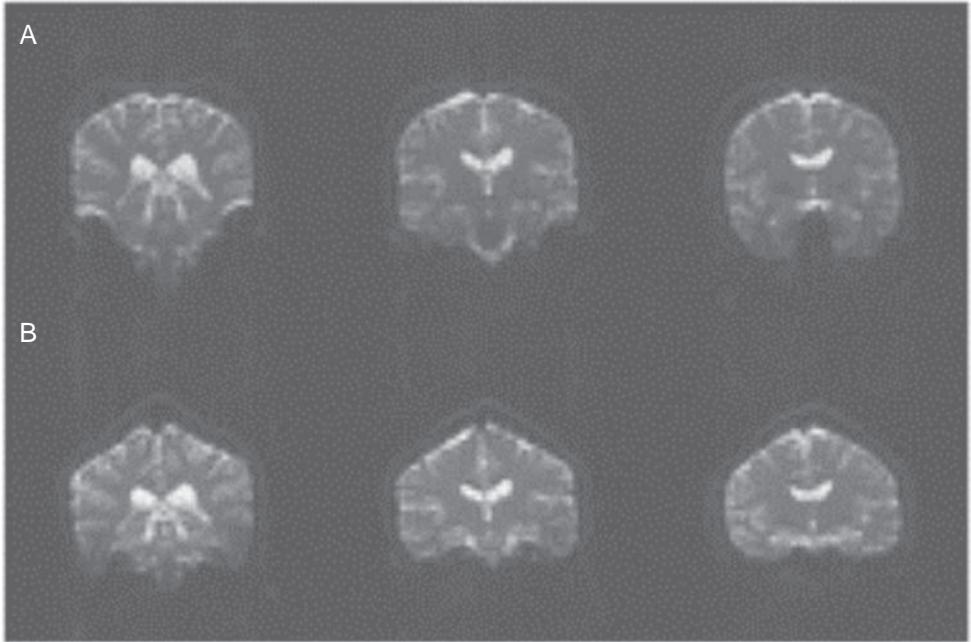


**Fig. 11.8.** Off-resonance distortions in echo planar imaging. Coronal single-shot images for three slices (columns) are shown. The phase-encoding gradient is vertical, but reversed in direction in (B) compared with (A) (compare with Fig. 11.9 C, D). Note the vertical shift of the temporal lobes and the distortion of the top of the head. (Data courtesy of E. Wong.)

a continuous gradient with the same integrated area between samples as the blipped gradient. Because the equivalent gradient is so weak, the bandwidth per resolution element is small, and the shift of the fat image along  $y$  is many resolution elements.

The magnitude of the off-resonance effect can be characterized in terms of how much time is required to scan completely through one axis in  $k$ -space. In EPI, for example, a single pass through the  $k_x$ -direction might require approximately 1 ms or less, whereas a full pass through  $k_y$  might take approximately 60 ms (the full data acquisition time). Now consider the signals from two positions separated by one resolution element in  $x$ . In moving from the  $k_x = 0$  sample to the  $k_x = k_{\max}$  sample, the gradient-induced relative phase between these two signals is  $180^\circ$ , so after a full pass along  $k_x$  from  $-k_{\max}$  to  $+k_{\max}$  the induced phase offset is  $360^\circ$ .

We can use this to calibrate the off-resonance effect, relating the observed shift in the image to the amount of artifactual phase evolution from off-resonance precession. The fat is shifted by one resolution element for each  $360^\circ$  of phase evolution during the time required to sample from  $-k_{\max}$  to  $+k_{\max}$ , and the same argument applies to both the frequency-encoded and the phase-encoded directions. For fat at 1.5 T, the 3.5 ppm frequency offset is approximately 220 Hz. Then, during a 1 ms scan through  $k_x$ , the additional phase evolution is only 0.22 cycles ( $79^\circ$ ), and so the displacement in the image is only 0.22 resolution elements along  $x$ . But if a full scan from  $-k_{\max}$  to  $+k_{\max}$  in  $y$  requires 60 ms, the extra phase accumulation of the fat signal is 13.2 cycles, and so the fat image is shifted approximately 13 resolution elements in  $y$ . For an image with only 64 total resolution elements across the FOV, this is a substantial shift.

This discussion has focused on the chemical shift artifact from fat and water, but the arguments also apply to other sources of off-resonance precession, such as field inhomogeneities caused by magnetic susceptibility differences. Unlike chemical shift effects, which involve pure resonant frequency offsets, field inhomogeneities generally produce smooth field variations, resulting in image distortions (Fig. 11.8). We can picture the full effect of image distortions similar to the way that we described the effects of  $T_2^*$  variation across the image plane by considering the full image to be a sum of subimages corresponding to one value of  $T_2^*$ . Now we want to divide the full image into subimages corresponding to different field offsets. Then each of these planes is shifted along the phase-encoded axis ( $y$ ) in an EPI acquisition in proportion to its field offset, and the resulting reconstructed image is then the sum of each of these separately shifted images.

As described above, the shifts along the  $y$ -axis are proportional to the data acquisition time and also to  $B_0$ . Magnetic susceptibility differences between tissues create magnetic field offsets that are proportional to  $B_0$ , so it is convenient to define a dimensionless number  $\nu$ , such that the field offset  $\Delta B = B_0\nu$ . Typical field offsets in the brain owing to inhomogeneous tissues are on the order of 1 ppm, and so  $\nu$  is expressed in parts per million. With  $B_0$  expressed in Tesla and the acquisition time expressed in seconds, the local signal is shifted  $\Delta y$  pixels in an EPI image (assuming one pixel is equal to the true resolution) given by

$$\Delta y(\text{pixels}) = 42.6B_0(\text{T}) \cdot \nu(\text{ppm}) \cdot T_{\text{acq}}(\text{s}) \quad (11.3)$$

The magnitude of the distortions in EPI images is proportional to the main magnetic field and to the total data acquisition time. The magnitude of  $\nu$  is determined by the shape and composition of the human head and is not affected by field strength. Equations (11.1) and (11.3) illustrate the central conflict involved in trying to achieve both high SNR and minimal distortions. The distortions can be minimized by decreasing the acquisition time, but this also decreases SNR. Similarly, increasing the magnetic field strength increases the intrinsic SNR but also increases the magnitude of the distortions. Consequently, there is always a trade-off between SNR and image distortion, and the optimal balance depends on the part of the brain being imaged. In the parietal and occipital lobes, the field is reasonably uniform, so SNR in these regions can be improved with a longer acquisition time at the expense of increased distortions in the frontal and temporal lobes.

One further complication results from these distortions of the image. In the preceding thought experiment of adding up a stack of shifted subimages, each corresponding to a different field offset, each subimage is a complex image. With a gradient echo acquisition, the signal from each subimage also develops a phase offset proportional to the field offset and the TE. When the subimages are added back together, these phase offsets can produce signal cancellation, and will, therefore, affect how the net signal mapped to one pixel location evolves in time. This effect on the net signal at a point is described as a  $T_2^*$  effect, but this argument emphasizes that the nature of  $T_2^*$  effects is subtle. The signals that are combined in one pixel of the image and interfere to cause  $T_2^*$  signal loss do not necessarily arise from the same location! Field inhomogeneities, therefore, affect both image distortions and  $T_2^*$  effects in a complicated way.

Fig. 11.9 illustrates how field inhomogeneities lead to distortions, signal dropouts, and  $T_2^*$  effects. It shows simulations for a simple spherical object, representing the head, containing a smaller spherical cavity near the bottom, representing a sinus cavity. The cavity creates a dipole field distortion throughout the head, and Fig. 11.9A shows contours of the field offset  $\Delta B$ . The

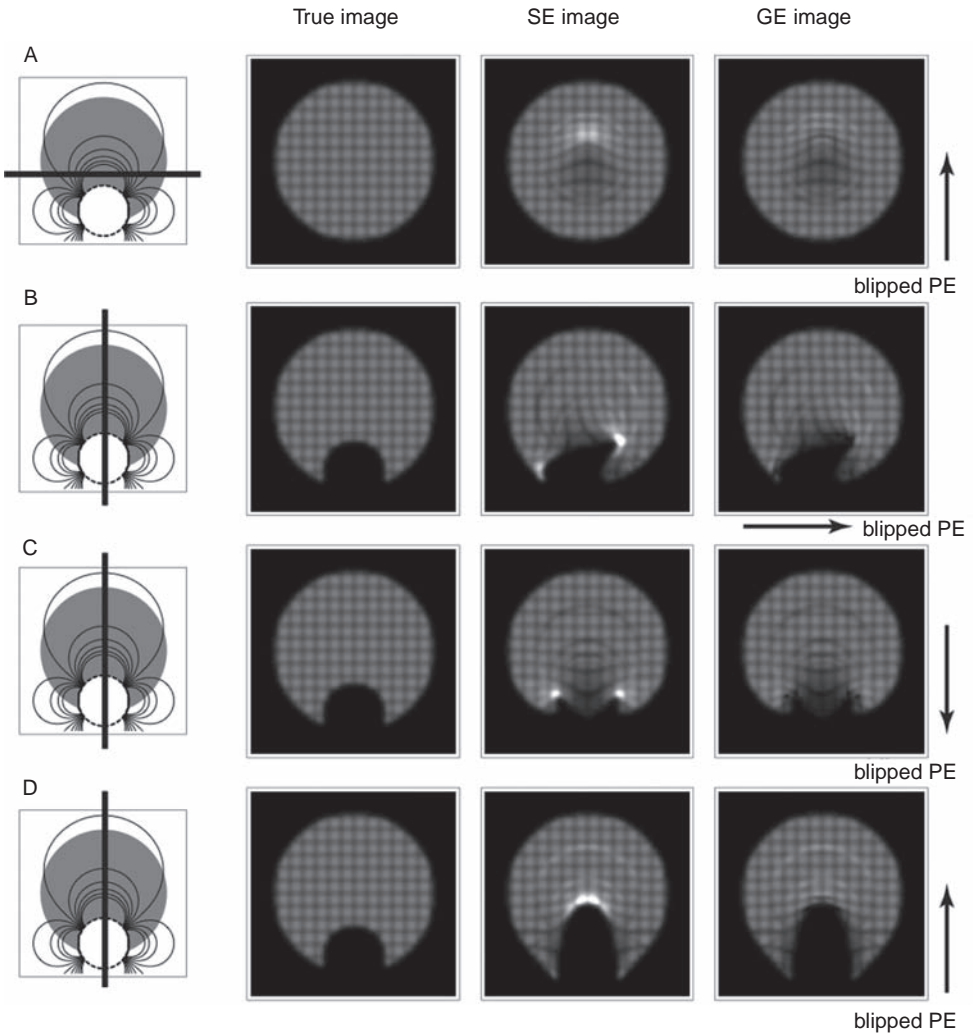


**Fig. 11.9.** Simulation of off-resonance distortions in echo planar imaging. Simulations show the distortions of images of a sphere (representing the head) with a smaller off-center spherical air space inside (representing a sinus cavity). (A) The magnetic field distribution and imaging plane; (B) the true (undistorted) image; (C) the spin echo (SE) image; (D) the gradient recalled echo (GRE) image. The distorted maps were calculated by appropriately shifting each local signal along the blipped phase-encoded (PE) direction, indicated by the arrows. For the GRE images, the phase of each local signal was included in the calculations, so the GRE image shows signal dropouts in addition to the distortions exhibited by the SE images. Grid lines indicate the distortions of the local voxel shapes.

strength of the dipole field was chosen to give  $\Delta B = 1$  ppm of  $B_0$  at the upper pole of the cavity. This is a modest field distortion, and for conventional imaging the distortions are minor. But for EPI the distortions are substantial, as shown in the simulated images.

In these simulations, it was assumed that the  $x$ - and  $z$ -coordinates of the local signal are accurately mapped, and it is only the  $y$ -position that is mismapped. In each example, images are shown for an SE acquisition and a GRE acquisition, to bring out the two distinct effects of field distortions: (1) signals are mapped to the wrong locations in both SE and GRE acquisitions; and (2) in GRE imaging, there is an additional  $T_2^*$  effect owing to phase

cancellation of signals from different locations mapped to the same voxel. In these simulations, we have neglected any  $T_2^*$  effects resulting from slice thickness, such as those illustrated in Fig. 11.7, to show the effects that come just from the mismapping in  $y$ . In these examples, the intrinsic signal is uniform, and any variations of intensity in the SE images result from bunching or spreading of the mapped locations of the individual signals (i.e., a distortion of the voxel shape). In the GRE images, the additional effects of phase cancellation are included. The common pattern is that the field distortions will create some bright spots in the SE images where signals are bunched together, but these same areas will often show signal reductions in the GRE image because spins from a wider range of fields are interfering. There are, therefore, two sources of signal dropouts in GRE images illustrated here: a dispersion of the signal into a wider area, which lowers the intensity of both SE and GRE images, and a  $T_2^*$  effect from phase variations within the voxel.

The nature of the distortion is quite simple in principle but rather complicated in appearance. For a positive field offset, the signal is shifted toward the positive end of the  $y$ -gradient axis, so the distortion depends on the direction of the gradient and also its sign (i.e., the order of collection of  $k$ -space samples in  $k_y$ ). Figure 11.9A shows axial images collected just above the cavity. At all points, the field offset is positive, and the central points are shifted the most. Figure 11.9B and C shows the distortions when the blipped gradient is horizontal and vertical, respectively, and Fig. 11.9D shows the effect of reversing the gradient. Note that reversing the sign of the gradient has a significant effect. In the GRE image in Fig. 11.9C, the regions near the sinus cavity are distorted but measurable because the dominant displacement is down, spreading out the signals. But with the sign of the gradient reversed (Fig. 11.9D), the regions near the sinus cavity are shifted up, bunching the signals together, and the net signal is largely gone as a result of phase cancellation.

If the image signal is not lost through signal dropouts, it is possible to unwarped the spatial distortions in EPI images by measuring a magnetic field map for each slice with a GRE pulse sequence and using Eq. (11.3) to estimate the expected shift. With a GRE sequence, the phase evolution from field offsets is not refocused, so the phase change between images with two different TEs directly reflects the field offset. Because the distortion is directly related to the local field offset, this provides the needed information to unwarped the EPI images (Jezzard and Balaban 1995; Reber *et al.* 1998). However, it should be noted that there are limits to what can be corrected. If the signals from two regions are mapped to the same voxel, it will not be possible to separate the two contributions. Often, however, the distortion is a smooth local stretching, and unwarped works reasonably well.

The preceding arguments emphasize the trade-offs between SNR and image distortions in EPI acquisitions. Increasing the acquisition time can improve SNR, but this beneficial effect must be balanced against the costs of increased distortions and signal dropouts. The latter may entirely offset the nominal SNR gain, just as increasing the slice thickness will increase SNR in a uniform field, but the decrease of  $T_2^*$  as a result of broad field gradients through the voxel may nullify the SNR improvement. For fMRI at higher fields, the problems of distortions and signal dropouts are a serious concern.

## Motion artifacts

Any motion during the acquisition of an MR image will produce artifacts (Wood and Henkelman 1985). Such motions include subject movement, such as head motion, coughing or swallowing, and physiological motions such as pulsatile blood flow, CSF motions, and respiratory motions. In a conventional MR image, motion artifacts appear as a ghosting or

diffuse blurring that extends along the phase-encoded direction over the full FOV of the image. Note that this is distinctly different from motion artifacts in other imaging settings, such as photography. With a camera, any motion while the shutter is open produces a blurred image on the film, but the blurring extends only over the range of motion of the object, not over the whole frame.

In MRI, any motion during the image acquisition means that the different samples in  $k$ -space are inconsistent with one another. If a subject tips his head slightly in the middle of a scan, the early  $k$ -space samples are appropriate for an image of the head in the first position, but the later samples are consistent with the new position. Each  $k$ -space sample describes a wave extending across the entire image plane, and so inconsistencies in the sampling can lead to artifacts over the full FOV. For example, with a consistent set of  $k$ -space samples, the contributions of all the different wave patterns cancel outside the head and add constructively inside the head to give a clear brain image. If the samples are inconsistent, the cancellation outside the head is incomplete, and so the artifacts can appear far removed from the moving tissues themselves.

In conventional MRI, motion artifacts are spread out in the phase-encoded direction. The reason the frequency-encoded direction is little affected is that each data line in  $k_x$  is collected quickly (i.e., in approximately 8 ms), so most motions are frozen during this short interval, and all the collected samples are consistent with the same image. But the time between  $k_y$ -samples (i.e., TR between phase-encoding steps) is much longer, and so the inconsistencies that arise in the  $k$ -space data are between different  $k_y$ -lines.

If the motion is periodic, such as pulsatile flow in blood vessels, the artifacts can appear as distinct ghosts rather than just as a blurring. [Figure 11.10](#) shows an example of a conventional axial fast low-angle shot (FLASH) image with TR = 0.25 s, windowed to expose the line of ghosts arising from the sagittal sinus. The two largest ghosts are approximately 80 resolution elements on either side of the sagittal sinus. The spatial shift of the ghosts depends on how the heart rate compares with the TR. To see how such ghosts arise, consider again how the sampling in  $k$ -space is done in conventional imaging. Each  $k_x$ -line is measured after a separate RF excitation pulse, and the lines at different values of  $k_y$  are measured in order from  $-k_{\max}$  to  $+k_{\max}$  with a time interval TR between each measurement. Suppose that the signal from a blood vessel varies sinusoidally with the frequency of the heart rate. If the heart beats once per second, then the measured samples in  $k$ -space representing the image of the vessel will have an additional sinusoidal modulation in the  $k_y$ -direction.

For example, with a TR of 0.5 s, the modulation is very rapid, alternating with each  $k_y$ -line. If the TR is 1.0 s, the scanning is effectively gated to the heart rate and so there is no modulation of the  $k$ -space samples. But if the TR is 1.1 s, there is a slow modulation of the  $k_y$ -samples because the sampling is slightly off in frequency from the heart rate. If the first  $k_y$ -sample is synchronous with a heartbeat, the next sample 1.1 s later will occur 1/10 of the way into the next heart cycle, and each subsequent sample will occur an additional 1/10 of the way into the heart cycle. The modulation period for the  $k_y$ -samples is then 10 s, because that is how long it will take for another measured sample to fall on the same phase of the heart cycle.

This is another example of *aliasing*, in which a high-frequency oscillation appears to be a much lower frequency in a set of measured samples because the sampling frequency was too low. (Aliasing also leads to the wraparound effect associated with the FOV, as described in [Ch. 9](#).) The critical sampling frequency, called the Nyquist frequency, required to detect accurately a maximum frequency  $f_{\max}$  is  $2f_{\max}$ . In this example, the TR of 0.5 s (2 Hz sampling rate) critically samples the heart rate with a period of 1 s (1 Hz), but in the other cases, the

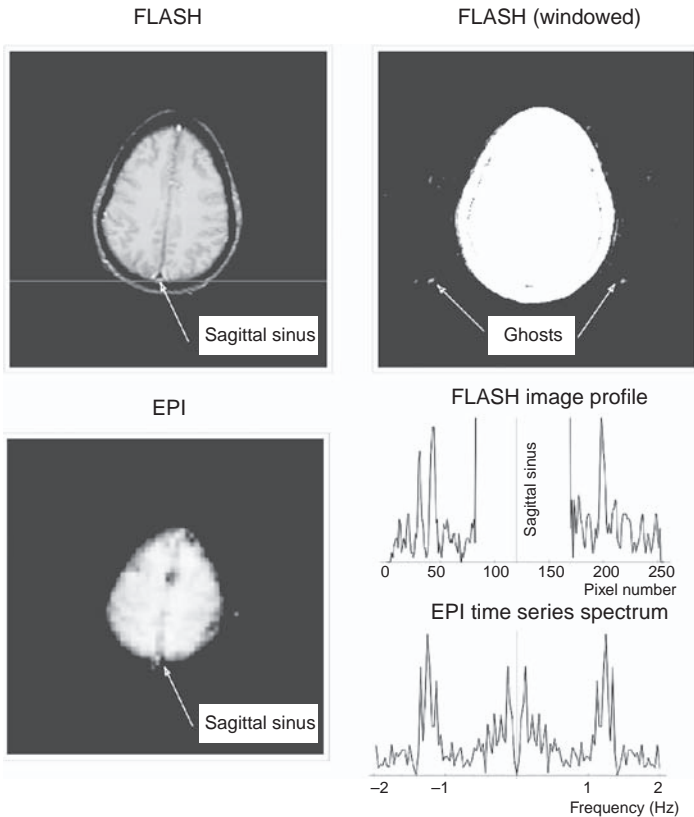


**Fig. 11.10.** Physiological motion artifacts. Pulsatile flow in the sagittal sinus creates ghost images of the vessel in a conventional fast low-angle shot (FLASH) image acquired in 32 s with a repetition time of 250 ms, 128 phase-encoding steps (along a left/right axis), and reconstructed as a 256 matrix (so one resolution element is 2 pixels). The spectrum of a dynamic time series of echo planar imaging (EPI) images of the same section acquired with the same repetition time for an equal period of time show strong cardiac components at approximately 1.2 Hz. The ghosting pattern in the FLASH image is directly related to the spectrum of the fluctuations graphs (See plate section for color version.)

heart frequency is aliased to a lower frequency. When the TR is the same as the heart period, the apparent heart rate in the data is shifted to zero frequency, and when TR is 1.1 s the apparent heart rate is shifted from a frequency of 1 Hz to a frequency of 0.1 Hz.

The effect of a periodic signal variation during a conventional MRI acquisition is, therefore, to create a periodic modulation of the  $k$ -space samples. But a periodically varying signal looks exactly like a constant signal arising from a displaced position along  $y$ . We can look at this effect in the same way as we looked at distortions in EPI images caused by field inhomogeneities. The signals from two voxels separated by one resolution element will acquire a phase difference of  $360^\circ$  between the first  $k_y$ -line and the last. So any signal varying periodically will be shifted in the image by one resolution element for each  $360^\circ$  of phase evolution during data acquisition. Note, though, that this phase evolution is between  $k$ -space samples, so the apparent periodicity with aliasing taken into account is important (e.g., if TR is equal to the heart period, there are no artifacts).

The practical result of these arguments is a simple rule for the displacement of the ghost. If the period of the pulsation is  $T$ , and there are  $N$  phase-encoding steps separated by a time TR in the image acquisition, then the shift of the ghost image in resolution elements is  $N \times TR/T$ . This relation holds, even if the heart rate is not critically sampled, if the shift is understood to mean the total number of pixels shifted, such that a shift past the edge of the FOV is wrapped around to the other side (aliased). For example, if  $TR = T$ , the ghost is shifted

by  $N$  pixels – one full image – and this leaves it in the same spot. Returning to the example of Fig. 11.10, a shift of 40 pixels out of a FOV of 128 pixels with  $TR = 250$  ms is consistent with a heart period of 0.8 s (a heart rate of 75 beats/min).

In this simple example, we considered the blood signal to consist of a constant average term plus one oscillatory term. In fact, these are just the first two terms of the Fourier series expansion of the blood signal in terms of temporal frequencies. The contributions of higher harmonics of the signal could also be included, and these terms would create additional ghosts. These terms correspond to higher frequency modulation of the  $k$ -space samples, and each will be shifted in proportion to the frequency (i.e., the ghost from the second harmonic is shifted twice as far as the ghost from the first harmonic of the fundamental frequency).

The result is that the temporal Fourier transform of the local signal during data collection is transformed into a string of ghost images in the image domain. The correspondence between the pattern of ghosts and the Fourier spectrum of the time variations is illustrated in Fig. 11.10. In addition to the conventional image showing the ghosting pattern from the sagittal sinus, a set of dynamic EPI images were also acquired in the same subject. The Fourier transform of the temporal variation of the sagittal sinus signal agrees reasonably well with a profile through the conventional FLASH image showing the ghosting pattern. (The EPI and the FLASH data were acquired in separate runs, so the spectrum of fluctuations is not identical.)

In this example, we considered the case in which the signal variation is characterized by a fundamental frequency and its harmonics, which produces distinct ghosts. But neither cardiac pulsations nor respiration are truly periodic, and so we would expect that the more general case of signal variation is described by a Fourier series with contributions from many frequencies. The ghosting pattern is then a more diffuse spread of signal along  $y$ . This same effect, in which the signal from a voxel is spread out in space in the image depending on the temporal Fourier transform of the local signal, happens for every point in the image, and the net image is then the sum of the spread-out image of each of the local signals.

In fact, this brings us back to the same way of looking at imaging and image artifacts that we have used throughout this chapter. The effect of any process on an MR image can be analyzed by looking at how the  $k$ -space representation of the true image is modified. Earlier in the chapter we used this idea to understand the effects of finite  $k$ -space sampling, smoothing the images in post-processing, and distortions caused by field offsets. This is simply the generalization of that idea to any temporal variation of the signal during data acquisition that modifies the  $k$ -space samples. It is important to remember that with motion artifacts, as with distortions caused by field inhomogeneity, we are no longer dealing with a global windowing function applied to the full image data. Instead, the image of each point in the object is spread out in a way that depends on the Fourier transform of the signal from that point. The signal from another point, with a different temporal pattern of signal variation, will produce a different pattern of ghosts. The full image with motion artifacts is then the sum of the spread-out signals from each of these points. Understandably, the resulting image can be severely degraded, and even though the source of the ghosting patterns can sometimes be easily recognized (such as pulsatile flow artifacts), motion artifacts are often uninterpretable in practice.

## Physiological noise

The earlier part of the chapter has dealt with the nature of the motion artifacts that can occur in conventional imaging. Such artifacts can completely destroy the diagnostic value of the

image, and this has been a primary motivating factor in the development of fast imaging techniques. If the total acquisition time is short, it is easier for the subject to hold still. If the imaging time is short enough, the most problematic physiological motions (cardiac and respiratory) are essentially frozen. With EPI and total data acquisition times of 30–50 ms, there are virtually no motion artifacts.

However, fMRI studies are based on dynamic imaging, so a single image is not sufficient. With contrast agent studies, rapidly repeated images are required to follow the kinetics of the contrast agent. In blood oxygenation level dependent (BOLD) fMRI studies, dynamic images are acquired over several minutes while a subject alternates between task and control states. In these applications, we must deal with a time series of images, and although each image is free of motion artifacts, fluctuations in the local signal over time now appear directly as shot-to-shot variations of the local signal (as in Fig. 11.10). In other words, the temporal variation of the local signal in a time series of EPI images will have a noise component resulting from physiological motions in addition to the standard thermal noise discussed above (Glover and Lee 1995).

In the broadest sense, this physiological noise includes outright subject movement in addition to effects of cardiac and respiratory motions. Movement of the subject's head during a BOLD-fMRI run is a critical problem. In BOLD studies, the signal change associated with brain activation is only a small percentage. Head movement of only a small fraction of a voxel can also produce signal changes of this order, particularly when the voxel is at the border of two regions with different signal intensities (i.e., an edge in the image). Then a small shift of the location of the voxel across this boundary as a result of motion can create substantial changes in the voxel signal. If the motion is correlated with the stimulus (e.g., if the subject's head is tipped slightly each time a visual stimulus is presented), this can create large apparent activations that are purely artifactual (Hajnal *et al.* 1994).

For this reason, the subject's head is tightly restrained, and a bite-bar system is often used to further stabilize the head. In addition, after the data are collected, the images are processed with a motion correction algorithm that applies small translations and rotations to the images to produce the best mutual alignment (Cox 1996; Friston *et al.* 1995; Woods *et al.* 1993). However, even with preventive measures and post-processing corrections such as these, head movement remains one of the most common problems in BOLD studies, particularly in patient populations (Friston *et al.* 1996).

Assuming that head motion can be prevented and/or corrected, the more physiological sources of noise still remain. If physiological data (e.g., heart beats and respiration) are recorded during the fMRI experiment, these data can be used to estimate retrospectively and remove the physiological fluctuations from the fMRI time series (Glover *et al.* 2000; Hu *et al.* 1995; Restom *et al.* 2006). This approach can considerably improve the fMRI data, but it is not always feasible to perform the necessary physiological monitoring. The effect of physiological noise is that the standard deviation of the local signal over time is larger than what one would estimate from the variation of the background of a single image, which is an estimate of the thermal noise alone. In fact, the temporal noise in images of the brain is often several times larger than the thermal noise, suggesting a strong contribution from physiological noise. If one maps the standard deviation of the temporal noise in different regions of the brain, the distribution correlates strongly with brain structures; indeed, a map of the noise standard deviation often looks much like a map of CSF.

In addition to increasing the magnitude of the noise, physiological fluctuations can also introduce temporal and spatial correlations in the noise. For example, respiratory motions have periods of several seconds and are likely to affect large regions in a similar way. Indeed,



respiratory motions can affect the signal from the brain even if the head is still. Noll (1995) concluded that signal variations at the respiratory frequency arise from magnetic field variations in the brain of the order of a few parts per billion, likely caused by changes in the shape of the body with respiration. As a result of such effects with long temporal correlations and broad spatial patterns, the noise component of the signal from a voxel in one image may not be independent of the noise in the next image in a time series. In addition, the noise in the signal from one voxel may not be independent of the noise in nearby voxels.

The presence of temporal and spatial noise correlations substantially complicates the analysis of the statistical significance of detected activations. The problem of correlated noise is the problem outlined above: how much does the noise go down with averaging? The detection of an activated voxel essentially depends on detecting a signal difference between the task and control states, but the statistical significance of any measured average signal difference depends on the number of degrees of freedom, the number of independent measurements involved. The temporal correlations of the noise may significantly reduce the degrees of freedom. Spatial correlations of the noise affect spatial smoothing and the statistical significance of clusters of activated pixels (Friston *et al.* 1994). Often the statistical threshold for defining activations is relaxed for clusters of adjacent pixels, on the theory that clusters of random apparent activation are unlikely to occur if the noise is independent. But stimulus-correlated motion regularly produces many contiguous, artifactually activated pixels at the edge of the brain. So the statistical significance of clusters of activation critically depends on the spatial correlations. Unfortunately, however, physiological noise is still not understood in a quantitative way, and the full significance of noise correlations in BOLD studies is still being investigated.

## References

- Cox RW (1996) AFNI: software for analysis and visualization of functional magnetic resonance neuroimages. *Comput Biomed Res* **29**: 162–173
- Friston KJ (1996) Statistical parametric mapping and other analyses of functional imaging data. In *Brain Mapping: The Methods*, Toga AW, Mazziotta JC, eds. New York: Academic Press, pp. 363–386
- Friston KJ, Worsley KJ, Frackowiak RSJ, Mazziotta J, Evans A (1994) Assessing the significance of focal activations using their spatial extent. *Hum Brain Mapping* **1**: 210–220
- Friston KJ, Ashburner J, Poline JB *et al.* (1995) Spatial registration and normalization of images. *Hum Brain Mapping* **2**: 165–189
- Friston KJ, Williams S, Howard R, Frackowiak RSJ, Turner R (1996) Movement related effects in fMRI time-series. *Magn Reson Med* **35**: 346–355
- Glover GH, Lee AT (1995) Motion artifacts in fMRI: comparison of 2DFT with PR and spiral scan methods. *Magn Reson Med* **33**: 624–635
- Glover GH, Li TQ, Ress D (2000) Image-based method for retrospective correction of physiological motion effects in fMRI: RETROICOR. *Magn Reson Med* **44**: 162–167
- Grant PE, Vigneron DB, Barkovich AJ (1998) High resolution imaging of the brain. *MRI Clin N Am* **6**: 139–154
- Hajnal JV, Myers R, Oatridge JE, *et al.* (1994) Artifacts due to stimulus correlated motion in functional imaging of the brain. *Magn Reson Med* **31**: 283–291
- Hoult DI, Richards RE (1979) The signal to noise ratio of the nuclear magnetic resonance experiment. *Magn Reson* **24**: 71–85
- Hu X, Le TH, Parrish T, Erhard P (1995) Retrospective estimation and correction of physiological fluctuation in functional MRI. *Magn Reson Med* **34**: 201–212
- Jezzard P, Balaban RS (1995) Correction for geometric distortion in echo planar images  $B_0$  from field distortions. *Magn Reson Med* **34**: 65–73

- Lange N (1996) Statistical approaches to human brain mapping by functional magnetic resonance imaging. *Stat Med* **15**: 389–428
- Macovski A (1996) Noise in MRI. *Magn Reson Med* **36**: 494–497
- Noll DC (1995) Methodologic considerations for spiral k-space functional MRI. *Int J Imaging Syst Tech* **6**: 175–183
- Parker DL, Gullberg GL (1990) Signal to noise efficiency in magnetic resonance imaging. *Med Phys* **17**: 250–257
- Poline J-B, Worsley KJ, Evans AC, Friston KJ (1997) Combining spatial extent and peak intensity to test for activations in functional imaging. *Neuroimage* **5**: 83–96
- Reber PJ, Wong EC, Buxton RB, Frank L (1998) Correction of off resonance-related distortion in echo-planar imaging using EPI-based field maps. *Magn Reson Med* **39**: 328–330
- Restom K, Behzadi Y, Liu TT (2006) Physiological noise reduction for arterial spin labeling functional MRI. *Neuroimage* **31**: 1104–1115
- Wood ML, Henkelman RM (1985) MR image artifacts from periodic motion. *Med Phys* **12**: 143–151
- Woods RP, Mazziota JC, Cherry S (1993) MRI–PET registration with automated algorithm. *J Comput Assist Tomogr* **17**: 536–546



Part

# Principles of functional magnetic resonance imaging

## Part IIIA Perfusion imaging

- 12 Contrast agent techniques
- 13 Arterial spin labeling techniques

## Part IIIB Blood oxygenation level dependent imaging

- 14 The BOLD effect
- 15 Design and analysis of BOLD experiments
- 16 Interpreting the BOLD response



**Part**

**IIIA**

**Perfusion imaging**



<b>Introduction</b>	<i>page</i> 281
Perfusion imaging	281
The beginning of fMRI	282
<b>Basic concepts of tracer kinetics</b>	283
Time–activity curves	283
Volume of distribution of the agent	284
<b>Interpreting the tissue concentration–time curve</b>	285
A simple example	285
Measuring cerebral blood flow and volume	287
The general form of the tissue concentration–time curve	288
The residue function	292
Sensitivity of the tissue concentration–time curve to local blood flow and the volume of distribution	294
<b>Bolus tracking</b>	296
The bolus tracking experiment	296
Relating MR signal changes to agent concentration	297
Measuring cerebral blood volume from bolus tracking data	298
Recirculation of the agent	298
The mean transit time	299
Estimating cerebral blood flow from bolus tracking data	300
<b>Other contrast agent methods</b>	302
<b>Clinical applications</b>	303

## Introduction

### Perfusion imaging

The previous chapters considered MRI as a sensitive technique for depicting human anatomy. The MR signal is intrinsically sensitive to several properties of tissues, such as relaxation times and diffusion, and the flexibility of pulse sequence design makes possible a variety of imaging techniques. Over time, the field of MRI has expanded to include studies of tissue function in addition to anatomy. The remaining chapters describe how subtle MR effects are exploited to measure different aspects of the perfusion state of tissue. Although the blood oxygenation level dependent (BOLD) effect is most often used in brain activation studies, a drawback of this technique is that it only provides information on the change in activity between one state and another. For example, measurements made while a subject alternates between a control state and a task state reveal regions of the brain showing a significant signal difference between the

two states. But BOLD techniques provide no information on the resting or chronic perfusion state.

In this chapter and the following one we describe two classes of MRI technique that do provide measures of the resting perfusion state. The first class, *bolus tracking* techniques, is based on the use of intravascular contrast agents that alter the magnetic susceptibility of blood and so affect the MR signal. The second class of techniques is *arterial spin labeling* (ASL), in which arterial blood is magnetically tagged before it arrives in the tissue, and the amount of blood delivered to the tissue is then measured. These two approaches are quite different, and, as we will see, the two techniques essentially measure different aspects of the perfusion state of the tissue. The contrast agent techniques provide a robust measurement of cerebral blood volume (CBV), whereas the ASL techniques measure cerebral blood flow (CBF).

In the healthy brain, CBF and CBV are believed to be closely correlated, in the sense that an increase in CBF is accompanied by an increase in CBV (Grubb *et al.* 1974). However, as discussed in Ch. 2, it is best to view this relationship simply as a correlation, rather than as a tight link. Blood flow is controlled by changes in the caliber of the arterioles, but the small blood volume changes associated with arteriolar dilatation are likely much smaller than the measured total CBV changes. Furthermore, there is evidence that the correlation between CBF and CBV found in the healthy brain is disrupted in disease. For example, ischemic states are often marked by a reduced CBF but an elevated CBV, a situation described as a reduced perfusion reserve (Gibbs *et al.* 1984; Kluytmans *et al.* 1998). For these reasons, measurements of both CBF and CBV have important clinical roles.

## The beginning of fMRI

In clinical MRI studies contrast agents are used to alter local relaxation times (Lauffer 1996). Gadolinium (Gd) compounds such as gadolinium-linked diethylenetriaminepentaacetic acid (Gd-DTPA) are the most commonly used agents. Gadolinium is a lanthanide metal ion with the unique property of having seven unpaired electrons. In most atoms, electrons in an orbital pair up with opposite spin so that the net magnetic moment from the electrons is zero. Unpaired electrons create a strong, fluctuating magnetic field in their vicinity, which promotes relaxation of nuclear magnetic moments. When gadolinium reaches a tissue water pool, the  $T_1$  of the local water protons is reduced, increasing the signal in a  $T_1$ -weighted image. In the healthy brain, Gd-DTPA does not cross the blood-brain barrier, and because the agent remains confined to the vasculature, there is little relaxivity effect. The  $T_1$  of the intravascular component is reduced, so the blood signal increases, but the extravascular spins are unaffected. The typical blood volume in brain tissue is only around 4%, so the net signal increase from the presence of gadolinium is small. However, in a tumor with leaky capillaries, the gadolinium readily diffuses into the extravascular space, and the tumor enhances on the MR image.

In the late 1980s, Villringer and co-workers (1988) discovered an additional effect of gadolinium that forms the basis for using contrast agents in fMRI. By observing the healthy brain with rapid dynamic MRI, they were able to track the bolus of Gd-DTPA as it passed through the brain in a rat model. The surprising result was that the MR signal dropped transiently as the bolus passed through. Given the common use of Gd-DTPA as a relaxivity agent to enhance the signal from specific tissues, it was clear that this effect was caused by something other than the relaxation effect.

The source of the new effect is that gadolinium also possesses a large magnetic moment, which alters the local magnetic susceptibility (Fisel *et al.* 1991; Rosen *et al.* 1990). Because the



gadolinium is confined to the blood vessels, the susceptibility difference between the intravascular and extravascular spaces creates microscopic field gradients in the tissue. As spins precess at different rates in the inhomogeneous field, their signals get out of phase with one another, and the net signal in a gradient recalled echo (GRE) image is reduced. This is described as a shortening of  $T_2^*$ . Furthermore, the signal is also reduced in a spin echo (SE) image because diffusion through the microscopic field gradients causes the SE to be less effective in refocusing the phase offsets caused by field inhomogeneities (Ch. 8). The magnetic susceptibility effect of gadolinium requires a sharp bolus injection to produce a high-enough concentration of gadolinium in the vessels to produce a significant susceptibility change, and it also requires an intact blood–brain barrier to produce a susceptibility difference between the intravascular and extravascular spaces.

The discovery of this magnetic susceptibility effect and the development of techniques to follow the passage of an agent through the brain marked the beginning of fMRI, opening the door to physiological studies in addition to anatomy (Rosen *et al.* 1989). The first demonstration of brain activation with MRI used serial injections of Gd-DTPA to measure the increased blood volume in the visual cortex when subjects viewed a flashing light (Belliveau *et al.* 1991). In the activated state, the signal drop as the gadolinium passed through the brain was deeper and shifted slightly earlier. For brain activation studies, BOLD techniques have superseded these contrast agent techniques, but as newer long-lasting agents are developed and approved for human use, we are likely to see a resurgence in interest in using contrast agents for fMRI studies. Dynamic contrast agent studies are now a standard clinical tool for investigating a number of disease states involving altered perfusion (Edelman *et al.* 1990; Rosen *et al.* 1991).

Given that we can measure such bolus-tracking curves as an agent passes through the tissue, how can we interpret them in a quantitative way in terms of underlying physiological quantities such as CBF and CBV? Answering this question involves some subtle complications. Bolus-tracking techniques draw heavily on ideas of tracer kinetics developed over the last 50 years, and we will use these ideas as the framework for understanding the MR methods. In addition, the principles of tracer kinetic methods are also the foundation for understanding ASL methods discussed in Ch. 13.

## Basic concepts of tracer kinetics

### Time–activity curves

Tracer kinetic modeling has a long history in the study of physiology (Axel 1980; Lassen and Perl 1979; Meier and Zierler 1954; Zierler 1962). In a tracer study, an agent is injected into the blood, and the kinetics of the agent as it passes through the tissue are monitored. Radioactive labels make possible a direct measurement of the tissue concentration of the agent, as in positron emission tomography (PET) studies. Technically speaking, a tracer study usually means that the agent is a labeled version of a metabolic substrate (e.g., [ $^{11}\text{C}$ ]-glucose or  $^{15}\text{O}_2$ ), and the agent then traces the fate of that substrate. However, the same principles apply to other agents that are not a modified form of a metabolic substrate (e.g.,  $^{133}\text{Xe}$  or nitrous oxide) but nevertheless distribute through the tissue in a way that reflects some underlying physiological parameter, such as blood flow. In fact, the question of whether a particular agent acts as a tracer of a particular metabolic substrate can be subtle. Deoxyglucose differs from glucose yet it is used as a tracer of the early stages of glucose metabolism (Sokoloff *et al.* 1977). The differences between the two molecules appear in a correction factor called the

*lumped constant*, as described in Ch. 1. In contrast,  $^{11}\text{CO}_2$  is a labeled form of  $\text{CO}_2$  but does not act as a tracer of  $\text{CO}_2$  in the body because intrinsic  $\text{CO}_2$  is not only delivered to tissues by blood flow, like the labeled agent, but also is created in the tissue by oxidative metabolism, unlike the agent (Buxton *et al.* 1984).

In the following, we will take the broad view of tracer kinetics as a description of the dynamic tissue concentration of any agent that is delivered to the tissue by blood flow. The essential data in a tracer study then are the tissue concentration of the agent measured over time,  $C_T(t)$ , and the agent concentration measured in arterial blood,  $C_A(t)$ . These curves are described as *time-activity curves*, where activity refers to concentration of the agent, often measured as an amount of radioactivity, and not to neural activity. A basic assumption of tracer studies is that the physiological system is in a steady state during the measurement so that neural activity and flow are constant. Then  $C_A(t)$  is the driving function of the system, and  $C_T(t)$  is the output. Connecting the input and the output is a model for the kinetics of the agent that involves several physiological parameters, and the goal of tracer kinetic analysis is to estimate these parameters from the data.

## Volume of distribution of the agent

For MR applications of tracer kinetics, we are primarily concerned with agents that are not metabolized in the brain and so are simply passively distributed. For these agents, the two physiological parameters that directly affect the kinetics are the local CBF and the *partition coefficient*, or *volume of distribution*, of the agent. The local CBF is most often expressed as the volume of arterial blood delivered per minute to 1 g tissue. But for imaging applications, the natural unit for an element of tissue is volume, rather than mass, because an image voxel refers to a volume of tissue. Expressed in these terms, the local CBF, which we will abbreviate as  $f$ , is the milliliters of arterial blood delivered per milliliter of tissue per minute. The units of  $f$  are, therefore, simply inverse time, and we can often think of  $f$  as a rate constant governing the delivery of metabolic substrates, as described in Ch. 2. A typical value for the human brain is  $0.6 \text{ min}^{-1}$  (or  $60 \text{ mL/min per } 100 \text{ mL tissue}$ , or  $0.01 \text{ s}^{-1}$ ).

The partition coefficient  $\lambda$  describes how the agent would naturally distribute between blood and tissue if allowed to equilibrate. Specifically, if the concentration of the agent in blood is held constant for a very long time at a value  $C_0$ , the total tissue concentration of the agent in an element of brain tissue will approach a value  $C_T(\infty)$  such that  $\lambda = C_T(\infty)/C_0$ . The dimensions of  $\lambda$  (and the concentrations) must be defined in a way that is consistent with the dimensions of  $f$ . If  $f$  is expressed as milliliters of blood per minute per gram of tissue, then  $\lambda$  has the dimensions milliliters per gram (i.e., volume of distribution per gram of tissue), arterial concentration is expressed as moles per milliliter, and tissue concentration is expressed as moles per gram. But if, instead,  $f$  is defined as milliliters of blood per minute per milliliter of tissue, so its dimensions are simply inverse time, then  $\lambda$  is dimensionless (volume of distribution per volume of tissue). We will use the latter definition, so  $f$  is expressed as inverse time,  $\lambda$  is dimensionless, and all concentrations are expressed in moles per milliliter.

The simplest case is a *freely diffusible agent* that readily leaves the blood and diffuses into all the tissue spaces; therefore,  $\lambda = 1$ . If the agent only distributes through a part of the tissue space,  $\lambda$  is less than one. For example, if the agent freely diffuses into the interstitial space, but not the intracellular space, at equilibrium the interstitial concentration will be equal to the arterial concentration, but the intracellular concentration will be zero. The total tissue concentration will be proportional to the interstitial plus blood volume fractions, which is typically

approximately 20%, and so  $\lambda$  will be approximately 0.2. This is the reason why  $\lambda$  is often described as the volume of distribution of the agent, and for many agents this is a useful way to interpret  $\lambda$ .

However, thinking of  $\lambda$  as a tissue–blood partition coefficient, rather than a volume of distribution, is a more general description that applies to any agent. An agent could have a value for  $\lambda$  that is greater than one or much less than one even though it has access to the full volume of the tissue. For example,  $O_2$  diffuses throughout the tissue space but is more soluble in lipids than in water (Kassissia *et al.* 1995). At equilibrium, there is a higher concentration in the tissue space than in blood plasma because of the greater concentration of cell membranes, and so  $\lambda$  is greater than one. But the case of  $O_2$  is even more complicated because most of the  $O_2$  in blood is bound to hemoglobin, and so if  $\lambda$  is defined in terms of the total arterial blood content, rather than the plasma content, it will be less than one. Another example is  $CO_2$ , which freely enters all the tissue spaces but also combines with water to form bicarbonate ions. If labeled  $CO_2$  is introduced into the blood, the label will distribute between dissolved gas and bicarbonate ions, and this distribution depends on the local pH. The  $\lambda$  for labeled  $CO_2$  then depends on the arterial and tissue pH values (Buxton *et al.* 1984) and can be greater or less than one despite the fact that the  $CO_2$  enters all the tissue space.

These examples indicate that the interpretation of  $\lambda$  can involve some subtleties. But for the agents of interest in MRI, it is reasonable to think of  $\lambda$  as a measure of the fraction of the total tissue volume that the agent can enter. Then a diffusible tracer, such as tagged water, that enters the full tissue space, has  $\lambda = 1$ . In contrast, an intravascular tracer, such as Gd-DTPA, that remains confined to the vasculature in the healthy brain, has  $\lambda = \text{CBV}$  (typically approximately 4% in the brain).

Furthermore, if the agent readily fills its volume of distribution, in the sense that there is no impediment to the agent (i.e., it freely diffuses into its volume of distribution), then a useful time constant is  $\tau = \lambda/f$ , the mean transit time of the agent. This time constant is also the characteristic time required for the tissue to come into equilibrium with the blood. In other words, for the same flow, the volume of distribution of an intravascular agent is quickly filled because the blood volume is only a small fraction of the total volume, while the volume of distribution of a freely diffusible agent requires a much longer time to fill. For example, with a CBF of 60 mL/(min · mL) tissue ( $0.01 \text{ s}^{-1}$ ),  $\tau$  for an intravascular tracer with a CBV of 4% is approximately 4 s, but for a diffusible tracer the equilibrium time is approximately 100 s.

As we will see, this huge difference in the time constants is critical for interpreting tissue time–activity curves in terms of local physiological parameters. The kinetics of an agent, as reflected in the local tissue concentration–time curve, depend on both  $f$  and  $\lambda$ . The goal in analyzing such curves is to derive a measurement of one or both of these physiological quantities, and the quality of these measurements will depend on how sensitive the tissue curve is to each quantity.

## Interpreting the tissue concentration–time curve

### A simple example

As the simplest example, suppose that the arterial concentration of the agent is maintained at a constant level  $C_A$  for a long time, after which the concentration falls abruptly to zero (Fig. 12.1). What will the tissue time–activity curve look like? Initially, the curve will smoothly increase as flow delivers the agent to the tissue element, and the slope can be directly quantified in terms of the local flow  $f$ . In a short time  $\Delta t$ , the volume of blood delivered per milliliter of tissue is  $f\Delta t$ , and because each unit volume of blood carries  $C_A$  moles of

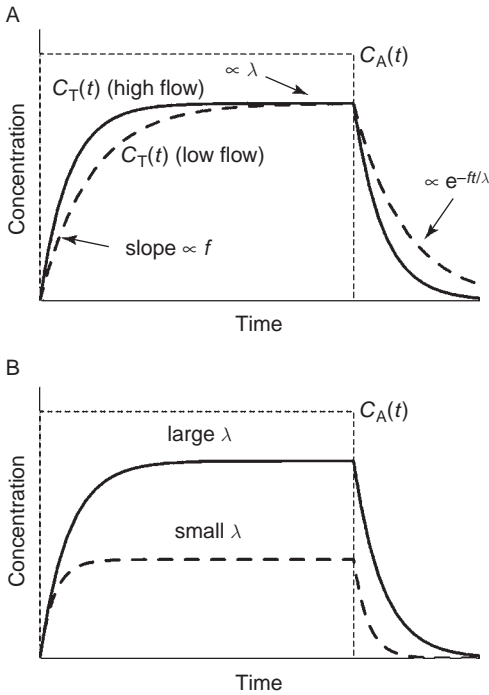


**Fig. 12.1.** Tracer kinetics. Idealized examples of tracer kinetic curves are shown, with the arterial concentration  $C_A(t)$  represented as a perfectly rectangular bolus. (A) Two tissue concentration  $C_T(t)$  curves for different local flows ( $f$ ) but the same volume of distribution ( $\lambda$ ). (B) Tissue curves for the same  $f$  value but different  $\lambda$ . The agent is delivered in proportion to  $f$ , so the slope of the early part of  $C_T(t)$  depends just on  $f$ . After a steady-state plateau is reached,  $C_T(t)$  is proportional to  $\lambda$  and independent of  $f$ . Finally, after delivery stops, the clearance of the agent depends on the ratio  $f/\lambda$ .

the agent, the change in the tissue concentration of the agent is  $\Delta C_T = f C_A \Delta t$ . Thus, the slope of the initial portion of the tissue concentration–time curve is simply proportional to  $f$  and the arterial concentration. In this initial linear period, before any of the agent has had a chance to leave the tissue volume, the tissue concentration depends only on  $f$  and is independent of  $\lambda$ .

As time goes on, some of the agent that arrived early will begin to clear from the tissue by venous flow, and the linear rise of the tissue concentration–time curve will begin to taper off. Eventually, if the duration of the arterial input curve is long enough, the tissue curve will reach a steady-state plateau. From this time on, the volume of distribution of the agent is filled to the same concentration as in the artery, and the rate of delivery of new agent by arterial flow is matched with the rate of clearance by venous flow. Within the volume of distribution of the agent, the concentration is equal to the arterial concentration,  $C_A$ , but since this volume only occupies a fraction  $\lambda$  of the total volume of the tissue element, the net tissue concentration at the plateau is  $\lambda C_A$ . Therefore, on the plateau, the tissue concentration directly reflects  $\lambda$  and is independent of  $f$ .

After the arterial concentration is reduced to zero, with no more delivery of new agent, the tissue concentration will decrease over time as the agent is cleared by venous flow. The exact shape of this portion of the curve will depend on details of the particular agent and its volume of distribution. But a simple model that is often used is to assume that the agent passes rapidly from the blood throughout its volume of distribution, so that the venous blood remains in equilibrium with the rest of the tissue even as the total concentration is decreasing. That is, the venous concentration  $C_V$  quickly adjusts so that it is always equal to  $C_T/\lambda$  as  $C_T$  decreases. In each short time interval  $\Delta t$ , the amount of the agent carried out is

$fC_V\Delta t = (f/\lambda)C_T\Delta t$ ; therefore, the fraction of the tissue concentration removed in  $\Delta t$  is  $f\Delta t/\lambda$ . This produces an exponential decay of the tissue concentration,  $e^{-t/\tau}$ , with  $\tau = \lambda/f$ ; the clearance of the agent does not depend on the exact value of either  $f$  or  $\lambda$ , but only on their ratio.

To summarize, the tissue concentration–time curve depends on the local flow and the volume of distribution of the agent to different degrees at different times. The initial upslope of the curve depends only on  $f$ , the plateau depends only on  $\lambda$ , and the clearance portion depends on the ratio  $f/\lambda$ . During the upslope portion of the curve, the tissue concentration provides a pure measurement of local flow, independent of  $\lambda$ . Because none (or very little) of the delivered agent has cleared, the agent is acting essentially like a microsphere, which is delivered to the tissue in proportion to flow and then remains trapped in the capillary bed (Ch. 2). On the plateau, the tissue concentration provides no information on the local flow and, instead, provides a direct measurement of the local volume of distribution of the agent. The clearance portion of the curve again provides information on flow, but only in the form of  $f/\lambda$ . That is, from a clearance measurement alone, only the ratio  $\lambda/f$  can be measured, and to extract a measurement of flow alone, the volume of distribution must be known or measured separately.

## Measuring cerebral blood flow and volume

With these arguments in mind, the essential difference between the kinetics of a diffusible agent and an intravascular agent can be understood. The time to reach the plateau and the time required for clearance are both on the order of  $\lambda/f$ . For an intravascular tracer this is only approximately 4 s, but for a diffusible tracer it is over 1 min. For an intravascular tracer, the transition periods before and after the equilibrium plateau are very short and so are difficult to measure. In addition, because these are the only times when the curve is sensitive to flow, it is difficult to measure flow with an intravascular agent. However, because the plateau is quickly reached and can be maintained for a long time, the volume of distribution is readily measured. And  $\lambda$  for an intravascular agent is simply the local CBV. In contrast, for a diffusible agent the transition regions when the tissue curve depends strongly on flow are much longer and so are much more easily measured.

In practice, a complete tissue concentration–time curve such as this is rarely measured. Instead, different techniques focus on different aspects of the curve. In  $^{133}\text{Xe}$  studies, the radioactive xenon is an inert gas that freely diffuses into the tissue (Obrist *et al.* 1967). After breathing in the gas, the clearance of the agent from the subject's brain is monitored with external detectors that measure the gamma rays emitted by the radioactive xenon. By placing an array of detectors around the head, the clearance from local regions can be measured. However, this is not the same thing as a true measurement of tissue concentration. The sensitivity pattern of a single detector is indeed localized, so each activity measurement can be taken as being proportional to the local tissue concentration of the agent, but it is difficult to turn this into an absolute tissue concentration. However, for measuring a decay time for the tissue activity, this type of proportional measurement is sufficient. If the clearance is indeed exponential, then the measured activity will fall by a factor of  $1/e$  during the time  $\tau = \lambda/f$ . To convert a measurement of  $\tau$  into an estimate of local flow,  $\lambda$  must be known, or a value must be assumed. Clearance studies with  $^{133}\text{Xe}$  can thus provide a robust measurement of  $f/\lambda$  but uncertainties in the value of  $\lambda$  and how it might vary from one tissue to another (e.g., gray matter compared with white matter) make this a less robust measurement of blood flow.

With PET and  $\text{H}_2^{15}\text{O}$ , however, the local concentration of the agent is accurately measured, and so it is possible to focus on the early part of the tissue time–activity curve. In the bolus administration method, data are collected over the first 40 s following a rapid injection of the tracer (Raichle 1983). Because the tissue concentration during this period is dominated by delivery by arterial flow, the measured PET counts in each image voxel are primarily sensitive just to local CBF and are only weakly sensitive to  $\lambda$ . For longer data acquisition times, the signal to noise ratio (SNR) would improve, but the signal would become more dependent on  $\lambda$ . The method is, thus, designed to provide a robust measurement of flow independent of any uncertainties about  $\lambda$ .

## The general form of the tissue concentration–time curve

The earlier simple example assumed an ideal arterial concentration–time curve that increases immediately to a plateau value, stays constant at that value for a time, and then falls immediately back to zero. The delivery, plateau, and clearance portions of the curve were determined by  $f$ ,  $\lambda$ , and  $\lambda/f$ , respectively. However, in practice, the arterial concentration–time curve is never a rectangular function, and the borders between delivery, plateau, and clearance regions become blurred, and it is more difficult to see directly how sensitive the tissue concentration–time curve is to these three physiological parameters. In Box 12.1, a more general mathematical treatment of tracer kinetics is developed for an arbitrary arterial concentration  $C_A(t)$  from which it is possible to draw some general conclusions about how blood flow, blood volume, and  $\tau$  affect the tissue concentration–time curve. In general, the tissue concentration–time curve can be written as (from Eq. (B12.1))

$$C_T(t) = C_A(t) * [fr(t)] \quad (12.1)$$

where the  $*$  indicates convolution,  $C_T(t)$  is the tissue concentration–time curve,  $C_A(t)$  is the arterial concentration–time curve,  $f$  is the local CBF, and  $r(t)$  is the local *residue function* (Fig. 12.2), which contains most of the details of the distribution and kinetics of the agent. Specifically,  $r(t_2 - t_1)$  is the fraction of the number of moles of the agent that entered the tissue at time  $t_1$  that are still in the tissue at time  $t_2$ . Then  $r(t) = 1$  for  $t = 0$  because there has been no time for any of the agent to leave, and with increasing  $t$ , it must decrease monotonically. As shown in Box 12.1, the integral of  $r(t)$  over all  $t$  is equal to  $\tau$ . Using Eq. (12.1), one can show that for *any* shape of  $r(t)$ ,  $\tau$ ,  $f$ , and  $\lambda$  are always related by the *central volume principle* as  $\tau = \lambda/f$ .

It is useful to look at Eq. (12.1) in the context of linear systems, such that the arterial concentration–time curve is the input function and the combination  $fr(t)$  is the *impulse response* (the term in brackets in Eq. [12.1]). Then the output (the tissue concentration–time curve) is the convolution of the input function with the impulse response, as illustrated in Fig. 12.2. From the definition of  $r(t)$ , we can see two important characteristics of the local impulse response of the tissue. First, the initial amplitude of the impulse response is  $f$ , because  $r(0) = 1$ . Second, because the integral of  $r(t)$  is  $\tau (= \lambda/f)$ , the area under the impulse response is  $\lambda$ . The extent to which a tissue concentration–time curve depends on  $f$  or  $\lambda$  will then depend on whether it depends on the peak value of the impulse response or just the area under it. This approach is used to analyze the sensitivity of the curve for an intravascular agent to CBF and CBV below.

**Box 12.1. A general model for tracer kinetics**

The goal in tracer kinetic modeling is to develop a mathematical relation between the arterial concentration of the agent  $C_A(t)$  and the resulting tissue concentration  $C_T(t)$ . One can think of  $C_A(t)$  as the driving function of the system, the input function, and  $C_T(t)$  as the output. For the agents of interest for MRI (both diffusible and intravascular tracers), the kinetic model will depend primarily on just two local physiological parameters: the local cerebral blood flow  $f$  and the partition coefficient (or volume of distribution) of the agent  $\lambda$ . We can construct a general expression for the tissue concentration curve at time  $t$  by adding up the amount of agent delivered up to  $t$  weighted by the probability that the agent is still in the tissue voxel at  $t$ . To do this, we define a residue function  $r(t - t')$ , the probability that a molecule of the agent that entered the tissue voxel at time  $t'$  is still there at time  $t$ . We assume that the underlying physiology is in a steady state (e.g., constant flow throughout the experiment) so that  $r$  only depends on the interval  $t - t'$  and not the absolute values of  $t$  or  $t'$ . Then the number of molecules of the agent delivered during a short interval between  $t'$  and  $dt'$  is  $fC_A(t')dt'$ , and the probability that they are still in the tissue element at time  $t$  is  $r(t - t')$ . The net tissue concentration at time  $t$  is then

$$C_T(t) = \int_0^t f C_A(t') r(t - t') dt' = f C_A(t) * r(t) \quad (\text{B12.1})$$

where the  $*$  symbolizes convolution as defined by this equation.

The essential condition required for the validity of Eq. (B12.1) is that when each molecule of the agent enters the capillary bed it has the same possible fates as every other molecule of the agent. This condition could break down if the underlying physiology is not in a steady state (e.g., a changing  $f$  during the experiment). Or, this equation could break down if the agent is present in such a high concentration that there is competition for a saturable transport system, such as glucose extraction from the capillary bed in the brain, which has a limited capacity. In the latter case, a molecule that enters when the agent concentration is low would have a higher probability of being extracted than one that entered when the concentration is high. But for most MRI studies, Eq. (B12.1) is appropriate as a general expression for the tissue concentration of the agent as a function of time.

Equation (B12.1) applies to a wide range of agents, but we have achieved this generality by lumping all the details of transport and uptake of the agent into the single function  $r(t)$ . In particular, Eq. (B12.1) hides the full dependence of the tissue concentration curve on perfusion because  $r(t)$  depends on  $f$  as well. A more detailed consideration of the form of  $r(t)$  for different agents is necessary to clarify how the measured kinetics of an agent can be used to measure the local perfusion. By definition,  $r(t)$  is the probability that a molecule of the agent that entered the capillary bed at  $t=0$  is still there at time  $t$ , so  $r(0)=1$  since there has been no time for any of the agent to leave.

Furthermore,  $r(t)$  must monotonically decrease with increasing time because the probability that a particular molecule is still present cannot be higher at a later time than at an earlier time. The residue function is closely related to the distribution of transit times through the tissue voxel,  $h(t)$ . If many particles enter the tissue at the same moment, the fraction that will stay in the tissue voxel for a total time between  $t$  and  $t + dt$  is  $h(t)dt$ . But this fraction that leaves at time  $t$  is also the change in the fraction that remains at time  $t$ , which is  $(dr/dt)dt$ . Therefore, the relation between the residue function and the distribution of transit times is

$$\frac{dr(t)}{dt} = -h(t) \quad (\text{B12.2})$$

The mean transit time,  $\tau$ , is then

$$\tau = \int_0^{\infty} th(t)dt = \int_0^{\infty} r(t)dt \quad (\text{B12.3})$$

From Eq. (B12.1), we can derive an important general relationship called the *central volume principle*, which was introduced in Ch. 2. Suppose that the arterial concentration is maintained at a constant value  $C_A$  for a very long time  $t$ . As  $t$  approaches infinity, the tissue concentration must approach its equilibrium value  $\lambda C_A$ . From Eqs. (B.12.1) and (B12.3), as  $t$  approaches infinity with  $C_A$  held constant,  $C_T$  approaches  $f\tau C_A$ ; so equating this with the equilibrium condition requires

$$\tau = \frac{\lambda}{f} \quad (\text{B12.4})$$

This simple relationship between the flow, the volume of distribution, and the mean transit time is completely general, regardless of the exact form of  $r(t)$ . It also shows how the form of  $r(t)$  is constrained by our two local physiological variables  $f$  and  $\tau$  such that the integral of  $r(t)$  must be equal to  $\lambda/f$ .

The distinction between  $h(t)$  and  $r(t)$  can be confusing because both appear in the literature of tracer kinetics, but they actually play different roles, depending on the nature of the experiment. In animal experiments, particularly those carried out before imaging techniques became available, the measured quantity is often the venous outflow concentration of the agent rather than the tissue concentration. The venous concentration can be modeled as the convolution of  $h(t)$  with the arterial curve  $C_A(t)$  because  $h(t)$  directly describes how long it is likely to take for a molecule of the agent delivered to the vascular bed to transit the bed and show up in the venous concentration. But for imaging studies, the tissue concentration is measured, and this is modeled as the convolution of  $C_A(t)$  with  $fr(t)$  rather than  $h(t)$ .

To put this another way, we are treating the system as linear so that both the venous concentration and the tissue concentration result from a convolution of the arterial input function with an appropriate impulse response function. For the venous concentration, the impulse response is  $h(t)$ ; for the tissue concentration, the impulse response is the product  $fr(t)$ . The tissue impulse response depends on both flow and the volume of distribution, with an initial amplitude of  $f$  and an area equal to  $\lambda$ . In contrast,  $h(t)$  depends primarily on  $\tau$ , which is the ratio  $\lambda/f$ . For this reason, the difference in the impulse responses for the venous concentration and the tissue concentration is not a simple difference in form; the tissue concentration curve actually carries more information than the venous concentration curve because the impulse response depends on the values of both  $f$  and  $\lambda$  and not just on their ratio.

A common approach to modeling tracer kinetic curves is *compartmental modeling*, and it is useful to consider how such models fit into the more general framework developed here. For example, suppose that the tissue is modeled as a single well-mixed compartment. The rate of delivery of agent to the tissue compartment is  $fC_A(t)$ , and the rate of clearance of the agent from tissue is  $fC_V(t)$ , where  $C_V(t)$  is the concentration of the agent in venous blood. If the exchange of the agent between blood and tissue is very rapid, so that the two pools stay in equilibrium even as the overall concentration is changing, then we can equate  $C_T$  with  $\lambda C_V$ , and the rate of clearance then is  $fC_T\lambda$ . The rate of change of the tissue concentration is then the difference between the rate of delivery and the rate of clearance:

$$\frac{dC_T(t)}{dt} = fC_A(t) - \frac{f}{\lambda} C_T(t) \quad (\text{B12.5})$$

The solution of this differential equation is given by Eq. (B12.1) with  $r(t) = e^{-ft/\lambda}$ . In other words, a single-compartment model is described by the general model with an exponential form for  $r(t)$ .

Compartmental models are often useful in analyzing tracer kinetic data, but it is important to determine which results strongly depend on the restrictive assumptions of compartmental models



and which follow from the more general model and, therefore, are more robust. An important example concerns the interpretation of kinetic curves for an intravascular agent in terms of local CBV. Suppose that an agent is delivered in a bolus form so that the arterial concentration falls back down to zero after a time. The integral of the arterial concentration curve is then finite, and the integral of the tissue concentration curve will also be finite. What is the relation between these two integrated values? To answer this, we can turn to the general model. Mathematically, the integral of a convolution of two functions is the product of the separate integrals of the two functions. Then from Eq. (B12.1) we have

$$\int_0^{\infty} C_T(t) dt = \lambda \int_0^{\infty} C_A(t) dt \quad (\text{B12.6})$$

In other words, for any agent that is not metabolized, the integral of the local tissue concentration curve over all time is proportional to the local partition coefficient multiplied by the integral of the arterial concentration curve. If the agent remains confined to the vasculature,  $\lambda = \text{CBV}$ . So for an intravascular agent, the integrated tissue concentration curve provides a robust measurement of CBV, regardless of the exact form of either the tissue concentration curve or the arterial concentration curve. The arterial concentration curve is global, rather than local, so a map of the local integrated tissue activity is, in fact, directly proportional to a map of CBV.

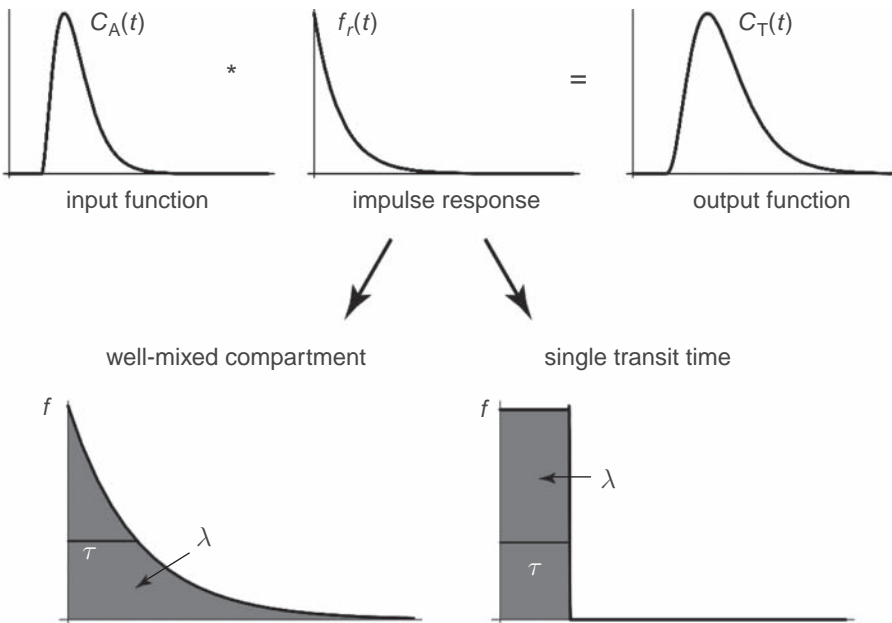


**Fig. 12.2.** General form of the tissue concentration curve. From Eq. (12.1), for any agent, the tissue concentration curve  $C_T(t)$  is the convolution of the arterial concentration curve  $C_A(t)$  with the local impulse response, which is the product of the local flow  $f$  and  $r(t)$ , the probability that a molecule of the agent entering the tissue element at  $t=0$  will still be there at  $t=t$ . The peak of the impulse response is  $f$ , and the area under the impulse response is the partition coefficient or volume of distribution of the agent,  $\lambda$ . Two examples of the impulse response are shown. For a well-mixed compartment,  $r(t)$  is an exponential, and for an intravascular agent with plug flow through identical capillaries, so that the transit time is identical for all molecules of the agent,  $r(t)$  is a rectangle. For either case, the mean transit time  $\tau$  is  $\lambda/f$ .

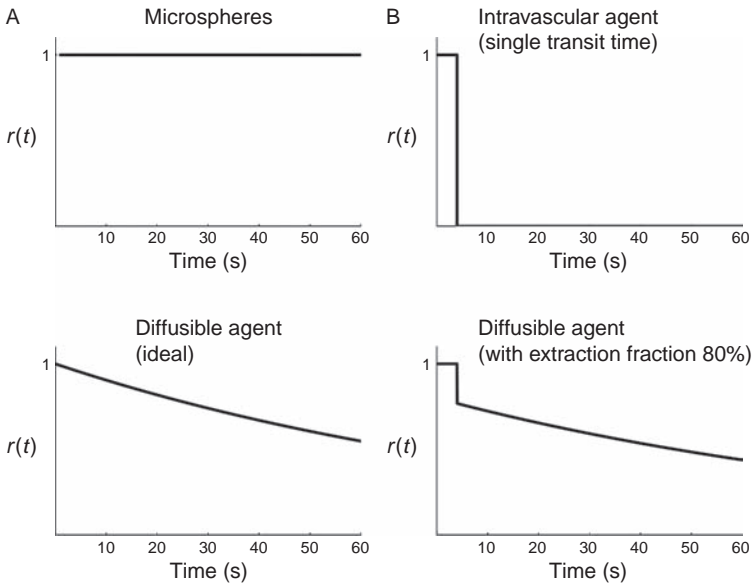


**Fig. 12.3.** The shape of the residue function. The impulse response of the tissue curve is  $f r(t)$ , where  $f$  is the local flow and  $r(t)$  is the probability that a molecule of agent entering a tissue element at  $t=0$  will still be there at  $t=t$ . Several shapes for the residue function  $r(t)$  are illustrated. (A) Microspheres are trapped in the tissue, so  $r(t) = 1$ . (B) For an intravascular agent traversing identical capillaries with plug flow, there is only one transit time, so  $r(t)$  is a narrow rectangle. (C, D) For the ideal diffusible tracer,  $r(t)$  is an exponential (C), and for a partially extracted diffusible tracer,  $r(t)$  must describe the fact that a fraction of the agent quickly traverses the capillary bed and is cleared, while the remaining extracted fraction has a much longer transit time (D).

## The residue function

The form of Eq. (12.1) may seem remarkably simple for a general description of tracer kinetic curves, but we have achieved this simplicity by hiding all the complexities of the transport and distribution of the agent in the shape of  $r(t)$ . The shape of  $r(t)$  is constrained such that  $r(0) = 1$  and the integral is  $\lambda/f$ , but within these constraints a wide range of shapes is possible. To give a sense of what  $r(t)$  looks like under different conditions, we can examine several examples (Fig. 12.3). To begin with, consider the classic case of microsphere studies introduced in Ch. 2. Labeled microspheres are injected in an artery and delivered to a capillary bed, but because the spheres are designed to be too large to fit through the capillaries, they remain lodged in the tissue. For this agent,  $r(t) = 1$  for all time (since the microspheres never leave the tissue), and so by Eq. (12.1) the measured tissue concentration is simply the perfusion  $f$  multiplied by the integral of the arterial concentration. This is a robust method for measuring  $f$  and is usually considered the gold standard for perfusion measurements. The integrated arterial curve can be measured from any convenient artery and need not be measured locally. Note that the form  $r(t) = 1$  does satisfy the central volume principle because both the integral of  $r(t)$  and  $\lambda$  are infinite. In other words, a microsphere behaves as if it is filling an infinite volume of distribution so that none of it ever leaves because  $\tau$  is also infinite.

A diffusible tracer is one that freely crosses the blood–brain barrier and enters the extravascular space, such as an inert gas (e.g.,  $^{133}\text{Xe}$ ) or labeled water (e.g.,  $\text{H}_2^{15}\text{O}$ ). A simple

form for  $r(t)$  that satisfies the central volume principle and is commonly used to model the kinetics of these agents is  $r(t) = e^{-ft/\lambda}$ . This exponential form naturally arises in compartmental models in which the rate of transport out of a compartment is taken to be a rate constant times the concentration in the compartment. This simple form is equivalent to modeling the tissue as a single well-mixed compartment (Box 12.1).

This example shows how  $f$  affects the tissue concentration–time curve in two distinct ways: the amount of agent delivered to the tissue is directly proportional to  $f$ , and the clearance of the agent depends on  $f$  through the form of  $r(t)$ . So either delivery or clearance of the agent can be used as the basis for a measurement of  $f$ , as discussed above. With the  $\text{H}_2^{15}\text{O}$  method, the tracer is administered rapidly, and the initial concentration in the tissue (averaged over the first 40 s) is measured locally with PET, directly yielding a measurement proportional to  $f$  based on the delivery of the agent. The concentration maps can be calibrated by also measuring the arterial curve. In the  $^{133}\text{Xe}$  method, the agent is administered by inhalation, and the clearance curve is measured with an external detector. The measured tissue curve can then be fit to a decaying exponential, and the time constant  $\tau$  for clearance is  $\lambda/f$ . Provided that  $\lambda$  is known (and for diffusible tracers it is near one),  $f$  can be measured directly from the clearance curve.

Although perfusion can be measured with a diffusible tracer either from delivery or from clearance of the agent, measurements based on delivery are more robust. Delivery is always proportional to flow, as with microspheres, and is independent of  $r(t)$ . That is, for delivery,  $f$  enters directly as a multiplicative factor in Eq. (12.1), regardless of the form of  $r(t)$ . But to model clearance, a form of  $r(t)$  must be assumed, and calculated perfusion will always be somewhat model dependent. For example, consider measuring  $f$  in a voxel that contains two types of tissue with different values of perfusion (e.g., gray and white matter). Delivery of the tracer is then governed simply by the average value of  $f$  in the voxel, but clearance is now more complicated than the simple exponential form, and  $r(t)$  should be modeled as a biexponential form.

An exponential form for  $r(t)$  is often used to model diffusible tracers, but what is an appropriate form for an intravascular agent? One could use an appropriate exponential (e.g., with  $\lambda = 0.04$  instead of  $\lambda = 1$ ). But a single well-mixed compartment seems to be a poor approximation for blood flow through a vascular tree. As a counter-example, suppose that the capillary bed consists of identical capillaries, with plug flow at the same velocity in each one. Then  $\tau$  through the tissue is identical for all molecules of the agent, with each molecule spending precisely a time  $\tau$  in the tissue, and  $r(t)$  is rectangular with a width  $\tau$  (Figs. 12.2 and 12.3). This also is an extreme form for  $r(t)$ , and the true form likely lies somewhere between the rectangle and the exponential.

Even for a diffusible tracer with  $\lambda = 1$ , the exponential form of  $r(t)$  will only apply if the agent rapidly enters its volume of distribution. What happens if, instead, there is an impediment to rapid filling? For example, if the permeability of the capillary wall to the agent is low, some of the agent delivered to the capillary bed will not even leave the blood and will be carried away by venous flow. For example, labeled water is not fully extracted in the brain and so, even though its volume of distribution is the whole tissue volume, it can require some time to diffuse into it. This leads to systematic errors in the estimation of CBF in PET studies with  $\text{H}_2^{15}\text{O}$ .

A useful measure of this effect is the unidirectional extraction fraction  $E$ , the fraction of the delivered agent that leaves the blood during its passage through the capillary bed. If  $E$  is close to 100%, then the exponential form for  $r(t)$  is likely to be accurate. But if  $E$  is only 80%,

then 20% of the agent will clear much more rapidly. To describe the effects of limited extraction, we must modify the form of  $r(t)$ . Figure 12.3D illustrates what  $r(t)$  would look like if 20% of the delivered agent passes through without entering the tissue, with each unextracted molecule having a capillary transit time of 4 s. The remaining 80% of the delivered agent is extracted and follows the exponential behavior of a diffusible tracer.

This example illustrates the importance of having a more general model for tracer kinetics than that provided by compartmental models alone. The assumptions of compartmental models are often not true in practice, and the more general treatment makes possible more accurate modeling and analysis of errors in the techniques. These examples also serve as a reminder that even though we often adopt a model in which the kinetics of the agent are described just by  $f$  and  $\lambda$ , the shape of  $r(t)$  also is important.

## Sensitivity of the tissue concentration–time curve to local blood flow and the volume of distribution

In tracer studies, or contrast agent studies in MRI, the goal is to derive estimates of  $f$  or  $\lambda$  from the measured concentration–time curves. With a diffusible agent,  $\lambda$  is approximately equal to one, and so the goal is to measure  $f$ . With an intravascular agent, such as Gd-DTPA in MR studies of the brain,  $\lambda = \text{CBV}$ , so it is desirable to extract estimates of both  $f$  and  $\lambda$  from the kinetic curves. The precision of any estimate of these physiological parameters depends on how sensitive the shape and magnitude of the tissue concentration–time curve are to these parameters. For example, if we can change CBF by a factor of two and this produces a negligible change in the tissue concentration–time curve of an agent, then we have no hope of measuring  $f$  from such data. Furthermore, for an intravascular agent, the curve is affected by both  $f$  and  $\lambda$ , and we are concerned with how well we can separate these effects to produce accurate measurements of each.

Equation (12.1) provides the basis for drawing some general conclusions about the sensitivity of the tissue concentration–time curve to  $f$  and  $\lambda$ . In this equation, the tissue concentration–time curve is represented as a convolution of the arterial input function  $C_A(t)$  and the tissue impulse response function  $fr(t)$ . For any agent, the tissue impulse response has an initial amplitude equal to  $f$  and an area of  $\lambda$ . Accurately measuring the *shape* of the tissue concentration–time curve requires high temporal resolution and a good SNR. However, a relatively straightforward quantity to measure is the *area under the tissue concentration–time curve*. As discussed in Box 12.1, a useful mathematical property of convolutions is that the integral of a convolution of two functions over all time is equal to the product of the separate integrals of the two functions. The integral of the impulse response is  $\lambda$ , so the integral of the tissue concentration–time curve over all time is simply  $\lambda$  multiplied by the integral of the arterial concentration–time curve, *independent* of  $f$  or the shape of  $r(t)$ . This means that  $\lambda$  can be measured in a very robust way from the integral of the tissue concentration–time curve, and this is the basis for using Gd-DTPA to measure CBV. Furthermore, even without any measurements of the arterial concentration–time curve, just the integral of the tissue concentration–time curve alone is directly proportional to local CBV because the integrated arterial concentration–time curve should be the same for all capillary beds.

Deriving an estimate of CBF from the dynamics of an intravascular tracer is more problematic, because the characteristic time required for the tissue concentration to come into equilibrium with the blood concentration is  $\tau$ . As discussed above, the tissue concentration–time curve is only sensitive to flow during the approach to equilibrium, and at equilibrium the

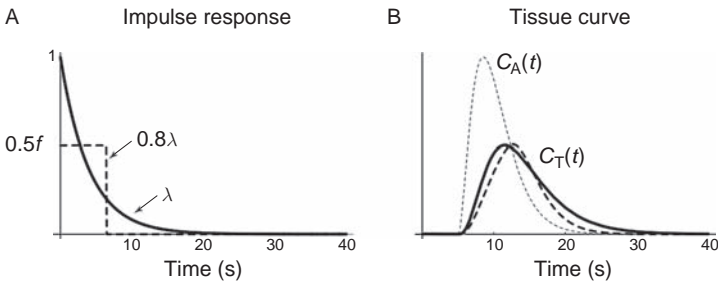


**Fig. 12.4.** Ambiguities in estimating cerebral blood flow (CBF) from the tissue concentration curve. The essential difficulty in estimating CBF from the tissue concentration curve of an intravascular agent is that different values of flow with different shapes of the impulse response function can nevertheless produce similar tissue concentration curves. The two impulse response shapes describe local flow values that differ by a factor of two (A), yet the tissue curves are nearly identical (B).

curve just depends on  $\lambda$ . So for a broad bolus, with the arterial concentration–time curve changing slowly relative to  $\tau$ , the tissue concentration of the agent quickly equilibrates with the current value of the arterial concentration. The result is that the tissue concentration–time curve is essentially a replica of the arterial concentration–time curve scaled by  $\lambda$  and carries no information on flow. For the tissue concentration–time curve of an intravascular agent to reflect  $f$ , a very narrow bolus is required, so that the arterial concentration is changing so fast that the tissue concentration cannot catch up. The tissue concentration–time curve then reflects how fast the local tissue concentration can change, which depends on  $\tau$  and thus depends on flow.

Because  $\tau$  for a diffusible agent is very long, nuclear medicine techniques all employ diffusible tracers to measure flow; it is easy to produce an arterial bolus that is much shorter than  $\tau$  so that the local tissue concentration–time curve will be sensitive to flow. To use an intravascular agent for a flow measurement requires a much sharper arterial bolus because  $\tau$  is so short (approximately 4 s). Indeed, it was suggested in the nuclear medicine literature that measurement of CBF with an intravascular tracer is not possible (Lassen 1984). The slight delay in the peak of the tissue concentration–time curve relative to the arterial concentration–time curve is difficult to measure, and unless the arterial bolus is only a few seconds wide, the amplitude of the tissue concentration–time curve will depend primarily on CBV rather than CBF. In addition, the shape of  $r(t)$  is critical for interpreting such curves, as illustrated in Fig. 12.4. In this example, two forms for  $r(t)$  are used to show that two regions with a CBF difference of a factor of two can yield nearly identical tissue concentration–time curves. Even with an accurate estimate of the arterial input curve, it would be very difficult to untangle the separate influences of  $r(t)$  and  $f$  on the tissue concentration–time curve to derive a reliable estimate of CBF.

In summary, measurements of the kinetics of an intravascular agent provide a robust measurement proportional to CBV based on the area under the tissue concentration–time curve. That is, the area under the local tissue concentration–time curve is a direct reflection of CBV, lacking only a global scaling factor: the area under the arterial concentration–time curve. However, extracting an estimate of CBF from such data is more difficult, requiring rapid imaging, a narrow arterial bolus of the agent, and a measurement of the arterial concentration–time curve. The CBF estimate is likely to be more accurate in states of reduced flow than in states of increased flow; consequently, it is more useful in ischemia studies than in activation studies.

## Bolus tracking

### The bolus tracking experiment

We now turn back to the bolus tracking experiment, in which an agent such as Gd-DTPA is rapidly injected, and consider how to interpret the dynamic curves in the light of the preceding discussion of classical tracer kinetics. In qualitative terms, we expect that the larger the concentration of the agent within the voxel, the greater the field gradients produced, and the larger the signal dip will be. But how, exactly, is the dynamic MR signal curve of an element of brain tissue related to the CBF and CBV of that tissue?

The underlying events in a dynamic contrast agent study are shown schematically in Fig. 12.5. After a rapid venous injection, the agent passes through the heart and produces an arterial bolus, shown as a plot of the time-dependent arterial concentration  $C_A(t)$ . This bolus is delivered to each tissue element, creating a local tissue concentration–time curve  $C_T(t)$ . The tissue concentration–time curve is the convolution of the arterial concentration–time curve with a local impulse response function that depends on  $f$ , and  $r(t)$ . The tissue concentration of the agent, in turn, shortens the local  $T_2^*$ , creating a dip in the MR signal curve measured over time. The signal fall as gadolinium passes through the microvasculature of the brain is transient, but it can be measured with fast imaging techniques such as echo planar imaging (EPI), with a typical temporal resolution of one image per second on each slice.

Modeling the dynamic curve of concentration of an intravascular agent was discussed in the previous sections, but the MR experiment introduces a new element: the MR signal, rather than the agent concentration, is the measured quantity. So the modeling requires two steps: (1) relating agent concentration  $C_T(t)$  to MR signal  $S(t)$ , and (2) relating physiological parameters such as blood flow and blood volume to  $C_T(t)$ . The first stage is modeling the biophysics of MR signal loss caused by magnetized blood vessels, and the second stage is modeling the kinetics of how inflow and outflow control the tissue concentration of an injected intravascular agent.

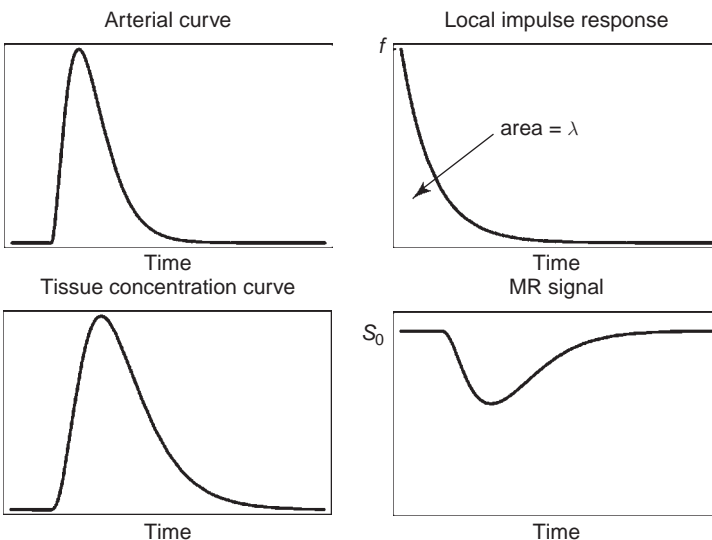


**Fig. 12.5.** Dynamics of MR contrast agents. The effects of an agent such as Gd-DTPA are illustrated. A rapid venous injection produces an arterial bolus of the agent. The local tissue concentration curve is the convolution of the arterial concentration curve with a local impulse response function that depends on the local cerebral blood flow  $f$  and the cerebral blood volume  $\lambda$ . As the agent passes through the tissue,  $T_2^*$  is shortened, creating a dip in the local signal measured with dynamic MRI.

## Relating MR signal changes to agent concentration

In the first stage of modeling, the change in the MR signal  $S(t)$  is related to the change in the gadolinium concentration. The general question of modeling the MR signal effects caused by altered susceptibility of blood has received a great deal of attention (Boxerman *et al.* 1995; Kennan *et al.* 1994; Weisskoff *et al.* 1994; Yablonsky and Haacke 1994). The question is important not only for the interpretation of contrast agent curves but also for the interpretation of BOLD contrast in altered blood oxygenation. The MR signal depends on the pulse sequence used, but for this application, the effect we are analyzing is an altered transverse relaxation, so the essential difference between pulse sequences is whether it is a GRE or SE acquisition. For a GRE acquisition, the additional signal loss owing to gadolinium is primarily just a result of microscopic field distortions creating an inhomogeneous field; the additional dephasing of precessing spins reduces  $T_2^*$ .

We can then describe the dynamic MR signal for a GRE experiment as

$$S(t) = S_0 e^{-TE \Delta R_2^*(t)} \quad (12.2)$$

where TE is the echo time and  $S_0$  is the signal when there is no gadolinium present. The  $T_2^*$  relaxation has been written in terms of a change in the relaxation rate  $R_2^*$ , and that rate is simply  $1/T_2^*$ . In short, the effect of the agent is modeled as a transient change  $\Delta R_2^*$ , which depends on the concentration of the agent,  $C_A(t)$ . The essential connection between the MR signal and the gadolinium concentration then depends on how  $\Delta R_2^*$  depends on  $C_T(t)$ . The standard assumption is to model this as a simple linear dependence

$$\Delta R_2^*(t) = k C_T(t) \quad (12.3)$$

where  $k$  is a constant of proportionality.

The first step in analyzing dynamic contrast agent data is to use Eqs. (12.2) and (12.3) to convert the local MR signal measured over time  $S(t)$  into a curve proportional to the tissue concentration  $C_T(t)$  (Fig. 12.6). This is done by calculating  $\Delta R_2^*(t)$  for each time point, by normalizing the MR signal intensities to the initial intensity  $S_0$  prior to injection, and then taking the natural logarithm.

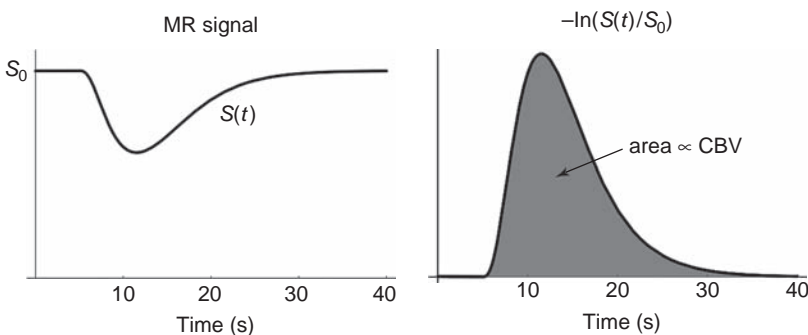


**Fig. 12.6.** Analysis of dynamic contrast agent data. The MR signal over time  $S(t)$  is first converted to a measure proportional to  $\Delta R_2^*$  by normalizing each measured value  $S(t)$  to the mean value  $S_0$  before injection, and taking the natural logarithm. The area under this curve is then directly proportional to local cerebral blood volume.

Although the simple modeling of the relationship between  $\Delta R_2^*$  (or  $\Delta R_2$ ) and the concentration of the contrast agent expressed in Eq. (12.3) is widely used, there is substantial evidence that this is too simple an approximation. Specifically, Springer and colleagues have shown that an implicit assumption of the modeling is that there is fast exchange between water compartments in the tissue, and there is strong evidence against this idea (Landis *et al.* 2000; Li *et al.* 2005; Yankeelov *et al.* 2003, 2005). In addition, the mechanisms that lead to signal loss are complex, and different in tissue and blood (Kjolby *et al.* 2006). For these reasons, the quantitative interpretation of bolus tracking curves, particularly in disease, is potentially quite complicated. Nevertheless, the simple analysis outlined above is still the standard one used in clinical applications.

## Measuring cerebral blood volume from bolus tracking data

With the assumption that Eq. (12.3) applies, making the connection between the dynamic MR curve and the local concentration of the agent, we can now apply the principles of tracer kinetics. In particular, from Eq. (B12.6) in Box 12.1, the integral of the tissue concentration–time curve is equal to  $\lambda$  multiplied by the integral of the arterial concentration–time. Combining this with Eq. (12.3) gives

$$\int_0^{\infty} \Delta R_2^*(t) dt = \lambda \left[ k \int_0^{\infty} C_A(t) dt \right] \quad (12.4)$$

where  $k$  is a proportionality constant. In the healthy brain, Gd-DTPA is an intravascular agent, so  $\lambda = \text{CBV}$ .

This equation represents a simple relationship: the area under the  $\Delta R_2^*$  curve is proportional to the local CBV. The constant of proportionality is  $k$  (from Eq. [12.3]) multiplied by the integral of the arterial concentration–time curve. The constant  $k$  is generally unknown, and the arterial concentration–time curve is usually not measured. However, the integral of the arterial concentration–time curve is a global property, and so is the same everywhere. If  $k$  also is the same in each region of the brain, then the overall proportionality constant, represented by the terms in brackets in Eq. (12.4), is a *global scaling factor*. This means that a pixel-by-pixel map of the integral of  $\Delta R_2^*$  is a map of CBV, lacking only a global scaling factor to convert the image intensities into units of absolute blood volume (i.e., milliliters of blood per milliliter of tissue).

The preceding arguments specifically applied to GRE studies, for which we can assume that  $\Delta R_2^*$  varies approximately linearly with the local gadolinium concentration. For SE studies, this relationship is likely to be non-linear. Nevertheless, Boxerman and co-workers (1995) have argued that the integrated  $R_2$  curve should still yield an accurate measurement proportional to local CBV as long as the form of this non-linearity is reasonably uniform across the brain. In practice, dynamic SE data are analyzed in the same way as dynamic GRE data.

## Recirculation of the agent

In a typical implementation of a CBV measurement from Gd-DTPA kinetics, dynamic images are collected for 40–60 s after rapid injection of the agent. To optimize the SNR of the CBV measurement, it is important that a sufficiently long period of baseline images be collected before the bolus of the agent arrives in the imaging voxel, so it is best to start the imaging



series well before the agent is injected (Boxerman *et al.* 1997). If the imaging is continued for 30–60 s after the arrival of the initial bolus, a broad but weaker second signal dip sometimes occurs from the recirculation of the agent. In principle, recirculation of the agent and reappearance in tissue is not a concern for the preceding analysis. This just makes the arterial concentration–time curve have a more complicated shape, but the integrated tissue concentration–time curve should still be simply proportional to the integral of this arterial concentration–time curve including the second pass.

However, if there is any leakage of the agent into the extravascular space, as might occur in tumors, or any tendency for the agent to bind to the endothelium and remain in the voxel, then recirculation poses a problem for accurate measurements of CBV. Furthermore, the integral of the arterial concentration–time curve (or the tissue concentration–time curve) is only a well-defined number if the curve returns to zero before the end of the experiment, because otherwise it will depend on local transit delays as well. In practice, the tissue signal is often reduced at the end of the dynamic imaging, indicating that the agent is still circulating through the tissue. For these reasons, a useful approach is to fit the early part of the tissue concentration–time curve, covering the initial first-pass bolus, to an assumed shape – usually a gamma-variate function – and use the parameters of that fit to determine the area (Belliveau *et al.* 1991; Boxerman *et al.* 1997). The gamma-variate fitting approach generally works well when the SNR is reasonably high, but for very noisy data, it may actually make the SNR worse (Boxerman *et al.* 1997).

## The mean transit time

The mean transit time  $\tau$  through a tissue element is equal to  $\lambda/f$ , as described by the central volume principle in earlier sections of this chapter. But in the analysis of Gd-DTPA kinetic curves, a different parameter has been introduced and called the “mean transit time,” abbreviated as MTT. This quantity is the time from injection of the bolus to the mean of the local tissue concentration curve and so is distinctly different from  $\tau$ . The MTT parameter is readily measured from the MR data and is routinely calculated. Furthermore, MTT is lengthened in ischemia, so the measurement has important value in assessing low flow states. However, it is unfortunate that this quantity is called the mean transit time because it creates confusion with the true mean transit time  $\tau$  (Weisskoff *et al.* 1993).

Most recent papers recognize that MTT as originally defined is not  $\tau$ , and emphasize that to get a true value of MTT, a deconvolution of the measured curve is required to separate the effects of the arterial input function. These papers then refer correctly to the true MTT, but the literature is confusing because one must read carefully to determine whether the definition is the correct one or the original one. Data analysis software provided by the scanner manufacturers often reports MTT or an equivalent number, because this is a readily calculated empirical number. In the following, we will continue to use the original terminology of MTT for this quantity and consider how it is related to  $\tau$ .

The concept of the MTT comes from thinking about a concentration curve as a kind of probability distribution, with MTT as the mean value. However, relating MTT to other physiological parameters is rather complicated. For example, suppose that the entire bolus of the agent was delivered to a tissue voxel instantaneously. The tissue concentration–time curve would then simply be proportional to  $r(t)$ , the residue function discussed above. Now consider the two forms of  $r(t)$  for an intravascular agent that were discussed above (Fig. 12.2): a decaying exponential with mean  $\tau$ , and a rectangular function, corresponding to a capillary bed with an identical transit time  $\tau$  in each capillary. Would these curves give

the same MTT? Somewhat surprisingly, they do not. For the exponential decay, the mean of  $r(t)$  is equal to  $\tau$ , but for the rectangular function the MTT is  $\tau/2$  (the width of the rectangular curve is  $\tau$ , so the mean is  $\tau/2$ ). This example illustrates that while MTT is a simple number to measure, it is difficult to interpret reliably in terms of basic physiological parameters.

In practice, the problem of interpreting MTT is much greater because the agent is delivered over an extended time. Even with a rapid venous injection, the bolus is broadened and delayed as it passes through the heart and the arterial vasculature. And even if the resulting shape of the arterial concentration–time curve can be taken to be global, and so the same for each tissue voxel, the transit delay from the time of injection to the time of arrival at the tissue voxel is really a local parameter, varying across the brain.

For these reasons, although the true mean transit time  $\tau$  does contribute to MTT, the local value of MTT is primarily driven by the arterial transit delay and the broadening of the arterial concentration–time curve. So it is an incorrect application of the central volume principle to take the ratio of CBV to MTT as a measure of CBF. For example, consider a region of brain whose primary arterial delivery is somewhat compromised, but the region is receiving adequate blood flow through collateral pathways. In this case, the local CBF and CBV could be normal, but the blood takes longer to get there because of the collateral route, and so MTT would be lengthened.

The measured MTT is, therefore, difficult to interpret in a rigorous quantitative way. But it is, nevertheless, a useful measurement, as suggested by the example above. In ischemic states, several factors may combine to create a lengthened MTT. A partial stenosis of a major artery feeding the local capillary bed may result in a longer transit delay in addition to a reduced perfusion. Collateral circulation feeding the affected area may also lead to a longer delay because the blood follows a longer route in getting to the tissue capillary bed. A decrease in local CBF will increase  $\tau$ , and so this will lengthen MTT. In addition, based on PET studies, it has been suggested that tissue at risk of infarction also has an elevated CBV (Gibbs *et al.* 1984), and this would further increase  $\tau$  and MTT. Although the terminology is confusing, the MTT, nevertheless, is likely to be a sensitive indicator of ischemia.

## Estimating cerebral blood flow from bolus tracking data

The preceding arguments suggest that the effects of CBF on the tissue concentration of an intravascular agent are subtle. Not only does the apparent MTT depend on CBF, but it also depends more strongly on the width of the arterial bolus, the transit delays to the tissue vascular bed, and the shape of  $r(t)$  in addition to  $\tau$ . As discussed above, estimating CBF from the dynamics of an intravascular agent is difficult because  $\tau$  is so short; when the arterial bolus is much broader than  $\tau$ , the tissue concentration–time curve of the agent depends only on CBV. However, with current MR imagers, it is possible to collect full images at rates faster than one image per second. Furthermore, with a rapid venous injection, it is possible to create an arterial bolus with a width of 4–8 s, which is comparable to  $\tau$  for an intravascular agent in the resting human brain. Even though this is not sufficiently narrow to enter the regimen where the peak of the curve depends only on CBF, it does produce some sensitivity of the tissue concentration–time curve to the local CBF. However, estimating CBF generally requires an accurate estimate of the local *arterial input function* (AIF, equivalent to our arterial concentration–time curve  $C_A(t)$ ).

A possible approach to resolving these ambiguities, and obtaining a measurement of CBF from measurements of the tissue concentration–time curve alone, is to measure the initial slope as the agent first arrives in the tissue. During the initial delivery phase, before any of the agent has had time to clear from the tissue, the quantity present in the tissue is directly proportional to how much has been delivered and so is proportional to local CBF. However, the measurement of this initial slope is difficult. The first arrival of the agent in a voxel must be estimated, and the slope must be estimated over a narrow time window smaller than  $\tau$  (after a delay of  $\tau$ , much of the initially delivered agent will have cleared from the voxel). In the healthy brain, with  $\tau$  of approximately 4 s, only a small part of the measured tissue curve can be used. In ischemia, this measurement becomes more feasible because  $\tau$  is substantially lengthened. With this approach, the measured quantity is proportional to local CBF, and the unknown proportionality constant depends on the early shape of the arterial input curve. In other words, a map of the initial slope would be a quantitative map of CBF, lacking only a global calibration factor to convert the map values into units of absolute CBF, in the same sense that a map of the integral of  $\Delta R_2^*(t)$  is a quantitative map of CBV.

Given that CBF does have some effect on the shape of the entire tissue concentration–time curve, a more general approach is to measure the arterial concentration–time curve in addition to the tissue curve and then to model the tissue curve as a convolution of the arterial curve with an unknown impulse response function. The goal is to deconvolve the measured tissue concentration–time curve to produce an estimate of the impulse response (Østergaard *et al.* 1996a, b; Rempp *et al.* 1994). From the foregoing modeling considerations, the impulse response is  $fr(t)$ , so the initial amplitude is the local CBF.

Measuring the arterial input function presents a number of technical challenges, particularly because it is not identical for every tissue element. As the example in Fig. 12.4 suggests, an accurate estimate of the shape of the impulse response is required. However, since the only data available are the convolution of the impulse response with the AIF, the AIF must be known very accurately to deconvolve the tissue concentration–time curve. Any systematic errors, such as a broadening or delay of the AIF for that particular voxel, can lead to significant errors in the estimates of CBF. For this reason, an active field of research has grown around questions of determining an accurate local AIF (Calamante 2005; Calamante *et al.* 2004, 2006; Duhamel *et al.* 2006; Ko *et al.* 2007; Mouridsen *et al.* 2006; Rempp *et al.* 1994; Wu *et al.* 2003).

With an accurate estimate of the AIF in hand, the next problem is how to deconvolve the arterial concentration–time curve from the tissue concentration–time curve to estimate the local impulse response function. The difficulty in any deconvolution problem is that two different impulse response functions may produce similar output curves when convolved with the same input curve (an example is shown in Fig. 12.4.). This makes the deconvolution process very sensitive to noise in that a small change in the data leads to a radically different estimate of CBF. A number of approaches have been developed to try to deal with this problem (Østergaard 2004, 2005; Østergaard *et al.* 1996a, b).

The large body of literature that has focused on the problem of obtaining accurate estimates of CBF from dynamic contrast agent data suggests that this approach can be made to work, but deriving reliable routine measurements of CBF from the dynamics of an intravascular agent remains a challenging task. In particular, resolving ambiguities such as the one illustrated in Fig. 12.4 requires high SNR measurements and very accurate estimates of the local arterial input function. As our understanding of the shape of the impulse

response function in health and disease improves, our ability to estimate CBF from contrast agent data will improve.

## Other contrast agent methods

The foregoing description of contrast agent studies is shaped around a bolus injection of Gd-DTPA, and this is the standard approach. But a number of variations have also been developed. Gadolinium has a  $T_1$  effect in addition to the  $T_2^*$  or  $T_2$  effect, and potentially this can complicate the quantitative analysis of the dynamic data, particularly in tumor studies in which there may be some leakage of the agent out of the vasculature. Dysprosium agents have been used as an alternative to gadolinium agents because dysprosium creates a stronger  $T_2^*$  effect for the same dose but has no  $T_1$  effect (Lev *et al.* 1997; Villringer *et al.* 1988; Zaharchuk *et al.* 1998).

A limitation of Gd-DTPA studies is the short lifetime of the agent in the blood. Measurements of CBF with an intravascular agent are only possible when the agent is delivered as a sharp bolus, but simpler measurements of CBV could be done with an agent that remains in the blood for a longer time. If the agent exerts a susceptibility effect, then the signal difference before and after the administration of the agent would provide a direct measure of the local CBV. In contrast, with a dynamic injection, the tissue concentration must be integrated over time, requiring fast dynamic imaging – and the cost of fast imaging is reduced image resolution and SNR. For this reason, a blood pool agent that creates a  $T_2^*$  effect could be used for higher-resolution imaging of CBV.

The approach to the measurement of CBV with Gd-DTPA described above is based on the susceptibility effect of gadolinium, which alters local tissue  $T_2$  and  $T_2^*$ . However, gadolinium also decreases the  $T_1$  of blood, and so in a  $T_1$ -weighted image this will increase the blood signal. This is the basis for using a bolus of Gd-DTPA to enhance the signal of blood and improve MR angiography images. This can also serve as the basis for measuring CBV with  $T_1$ -weighted images (Lin *et al.* 1997, 1999; Moreno *et al.* 2007). Images are acquired before and several minutes after administration of Gd-DTPA, and the difference is interpreted as being the result of the altered signal of the blood from  $T_1$  shortening. To scale this difference image, the signal change in a voxel in the sagittal sinus is used to estimate the full effect in a voxel full of blood. However,  $T_1$ -based studies are potentially more sensitive to the effects of water exchange between blood and tissue because  $T_1$  relaxation is much slower than  $T_2$  relaxation (Donahue *et al.* 1997; Landis *et al.* 2000).

Another important class of contrast agents are based on superparamagnetic iron oxide crystals such as MION (Bjornerud and Johansson 2004; Majumdar *et al.* 1988; Weissleder *et al.* 1989, 1990). These particles are small (4–25 nm) and structurally similar to magnetite. The term *superparamagnetic* describes the fact that the magnetic properties of these crystals lie between paramagnetism and ferromagnetism. As described in Ch. 6, in paramagnetism individual magnetic moments tend to align with an externally applied magnetic field. However, this alignment results from just the independent interaction of each magnetic moment with the field; there is little interaction between the magnetic moments. In ferromagnetism, however, there is a strong interaction among the individual magnetic moments and so neighboring particles align together.

This ordering extends over a certain range of distance and defines a domain of magnetization. A large crystal contains a number of domains, each with a different local orientation of the magnetization. At the domain boundaries, there is a sharp change in the magnetization

orientation. When placed in a magnetic field, the domains aligned with the field grow at the expense of the other domains, producing a net magnetization that remains after the magnetic field is removed. Superparamagnetic crystals are sufficiently small that they only contain one domain and so do not display all the ferromagnetic properties of a larger crystal. Because of the iron spins, they become strongly magnetized in a magnetic field but do not retain the magnetization when the field is removed. Superparamagnetic iron agents produce strong  $T_2^*$  effects when confined to the vasculature, similar to gadolinium and dysprosium.

Most of the alternative blood pool agents already described are currently used only in animal studies (Forsting *et al.* 1994; Kent *et al.* 1990; Mandeville *et al.* 1996, 1998; Simonsen *et al.* 1999; Yacoub *et al.* 2006). If similar agents are approved for human studies, they will provide a potentially important alternative to BOLD techniques for activation studies.

## Clinical applications

Contrast agent techniques for assessing perfusion have become standard clinical tools and have been applied to the study of a variety of disease states, including stroke, vascular stenosis, arteriovenous malformation, cerebral neoplasm, and multiple sclerosis (Edelman *et al.* 1990; Provenzale *et al.* 2006; Wuerfel *et al.* 2007). In particular, MR contrast agent techniques have been used in many studies of ischemic disease and have helped to establish the current view of the evolution of stroke (Baird and Warach 1998; Guadagno *et al.* 2004; Hossmann and Hoehn-Berlage 1995; Kucharczyk *et al.* 1991; Muir *et al.* 2006). In embolic stroke, the blockage of an artery reduces flow to a region of brain. If flow is not restored, an infarction will develop. The current view of stroke is that there is often an ischemic core in which the flow is reduced to such a low level that cellular ionic levels cannot be maintained, leading over time to irreversible neuronal damage. However, surrounding this ischemic core is a region called the ischemic *penumbra*, characterized by reduced flow that is unable to supply sufficient metabolic energy to maintain electrical activity but is above the threshold for breakdown of cellular ionic gradients (Obrenovitch 1995). This tissue is at risk of infarction but potentially can be saved; consequently, it is the target for therapeutic intervention.

The central idea associated with the evaluation of stroke by MRI techniques is that the mismatch of diffusion and perfusion imaging identifies the penumbra. As noted in Ch. 8, a clinically important finding is that the apparent diffusion coefficient decreases quickly, before any change in the relaxation times, and the area of diffusion change is predictive of the area that is infarcted. Perfusion imaging with dynamic susceptibility contrast also shows a rapid fall, but over a larger region. The underlying idea is that the area with a perfusion fall but no change in diffusion is the penumbra, an affected area that has not yet progressed to an irreversible infarct and potentially could be saved with prompt therapy. The therapeutic window for acute stroke is the first few hours, before irreversible damage is done (Brott *et al.* 1992; Neumann-Haefelin and Steinmetz 2007). While this basic picture is probably too simple, the approach of combining diffusion and perfusion imaging is still the standard method for evaluating stroke (Guadagno *et al.* 2004; Moustafa and Baron 2007).

## References

- Axel L (1980) Cerebral blood flow determination by rapid-sequence computed tomography: a theoretical analysis. *Radiology* **137**: 679–686
- Baird AE, Warach S (1998) Magnetic resonance imaging of acute stroke. *J Cereb Blood Flow Metab.* **18**: 583–609

- Belliveau JW, Kennedy DN, McKinstry RC, *et al.* (1991) Functional mapping of the human visual cortex by magnetic resonance imaging. *Science* **254**: 716–719
- Bjornerud A, Johansson L (2004) The utility of superparamagnetic contrast agents in MRI: theoretical consideration and applications in the cardiovascular system. *NMR Biomed* **17**: 465–477
- Boxerman JL, Hamberg LM, Rosen BR, Weisskoff RM (1995) MR contrast due to intravascular magnetic susceptibility perturbations. *Magn Reson Med* **34**: 555–566
- Boxerman JL, Rosen BR, Weisskoff RM (1997) Signal-to-noise analysis of cerebral blood volume maps from dynamic NMR imaging studies. *J Magn Reson Imaging* **7**: 528–537
- Brott TG, Haley EC, Levy DE, *et al.* (1992) Urgent therapy for stroke I: pilot study of tissue plasminogen activator administered within 90 minutes. *Stroke* **23**: 632–640
- Buxton RB, Wechsler LR, Alpert NM, *et al.* (1984) The measurement of brain pH using  $^{11}\text{-CO}_2$  and positron emission tomography. *J Cereb Blood Flow Metab* **4**: 8–16
- Calamante F (2005) Bolus dispersion issues related to the quantification of perfusion MRI data. *J Magn Reson Imaging* **22**: 718–722
- Calamante F, Morup M, Hansen LK (2004) Defining a local arterial input function for perfusion MRI using independent component analysis. *Magn Reson Med* **52**: 789–797
- Calamante F, Willats L, Gadian DG, Connelly A (2006) Bolus delay and dispersion in perfusion MRI: implications for tissue predictor models in stroke. *Magn Reson Med* **55**: 1180–1185
- Donahue KM, Weisskoff RM, Burstein D (1997) Water diffusion and exchange as they influence contrast enhancement. *J Magn Reson Imaging* **7**: 102–110
- Duhamel G, Schlaug G, Alsop DC (2006) Measurement of arterial input functions for dynamic susceptibility contrast magnetic resonance imaging using echoplanar images: comparison of physical simulations with in vivo results. *Magn Reson Med* **55**: 514–523
- Edelman RR, Mattle HP, Atkinson DJ, *et al.* (1990) Cerebral blood flow: assessment with dynamic contrast-enhanced T2\*-weighted MR imaging at 1.5 T. *Radiology* **176**: 211–220
- Fisel CR, Ackerman JL, Buxton RB, *et al.* (1991) MR contrast due to microscopically heterogeneous magnetic susceptibility: numerical simulations and applications to cerebral physiology. *Magn Reson Med* **17**: 336–347
- Forsting M, Reith W, Dorfler A, *et al.* (1994) MRI in acute cerebral ischemia: perfusion imaging with superparamagnetic iron oxide in a rat model. *Neuroradiology* **36**: 23–26
- Gibbs JM, Wise RJ, Leenders KL, Jones T (1984) Evaluation of cerebral perfusion reserve in patients with carotid artery occlusion. *Lancet* **i**: 310–314
- Grubb RL, Raichle ME, Eichling JO, Ter-Pogossian MM (1974) The effects of changes in PaCO<sub>2</sub> on cerebral blood volume, blood flow, and vascular mean transit time. *Stroke* **5**: 630–639
- Guadagno JV, Donnan GA, Markus R, Gillard JH, Baron JC (2004) Imaging the ischaemic penumbra. *Curr Opin Neurol* **17**: 61–67
- Hossmann KA, Hoehn-Berlage M (1995) Diffusion and perfusion MR imaging of cerebral ischemia. *Cerebrovasc Brain Metab Rev* **7**: 187–217
- Kassissia IG, Goresky CA, Rose CP, *et al.* (1995) Tracer oxygen distribution is barrier-limited in the cerebral microcirculation. *Circ Res* **77**: 1201–1211
- Kennan RP, Zhong J, Gore JC (1994) Intravascular susceptibility contrast mechanisms in tissues. *Magn Reson Med* **31**: 9–21
- Kent T, Quast M, Kaplan B, *et al.* (1990) Assessment of a superparamagnetic iron oxide (AMI-25) as a brain contrast agent. *Magn Reson Med* **13**: 434–443
- Kjolby BF, Ostergaard L, Kiselev VG (2006) Theoretical model of intravascular paramagnetic tracers effect on tissue relaxation. *Magn Reson Med* **56**: 187–197
- Kluytmans M, van der Grond J, Viergever MA (1998) Gray matter and white matter perfusion imaging in patients with severe carotid artery lesions. *Radiology* **209**: 675–682
- Ko L, Salluzzi M, Frayne R, Smith M (2007) Reexamining the quantification of perfusion MRI data in the presence of bolus dispersion. *J Magn Reson Imaging* **25**: 639–643
- Kucharczyk J, Mintorovitch J, Asgari HS, Moseley M (1991) Diffusion/perfusion MR

- imaging of acute cerebral ischemia. *Magn Reson Med* **19**: 311–315
- Landis CS, Li X, Telang FW, *et al.* (2000) Determination of the MRI contrast agent concentration time course in vivo following bolus injection: effect of equilibrium transcytolemmal water exchange. *Magn Reson Med* **44**: 563–574
- Lassen NA (1984) Cerebral transit of an intravascular tracer may allow measurement of regional blood volume but not regional flow. *J Cereb Blood Flow Metab* **4**: 633–634
- Lassen NA, Perl W (1979) *Tracer Kinetic Methods in Medical Physiology*. New York: Raven Press
- Lauffer RB (1996) MR contrast agents: basic principles. In *Clinical Magnetic Resonance Imaging*, Edelman RR, Hesselink JR, Zlatkin MB, eds. Philadelphia, PA: WB Saunders, pp. 177–191
- Lev MH, Kulke SF, Sorensen AG, *et al.* (1997) Contrast-to-noise ratio in functional MRI of relative cerebral blood volume with sprodiamide injection. *J Magn Reson Imaging* **7**: 523–527
- Li X, Huang W, Yankeelov TE, *et al.* (2005) Shutter-speed analysis of contrast reagent bolus-tracking data: preliminary observations in benign and malignant breast disease. *Magn Reson Med* **53**: 724–729
- Lin W, Paczynski RP, Kuppusamy K, Hsu CY, Haacke EM (1997) Quantitative measurements of regional cerebral blood volume using MRI in rats: effects of arterial carbon dioxide tension and mannitol. *Magn Reson Med* **38**: 420–428
- Lin W, Celik A, Paczynski RP (1999) Regional cerebral blood volume: a comparison of the dynamic imaging and the steady state methods. *J Magn Reson Imaging* **9**: 44–52
- Majumdar S, Zoghbi SS, Gore JC (1988) Regional differences in rat brain displayed by fast MRI with superparamagnetic contrast agents. *Magn Reson Imaging* **6**: 611–615
- Mandeville JB, Marota J, Keltner JR, *et al.* (1996) CBV functional imaging in rat brain using iron oxide agent at steady state concentration. In *The Fourth Scientific Meeting of the International Society for Magnetic Resonance in Medicine*, New York, p. 292
- Mandeville JB, Marota JJA, Kosofsky BE, *et al.* (1998) Dynamic functional imaging of relative cerebral blood volume during rat forepaw stimulation. *Magn Reson Med* **39**: 615–624
- Meier P, Zierler KL (1954) On the theory of the indicator-dilution method for measurement of blood flow and volume. *J Appl Physiol* **6**: 731–744
- Moreno H, Wu WE, Lee T, *et al.* (2007) Imaging the Abeta-related neurotoxicity of Alzheimer disease. *Arch Neurol* **64**: 1467–1477
- Mouridsen K, Christensen S, Gyldensted L, Ostergaard L (2006) Automatic selection of arterial input function using cluster analysis. *Magn Reson Med* **55**: 524–531
- Moustafa RR, Baron JC (2007) Clinical review: Imaging in ischaemic stroke: implications for acute management. *Crit Care* **11**: 227
- Muir KW, Buchan A, von Kummer R, Rother J, Baron JC (2006) Imaging of acute stroke. *Lancet Neurol* **5**: 755–768
- Neumann-Haefelin T, Steinmetz H (2007) Time is brain: is MRI the clock? *Curr Opin Neurol* **20**: 410–416
- Obrenovitch TP (1995) The ischaemic penumbra: twenty years on. *Cerebrovasc Brain Metab Rev* **7**: 297–323
- Obrist WD, Thompson HK, King CH, Wang HS (1967) Determination of regional cerebral blood flow by inhalation of 133-xenon. *Circ Res* **20**: 124–135
- Ostergaard L (2004) Cerebral perfusion imaging by bolus tracking. *Top Magn Reson Imaging* **15**: 3–9
- Ostergaard L (2005) Principles of cerebral perfusion imaging by bolus tracking. *J Magn Reson Imaging* **22**: 710–717
- Ostergaard L, Sorensen AG, Kwong KK, *et al.* (1996a) High resolution measurement of cerebral blood flow using intravascular tracer bolus passages. Part II: experimental comparison and preliminary results. *Magn Reson Med* **36**: 726–736
- Ostergaard L, Weisskoff RM, Chesler DA, Gyldensted C, Rosen BR (1996b) High resolution measurement of cerebral blood flow using intravascular tracer bolus passages. Part I: mathematical approach and statistical analysis. *Magn Reson Med* **36**: 715–725
- Provenzale JM, Mukundan S, Barboriak DP (2006) Diffusion-weighted and perfusion MR imaging for brain tumor characterization and assessment of treatment response. *Radiology* **239**: 632–649

- Raichle ME (1983) Brain blood flow measured with intravenous  $H_2O-15$ : implementation and validation. *J Nucl Med* **24**: 790–798
- Rempp KA, Brix G, Wenz F, *et al.* (1994) Quantification of regional cerebral blood flow and volume with dynamic susceptibility contrast-enhanced MR imaging. *Radiology* **193**: 637–641
- Rosen BR, Belliveau JW, Chien D (1989) Perfusion imaging by nuclear magnetic resonance. *Magn Reson Quart* **5**: 263–281
- Rosen BR, Belliveau JW, Vevea JM, Brady TJ (1990) Perfusion imaging with NMR contrast agents. *Magn Reson Med* **14**: 249–265
- Rosen BR, Belliveau JW, Aronen HJ, *et al.* (1991) Susceptibility contrast imaging of cerebral blood volume: human experience. *Magn Reson Med* **22**: 293–299
- Simonsen CZ, Ostergaard L, Vestergaard-Poulsen P, *et al.* (1999) CBF and CBV measurements by USPIO bolus tracking: reproducibility and comparison with Gd-based values. *J Magn Reson Imaging* **9**: 342–347
- Sokoloff L, Reivich M, Kennedy C, *et al.* (1977) The [ $^{14}C$ ]deoxyglucose method for the measurement of local cerebral glucose utilization: theory, procedure, and normal values in the conscious and anesthetized albino rat. *J Neurochem* **28**: 897–916
- Villringer A, Rosen BR, Belliveau JW, *et al.* (1988) Dynamic imaging with lanthanide chelates in normal brain: contrast due to magnetic susceptibility effects. *Magn Reson Med* **6**: 164–174.
- Weisskoff RM, Chesler D, Boxerman JL, Rosen BR (1993) Pitfalls in MR measurements of tissue blood flow with intravascular tracers: which mean transit time? *Magn Reson Med* **29**: 553–559
- Weisskoff RM, Zuo CS, Boxerman JL, Rosen BR (1994) Microscopic susceptibility variation and transverse relaxation: theory and experiment. *Magn Reson Med* **31**: 601–610
- Weissleder R, Stark DD, Engelstad BL, *et al.* (1989) Superparamagnetic iron oxide: pharmacokinetics and toxicity. *Am J Roentgenol* **152**: 167–173
- Weissleder R, Elizondo G, Wittenberg J, *et al.* (1990) Ultrasmall paramagnetic iron oxide: characterization of a new class of contrast agents for MR imaging. *Radiology* **175**: 489–493
- Wu O, Ostergaard L, Koroshetz WJ, *et al.* (2003) Effects of tracer arrival time on flow estimates in MR perfusion-weighted imaging. *Magn Reson Med* **50**: 856–864
- Wuerfel J, Paul F, Zipp F (2007) Cerebral blood perfusion changes in multiple sclerosis. *J Neurol Sci* **259**: 16–20
- Yablonsky DA, Haacke EM (1994) Theory of NMR signal behavior in magnetically inhomogenous tissues: the static dephasing regime. *Magn Reson Med* **32**: 749–763
- Yacoub E, Ugurbil K, Harel N (2006) The spatial dependence of the poststimulus undershoot as revealed by high-resolution BOLD- and CBV-weighted fMRI. *J Cereb Blood Flow Metab* **26**: 634–644
- Yankeelov TE, Rooney WD, Li X, Springer CS, Jr. (2003) Variation of the relaxographic “shutter-speed” for transcytolemmal water exchange affects the CR bolus-tracking curve shape. *Magn Reson Med* **50**: 1151–1169
- Yankeelov TE, Rooney WD, Huang W, *et al.* (2005) Evidence for shutter-speed variation in CR bolus-tracking studies of human pathology. *NMR Biomed* **18**: 173–185
- Zaharchuk G, Bogdanov AA, Marota JJA, *et al.* (1998) Continuous assessment of perfusion by tagging including volume and water extraction (CAPTIVE): a steady-state contrast agent technique for measuring blood flow, relative blood volume fraction, and the water extraction fraction. *Magn Reson Med* **40**: 666–678
- Zierler KL (1962) Theoretical basis of indicator-dilution methods for measuring flow and volume. *Circ Res* **10**: 393–407



# Arterial spin labeling techniques

<b>Introduction</b>	<i>page</i> 307
<b>Arterial spin labeling</b>	308
The basic experiment	308
Continuous arterial spin labeling	313
Pulsed arterial spin labeling	315
The importance of creating a well-defined arterial bolus	318
<b>Quantitative cerebral blood flow measurements</b>	320
Sources of systematic errors	320
Controlling for transit delay effects	322
Relaxation effects	326
Absolute cerebral blood flow calibration	328
<b>Current issues</b>	329
Tagged water in arteries	329
The arterial input function	330
Recent innovations	330
<b>Applications in fMRI</b>	332
Activation studies with arterial spin labeling	332
Simultaneous cerebral blood flow and O <sub>2</sub> imaging	333
The calibrated-BOLD method	334

## Introduction

Bolus tracking studies with intravascular contrast agents provide a robust measurement of blood volume, but as discussed in [Ch. 12](#) a measurement of cerebral blood flow (CBF) is more difficult. The kinetic curve of an intravascular contrast agent is more sensitive to decreases in CBF than increases, making these techniques a useful tool for clinical studies of ischemia but less useful for measurements of CBF changes with activation in the healthy brain. In recent years, a different class of techniques for measuring local tissue perfusion with MRI has been developed based on arterial spin labeling (ASL) (Detre *et al.* 1992).

Arterial spin labeling techniques provide non-invasive images of local CBF with better spatial and temporal resolution than any other technique, including nuclear medicine methods. The development of ASL techniques is an active area of research, and although they are not yet widely available on standard MR imagers, ASL applications are steadily growing. The standard technique for mapping patterns of activation in the healthy brain is still blood oxygenation level dependent (BOLD) imaging, but questions remain about the accuracy of localization of BOLD changes and the quantitative interpretation of the magnitude of BOLD signal changes (see Part IIIB). Techniques using ASL have already become standard tools for investigations of the mechanisms underlying the BOLD effect, and the

applications of ASL to basic activation studies are continuing to expand. One limitation of the BOLD technique is that it is sensitive only to changes in perfusion associated with a particular task and insensitive to chronic alterations of perfusion. Because ASL provides a direct measurement of CBF, methods based on ASL are likely to find wider clinical applications in studies of disease progression, in the evaluation of pharmacological treatments, and in routine diagnosis of diseases marked by altered CBF (Alsop *et al.* 2000; Brown *et al.* 2007; Wolf and Detre 2007).

For fMRI studies, ASL methods provide several advantages over BOLD methods (Liu and Brown 2007). They measure a well-defined physiological parameter, CBF, and provide measurements of both the chronic baseline value as well as acute changes with activation. The nature of the ASL method requires a running subtraction of two images, and this provides a great deal of stability against slow signal drifts, making possible experiments with long stimuli. These methods can make use of imaging techniques with reduced sensitivity to magnetic susceptibility effects, and thus improve over the distortion and signal dropout effects that occur with BOLD imaging. Finally, because ASL measures the delivery of arterial blood, the signal is better localized to the capillary beds than with BOLD imaging, because the BOLD signal arises more from venous oxygenation changes.

However, there are some significant disadvantages of ASL compared with BOLD imaging. The intrinsic signal to noise ratio (SNR) of ASL is worse than with BOLD imaging, so sensitivity to weak activations is better with BOLD imaging. Technical requirements of ASL make the temporal resolution poorer and the number of slices that can be measured is reduced compared with BOLD imaging. For these reasons, ASL methods are not likely to replace BOLD methods. Instead, a promising approach is to use ASL methods in conjunction with BOLD methods. This provides a richer context for interpreting the observed BOLD response, particularly in disease states (Fleisher *et al.* 2008). In addition, the combination of ASL and BOLD imaging makes possible a calibrated-BOLD technique (Davis *et al.* 1998), which provides measurements of the change in the cerebral metabolic rate of O<sub>2</sub> (CMRO<sub>2</sub>) with activation (discussed in Part IIIB).

## Arterial spin labeling

### The basic experiment

The principle behind ASL techniques is relatively simple (Fig. 13.1). The goal is to measure CBF, the rate of delivery of arterial blood to a local brain voxel in an imaged slice of interest. Before acquiring the image, a 180° radiofrequency (RF) inversion pulse is applied to flip the magnetization of the water in arterial blood before the blood reaches the image slice. The water molecules carrying the labeled magnetization flow into each tissue element in proportion to the local CBF. After a sufficient delay, the inversion time (TI) to allow the tagged blood to reach the slice of interest, the *tag* image is made. The experiment is then repeated without labeling the arterial blood to create a *control* image, and the two images are subtracted to produce the ASL difference image. If the tag and control images are carefully done, the signal from static spins subtracts out in the difference image, leaving just the signal difference of arterial blood. The blood signal does not subtract out, because the arterial blood signal was fully relaxed in the control image, but inverted in the tag image, and the resulting ASL difference image signal is directly proportional to how much arterial blood was delivered during the interval TI.

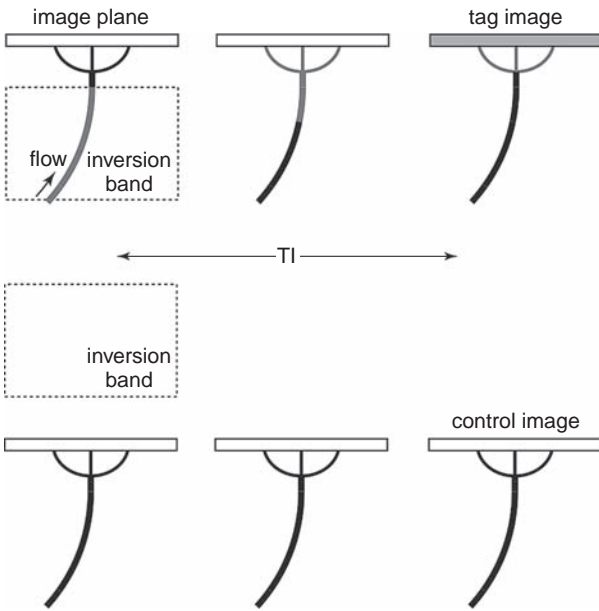


**Fig. 13.1.** Arterial spin labeling (ASL). The basic principle of ASL is to acquire two images of a slice through the brain, a *tag* image following inversion of the magnetization of arterial blood and a *control* image in which the magnetization of arterial blood is not inverted. The illustration shows one implementation of this idea in which a  $180^\circ$  inversion pulse is applied to a band below the image plane, and after a delay TI (the inversion time) to allow the tagged arterial blood (shown as a gray vessel) to be delivered to the slice, the tag image is acquired. For the control image (bottom row), the inversion pulse is applied above the slice so that blood is not tagged (but off-resonance effects on the static spins in the image plane are balanced), and the control image is also collected after a delay TI. If the control experiment is carefully designed, the static tissue subtracts out from the ASL difference signal (control – tag) leaving a direct image of the amount of arterial blood delivered to each voxel of the slice in the time interval TI.

This is the basic idea behind all ASL techniques. In the context of tracer kinetics, the “agent” used here is labeled water, a diffusible tracer, and these ASL techniques closely parallel positron emission tomography (PET) techniques using  $\text{H}_2^{15}\text{O}$  (Frackowiak *et al.* 1980; Raichle 1983). In fact, we can think of the ASL difference signal as a measurement of a tagged bolus of arterial blood that has been delivered to the tissue (Buxton *et al.* 1998a). However, there are two important differences between ASL and PET. First, because there is little time during TI for tagged blood to move all the way through the vasculature and exit on the venous side, the experiment is really closer to a microsphere experiment than a diffusible tracer study with PET (discussed further in Box 13.1) (Buxton 2005). Second, while PET requires an injection of the appropriate agent, in ASL the water is labeled magnetically and non-invasively, and the ASL experiment can be repeated many times to improve the SNR or to follow the dynamics of CBF change with activation.

To understand the ASL experiment more quantitatively, we can expand on the comparison of ASL to the gold standard for measuring CBF, a *microsphere* study (see Ch. 2 and Box 12.1). Labeled microspheres are injected into an artery, creating an arterial concentration of the agent  $C_A(t)$ . When the microspheres reach the capillary bed they stick, because they are too large to fit through the capillaries. If we wait long enough for all of the arterial bolus to be delivered, the number of microspheres trapped in the tissue will be directly proportional to  $f$ , the local CBF. The constant of proportionality relating the microsphere content of tissue to  $f$  is the area under the arterial input curve ( $A$ , i.e., the integral of  $C_A(t)$ ). In analogy with a microsphere study, we can define the ASL signal difference ( $\Delta S$ ) as

$$\Delta S = A_{\text{eff}} f \quad (13.1)$$

The term  $A_{\text{eff}}$  plays the role of the effective area under the arterial bolus in the ASL experiment, analogous to the microsphere experiment.

We can think of  $A_{\text{eff}}$  as a calibration factor that converts the local flow into a measured magnetization difference. This is a key factor, and much of the discussion of this chapter will focus on trying to understand what  $A_{\text{eff}}$  is in practice. But we can already see that it plays several important roles. The first is that  $A_{\text{eff}}$  controls the SNR of the experiment; for a larger  $A_{\text{eff}}$ , the same local flow will produce a larger ASL signal difference. The second critical aspect is that the extent to which the ASL signal reflects *only* local flow is described by the sensitivity of  $A_{\text{eff}}$  to other factors, such as transit delays from the tagging region to the image plane and relaxation times. Ideally,  $A_{\text{eff}}$  would only depend on global factors and so it would be the same for all voxels. Then even if  $A_{\text{eff}}$  is not known precisely, a map of the ASL difference signal would still be a quantitative reflection of the local CBF, lacking only the global scaling factor to convert image difference measurements into appropriate units for CBF. Finally, in order to convert the ASL signal into a measure of CBF in absolute units (e.g., milliliters of blood per milliliter of tissue per minute), we must know what  $A_{\text{eff}}$  is for the particular ASL experiment.

As a simple example of  $A_{\text{eff}}$ , consider the ideal case in which there is no relaxation and no transit delay effect. Defining the intrinsic magnetization of fully relaxed arterial blood as  $M_{0A}$ , in the ideal case the delivered arterial blood carries a magnetization  $M_{0A}$  in the control image and  $-M_{0A}$  in the tag image because of the inversion. Furthermore, the amount of blood delivered during the interval TI is  $f$ TI. Then for the ideal case, the signal in the ASL difference image results from a change in net magnetization  $\Delta M = 2M_{0A} f$ TI, so  $A_{\text{eff}} = 2M_{0A} f$ TI. For a CBF of 60 mL/min per 100 mL of tissue ( $= 0.01 \text{ s}^{-1}$ ) and a typical experiment time of TI = 1 s,  $\Delta M$  is on the order of 1% of  $M_{0A}$ , so the ASL difference signal is small compared with the raw image signal. Nevertheless, the signal intensity in the ASL difference image is directly proportional to local CBF, and with sufficient averaging CBF can be mapped reliably.

This simple example illustrates the basic components of  $A_{\text{eff}}$ . There must be a measure of equilibrium magnetization in scanner intensity units and a time constant, because these components are necessary to balance the dimensions in Eq. (13.1). Although the basic idea behind ASL is simple, the implementation of this idea requires careful attention to the details of the experimental design and to a number of confounding factors, which must be taken into account for the measurement to be a quantitative reflection of CBF. The various ASL techniques differ in how the tagging is done, how the control image is acquired, and how potential systematic errors are handled. The form of  $A_{\text{eff}}$  under these more general conditions is developed in Box 13.1. One advantage in thinking about  $A_{\text{eff}}$  is that it can be interpreted as an appropriately scaled area under the arterial bolus, and so can be visualized easily. We will use this approach throughout the chapter to illustrate how different factors affect the quantification of ASL measurements of CBF through their effect on  $A_{\text{eff}}$ .

Historically, two basic approaches to ASL perfusion imaging have been developed, which can be classified as pulsed ASL (PASL) and continuous ASL (CASL). However, both of the original approaches suffer from similar systematic errors caused by physiological factors other than CBF that affect the measurement, in particular the transit delay from the tagging region to the slice. For quantitative perfusion measurements, these techniques have been modified to deal with this problem, and with these changes the two approaches are, in fact, converging. For now, it is helpful to understand the original approaches.

**Box 13.1. Modeling the arterial spin labeling experiment**

To extract a quantitative measurement of perfusion from ASL data, a detailed model of the process combining kinetics and relaxation is needed. Detre and co-workers (1992) introduced a modeling approach based on combining single-compartment kinetics with the Bloch equations, and this approach was extended to the FAIR experiment by Kim (1995) and Kwong and co-workers (1992, 1995). In this approach, the Bloch equation for the longitudinal magnetization is modified to include delivery and clearance terms proportional to the local flow  $f$ :

$$\frac{dM(t)}{dt} = \frac{M_0 - M(t)}{T_1} + f M_A(t) - \frac{f}{\lambda} M(t) \quad (\text{B13.1})$$

where  $M_0$  is the equilibrium longitudinal magnetization of tissue,  $\lambda$  is the partition coefficient (or volume of distribution) for water, and  $M$  and  $M_A$  are the time-dependent longitudinal magnetizations of tissue and arterial blood, respectively. The flow-dependent parts of this equation are similar to compartmental models used in tracer kinetics studies (Box 12.1), and the implicit assumption is that water distribution in the brain can be treated as a single well-mixed compartment.

Equation (B13.1) has served as the basis for most of the early quantitative analyses of ASL. However, this equation is based on a restrictive premise, that labeled water delivered to the brain immediately mixes with the large pool of tissue water. This is the standard assumption used in PET studies with  $\text{H}_2^{15}\text{O}$ , so it seems plausible to apply the same model to ASL studies since both deal with labeled water. However, PET studies follow the kinetics of labeled water over a time period on the order of 1 min, while for ASL the kinetics over 1 s are important for the analysis. For example, a critical problem with quantitative ASL experiments is the transit delay of several hundred milliseconds from the tagging region to the image plane. Such small time intervals are negligible in a PET experiment but are the primary source of systematic errors in ASL. Other potential systematic errors in ASL include effects of capillary-tissue exchange of water on the relaxation of the tag and the effects of incomplete water extraction from the capillary bed.

A more general treatment is possible based on the kinetic model described in Box 12.1 (Buxton *et al.* 1998a) and we will use this approach here for describing both the pulsed and the continuous labeling techniques. With appropriate assumptions, this general model reproduces the earlier modeling work but is flexible enough to include the systematic effects described above. The first question in applying the general kinetic model developed in Box 12.1 to ASL is what precisely corresponds to agent concentration in the ASL experiment.

Assuming that the control experiment is well designed, the magnetization difference  $\Delta M(t)$  (control-tag) measured with ASL can be considered to be a quantity of magnetization that is carried into the voxel by arterial blood. That is, we treat  $\Delta M$  as a concentration of a tracer that is delivered by flow and then apply tracer kinetics principles as in Box 12.1. The amount of this magnetization in the tissue at a time  $t$  will depend on the history of delivery of magnetization by arterial flow and clearance by venous flow and longitudinal relaxation. These physical processes can be described by defining three functions of time: (1) the delivery function  $c(t)$  is the normalized arterial concentration of magnetization arriving at the voxel at time  $t$ ; (2) the residue function  $r(t)$  is the fraction of tagged water molecules that remain at a time  $t$  after their arrival; and (3) the magnetization relaxation function  $m(t)$  is the fraction of the original longitudinal magnetization tag carried by the water molecules that remains at a time  $t$  after their arrival in the voxel.

The arterial input function  $c(t)$  is defined to be equal to one if the blood arrives fully inverted in the tag experiment and fully relaxed in the control experiment. It will then be zero until tagged blood begins to arrive, greater than zero for the duration  $T$  of the bolus, and then return to zero again after the end of the bolus. The duration of the bolus  $T$  is a key parameter, and as we will see one goal in correcting for systematic errors is to control the value of  $T$ . In the CASL experiment  $T$  is the duration of the RF tagging pulse. But in the classical PASL techniques,  $T$  is poorly defined, and the QUIPSS II method was designed to create a well-defined bolus duration  $T$  (see the discussion in the main text).

As an example of how these functions are constructed, if there is no transit delay between the tagging region and the image plane, then  $c(t) = \exp[-t/T_{1A}]$  for pulsed ASL, where  $T_{1A}$  is the longitudinal relaxation time of arterial blood. That is,  $c(t)$  is reduced from one because as time goes on the magnetization of the arriving blood in the tag experiment is partly relaxed. If the clearance of water from the tissue follows single-compartment kinetics,  $r(t)$  is a single exponential. And if the labeled water immediately exchanges into the tissue space so that further decay occurs with the time constant  $T_1$  of the tissue space,  $m(t)$  is a decaying exponential with time constant  $T_1$ .

With these definitions,  $\Delta M(t)$  can be constructed as a sum over the past history of delivery of magnetization to the tissue weighted with the fraction of that magnetization which remains in the voxel. Following the inversion pulse, the arterial magnetization difference is  $2M_{0A}$ , where  $M_{0A}$  is the equilibrium magnetization of arterial blood. The amount delivered to a particular voxel between  $t'$  and  $t' + dt'$  is  $2M_{0A} f c(t') dt'$  where  $f$  is the cerebral blood flow (expressed in units of milliliters of blood per milliliter of voxel volume per second). The fraction of the magnetization that remains at time  $t$  is  $r(t-t') m(t-t')$ . Then, as in Box 12.1, we simply add up the contributions to  $\Delta M(t)$  over the full course of the experiment:

$$\begin{aligned} \Delta M(t) &= 2M_{0A} f \int_0^t c(t') r(t-t') m(t-t') dt' \\ &= 2M_{0A} f c(t) * [r(t) m(t)] \\ &= f A_{\text{eff}} \end{aligned} \tag{B13.2}$$

where  $*$  denotes convolution as defined in Eq. (B13.2). In the final line of Eq. (B13.2), all the complexities of the kinetics have been combined into the term  $A_{\text{eff}}$ . Physically, this term is the effective area of the arterial bolus. For example, if the delivered magnetization behaved like microspheres so that whatever is delivered to the voxel never leaves and never decays away, then  $A_{\text{eff}}$  is simply the integral of the arterial curve. For this ideal case  $r(t) = m(t) = 1$ , and the convolution in Eq. (B13.2) reduces to the integral of  $c(t)$ .

To understand the potential systematic errors in ASL experiments with Eq. (B13.2), we must first choose appropriate forms for the three functions  $c(t)$ ,  $r(t)$ , and  $m(t)$ . Two effects that we want to include are a transit delay  $\Delta t$  from the tagging region to the image slice and a delay  $T_{\text{ex}}$  after the labeled water arrives in the voxel before it exchanges into the extravascular space. The transit delay describes the fact that the tagged spins require some time to travel from the tagging region to the image plane. When the tagged spins enter the voxel, they must continue down the vascular tree until they reach the capillary bed before they can exchange into the tissue. While they are still in blood, they relax with the longitudinal relaxation time of blood,  $T_{1A}$ , and after exchange they relax with  $T_1$ , the tissue relaxation time. This is modeled in a very simple way by assuming that the spins leave the capillary and enter the tissue space at a time  $T_{\text{ex}}$  after they were inverted. The mathematical forms of the functions that describe these processes are

$$\begin{aligned}
 c(t) &= \begin{cases} 0 & 0 < t < \Delta t \\ \alpha e^{-t/T_{1A}} \quad (\text{PASL}) & \Delta t < t < \Delta t + T \\ \alpha e^{-\Delta t/T_{1A}} \quad (\text{CASL}) & \Delta t < t < \Delta t + T \\ 0 & \Delta t + T < t \end{cases} \\
 r(t) &= e^{-f t/\lambda} \\
 m(t) &= \begin{cases} e^{-t/T_{1A}} & t < T_{\text{ex}} \\ e^{-T_{\text{ex}}/T_{1A}} e^{-(t-T_{\text{ex}})/T_{1A}} & t > T_{\text{ex}} \end{cases}
 \end{aligned} \tag{B13.3}$$

where  $T$  is the duration of the tagged bolus,  $\Delta t$  is the transit delay from the tagging region to the image voxel,  $T_{\text{ex}}$  is the delay after the labeled water arrives in the voxel before it exchanges into the extravascular pool,  $T_{1A}$  is the longitudinal relaxation time of water in blood, and  $T_1$  is the relaxation time of water in the extravascular space.

For completeness, the expression for  $c(t)$  includes a factor  $\alpha$  that describes the inversion efficiency of the experiment (Alsop and Detre 1996; Zhang *et al.* 1993). Specifically,  $\alpha$  is the achieved fraction of the maximum possible change in longitudinal relaxation between the tag and control experiments. This describes the fact that the  $180^\circ$  inversion may not be complete (i.e., less than  $180^\circ$ ) or that the longitudinal magnetization in the control image may not be fully relaxed. For PASL experiments,  $\alpha$  is usually very close to one, but for CASL experiments this can be an important correction. Figure 13.7 shows example kinetic curves of  $\Delta M(t)$  based on Eq. (B13.3).

With these model functions, we can now examine how  $A_{\text{eff}}$  depends on different confounding factors. We will use the notation TI for the time of the measurement in analogy with an inversion recovery experiment, even though the way we interpret the data is in terms of delivery and decay of the tag. The kinetic curves shown in Fig. 13.7 are essentially plots of how  $A_{\text{eff}}$  varies with the inversion time TI. We can further illustrate how various factors influence  $A_{\text{eff}}$  by defining a function  $a(t)$  as the contribution of magnetization that entered the voxel at time  $t$  to the final net magnetization difference measured at TI. From Eq. (B13.2), this function is

$$a(t) = 2 M_{0A} c(t) r(\text{TI} - t) m(\text{TI} - t) \tag{B13.4}$$

and the integral of  $a(t)$  is  $A_{\text{eff}}$ . By plotting  $a(t)$  for each time  $t$  between the beginning of the experiment ( $t=0$ ) and the measurement time ( $t=\text{TI}$ ), we can visualize  $A_{\text{eff}}$  directly as the area under the curve. The area  $A_{\text{eff}}$  is our primary interest because this is what affects quantitative measurements of CBF, but it is often helpful to see in detail how a particular systematic error affects the contribution of spins entering at different times to the final measured signal.

## Continuous arterial spin labeling

The original demonstrations of ASL were based on CASL (Detre *et al.* 1992; Williams *et al.* 1992). In this approach, the magnetization of arterial blood is continuously inverted in the neck using a continuous RF pulse (Fig. 13.2). This technique of *adiabatic inversion* of flowing blood was originally introduced as a blood labeling technique for MR angiography applications (Dixon 1984). The essential idea of adiabatic inversion is that the effective RF field in the rotating frame is slowly swept from off-resonance to on-resonance and back to off-resonance again (Ch. 6). When the effective field reaches resonance, the magnetization begins to follow it and so can be cleanly inverted. In imaging applications, long adiabatic inversion pulses (e.g., 20–30 ms in length) are used to produce sharp slice profiles by varying the RF during the pulse. But in adiabatic inversion of flowing blood, the motion of the blood itself produces

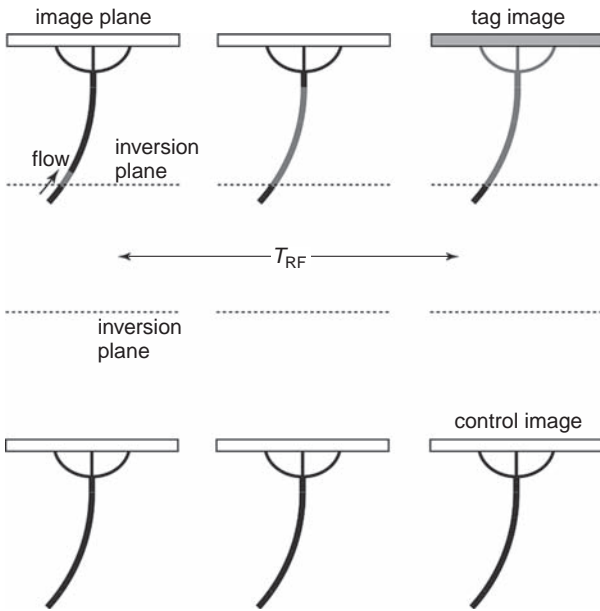


**Fig. 13.2.** Continuous arterial spin labeling. In the original arterial spin labeling technique, the magnetization of arterial blood is inverted continuously while a radiofrequency (RF) pulse is applied in the presence of a magnetic field gradient along the flow direction. As the blood passes through the location where the RF pulse is on-resonance (the inversion plane), the magnetization is inverted. A continuous stream of tagged arterial blood is created as long as the RF field is applied ( $T_{RF}$ ), typically 3–4 s. For the control image (bottom row) the same RF is applied with the inversion plane symmetrically placed above the slice, so no arterial blood is tagged.

a sweep of the effective field while the RF is constant. While the RF is on, a constant field gradient is applied in the flow direction. Then as the blood flows along the gradient axis, the local resonant frequency changes, causing the effective field to sweep through resonance and invert the magnetization of the blood.

The inversion of the magnetization of the arterial blood occurs over a small spatial region located at the position along the gradient axis where the RF pulse is on-resonance. That is, we can think of the combination of the RF and the gradient field as defining an inversion plane. As flowing blood crosses this plane, its magnetization is inverted. For example, for brain imaging, the tagging plane is a transverse plane cutting through the major arteries at the base of the brain. This process of adiabatic inversion of flowing blood creates a continuous stream of tagged blood originating at the inversion plane for as long as the RF pulse is turned on (Fig. 13.2). For a CASL experiment, the duration of the RF pulse is typically several seconds (Alsop and Detre 1996). This creates an arterial bolus of tagged blood with a duration equal to the duration of the RF pulse. After the end of the RF pulse, the tag image is acquired.

In all ASL experiments, the way the control image is acquired is a critical factor that affects the quantitative accuracy of the CBF measurement. Because the ASL signal difference (control – tag) that carries the CBF information is only around 1% of the control image intensity, a systematic error of 1% in the control image would produce a 100% error in the CBF measurement. The control experiment must satisfy two conditions: (1) the arterial blood is not tagged, so that it enters the tissue fully relaxed; and (2) the static spins within the image slice should generate precisely the same signal as they did in the tag image, so that a subtraction (control – tag) leaves nothing but the difference signal of the spins delivered by arterial flow.

The long RF pulse in the tag part of the CASL experiment is off-resonance for the slice of interest and so ideally should have no effect on the image slice. However, as discussed in Ch. 6, off-resonance pulses can produce a slight tipping of the magnetization directly, and through magnetization transfer effects the magnetization in the image slice can be affected



even more strongly (McLaughlin *et al.* 1997; Pekar *et al.* 1996; Zhang *et al.* 1992). These off-resonance effects of the RF pulse alter the longitudinal magnetization of the static spins in the image independently of any flow effect, so the control experiment must reproduce these effects as closely as possible. A typical control image in early CASL applications was acquired by applying a similar long RF pulse but with the frequency of the RF or the sign of the gradient switched so that blood entering from above the slice would be tagged rather than arterial blood entering from below. In this way, the off-resonance effects on the slice are approximately balanced, and because the inversion plane for the control image is often outside the head, nothing is tagged.

One problem with this scheme for the control pulse is that only one image plane is properly controlled. That is, to control for magnetization transfer effects, the control RF pulse must be off-resonance by the same amount as the tagging RF pulse, so the inversion planes of the two RF pulses must be symmetrically placed around the image slice. For multislice acquisitions, there will be systematic errors for all but the center slice. In practice, several other factors also need to be taken into account to make a quantitative measurement of CBF. For example, the tagged magnetization decays during the experiment, and a correction must be made for spatial variations in  $T_1$ . Other confounding factors include incomplete inversion of the arterial blood, relaxation during the transit from the inversion region to the slice, and signal contributions from large vessels. Several methods have been developed to deal with these problems and are discussed below. When these effects are taken into account, CASL provides a quantitative measurement of local perfusion.

## Pulsed arterial spin labeling

The basic description of ASL at the beginning of the chapter was essentially an ideal version of PASL (Fig. 13.1). Instead of a continuous RF pulse to invert blood as it flows through the inversion plane, a single  $180^\circ$  RF pulse is applied as a spatially selective pulse that tips over all spins in a thick band below the slice of interest. After a delay to allow the tagged blood to flow into the slice, the tag image is acquired. As with CASL, collecting a high-quality control image is critical for the accuracy of ASL. As noted previously, the goal is to acquire a control image in which arterial blood is not inverted but the signal from static spins in the slice is precisely the same as it was in the tagged image. Minimizing effects of the tagging on the image plane is the difficult part of this goal. For example, a slice-selective inversion slab, even when constructed to have as rectangular a profile as possible, will nevertheless have small wings that can extend into the imaging slice.

In EPISTAR (echo planar imaging and signal targeting with alternating radiofrequency), an early version of PASL, the tagging band is typically 10 cm thick with a gap of 1 cm between the edge of the band and the edge of the imaged slice (Edelman *et al.* 1994; Fig. 13.3). The control image is acquired with the same strategy used in CASL. An identical inversion pulse is applied on the other side of the imaging slice, inverting a band of spins above the image slice. Ideally the control pulse does not tag any arterial blood that will flow into the image slice but produces effects on the static spins through the wings of the slice profile that are similar to the off-resonance effects of the tagging pulse. In a CASL experiment, the tag and control RF inversion planes typically are several centimeters from the image plane, so the control plane may even be outside the head. However, with EPISTAR, the near edges of the tagging band and the control band are only approximately 1 cm from the edge of the image slice. An artifact that can result from this scheme is that venous blood entering from above

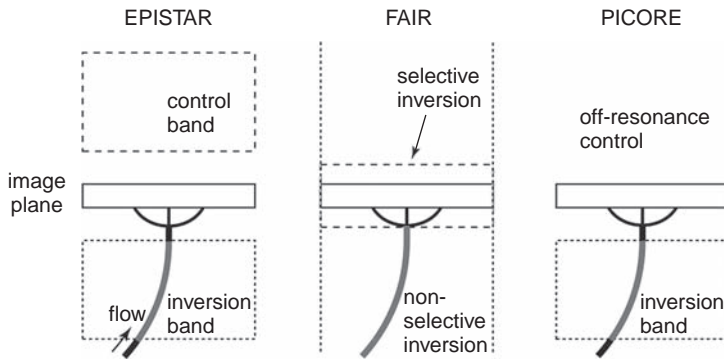


**Fig. 13.3.** Pulsed arterial spin labeling (PASL). Arterial magnetization is inverted all at once, and three variations of PASL are shown (see text for details). In EPISTAR, the tag is created with a spatially selective inversion slab below the image plane, and the control is the same inversion slab applied above the slice. In FAIR, the tag is created with a non-selective inversion that inverts everything within the RF coil, and the control is a selective inversion on the image plane. In PICORE, the tag is done as in EPISTAR, but the control is the same radiofrequency pulse applied off-resonance to the slice and with no gradient on, so nothing is inverted. All these schemes ideally invert the arterial magnetization for the tag image and leave it fully relaxed for the control image.

will actually be tagged by the control pulse and so will appear as focal dark spots in the subtraction image (Fig. 13.4).

In FAIR (flow-sensitive alternating inversion recovery), the tag image is acquired with a non-selective inversion pulse, and the control image is acquired with a slice-selective inversion pulse centered on the image slice (Kim 1995). If the two types of inversion pulse are carefully designed to have the same effect on the static spins in the image slice, then the entering arterial blood is inverted with the non-selective RF pulse but fully relaxed with the selective RF pulse. The static spins in the image slice are identically inverted (ideally) in both experiments, so their signal subtracts out.

As with all ASL experiments, the quality of the control experiment is critical. The difficulty in performing a FAIR experiment is to ensure that the slice-selective inversion produces a clean  $180^\circ$  pulse over the entire thickness of the imaged slice that matches the non-selective inversion. Because the slice profile is not perfectly rectangular, the spatial width of the selective inversion pulse is typically twice the width of the imaged slice so that the width of the image plane falls under the uniform center of the selective inversion (Kim 1995). Improvements in the design of slice-selective pulses may help to alleviate this problem, moving the technique closer to the ideal experiment of perfectly matched selective and non-selective inversions over the imaged slice. However, it is likely that the selective inversion will always have to be larger than the imaged slice thickness.

In comparison with the EPISTAR technique, instead of a tagging band with a set width, FAIR attempts to invert all spins outside the image plane with the non-selective inversion pulse. In practice, of course, there is a limit to the spatial extent of an RF pulse set by the size of the coil even if no field gradients are applied. One can think of the FAIR experiment as making the tagging band as large as the RF coil will allow in order to tip over the maximum number of arterial spins. Also, with this scheme, blood entering from either side of the slice is tagged, and so this technique is likely to be more robust when the imaging slice is fed by arterial flow from both directions. Here, however, artifacts from tagged veins will appear bright, rather than dark as in EPISTAR (Fig. 13.4).

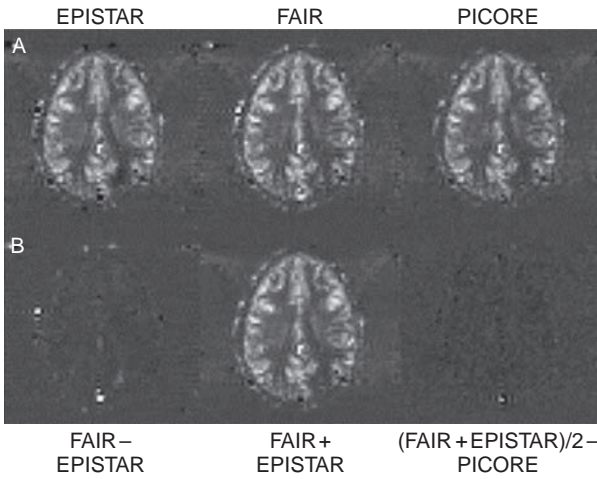


**Fig. 13.4.** Venous artifacts with pulsed arterial spin label (PASL) techniques. (A) One artifact in PASL is that venous blood entering from above the slice appears negative because it is inverted by the control pulse in EPISTAR and appears positive because it is inverted by the non-selective tagging pulse in FAIR. In PICORE, nothing above the slice is tagged. (B) This is illustrated by subtracting the EPISTAR image from the FAIR image so that all spins entering from above the slice appear bright. The PICORE image is essentially identical to the average of the EPISTAR and FAIR images. Techniques are described in the text. (Data courtesy of E. Wong.)

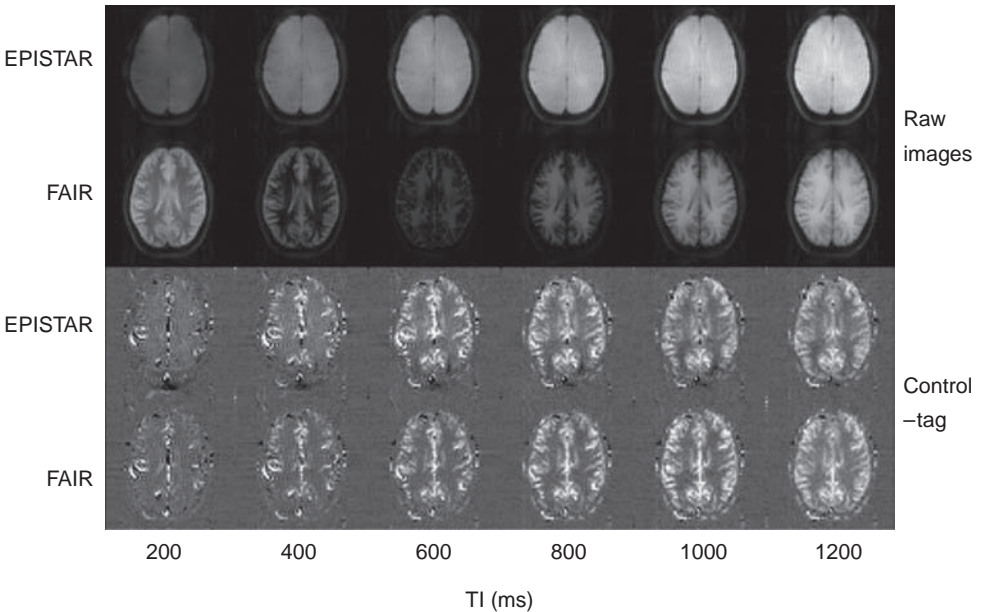


**Fig. 13.5.** The arterial spin labeling (ASL) difference signal is independent of the raw image contrast. Image series for a range of inversion times (TI) are shown for EPISTAR and FAIR to demonstrate that the cerebral blood flow information is carried in the ASL difference image (control - tag). Despite the very different intrinsic contrast in EPISTAR and FAIR, the difference images are quite similar. Techniques are described in the text. (Data courtesy of E. Wong.)

A third technique, PICORE (proximal inversion with a control for off-resonance effects), uses a tag similar to that of EPISTAR (Wong *et al.* 1997). For the control image, the same RF inversion pulse is applied as in the tag image with two exceptions: no field gradients are turned on and the frequency of the RF pulse is shifted so that the image plane experiences the same off-resonance RF pulse in both tag and control images. Because there are no gradients applied, the RF pulse is off-resonance for all spins, so nothing is inverted. This technique has

the advantage that venous blood entering from the superior side of the image plane is not tagged, in contrast to EPISTAR and FAIR (Fig. 13.4).

It is important to note that, in these PASL experiments, the flow information is carried in the difference signal (control – tag) and not in the intrinsic tissue signal. For this reason, the raw images may have quite different intrinsic contrast, as in the EPISTAR and FAIR images shown in Fig. 13.5, but the ASL difference images are very similar. Because the goal with ASL imaging is that the intrinsic tissue signals should subtract out, leaving only the signal difference of delivered blood, there is a useful trick to improve the accuracy of the subtraction. The essential problem is that the intrinsic tissue signal is much larger than the arterial blood signal, so we are subtracting two large numbers to estimate a small difference. If the intrinsic tissue signal can be reduced, the subtraction should be more robust. This is done by applying a  $90^\circ$  saturation pulse on the imaged slice just after the  $180^\circ$  tagging pulse (Edelman *et al.* 1994; Wong *et al.* 1997). In this way, the static tissue signal recovers from zero and so is weaker at the time of measurement, but the ASL difference signal from delivered arterial blood is unaffected.

These PASL techniques also suffer from potential systematic errors that make quantification of CBF more difficult. As with CASL, although the source of these effects is likely dominated by imperfect slice profiles rather than magnetization transfer effects (Frank *et al.* 1997a). For all these PASL approaches, we would ideally like to have the tagging band flush against the edge of the imaged slice. But because neither the slice profile of the inversion pulse nor the imaging excitation pulse are perfectly sharp, there must be a gap between the edge of the inversion band and the edge of the image slice. If there is a gap, then there will necessarily be a transit delay before the tagged blood arrives in the voxel. The transit delay in PASL is shorter than with CASL because the tagging band is usually closer, but this is still an important problem affecting quantitative measurements of CBF and will be discussed further below.

## The importance of creating a well-defined arterial bolus

The approaches to PASL described above also suffer from a more subtle problem related to the duration of the tagged bolus in the arterial blood. For the CASL experiment, the arterial bolus width is well defined by the experiment, as the duration of the RF tagging pulse (if we neglect any broadening of the bolus as it travels to the capillary bed) (Fig. 13.6). But what is the corresponding arterial bolus width in the PASL experiment? In the PASL experiment, the arterial tagging is done in *space* rather than in *time*. The duration of the arterial bolus in a PASL experiment is the average transit time of arterial blood out of the tagging band. For example, suppose that the arterial volume within the tagging band is  $V_0$ , and the net arterial flow through the tagging band is  $F_0$ , and to keep the argument simple, suppose that the arterial flow is plug flow. Then the duration of the arterial bolus is  $V_0/F_0$ , the total time required for all of the tagged blood to leave the tagging band. But this means that the duration of the arterial input function is determined by the physiological state and the details of the applied tag, and so has been taken out of the experimenter's hands.

For example, suppose that flow to the brain increases globally (e.g., as in a  $\text{CO}_2$  inhalation experiment). Then  $F_0$  would increase in proportion to the change in CBF, and so the duration of the arterial bolus would be decreased in proportion to the flow change. This could lead to the surprising effect of a resting CBF measurement producing a reasonable map of perfusion, but a similar map made with globally increased CBF showing no change in perfusion at all. If the delay after the tagging pulse is sufficiently long for all the tagged spins to be delivered to the tissue slice at rest, then the distribution of the tagged spins will accurately reflect local CBF. However, with a global activation so that the local flow at every point in the brain is

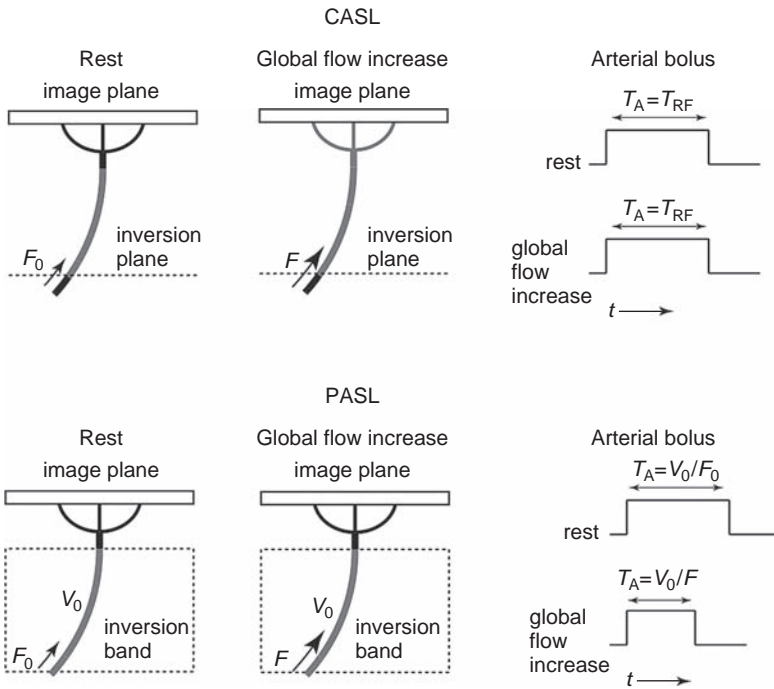


**Fig. 13.6.** Arterial bolus curves for pulsed arterial spin labeling (PASL) and continuous arterial spin labeling (CASL). A fruitful approach to modeling the ASL signal is to treat the magnetically tagged arterial blood as an “agent” delivered to the tissue. The driving function of such a kinetic model is the arterial concentration of the agent, the arterial bolus of tagged spins. Ideally, the arterial bolus has a well-defined time width  $T_A$ . The figure illustrates what happens when there is a global flow increase that increases the flow rate  $F$  through the large tagged vessels. For CASL, inverted blood is continuously produced for as long as the radiofrequency (RF) pulse is turned on ( $T_{RF}$ ), so  $T_A = T_{RF}$  independent of  $F$ . But for PASL, a volume  $V_0$  of spins is tagged (the arterial blood within the tagging band), and so the time width of the arterial bolus is set by  $V_0/F$ , the time required for the tagged blood to leave the inversion band, which depends on the physiological state. For this reason,  $T_A$  is not a well-defined quantity in a standard PASL experiment.

increased, the number of tagged spins is still the same because the same volume  $V_0$  of blood is inverted. These tagged spins are delivered in proportion to flow as before, and so the same number of tagged spins will be delivered to each voxel, yielding an identical perfusion map despite the global change in flow.

Note that this effect would not happen in a CASL experiment. In both PASL and CASL, the number of tagged spins leaving the tagging region is proportional to  $F_0 T$ . But in PASL, the duration of the arterial bolus is  $V_0/F_0$  so the number of tagged spins is fixed, but with CASL, the duration is determined by the experimenter and so is constant, independent of the physiological conditions. With CASL, a global increase in flow and  $F_0$  then increases the number of tagged spins produced, and the measured signal difference is larger, reflecting the global flow increase.

Another effect of a physiologically dependent duration for the arterial bolus in a PASL experiment is that the local value of this duration may vary from one region of the brain to another. The reason for this is that the tagging band will contain several arteries, and each will have a different bolus duration depending on the volume of the artery within the tagging band and the flow through that artery. The local width of the arterial input function may then vary between tissue regions fed by different arteries. In short, with the original PASL methods, the duration of the arterial bolus is poorly defined and varies with location in the

brain and with the physiological state, but with CASL the duration is a well-defined experimental parameter (the duration of the RF pulse).

We will return to this problem below in the discussion of a PASL technique called QUIPSS II (quantitative imaging of perfusion with a single subtraction, version II) that solves this problem.

## Quantitative cerebral blood flow measurements

### Sources of systematic errors

At the beginning of the chapter, the ASL experiment was compared with an ideal microsphere experiment. We will examine how the ASL experiment departs from this idealization by considering how other factors may affect the local value of  $A_{\text{eff}}$  in Eq. (13.1). The prominent factors that present a problem for quantifying CBF with ASL are the transit delay from the tagging region to each voxel, relaxation effects during the experiment, and the duration of the arterial bolus. Essentially, these factors all affect the shape of the arterial input function at each voxel. For this reason, ASL experiments should be designed to minimize the effects of these factors on  $A_{\text{eff}}$ , or methods need to be added to quantify these effects for each voxel.

We can illustrate these effects with a modeling framework that is sufficiently general to include them in a quantitative way (Box 13.1). For example, Fig. 13.7 shows kinetic curves for a PASL and CASL experiment when there is a transit delay before tagged blood reaches the image voxel, and  $T_1$  relaxation modifies the net signal that remains at the time of measurement. In these plots, the horizontal time axis essentially refers to TI, the time after tagging is initiated when the signal is measured. A particular experiment with a fixed TI would then measure a single point on these curves. Clearly, if the transit delay differs between two voxels – equivalent to shifting the curves to the left or right – the measured signal at a particular time point could change substantially even though the intrinsic flow in the two voxels is identical.

Similarly, correcting for relaxation of the tag is essential, as shown in the plot for the PASL experiment in Fig. 13.7, which shows the curve of the number of tagged spins delivered (dashed line) in comparison with the resulting ASL signal. In fact, properly accounting for relaxation is potentially complicated because the relaxation of the tagged spins is initially

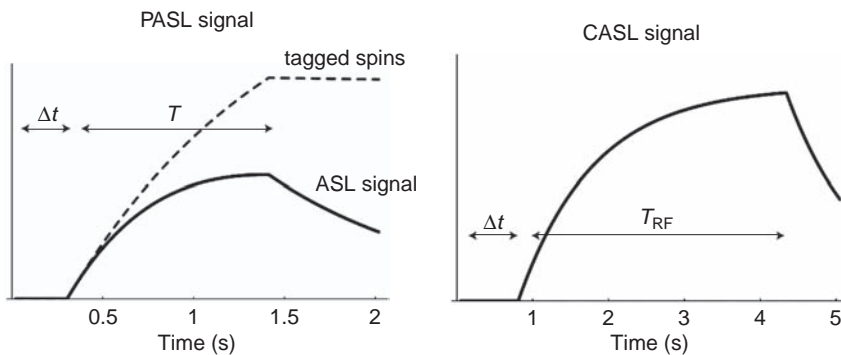


**Fig. 13.7.** Arterial spin labeling (ASL) kinetic curves. Illustration of the ideal ASL difference signal as a function of time (TI) for a pulsed ASL (PASL) experiment and a continuous ASL (CASL) experiment calculated with Eq. (B13.3). Labeled spins begin to arrive in the voxel after a transit delay  $\Delta t$  and continue to arrive for the duration of the bolus ( $T$  for PASL and  $T_{\text{RF}}$  for CASL). For the PASL experiment, the concentration of delivered spins (i.e., ignoring relaxation and venous clearance) is shown as a dashed line.

with the  $T_1$  of arterial blood ( $T_{1A}$ ), but as these spins leave the capillary and join the tissue water pool, they begin to relax with a different  $T_1$  characteristic of the extravascular water. As a simple way to approximate this effect we can define  $T_{ex}$  as the typical time between the first arrival of a tagged spin in an image voxel and the time when that spin leaves the capillary and joins the extravascular pool. Then at time  $T_{ex}$ , the relaxation rate constant changes from  $T_{1A}$  to  $T_1$ . Note that  $T_{ex}$  includes the time to move down the vascular tree within the voxel, plus the time for a water molecule in capillary blood to diffuse across the capillary wall.

A useful way to visualize the effects of these factors on the ASL signal is to plot a function  $a(t)$  defined as the contribution of spins that arrived in the voxel at time  $t$  to the net ASL signal measured at time TI. Then  $A_{eff}$  is the area under this curve. This method of visualization is a bit unusual, because  $t$  plays a subtle role here. We have described in Ch. 12 the idea of an arterial input function,  $C_A(t)$ , that defines the concentration in arterial blood that arrives at time  $t$ . The new function  $a(t)$  is not the same as  $C_A(t)$ , because we need to deal with relaxation and the possibility that some of the delivered tagged blood has left through venous clearance before

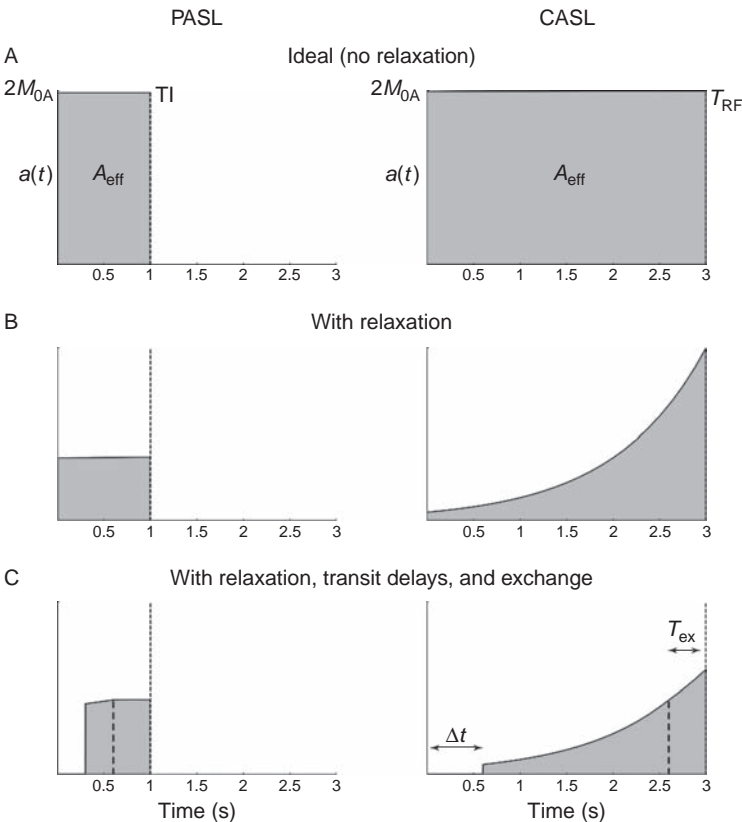


**Fig. 13.8.** The calibration factor  $A_{eff}$ . The arterial spin labeling (ASL) difference signal is modeled as  $\Delta M = f A_{eff}$ , where  $A_{eff}$  is the effective area under the arterial curve. This is illustrated by plotting  $a(t)$ , the contribution of the spins arriving in the voxel at time  $t$  to the measured signal at time TI. The calibration factor  $A_{eff}$  is the shaded area under  $a(t)$ . (A) (the ideal state) If there were no relaxation, all delivered spins would contribute equally to the measured signal. (B) With relaxation, the signal from all the delivered spins is attenuated in pulsed ASL (PASL) whereas the signal from recently arrived spins has decayed less for continuous ASL (CASL). (C) The more general case includes a transit delay  $\Delta t$  and a delay to exchange of the tagged water with tissue water,  $T_{ex}$ .

the signal is measured, both of which effectively make the delivered tag disappear over time. For this reason, the ASL signal depends not just on how much tagged magnetization arrived at time  $t$ , but also on how much of that tag survives to the time of measurement. Our definition of  $a(t)$  incorporates both delivery and survival effects, and  $A_{\text{eff}}$  is visualized as the area under  $a(t)$ .

This approach is illustrated in Fig. 13.8 for several examples of a PASL experiment with  $\text{TI} = 1$  s and a CASL experiment with a tagging time  $T_{\text{RF}} = 3$  s. For the ideal case of a perfect inversion with no relaxation and no venous clearance (Fig. 13.8A), all time points contribute equally to the final magnetization in the voxel, so  $a(t)$  is a rectangle for both the PASL and CASL experiments. Because of the longer tagging time with CASL,  $A_{\text{eff}}$  is larger and so the SNR is larger than for PASL. In practice, of course, this ideal form could not occur because relaxation does happen, but it serves to illustrate the meaning and interpretation of  $a(t)$  and  $A_{\text{eff}}$ .

Figure 13.8B illustrates relaxation effects with the assumptions that tagged water molecules begin to enter the voxel immediately after the inversion (transit delay,  $\Delta t$  is 0), that water molecules exchange into tissue and begin to relax with the  $T_1$  of tissue immediately after they enter the voxel ( $T_{\text{ex}} = 0$ ), and that clearance by venous flow is described by a single exponential. As shown in the figure, the effect of these assumptions is that spins that arrived earlier contribute less to the final magnetization, as we would expect when relaxation effects are included. Note, though, that the effect is different for PASL and CASL. In the PASL experiment, the tagging is done all at once, so all spins contributing to the ASL signal suffer the same relaxation decay. With CASL, new tagged magnetization is created continuously during the RF pulse, so the earliest tagged spins to arrive at the voxel have suffered significantly more attenuation. Note also that relaxation significantly decreases  $A_{\text{eff}}$  compared with the ideal form, and so relaxation strongly affects the SNR.

Figure 13.8C shows a more realistic model that illustrates the effects of the two parameters transit delay and  $T_{\text{ex}}$ . The transit delay shifts  $a(t)$ , and when the delay is long, the area  $A_{\text{eff}}$  is significantly reduced. There is a more subtle effect for  $T_{\text{ex}}$ , altering the slope of  $a(t)$  at a time  $T_{\text{ex}}$  before the image acquisition. This affects the area  $A_{\text{eff}}$ , but by a smaller amount than the transit delay effect. In the following sections, we use plots like those in Fig. 13.8 to illustrate the effects of potential systematic errors on the scaling factor  $A_{\text{eff}}$ .

## Controlling for transit delay effects

### Continuous arterial spin labeling

A key local variable that affects the ASL signal is the transit delay from the tagging region to the imaged voxel (Alsop and Detre 1996; Buxton *et al.* 1998a; Wong *et al.* 1997; 1998a; Zhang *et al.* 1993). If the transit delays to different parts of the imaged slice were all similar, this parameter would affect the magnitude of  $A_{\text{eff}}$  but would not cause it to vary across the brain. The ASL signal would then accurately reflect CBF differences between brain regions, although the effect of the transit delay would have to be taken into account in determining the value of  $A_{\text{eff}}$  to calibrate the flow measurement. Unfortunately, this is not the case (Fig. 13.9). The transit delay can vary by several tenths of a second across a single image plane (Wong *et al.*, 1997). Based on studies with different gaps between the tagging band and the slice, a rough estimate is that the transit delay increases by approximately 150 ms for each additional 1 cm gap (Wong *et al.* 1997). Furthermore, the transit delay is likely to decrease with activation. For these reasons, transit delays are a significant confounding factor for the interpretation of the ASL signal in terms of CBF.



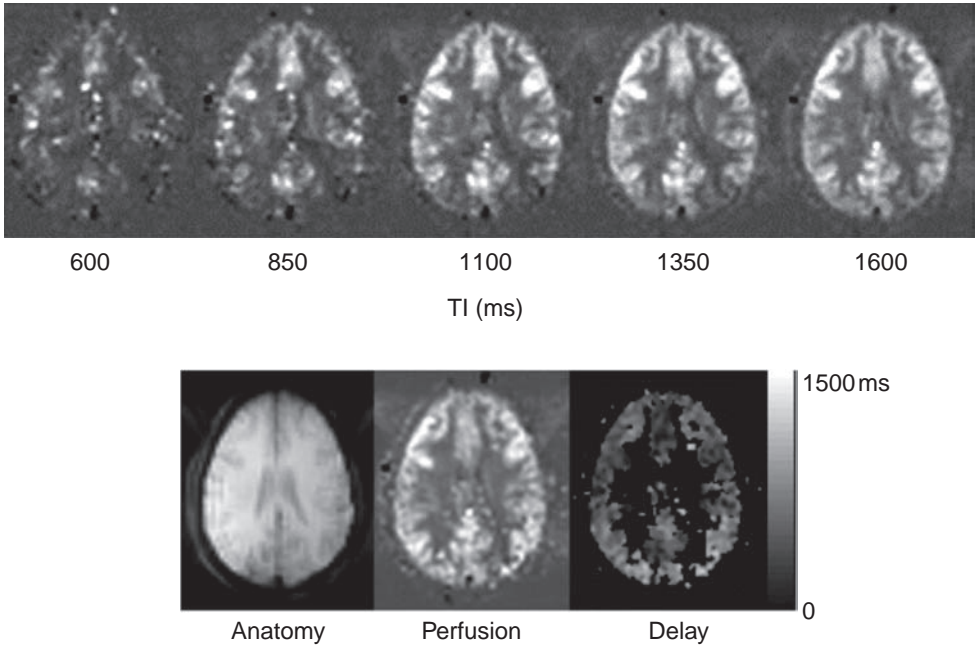


**Fig. 13.9.** Variable transit delays. Pulsed arterial spin labeling images made at different times TI after the inversion pulse show early delivery in large vessels for short TI and a slower spread of the signal to the brain parenchyma. Note, however, that the occipital region takes substantially longer to fill in because of a longer transit delay. The calculated map of transit delays is shown on the lower right. (Data courtesy of E. Wong.)

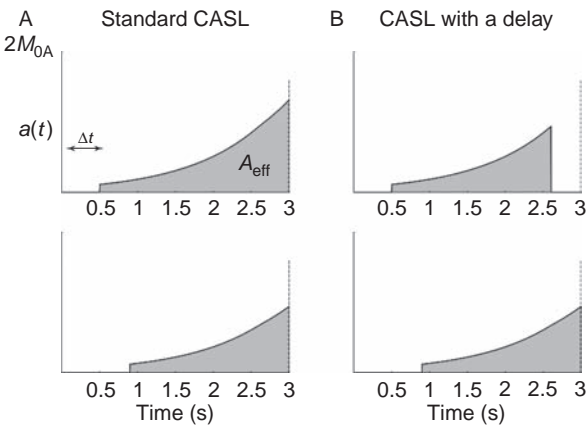


**Fig. 13.10.** Controlling for transit delay effects in continuous arterial spin labeling (CASL). (A) The problem posed by variable transit delays from the tagging plane to the image plane is illustrated. The calibration factor  $A_{eff}$  depends strongly on the delay because fewer of the tagged spins have reached the voxel with the longer transit delay  $\Delta t$  (0.9 s at bottom plot compared with 0.5 s in the upper plot) and so creates a large systematic error in the measurement of CBF. (B) The solution to the problem is to insert a delay  $\delta t$  after the end of the radiofrequency pulse interval ( $T_{RF}$ ) before imaging to allow complete delivery of the arterial bolus to all the image voxels. Plots for  $T_{RF}$  of 2.1 s and 0.9 s are shown. Note that the areas of the two lower plots ( $A_{eff}$ ) are nearly identical despite the transit delay difference.

The effect of a transit delay on  $A_{eff}$  for CASL is illustrated in Fig. 13.10. Curves of  $a(t)$ , the contribution to the measured  $\Delta M$  from spins arriving in the voxel at time  $t$ , are shown for two transit delays (0.5 and 0.9 s). For the tissue with the longer transit delay,  $A_{eff}$  is significantly reduced because many of the tagged spins have not reached the voxel by the time of the image. The solution to this problem, proposed by Alsop and Detre (1996), is illustrated in Fig. 13.10B. Instead of applying the long tagging pulse for a duration of the RF

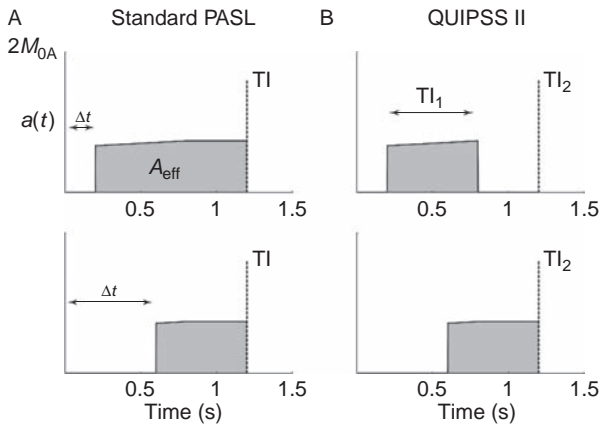


**Fig. 13.11.** Controlling for transit delay effects in pulse arterial spin labeling (PASL). (A) As with continuous arterial spin labeling, variable transit delays ( $\Delta t$ ) severely affect the calibration factor  $A_{\text{eff}}$ , producing systematic errors in the measurement of CBF. In this example, the image is measured at  $T_I = 1.2$  s, and the two illustrated delays are 0.2 and 0.6 s, creating a large difference in  $A_{\text{eff}}$ . (B) The solution to this problem in QUIPSS II (quantitative imaging of perfusion with a single subtraction, version II) is to create a well-defined arterial bolus width by applying a saturation pulse to the tagging band after a delay  $T_{I_1}$  and then to acquire the image at a time  $T_{I_2}$  after the arterial bolus has been delivered to all the voxels. Slight differences remain in  $A_{\text{eff}}$  for the two cases because of different relaxation times in blood and tissue, but these differences have a small effect on the CBF measurement.

pulse and then immediately acquiring an image, a delay  $\delta t$  is inserted after the end of tagging before the image acquisition. The effect of this is to create nearly equal values of  $A_{\text{eff}}$  despite the large difference in transit delay. If the inserted delay is greater than the longest transit delay, all the tagged arterial bolus will be delivered to all the image voxels. The only remaining effect of the different transit times will result from differing relaxation rates in blood and tissue. The tagged spins in the voxel with the longest transit delay spend more time in the blood and so relax somewhat less than spins that quickly exchange into tissue. However, this residual dependence of the local transit delay is small, and the trick of inserting a delay is effective in controlling for variability of the transit delay.

### Pulsed arterial spin labeling: QUIPSS II

Figure 13.11 shows the effect of transit delays in a PASL experiment. In these examples, smaller transit delays were used (0.2 and 0.6 s) because the tagging region is generally closer to the imaged slice with PASL than with CASL. Nevertheless, the area  $A_{\text{eff}}$  is still strongly affected by the transit delay interval. The solution to the problem is similar to the CASL solution. By waiting sufficiently long that all the tagged arterial bolus reaches all the voxels in the image, the only remaining sensitivity to the transit delay will be a small relaxation effect similar to that in CASL. However, there is a problem in applying this idea to PASL: the duration of the arterial bolus is not a well-defined quantity. As described above, an essential difference between CASL and PASL is that CASL tags spins in time so that the arterial bolus has a well-defined width set by the duration of the tagging pulse. But PASL tags in space, inverting all spins in a fixed volume, so the duration of the arterial curve depends on the flow in the large tagged arteries. For this reason, the duration of the arterial bolus can vary across the brain.

To apply the idea of adding a delay to the pulse sequence to allow all the tagged spins to arrive, the duration of the arterial bolus must be controlled. The technique QUIPSS II is designed to provide this needed control over the arterial bolus width (Wong *et al.* 1998b). The QUIPSS II modification to PASL is to add a  $90^\circ$  saturation pulse, after the inversion pulse and before the imaging excitation pulse, that hits the same tagging band as the inversion pulse. For example, with EPISTAR/QUIPSS II, the selective inversion pulse is applied in a

tagging band below the slice at  $t = 0$ , a saturation pulse is applied in the same band at  $t = TI_1$ , and the image is made at  $t = TI_2$ . The control image is done with the inversion band above the slice so that arterial blood is not tagged, but again the saturation pulse is applied to the original tagging band at  $t = TI_1$  (i.e., the saturation pulse is applied to the same spatial region in both the tag and control experiments).

The effect of the saturation pulse is to snip off the end of the arterial bolus and produce a well-defined bolus with a duration of  $TI_1$ . To see this, it is helpful to follow the fate of the arterial magnetization within the tagging band in the two parts of the experiment. For the tag image, all the arterial magnetization in the tagging band is initially inverted, and it then begins to flow out of the tagging band. But before all the labeled blood has had a chance to leave, the saturation pulse is applied. The magnetization of the originally tagged spins remaining in the tagging band is then flipped into the transverse plane, leaving a longitudinal magnetization of zero. Now consider the same spins in the control experiment. The initial inversion pulse has no effect on the arterial spins in the tagging band, so they remain fully relaxed and begin to flow out of the band carrying full magnetization. But the saturation pulse reduces the longitudinal magnetization of the remaining arterial spins to zero at time  $TI_1$ , just as in the tag experiment. The difference between the tag and control signals then drops to zero after a time  $TI_1$ .

For QUIPSS II to yield a quantitative flow image, two conditions must be satisfied: (1) the saturation pulse must be applied before all of the tagged spins have left the tagging band, and (2) the delay after the saturation pulse must be long enough for all the arterial tagged spins to reach the tissue voxel. If the natural duration of the tag is set by the volume and flow rate of the arterial blood in the tagging band, then these conditions for QUIPSS II to be accurate are that  $TI_1$  is less than this natural duration and that  $TI_2 - TI_1$  is greater than the transit delay. In practice, with the tagging band only 1 cm away from the image slice, typical values are  $TI_1 = 700$  ms and  $TI_2 = 1500$  ms. With the QUIPSS II modification, the quantification problems of the original PASL techniques can be corrected. For example, with global flow changes, the number of tagged spins is increased because more will flow out of the tagging band before the saturation pulse is applied, so the number of tagged spins delivered to a voxel will be proportional to the local flow. In other words, the QUIPSS II modification changes PASL from tagging in space to tagging in time, like CASL.

If these conditions are satisfied, the calibration factor for the QUIPSS II experiment is approximately

$$A_{\text{eff}} = 2M_{0A} TI_1 e^{-TI_2/T_{1A}} \quad (13.2)$$

The reason that this expression is only approximate is that the relaxation term really depends on the time of exchange  $T_{\text{ex}}$ . Equation (13.2) is accurate if  $T_{\text{ex}}$  is greater than the difference between  $TI_2$  and the transit delay, so that all the spins relax with the  $T_1$  of blood during the experiment. If this is not true, then the amount of decay will depend on precisely when the spins were extracted into the tissue, and this will depend on the transit delay as well as  $T_{\text{ex}}$ . We will consider these relaxation effects further in the next section.

In a typical multislice implementation of QUIPSS II, five to seven slices are imaged in rapid succession with a single-shot echo planar imaging (EPI) acquisition after a single tagging pulse is applied below the block of images (Wong *et al.* 1997). After a delay  $TI_1$ , the saturation pulse is applied to cut off the end of the arterial bolus, and after another delay,  $TI_2$ , the image of a slice is acquired. The imaging rate is approximately one image every 80 ms, so if the image time ( $TI_2$ ) for the first slice is 1200 ms, it is 1520 ms for the last slice. To control

for transit delays,  $TI_2 - TI_1$  should be longer than the delay from the tagging band to the slice, so the most distal slice with the longest delay should be collected last to allow time for the tagged spins to arrive. This proximal to distal order of slice collection could potentially create a problem if some of the tagged bolus destined for a more distal slice is still in a larger artery in a more proximal slice when the latter is imaged. Consequently, it is important that  $TI_2$  is sufficiently long that all tagged spins in large vessels that are simply flowing through the slice have had sufficient time to clear. Each imaging excitation pulse also alters the magnetization of the arterial blood within the slice, and so effectively retags the blood, which also could create a problem if this newly tagged blood reaches more distal slices. However, with sufficiently rapid image acquisition, there is not enough time for the blood saturated in one image acquisition to reach the next slice before the next image is acquired.

In practice, a potential source of error with QUIPSS II is the quality of the saturation pulse applied to the tagging band. Ideally, the edges of the  $90^\circ$  saturation pulse should precisely match the edges of the  $180^\circ$  inversion pulse. The quality of the saturation can be improved by replacing the single saturation pulse with a periodic train of thin-slice saturation pulses at the distal end of the tagging band to create a well-defined arterial bolus, a technique called Q2TIPS (Luh *et al.* 1999).

## Relaxation effects

For both CASL and PASL, the cost of controlling for transit delays is reduced sensitivity. As can be seen in Figs. 13.10 and 13.11, there is more relaxation and a reduction in the calibration factor  $A_{\text{eff}}$  with the added delays. Furthermore, because the  $T_1$  values of white matter and gray matter are significantly different, we must consider the role of variations in the local relaxation rate on  $A_{\text{eff}}$ . Initially, the tagged magnetization decays with the  $T_1$  of blood ( $T_{1A}$ ), but as the tagged water molecules enter the extravascular space, they decay with the  $T_1$  of tissue. In a CASL experiment, accounting for  $T_1$  decay is even more complicated because of magnetization transfer effects. In the presence of an off-resonance RF field, magnetization transfer effects alter the apparent  $T_1$  of the tissue, so the relevant apparent  $T_1$  for CASL experiments must include these effects (Zhang *et al.* 1992).

The time of exchange  $T_{\text{ex}}$  of labeled water molecules into the tissue space is not well known. This question has been addressed experimentally with MRI by partly destroying the signal from blood with diffusion-weighting gradients. The motion of blood leads to rapid dephasing of the transverse magnetization, even for relatively weak diffusion-sensitizing gradients. In effect, the apparent diffusion coefficient of water molecules in blood appears to be much higher than the apparent diffusion coefficient in the extravascular space. Studies in a rat model using CASL with a 3.5 s tagging time found that approximately 90% of the tagged spins exhibited an apparent diffusion coefficient similar to tissue, indicating that these spins had left the blood and joined the tissue water pool (Silva *et al.* 1997). In a human experiment using CASL with diffusion-weighting gradient pulses to destroy the blood signal, the mean time to exchange with tissue was found to be 0.94 s for a tagging plane 3 cm below the center of the imaged slice (Ye *et al.* 1997). This delay is really  $T_{\text{ex}}$  plus the transit delay as we have defined the terms, suggesting that  $T_{\text{ex}}$  may be on the order of a few tenths of a second.

Figure 13.12 illustrates the sensitivity of  $A_{\text{eff}}$  to differences in the tissue relaxation times for PASL. The curves show examples for assumed relaxation times ( $T_1$ ) of 1.0 s for gray matter, 0.7 s for white matter, and 1.2 s for blood. Clearly, if  $T_{\text{ex}}$  is long enough, the local relaxation time will have no effect on  $A_{\text{eff}}$  because the tagged spins always remain in blood during the experiment. Two values of the exchange time were used in Fig. 13.12,  $T_{\text{ex}} = 0.2$  s and  $T_{\text{ex}} = 0.7$  s,

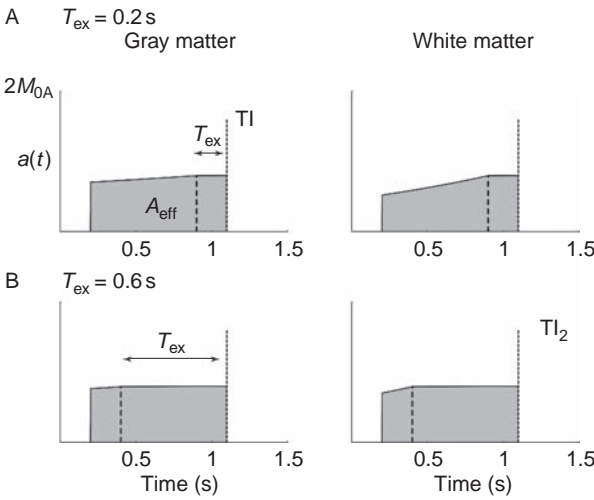


**Fig. 13.12.** Effects of relaxation on the calibration factor  $A_{\text{eff}}$  with pulsed arterial spin labeling. The tag is assumed to relax with the  $T_1$  of blood (approximately 1.2 s) while the labeled spins are still in the vasculature, and to relax with the  $T_1$  of tissue (approximately 1.0 s for gray matter and 0.7 s for white matter) after the spins have exchanged into the tissue. The calibration factor  $A_{\text{eff}}$  then depends somewhat on the local value of  $T_1$  (e.g., gray matter or white matter), but the magnitude of the effect also depends on  $T_{\text{ex}}$ , the time after arrival in the voxel when spins exchange from blood to tissue. For all these examples, relaxation effects related to the exchange time  $T_{\text{ex}}$  have a relatively minor impact on  $A_{\text{eff}}$ .

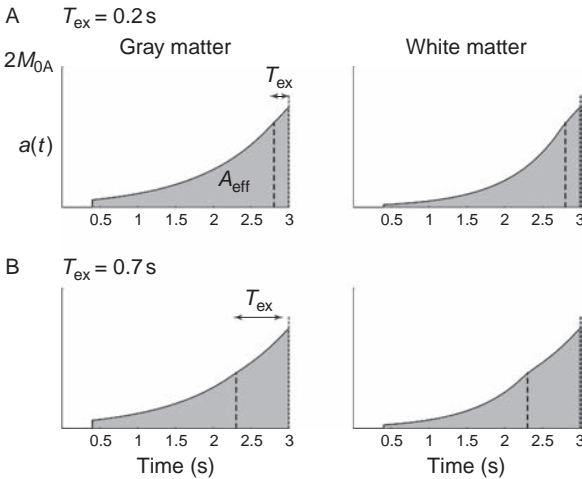


**Fig. 13.13.** Effects of relaxation on  $A_{\text{eff}}$  with continuous arterial spin labeling (CASL). Plots for CASL similar to those in Fig. 13.12 show a stronger effect of relaxation rate in the CASL experiment. Because the duration of the tagging (several seconds) is much longer with CASL, there is more time for tagged spins to exchange into tissue. The calibration factor  $A_{\text{eff}}$  then depends more strongly on the local  $T_1$ , and a correction for spatial variations in  $T_1$  is usually required.

with a measurement time of 1.1 s and a transit delay of 0.2 s. In these examples for a standard PASL experiment, the fractional difference of  $A_{\text{eff}}$  for white matter compared with gray matter is 6.5% when  $T_{\text{ex}} = 0.2$  s and 0.6% when  $T_{\text{ex}} = 0.7$  s. For the extreme case of  $T_{\text{ex}} = 0$  (curves not shown),  $A_{\text{eff}}$  differs between white matter and gray matter by only 10%. With PASL, even for the worst case of rapid exchange into tissue, variations in the local  $T_1$  have a relatively weak effect on the calibration factor  $A_{\text{eff}}$ .

For the CASL experiment, the examples in Fig. 13.13 were calculated with an RF pulse of 2.6 s and transit delay of 0.4 s, and the sensitivity of  $A_{\text{eff}}$  to differences in the relaxation times is quite a bit greater because of the long duration of the experiment. The fractional difference of  $A_{\text{eff}}$  for white matter compared with gray matter is 32% when  $T_{\text{ex}} = 0.2$  s and 21% when  $T_{\text{ex}} = 0.7$  s. For the extreme case of  $T_{\text{ex}} = 0$ , the fractional difference is 37%. For this reason, it is more critical to measure a local tissue  $T_1$  map together with the ASL data in a CASL experiment to correct for the variability in  $A_{\text{eff}}$  caused by variations in local  $T_1$ .

## Absolute cerebral blood flow calibration

To convert the ASL signal into absolute units of CBF we must know the appropriate value of  $A_{\text{eff}}$ . For pulsed ASL with QUIPSS II, the effects of water exchange into tissue are likely to be small, based on the estimates in the previous section, and Eq. (13.2) is usually used (Liu *et al.* 2004). This expression involves pulse sequence parameters  $TI_1$  and  $TI_2$ , plus two parameters related to arterial blood:  $T_{1A}$  and  $M_{0A}$ . Typically an assumed value for  $T_{1A}$  is used based on literature values. The term  $M_{0A}$ , the equilibrium magnetization of blood, could potentially be estimated by imaging a voxel full of blood. Because such a calibration signal is difficult to measure in a blood vessel, because of partial volume and motion effects, a useful approximation is to take the signal of cerebrospinal fluid (CSF) as a surrogate for blood (Chalela *et al.* 2000). In practice, this requires an additional quick scan of long repetition time (TR) with the slices shifted to capture CSF in the ventricles, holding the in-plane resolution parameters constant (Liu *et al.* 2004; Perthen *et al.* 2008).

However, even for this simple case, there are two other factors that should be taken into account. The first is receiver coil inhomogeneity. If the coil sensitivity pattern is not uniform across the field of view, then the same magnetization at different locations will generate different intensities in the ASL images, and this non-uniform scaling translates directly into a non-uniform scaling of the estimated CBF. With multichannel array coils, such non-uniformity is always present. A useful method for correcting for this is to collect a *minimum contrast* image designed to minimize the true contrast between different brain structures so that signal variations across the image reflect coil sensitivity variations (Wang *et al.* 2005). From these data, a correction map can be calculated to remove the effect of coil inhomogeneity.

A second factor that should be taken into account is  $T_2^*$  relaxation (St. Lawrence and Wang 2005). Equation (13.2) really refers to the longitudinal magnetization, before it is tipped over to generate a signal. This signal will decay by the local  $T_2^*$  (or  $T_2$  for a spin echo [SE] acquisition) during the echo time TE. Although the exchange of tagged water spins from blood into tissue has only a small effect on the  $T_1$  relaxation, because most of the time is spent in blood, the relevant  $T_2^*$  depends on where the spin is when the signal is collected. For this reason,  $T_2^*$  effects do depend strongly on exchange. Usually, a typical value of  $T_2^*$  is assumed. A better approach to this problem is to use a short TE, so that the exact value of  $T_2^*$  has little effect on the signal. This is difficult to accomplish with an EPI pulse sequence, but is possible with a spiral  $k$ -space acquisition (Perthen *et al.* 2008).

For CASL experiments, the longer tagging intervals allow more time for exchange of tagged spins between the intravascular and extravascular space, and quantifying CBF is more difficult. Because exchange is more important, the local tissue  $T_1$  becomes important and must be measured separately. In addition, a more complete model of exchange is needed to quantify the signal (Parkes 2005). Nevertheless, a simple approximation that is often used is to assume that the tagged spins immediately leave the vasculature as soon as they arrive in a voxel ( $T_{\text{ex}} = 0$ ), so that the decay of the tag is entirely by the  $T_1$  of tissue after arrival (Detre *et al.* 1992). This likely leads to a systematic error, but it is the usual method of analysis.

The analysis of CASL data also often involves the parameter  $\lambda$ , the partition coefficient of water between blood and brain tissue, based on the original formulation of the ASL signal model as an analogy with models used for diffusible tracers in PET (Buxton *et al.* 1998a; Detre *et al.* 1992). This formulation is often called a single-compartment model (Box 13.1). It differs from our current formulation by replacing  $M_{0A}$  with  $M_{0T}/\lambda$ , where  $M_{0T}$  is the

equilibrium magnetization of tissue. However, this usage is misleading in terms of the basic physics and physiology, because it suggests that the ASL signal depends on how much total water is in each voxel ( $M_{0T}$ ), which is a local parameter that varies across the brain.

Instead, by the basic reasoning underlying ASL, the signal difference is just a result of the signal difference of arterial blood – the static water signal subtracts out. The essential difference is that the approach taken in this chapter is to model the ASL signal in analogy with a microsphere experiment, rather than a diffusible tracer experiment, and this brings out the central role played by  $M_{0A}$  (Buxton 2005). This is a global scaling factor and not a property of the local tissue. Often in CASL experiments,  $M_{0T}$  is estimated as part of the  $T_1$  measurement, and then used with an assumed value of  $\lambda$ . However, this is likely to introduce systematic errors, because it amounts to a complicated way of measuring  $M_{0A}$ . The only way in which  $\lambda$  *does* enter the ASL signal equation is in the description of water that has left the capillary, mixed with the extravascular water, and returned to the capillary and cleared from the image voxel by venous flow. This is a negligibly small amount. In contrast, unextracted water that never left the capillary and is cleared by venous flow may be significant (Parkes 2005), but this does not depend on  $\lambda$ . In short, a fundamental strength of the ASL technique is that the signal is proportional to a global property ( $M_{0A}$ ) and not an unknown local property ( $M_{0T}$ ).

Several studies have compared quantitative CBF measurements from ASL with other techniques and have found generally good agreement, although the CBF values with ASL tend to be higher (Ewing *et al.* 2005; Koziak *et al.* 2008; Walsh *et al.* 1994; Ye *et al.* 2000a). This could reflect partly the different partial volume effects between different methods. Spatial resolution with ASL is better than with PET techniques, for example, and so with a better isolation of gray matter it would not be surprising to find higher flows. Another possibility is that the current modeling is systematically off in treating relaxation effects, as described above. The  $T_1$  of blood is longer than that of tissue, so if the tagged spins spend some time in the blood before exchanging into the tissue ( $T_{ex} > 0$ ), the assumption of decay of the tag by the  $T_1$  of tissue will overestimate the degree of signal loss, and so overestimate the CBF. And, as discussed in the next section, tagged blood in the larger arteries destined for a more distal capillary bed also may lead to an overestimate (Donahue *et al.* 2006).

In addition, a number of studies have examined the reproducibility of CBF measurements with ASL (Hermes *et al.* 2007; Jahng *et al.* 2005; Leontiev and Buxton 2007; Parkes *et al.* 2004). Although there is a wide variation of values across subjects, repeated measurements in the same individuals are quite similar, with variation typically less than approximately 10%. For this reason ASL provides a reasonably robust measurement of CBF.

## Current issues

### Tagged water in arteries

In addition to the transit delay effects and relaxation effects described above, there are a few other systematic factors that affect the accuracy of CBF measurements with ASL (Buxton *et al.* 1998a; Donahue *et al.* 2006; Wong *et al.* 1997). The first is the issue of tagged spins in large vessels that are simply flowing through the image voxel. The meaningful definition of perfusion is the amount of arterial blood delivered to a capillary bed within a voxel. Tagged spins in an artery within a voxel that are destined for a capillary bed in another region should not be counted as perfusing that voxel. For example, PASL experiments with short TI often

show focal bright spots in arteries because there has not been sufficient time for the tagged spins to reach the brain parenchyma.

With both QUIPSS II and CASL with a delay, this flow-through effect is likely to be small because both approaches use long delays to allow the tagged blood to distribute to the tissues. The effect can be further reduced by applying diffusion weighting to spoil the signal from large vessels (Ye *et al.* 1997). One might imagine that the best approach for ensuring that we do not suffer from this problem would be to apply large gradient pulses to destroy all vascular signal, so that only spins that have exchanged into tissue will contribute to the ASL signal. But, in fact, this would be overkill. The signal from tagged blood in small arteries that are feeding capillary beds within the voxel does not need to be destroyed because such spins are properly counted as contributing to the perfusion of that voxel. In effect, excessive diffusion weighting would increase the transit delay, in the sense that the tagged spins do not contribute to the voxel signal until a later time after they have reached the capillary bed and exchanged with tissue. In other words, for practical purposes, the transit delay is the time from the beginning of the experiment to the first appearance of the signal from tagged spins in the voxel. So excessive diffusion weighting will decrease the sensitivity of the measurement because fewer spins are measured and this will exacerbate the problem of transit delays without improving the accuracy.

## The arterial input function

Off-resonance excitation effects are always a potential problem with quantitative ASL. For PASL, the problem is primarily that the RF pulses do not have perfectly sharp slice profiles (Frank *et al.* 1997b). The essential effect of this is that the arterial input function is then not a simple rectangle. For example, in EPISTAR, the rounded edge of the tag slice profile on the distal side means that the first tagged spins to arrive in the voxel are not fully inverted, producing a rounded leading edge to the arterial curve. The same effect happens in FAIR, but here it occurs because the slice-selective control slice profile has a rounded edge. In both cases, the difference (control – tag) is important, so in both cases the effect is a rounded arterial input function. Effectively, this means that less tagged magnetization is delivered during the earlier part of the bolus than if the arterial curve had an ideal rectangular shape.

In nearly all ASL studies, the arterial input function is modeled in some way (Gallichan and Jezzard 2008). Yet these models are often quite simple (plug flow etc.) and may fail to capture the full effects of partial inversion or physiological broadening as the bolus travels down the vascular tree. An interesting approach to dealing with this problem is to collect sufficient data to estimate individual input functions, a technique called QUASAR (Petersen *et al.* 2006). By measuring a series of images with different inflow times both with and without crusher gradients to destroy the blood signal, the arterial input function can be measured directly and used in the calculation of CBF. Petersen and colleagues (2006) found CBF values approximately 10% lower when analyzed with this method compared with the standard method.

## Recent innovations

Research in ASL technique development is growing rapidly, with many innovative approaches to improve SNR, minimize systematic errors, and maximize coverage of the brain (Liu and Brown 2007). The following is a brief description of some of the key ideas.



### Background suppression

In conventional ASL, the signal of interest is the small difference of two large signals. Any systematic error that is proportional to the large signal, even if relatively small, can be a serious error for the estimate of CBF. Because it is only the difference signal that carries information on flow, suppression of the background signal can improve the quality of the signal. With multiple inversion pulses, it is possible to null the signal of tissue over a reasonably wide range of  $T_1$  values. Such techniques were originally developed in MR angiography applications and have been applied quite effectively in ASL (Garcia *et al.* 2005a; Mani *et al.* 1997; Ye *et al.* 2000b).

### Correction for physiological noise

An important feature of ASL methods for fMRI applications is that they can measure dynamic CBF responses to activation with a time resolution of a few seconds, a significant improvement over PET methods, which only provide CBF measurements in a few selected states. However, the contamination of the ASL time series with physiological noise is a significant problem that effectively lowers the sensitivity to weak activations. This problem can be corrected by recording cardiac and breathing fluctuations during the scan and removing these components from the data (Restom *et al.* 2006). Correcting for physiological noise significantly improves ASL time series.

### Separate labeling coil

Multislice imaging with CASL presents the problem of how to construct a control experiment that works for all slices. During the continuous RF, the spins in the image slice are off-resonance by an amount that depends on their position because of the constant gradient used for the adiabatic inversion. The off-resonance RF has a significant effect on the static magnetization in the slice because of magnetization transfer effects, and image slices in different locations will have different levels of off-resonance effects. In the original CASL, the control experiment used a similar RF pulse applied to an inversion plane symmetrically placed on the other side of the image plane, but this only works for one slice. A direct approach to solving this problem for CASL is to use a second, small coil to apply the tag in the neck (Silva *et al.* 1995). If the coil is sufficiently far away, the effects of the continuous RF are localized and do not affect the image slice, so a simple control image without the RF inversion works for all slices. Several groups have explored this approach (Mildner *et al.* 2003; Paiva *et al.* 2008; Talagala *et al.* 2004; Trampel *et al.* 2002). Although very promising, this method requires novel hardware that is not generally available on MR scanners.

### Amplitude-modulated pulses

Alsop and co-workers proposed a novel control pulse to allow multislice perfusion imaging without the additional hardware required for an extra RF coil (Alsop and Detre 1998). The control pulse is the same as the tagging pulse, except that it is modulated at 250 Hz. This amplitude modulation creates two closely spaced inversion planes so that flowing blood is first inverted and then almost immediately flipped back. The RF power used in the tagging pulses is the same, and the resonant frequency offset for any image plane is the same for the two pulses because the gradient is the same, so the magnetization transfer effects should be similar. However, one cost of this approach is that the tagging efficiency is reduced, which cuts into the potential SNR advantage of CASL techniques over PASL techniques (Wong *et al.* 1998a).

### Pseudo-continuous ASL

More recently, Garcia and colleagues (2005b) described a promising approach called pseudo-CASL. Rather than a continuous RF pulse in the presence of a constant gradient, both the RF and the gradient are broken into a series of very short pulses. This has the same effect of producing an adiabatic inversion of the magnetization of blood as it flows through the zero plane of the gradient. However, the gradient used during each pulse is stronger than the constant gradient used in traditional CASL, and this means that the slice to be imaged is farther off resonance, with reduced magnetization transfer effects.

### Three-dimensional imaging with a GRASE acquisition

A technique for fast imaging that was introduced in Ch. 10, GRASE (combination of rapid acquisition with relaxation enhancement [RARE] and gradient recalled acquisitions in a single multi-echo sequence) has been applied to rapid collection of three-dimensional ASL data (Gunther *et al.* 2005). Recently, this approach was combined with pseudo-continuous ASL and background suppression in a method that makes possible high-quality three-dimensional ASL images in under 1 min (Fernandez-Seara *et al.* 2008). This approach is exceptionally promising for future clinical applications.

### Vascular territory imaging

A number of *vessel-selective* methods have been developed to limit the RF pulses to particular arteries, so that the ASL image will specifically reflect the territories fed by those particular arteries (Golay *et al.* 2005; Hendrikse *et al.* 2004; Paiva *et al.* 2007; van Laar *et al.* 2008). A recent *vessel-encoding* approach should offer a significant SNR advantage over vessel-selective techniques because data are collected simultaneously for all vessels (Gunther 2006; Kansagra and Wong 2008; Wong 2007). The technique developed by Wong (2007) uses a pseudo-continuous labeling scheme with additional gradient pulses inserted between the RF pulses to differentially encode the signals from the main arteries feeding the brain. In post-processing, the different vascular territories can be resolved. Compared with other pulsed methods, this approach provides a significant SNR advantage through the use of pseudo-CASL and improved spatial specificity by encoding vessels within a single tagging plane.

### Velocity-selective imaging

The ASL approach is based on manipulations of the signal of arterial blood, and imaging this labeled blood after it arrives in a tissue of interest. As discussed above, this leads to the problem of transit delays from the tagging region to the image plane. This is potentially a serious limitation of ASL methods in applications to disease where the transit delay problems may be more severe, such as stroke. A radically different approach to measuring CBF is to use velocity-selective RF pulses essentially to image spins that are slowing down, and thus directly acquire signal from the arterial blood within the image plane (Wong *et al.* 2006). Although still in its infancy, this class of methods has considerable promise for clinical applications.

## Applications in fMRI

### Activation studies with arterial spin labeling

Cerebral blood flow changes during simple motor and sensory tasks were first demonstrated with flow-sensitive techniques by Kwong and co-workers and reported in the same seminal

paper that described human brain activations measured with the BOLD effect (Kwong *et al.* 1992). They used a slice-selective inversion recovery and found small signal increases consistent with increased inflow to the slice associated with simple activation tasks. Although not truly an ASL technique, this early study demonstrated the potential of detecting the effect of CBF changes on the MR signal.

Methods using ASL have now reached a sufficient level of maturity that they have been used for a number of basic studies of brain function. Two particular areas of promising applications are studies in disease populations, where it is difficult to know how the disease process alters the BOLD response, and studies where the time frame is longer than a few minutes, such as assessment of the effects of treatment (Brown *et al.* 2007; Detre and Wang 2002). Because ASL is able to measure the baseline CBF, as well as the change with activation, it is possible to make quantitative comparisons across groups. In addition, the repeated collection of tag and control images that are subtracted makes the measured CBF time series robust against slow drifts of the signal. In contrast, such drifts are a problem for BOLD imaging, and some correction must be applied. A striking example of how stable the CBF time series can be was provided by Wang and colleagues (2003). They asked subjects to perform a simple finger tapping task, comparing a block of finger tapping with a block of resting. They then increased the time between the blocks to as much as 24 h, and they were still able to produce activation maps based on the difference in flow in the motor area between the task and control conditions.

## Simultaneous cerebral blood flow and O<sub>2</sub> imaging

A powerful feature of ASL is that it is possible to map flow and BOLD activation patterns simultaneously and independently with an appropriately modified ASL sequence (Buxton *et al.* 1998b). The basic idea is that in a PASL data set, alternating between tag and control images, the time course of signal differences (control – tag) is flow weighted, whereas the time course of signal averages (control + tag) is BOLD weighted. For example, by collecting the tag and control images of the ASL sequence with a gradient recalled echo EPI pulse sequence with TE = 30 ms, each individual image is BOLD weighted. From the raw image time series of a voxel, a BOLD-weighted time series is calculated by averaging the signal at each time point with the mean of the signals just before and just after (Liu and Wong 2005). For each time point, this is equivalent to adding a control and a tag signal. From the raw time series, a flow-weighted time series is calculated by subtracting the mean of the two nearest neighbors from the signal at each time point. This is equivalent to subtracting a control and a tag signal at each time point. To produce a consistent time course, the sign must be flipped for alternate time points to correct for the fact that they alternate between control – tag and tag – control.

A better approach for simultaneous measurement of CBF and BOLD changes is the use of a dual-echo spiral acquisition (Liu and Brown 2007). With a spiral trajectory through  $k$ -space, the sampling starts with  $k=0$ , so the effective TE can be very short (a few milliseconds), improving the SNR of the ASL measurement. The second echo is collected with a TE more typical of a BOLD experiment (30–40 ms) to provide the BOLD time series. Figure 13.14 shows an example of simultaneous measurements of flow and BOLD changes during a simple sequential finger-tapping exercise measured with spiral QUIPSS II. The separate flow and BOLD time courses were calculated from the raw data as previously described. Note that the shapes of the two time courses are somewhat different, with the BOLD time course showing a pronounced post-stimulus undershoot (Fig. 13.14E).

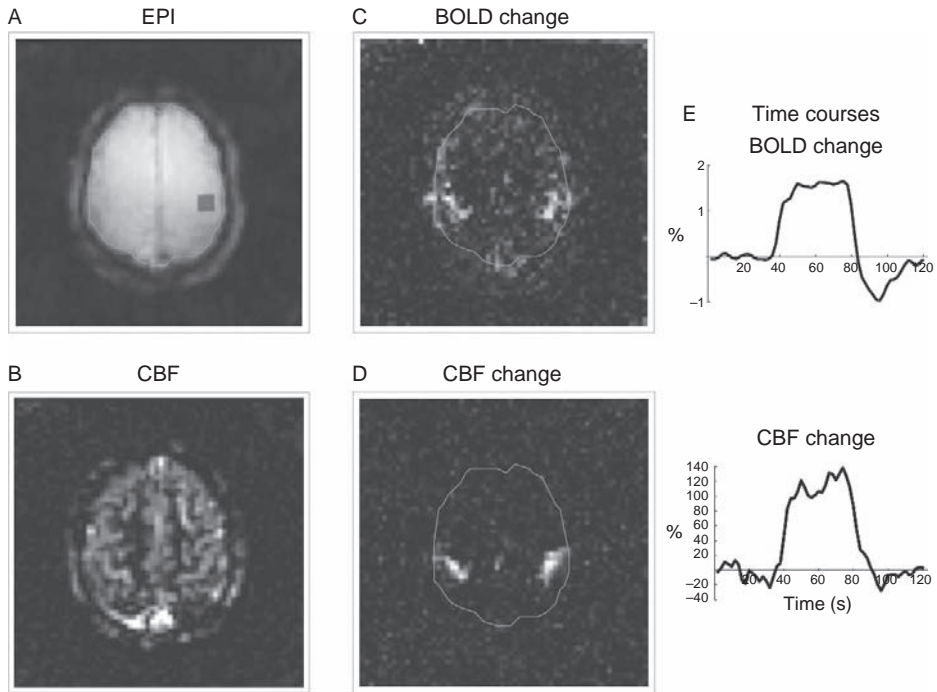


**Fig. 13.14.** Simultaneous measurements of flow and BOLD changes with activation. Data from a combined flow and BOLD finger-tapping study at 1.5 T acquired with a spiral dual-echo acquisition are shown. The arterial spin label pulse sequence was PICORE–QUIPSS II, with the flow time series calculated from the first echo ( $TE = 3$  ms) and the BOLD time series calculated from the second echo ( $TE = 30$  ms). (A) The echo planar image shows a  $3 \times 3$  region of interest (ROI), and the average time courses for the ROI are on the right (average of 16 cycles, 40 s of tapping alternated with 80 s of rest). (B) The average cerebral blood flow (CBF). Image (C, D) Maps of fractional signal change with activation measured for BOLD (C) and CBF (D). The activation maps are similar but not identical. (E) The flow and BOLD time courses are distinctly different, with the BOLD signal showing a distinct post-stimulus undershoot. (Data courtesy of T. Liu.) (See plate section for color version.)

Figure 13.14 also shows a simple subtraction of the images made during the tapping exercise from the images made during the rest period. The subtraction image for the flow-weighted series is much cleaner. The BOLD image shows two prominent areas of activation near the central sulcus but also shows a weaker diffuse and patchy pattern of signal change, possibly from residual motion artifacts or slow signal drifts. In contrast, the map of CBF changes shows only two bright focal areas of activation. The alternating subtractions in the construction of the flow series tend to cancel out slow motion effects that plague BOLD time series. Finally, these two maps also show that the locations of the prominent flow and BOLD changes do not necessarily coincide, consistent with the interpretation that BOLD is primarily sensitive to draining veins, while ASL is more closely associated with the capillary bed and the brain parenchyma. This is discussed further in Ch. 14.

## The calibrated-BOLD method

Combined measurements of flow and BOLD signal changes are a useful tool for studies of the basic mechanisms underlying the BOLD effect. The BOLD response is a complex phenomenon, because the change in the local level of deoxyhemoglobin depends on how much

deoxyhemoglobin is present in the baseline state, plus the balance of changes in CBF and the cerebral metabolic rate of O<sub>2</sub> (CMRO<sub>2</sub>) with activation. Davis and colleagues (1998) introduced an influential method for exploiting this complexity by combining ASL imaging with BOLD imaging to determine the CMRO<sub>2</sub> response as well as the CBF response. They measured CBF and BOLD responses to activation, and then also measured the same two responses to breathing CO<sub>2</sub> (hypercapnia), a physiological challenge that is thought to alter CBF but not CMRO<sub>2</sub>. The two sets of data – flow and BOLD responses to activation and to hypercapnia – were analyzed with a mathematical model for the BOLD effect. From the hypercapnia data, they calculated a scaling parameter in the model that described the effect of baseline deoxyhemoglobin content, and then with this calibration factor in hand they applied the model again to the activation data to derive an estimate of the change in CMRO<sub>2</sub> with activation.

This calibrated-BOLD approach takes BOLD imaging from a qualitative mapping tool to a true probe of physiology, and opens the door to quantitative studies of brain function. The combination of ASL and BOLD can thus provide much more information than either one alone, and it has become a primary tool for investigating the physiological mechanisms that underlie the BOLD response. In addition, the combination of ASL and BOLD studies, even without the calibration experiment, can provide a richer context for interpreting the BOLD response, particularly for studies of disease processes. For example, a recent study (Fleisher *et al.* 2008) found a weaker BOLD response to a memory task in subjects at risk for Alzheimer's disease compared with a low-risk group, suggesting that the neural activity associated with the task was altered in the high-risk group. However, CBF measurements with ASL in the same subjects and tasks suggested that the observed difference in the BOLD response could reflect a chronic difference in baseline CBF in the two groups, rather than the activation itself.

We will return to these themes in the later chapters, after first considering the BOLD response in more detail.

## References

- Alsop DC, Detre JA (1996) Reduced transit-time sensitivity in noninvasive magnetic resonance imaging of human cerebral blood flow. *J Cereb Blood Flow Metab* **16**: 1236–1249
- Alsop DC, Detre JA (1998) Multisection cerebral blood flow MR imaging with continuous arterial spin labeling. *Radiology* **208**: 410–416
- Alsop DC, Detre JA, Grossman M (2000) Assessment of cerebral blood flow in Alzheimer's disease by spin-labeled magnetic resonance imaging. *Ann Neurol* **47**: 93–100
- Brown GG, Clark C, Liu TT (2007) Measurement of cerebral perfusion with arterial spin labeling: Part 2. Applications. *J Int Neuropsychol Soc* **13**: 526–538
- Buxton RB (2005) Quantifying CBF with arterial spin labeling. *J Magn Reson Imaging* **22**: 723–726
- Buxton RB, Frank LR, Wong EC, *et al.* (1998a) A general kinetic model for quantitative perfusion imaging with arterial spin labeling. *Magn Reson Med* **40**: 383–396
- Buxton RB, Wong EC, Frank LR (1998b) Dynamics of blood flow and oxygenation changes during brain activation: the balloon model. *Magn Reson Med* **39**: 855–864
- Chalela JA, Alsop DC, Gonzalez-Atavales JB, *et al.* (2000) Magnetic resonance perfusion imaging in acute ischemic stroke using continuous arterial spin labeling. *Stroke* **31**: 680–687
- Davis TL, Kwong KK, Weisskoff RM, Rosen BR (1998) Calibrated functional MRI: mapping the dynamics of oxidative metabolism. *Proc Natl Acad Sci USA* **95**: 1834–1839
- Detre JA, Wang J (2002) Technical aspects and utility of fMRI using BOLD and ASL. *Clin Neurophysiol* **113**: 621–634

- Detre JA, Leigh JS, Williams DS, Koretsky AP (1992) Perfusion imaging. *Magn Reson Med* **23**: 37–45
- Dixon WT (1984) Simple proton spectroscopic imaging. *Radiology* **153**: 189–194
- Donahue MJ, Lu H, Jones CK, Pekar JJ, van Zijl PC (2006) An account of the discrepancy between MRI and PET cerebral blood flow measures. A high-field MRI investigation. *NMR Biomed* **19**: 1043–1054
- Edelman RR, Siewert B, Darby DG, *et al.* (1994) Qualitative mapping of cerebral blood flow and functional localization with echo-planar MR imaging and signal targeting with alternating radiofrequency (STAR) sequences: applications to MR angiography. *Radiology* **192**: 513–520
- Ewing JR, Cao Y, Knight RA, Fenstermacher JD (2005) Arterial spin labeling: validity testing and comparison studies. *J Magn Reson Imaging* **22**: 737–740
- Fernandez-Seara MA, Edlow BL, Hoang A, *et al.* (2008) Minimizing acquisition time of arterial spin labeling at 3T. *Magn Reson Med* **59**: 1467–1471
- Fleisher AS, Podraza KM, Bangen KJ, *et al.* (2008) Cerebral perfusion and oxygenation differences in Alzheimer's disease risk. *Neurobiol Aging* **7**: 812–826
- Frackowiak RSJ, Lenzi GL, Jones T, Heather JD (1980) Quantitative measurement of regional cerebral blood flow and oxygen metabolism in man using  $^{15}\text{O}$  and positron emission tomography: theory, procedure, and normal values. *J Comput Assist Tomogr* **4**: 727–736
- Frank LR, Wong EC, Buxton RB (1997a) Slice profile effects in adiabatic inversion: application to multislice perfusion imaging. *Magn Reson Med* **38**: 558–564
- Frank LR, Wong EC, Buxton RB (1997b) Slice profile effects in adiabatic inversion: application to multi-slice perfusion imaging using pulsed arterial spin labeling. In *Proceedings of the Fifth Meeting of the International Society for Magnetic Resonance in Medicine*, Vancouver, p. 1755
- Gallichan D, Jezzard P (2008) Modeling the effects of dispersion and pulsatility of blood flow in pulsed arterial spin labeling. *Magn Reson Med* **60**: 53–63
- Garcia DM, Duhamel G, Alsop DC (2005a) Efficiency of inversion pulses for background suppressed arterial spin labeling. *Magn Reson Med* **54**: 366–372
- Garcia DM, Bazelaire CD, Alsop D (2005b) Pseudo-continuous flow driven adiabatic inversion for arterial spin labeling. *Scientific Meeting of the International Society for Magnetic Resonance in Medicine*, Miami, p. 37
- Golay X, Petersen ET, Hui F (2005) Pulsed star labeling of arterial regions (PULSAR): a robust regional perfusion technique for high field imaging. *Magn Reson Med* **53**: 15–21
- Gunther M (2006) Efficient visualization of vascular territories in the human brain by cycled arterial spin labeling MRI. *Magn Reson Med* **56**: 671–675
- Gunther M, Oshio K, Feinberg DA (2005) Single-shot 3D imaging techniques improve arterial spin labeling perfusion measurements. *Magn Reson Med* **54**: 491–498
- Hendrikse J, van der Grond J, Lu H, van Zijl PC, Golay X (2004) Flow territory mapping of the cerebral arteries with regional perfusion MRI. *Stroke* **35**: 882–887
- Hermes M, Hagemann D, Britz P, *et al.* (2007) Reproducibility of continuous arterial spin labeling perfusion MRI after 7 weeks. *MAGMA* **20**: 103–115
- Jahng GH, Song E, Zhu XP, *et al.* (2005) Human brain: reliability and reproducibility of pulsed arterial spin-labeling perfusion MR imaging. *Radiology* **234**: 909–916
- Kansagra AP, Wong EC (2008) Quantitative assessment of mixed cerebral vascular territory supply with vessel encoded arterial spin labeling MRI. *Stroke* **39**: 2980–2985
- Kim S-G (1995) Quantification of regional cerebral blood flow change by flow-sensitive alternating inversion recovery (FAIR) technique: application to functional mapping. *Magn Reson Med* **34**: 293–301
- Koziak AM, Winter J, Lee TY, Thompson RT, St. Lawrence KS (2008) Validation study of a pulsed arterial spin labeling technique by comparison to perfusion computed tomography. *Magn Reson Imaging* **26**: 543–553
- Kwong KK, Belliveau JW, Chesler DA, *et al.* (1992) Dynamic magnetic resonance imaging of human brain activity during primary sensory stimulation. *Proc Natl Acad Sci USA* **89**: 5675–5679

- Kwong KK, Chesler DA, Weisskoff RM, *et al.* (1995) MR perfusion studies with T<sub>1</sub>-weighted echo planar imaging. *Magn Reson Med* **34**: 878–887
- Leontiev O, Buxton RB (2007) Reproducibility of BOLD, perfusion, and CMRO(2) measurements with calibrated-BOLD fMRI. *Neuroimage* **35**: 175–184
- Liu TT, Brown GG (2007) Measurement of cerebral perfusion with arterial spin labeling: Part 1. Methods. *J Int Neuropsychol Soc* **13**: 517–525
- Liu TT, Wong EC (2005) A signal processing model for arterial spin labeling functional MRI. *Neuroimage* **24**: 207–215
- Liu TT, Behzadi Y, Restom K, *et al.* (2004) Caffeine alters the temporal dynamics of the visual BOLD response. *Neuroimage* **23**: 1402–1413
- Luh WM, Wong EC, Bandettini PA, Hyde JS (1999) QUIPSS II with thin-slice T<sub>1</sub>, periodic saturation: a method for improving accuracy of quantitative perfusion imaging using pulsed arterial spin labeling. *Magn Reson Med* **41**: 1246–1254
- Mani S, Pauly J, Conolly S, Meyer C, Nishimura D (1997) Background suppression with multiple inversion recovery nulling: applications to projective angiography. *Magn Reson Med* **37**: 898–905
- McLaughlin AC, Ye FQ, Pekar JJ, Santha AKS, Frank JA (1997) Effect of magnetization transfer on the measurement of cerebral blood flow using steady-state arterial spin tagging approaches: a theoretical investigation. *Magn Reson Med* **37**: 501–510
- Mildner T, Trampel R, Moller HE, *et al.* (2003) Functional perfusion imaging using continuous arterial spin labeling with separate labeling and imaging coils at 3 T. *Magn Reson Med* **49**: 791–795
- Paiva FF, Tannus A, Silva AC (2007) Measurement of cerebral perfusion territories using arterial spin labelling. *NMR Biomed* **20**: 633–642
- Paiva FF, Tannus A, Talagala SL, Silva AC (2008) Arterial spin labeling of cerebral perfusion territories using a separate labeling coil. *J Magn Reson Imaging* **27**: 970–977
- Parkes LM (2005) Quantification of cerebral perfusion using arterial spin labeling: two-compartment models. *J Magn Reson Imaging* **22**: 732–736
- Parkes LM, Rashid W, Chard DT, Tofts PS (2004) Normal cerebral perfusion measurements using arterial spin labeling: reproducibility, stability, and age and gender effects. *Magn Reson Med* **51**: 736–743
- Pekar J, Jezzard P, Roberts DA, *et al.* (1996) Perfusion imaging with compensation for asymmetric magnetization transfer effects. *Magn Reson Med* **35**: 70–79
- Perthen JE, Lansing AE, Liao J, Liu TT, Buxton RB (2008) Caffeine-induced uncoupling of cerebral blood flow and oxygen metabolism: a calibrated BOLD fMRI study. *Neuroimage* **40**: 237–247
- Petersen ET, Lim T, Golay X (2006) Model-free arterial spin labeling quantification approach for perfusion MRI. *Magn Reson Med* **55**: 219–232
- Raichle ME (1983) Brain blood flow measured with intravenous H<sub>2</sub>O-15: implementation and validation. *J Nucl Med* **24**: 790–798
- Restom K, Behzadi Y, Liu TT (2006) Physiological noise reduction for arterial spin labeling functional MRI. *Neuroimage* **31**: 1104–1115
- Silva AC, Zhang W, Williams DS, Koretsky AP (1995) Multi-slice MRI of rat brain perfusion during amphetamine stimulation using arterial spin labeling. *Magn Reson Med* **33**: 209–214
- Silva AC, Williams DS, Koretsky AP (1997) Evidence for the exchange of arterial spin-labeled water with tissue water in rat brain from diffusion-sensitized measurements of perfusion. *Magn Reson Med* **38**: 232–237
- St. Lawrence KS, Wang J (2005) Effects of the apparent transverse relaxation time on cerebral blood flow measurements obtained by arterial spin labeling. *Magn Reson Med* **53**: 425–433
- Talagala SL, Ye FQ, Ledden PJ, Chesnick S (2004) Whole-brain 3D perfusion MRI at 3.0 T using CASL with a separate labeling coil. *Magn Reson Med* **52**: 131–140
- Trampel R, Mildner T, Goerke U, *et al.* (2002) Continuous arterial spin labeling using a local magnetic field gradient coil. *Magn Reson Med* **48**: 543–546
- van Laar PJ, van der Grond J, Hendrikse J (2008) Brain perfusion territory imaging: methods and clinical applications of selective arterial spin-labeling MR imaging. *Radiology* **246**: 354–364

- Walsh EG, Minematsu K, Leppo J, Moore SC. (1994) Radioactive microsphere validation of a volume localized continuous saturation perfusion measurement. *Magn Reson Med* **31**: 147–153
- Wang J, Aguirre GK, Kimberg DY, *et al.* (2003) Arterial spin labeling perfusion fMRI with very low task frequency. *Magn Reson Med* **49**: 796–802
- Wang J, Qiu M, Constable RT (2005) In vivo method for correcting transmit/receive nonuniformities with phased array coils. *Magn Reson Med* **53**: 666–674
- Williams DS, Detre JA, Leigh JS, Koretsky AP (1992) Magnetic resonance imaging of perfusion using spin-inversion of arterial water. *Proc Natl Acad Sci USA* **89**: 212–216
- Wolf RL, Detre JA (2007) Clinical neuroimaging using arterial spin-labeled perfusion magnetic resonance imaging. *Neurotherapeutics* **4**: 346–359
- Wong EC (2007) Vessel-encoded arterial spin-labeling using pseudocontinuous tagging. *Magn Reson Med* **58**: 1086–1091
- Wong EC, Buxton RB, Frank LR (1997) Implementation of quantitative perfusion imaging techniques for functional brain mapping using pulsed arterial spin labeling. *NMR Biomed* **10**: 237–249
- Wong EC, Buxton RB, Frank LR (1998a) A theoretical and experimental comparison of continuous and pulsed arterial spin labeling techniques for quantitative perfusion imaging. *Magn Reson Med* **40**: 348–355
- Wong EC, Buxton RB, Frank LR (1998b) Quantitative imaging of perfusion using a single subtraction (QUIPSS and QUIPSS II). *Magn Reson Med* **39**: 702–708
- Wong EC, Cronin M, Wu WC, *et al.* (2006) Velocity-selective arterial spin labeling. *Magn Reson Med* **55**: 1334–1341
- Ye FQ, Matay VS, Jezzard P, *et al.* (1997) Correction for vascular artifacts in cerebral blood flow values measured by using arterial spin tagging techniques. *Magn Reson Med* **37**: 226–235
- Ye FQ, Berman KF, Ellmore T, *et al.* (2000a) H<sub>2</sub>(15)O PET validation of steady-state arterial spin tagging cerebral blood flow measurements in humans. *Magn Reson Med* **44**: 450–456
- Ye FQ, Frank JA, Weinberger DR, McLaughlin AC (2000b) Noise reduction in 3D perfusion imaging by attenuating the static signal in arterial spin tagging (ASSIST). *Magn Reson Med* **44**: 92–100
- Zhang W, Williams DS, Detre JA, Koretsky AP (1992) Measurement of brain perfusion by volume-localized NMR spectroscopy using inversion of arterial water spins: accounting for transit time and cross-relaxation. *Magn Reson Med* **25**: 362–371
- Zhang W, Williams DS, Koretsky AP (1993) Measurement of rat brain perfusion by NMR using spin labeling of arterial water: in vivo determination of the degree of spin labeling. *Magn Reson Med* **29**: 416–421



**Part**

**IIIB**

**Blood oxygenation level  
dependent imaging**



<b>The discovery of the BOLD effect</b>	<i>page</i> 341
<b>The biophysical basis of the BOLD effect</b>	342
Magnetic field distortions shorten $T_2^*$	342
Field distortions around a magnetized cylinder	348
The moderating effect of diffusion on $T_2^*$ changes	350
The intravascular contribution to the BOLD signal	352
Spin echo BOLD signal changes	353
<b>The physiological basis of the BOLD effect</b>	355
The BOLD effect depends on multiple physiological changes	355
What does the BOLD response measure?	355
The calibrated-BOLD method	357
Coupling of cerebral blood flow and $O_2$ metabolism during activation	358
<b>Optimizing BOLD image acquisition</b>	358
Magnetic field dependence	358
Image acquisition parameters	359
Motion artifacts	362
Image distortions	363

## The discovery of the BOLD effect

The previous chapters described MRI techniques for measuring cerebral blood flow (CBF) and cerebral blood volume (CBV). By introducing contrast agents or manipulating the magnetization of arterial blood before it arrives in a tissue voxel, the MR signal becomes sensitive to aspects of local tissue perfusion. Such techniques are clinically valuable for investigating disorders characterized by perfusion abnormalities, such as stroke and tumors, and these techniques have also seen limited use in investigations of normal brain function. But the fMRI technique that has created a revolution in research on the basic functions of the healthy human brain is based on an intrinsic sensitivity of the MR signal to local changes in perfusion and metabolism. When neural activity increases in a region of the brain, the local MR signal produced in that part of the brain increases by a small amount owing to changes in blood oxygenation. This blood oxygenation level dependent (BOLD) effect is the basis for most of the fMRI studies done today to map patterns of activation in the working human brain.

The BOLD effect is most pronounced on gradient recalled echo (GRE) images, indicating that the effect is primarily an increase of the local value of  $T_2^*$ . The fact that the oxygenation of the blood has a measurable effect on the MR signal from the surrounding tissue was discovered by Ogawa and co-workers (1990) imaging a rat model at 7 T. They found that the MR signal around veins decreased when the  $O_2$  content of the inspired air was reduced,

and the effect was reversed when the  $O_2$  was returned to normal values. The  $O_2$  sensitivity of the MR signal from blood was known from previous studies, which had shown that blood  $T_2$  depends strongly on the oxygenation of the hemoglobin (Thulborn *et al.* 1982). Ogawa and co-workers (1990) demonstrated an additional feature in their rat studies. They observed that the signal reductions were not just in the blood itself but also in the tissue space around the vessels, suggesting that  $T_2^*$  was reduced in both the intravascular and extravascular spaces. They proposed that this effect resulted from changes in the magnetic susceptibility of blood, similar to (but weaker than) the susceptibility changes caused by contrast agents. The important difference, however, is that this alteration of the susceptibility of blood is an intrinsic physiological effect. Shortly after this, a reduced MR signal was observed in an ischemia model and attributed to the same cause: a reduction of  $T_2^*$  with decreasing oxygenation of the blood (Turner *et al.* 1991).

These early physiological manipulations demonstrated that reductions in blood oxygenation led to a signal decrease. Kwong and co-workers (1992) demonstrated that brain activation in human subjects produced a local signal increase that could be used for functional brain mapping, and several other groups reported the same finding that year (Bandettini *et al.* 1992; Frahm *et al.* 1992; Ogawa *et al.* 1992). The discovery that activation produces a signal increase was somewhat surprising because it indicated that the  $T_2^*$  had increased, rather than decreased, suggesting that blood is more oxygenated with activation.

Earlier chapters in this book have laid the foundation for understanding how fMRI based on the BOLD effect works. The BOLD effect comes about for two reasons, one biophysical and one physiological: (1) deoxyhemoglobin produces magnetic field gradients around and through the blood vessels that decrease the MR signal, and (2) brain activation is characterized by a fall in the local  $O_2$  extraction fraction (OEF) and a corresponding fall in the local concentration of deoxyhemoglobin. The reduction in deoxyhemoglobin during activation then produces a small increase in the MR signal. The BOLD effect is widely used for mapping patterns of activation in the working human brain and has also been applied in a number of animal models. However, the interpretation of the results of these studies requires a careful consideration of the nature of the BOLD response.

In this chapter, we consider the biophysical and physiological origins of the BOLD response, and practical matters related to optimizing the detection of the BOLD signal. Chapter 15 is an introduction to the design and statistical analysis of BOLD-fMRI experiments, and in Chapter 16 we consider the challenges involved in interpreting the BOLD response.

## The biophysical basis of the BOLD effect

### Magnetic field distortions shorten $T_2^*$

The physical basis of the BOLD sensitivity of the MR signal is that deoxyhemoglobin alters the *magnetic susceptibility* of blood. The concept of magnetic susceptibility was discussed in Ch. 6. Whenever a material is placed in a magnetic field, it becomes slightly magnetized as magnetic dipoles within the material partially align with the field, and magnetic susceptibility is a measure of the resulting magnetization. Specifically, the local magnetization is proportional to the magnetic field, and the constant of proportionality is the magnetic susceptibility. The effect of this magnetization is that the field within the material is slightly shifted from the main magnetic field, and the shift is proportional to the

magnetic susceptibility. The full magnetic susceptibility of a material has several contributions: unpaired electron spins, orbital motions of electrons, and unpaired nuclear spins. The last is, of course, the magnetization we exploit in NMR to generate a signal, but the nuclear magnetization makes a negligible contribution to the total magnetic susceptibility. In paramagnetic materials, the unpaired electrons are the primary determinant of the magnetic susceptibility.

The magnetic properties of hemoglobin, and their dependence on the oxygenation state of the heme groups, has been known for some time (Pauling and Coryell 1936). Deoxyhemoglobin is paramagnetic, and when O<sub>2</sub> binds to the heme group, the paramagnetic effect is reduced. The result is that the magnetic susceptibility of blood varies linearly with the blood oxygenation (Weisskoff and Kiihne 1992). However, the susceptibility shift caused by deoxyhemoglobin is an order of magnitude smaller than the susceptibility shift produced by a standard injection of a contrast agent such as gadolinium-linked diethylenetriaminepenta-acetic acid (Gd-DTPA), and so the magnitude of the effect on the MR signal is much smaller than the effects described in Ch. 12.

When two dissimilar materials are placed next to each other, field gradients are produced as a result of the difference in magnetic susceptibility. This is commonly seen on a large spatial scale in MRI, where field gradients occur in the vicinity of bone, air, and tissue interfaces. In a non-uniform field, spins precess at different rates, and the local signals gradually become out of phase with each other. For broad gradients, with spatial scales much larger than an image voxel, such susceptibility effects show up as local phase variations in a GRE image (Fig. 14.1). In these phase maps, the sharp jumps from white to black simply reflect the fact that the phase angle is cyclic (i.e., the jump corresponds to the smooth phase increase from 359° to 0°). The field distortions vary smoothly, and the black-to-white transitions in the phase image are effectively contour lines of the field distribution. In the case of broad field gradients, the spins within a voxel precess reasonably coherently, but at a different rate from spins in another part of the brain. However, if the spatial scale of the field gradients is microscopic (smaller than an image voxel), then the net signal from the voxel is reduced through the dephasing of the spins that contribute to the voxel signal. This signal fall is described as a  $T_2^*$  effect, a reduction in the apparent transverse relaxation time measured with a GRE pulse sequence.

An imaging voxel in the brain contains blood in arteries, capillaries, and veins. Moving down the vascular tree, the deoxyhemoglobin content steadily increases, from near zero in the arteries to about 40% of the total hemoglobin concentration in the veins. Venous blood suffers the largest change in magnetic susceptibility, but capillary blood is affected as well. The presence of deoxyhemoglobin creates magnetic field gradients around the red cells and in the tissue space surrounding the vessels. These field gradients shorten  $T_2^*$  and reduce the MR signal at rest from what it would be if there were no deoxyhemoglobin present. Based on calibration studies of the BOLD effect, described in more detail in Box 14.1, the signal is reduced by approximately 8% at 1.5 T from the signal with fully oxygenated blood (Davis *et al.* 1998). Brain activation leads to a much larger increase in blood flow than O<sub>2</sub> metabolism, so the net OEF drops with activation. The capillary and venous blood is more oxygenated, and so there is less deoxyhemoglobin present in the voxel. With less deoxyhemoglobin, the susceptibility of the blood moves closer to the susceptibility of the surrounding tissue, and the field gradients are reduced. The  $T_2^*$  becomes longer, and the signal measured with a  $T_2^*$ -weighted pulse sequence increases by a small percentage.

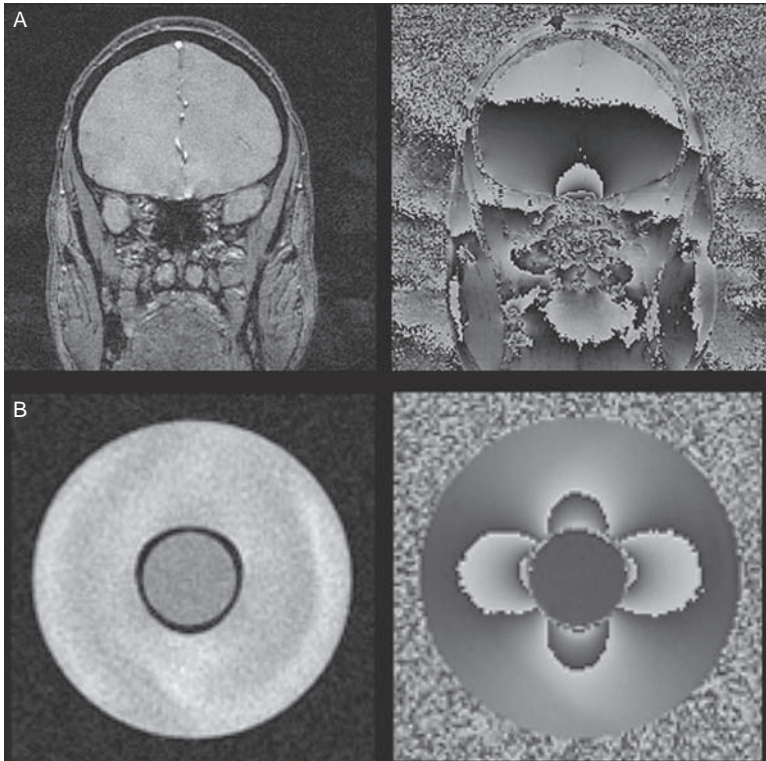


**Fig. 14.1.** Magnetic field distortions resulting from magnetic susceptibility differences. Gradient echo magnitude (left) and phase (right) images of a coronal section through the brain (A) and two concentric cylinders with different susceptibilities (B). With a gradient recalled echo acquisition, the image phase is proportional to the local magnetic field offset (the sharp transition from black to white results from the cyclic nature of the phase angle and not a jump in field offset). In the brain image, the field is distorted by the different susceptibility of the air space in the sinus cavity. The magnetized cylinder is a model for a blood vessel containing deoxyhemoglobin, showing a dipole field distortion in the surrounding space.

### Box 14.1. Modeling the BOLD signal

The BOLD effect arises when the magnetic susceptibility of blood is altered by a change in the concentration of deoxyhemoglobin, producing field gradients around the vessels and an attenuation of the MR signal. A quantitative model of this process is important for understanding the basic mechanisms of the BOLD effect, for optimizing the image acquisition technique to maximize sensitivity, and for calibrating the BOLD signal to measure local cerebral metabolic rate for  $O_2$  ( $CMRO_2$ ). In this box, we will consider the gradient echo signal only, because that is the most common technique used in fMRI and the modeling is simplified because diffusion effects are not as pronounced. The simplest model of the MR signal  $S$  involves two tissue parameters, an intrinsic local signal  $S_0$  and a transverse decay rate  $R_2^*$ :

$$S = S_0 e^{-TE R_2^*} \quad (\text{B14.1})$$

where TE is the echo time. We can further break down  $R_2^*$  into a component  $R_2^*(\text{dHb})$ , which depends on the concentration of deoxyhemoglobin in blood, and a component  $R_2^*(0)$ , which describes what the  $R_2^*$  would be if there was no deoxyhemoglobin present:

$$R_2^* = R_2^*(0) + R_2^*(\text{dHb}) \quad (\text{B14.2})$$

Note that the part of the total  $R_2^*$  that depends on deoxyhemoglobin is small, with rough typical values of about  $25 \text{ s}^{-1}$  for  $R_2^*(0)$  and  $2 \text{ s}^{-1}$  for  $R_2^*(\text{dHb})$ . For this reason we cannot use the raw baseline  $R_2^*$  as a reflection of baseline activity because  $R_2^*(0)$  is determined by other factors such as the intrinsic tissue  $T_2$  and field inhomogeneities. However, we can detect dynamic modulations of the signal with activation through changes in  $R_2^*(\text{dHb})$ .

The goal of modeling the BOLD signal is to describe the dependence of  $R_2^*(\text{dHb})$  on blood volume and blood oxygenation. This physical process has been extensively studied with Monte Carlo simulations (Boxerman *et al.* 1995a, b; Ogawa *et al.* 1993; Weisskoff *et al.* 1994), analytical calculations (Yablonsky and Haacke 1994), and experiments in model systems (Weisskoff and Kiihne 1992; Weisskoff *et al.* 1994). A useful empirical model that has grown out of these studies has a very simple dependence on blood volume  $V$  and the deoxyhemoglobin concentration in blood [dHb] (Davis *et al.* 1998):

$$R_2^*(\text{dHb}) = kV[\text{dHb}]^\beta \quad (\text{B14.3})$$

where  $k$  is a proportionality constant that depends on the magnetic field.

The exponent  $\beta$  indicates that the dependence on blood oxygenation is not necessarily a simple proportionality. For the simplest case of looking just at the extravascular signal changes around larger veins,  $\beta = 1$  would be a good approximation. In this case,  $R_2^*$  depends just on the total deoxyhemoglobin in the voxel (the product of the blood volume and the deoxyhemoglobin concentration in blood). However, this simple picture does not adequately describe two other effects. The first is diffusion of the water molecules through the field gradients around the vessels. This effect is important for the capillaries, which have a radius smaller than typical diffusion distances during an experiment. With diffusion,  $\beta > 1$ , and this is usually given as the reason for choosing  $\beta > 1$ . Based on Monte Carlo simulations, the estimated value that is typically assumed for  $\beta$  is 1.5 (Boxerman *et al.* 1995a; Davis *et al.* 1998).

However, a larger value for  $\beta$  also provides an approximate description for another important effect, the signal change of the blood itself (Buxton *et al.* 2004). At 1.5 T, a large fraction of the BOLD signal change results from the large change in the blood signal, resulting from both the increased oxygenation and the increased blood volume. To see why it is important for  $\beta$  to be  $> 1$ , imagine the special case in which the increase of blood volume and the decrease of blood deoxyhemoglobin concentration are perfectly balanced to leave the total amount of deoxyhemoglobin in the voxel unchanged. Then if  $\beta = 1$ , the model prediction would be that there is no BOLD effect because the product  $V[\text{dHb}]$  is unchanged and so  $R_2^*$  is unchanged. This constancy of the signal would be approximately correct for the extravascular signal around larger vessels, but it would not account for the increase of the intrinsic blood signal resulting from the decrease in the intravascular concentration of deoxyhemoglobin. That is, in this hypothetical scenario, the MR signal would increase even though total deoxyhemoglobin did not change, because the MR signal depends on both total deoxyhemoglobin and on the blood concentration of deoxyhemoglobin. For this reason,  $\beta > 1$  provides a better empirical description of the signal change because it captures this behavior: if the product  $V[\text{dHb}]$  stays constant, but [dHb] decreases,  $R_2^*(\text{dHb})$  will decrease if  $\beta > 1$ . A reduction of  $R_2^*(\text{dHb})$  produces a signal increase.

Consequently, Eq. (B14.3) is likely to be a better approximation than one might have thought based on the original assumptions that led to it. Although the original derivation did not include intravascular signal changes, the argument above suggests that with  $\beta = 1.5$  the model can also

describe these effects. A theoretical comparison of this model with a more complete model that includes intravascular signal changes showed that the simple form in Eq. (B14.3) is a good approximation with  $\beta = 1.5$  (Buxton *et al.* 2004; Obata *et al.* 2004).

Armed with Eq. (B14.3) as a model for the deoxyhemoglobin contribution to  $R_2^*$ , the difference  $\Delta R_2^*$  between the activated and baseline states is

$$\begin{aligned}\Delta R_2^* &= k \left( V [\text{dHb}]^\beta - V_0 [\text{dHb}]_0^\beta \right) \\ &= k V_0 [\text{dHb}]_0^\beta (v c^\beta - 1)\end{aligned}\quad (\text{B14.4})$$

where  $V_0$  and  $V$  are the venous blood volume in the baseline state and during activation, respectively, and  $v = V/V_0$  is the normalized activated blood volume. Similarly,  $c = [\text{dHb}]/[\text{dHb}]_0$  is the normalized deoxyhemoglobin concentration in blood during activation. For small signal changes, the measured fractional signal change is then

$$\frac{\Delta S}{S_0} = \frac{S - S_0}{S_0} \approx -\text{TE} \Delta R_2^* = M(1 - v c^\beta) \quad (\text{B14.5})$$

$$M = k V_0 [\text{dHb}]_0^\beta \text{TE} \quad (\text{B14.6})$$

All the parameters in the final form of Eq. (B14.5) are dimensionless. If there is no change in blood volume or deoxyhemoglobin concentration, then  $v = c = 1$ , and there is no signal change. The constant  $M$  in front lumps together several factors and describes the maximum signal change that could be observed. If blood flow increased by such an enormous amount that there is no deoxyhemoglobin left in the voxel, then  $c = 0$  and the fractional signal change is  $M$ . The parameter  $M$  plays a critical role by setting the scale of BOLD signal changes, in the sense that the same changes in blood volume and oxygenation can produce different BOLD signal changes if  $M$  differs.

Equation (B14.6) represents the biophysical side of the modeling, relating the BOLD signal to the change in blood volume and blood oxygenation. The physiological side of the modeling involves relating the change in blood oxygenation to the changes in  $\text{CMRO}_2$  and CBF. The former can always be written in terms of the local CBF and the net OEF ( $E$ ) the fraction of  $\text{O}_2$  delivered to the capillary bed by arterial flow that is consumed by metabolism in the tissue:

$$\text{CMRO}_2 = E \text{CBF}[\text{O}_2]_{\text{art}} \quad (\text{B14.7})$$

where  $[\text{O}_2]_{\text{art}}$  is the arterial concentration of  $\text{O}_2$ . At this point, it is useful to normalize  $\text{CMRO}_2$  and CBF to their values at baseline (as we already did with blood volume  $v$ ), with  $m = \text{CMRO}_2(\text{activation})/\text{CMRO}_2(\text{baseline})$  and  $f = \text{CBF}(\text{activation})/\text{CBF}(\text{baseline})$ . Then the normalized CBF and  $\text{CMRO}_2$  ratios are related to OEF with activation ( $E$ ) and at baseline ( $E_0$ ) by

$$\frac{E}{E_0} = \frac{m}{f} \quad (\text{B14.8})$$

Nearly all of the  $\text{O}_2$  in blood is carried bound to hemoglobin, and assuming that arterial blood is fully saturated, the deoxyhemoglobin concentration in venous blood is  $E[\text{Hb}]$ , where  $[\text{Hb}]$  is the equivalent hemoglobin concentration in blood (equivalent here means that  $[\text{Hb}]$  is the concentration of  $\text{O}_2$  when hemoglobin is fully saturated with four  $\text{O}_2$  molecules per hemoglobin molecule). The deoxyhemoglobin ratio then is  $c = E/E_0$ . Combining this with Eq. (B14.5), the BOLD signal expressed in terms of the local normalized changes in blood volume  $v$ , blood flow  $f$ , and  $\text{O}_2$  metabolism  $m$ , is

$$\frac{\Delta S}{S_0} = M \left[ 1 - v \left( \frac{m}{f} \right)^\beta \right] \quad (\text{B14.9})$$



Equation (B14.9) is the *Davis model*, with the parameter  $\beta = 1.5$  (Davis *et al.* 1998). The parameter  $M$  can be expressed in terms related to the baseline state through Eqs. (B14.6) and (B14.8) as

$$M = k \text{ TE } V_0 (E_0 [\text{Hb}])^\beta \quad (\text{B14.10})$$

Note that  $M$  depends on magnetic field strength through the parameter  $k$ , the pulse sequence used through TE, and the baseline physiological state through the baseline blood volume, the baseline OEF, and the hemoglobin concentration in the subject's blood. A useful way to think about  $M$  is that it represents the amount of deoxyhemoglobin present in the baseline state, and so sets the scale of any BOLD response from that baseline state.

Equation (B14.9) offers a way to estimate local CMRO<sub>2</sub> from the BOLD signal change, if  $f$ ,  $v$ , and  $M$  can be determined independently (Davis *et al.* 1998). The blood flow change  $f$  can be measured with arterial spin labeling (ASL) methods (Ch. 13). The blood volume change  $v$  is more difficult to determine directly, although it can be measured with contrast agents in animal studies (Mandeville *et al.* 1998). Instead, the usual procedure is to assume that  $v$  is tightly coupled to the flow change, with  $v = f^\alpha$ . The value usually assumed is  $\alpha = 0.4$  based on early, whole-brain measurements in monkeys (Grubb *et al.* 1974). It is not known how variable  $\alpha$  is in the human brain. With this assumption the BOLD signal model can be written as

$$\frac{\Delta S}{S_0} = M [1 - f^{\alpha - \beta} m^\beta] \quad (\text{B14.11})$$

The central idea of the *calibrated-BOLD* method is that if the local value of the scaling parameter  $M$  can be measured, then a combined measurement of the BOLD response ( $\Delta S/S_0$ ) and the CBF response ( $f$ ) to activation would make it possible to calculate the CMRO<sub>2</sub> response ( $m$ ) from Eq. (B14.11).

To measure  $M$ , and thus calibrate the BOLD effect, a CO<sub>2</sub> inhalation (hypercapnia) experiment is performed, measuring both the local BOLD change and the local CBF change with ASL. Breathing CO<sub>2</sub> elevates CBF throughout the brain, but for mild levels of hypercapnia is thought to leave CMRO<sub>2</sub> unchanged. For this experiment, then,  $m = 1$ , and from the measured BOLD change and the measured flow change,  $M$  can be estimated locally using Eq. (B14.11). Following the calibration experiment, an activation study is performed, again measuring both the BOLD change and the flow change. From these measurements and the map of  $M$  from the CO<sub>2</sub> experiment, the CMRO<sub>2</sub> change during activation can be calculated. If CMRO<sub>2</sub> increases with activation ( $m > 1$ ), then for the same change in CBF, the BOLD change should be larger for the CO<sub>2</sub> experiment than for the activation experiment because the increased CMRO<sub>2</sub> and the corresponding increased rate of production of deoxyhemoglobin partially offsets the dilution of deoxyhemoglobin by the large flow increase.

Finally, it is useful in thinking about the BOLD response to consider the ratio of the fractional change in CBF to the fractional change in CMRO<sub>2</sub>, because this ratio  $n$  defines the mismatch of CBF and CMRO<sub>2</sub> that leads to the BOLD response, as described in the main text. However, in formulating the Davis model in Eq. (B14.11), it was more convenient to use the full activated values, normalized to their values at rest, rather than the fractional change values. In terms of these normalized values,

$$n = \frac{f - 1}{m - 1} \quad (\text{B14.12})$$

The BOLD response then can be viewed as being driven by the change in CBF through Eq. (B14.11), but modulated by the local values of  $M$  and  $n$ .

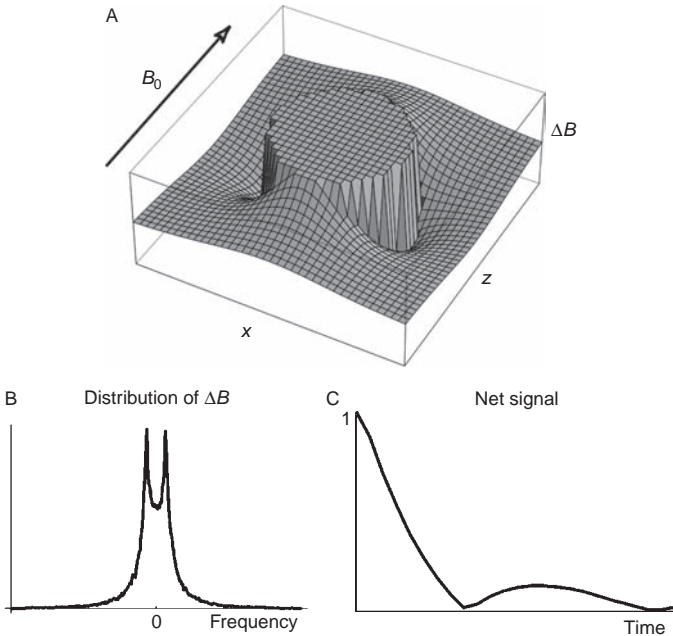


**Fig. 14.2.** Field distortions around a magnetized blood vessel. (A) A single magnetized cylinder oriented perpendicularly to the magnetic field  $B_0$  creates field offsets ( $\Delta B$ ) in the surrounding space, with the field increased along the main field axis and decreased along a perpendicular axis. (B) The distribution of fields creates a resonant frequency spectrum with two peaks. (C) The Fourier transform of the frequency spectrum shows how the net signal evolves in time. (See plate section for color version.)

## Field distortions around a magnetized cylinder

To see more precisely how this  $T_2^*$  effect on the extravascular spins comes about, consider the simplified picture of a long cylinder surrounded by a medium with a different magnetic susceptibility, a model for a capillary or vein containing deoxyhemoglobin. If the capillary is oriented perpendicularly to the magnetic field, the  $z$ -component of the magnetic field is distorted, as shown in the cross-sectional view image in Fig. 14.1. The field pattern has a dipole shape, with opposite field offsets along the main field direction and perpendicular to the main field. An important feature of this pattern is that the magnitude of the field offset at the surface of the cylinder depends only on the susceptibility difference and not on the radius of the cylinder, whereas the spatial extent of the field distortion is proportional to the radius. Figure 14.2 shows the histogram of field offsets within a range of four times the vessel radius (calculated by simply sampling many random points around the vessel). We can think of the net signal from this volume as the signal measured in a single voxel. Because the rate of precession of each of the spin groups within the box is directly proportional to the field offset, this histogram is also the NMR spectrum that would be measured, and the net signal as a function of time  $A(t)$  is simply the Fourier transform of this histogram. For simplicity, we neglect the true  $T_2$  decay, so  $A(t)$  represents the additional attenuation of the signal caused by the difference in magnetic susceptibility between the vessel and the surrounding space.

The decay curve shown in Fig. 14.2 is not a simple exponential because the distribution of field offsets has a rather irregular shape. However, this simple model is for one vessel oriented perpendicularly to the magnetic field. A better model for a voxel containing many vessels is a collection of randomly oriented cylinders. When the same cylinder is tipped at an angle to the field, the same basic pattern of field offsets results but with a decreased range. Indeed, for a cylinder parallel to the field, there is no field offset outside (the range is compressed to zero). For a collection of randomly oriented cylinders, the field distribution and attenuation curves

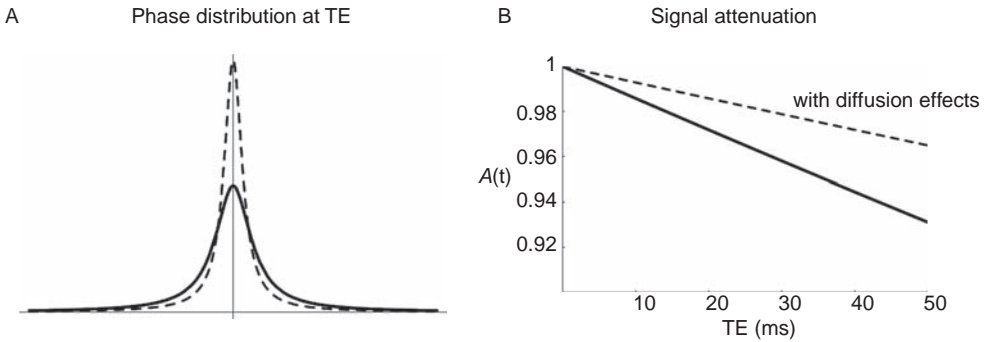


**Fig. 14.3.** The net effect of many randomly oriented magnetized blood vessels on the gradient recalled echo signal. (A) With many cylinders, the distribution of fields has only a single peak. (B) This produces an approximately exponential decay of the signal. When diffusion effects are included, the signal is no longer the Fourier transform of the field distribution, but for any echo time TE the signal attenuation  $A$  is the Fourier transform of the local *phase* distribution. Without diffusion, the phase distribution is identical to the field distribution. But with diffusion effects (dashed line), the phase distribution at any time point is narrower because the motion of the spins effectively averages over the field distribution.

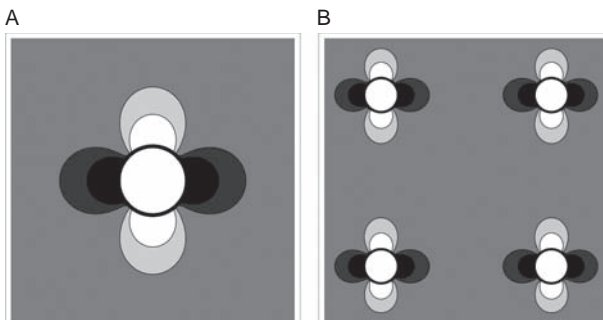


**Fig. 14.4.** The spectrum of field offsets depends primarily on the total volume of the blood vessels containing deoxyhemoglobin. The magnetic field of a magnetized cylinder falls off inversely with the square of distance. A single large vessel creates a larger pattern of field offsets (A) than a smaller vessel (B), but the magnitude of the field offset at the surface of the cylinder is the same. For this reason, the pattern of vessels in (B), with the same total blood volume, affects the same volume of spins as the single vessel in (A). So when diffusion effects are negligible, the BOLD effect is proportional to the local venous blood volume.

are shown in Fig. 14.3. In this more realistic case, the attenuation is closer to exponential, and we can write this attenuation as

$$A(t) = e^{-t \Delta R_2^*} \quad (14.1)$$

where  $\Delta R_2^*$  is the change in the transverse relaxation rate  $R_2^*$  ( $= 1/T_2^*$ ) resulting from the magnetic susceptibility difference between the blood and the surrounding tissue.

To a first approximation,  $\Delta R_2^*$  depends simply on the total venous volume of the vessels within the voxel, and not on the size of the vessels. (This conclusion will be modified when we consider the effects of diffusion next.) The reason for this is shown graphically in Fig. 14.4. Figure 14.4A shows a single large vessel within the box, and Fig. 14.4B shows four cylinders with half the radius but the same total blood volume. The extent of the field distortions is scaled down in proportion to the radius for each of the smaller vessels, but the total volume affected remains the same. So the spectrum of field offsets depends just on the total blood volume and not on the vessel size. If there is no motion of the spins during the experiment, then the net signal is simply the Fourier transform of this spectrum.

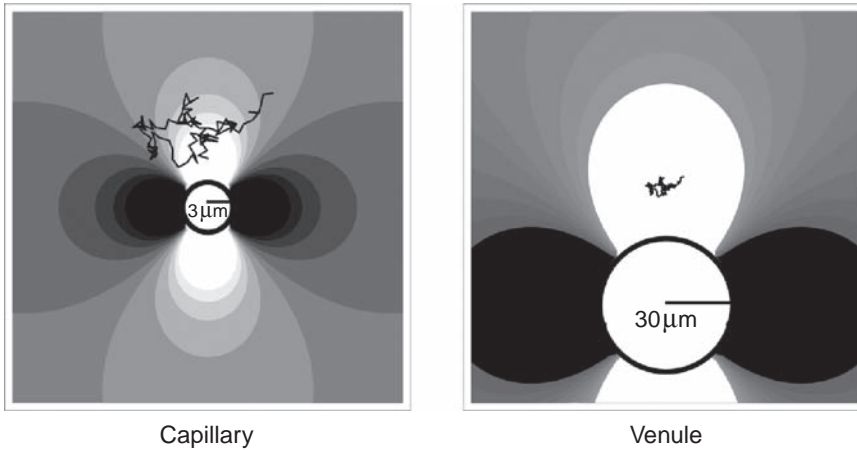


**Fig. 14.5.** Diffusion produces an averaging over field offsets that is more effective for the smallest vessels. The random walk of a diffusing water molecule is shown as a wiggly black line overlaid on the field distortion pattern around a capillary (radius  $3\ \mu\text{m}$ ) and a venule (radius  $30\ \mu\text{m}$ ). A molecule diffusing around a capillary will experience a larger range of field offsets, and the net phase will reflect the average of these fields. This averaging reduces the phase dispersion of all the diffusing spins. In contrast, a molecule diffusing near a larger venule or vein experiences a more constant field, and the phase dispersion among spins then reflects the full distribution of magnetic field offsets. The signal attenuation is greater around the venous vessels.

## The moderating effect of diffusion on $T_2^*$ changes

The argument presented in the previous section, that the extravascular signal attenuation depends only on total blood volume and is independent of the size of the vessels holding that blood, is not strictly true because of the effects of diffusion (Ch. 8). As a water molecule randomly moves through spatially varying fields, the precession rate of the nuclei is always proportional to the current value of the field, so the precession rate for each spin will vary randomly (Fig. 14.5). Because the precession rate is not constant, the attenuation is not simply the Fourier transform of the distribution of field offsets. Instead, one must follow each spin as it randomly diffuses, adjusting its precession rate as it moves to a region with a different field offset, and then adding up the net signal from each spin with its acquired phase offset. Numerical analyses of just this sort (Monte Carlo simulations) have been done to explore these effects of diffusion, and the results are in good agreement with analytical calculations and experiments in model systems with small field perturbers (Boxerman *et al.* 1995a; Fisel *et al.* 1991; Ogawa *et al.* 1993; Weisskoff *et al.* 1994; Yablonsky and Haacke 1994).

The effect of these motions created by diffusion is an averaging of the field offset felt by any one spin, resulting in a reduced phase dispersion (Fig. 14.3). It is really this dispersion of phases after the spins have evolved for an echo time TE that determines the attenuation at TE. One can think of this as plotting the histogram of phase offsets at TE, and then adding up vectors with these phase offsets to produce a net signal. In the absence of diffusion, each spin sits in the same location, with its phase evolving at a rate proportional to the local field offset. For this case, the distribution of phases is simply proportional to the distribution of field offsets. But if the spins move during the experiment and sample different field offsets, the net phase at TE reflects the past history of motions of each spin. In the extreme case of very rapid diffusion, each spin feels all of the field offsets, and so each has a similar history. But if all of

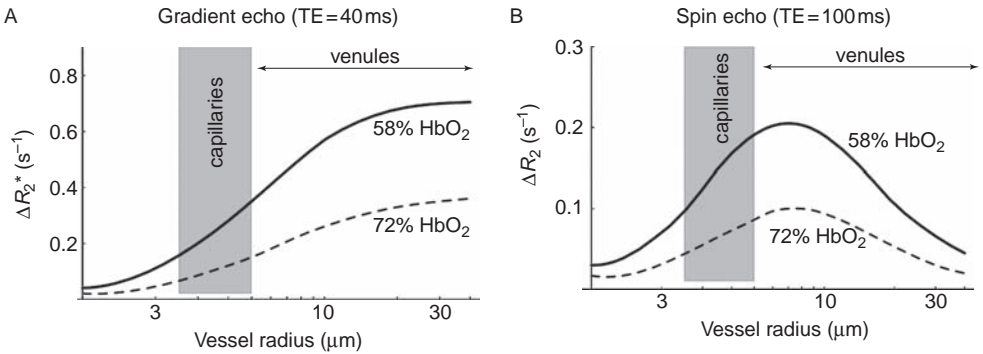


**Fig. 14.6.** Calculated curves of the change in the extravascular transverse relaxation rate at 1.5T as a function of vessel size. Curves are shown for two levels of hemoglobin O<sub>2</sub> saturation (HbO<sub>2</sub>) for the gradient recalled echo (GRE) signal (A) and the spin echo (SE) signal (B). The two curves correspond approximately to the oxygenation of venous blood at rest (solid line) and during strong activation (dashed line). For the GRE signal, diffusion effects around the smallest vessels reduce the BOLD effect. For the SE signal, the BOLD effect is largest for the capillaries and smaller venules. Note that the vertical scale is three times larger for the GRE effect, reflecting the weakness of the extravascular SE-BOLD effect. (Adapted from Weisskoff 1999.)

the spins are experiencing the same range of field offsets, then there will be very little phase dispersion and so very little attenuation, and it appears as if the range of field offsets has narrowed (Fig. 14.3). In short, any diffusion of the water molecules will reduce the GRE-BOLD effect.

The magnitude of the diffusion effect on the signal depends on how far a water molecule diffuses during the experiment, and how this distance compares with the spatial scale of the field variations (Fig. 14.5). As described in Ch. 8, the “average” displacement of a water molecule with diffusion coefficient  $D$  during a time interval  $T$  is given by  $\Delta x^2 = 2DT$ . This is the size of the expected displacement along any spatial axis, so the full displacement in space is  $\Delta x^2 + \Delta y^2 + \Delta z^2 = 6DT$ . For considering the diffusion effects around long magnetized blood vessels, displacement along the length of the vessel does not alter the field offset, and so these displacements do not affect the relaxation rate. For this reason, we can take as a typical diffusion distance the expected displacement in a cross-sectional plane,  $4DT$ . A typical TE in a GRE-BOLD experiment is 40 ms. In the brain, with a water diffusion coefficient of approximately  $1 \mu\text{m}^2/\text{ms}$ , the typical distance moved is then about 13  $\mu\text{m}$ . This distance is larger than the radius of a capillary, comparable to the radius of smaller venules, and smaller than the radius of a small vein. The variation of  $\Delta R_2^*$  with vessel size is shown in Fig. 14.6A. If the vessel is a larger venule or vein, so the typical distance moved by a molecule through diffusion is much smaller than the radius of the vessel, there will be little variation in the field offset felt by the spin. In this case, the GRE-BOLD effect is large, and the attenuation factor is simply the Fourier transform of the distribution of field offsets. By comparison, for capillaries, the distance moved is larger than the radius of the vessel, and  $\Delta R_2^*$  is reduced by the averaging caused by diffusion. For a gradient echo signal, the attenuation varies smoothly between these two extremes.

Figure 14.7A shows calculated curves for the attenuation of the GRE-BOLD extravascular signal around capillaries and veins as a function of the O<sub>2</sub> saturation of the hemoglobin. The two curves are based on the numerical simulations of Ogawa *et al.* (1993) for the same total blood volume (2%) and for a magnetic field strength of 1.5T. For the same level of O<sub>2</sub>

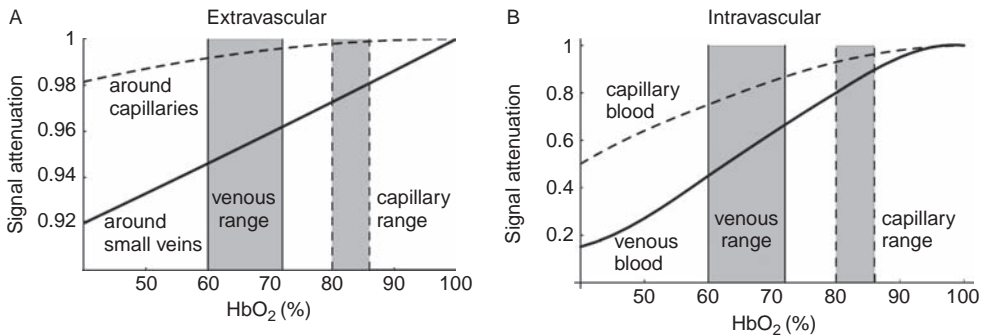


**Fig. 14.7.** Extravascular and intravascular components of the gradient recalled echo (GRE) BOLD signal change. The signal change of the extravascular (A) and intravascular (B) signals are plotted as a function of the O<sub>2</sub> saturation of hemoglobin (HbO<sub>2</sub>). In each plot, the bars indicate the range of variation of the venous and capillary oxygenation between rest and activated states (taking the average capillary saturation to be the average of the arterial and venous saturations). Signal is plotted as the attenuation from the signal with fully oxygenated blood. The signal changes in blood itself are more than an order of magnitude larger than the extravascular signal changes; consequently, despite the low volume fraction occupied by blood, the intravascular and extravascular contributions to the BOLD signal at 1.5 T are comparable. At higher fields, the blood contribution diminishes. (Extravascular curves are calculated from the results of Ogawa *et al.* [1993]; the intravascular curves are adapted from Boxerman *et al.* [1995b].)

saturation of the hemoglobin, the attenuation around veins is typically about five times larger than the attenuation around capillaries because of the effect of diffusion. Furthermore, hemoglobin is significantly less saturated in the veins than in the capillaries. At rest, the venous oxygenation in the brain is about 60%, corresponding to a typical OEF of 40%. With activation, the venous hemoglobin saturation can increase to more than 70%. For the capillaries, the changes are less dramatic. Assuming that the average capillary hemoglobin saturation is midway between the arterial and venous saturation levels, the same range of variation of the saturation from the resting state to the activated state is only 80–85%. It is clear that the extravascular BOLD effect is dominated by the venous side of the vasculature, resulting from both the reduced range of variation of the hemoglobin saturation in capillaries and the moderating action of diffusion on the BOLD effect around capillaries. In short, GRE-BOLD experiments are primarily sensitive to the veins, and because the veins are large compared with a typical diffusion distance, diffusion effects are small.

## The intravascular contribution to the BOLD signal

The intravascular compartment is a small fraction of the total tissue volume (only approximately 4%), and so it is tempting to suppose that the intravascular spins would contribute a comparably small amount to the net BOLD signal change. In fact, the vascular contribution is comparable to the extravascular contribution at 1.5 T (Boxerman *et al.* 1995b). The reason for this is that the intrinsic signal change in the blood is more than an order of magnitude larger than the extravascular signal change (Fig. 14.7). Within the blood, large field gradients are produced around the red blood cells carrying the deoxyhemoglobin (Thulborn *et al.* 1982); consequently, at rest, the venous blood signal may be reduced by as much as 50% compared with what it would be if the blood were fully oxygenated (Boxerman *et al.* 1995b). This provides a much wider dynamic range for the intravascular signal change, and even though the blood occupies a small fraction of the volume, the absolute intravascular signal change is comparable to the extravascular signal change at 1.5 T.

The intravascular contribution to the BOLD signal can be measured by performing a BOLD experiment with and without bipolar gradient pulses added to the sequence. A bipolar gradient pulse is simply two matched gradient pulses with the same amplitude and duration, but opposite sign. Such pulses are commonly used to add diffusion weighting to the signal because a bipolar gradient adds sensitivity to motion (Ch. 8). With a bipolar gradient pulse, each spin acquires a phase offset proportional to the distance it moves between the two pulses. The random motions from diffusion create a spread of phases and an attenuation of the signal. For smaller vessels within a voxel, the uniform motion of the blood, but in randomly oriented vessels, produces a dephasing effect similar to diffusion. However, the distances moved by flowing blood are much greater than the displacements from diffusion, so the blood signal can be destroyed with only modest diffusion weighting (although fully suppressing the signal of the slow-moving capillary blood does require significant gradient strength). So by adding a bipolar gradient pulse, most of the signal of flowing blood can be selectively suppressed with only a small effect on the extravascular signal.

Experiments comparing the BOLD signal with and without diffusion weighting have confirmed that at lower fields (1.5–3 T) a significant fraction of the BOLD signal is reduced with diffusion weighting. Boxerman and co-workers (1995a) found that about 70% of the signal could be eliminated with a large degree of diffusion weighting. At 3 T, even a much more modest level of diffusion weighting reduced the BOLD signal by about 35% (Buxton *et al.* 1998). These data confirm that at field strengths of 1.5–3 T a substantial fraction of the GRE signal change is intravascular.

In these sections, we have tried to dissect the BOLD effect into small-vessel and large-vessel effects, and into separate contributions from extravascular and intravascular signal changes. For practical applications, however, it is useful to combine these different sources of the BOLD effect into one empirical relationship that describes the total BOLD signal change as a function of blood volume and blood oxygenation. This relation is derived in Box 14.1 for the GRE-BOLD signal (Davis *et al.* 1998). Using such a relationship we can model how the physiological changes in CBF, CBV, and cerebral metabolic rate of O<sub>2</sub> (CMRO<sub>2</sub>) combine to produce a BOLD signal change.

## Spin echo BOLD signal changes

With a spin echo (SE) pulse sequence, the 180° radiofrequency (RF) pulse refocuses the phase offsets caused by precession in an inhomogeneous field, so at first glance it might appear that there should be no BOLD effect with SE imaging. However, an SE works only if the spins remain in the same field throughout the experiment. Phase offsets acquired during the first half of the TE are reversed by the 180° pulse, and the same phase offset acquired in the second half of the TE then precisely cancels the phase from the first half. But because of diffusion, each water molecule wanders randomly during the course of the experiment. If the spatial scale of the field inhomogeneities is smaller than the typical distance moved by a water molecule, then the spins are in different fields (and precessing at different rates) during the first and second half of the experiment. The SE does not refocus the phase offsets completely, and the remaining phase dispersion will produce a reduction in the net signal. As with the GRE signal, we can write this additional attenuation of the SE signal from deoxyhemoglobin in the vessels as

$$A(t) = e^{-t \Delta R_2} \quad (14.2)$$

where  $\Delta R_2$  is the change in the transverse relaxation rate  $R_2$  ( $= 1/T_2$ ). Because of the partial refocusing effect of the SE,  $\Delta R_2$  is always less than  $\Delta R_2^*$ , and so the SE-BOLD effect is always weaker than the GRE-BOLD effect.

In a typical SE-BOLD experiment, TE is longer than in a GRE-BOLD experiment (e.g., TE is 100 ms compared with 40 ms) to maximize the signal change resulting from a small change in  $R_2$ . The change in  $\Delta R_2$  in an SE experiment is plotted in Fig. 14.6B. Not only are the changes in  $R_2$  much smaller than the changes in  $R_2^*$ , but the dependence on vessel size is also quite different. For the larger vessels, diffusion effects are negligible, so the SE efficiently refocuses the field offsets that produce a large GRE-BOLD effect. The change in  $R_2$  is minimal, so the SE-BOLD effect is negligible. As we move to smaller vessels, diffusion makes the SE less effective at refocusing the phase dispersion from field offsets, and  $\Delta R_2$  becomes larger. However, the SE-BOLD effect peaks for a vessel radius around  $7\ \mu\text{m}$  in these calculations and diminishes for smaller vessels. In this situation, the SE does a poor job of refocusing, but the extensive field averaging by diffusion narrows the range of phase offsets and reduces  $\Delta R_2$  just as it reduces  $\Delta R_2^*$ .

Because of this sensitivity to vessel size, SE-BOLD is more selective for the smallest vessels: the capillaries and small venules. This has been a primary motivation for using SE-BOLD for brain mapping despite the lower sensitivity, based on the assumption that the SE signal changes would map more tightly to the capillary bed than to draining veins. In other words, the SE pulse sequence trades sensitivity for increased specificity. In practice, an asymmetric SE sequence often is used (Ch. 7). An ASE sequence is intermediate between a GRE and an SE pulse sequence in its sensitivity to local field offsets.

However, the argument for the greater selectivity of the SE technique is based on considerations of the extravascular signal change. As with the GRE technique, the total BOLD effect has a strong contribution from the intravascular compartment. Theoretical studies suggest that with an SE method the BOLD effect is strongly dominated by intravascular signal changes at 1.5 T (Oja *et al.* 1999; van Zijl *et al.* 1998). In addition, because the venous blood exhibits the largest signal change with decreasing deoxyhemoglobin, the largest SE-BOLD changes are in the veins as well. This implies that SE-BOLD may be more sensitive to draining veins than GRE-BOLD, where the extravascular and intravascular contributions are closer to being equal. In other words, although the extravascular SE-BOLD signal change is likely to be more sensitive to the capillary changes, at lower fields this weak signal change is swamped by the much larger signal change in the veins. To regain the capillary selectivity, one could apply spoiler gradients to destroy the intrinsic signal of the veins. However, this would reduce an already weak signal even further, and so in practice the method would be very insensitive.

At higher fields (7 T and higher), the blood signal is naturally reduced because the  $T_2$  of blood shortens with increasing field. The reduced blood signal, combined with the increased signal to noise ratio (SNR) at high field, makes SE imaging a desirable technique at high field (Yacoub *et al.* 2003). In short, although early studies of SE-BOLD indicated a greater selectivity for the capillary bed compared with draining veins, this selectivity requires high magnetic field strengths where the signal from blood is suppressed. One estimate is that if the TE used is equal to the tissue  $T_2$ , the fractional contribution of the venous blood signal change itself to the net SE-BOLD signal change is 60% at 1.5 T, 8% at 4.7 T, and 1% at 9.4 T (Lee *et al.* 1999).



## The physiological basis of the BOLD effect

### The BOLD effect depends on multiple physiological changes

The BOLD effect is not a direct measure of neural activity but rather depends on the blood flow and energy metabolism changes that accompany neural activity. In this sense BOLD-fMRI is similar to PET techniques, measuring indirect effects of neural activity. However, positron emission tomography (PET) techniques at least have the advantage of measuring well-defined physiological quantities such as CBF, the cerebral metabolic rate of glucose (CMRGlc), CMRO<sub>2</sub>, or CBV. All these quantities increase with activation, as described in Chs. 1 and 2. However, the BOLD effect is not a simple reflection of any one of these physiological changes, because changes in CBF, CMRO<sub>2</sub>, and venous CBV all affect the local deoxyhemoglobin content.

Furthermore, the complexity of the BOLD response is not just that it depends on the changes in several physiological parameters, but also that the expected changes in these parameters with activation have conflicting effects on the resulting BOLD signal. With activation, CBF increases dramatically, CBV increases moderately, and CMRO<sub>2</sub> increases by a much smaller amount (Chs. 1 and 2). The increase of CBF produces a positive BOLD response, but the increase of CMRO<sub>2</sub> partly counteracts this, tending to produce a negative BOLD response. With a large CBF change, the resulting drop in the OEF tends to increase the MR signal, whereas an increase of venous CBV tends to decrease the MR signal. In the adult brain, the oxygenation change overwhelms the volume change, and the result is a positive BOLD effect (an increase of the MR signal). In addition, this complexity of the BOLD response may account for some of the observed transient features of the response, if the time courses for the changes in CBF, CMRO<sub>2</sub>, and CBV are not the same (discussed further in Ch. 16).

### What does the BOLD response measure?

Based on the discussion above, it is clear that the BOLD response is a complex phenomenon, and it is important to try to understand exactly what is being measured. To put the question another way: If two regions have the same neural activity change, what could make the BOLD response different? An instructive way to think about the BOLD response is in terms of the *Davis model*, an early mathematical model that still is widely used (Davis *et al.* 1998). The derivation and justification for the model are discussed in Box 14.1, but the key implications can be understood rather simply. In this picture, the BOLD response associated with brain activation depends on three physiological factors: (1) the CBF response ( $f$ ) expressed as the CBF during activation normalized to the CBF in the baseline state; (2) the ratio  $n$  of the fractional change in CBF to the fractional change in CMRO<sub>2</sub>; and (3) a local scaling factor  $M$  that depends on the amount of deoxyhemoglobin present in the baseline state.

We can think of the BOLD response as primarily reflecting the flow change but strongly modulated by the other two factors. The factor  $n$  is important because it is the mismatch of CBF and CMRO<sub>2</sub> changes with activation that lead to local changes in deoxyhemoglobin, and  $n$  describes this mismatch. For example, if CBF increases by 20% but CMRO<sub>2</sub> increases by only 10%, then  $n = 2$ . Another way to think about  $n$  is that it describes how the OEF changes with activation. If  $n = 1$  there is no change in OEF with activation, because the ratio of CBF to CMRO<sub>2</sub> stays the same, but for  $n > 1$  there is a fall in the OEF with activation. The factor  $n$

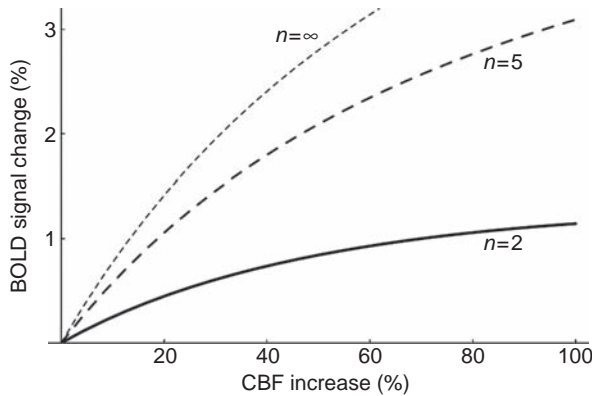


**Fig. 14.8.** Theoretical curves of the gradient recalled echo BOLD signal as a function of the change in cerebral blood flow (CBF). Curves were calculated from the model in Box 14.1. All curves assume that the blood volume varies as  $f^\alpha$  where  $f$  is the normalized CBF and the exponent  $\alpha$  is 0.4. All curves also assume that the change in the cerebral metabolic rate of  $O_2$  (CMRO<sub>2</sub>) is coupled to the CBF change. For simplicity, this is expressed in terms of  $n$ , the ratio of the fractional change in CBF to the fractional change in CMRO<sub>2</sub> (e.g., if  $n=2$ , then a 40% change in CBF is accompanied by a 20% change in CMRO<sub>2</sub>). The curve for  $n=2$  corresponds to the calibrated BOLD data of Hoge *et al.* (1999); the curve for  $n=5$  corresponds approximately to the original PET data of Fox and Raichle (1986); and the curve for  $n=\infty$  corresponds to the case when there is no change in CMRO<sub>2</sub>, which occurs when breathing CO<sub>2</sub>.

thus describes the essentially conflicting roles of CBF and CMRO<sub>2</sub> changes with activation in terms of their effect on the BOLD signal. Increased CBF tends to increase the BOLD signal, while increased CMRO<sub>2</sub> tends to decrease the BOLD signal. In short, for the same CBF change, a larger value of  $n$  will lead to a larger BOLD response (Fig. 14.8).

The parameter  $M$  also is important because it characterizes the maximum BOLD response that could occur in a brain region. Because the BOLD response is driven by a reduction of deoxyhemoglobin, there is a ceiling on how large the BOLD response can be, corresponding to complete elimination of deoxyhemoglobin. That ceiling is set by  $M$ , so  $M$  is typically expressed as a fraction. A typical value is 8%, meaning that the maximum possible BOLD signal change is 8%. However, the exact value of  $M$  depends on field strength, the pulse sequence, and the local physiology (Box 14.1).

We can visualize the effects of  $M$  and  $n$  on the BOLD response by plotting the BOLD response as a function of the CBF response  $f$ , as in Fig. 14.8. The BOLD response increases as the CBF response increases, but tends toward a plateau because of the BOLD ceiling effect. The factor  $M$  directly scales this curve, so that if the fractional CBF change is identical in two regions, but  $M$  differs by a factor of two, the BOLD response will be twice as large in the region with higher  $M$ . The factor  $n$  affects the BOLD response in a less linear way. The BOLD response for the same change in CBF increases as  $n$  grows larger, but once  $n$  is larger than 5 or so it makes little difference. The reason is that the CMRO<sub>2</sub> increase tends to counteract the effect of the CBF increase, and so if this is small it has little effect. For this reason, the BOLD signal is most sensitive to the exact value of  $n$  when  $n < 3$ . As described below, a number of studies have found  $n$  values of around 2, so in this situation the magnitude of the BOLD response is sensitive to the exact value of  $n$ .

Based on this description, we cannot think of the BOLD response as a simple reflection of CBF changes because of the strong effects of  $M$  and  $n$ . An important complexity of the BOLD response from this picture is the dependence on the baseline state. It is not the absolute CBF

change, but rather the fractional CBF change that matters in determining the BOLD response. In addition, the parameter  $M$  depends directly on the baseline blood volume and  $O_2$  extraction. For this reason, any change in the baseline physiological state could affect the magnitude of the BOLD response. Medications, caffeine, disease processes, and even the anxiety level of the subject can all potentially alter the baseline state. We will return to this issue in [Ch. 16](#) in the context of recent studies.

## The calibrated-BOLD method

In the early thinking about the BOLD effect it was common to neglect the  $CMRO_2$  change associated with activation. This was in part because in Fox and Raichle's seminal work (1986) discovering the mismatch between CBF and  $CMRO_2$  changes, the ratio of the two changes ( $n$ , in our current terminology) was approximately 6. Although the  $CMRO_2$  change was statistically significant, it was quite small, and when  $n$  is that large the  $CMRO_2$  change does indeed have a negligible effect on the BOLD signal. If that result is general for other parts of the brain and activation tasks, then the BOLD response could be viewed as simply a surrogate for the CBF response.

However, Davis and colleagues (1998) directly challenged this view in an influential paper. They combined ASL and BOLD techniques to examine the relationship between BOLD and CBF responses to activation. Their innovation was to compare these two responses to brain activation with the same responses in the same part of the brain to a physiological stimulus: breathing  $CO_2$ . Breathing a gas mixture with 5% added  $CO_2$  increases the partial pressure of  $CO_2$  of the arterial blood (hypercapnia), and this causes a sharp increase in CBF ([Ch. 2](#)). However, it is thought that mild hypercapnia has no effect on  $CMRO_2$ , so this is a pure CBF change. The interesting finding was that, for the same CBF response, the BOLD response was substantially weaker in the activation experiment than in the hypercapnia experiment. This is consistent with the idea that  $CMRO_2$  increases with activation, and by such a significant amount that it counteracts part of the CBF effect on the BOLD response.

Davis and colleagues (1998) then proposed that this sensitivity of the BOLD signal to the change in  $CMRO_2$  could be exploited to measure the  $CMRO_2$  response to activation ([Box 14.1](#)). The essential idea was to exploit the fact that the ASL signal depended just on CBF, while the BOLD signal depended on both the CBF and  $CMRO_2$  changes. With an appropriate mathematical model for how the BOLD signal depended on these changes, the  $CMRO_2$  change could be calculated. The trick in doing this, however, is that there is an unknown calibration factor ( $M$ , the scaling factor introduced above) in the Davis model that must first be measured. With the assumption that mild hypercapnia does not change  $CMRO_2$ , the factor  $M$  can be calculated from the  $CO_2$  experiment and then applied to the measured activation data. In short, the calibrated-BOLD approach requires four measurements: ASL and BOLD responses to activation and to hypercapnia. From these measurements, the  $CMRO_2$  change can be calculated, and from this the ratio of the fractional changes  $n$  can be calculated.

The calibrated-BOLD method depends on the assumption that mild hypercapnia does not alter  $CMRO_2$ . However, this is still somewhat controversial. The problem is that with high enough levels  $CO_2$  acts as an anesthetic, and so it will reduce  $CMRO_2$ . The primary question is then whether mild hypercapnia as used in a calibrated-BOLD experiment changes  $CMRO_2$ . While some studies found that it does not (Sicard and Duong 2005), other studies indicate that this question should be examined further (Zappe *et al.* 2008). Recently, an alternative calibration approach was introduced based on using hyperoxia rather than

hypercapnia (Chiarelli *et al.* 2007a), and a direct comparison of these methods could shed light on the issue.

The calibrated-BOLD experiment provides measurements of the three primary factors,  $f$ ,  $M$  and  $n$ , that affect the BOLD response. For this reason, it has become a primary tool for understanding the mechanisms underlying the BOLD effect, and for addressing basic questions regarding how we should interpret the BOLD response.

## Coupling of cerebral blood flow and $O_2$ metabolism during activation

The observed mismatch in the changes of CBF and  $CMRO_2$  with activation was originally termed an uncoupling, in the sense that it appeared that the CBF increased much more than was necessary to support the small change in  $CMRO_2$  (Fox and Raichle 1986). Here we will use the term coupling in a looser sense, described by the ratio  $n$  of the fractional changes in CBF and  $CMRO_2$ , and call  $n$  an index of CBF/ $CMRO_2$  coupling. In this sense, “coupling” does not necessarily imply a mechanistic connection, and  $n$  simply quantifies the empirical finding of a mismatch.

Following from the work of Fox and Raichle (1986), a number of later studies – testing different brain regions, with different stimuli, and with different experimental techniques – have found larger changes in  $CMRO_2$  (lower values of  $n$ , although still greater than one). These are discussed below.

*Positron emission tomography studies.* Measurements of CBF and  $CMRO_2$  using PET have yielded a range of  $n$  values. Some PET studies found significant increases in CBF with little or no  $CMRO_2$  increases accompanying brain activation, leading to relatively large  $n$  values (Fox and Raichle 1986; Kuwabara *et al.* 1992). Other studies have observed larger  $CMRO_2$  changes, with  $n \sim 1$  (Roland *et al.* 1987) or  $n \sim 2-4$  (Marrett and Gjedde 1997; Seitz and Roland 1992; Vafae and Gjedde 2004; Vafae *et al.* 1998).

*Calibrated-BOLD studies.* Several groups have adopted the fMRI calibrated-BOLD approach and reported larger  $CMRO_2$  changes with  $n$  lying within the range 1.7–4.5 for cortical regions including the motor and visual areas (Ances *et al.* 2008, 2009; Chiarelli *et al.* 2007b; Davis *et al.* 1998; Hoge *et al.* 1999; Kastrup *et al.* 2002; Kim *et al.* 1999; Leontiev and Buxton 2007; Leontiev *et al.* 2007; Pasley *et al.* 2007; St. Lawrence *et al.* 2002; Stefanovic *et al.* 2004, 2005; Uludag and Buxton 2004).

In general, these studies support the basic physiological response that underlies the BOLD effect: CBF increases much more than  $CMRO_2$ , with  $n \sim 2-4$ . However, the important result is that these smaller changes in  $CMRO_2$  are not negligible in terms of their effect on the BOLD signal. Although the BOLD response is often described as a hemodynamic response, this is an oversimplification. The BOLD response is better described as a combined hemodynamic/metabolic response. This more complex picture of the BOLD response complicates the interpretation of BOLD-fMRI experiments, and this is discussed in Ch. 16.

## Optimizing BOLD image acquisition

### Magnetic field dependence

A critical aspect of the BOLD effect is that the fractional signal changes are larger with larger main magnetic fields. A larger magnetic field creates a larger magnetization within a body,

and so the field gradients caused by magnetic susceptibility differences increase in proportion to the field. On top of this, the intrinsic SNR also increases with increasing field, for a similar reason. A larger field produces a more pronounced alignment of the nuclear spins and creates a larger equilibrium magnetization. With any MRI pulse sequence, the signal is proportional to the equilibrium magnetization, so the SNR increases with increasing field. The field dependence of the BOLD effect has spurred much of the continuing interest in moving MRI to higher fields, and there are now a number of instruments using 7 T and a few at even higher fields.

The primary effect of increasing the magnetic field is an increase of the magnitude of the BOLD effect, which naturally increases the SNR of a BOLD experiment. However, other factors that conflict with this SNR increase also change and partially offset the increase in practice. Two intrinsic tissue time constants that affect the timing parameters in an MRI experiment are  $T_2^*$  and  $T_1$ . The time available for measuring a signal after it is created by an RF pulse is governed by the local  $T_2^*$ , which is determined by the magnitude of local field inhomogeneities. Just as with the BOLD effect, the field offsets caused by large-scale magnetic susceptibility effects (e.g., near air–tissue boundaries) are proportional to the main magnetic field, so  $T_2^*$  is decreased with increasing field. Furthermore, in addition to  $T_2^*$  effects, these field offsets produce distortions in the images (Ch. 11). To compensate for these larger effects at higher field, the data acquisition time can be reduced, but this also reduces SNR. However, even if some of the potential increase in SNR is sacrificed to compensate for increased distortion and  $T_2^*$  effects from field inhomogeneities, there is still a net gain in SNR with increasing the main magnetic field.

The longitudinal relaxation time  $T_1$  also increases with increasing the main magnetic field. To produce the same degree of recovery of the magnetization between RF pulses, the repetition time (TR) must be increased in proportion to  $T_1$ , lengthening the duration of a study. Other factors being equal, if fewer images are collected during a given time frame, the SNR per unit time is reduced. This issue is considered in more detail below.

At 4 T and higher, another effect that alters the quality of the images comes into play in human imaging. When imaging at 1.5 T, the wavelength of the RF pulse is larger than the human head. However, at 4 T, this wavelength is comparable to the size of the head, and at 7 T it is smaller. This difference creates a more complicated coupling between the RF coil and the head. Consequently, it is difficult to design an RF coil that produces a uniform RF field over the whole brain. This leads to variable flip angles across the brain when the coil is used as a transmitter, and a non-uniform sensitivity pattern for detection when it is used as a receiver. In short, this effect makes uniform imaging of the entire brain more problematic at high fields.

Despite these potential limitations of high-field imaging, it is clear that SNR for imaging the human brain continues to increase at least to 7 T, improving the sensitivity for BOLD experiments (Harel *et al.* 2006). With increased SNR, spatial resolution can be reduced to the point that the columnar architecture of the brain can be resolved (Yacoub *et al.* 2008).

## Image acquisition parameters

The SNR of the image acquisition is a critical factor in determining the sensitivity of BOLD imaging, and the SNR depends on several parameters in addition to the main magnetic field strength. As we will see, the choice of experimental parameters usually involves a trade-off between SNR and a systematic artifact. Most BOLD studies use a GRE echo planar imaging (EPI) single-shot acquisition, so we will focus on this technique in considering how to

optimize the acquisition, but the basic ideas apply to other techniques as well. The primary pulse sequence parameter that makes the MR signal sensitive to the BOLD effect is TE. If TE is very short, the signal is insensitive to  $T_2^*$ , and so the signal change with activation is minimal. If TE is very long, most of the signal decays away before it is measured, so again the sensitivity is low because the signal is lost in the noise. To maximize the SNR, we must maximize the signal change resulting from change in  $T_2^*$ . If the noise is purely additive and so the magnitude of the noise fluctuations in a voxel is independent of the intrinsic resting signal in the voxel, then the optimal TE is approximately equal to the local  $T_2^*$ . In the brain at field strengths of 1.5–3 T, typical  $T_2^*$  values are in the range 40–60 ms, and most BOLD studies use TEs in this range.

The voxel dimensions strongly affect the SNR. In general, the SNR is proportional to the number of spins that contribute to the signal from a voxel, and so for a uniform tissue the SNR is proportional to the voxel volume (Ch. 11). If the voxel volume is larger than the activated area in a BOLD experiment, then the measured signal change will be diluted by partial volume averaging. From this argument alone, the optimal voxel size for maximizing SNR should be relatively large, just small enough to resolve the activated area but no smaller. However, in practice, another factor comes into play: magnetic field inhomogeneities. Field variations within a voxel lead to different precession rates and phase dispersion, so the net signal can be drastically reduced from what it would be if all the spin signals added coherently. In this case, increasing the voxel size can decrease the net signal by bringing in a wider range of field variations. The microscopic field distortions caused by the BOLD effect should be independent of voxel size, but for broader field gradients caused by macroscopic susceptibility differences (e.g., near sinus cavities), the range of field variations is directly proportional to voxel size. The effect on an image is a signal dropout (as discussed in Ch. 11).

For these reasons, the choice of voxel size is a trade-off between SNR and the need for sufficient spatial resolution to reduce signal dropout problems to an acceptable level. The SNR decreases with small voxels because there are fewer spins contributing to the signal; it also decreases with very large voxels because of magnetic field variations within the voxel. At 1.5 T, typical voxel volumes for fMRI range from approximately 20 to 100 mm<sup>3</sup>. The optimum voxel size depends on the magnitude of the field variations in the area of the brain under investigation. In regions of the brain prone to field distortions, such as the frontal and temporal lobes, smaller voxels may produce better SNR.

The sensitivity of a BOLD signal measurement depends on the ratio of the absolute signal change to the added noise amplitude. A change in blood oxygenation produces a corresponding fractional change in the MR signal; consequently, we should maximize the resting MR signal to maximize the absolute signal change. The resting signal primarily depends on two pulse sequence parameters, TR and the flip angle. The TR has two practical effects that govern the SNR. The first effect is that TR controls how much longitudinal ( $T_1$ ) relaxation occurs between RF pulses, which then affects the measured signal when the magnetization is flipped into the transverse plane. In other words, there is a saturation effect with repeated images with TR shorter than  $T_1$ . This saturation effect also is partly controlled by the flip angle: a smaller angle leaves some of the magnetization along the longitudinal axis and produces less saturation.

In addition to the saturation effect, TR also controls how many separate measurements can be made in a fixed time. The statistical analysis of BOLD voxel time series can be quite involved (Ch. 15), but the detection of a BOLD signal change essentially amounts to comparing the average signal during the stimulus intervals with the average signal during

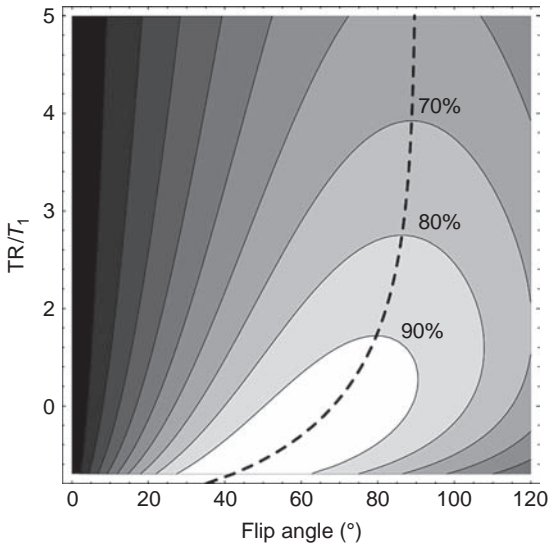


**Fig. 14.9.** Optimizing the repetition time (TR) and flip angle to maximize the signal to noise ratio (SNR). For a gradient recalled echo pulse sequence, the SNR that can be achieved in a given total imaging time is shown as a contour plot. The contours indicate the percentage of the maximum possible SNR for each combination of the ratio of TR to the longitudinal relaxation time ( $TR/T_1$ ) and the flip angle. The dashed line shows the optimal flip angle for each value of  $TR/T_1$ . Using a long TR is costly in terms of SNR, but when the TR is reduced to approximately the value of  $T_1$  there is little gain in SNR in shortening it further provided that the flip angle is appropriately adjusted.

the control intervals. If the noise in each measured image is independent, then the SNR will be proportional to  $\sqrt{N}$ , where  $N$  is the number of measurements that go into the average. And  $N$ , in turn, is proportional to  $1/TR$ : a shorter TR allows more averages to be done in the same total experiment time. Taking this into account, the SNR that can be achieved depends on the choice of  $TR/T_1$  and the flip angle, as shown in Fig. 14.9.

For any TR, there is an optimum flip angle that maximizes the available SNR. When TR is long compared with  $T_1$ , the optimum flip angle is  $90^\circ$ , which flips all the longitudinal magnetization into the transverse plane, but the maximum SNR is less than that which can be achieved with a shorter TR. As TR is reduced, the optimum flip angle also reduces. With very short TR, the available SNR plateaus at a maximum level with small flip angles. So shortening TR until it is approximately equal to  $T_1$  is desirable, but making it even shorter does not produce much further improvement. It is helpful to consider some examples. For gray matter with  $T_1$  of approximately 1 s, a TR of 1 s with a flip angle of  $68^\circ$  achieves 96% of the theoretical maximum SNR, whereas a TR of 4 s and a  $90^\circ$  flip angle produces only 69% of the maximum SNR. This is a large difference. To improve the SNR of the longer TR experiment to the same level as the shorter TR experiment by averaging longer runs would nearly double the total imaging time.

It is important to note that these examples are based on the assumption that the relevant  $T_1$  is that of gray matter. However, because GRE images are primarily sensitive to veins, and the largest field gradients occur in the perivascular space, the relevant  $T_1$  for SNR optimization at lower fields may be that of cerebrospinal fluid (CSF), which is approximately 3–5 s. The plot in Fig. 14.9 still applies because the shape of the curves depends only on the ratio  $TR/T_1$ . That is, if the relevant  $T_1$  is 4 s, then TR of 4 s and a flip angle of  $68^\circ$  would yield 96% of the available SNR, just as in the preceding example. However, the maximum available SNR also depends on  $T_1$ , decreasing as  $1/\sqrt{T_1}$ . If the TR is increased in proportion to the  $T_1$ , the signal generated with each repetition will be the same, but fewer signals are generated for averaging during the same fixed total imaging time. So the maximum available SNR for CSF is approximately half ( $1/\sqrt{4}$ ) of the

maximum SNR for gray matter. In practice, the GRE-BOLD signal is likely a combination of gray matter and perivascular CSF signal changes.

In practice, reducing the TR to approximately 1 s creates a conflict with coverage of the brain. Most modern scanners have a maximum image acquisition rate of about  $20 \text{ s}^{-1}$ . These images could be repeated images on the same slice or cycling through a number of different slice locations to cover the whole brain. For example, 40 sagittal slices 4 mm thick will cover nearly all human brains, but if the maximum imaging rate is  $20 \text{ s}^{-1}$ , the minimum TR that is possible is 2 s, longer than the optimum for gray matter SNR. For more focal studies, covering only a limited part of the brain, more optimal TRs are possible.

## Motion artifacts

The simplest interpretation of a dynamic series of MR images is that each image is measuring the net signal from an array of spatially defined voxels. In other words, the time course of a particular voxel is the average signal in a small volume of space centered at position  $(x, y, z)$ . Ideally, this position also corresponds to a fixed location in the brain. For this reason, a persistent problem in BOLD experiments is subject motion. Any slight movement of the subject's head will move parts of the subject's brain to different voxel locations. If there are sharp edges in the intensity pattern of the image, such as near the edge of the brain, then movements much smaller than a voxel dimension can produce a signal change larger than the expected signal change from the BOLD effect. This effect is particularly troublesome if the motion is correlated with the stimulus (Friston *et al.* 1996; Hajnal *et al.* 1994). For example, if the subject tips his head slightly when a visual stimulus is presented or if his head slides out of the coil slightly during a motor task, the result can be signal changes that nicely correlate with the stimulus but that are entirely artifactual. A useful check is to be sure that activations are not right at a sharp boundary in the image. Often stimulus-correlated motion will present as a positive correlation on one side of the brain and a negative correlation on the other side. But this is not the only possible pattern. For example, superior axial slices at a level where the cross-section of the brain is significantly different from one slice to the next could show symmetric artifactual activation around the edge of the brain caused by motion in the slice selection direction.

There are several approaches to dealing with motion artifacts. The best is perhaps to try to prevent motion as much as possible by carefully coaching the subject about the importance of remaining still and by using head restraints. These could include foam pads between the coil and the head and restraining straps. A number of groups have found that a bite bar molded to the subject's teeth with dental plastic is very effective in stabilizing the head.

After data collection, motion effects can be somewhat corrected with post-processing software (Ashburner and Friston 1999; Cox 1996; Friston *et al.* 1995; Woods *et al.* 1993). The primary goal of such techniques is realignment of the individual images. If the motion is in the plane of the images, then a two-dimensional registration is adequate. For example, if the subject's motion is a tipping forward of the head, with no rotational component, and the images are sagittal in orientation, then the motion is entirely within the plane of the image. The correction is then a translation and rotation to align optimally the image with a reference image (e.g., the first image in the dynamic series or the average image of the series). The corrections required are subpixel shifts, so the new image matrix is an appropriate interpolation of the original image on to the new registered grid. If the motion does not lie in the image plane, then a three-dimensional registration is required. In addition to being a more time-consuming calculation, a problem for three-dimensional registration is that the



two-dimensional images are acquired sequentially in time. This means that at any one time point we do not have a complete three-dimensional image of the brain to compare with the three-dimensional image at another time point. Nevertheless, three-dimensional registration schemes have been developed to deal with these problems.

However, there are a few other problems caused by motion that need to be corrected in addition to image registration (Ashburner and Friston 1999). The first is the spin history effect. With a reasonably short TR, the MR signal is not fully relaxed, but if everything is repeated exactly the same, a steady state develops such that with each repetition the signal generated is the same. If motion causes a group of spins to move out of the selected slice, then these spins will not feel the next RF pulse. If they are later moved back into the slice, their spin history, the combined effects of RF pulses and relaxation, will be different from that of spins that remained within the selected slice. This disrupts the steady-state signal in a way that depends on the past motion. This effect can be estimated by using the history of the motion estimated from the image registration algorithm (i.e., the translations and rotations necessary to put each image into alignment).

A more subtle motion-related problem is that the basic picture measured by MRI, the signal from a set of fixed voxels in space, is not correct. Magnetic field variations within the head distort the images, as discussed in Ch. 11. This creates problems in aligning EPI images with higher-resolution anatomical images that are less sensitive to these distortions. Because the source of the distortions is the head itself, any motion will also shift the pattern of distortions. In other words, the location in space corresponding to a particular voxel is not fixed. This fact adds another layer of complexity to motion correction (Jezzard and Clare 1999). The nature of these distortions and approaches for correction are described in the next section.

## Image distortions

Localization with EPI is based on the frequency of the local signal in the presence of field gradients. The key assumption is that if no gradients are applied, all spins resonate at precisely the same frequency. This is not true in general because the inhomogeneities of the head create magnetic field variations, and the resulting image is distorted. Consider a small sample of tissue in the brain in which the magnetic field is offset by these field variations. The primary distortion of the image is that this signal will be displaced along the phase-encoded axis by a distance proportional to the field offset (Ch. 11). Note that this effect is in addition to the signal dropout effect described above, which also results from local field gradients. The apparent location of the signal from a small element of tissue is shifted in the reconstructed image in proportion to the mean field offset. If there is a large spread in the field offsets within the tissue element, the signal will be reduced as well.

The basic approach to correcting image distortions caused by field inhomogeneity is to first map the field distribution within the brain. This can be done with a series of gradient echo images with a progression of closely spaced TEs, reconstructing the phase images in addition to the magnitude images. At each voxel, the phase change between one TE and the next is proportional to the local field offset. The echo spacing must be short enough to prevent phase ambiguities from precession greater than  $360^\circ$ . At 1.5 T, a 1 ppm field offset (64 Hz) will produce a phase change of  $23^\circ$  if TE is changed by 1 ms, so the spacing should be no more than a few milliseconds. Field maps can be made using standard two- or three-dimensional imaging techniques, which are not strongly distorted, or with EPI images

themselves. With the first approach, the true distribution of fields is calculated, and from this map the location of where each tissue element will appear in the distorted EPI image can be calculated (Jezzard and Balaban 1995). With EPI field maps, the locations are distorted, but from the measured field offset one can calculate where that signal must have originated (Reber *et al.* 1998).

With subject motion, the pattern of field offsets changes, creating a different pattern of distortions in the EPI image. In this case, a single field map collected before the fMRI experiment will not be adequate for correcting the distortions of all the images. To deal with this motion problem, which produces a dynamically changing pattern of distortions, Jezzard and Clare (1999) suggested using the phase changes of the individual EPI images in the time series to make the additional dynamic distortion corrections necessary in addition to realignment.

Correction for distortions with field mapping is often very helpful, particularly when overlaying functional EPI images on higher-resolution structural images. However, it is important to note that such distortions cannot always be corrected. The nature of these distortions is that signals from two different regions can be added within the same distorted voxel. This can happen if the imaging gradients and the intrinsic field inhomogeneity combine to produce the same field in two separate regions. In this case, all we can measure is the combined signal, and we have no way of knowing how much came from one region and how much from the other. Because only the phase-encoded axis is strongly distorted in an EPI image, the pattern of distortions can be altered radically by changing the orientation of the phase-encoding axis. So for different parts of the brain, some imaging orientations may work much better than others for minimizing the distortions and for making the distortions more correctable.

The magnitude of image distortions depends on the total acquisition time for each image. For an EPI acquisition, the total data collection time typically is in the range of 40–100 ms. There is a simple rule for how far the signal from an area with an offset field will be displaced in the reconstructed image: for each additional phase evolution of  $360^\circ$  during the data acquisition time caused by the field offset, the signal is shifted one pixel along the  $y$ -axis. The shift is, therefore, directly proportional to the data acquisition time, and minimizing that time will minimize the distortions. The acquisition time can be reduced and still allow sampling of the same points in  $k$ -space by increasing the read-out gradient strength (Ch. 11). This spreads the signal from the head over a larger range of frequencies, and so is described as increasing the bandwidth of the acquisition.

However, the problem with this approach is that the SNR of the acquisition is proportional to the square root of the acquisition time (one can think of the data acquisition time as equivalent to averaging a continuous signal over that interval, and SNR increases with the square root of the number of averages). So minimizing distortions also minimizes SNR, and again we are faced with a trade-off between maximizing SNR and minimizing artifacts. Note that the argument that SNR increases with increasing acquisition time does not hold when the acquisition time becomes much larger than  $T_2^*$ . With such a long acquisition time, most of the signal has decayed away, so additional measurements are simply adding noise. The optimal choice for SNR is to have acquisition time approximately equal to  $T_2^*$  so that the full available signal is used.

Parallel imaging provides a useful solution to reducing distortions (de Zwart *et al.* 2006). Multiple small receiver coils are used in parallel to measure the signal. Because these coils have some intrinsic spatial selectivity, the  $k$ -space sampling can be reduced. And by reducing the acquisition time, the distortions are reduced. However, there is still some loss of SNR.

Most current scanners have head coils with at least eight channels, and some version of parallel imaging available.

As with many aspects of MRI, optimizing the imaging protocol is a matter of balancing the trade-offs between SNR and systematic artifacts, and this depends on the goals of the study. For imaging a small region of the brain, more severe distortions in other parts of the brain may be tolerable. But distortions in the EPI images always complicate detailed comparisons with other images. It is common practice to display areas of activation calculated from the EPI images as a color overlay on a higher-resolution anatomical image. High-resolution MR images are not as distorted as the EPI images, so correction for distortions is critical for accurate localization. Furthermore, correction for distortions and motion artifacts is important if the images of individual subjects are to be warped into a common brain atlas (Woods *et al.* 1999).

## References

- Ances BM, Leontiev O, Perthen JE, *et al.* (2008) Regional differences in the coupling of cerebral blood flow and oxygen metabolism changes in response to activation: implications for BOLD fMRI. *Neuroimage* **39**: 1510–1521
- Ances BM, Liang CL, Leontiev O, *et al.* (2009) Effects of aging on cerebral blood flow, oxygen metabolism, and blood oxygenation level dependent responses to visual stimulation. *Hum Brain Mapp*, **30**: 1120–1132
- Ashburner J, Friston KJ (1999) Image registration. In *Functional MRI*, Moonen CTW, Bandettini P, eds. Berlin: Springer, pp. 285–299
- Bandettini PA, Wong EC, Hinks RS, Hyde JS (1992) Time-course spin-echo and gradient-echo EPI of the human brain during a breath hold. In *Proceedings of the Society of Magnetic Resonance in Medicine*, Berlin, p. 1104
- Boxerman JL, Hamberg LM, Rosen BR, Weisskoff RM (1995a) MR contrast due to intravascular magnetic susceptibility perturbations. *Magn Reson Med* **34**: 555–566
- Boxerman JL, Bandettini PA, Kwong KK, *et al.* (1995b) The intravascular contribution to fMRI signal change: Monte Carlo modeling and diffusion-weighted studies in vivo. *Magn Reson Med* **34**: 4–10
- Buxton RB, Luh W-M, Wong EC, Frank LR, Bandettini PA (1998) Diffusion weighting attenuates the BOLD peak signal change but not the post-stimulus undershoot. In *Proceedings of the Sixth Meeting of the International Society for Magnetic Resonance in Medicine*, Sydney, Australia, p. 7
- Buxton RB, Uludag K, Dubowitz DJ, Liu TT (2004) Modeling the hemodynamic response to brain activation. *Neuroimage* **23** (Suppl 1): S220–S233
- Chiarelli PA, Bulte DP, Wise R, Gallichan D, Jezzard P (2007a) A calibration method for quantitative BOLD fMRI based on hyperoxia. *Neuroimage* **37**: 808–820
- Chiarelli PA, Bulte DP, Gallichan D, *et al.* (2007b) Flow-metabolism coupling in human visual, motor, and supplementary motor areas assessed by magnetic resonance imaging. *Magn Reson Med* **57**: 538–547
- Cox RW (1996) AFNI: software for analysis and visualization of functional magnetic resonance neuroimages. *Comput Biomed Res* **29**: 162–173
- Davis TL, Kwong KK, Weisskoff RM, Rosen BR (1998) Calibrated functional MRI: mapping the dynamics of oxidative metabolism. *Proc Natl Acad Sci USA* **95**: 1834–1839
- de Zwart JA, van Gelderen P, Duyn JH (2006) Receive coil arrays and parallel imaging for functional magnetic resonance imaging of the human brain. *Conf Proc IEEE Eng Med Biol Soc* **1**: 17–20
- Fisel CR, Ackerman JL, Buxton RB, *et al.* (1991) MR contrast due to microscopically heterogeneous magnetic susceptibility: numerical simulations and applications to cerebral physiology. *Magn Reson Med* **17**: 336–347
- Fox PT, Raichle ME (1986) Focal physiological uncoupling of cerebral blood flow and oxidative metabolism during somatosensory stimulation in human subjects. *Proc Natl Acad Sci USA* **83**: 1140–1144

- Frahm J, Bruhn H, Merboldt K-D, Hanicke W, Math D (1992) Dynamic MR imaging of human brain oxygenation during rest and photic stimulation. *J Magn Reson Imaging* 2: 501–505
- Friston KJ, Ashburner J, Frith CD, *et al.* (1995) Spatial registration and normalization of images. *Hum Brain Mapp* 2: 165–189
- Friston KJ, Williams S, Howard R, Frackowiak RSJ, Turner R (1996) Movement related effects in fMRI time-series. *Magn Reson Med* 35: 346–355
- Grubb RL, Jr., Raichle ME, Eichling JO, Ter-Pogossian MM (1974) The effects of changes in  $\text{Paco}_2$  on cerebral blood volume, blood flow, and vascular mean transit time. *Stroke* 5: 630–639
- Hajnal JV, Myers R, Oatridge A, *et al.* (1994) Artifacts due to stimulus correlated motion in functional imaging of the brain. *Magn. Reson. Med* 31: 283–291
- Harel N, Ugurbil K, Uludag K, Yacoub E (2006) Frontiers of brain mapping using MRI. *J Magn Reson Imaging* 23: 945–957
- Hoge RD, Atkinson J, Gill B, *et al.* (1999) Linear coupling between cerebral blood flow and oxygen consumption in activated human cortex. *Proc Natl Acad Sci USA* 96: 9403–9408
- Jezzard P, Balaban RS (1995) Correction for geometric distortion in echo planar images from  $B_0$  field distortions. *Magn Reson Med* 34: 65–73
- Jezzard P, Clare S (1999) Sources of distortion in functional MRI data. *Hum Brain Mapp* 8: 80–85
- Kastrup A, Kruger G, Neumann-Haefelin T, Glover GH, Moseley ME (2002) Changes of cerebral blood flow, oxygenation, and oxidative metabolism during graded motor activation. *Neuroimage* 15: 74–82
- Kim SG, Rostrup E, Larsson HBW, Ogawa S, Paulson OB (1999) Determination of relative CMRO<sub>2</sub> from CBF and BOLD changes: significant increase of oxygen consumption rate during visual stimulation. *Magn Reson Med* 41: 1152–1161
- Kuwabara H, Ohta S, Brust P, Meyer E, Gjedde A (1992) Density of perfused capillaries in living human brain during functional activation. *Prog Brain Res* 91: 209–215
- Kwong KK, Belliveau JW, Chesler DA, *et al.* (1992) Dynamic magnetic resonance imaging of human brain activity during primary sensory stimulation. *Proc Natl Acad Sci USA* 89: 5675–5679.
- Lee SP, Silva AC, Ugurbil K, Kim SG (1999) Diffusion-weighted spin-echo fMRI at 9.4 T: microvascular/tissue contribution to BOLD signal changes. *Magn Reson Med* 42: 919–928
- Leontiev O, Buxton RB (2007) Reproducibility of BOLD, perfusion, and CMRO(2) measurements with calibrated-BOLD fMRI. *Neuroimage* 35: 175–184
- Leontiev O, Dubowitz DJ, Buxton RB (2007) CBF/CMRO<sub>2</sub> coupling measured with calibrated BOLD fMRI: sources of bias. *Neuroimage* 36: 1110–1122
- Mandeville JB, Marota JJA, Kosofsky BE, *et al.* (1998) Dynamic functional imaging of relative cerebral blood volume during rat forepaw stimulation. *Magn Reson Med* 39: 615–624
- Marrett S, Gjedde A (1997) Changes of blood flow and oxygen consumption in visual cortex of living humans. *Adv Exp Med Biol* 413: 205–208
- Obata T, Liu TT, Miller KL, *et al.* (2004) Discrepancies between BOLD and flow dynamics in primary and supplementary motor areas: application of the balloon model to the interpretation of BOLD transients. *Neuroimage* 21: 144–153
- Ogawa S, Lee TM, Nayak AS, Glynn P (1990) Oxygenation-sensitive contrast in magnetic resonance image of rodent brain at high magnetic fields. *Magn Reson Med* 14: 68–78.
- Ogawa S, Tank DW, Menon R, *et al.* (1992) Intrinsic signal changes accompanying sensory stimulation: functional brain mapping with magnetic resonance imaging. *Proc Natl Acad Sci USA*. 89: 5951–5955
- Ogawa S, Menon RS, Tank DW, *et al.* (1993) Functional brain mapping by blood oxygenation level-dependent contrast magnetic resonance imaging: a comparison of signal characteristics with a biophysical model. *Biophys J* 64: 803–812
- Oja JME, Gillen J, Kaupinnen RA, Kraut M, Zijl PCMV (1999) Venous blood effects in spin-echo fMRI of human brain. *Magn Reson Med* 42: 617–626
- Pasley BN, Inglis BA, Freeman RD (2007) Analysis of oxygen metabolism implies a neural origin for the negative BOLD

- response in human visual cortex. *Neuroimage* **36**: 269–276
- Pauling L, Coryell CD (1936) The magnetic properties and structure of hemoglobin, oxyhemoglobin, and carbonmonoxyhemoglobin. *Proc Natl Acad Sci USA* **22**: 210–216
- Reber PJ, Wong EC, Buxton RB, Frank LR (1998) Correction of off resonance-related distortion in echo-planar imaging using EPI-based field maps. *Magn Reson Med* **39**: 328–330
- Roland PE, Eriksson L, Stone-Elander S, Widén L (1987) Does mental activity change the oxidative metabolism of the brain? *J Neurosci* **7**: 2373–2389
- Seitz RJ, Roland PE (1992) Vibratory stimulation increases and decreases the regional cerebral blood flow and oxidative metabolism: a positron emission tomography (PET) study. *Acta Neurol Scand* **86**: 60–67
- Sicard KM, Duong TQ (2005) Effects of hypoxia, hyperoxia, and hypercapnia on baseline and stimulus-evoked BOLD, CBF, and CMRO<sub>2</sub> in spontaneously breathing animals. *Neuroimage* **25**: 850–858
- St. Lawrence KS, Ye FQ, Lewis BK, *et al.* (2002) Effects of indomethacin on cerebral blood flow at rest and during hypercapnia: an arterial spin tagging study in humans. *J Magn Reson Imaging* **15**: 628–635
- Stefanovic B, Warnking JM, Pike GB. (2004) Hemodynamic and metabolic responses to neuronal inhibition. *Neuroimage* **22**: 771–778
- Stefanovic B, Warnking JM, Kobayashi E, *et al.* (2005) Hemodynamic and metabolic responses to activation, deactivation and epileptic discharges. *Neuroimage* **28**: 205–215
- Thulborn KR, Waterton JC, Matthews PM, Radda GK (1982) Oxygenation dependence of the transverse relaxation time of water protons in whole blood at high field. *Biochim Biophys Acta* **714**: 265–270
- Turner R, LeBihan D, Moonen CTW, Despres D, Frank J (1991) Echo-planar time course MRI of cat brain oxygenation changes. *Magn Reson Med* **27**: 159–166
- Uludag K, Buxton RB (2004) Measuring the effects of indomethacin on changes in cerebral oxidative metabolism and cerebral blood flow during sensorimotor activation. *Magn Reson Med* **51**: 1088–1089; author reply 1090
- Vafaee MS, Gjedde A (2004) Spatially dissociated flow-metabolism coupling in brain activation. *Neuroimage* **21**: 507–515
- Vafaee M, Marrett S, Meyer E, Evans A, Gjedde A (1998) Increased oxygen consumption in human visual cortex: response to visual stimulation. *Acta Neurol Scand* **98**: 85–89
- van Zijl PCM, Eleff SE, Ulatowski JA, *et al.* (1998) Quantitative assessment of blood flow, blood volume and blood oxygenation effects in functional magnetic resonance imaging. *Nature Med* **4**: 159–167
- Weisskoff RM (1999) Basic theoretical models of BOLD signal change. In *Functional MRI*, Moonen CTW, Bandettini PA, eds. Berlin: Springer, pp. 115–123
- Weisskoff RM, Kiihne S (1992) MRI susceptibility: image based measurement of absolute susceptibility of MR contrast agents and human blood. *Magn Reson Med* **24**: 375–383
- Weisskoff RM, Zuo CS, Boxerman JL, Rosen BR (1994) Microscopic susceptibility variation and transverse relaxation: theory and experiment. *Magn Reson Med* **31**: 601–610
- Woods RP, Mazziotta JC, Cherry SR (1993) MRI–PET registration with automated algorithm. *J Comput Assist Tomogr* **17**: 536–546
- Woods RP, Dapretto M, Sicutte NL, Toga AW, Mazziotta JC (1999) Creation and use of a Talairach-compatible atlas for accurate, automated, nonlinear intersubject registration, and analysis of functional imaging data. *Hum Brain Mapp* **8**: 73–79
- Yablonsky DA, Haacke EM (1994) Theory of NMR signal behavior in magnetically inhomogeneous tissues: the static dephasing regime. *Magn Reson Med* **32**: 749–763
- Yacoub E, Duong TQ, van de Moortele PF, *et al.* (2003) Spin-echo fMRI in humans using high spatial resolutions and high magnetic fields. *Magn Reson Med* **49**: 655–664
- Yacoub E, Harel N, Ugurbil K (2008) High-field fMRI unveils orientation columns in humans. *Proc Natl Acad Sci USA* **105**: 10607–10612
- Zappe AC, Uludag K, Oeltermann A, Ugurbil K, Logothetis NK (2008) The influence of moderate hypercapnia on neural activity in the anesthetized nonhuman primate. *Cereb Cortex* **18**: 2666–2673

# Design and analysis of BOLD experiments

<b>Introduction to the statistical analysis of BOLD data</b>	<i>page</i> 368
Separating true activations from noise	369
The <i>t</i> -test	371
Correlation analysis	372
Fourier analysis	373
The Kolmogorov–Smirnov test	374
Noise correlations	375
Interpreting BOLD activation maps	376
<b>The general linear model</b>	376
The hemodynamic response	377
Fitting the data with a known model response	378
Statistical significance	380
Fitting the data with a more general linear model	381
The variance of the parameter estimates	385
Statistical significance revisited	388
<b>Design of fMRI experiments</b>	389
Block designs and event-related designs	389
Detection power for a known hemodynamic response	391
Estimating an unknown hemodynamic response	394
Detecting an unknown hemodynamic response	396
Detection and estimation sensitivity	397

## Introduction to statistical analysis of BOLD data

The statistical analysis of blood oxygenation level dependent (BOLD) data is a critical part of brain mapping with fMRI. Many creative statistical methods have been proposed and, given the flexibility of fMRI and the range of experiments that is possible, it seems likely that a number of different statistical processing approaches can be applied to yield useful data. Indeed, a pluralistic analysis strategy applying several methods to the same data may be the best approach for pulling out and evaluating the full information content of the fMRI data (Lange *et al.* 1999). The goal of this chapter is to introduce some of the basic aspects of statistical thinking about BOLD data analysis, rather than to provide a comprehensive review of different approaches (e.g., see Price *et al.* 2006; Smith 2004; Smith *et al.* 2004). We will focus on the general linear model, which encompasses many of the techniques commonly used (Boynton *et al.* 1996; Friston *et al.* 1994, 1995; Worsley *et al.* 1997).

In the first section, we introduce the need for a statistical analysis and some of the basic ideas and strategies. In the second section, the general linear model is considered in more detail, emphasizing the geometrical view of the analysis. The third section focuses on how the

statistical analysis sheds light on how to design an efficient experiment and provides a framework for comparing the relative merits of blocked and event-related stimulus paradigms.

## Separating true activations from noise

The MR signal change during activation caused by the BOLD effect is quite small, on the order of 1% for a 50% change in cerebral blood flow (CBF) at 1.5 T. To use these weak signals for brain mapping, they must be reliably separated from the noise. With echo planar imaging (EPI), the intrinsic signal to noise ratio (SNR) in a single-shot image is often quite large, in the range 100–200, but this is still not large enough to reliably detect a 1% signal change in a voxel from a single image in the stimulus state and a single image in the control state. For this reason, a large number of images are required to allow sufficient averaging to detect the small signal changes.

An example of data from a BOLD experiment was shown in Fig. 5.3. The subject performed a simple finger-tapping task for 16 s, followed by an equal rest period, with a total of eight cycles of this task/control cycle repeated in one run. Echo planar imaging was performed throughout the run measuring 128 images per slice, with a repetition time (TR) of 2 s. The voxel resolution of the EPI images was  $3.75 \times 3.75 \times 5$  mm. This experiment produced a four-dimensional data set (three spatial dimensions plus time). Figure 5.3 shows one image plane and a grid of pixel time courses in the vicinity of the primary motor area. Because the motor BOLD response is large, a number of clearly activated voxels are detectable by eye. In general, however, we want to be able to detect activations that are not apparent to the eye but that are nevertheless statistically significant.

The most obvious processing strategy to identify activated voxels would be to simply subtract the average of all the images made during the control task from the average of all the images made during the stimulus task. If the signal variations caused by noise are random with a normal distribution and independent for each time point, this averaging will improve the SNR and should provide a map of the activated areas. However, this naive approach to the data processing does not work well, and in practice the data processing can become quite a bit more involved.

The first problem with the simple averaging scheme is that the standard deviation of the noise is different in different voxels and so the noise is not uniform across the image plane. The noise that adds into the signal from a particular voxel has two sources: random thermal noise and physiological fluctuations. The random thermal noise arises primarily from stray currents in the body that induce random signals in the receiver coil. This thermal noise is spread throughout the raw acquired data, and when the image is reconstructed this noise is spread throughout the voxels of the image. The result is that this thermal noise can be accurately described as uniform random Gaussian noise, with the noise in each voxel having the same standard deviation and being independent of the noise in the other voxels. If this thermal noise were the only source of fluctuations in the MR signal, the noise would have no spatial structure. But, in fact, the variance of the signal over time measured in a human brain is several times larger than would be expected from thermal noise alone, and it exhibits both temporal and spatial structure (Purdon and Weisskoff 1998; Zarahn *et al.* 1997a).

The additional variance of the MR signal *in vivo* is attributed to physiological fluctuations, which include several effects. Cardiac pulsations create a pressure wave that strongly affects the signal of flowing blood, but it also creates pulsations in cerebrospinal fluid (CSF) and in the brain parenchyma itself. Although these motions are small, they nevertheless can easily produce signal fluctuations on the order of 1%, and the magnitude of the fluctuations varies strongly across the image plane. Figure 15.1 shows the frequency spectrum for a voxel time

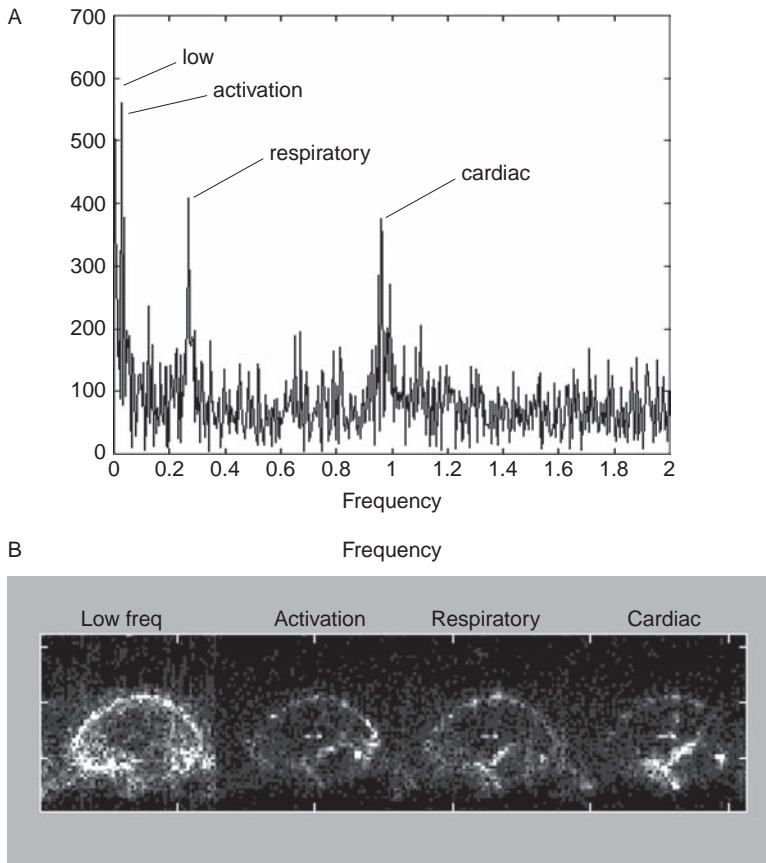


**Fig. 15.1.** Spectrum of noise fluctuations in the brain. (A) The Fourier transform of the MR signal measured during a simple block design, finger-tapping experiment with a repetition time of 250 ms shows a strong peak at the fundamental period of the stimulus plus peaks from cardiac and respiratory pulsations. There is also considerable noise power at low frequencies from baseline drifts and possibly also physiological vasomotion. (B) The images show the amplitudes of different components in sagittal images, suggesting the strong spatial as well as temporal structure of the noise. (Data courtesy of L. Frank.)

course measured in the primary visual cortex with a simple block design, flashing checkerboard stimulus, showing a strong spike at the fundamental frequency of the stimulus. For simple Gaussian noise, the frequency spectrum should be flat except for this spike and its harmonics, but there are additional clear peaks that can be identified with cardiac and respiratory fluctuations. Note that the cardiac peak is easily identified in this study because the TR was unusually short in this experiment (250 ms). For a more typical TR of 2 s, the cardiac pulsations would be aliased in the data and could appear at lower frequencies associated with the stimulus presentation. In the spectrum, there are also true low-frequency variations that could result from drifts caused by scanner hardware and that may also include additional slow physiological pulsations. A regular oscillation of blood flow and oxygenation called *vasomotion* has been observed in numerous optical studies at frequencies around 0.1 Hz (Mayhew *et al.* 1999). The source and physiological significance of these vasomotion oscillations are poorly understood, but because they involve slow oscillations in blood oxygenation, they can contribute to low-frequency oscillations of the BOLD signal, particularly at high magnetic fields.



This brings us to the central problem created by non-uniform noise. When two noisy images are subtracted to calculate a difference image, the signals should subtract out if there is no activation in a voxel. However, because of noise, there will be a residual difference, and the size of this random residual is on the order of the local noise standard deviation. In other words, the voxels with the largest signal fluctuations will show the largest random difference signal, and so we would expect that a simple difference map would be dominated by vessel and CSF artifacts. The maps of particular frequency components of the noise fluctuations shown in Fig. 15.1A show substantial spatial structure. Therefore, the essential problem with a simple image-difference approach is that there is no way to distinguish between a weak but true activation and a strong but false physiological fluctuation. To put it another way, a difference map alone carries no information on the statistical quality of the measured difference in a voxel. If the run were repeated, a true activation would show up with approximately the same signal difference, whereas the difference signal from a voxel dominated by a blood vessel or CSF fluctuations might vary over a wide range.

To remove these artifacts resulting from voxels with highly variable signals, we can normalize each measured difference signal between task and control states by dividing by an estimate of the intrinsic variability of the signal from that voxel. In effect, this creates a map of the SNR of the difference measurement. Then voxels with a large signal difference only because they have a large intrinsic variance will be suppressed, whereas true activations in which the signal change is much larger than the intrinsic variance will remain. The resulting map is, therefore, a map of the statistical quality of the measurement, rather than a map of the effect itself (i.e., the fractional signal change). Such *statistical parametric maps* are the standard statistical tool used for evaluating fMRI data (Friston *et al.* 1995; Gold *et al.* 1998).

## The *t*-test

One of the standard statistical parameters used to quantify the validity of a measured activation is the *t*-statistic, which is closely related to the SNR of the difference measurement. In its simplest form, the signals measured from a particular voxel are treated as samples of two populations (active and rest); the *t*-test is used to assess whether there is a significant difference between the means of the two groups. The *t*-statistic is essentially a measure of how large the difference of the means is compared with the variability of the populations; as *t* gets larger, the probability that such data could have arisen from two populations with equal means becomes more and more unlikely. This measure is quantified with the *t*-distribution, from which one can calculate the probability that a particular value of *t* or larger could arise by chance if the means really are identical. Then the procedure for analyzing BOLD data begins with the calculation of the *t*-statistic for each voxel. One can then choose a threshold value of probability, such as  $p < 0.01$ , which corresponds to a particular threshold on *t*, and pick out all voxels whose *t*-value passes the threshold. These voxels are then displayed in color on an underlying map of the anatomy for ease of visualization.

The choice of a threshold on *t* for constructing the activation map involves consideration of the fact that the signals from many voxels are being measured simultaneously. For example, if we were considering the difference of means of only a single voxel, we could adopt the conventional criterion that if  $p < 0.05$  the measured difference is considered to be significantly different from zero. But at this level of significance, the same or larger value of *t* will arise by chance 5% of the time. For a typical whole-brain fMRI study, there may be around 10 000 brain voxels analyzed, and so at this level of significance approximately 500 voxels should appear to be activated by chance alone. To account for these multiple

measurements, a more conservative  $p$  value is chosen. For example, to reduce the probability of finding any false-positive activations to the 5% level, the  $p$ -value chosen should be 5% divided by the number of voxels (Bonferroni correction), or  $p = 0.000005$  for this example.

However, a second problem that must be dealt with when applying the  $t$ -test is that the hemodynamic response of the brain does not precisely match the stimulus. For example, consider a simple block-design experiment in which the stimuli are presented in long blocks alternated with equal periods of rest. Then the stimulus as a function of time can be represented as a square wave equal to one during the stimulus task and zero during the control task. The simplest assumption we could make for the response of the BOLD function would be that it would follow the same curve, with the signal changing immediately at the start of each cycle of the square wave and returning cleanly to baseline at the end of each stimulus period. However, even if the neural activity closely follows the stimulus (e.g., within a few hundred milliseconds or so), the hemodynamic response is measurably delayed and broadened. A typical activated voxel will show a delay of approximately 2 s after the beginning of the stimulus period before the BOLD response begins, followed by a ramp of approximately 6 s duration before a new plateau of the signal is reached. After the end of the stimulus period, the BOLD signal ramps back down to the baseline over several seconds and often undershoots the baseline, with the undershoot lasting for 20 s or more (Ch. 16).

## Correlation analysis

The statistical analysis can be enlarged to include the expected hemodynamic response with a correlation analysis (Bandettini *et al.* 1993). Instead of assuming that the hemodynamic response precisely matches the stimulus pattern, the delay and smoothing are incorporated by defining a *model response function*. A simple approximation for the model response to a block-stimulus pattern is a trapezoid with 6 s ramps delayed by 2 s from the onset of the stimulus block. Having chosen a model response function, each measured voxel time course is analyzed by calculating the correlation coefficient  $r$  between the data and the model function. The value of  $r$  ranges from  $-1$  to  $1$  and it expresses the degree to which the measured signal follows the model function. The  $r$ -value is then used as the statistical parameter for mapping, and a threshold on  $r$  is chosen to select pixels that are reliably activated. Figure 5.4 shows an example of an activation map calculated from the correlation coefficient map.

In fact, a correlation analysis is closely related to the simple  $t$ -test comparison of means. The previously described test, in which the time course data are divided into two groups and the means compared, is equivalent to using a model reference function that precisely matches the square-wave stimulus pattern (instead of a delayed trapezoid). Then there is a one-to-one correspondence between the  $t$ -value calculated from the  $t$ -test and the  $r$ -value calculated from the correlation analysis. Any threshold based on  $t$  would precisely correspond to a particular threshold on  $r$ . The correlation analysis is more general, however, in that it allows one to use any model function, so the true response can be better approximated.

Correlation analysis, in turn, is a component of a more general linear regression analysis. In effect, what we are doing is trying to model the data as a linear combination of one or more model functions plus noise. With the single model function described above, we are trying to fit the data as well as we can by treating the data as a scaled version of the model function. That is, we try to determine the best value for a multiplicative parameter  $a$ , such that when the model function is multiplied by  $a$  the resulting time series best approximates the real data. Ideally, if we subtract this best-fit model curve from the data, the residuals should result only in noise. The  $r$ -value is then a measure of how much of the original variance of the data can be removed by subtracting the best-fit estimate of the model function.

In this case, there is only one model function, but the analysis can be generalized to include any number of model functions. For example, it is not uncommon for the MR signal from a voxel to drift slightly over the course of an experiment. One can try to take this into account by including an additional model function that is a linear function of time. Then the data are modeled as a linear combination of the hemodynamic response function and a linear drift. Quadratic and higher-order drift terms can also be included as additional model functions. This basic multiple regression approach is referred to as the *general linear model* (Friston *et al.* 1995). It is important to remember here that “linear” refers to the fact that the data are modeled as a linear combination of model functions and the model functions themselves need not be linear. The general linear model is described in more detail later in the chapter.

## Fourier analysis

Another closely related approach to analyzing BOLD data for block design experiments is to calculate the Fourier transform of the measured time course and examine the component at the fundamental frequency of the stimulus pattern (Engel *et al.* 1994; Sereno *et al.* 1995). For example, if four cycles of stimulus/control are performed, then the amplitude for the four-cycle frequency in the Fourier spectrum should be a strong spike wherever there is activation. [Figure 15.2](#) shows a blocked stimulus pattern, the expected hemodynamic response, and simulated data including noise. The Fourier spectrum of the stimulus pattern itself shows a prominent fundamental frequency, and a series of odd multiples of the fundamental frequency. (By symmetry, the even multiples of the fundamental frequency

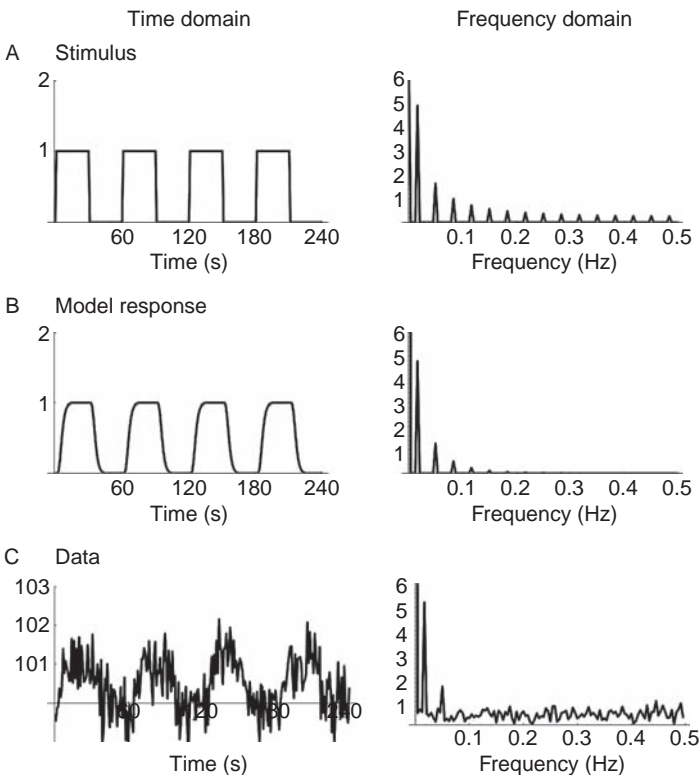


**Fig. 15.2.** Fourier components of the BOLD signal. (A) The spectral components of a blocked-design stimulus pattern show a prominent fundamental frequency and a series of odd multiples of the fundamental frequency. (B) The smoothed hemodynamic response attenuates the higher harmonics. (C) In the data with noise, only one harmonic is apparent.

do not contribute to the stimulus waveform.) The smoothing effect of the hemodynamic response attenuates the high frequencies of the stimulus pattern, and in the data only one or two harmonics are apparent. Fourier analysis can be viewed as another variation on the general linear model. Calculating the Fourier component at the fundamental stimulus frequency is equivalent to a multiple regression analysis with a sine wave and a cosine wave, both at the fundamental frequency, as the two model functions.

A Fourier analysis has the added advantage for some applications that the delay of the response is easily calculated. There is accumulating evidence that the hemodynamic delay may vary from one part of the brain to another, and this can present a problem with a standard correlation analysis. If the delay used in the model for the hemodynamic response function does not match the true delay, the value of  $r$  will be reduced, and activated pixels, which should be identifiable, could be missed. To account for this problem, the  $r$ -value for the same model shape but different delays can be calculated, and the one giving the highest value of  $r$  chosen as the best fit to those voxel data. However, if the model response function is a sine wave, the best fit of the delay can be calculated directly from the Fourier transform. For a sine wave model function, a hemodynamic delay is equivalent to a phase offset, and the Fourier transform directly provides the amplitude and phase at each frequency.

Another way of looking at a Fourier transform analysis in the context of a correlation analysis is to note that the comparison of a data time course with a model response function could be made in the frequency domain as well as in the time domain. The Fourier transform of the model response function shows spikes at multiples of the fundamental stimulus frequency, and the relative amplitudes and phases of these spikes depend on the shape of the response function in the time domain (Fig. 15.2). The Fourier transform of an activated pixel should also show spikes at the same frequencies as the model response function; however, there will also be noise present in all the frequencies. The correlation analysis is then equivalent to comparing the amplitudes of the model and data frequency spectra at the fundamental frequency and each of its harmonics and determining whether these amplitudes in the data are sufficiently larger than the noise. For a general model response function, all the harmonics can contribute to the comparison and should be used to improve sensitivity. However, as the model function approaches a single sine wave at the fundamental frequency, the Fourier transform reduces to just a single spike at the fundamental frequency. For a sustained activation of 30 s or more, the response function is better approximated with a trapezoid than a sine wave, and so the more general correlation analysis that uses all the harmonics will give a more sensitive estimate of activation than achieved with just the amplitude of the fundamental frequency in the Fourier transform of the data. However, when the stimulus is cycled more rapidly, a sine wave is a reasonable approximation to the response function, and a simple Fourier analysis should yield comparable results to a correlation with a trapezoid.

## The Kolmogorov–Smirnov test

Another statistical test used in the early days of fMRI (less so now) is to evaluate the statistical significance of detected activations in block design experiments with the Kolmogorov–Smirnov (KS) test. Like the  $t$ -test, the KS test treats the signal values measured during the task and control periods as two populations and then tests whether the two populations are significantly different. With the  $t$ -test, the focus is on whether the means of the two populations are different. With the KS test, the focus is on whether the cumulative distributions of the two populations are significantly different. For each population (e.g., all signal values measured in the activated state), the measured values are sorted into ascending order.

An estimate of the cumulative distribution is formed by calculating  $P(x)$ , the fraction of signal values greater than  $x$  for each  $x$ . From the two distributions  $P_{\text{act}}(x)$  and  $P_{\text{rest}}(x)$ , the KS statistic is calculated as the maximum difference between the two cumulative distributions. Under the null hypothesis, the distribution of the KS statistic can be calculated, so the significance of any measured value can be estimated.

In general, the KS test is less sensitive (or more conservative) than the other approaches described. In other words, some weak activations could be missed with the KS test, but the ones that are deemed to be significant are likely to be highly reliable. One potential interesting aspect of the KS test is that, in principle, it could detect a difference between two populations which have the same mean but different standard deviations. If the variance of the MR signal changed with activation, even though the mean signal remained constant, the KS test could potentially detect this change. Such a physiological effect has not been observed, so whether this mathematical property has any significance for brain activation studies is not known.

## Noise correlations

The foregoing discussion has focused on identifying whether the expected signal response is present in the data. But a complete determination of the significance of a detected activation depends on a full understanding of the noise in the data, and the noise in BOLD measurements of the brain is still not understood in a quantitative way. To clarify the problem this creates, we can return to the simplest method of a  $t$ -test comparison of the mean signals during stimulus and rest conditions. To assess the significance of the measurement of a particular value of  $t$ , we need to know the degrees of freedom, which are essentially the number of independent measurements that went into the calculation. For example, with only two measurements each in the stimulus and control states, a value of  $t > 3.0$  or larger is borderline significant ( $p = 0.029$ ), but with 50 measurements in each state,  $t > 3.0$  is highly significant ( $p = 0.0017$ ). However, these estimates of the significance of  $t$  are based on two assumptions about the noise: the noise is normally distributed, and the noise in each measurement is independent of the noise in the other measurements. Although these assumptions are good for the thermal noise component, the physiological contribution is likely to violate both (Purdon and Weisskoff 1998; Zarahn *et al.* 1997a). For example, added low-frequency noise components from respiration are likely to be quite structured and not normally distributed. Furthermore, because this noise has low frequencies, the noise added into a measurement at one time point is likely to be similar to the noise added in at the next time point, so the noise is not independent.

A similar question arises when we consider multiple voxels: is the noise in one voxel independent of the noise in a neighboring voxel? Again, random thermal noise is independent, but physiological noise is likely to have strong spatial correlations. For example, CSF pulsations are likely to affect nearby pixels in a similar way. The nature of these correlations will have a strong effect on calculating the significance of clusters of pixels. For example, any motion of the subject's head in synchrony with the stimulus will lead to a bulk shift in the MR images. At any edge in the image where there is a contrast difference, even small subpixel shifts will lead to a time-dependent signal that correlates strongly with the motion. Such stimulus-correlated motion artifacts are a common problem in fMRI, and the spurious correlations tend to occur in many contiguous pixels around the edge of the brain. As a result, clusters of false-positive activations can occur much more frequently than would be expected for voxels with independent noise.

In short, structured noise remains a problem for the analysis of BOLD data, and further work is needed to understand these signal fluctuations so that they can be taken into account

in the statistical analysis. For the remainder of this chapter, we will ignore these complications in order to clarify the basic ideas of the statistical analysis.

## Interpreting BOLD activation maps

This chapter has introduced some of the complexities of the statistical analysis. Although it often seems like many different approaches are used, in fact there is an underlying unity to these methods. In this section, we will step back from the details of the analysis to look at how the resulting maps can be interpreted. For this purpose, it is sufficient to return to the simple  $t$ -test comparing means, and forget complications such as the hemodynamic response function, systematic signal drift, and correlated noise. This basic approach is the simplest type of analysis of BOLD data; nevertheless, it captures the basic reasoning behind the analysis. The choice of the statistic and the justification for choosing a particular threshold may differ, but the basic structure is the same. It is important to be clear on the philosophy behind this approach. The goal is not to identify all voxels whose magnitude of change is greater than some threshold (e.g., all voxels with a fractional signal change greater than 1%). Instead, the goal is to identify all voxels whose signal change is sufficiently larger than what would be expected by chance alone, and the level of our statistical confidence depends on the threshold applied to the map of the statistical parameter.

But this makes the interpretation of activation maps such as Fig. 5.4, somewhat subtle, and some of our natural impulses when viewing such maps need to be curbed. It is tempting to look at such a map and interpret it as a map of the activated regions. We can say with confidence, and we can specify exactly what level of confidence, that the voxels that are colored are “activated” (we will ignore for the moment various artifacts that might lead to false-positive activations). But we cannot conclude that the pixels that are not colored are not activated. We can only say that the statistical quality of the measurements in those voxels is too low for us to be confident that there *is* an activation. In other words, strictly speaking, our failure to detect an activation in a particular voxel at a desired level of statistical quality cannot be taken as evidence of a lack of activation in that voxel. For example, one can imagine the simple, idealized case of two voxels with identical changes in CBF, which lead to identical 1% changes in the BOLD signal, but the intrinsic signal standard deviation in one voxel is 0.1% and in the other is 1%. The first would be detected and classified as an activated area, whereas the second would not, even though the CBF change is the same.

Another way of explaining this approach is that in analyzing BOLD data we are primarily concerned with eliminating false positives, such as vessels with high intrinsic signal variability. But we are not concerned with false negatives, in the sense that the analysis is not directed at eliminating false negatives. In fact, no negative finding is ever meaningful with this type of analysis alone. It is possible to carry the analysis further, for example to define confidence intervals for how much absolute activation (i.e., the signal change) might be present in a voxel (Frank *et al.* 1998), but this is not usually done. Similarly, the value of the statistic itself, such as  $t$ , should never be taken as a measure of the *degree* of activation: a larger value of  $t$  in one voxel than another does not imply that the level of activation is larger in the first. To draw such a conclusion, one must show that the difference in the  $t$ -values results from a difference in the signal change, rather than a difference in the intrinsic variability of the signal.

## The general linear model

With these basic ideas in mind, we can consider in more detail how the general linear model works. This method provides a powerful and flexible tool for analyzing BOLD data and also for

designing experiments to maximize the likelihood of detecting weak activations. As introduced above, this approach models the data as a linear combination of a set of model functions plus random noise. The model functions themselves have a known shape, but the amplitudes multiplying each model function are unknown. The analysis consists of finding the estimates of these amplitudes that provide the best fit of the model to the data in a least-squares sense. That is, the quality of a particular set of model parameters is gauged by calculating the sum of squares of the residuals after the model is subtracted from the data, and the best-fit set of parameters is the one that minimizes this sum. The general linear model is the framework for many commonly used statistical analysis techniques, including multiple regression analysis and analysis of variance (ANOVA). In thinking about the statistical analysis of BOLD data, a useful conceptual tool is to view the process as an exercise in multidimensional geometry, and throughout this chapter we will emphasize this geometric view (Frank *et al.* 1998). A useful introduction to this way of thinking is given by Saville and Wood (1991).

## The hemodynamic response

The first step in applying a linear model analysis is to predict the shape of the BOLD response to a given stimulus pattern so that only the amplitude of this response is unknown. The hemodynamic response is not a simple function of the stimulus pattern, as it often includes transient features such as a post-stimulus undershoot. In addition, the response is not a linear function of the stimulus duration, in the sense that the response to a sustained stimulus is not as large as one would predict from the response to a brief stimulus (Boynton *et al.* 1996; Friston *et al.* 1998a; Glover 1999; Vasquez and Noll 1998). Furthermore, the hemodynamic response varies among individuals and regions of the brain (Aguirre *et al.* 1998). Nevertheless, a fruitful approach to the analysis of the data is to ignore the complications and use the simplified assumption that the hemodynamic response is linear with stimulus duration. Although not true, this assumption likely does not introduce large errors, but this question requires further attention.

To emphasize how the analysis works, we will assume that the response to a brief stimulus looks something like the curve shown in Fig. 15.3A. If this is the response to a single brief stimulus, what is the response to a more complicated stimulus pattern? We can describe the stimulus pattern as  $X(t)$ , which takes on a value of 1 when the stimulus is on and 0 when the stimulus is off. Assuming linearity, the response to a more complex stimulus is the convolution of the stimulus pattern  $X(t)$  and the hemodynamic response (or impulse response) function  $h(t)$ , written as  $X(t) * h(t)$ . Figure 15.3B shows the model response for a sustained

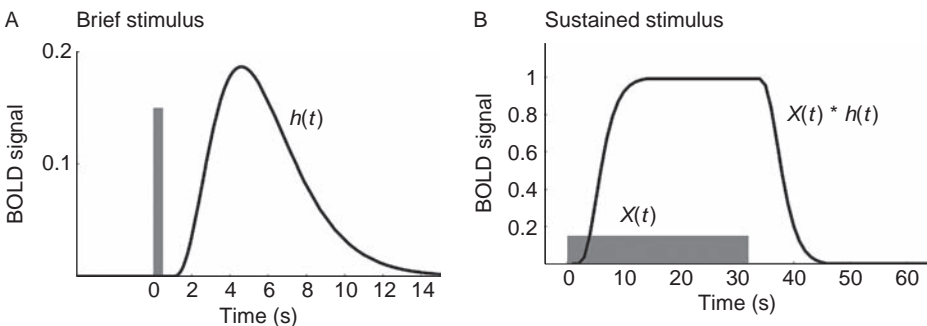


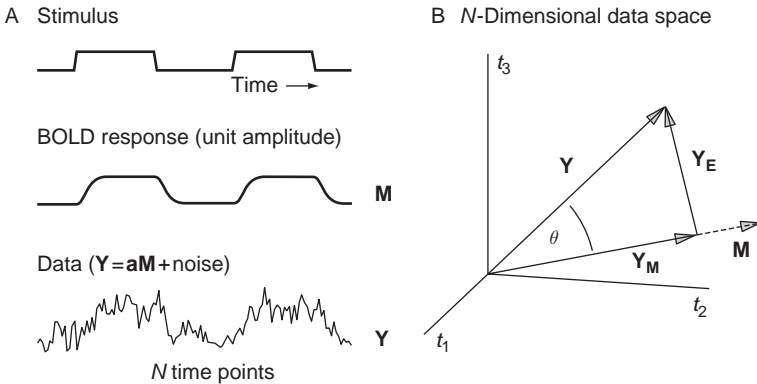
**Fig. 15.3.** The hemodynamic response. (A) A brief stimulus produces a BOLD hemodynamic response that is delayed and broadened, modeled as a gamma-variate function. (B) Assuming that the BOLD response is linear, the response to a stimulus of longer duration is the convolution of the impulse response  $h(t)$  with the stimulus pattern  $X(t)$ .

stimulus. The signal ramps up to a plateau level and then remains constant until the end of the stimulus. The ramp time is directly proportional to the width of  $h(t)$ , and the plateau level is proportional to the area under  $h(t)$ .

The hemodynamic response model shown in Fig. 15.3 is a reasonable approximation to a typical response, but there is nothing special about the mathematical form used (a gamma-variate function in this case). Other forms have been suggested, but all are based just on the convenience of the mathematical shape, rather than on a physiological model that would predict that particular form (Boynton *et al.* 1996; Friston *et al.* 1994). There is not yet an underlying mathematical theory of the blood flow response that would predict a particular flow response shape. For this reason, choosing a particular shape is simply an empirical convenience, and other shapes may work equally well. For now we consider the simple case of a known hemodynamic response  $h(t)$ .

## Fitting the data with a known model response

To be specific, suppose that we are examining a BOLD time series from one voxel, consisting of  $N$  measurements of the signal, with a time separation TR between measurements. The stimulus pattern consists of two cycles of stimulus and control, as illustrated in Fig. 15.4A. The



Vectors in data space:

$M$  = mode vector for unit amplitude response

$Y$  = data vector

$Y_M = \left( \frac{Y \cdot M}{M \cdot M} \right) \left( \frac{M}{M \cdot M} \right)$  = projection on-to model

$Y_E = Y - Y_M$  = error vector

Parameter estimates:

$a = \frac{Y_M}{M}$  = response amplitude

$\sigma^2 = \frac{Y_E^2}{N-1}$  = noise variance

Statistics:

$r = \cos(\theta) = \frac{Y_M}{Y}$  = correlation coefficient

$t = \sqrt{N-1} \cos(\theta) = t = \sqrt{N-1} \frac{Y_M}{Y}$  =  $t$ -statistic

**Fig. 15.4.** The basic linear model analysis of BOLD data. For a time series of  $N$  measurements, the data  $Y$  and the expected BOLD response  $M$  (A) are (B) viewed as vectors in an  $N$ -dimensional data space. (B) The data are modeled as an unknown amplitude  $a$   $M$  plus noise with standard deviation  $\sigma$ . The best-fit value of  $a$  is given by the projection of the data on to the model vector,  $Y_M$ , and  $\sigma$  is calculated from the remainder of the data,  $Y_E$ . The  $t$ -statistic and the correlation coefficient  $r$  are calculated from the triangle in the upper right. The mathematical relations are shown below the figure.



expected model response to this stimulus pattern is  $X(t) * h(t)$ , a smoothed and delayed version of the stimulus as shown in the second line. The activation signal is modeled as an unknown amplitude  $a$  multiplied by the model response, and this BOLD response is sampled at each of the measurement times. The full measured data include this sampled signal plus added noise at each of the measurement times. We assume that each noise value is independently drawn from a normal distribution with a mean of zero and a standard deviation ( $\sigma$ ).

For this analysis, we focus on the variance of the data. Part of the variance results from the activation, and so depends on the magnitude of  $a$ , and the rest comes from the noise component. The goal of the analysis is to estimate  $a$  and the standard deviation and to assess the significance of the estimate of  $a$ . Because we are only interested in the variance, the first step is to remove the mean value of both the model function and the data, to create a vector of model response values  $M_i$  ( $i = 1$  to  $N$ ) and a vector of data values  $Y_i$ .

The essence of the geometric view of this analysis is to imagine an  $N$ -dimensional space in which each axis corresponds to one time point. Of course, we cannot picture more than three dimensions, but mathematically there is no problem in defining an  $N$ -dimensional space. Each of the measured data values  $Y_i$  is a coordinate along the  $i$ th axis, so the full measured time course corresponds to one point in this space. We can think of this point as defining a vector from the origin to the point, and the projection of this data vector  $\mathbf{Y}$  onto the  $i$ th axis is simply the measured signal  $Y_i$ . We will use boldface symbols to denote a vector, and plain text to denote a scalar, or the magnitude of a vector. In other words,  $\mathbf{Y}$  denotes the full data vector, whereas  $Y$  is the length of that vector.

In a similar fashion, the model response is also a vector ( $\mathbf{M}$ ) in the  $N$ -dimensional data space, as illustrated in Fig. 15.4B. It is important to be clear about the meaning of the magnitude  $M$  of this vector. As we will see,  $M$  is the key number that characterizes the sensitivity of an experimental design. The model response  $\mathbf{M}$  is the unit amplitude response. For example, if the BOLD response is measured in image signal units, then  $\mathbf{M}$  is the response for an activation-induced hemodynamic response of one signal unit. If the best-fit value of  $a$  is 2, this means that the signal change is twice as large as that described by  $\mathbf{M}$ .

If there was no noise, then we would expect that the vector  $\mathbf{Y}$  would lie along the same direction as  $\mathbf{M}$ , and the estimate of  $a$  then would be simply  $Y/M$ . With noise, however,  $\mathbf{Y}$  no longer lies along  $\mathbf{M}$ , and so the analysis is slightly more difficult. For any value of  $a$ , we could multiply the model function by  $a$  and subtract this prediction from the measured data to form the residuals. Our goal is to find the value of  $a$  that minimizes the sum of the squared residuals. But this process can be directly visualized with the geometric picture. Any value of  $a$  produces a vector with amplitude  $aM$  along the axis defined by  $\mathbf{M}$ . Subtracting this vector from  $\mathbf{Y}$  creates a residual vector (or *error vector*)  $\mathbf{Y}_E$ . The sum of the squared residuals is the sum of the squares of each component of  $\mathbf{Y}_E$ , which is just  $Y_E^2$ , the length squared of the vector  $\mathbf{Y}_E$ . In other words, the sum of the squared residuals is simply the distance squared from the point defined by the model vector  $a\mathbf{M}$  to the point defined by  $\mathbf{Y}$  in the  $N$ -dimensional space. This is minimized by minimizing  $\mathbf{Y}_E$ , so the best fit of  $a$  is calculated by finding the point along the direction defined by  $\mathbf{M}$  that is closest to the data point defined by  $\mathbf{Y}$ . It is this close connection of least squares with distance that makes the geometric picture a natural conceptual tool.

For this case of a single model function, the best-fit amplitude is calculated by taking the projection  $\mathbf{Y}_M$  of the data onto the axis defined by  $\mathbf{M}$ . The best-fit value of  $a$  is given directly by the magnitude of  $\mathbf{Y}_M$ , as  $a = Y_M/M$ . (Remember that the magnitude of  $\mathbf{M}$  corresponds to a unit amplitude response, so  $M$  essentially calibrates the projection of the data in signal amplitude units.) Another way of looking at this is that we are breaking the data vector into

two perpendicular components: the projection on to the model vector,  $\mathbf{Y}_M$ , and a remaining error component  $\mathbf{Y}_E$  with  $Y^2 = Y_M^2 + Y_E^2$  (Fig. 15.4). Because the mean of the data has been removed,  $Y^2$  is the total variance of the signal. The decomposition of  $\mathbf{Y}$  into  $\mathbf{Y}_M$  and  $\mathbf{Y}_E$  thus partitions the variance between the activation and the noise. The component of the variance from the activation is  $Y_M^2$  and the remaining variance from noise is  $Y_E^2$ .

From the magnitude of  $\mathbf{Y}_E$ , we can estimate the noise variance  $\sigma^2$ . The length squared  $Y_E^2$  is the sum of the squared values of each component of the vector, and each component corresponds to the random noise signal added in at a particular measurement time. For each of these noise signals, the expected squared value is  $\sigma^2$ . So in calculating the magnitude of  $Y_E^2$ , each dimension adds in a value of  $\sigma^2$ .

This brings us to a critical question: how many dimensions contribute? At first glance, the answer appears to be  $N$  because that is the full dimensions of the data space. However, in the construction of  $\mathbf{Y}_E$ , we have first removed the component along a single dimension in the direction of  $\mathbf{M}$ , so  $\mathbf{Y}_E$  is really a vector in an  $N - 1$  dimensional space. One can think of this as dividing the  $N$ -dimensional space into a model space and an error space. In this case, the model space is a single dimension, and the error space has  $N - 1$  dimensions. In a more general model with  $m$  model functions (discussed below), the model space has  $m$  dimensions, and the error space has  $N - m$  dimensions. The number of dimensions in the error space is usually called the *degrees of freedom*,  $\nu = N - m$ . Returning to our estimate of  $\sigma^2$ , if the error space has  $\nu$  dimensions, then the expected magnitude of  $Y_E^2$  is  $\nu\sigma^2$  and so our estimate of the noise variance is  $\sigma^2 = Y_E^2/\nu$ .

The decomposition of the data vector into a model component and a noise component leads to direct estimates of the amplitude of the activation  $a$  and the noise variance  $\sigma^2$ . On average, the estimate of  $a$  should be the true value, but there will be some variance in the estimate owing to the noise signal that falls along the direction of  $\mathbf{M}$ . In other words, if we were to perform the experiment many times, with the same activation response but different noise samples, the estimates of  $a$  would have a variance we can call  $\sigma_a^2$ . The statistical significance of a measured value of  $a$  then depends directly on the magnitude of  $\sigma_a$ . For the current case of a single model vector, the variance of the estimate of  $a$  can be calculated in a direct way. Noise contributes to all dimensions of the data space equally, so there will be a noise component along  $\mathbf{M}$  with variance  $\sigma^2$ . Scaling this variance to the units of the model function, the variance of  $a$  is  $\sigma_a^2 = \sigma^2/M^2$ .

A natural measure of the statistical quality of a measurement of  $a$  is the ratio of the measured value to the uncertainty of the measurement, the SNR,

$$SNR = \frac{a}{\sigma_a} = \frac{aM}{\sigma} \quad (15.1)$$

This is an important relationship, and, as we will see, it provides a useful way of comparing the sensitivity of different experimental designs.

## Statistical significance

So far we have considered statistical significance in terms of the SNR of the estimate of the activation amplitude. A related and more common approach is to test how likely it is that a given measured model amplitude could have arisen by chance owing to noise alone. In other words, this approach tests the significance of the null hypothesis that  $a = 0$  (i.e., that there is no activation). This type of test can be done with either a  $t$ -test or an  $r$ -value, and both statistics have a natural geometric interpretation as shown in Fig. 15.4.

Under the null hypothesis, the sum of squares of the data given by the magnitude  $Y^2$  results entirely from noise. The expected magnitude squared of each component of the

$N$ -dimensional data space is  $\sigma^2$ . If we isolate any one axis of the  $N$ -dimensional data space, the expected mean value of that component is zero with a variance  $\sigma^2$ . The  $t$ -statistic with  $\nu$  degrees of freedom ( $t_\nu$ ) is the ratio of the amplitude measured along one axis to the noise standard deviation estimated from the remaining  $\nu$  dimensions of the data space. If the component along the model vector is caused only by noise, then its amplitude should be on the order of  $\sigma$ , and  $t$  is approximately equal to one. As  $t$  grows larger, the probability of such a large noise amplitude appearing along the model vector becomes less and less likely. From the arguments in the previous sections, the estimate of the standard deviation is  $Y_E/\sqrt{\nu}$ , and the component along the model vector is  $Y_M$ , so  $t = \sqrt{\nu} Y_M/Y_E$ . In this way,  $t$  is proportional to the ratio of two legs of the triangle in Fig. 15.4B. Furthermore, this expression for  $t$  reduces precisely to the ratio of the estimate of  $a$  to the standard deviation of that estimate. In short,  $t$  is identical to our expression for the SNR (Eq. (15.1)).

The  $r$ -value is the scalar product of  $\mathbf{Y}$  and  $\mathbf{M}$ , normalized by their respective magnitudes. In other words,  $r = \cos \theta$ , where  $\theta$  is the angle between  $\mathbf{Y}$  and  $\mathbf{M}$  in the data space. Because both  $t$  and  $r$  are calculated from the same triangle, there is a simple relation between them:

$$t = \sqrt{\nu} \cot \theta = \sqrt{\nu} \frac{r}{\sqrt{1 - r^2}} \quad (15.2)$$

The test of significance then amounts to asking how often a value greater than a given value of  $t$  or  $r$  should occur as a result of noise. These distributions are calculated from the geometry shown in Fig. 15.4 under the null hypothesis and are tabulated in standard statistics software packages. Given a measured value of  $t$  or  $r$  and the degrees of freedom  $\nu$ , the calculated probability of that result occurring by chance is the statistical significance. That is, the statistical significance reflects the confidence with which we can reject the null hypothesis that there is no activation.

## Fitting the data with a more general linear model

The preceding sections introduced the basic ideas of the general linear model, but in the limited context of a single model function. There are a number of experimental designs where more than one model function is desirable. Some examples follow.

*Removal of baseline trends* In addition to the model response and noise, a real data time course often shows a drift over time. This can be taken into account by including other model functions (e.g., a linear drift term, a quadratic term) to account for this added variance.

*Two types of stimuli* In more sophisticated BOLD experiments, multiple stimuli are used, and it is desirable to separate the responses to the different stimuli. Or, it may be useful to treat different aspects of the same stimulus as different events (e.g., in a simple motor task some areas may activate only at the beginning and end of the task, whereas other areas are activated throughout). Each type of stimulus can be modeled with a different response function.

*Unknown hemodynamic response* The exact shape of the hemodynamic response is unknown and is likely to vary across the brain. Rather than using a single model function, a small set of model functions can be used to describe a range of shapes.

*Event-related fMRI* The hemodynamic response itself can be estimated for each voxel by treating the response at each time point after an event as a separate model function.

To make the linear model more general by including these applications, we will consider the case of two model functions. The jump from one function to two may not sound like much of a generalization, but in fact this brings in all the new features of the general linear model that

$$\mathbf{Y} = \mathbf{M} \cdot \mathbf{a} + \mathbf{e}$$

$\mathbf{Y}$  = data vector  
 $\mathbf{M}$  = matrix of model functions  
 $\mathbf{a}$  = amplitude vector  
 $\mathbf{e}$  = noise vector

$$\begin{matrix} \text{N time points} \downarrow \\ \begin{pmatrix} Y(t_1) \\ Y(t_2) \\ \dots \\ Y(t_N) \end{pmatrix} = \begin{pmatrix} M_1(t_1) & M_2(t_1) \\ M_1(t_2) & M_2(t_2) \\ \dots & \dots \\ M_1(t_N) & M_2(t_N) \end{pmatrix} \begin{pmatrix} a_1 \\ a_2 \end{pmatrix} + \begin{pmatrix} e_1(t_1) \\ e_2(t_2) \\ \dots \\ e_N(t_N) \end{pmatrix} \end{matrix}$$

data                      design matrix                      amplitudes                      noise

$$\mathbf{a} = (\mathbf{M}^T \mathbf{M})^{-1} \mathbf{M}^T \mathbf{Y}$$

$$\mathbf{c} = (\mathbf{M}^T \mathbf{M})^{-1} = \text{covariance matrix}$$

**Fig. 15.5.** The mathematical structure of the general linear model. The data are modeled as a linear combination of a set of model functions with unknown amplitudes plus noise. The design matrix  $\mathbf{M}$  contains one column for each model function, and the amplitudes form a vector  $\mathbf{a}$ . The best-fit estimates of the amplitudes are calculated from the design matrix as shown in the lower part of the figure, and the variances of the estimated amplitudes are calculated from the covariance matrix (see Box 15.1 for mathematical details).

did not appear in the single model function, and with only two model functions it is still possible to visualize the geometry.

The mathematical form of the general linear model is shown in Fig. 15.5, and the geometry is illustrated in Fig. 15.6. Instead of a single model vector, we now have a matrix of model vectors, with the first column representing  $\mathbf{M}_1$  and the second column representing  $\mathbf{M}_2$ , the two model vectors. We will denote the matrix with the symbol  $\mathbf{M}$ , and continue to use the symbol  $\mathbf{M}$  for individual vectors that make up the design matrix. For example, if two types of stimulus are intermixed during an experimental run, then  $\mathbf{M}_1$  and  $\mathbf{M}_2$  could represent the separate responses to the two stimuli. That is,  $\mathbf{M}_1$  is calculated by convolving the first stimulus pattern  $X_1(t)$  with a hemodynamic response function, and  $\mathbf{M}_2$  is the convolution of the other stimulus pattern  $X_2(t)$  with the hemodynamic response. (More explicitly,  $\mathbf{M}_1$  is the magnitude of  $X_1(t) * h(t)$  with the mean removed.) The implicit assumption here is that the responses simply add, so that the response to both stimuli is the sum of the responses to each separate stimulus.

There are now two amplitudes to be estimated, so the single amplitude  $a$  is replaced with a vector  $\mathbf{a}$  consisting of two amplitudes,  $a_1$  and  $a_2$ . We can think of  $\mathbf{a}$  as a vector in a parameter space that defines the amplitudes of the model functions (i.e., the vector  $\mathbf{a}$  defines a point in a two-dimensional parameter space in which one axis corresponds to  $a_1$  and the other corresponds to  $a_2$ ). But the basic form of the model is the same. The data are modeled as a sum of two model vectors with a known shape but with unknown amplitudes  $a_1$  and  $a_2$ , plus noise with variance  $\sigma^2$ . From the geometric viewpoint (Fig. 15.6), the model space now has two dimensions, defined as the plane that includes both  $\mathbf{M}_1$  and  $\mathbf{M}_2$ , and the dimension of the error space is  $v = N - 2$ .

The procedure for fitting the data is similar to the earlier case of a single model function. The goal is to find the point in the model space that is closest to the data point defined by  $\mathbf{Y}$ , and this point is the projection  $\mathbf{Y}_M$  on to the model plane. Although conceptually similar to the case of the single model function, the mathematics is now more complicated because the projection on to the model space does not fall on either of the model vectors, but rather the plane formed by those vectors, and so  $\mathbf{Y}_M$  cannot be calculated as readily. For the ideal case in which  $\mathbf{M}_1$  and  $\mathbf{M}_2$  are perpendicular, the analysis is simple, and the projection of  $\mathbf{Y}$  separately on to  $\mathbf{M}_1$  and  $\mathbf{M}_2$  works just as it did for the single model function case. If we call the magnitudes of these two projections  $Y_{M1}$  and  $Y_{M2}$ , then the amplitudes are simply the appropriately scaled versions:  $a_1 = Y_{M1}/M_1$  and  $a_2 = Y_{M2}/M_2$ .

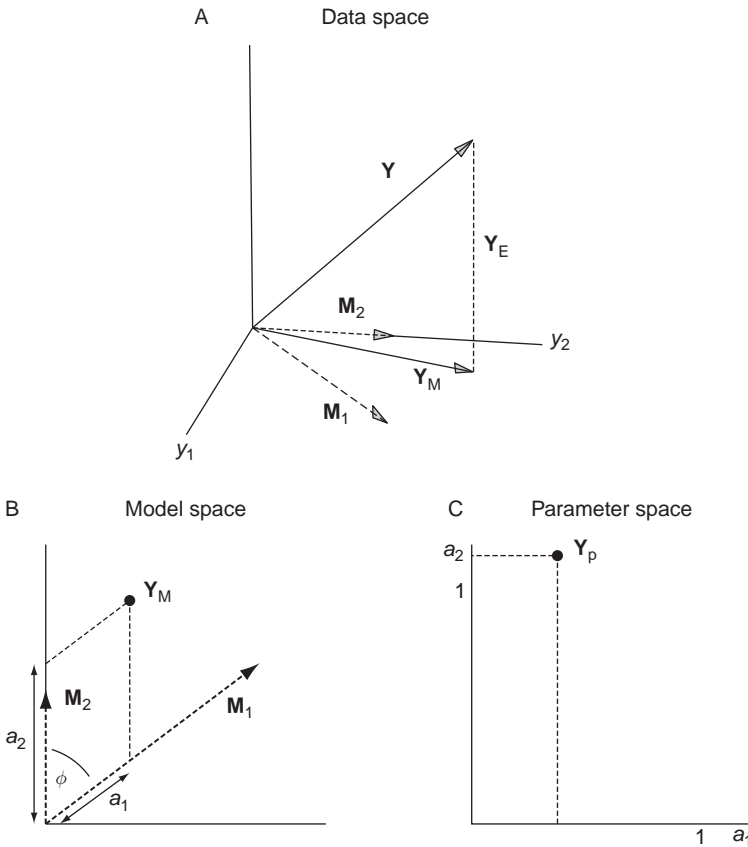


**Fig. 15.6.** The geometric structure of the general linear model. The illustration shows two model functions that define a two-dimensional model space. The projection  $\mathbf{Y}_M$  of the data on to the model space (A) is modeled as a linear combination of the two model functions, and the remaining component  $\mathbf{Y}_E$  provides a measure of the noise. The point  $\mathbf{Y}_M$  in the model space (B) is transformed to a parameter space in which the axes correspond to the amplitudes  $a_1$  and  $a_2$ . (C) This transformation accounts for the different amplitudes of the model functions and the fact that they may not be orthogonal (the mathematical details are in [Box 15.1](#)).

The complication comes in when the two model functions are not perpendicular, as illustrated in [Fig. 15.6B](#). Our goal is to find amplitudes  $a_1$  and  $a_2$  such that  $a_1\mathbf{M}_1 + a_2\mathbf{M}_2 = \mathbf{Y}_M$ , the full projection of the data onto the model space. But the correct amplitudes are not given by the separate projections  $Y_{M1}$  and  $Y_{M2}$  on to  $\mathbf{M}_1$  and  $\mathbf{M}_2$ . The correct values come from the parallelogram shown because this represents the vector sum that produces  $\mathbf{Y}_M$ . Mathematically, we can think of representing the projection  $\mathbf{Y}_M$  in two spaces: the model space (the subspace of the full data space that is spanned by the model functions) and the parameter space in which one axis corresponds to  $a_1$  and the other to  $a_2$ . The goal is to transform the coordinates of  $\mathbf{Y}_M$  in the model space into the coordinates of the parameter space. The essential problem is that in the general case the parameter space is defined by two vectors that are not orthogonal to each other and that, in addition, have unequal lengths  $M_1$  and  $M_2$ . Both these factors are taken into account in the coordinate transformation shown graphically in [Fig. 15.6](#). The mathematical details are described in [Box 15.1](#).

**Box 15.1. Estimating the model function amplitudes and their variance**

The calculation of the best-fit amplitudes  $\mathbf{a}$  is done in terms of the matrices and vectors illustrated in Fig. 15.6. The total data vector is  $\mathbf{Y} = \mathbf{Y}_M + \mathbf{Y}_E$ , with  $\mathbf{Y}_M = \mathbf{M}\mathbf{a}$ , where  $\mathbf{M}$  is the design matrix formed from the model vectors  $\mathbf{M}_1$  and  $\mathbf{M}_2$ . Now consider the scalar products of  $\mathbf{Y}$  with each of the model vectors  $\mathbf{M}_1$  and  $\mathbf{M}_2$ . In matrix terms, these components are given as a vector by multiplying  $\mathbf{Y}$  by the transpose of  $\mathbf{M}$ :

$$\mathbf{M}^T \mathbf{Y} = \mathbf{M}^T \mathbf{Y}_M + \mathbf{M}^T \mathbf{Y}_E = \mathbf{M}^T \mathbf{M} \mathbf{a} \quad (\text{B15.1})$$

Because we have constructed  $\mathbf{Y}_E$  to be perpendicular to  $\mathbf{M}_1$  and  $\mathbf{M}_2$ , the second term is zero, and we have used the relation  $\mathbf{Y}_M = \mathbf{M}\mathbf{a}$ . The vector of best-fit amplitudes is then:

$$\mathbf{a} = (\mathbf{M}^T \mathbf{M})^{-1} \mathbf{M}^T \mathbf{Y} \equiv \mathbf{L} \mathbf{Y} \quad (\text{B15.2})$$

where the superscript  $-1$  indicates matrix inverse, and  $\mathbf{L}$  is defined as the combined linear transformation matrix that converts the data to best-fit amplitude estimates.

If the model vectors are not perpendicular, then there will be some covariance in the errors of each of the amplitude estimates. In some cases, we are interested only in the error of a particular amplitude, such as when one model function is a known hemodynamic response and the second model function is a linear drift of the signal. In this case, we do not care what the drift slope actually is; we simply want to account for it and remove it in order to improve the estimate of  $a_1$ , the activation response. If, however, the two model functions represent the responses to two different stimuli, the errors in each amplitude and different linear combinations are important. For example,  $a_1 - a_2$  is a measure of the differential response to the two stimuli, and so the uncertainty in the estimate of  $a_1 - a_2$  is of interest.

Now we can consider how noise in the data space propagates into uncertainties of the parameter estimates. In general, any linear combination of the model amplitudes can be thought of as a contrast of the form  $c = w_1 a_1 + w_2 a_2$  and the weights  $w_1$  and  $w_2$  are treated as the components of a vector in the parameter space (Friston *et al.* 1999). In matrix form, this contrast can be written as  $c = \mathbf{a}^T \mathbf{w}$ . For example, if the contrast of interest is simply the amplitude  $c = a_1$ , then  $w_1 = 1$  and  $w_2 = 0$ , whereas if the contrast of interest is the differential response to the two stimuli  $c = a_1 - a_2$ , then  $w_1 = 1$  and  $w_2 = -1$ . The variance of the chosen contrast,  $\sigma_w^2$ , is calculated from the expected value of  $c^2$ :

$$\begin{aligned} c^2 &= (\mathbf{a}^T \mathbf{w})^T (\mathbf{a}^T \mathbf{w}) = \mathbf{w}^T (\mathbf{a} \mathbf{a}^T) \mathbf{w} \\ \langle c^2 \rangle &= \mathbf{w}^T \langle \mathbf{a} \mathbf{a}^T \rangle \mathbf{w} \end{aligned} \quad (\text{B15.3})$$

where we have used the matrix relation  $(\mathbf{A}\mathbf{B})^T = \mathbf{B}^T \mathbf{A}^T$  for matrices  $\mathbf{A}$  and  $\mathbf{B}$ , and the notation  $\langle b \rangle$  indicates the expected value of a scalar  $b$ . Because only the projection of the data into the model space determines the amplitudes, we can rewrite Eq. (B15.2) as  $\mathbf{a} = \mathbf{L} \mathbf{Y}_M$  and substitute this in Equation (B15.3):

$$\begin{aligned} \mathbf{a} \mathbf{a}^T &= (\mathbf{L} \mathbf{Y}_M) (\mathbf{L} \mathbf{Y}_M)^T = \mathbf{L} (\mathbf{Y}_M \mathbf{Y}_M^T) \mathbf{L}^T \\ \langle \mathbf{a} \mathbf{a}^T \rangle &= \mathbf{L} \langle \mathbf{Y}_M \mathbf{Y}_M^T \rangle \mathbf{L}^T \end{aligned} \quad (\text{B15.4})$$

If each component is independent Gaussian noise, then  $\langle \mathbf{Y}_M \mathbf{Y}_M^T \rangle = \sigma^2 \mathbf{I}$ , where  $\mathbf{I}$  is the identity matrix with ones down the diagonal and zeroes everywhere else. Then

$$\begin{aligned} \langle \mathbf{a} \mathbf{a}^T \rangle &= \sigma^2 \mathbf{L} \mathbf{L}^T = [(\mathbf{M}^T \mathbf{M})^{-1} \mathbf{M}^T] [\mathbf{M} (\mathbf{M}^T \mathbf{M})^{-1}] \\ \langle \mathbf{a} \mathbf{a}^T \rangle &= \sigma^2 (\mathbf{M}^T \mathbf{M})^{-1} \end{aligned} \quad (\text{B15.5})$$

So for any contrast of interest defined by a vector of weights  $\mathbf{w}$ , the variance is

$$\sigma_w^2 = \sigma^2 \mathbf{w}^T (\mathbf{M}^T \mathbf{M})^{-1} \mathbf{w} \quad (\text{B15.6})$$

This is a very useful equation for evaluating the sensitivity of an fMRI experiment. As one would expect, the variance of any combination of estimated amplitudes is proportional to the intrinsic noise variance  $\sigma^2$ , but there is an additional scaling factor determined by the design of the experiment through the matrix of model functions  $\mathbf{M}$  (the design matrix). Combining this equation with the estimated value of the contrast  $c = \mathbf{a}^T \mathbf{w}$ , we can write a general expression for the SNR of this contrast as

$$\text{SNR}(\mathbf{w}) = \frac{\mathbf{a}^T \mathbf{w}}{\sigma \sqrt{\mathbf{w}^T (\mathbf{M}^T \mathbf{M})^{-1} \mathbf{w}}} \quad (\text{B15.7})$$

This expression is the generalization of Eq. (15.1). Under the null hypothesis that the contrast is zero, this quantity should follow a  $t$ -distribution with  $\nu$  degrees of freedom.

## The variance of the parameter estimates

With any statistical analysis, a critical question is whether the estimated amplitudes are statistically significant. As we found in considering a single model function, there are two related ways to address this question. The first is to estimate the SNR of the measurement, the ratio of the measured amplitude to the expected variance in that measurement. The second approach is to define a  $t$ -statistic and ask how likely it would be for that value of  $t$  or larger to occur just through random noise even though the true amplitude of the model function is zero (i.e., there is no activation). We found that these two dimensionless numbers, the SNR and the  $t$ -statistic, were identical for the single model function. We now want to consider the same question for the more general linear model.

Random noise occurs along all the axes of the data space, and so noise components also fall in the model space and are transformed into variance of the model parameter estimates. Figure 15.6 illustrates the transformation from the model space to the parameter space defined by the amplitudes  $a_1$  and  $a_2$ . To begin with, suppose that there is no activation, so the true values of  $a_1$  and  $a_2$  are zero. In the model space, noise is isotropic, in the sense that the random component along any axis has the same variance  $\sigma^2$ . If the experiment were performed many times, the random data points that fall in the model space would form a symmetric cloud centered on the origin. We can represent this by drawing a circular set of points in the model space with each point a distance  $\sigma$  from the origin and then ask how this ring of points is transformed into the parameter space (i.e., transformed into values of  $a_1$  and  $a_2$ ).

Figure 15.7 illustrates this transformation into the parameter space for several examples. If  $\mathbf{M}_1$  and  $\mathbf{M}_2$  have the same amplitude and are perpendicular to each other, the ring of noise points transforms into another ring. But if  $\mathbf{M}_1$  and  $\mathbf{M}_2$  are not perpendicular, the noise points are spread into an ellipse oriented at  $45^\circ$  to the  $a_1$ - and  $a_2$ -axes in the parameter space. As the angle between  $\mathbf{M}_1$  and  $\mathbf{M}_2$  decreases, the ellipse becomes more elongated but remains at the same orientation as long as the magnitudes  $\mathbf{M}_1$  and  $\mathbf{M}_2$  are equal. When  $\mathbf{M}_1$  and  $\mathbf{M}_2$  have different magnitudes the axes are scaled differently, changing the orientation of the ellipse.

We can now return to the more general case in which the values of  $a_1$  and  $a_2$  are not necessarily zero. If we performed the same experiment many times with the same stimuli and the same true responses, the projections into the model space would transform into a cloud of points in the parameter space centered on the correct values of  $a_1$  and  $a_2$  (shown as a contour

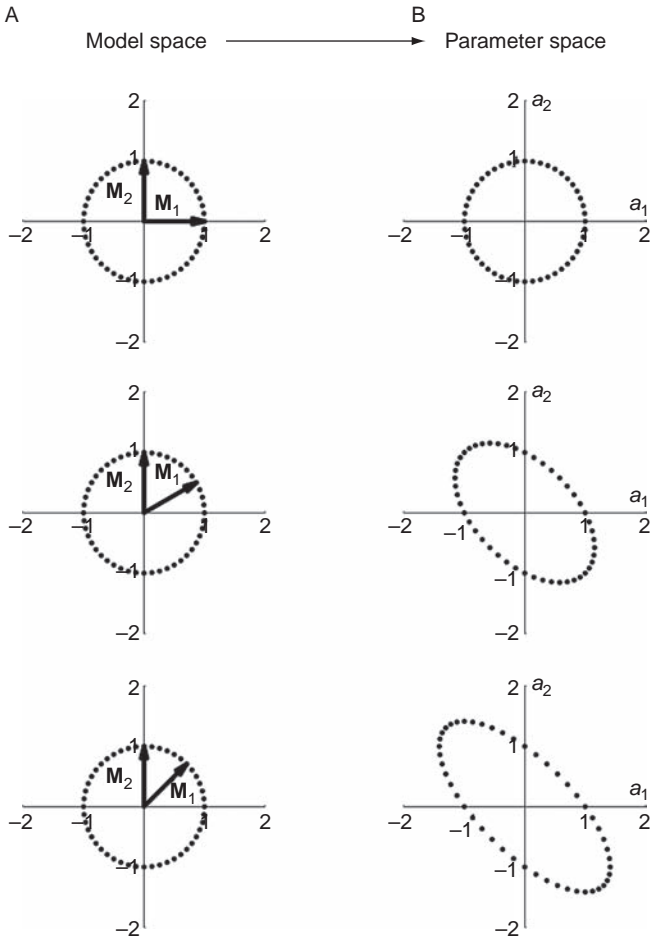


**Fig. 15.7.** Noise transformations from the model space (A) to the parameter space (B). Noise contributes to all dimensions of the data space, including the model space. The noise is assumed to be isotropic and is illustrated as a ring of points with a radius  $s$  to represent the uncertainty of the projected data point in the model space (A). When transformed to the parameter space (B), the ring is distorted into an ellipse at an angle of  $45^\circ$  (for equal amplitudes  $M_1$  and  $M_2$  when the model functions are not orthogonal (right), and this distortion increases the variance of the estimated parameters.

map in Fig. 15.8). If the model functions are not orthogonal, the cloud is elongated as discussed above. The variance of the estimate of a particular parameter or a linear combination of parameters is calculated from this distribution by projecting the two-dimensional distribution on to an appropriate axis (Fig. 15.8). For example, to find the variance of the estimate of  $a_1$  independent of the estimate of  $a_2$ , we project all the points on to the  $a_1$ -axis and calculate the variance of this distribution. The same procedure applies to any linear combination of the amplitudes. For example, suppose that  $M_1$  and  $M_2$  represent model functions for the responses to two different stimuli. Then we would certainly be interested in the separate responses to the two stimuli ( $a_1$  or  $a_2$ ), but we might also be interested in the combined response ( $a_1 + a_2$ ) or the differential response ( $a_1 - a_2$ ) to the two stimuli. Any linear combination of  $a_1$  and  $a_2$  corresponds to a line in the  $a_1$ - $a_2$  plane, and the variance of the estimate of that linear combination is the variance of the projection of the points on to that line. Fig. 15.8 shows examples of projections for  $a_1$ ,  $a_1 + a_2$  and  $a_1 - a_2$  for two model functions with equal amplitudes oriented  $45^\circ$  apart (the example from the third row of Fig. 15.7). Note that for this case the variance of the estimate of  $a_1 + a_2$  is much smaller than the variance of the estimate of  $a_1 - a_2$ , and the variance of  $a_1$  alone (or  $a_2$  alone) is intermediate between these two.



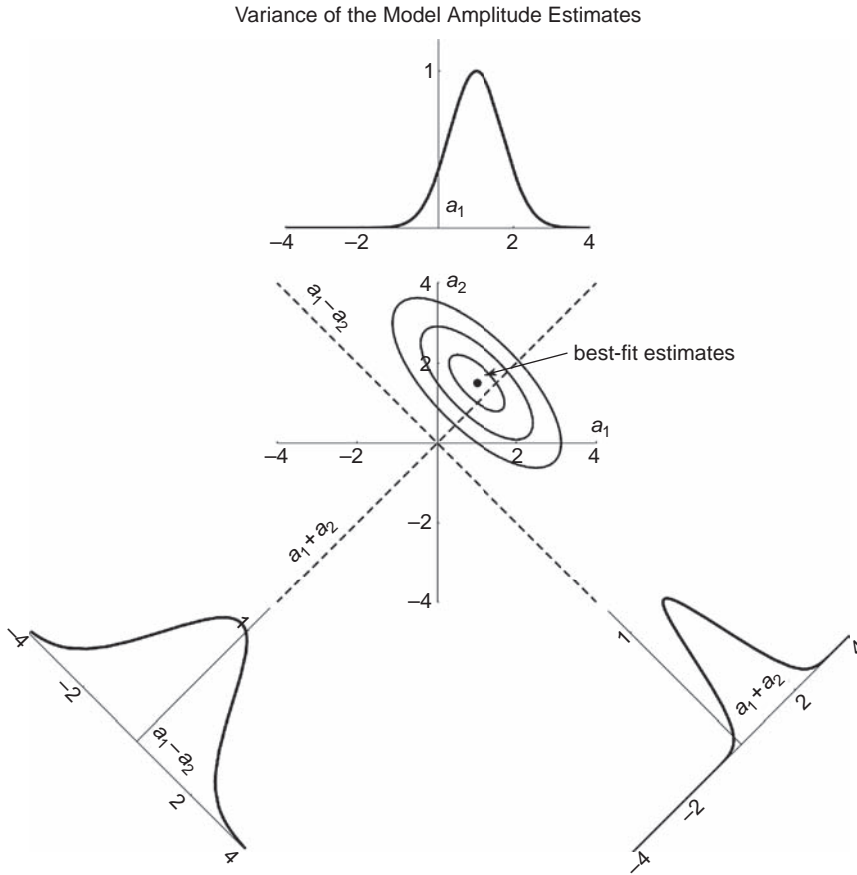


**Fig. 15.8.** Variance of the estimated parameters. The variance of any parameter, or linear combination of parameters, is calculated by projecting the two-dimension distribution of noise points onto the appropriate axis. In this example, the model functions form an angle of  $45^\circ$ , and this nonorthogonality makes some projections have a lower variance than others. For example, the estimate of  $a_1 + a_2$  has a much lower variance (the narrower distribution on the lower right) than the estimate of  $a_1 - a_2$  (lower left).

These illustrations are meant to show graphically how the noise is amplified when the model functions are not perpendicular to each other, increasing the variances of the estimates of both  $a_1$  and  $a_2$ . Furthermore, the sensitivity of the experimental design to different linear combinations of the amplitudes clearly depends strongly on the geometry of the model functions. For example, the pattern of two stimuli that yielded the model vectors  $\mathbf{M}_1$  and  $\mathbf{M}_2$  of Fig. 15.7 would be a poor design for measuring the differential response to the two stimuli because the variance of such a measurement is so high. In practice, the calculation of the variance of any linear combination of the model functions can be done in a straightforward way with the covariance matrix of the model functions, as described in Box 15.1. From the matrix calculations, a more general expression for the SNR can be derived (Eq. (B15.7)), analogous to Eq. (15.1) for the single model function case.

Another equivalent way to look at the uncertainties of the parameter estimates is to interpret the distribution shown in Fig. 15.8 as a two-dimensional probability distribution

for particular amplitudes of  $a_1$  and  $a_2$  given the measured data, called the a-posteriori (or simply posterior) probability (Frank *et al.* 1998). The posterior probability distribution has the elliptical shape shown in Fig. 15.8 and peaks at the best-fit values of  $a_1$  and  $a_2$ . This is a two-dimensional probability distribution, and the one-dimensional probability distribution for a particular amplitude is a projection on to the appropriate axis. For example, projecting the two-dimensional distribution on to the  $a_1$ -axis is equivalent to integrating over all possible values of  $a_2$  and gives the one-dimensional probability distribution of  $a_1$  independent of the estimate of  $a_2$ . The significance of the estimate can be calculated from the degree to which these one-dimensional projected probability distributions overlap zero. Specifically, the probability that the data could have arisen just from noise alone is the area under the curve on the opposite side of zero from the peak. This is equivalent to sliding the one-dimensional distribution until it is centered on zero (the null hypothesis) and calculating the area from the estimated parameter value to infinity (or negative infinity, if the amplitude estimate is negative), which is the probability of obtaining that value or greater by chance alone. For example, in Fig. 15.8 the estimate of  $a_1 + a_2$  is reasonably significant because there is very little area under the curve to the left of zero. The estimate of  $a_1$  is somewhat less significant, and the estimate of  $a_1 - a_2$  is not significant at all.

## Statistical significance revisited

In the [previous section](#) (and in [Box 15.1](#)), we discussed the variance of the parameter estimates with a view toward deriving a more general expression for the SNR of the measurement of any combination of the model function amplitudes. As with the case of the single model function, we can also approach the question of statistical significance by constructing a statistic whose distribution is well known under the null hypothesis that there is no activation. However, the appropriate statistic depends on what the model functions actually represent. We can illustrate the basic reasoning with two examples.

For the first example, suppose that we are dealing with a single stimulus type and that we know the hemodynamic response quite well but, in addition, that we want to account for a linear drift of the signal. The activation response is modeled as  $M_1$ , and  $M_2$  is the linear drift. Both  $a_1$  and  $a_2$  are calculated from Eq. (B15.2), but we are primarily interested in just the amplitude  $a_1$ . In other words, we include a second model function to model the data better, but we do not really care about the value of  $a_2$ . In mathematical terms, we simply want to project the two-dimensional probability distribution onto the  $a_1$ -axis. The ratio of the estimate of  $a_1$  to the expected variance of  $a_1$  is calculated from Eq. (B15.7), and just as with the single model function, this SNR estimate follows a  $t$ -distribution under the null hypothesis. However, the degrees of freedom is now  $N - 2$ , because the model space has two dimensions. So the SNR of the measurement of  $a_1$  can be taken as  $t_\nu$ , and the significance can be assessed just as for the single model function.

For the second example, we consider the case where both model functions are necessary to describe the hemodynamic response to a single stimulus. Suppose that the shape of the response is well known but that the delay after stimulus onset and the amplitude of the response are unknown. This can be cast in the form of a linear model by the clever trick of defining  $h(t) = h_1(t) + h_2(t)$ , where  $h_1(t)$  is the hemodynamic response for a fixed delay and  $h_2(t)$  is the first time derivative of  $h_1(t)$  (Friston *et al.* 1998b). To first order, a linear combination of a function and its first derivative simply shifts the same function shape along the time axis. Then if  $X(t)$  is the stimulus pattern, the model function  $M_1$  is  $X(t) * h_1(t)$  with the mean removed, and  $M_2$  is  $X(t) * h_2(t)$  with the mean removed. The amplitude  $a_1$  then

describes the magnitude of the response, and the amplitude  $a_2$  is proportional to the delay after stimulus onset.

The important difference with the first example is that now both amplitudes are necessary to describe the activation response. In geometric terms, there is no longer a single axis in the model space that is of interest. Instead, we are interested in the significance of the full model estimate, including  $a_1$  and  $a_2$ . To test the significance of the model fit, we use an  $F$ -statistic, which is essentially a generalization of the  $t$ -statistic to model spaces with more than one dimension (Friston *et al.* 1998b). By the null hypothesis, if there is no activation, then any projection of the data into the model space is entirely from noise. For any subspace of the data space, we can estimate the noise variance by dividing the length squared of the projection onto that space by  $n$ , the dimensions of the space. (Again, this is just the argument that, with independent Gaussian noise, each dimension of a subspace contributes a component  $\sigma^2$  to the net length squared of the vector in that subspace.) Now consider dividing the data space into a model space with  $m$  dimensions and an error space with  $v = N - m$  dimensions. In each space, we can calculate an estimate of  $\sigma^2$ , and the ratio of these two estimates is  $F$ . Under the null hypothesis,  $F$  should be approximately equal to one, and the question is whether  $F$  is sufficiently larger than one to justify rejection of the null hypothesis. The distribution of  $F$  depends on the dimensions of the two spaces, and so is usually written as  $F_{m,v}$ .

Using our earlier notation in which  $Y_M$  is the magnitude of the projection onto the model space and  $Y_E$  is the length of the component remaining in the error space, we have for our example:

$$F_{2,v} = \frac{Y_M^2/2}{Y_E^2/v} \quad (15.3)$$

The connection between  $F$  and  $t$  is clear when the model space has only one dimension, so  $F_{1,v} = t_v^2$ . From the value of  $F$ , the probability that such a large projection in the model space could have arisen by chance alone can be calculated to determine the statistical significance. Note that this test of significance does not depend on how we decompose  $Y_M$  into a set of model amplitudes, and so does not depend on the orthogonality of the model functions (Friston *et al.* 1998b). The model vectors define the model space, but  $F$  depends only on the length of the projection in that space. This point will be important in the next section where we consider event-related fMRI experimental paradigms.

## Design of fMRI experiments

### Block designs and event-related designs

The general linear model discussed in the previous section is a powerful and highly flexible technique for analyzing fMRI data to estimate the strength and significance of activations. In addition, it provides a useful framework for designing fMRI experiments and comparing the sensitivity of different experimental paradigms. For most fMRI applications, the goal is to detect a weak signal change associated with the stimulus, and a direct measure of the sensitivity is the SNR of the measured activation amplitude. Much of the discussion of the general linear model in the previous section was geared toward deriving expressions for the SNR and for the associated statistical measures such as  $t$  and  $F$ . This section focuses on the implications of these SNR considerations for the design of fMRI experiments.

The classic design for an fMRI experiment is a *block design* of stimulus presentation, with individual trials or events tightly clustered into “on” periods of activation alternated with equally long “off” control periods. However, for many applications, a block design is not feasible, or at least introduces an artificial quality into the stimulus that makes the results difficult to interpret. An *event-related* (or trial-based) design significantly broadens the types of neural processes that can be investigated (Buckner *et al.* 1996, 1998; Burock *et al.* 1998; Dale 1999; Dale and Buckner 1997a; Friston *et al.* 1998, 1999; Josephs *et al.* 1997; Zarahn *et al.* 1997b). A block design, by definition, presents similar stimuli together, which makes it difficult to study processes where predictability of the stimulus is an important consideration. For example, studies of recognition using familiar stimuli and novel stimuli are hampered if all the familiar stimuli are presented together. An event-related design allows randomization of different stimuli and a more sophisticated experimental design.

The general linear model approach described in the previous section can easily handle either block or event-related designs. The appropriate model function is the convolution of the arbitrary stimulus pattern  $X(t)$  with the hemodynamic impulse response function  $h(t)$ , and the analysis will identify voxels for which that model function describes a significant amount of the variance. But this approach assumes that the hemodynamic response  $h(t)$  is known, and it is likely to be variable across brain regions and subjects. Event-related experiments offer a different way to approach the data: no assumptions are made about the shape of the hemodynamic response, and instead the function  $h(t)$  is estimated from the data.

One reason for this shift in the analysis approach is that the response to an event-related design is more sensitive to the exact shape of  $h(t)$ , because of the mathematical nature of a convolution. When  $h(t)$  is convolved with a block design, the value of the response on the plateau depends only on the area under  $h(t)$ , and not the details of its shape. (We used this same principle to discuss the sensitivity of tracer kinetic curves to blood volume and blood flow in Ch. 12.) The shape of  $h(t)$  only affects the transition regions between blocks. In contrast, with an event-related design, all time points are essentially transition regions, because there is no equivalent of a plateau period. For this reason, the exact shape of the assumed hemodynamic response function is not critical for block designs but is very critical for event-related designs.

In the simplest approach for estimating  $h(t)$  from an event-related design, one can do an fMRI experiment analogous to an evoked potential experiment. Single trials of a particular stimulus are presented, and the responses are averaged time-locked to the stimulus presentation. That is, the images are rearranged into time order following a stimulus and appropriately averaged. If the separation between trials is sufficiently long so that there is no overlap of responses, this selective averaging approach directly provides a measure of the hemodynamic response on a voxel-by-voxel basis. In practice, though, a more sophisticated approach corrects for overlap of responses and makes it possible to study randomized events with average spacing much shorter than the width of  $h(t)$ .

Given the possibilities of block designs versus event-related designs, and analysis strategies of assuming a form for  $h(t)$  or estimating it, what is the most sensitive design for an fMRI study? This turns out to be a more subtle question than one might have thought. The essential problem is that there are really two ways one could ask a question about sensitivity. What is the most efficient design for *detecting* an activation? What is the most efficient design for *estimating* the hemodynamic response? These are distinct questions, and it turns out that the answers are different. The short answer is that block designs are better for detection, and

event-related designs are better for estimation, and the rest of this section focuses on trying to clarify these ideas (Dale 1999; Friston *et al.* 1999; Liu 2004; Liu and Frank 2004; Liu *et al.* 2001).

To explore these questions, we turn to a relatively simple example that allows us to examine a range of designs. We consider an idealized stimulus that could be presented in a block design, as periodic single trials, or in randomized single trials. This is somewhat artificial, because for many applications the choice of experimental design is dictated by the cognitive processes under investigation, and the experimenter may have little flexibility about when events occur. For example, to correlate neural activity separately with correct and incorrect identifications of target stimuli, the pattern of correct responses is not known until after the experiment is completed. For such an experiment, there may be little room for optimizing the stimulus presentation.

However, it is important to consider the efficiency of different designs in a more general way so that the potential costs of one design over another can be compared. In this section, we will focus on this more general question of sensitivity, as if we have complete control over when stimuli occur. In all cases, we assume that each trial (or event) elicits the same hemodynamic response. With this simple model, we can address the two questions posed earlier. Which design is best for estimating the hemodynamic response? Which design is best for detecting an activation?

## Detection power for a known hemodynamic response

Suppose that the hemodynamic response function  $h(t)$  is known. We can compare the sensitivity of different stimulus patterns for detecting a significant response in the data by looking at the SNR of each design. From the earlier arguments for the case of a known hemodynamic response represented by a single model function  $\mathbf{M}$ , the SNR is given by the simple expression  $aM/\sigma$  (Eq. (15.1)). The vector  $\mathbf{M}$  is the unit amplitude response to the stimulus pattern with the mean removed, and  $M$  is the amplitude of  $\mathbf{M}$ . The true amplitude of the response in the data is  $a$ , and  $\sigma$  is the standard deviation of the noise added in to each measurement. The intrinsic activation amplitude is set by brain physiology, and the noise standard deviation is set by the imaging hardware and the pulse sequence used for image acquisition, so we can think of these as being fixed aspects of the experiment. But  $M$ , which is proportional to the standard deviation of the data produced by a unit amplitude hemodynamic response, depends on how the stimuli are presented and the shape of the hemodynamic response function.

To focus this point, consider a simple experiment with the goal of identifying areas of the brain that respond to a brief stimulus, an event. For example, the stimulus could be a single finger tap or a brief flash of light. Suppose that a single run of the experiment consists of a fixed number of events. How should the timing of the events be designed to maximize the sensitivity of the experiment for detecting weak activations? At first glance, it might appear that the timing of the stimuli does not really matter because it will always be the responses to the same number of events that are averaged. However, the somewhat surprising result is that the sensitivity depends strongly on the design of the stimulus presentation.

To be concrete, suppose that we divide the time axis into steps of duration  $\delta t$  smaller than any of the other time intervals of interest in the experiment. For any pattern of identical events, we can describe the stimulus pattern by a function  $X_i$ , where  $X_i$  has a value of one if an event occurs at the  $i$ th time step and zero if there is no event. The unit amplitude hemodynamic response is  $h_i$ , where  $h_i$  is the amplitude of the signal change at  $i$  time steps after an event. The terminology “unit amplitude” means that this is the amplitude of response corresponding to  $a = 1$  in our analysis. Then the unit amplitude BOLD response to the stimulus

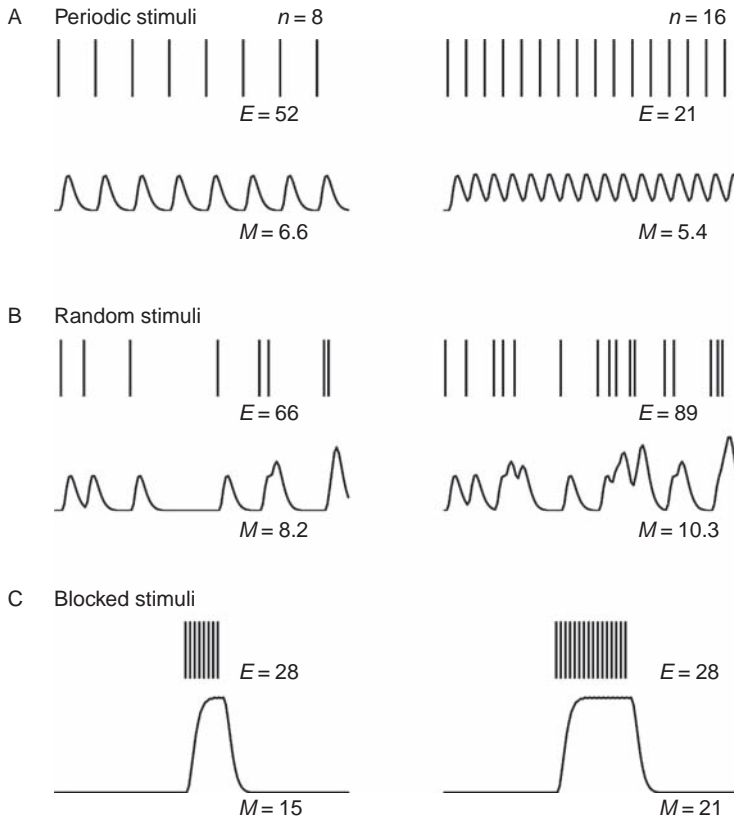


**Fig. 15.9.** The sensitivity of different experimental designs. Timing patterns of stimuli and the expected hemodynamic response are shown for periodic single trials (A), randomized single trials (B), and blocked stimuli (C). Examples for 8 trials (left) and 16 trials (right) within a 1 min time frame are shown. The sensitivity of each pattern (the expected SNR) for *detecting* an activation is proportional to the standard deviation of the response vector measured by  $M$ . The efficiency of each pattern for *estimating* the shape of the hemodynamic response  $E$  is calculated from Eq. (15.4). Note that the blocked design is best for detecting an activation; the randomized pattern is best for estimating the shape of the hemodynamic response, and the periodic single trial pattern is poor for both tasks.

pattern is the convolution of the stimulus pattern with the hemodynamic response  $X_i^*h_i$ . This response is then sampled at intervals of TR, and the vector  $\mathbf{M}$  consists of these sampled values with the mean subtracted. If there are  $N$  images in the experimental run, then  $\mathbf{M}$  is a vector in an  $N$ -dimensional data space. The magnitude of  $\mathbf{M}$  directly reflects the variance in the data from a unit amplitude response. Specifically, the variance is  $M^2/(N-1)$ . The sensitivity for detection of a response depends on how large this variance is compared with the noise variance  $\sigma^2$ , so the magnitude of  $\mathbf{M}$  is a useful index of the sensitivity of an experiment.

Figure 15.9 shows three types of timing pattern for an fMRI experiment: evenly spaced single trials, randomized single trials, and blocked stimuli, with examples for 8 and 16 stimuli presented in a 1 min run. For each example, the hemodynamic response to each stimulus (modeled as a gamma-variate function) is the same. However, the magnitude of  $M$  for these different experimental designs differs by more than a factor of two for the example with eight stimuli and by nearly a factor of four for the example with 16 stimuli! For the case of 16 stimuli, the hemodynamic response smoothes out the individual responses in the periodic

single-trial paradigm, creating little variance in the net response and a corresponding low value of  $M$ . In contrast, with the blocked design, the combination of long off-periods without a response and overlapping responses from different events when they are bunched together creates a large variance. Because  $M$  is four times larger with the blocked design, the SNR is also four times larger for the same response. To match the sensitivity of the blocked design, by repeating the single-trial paradigm and averaging, would require 16 times as many stimuli because SNR increases only with the square root of the number of averages.

The sensitivity of the SNR to the exact stimulus pattern comes about because the hemodynamic response is broad compared with the minimum interval between the onsets of repeated events. In this analysis, we assume that each event produces the same, stereotypical BOLD response, and that overlapping responses to different events simply add. There is a limit to how close together two events can be such that the neural activity evoked by each event is the same. But this limiting interval typically is on the order of 1 s or less (Friston *et al.* 1999). If we take this as a practical lower limit for event spacing to maintain approximate linearity of the response, this minimum interval is still much less than the width of the hemodynamic response. If the hemodynamic response had a comparable width of approximately 1 s, then the response to each event would be essentially finished before the next event occurs. In this case, the exact timing of the events would not make any difference. Each event would elicit a brief response, and the SNR of the average response would just depend on the total number of events presented.

With a broader hemodynamic response, there is much more opportunity for responses to overlap. Interestingly, this overlap can either increase or decrease  $M$ . In the block design, the signal difference between the control and activated states is maximized because of the constructive build up of overlapping responses during the activation; thus,  $M$  is maximized with a block design for any given number of stimuli. However, for periodic single trials, the regularity of the overlap of responses tends to smooth out the intrinsic variance of the stimulus pattern and produces a minimum value for  $M$  for any given number of stimuli. For a periodic single-trial design, the dependence of  $M$  on the number of stimuli is a little subtle.

Suppose that we start with a single stimulus, and each time we add another we rearrange them into a periodic pattern. When the stimuli are widely separated, each new stimulus adds to the variance and so increases  $M$ . However, once the responses from different stimuli begin to overlap, the smoothing effect of the hemodynamic response reduces the variance, so  $M$  decreases with any further increase in the number of stimuli (e.g., in going from 8 to 16 stimuli in Fig. 15.9). For this reason, there is an optimal spacing of approximately 12–15 s between stimuli that maximizes  $M$  for a periodic design. However, even at this optimal spacing, the sensitivity of the periodic single-trial design is much less than a block design with the same number of stimuli.

Randomized events allow for longer off-periods and some constructive bunching of the stimuli, creating a value of  $M$  intermediate between the optimal block design and a periodic single-trial design. Increasing the number of events in a randomized design produces a rather counterintuitive effect. Naively, we might expect that the overlap of responses would decrease the sensitivity just as it does for periodic single trials. However, the result is just the opposite (Fig. 15.9). Increasing the number of stimuli in a randomized pattern continues to increase the variance of the response, creating a larger  $M$  and improved sensitivity.

One way to understand these effects of experimental design is to look at the frequency content of the stimulus pattern (Fig. 15.10). For a fixed number of stimuli, the variance of the stimulus pattern itself is always the same, but the distribution of that variance among different frequency components depends strongly on the exact timing of the stimuli. The hemodynamic response is essentially a smoothing function that attenuates the higher

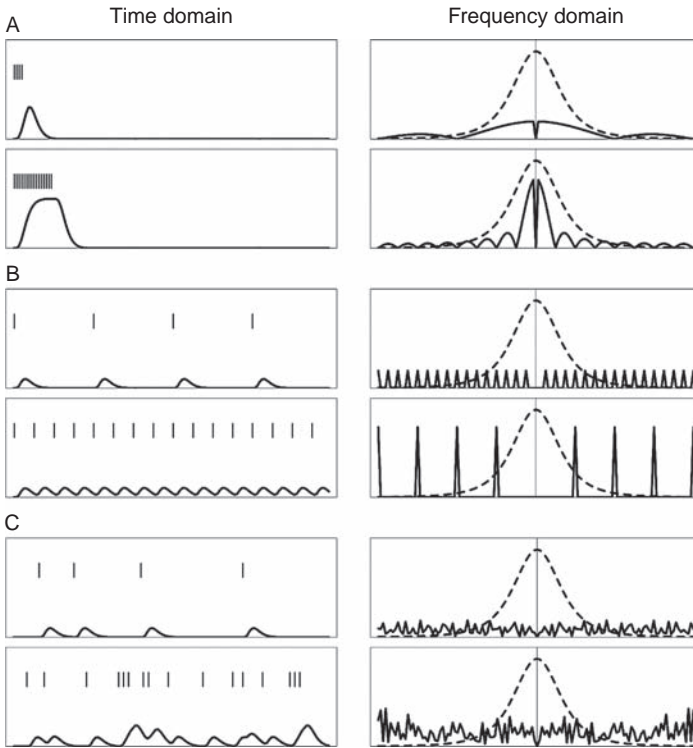


**Fig. 15.10.** Frequency domain analysis of the sensitivity of different experimental designs. Panels show examples of blocked (A), periodic single-trial (B), and randomized (C) stimulus events. Time domain plots show the stimulus events and the expected BOLD signal changes calculated by convolving the stimulus pattern with the hemodynamic response. In the frequency domain, the convolution multiplies the hemodynamic response (dashed curve) with the frequency spectrum of the stimulus pattern, attenuating the high frequencies. The sensitivity is roughly proportional to the area of the stimulus spectrum under the envelope of the hemodynamic response. Sensitivity of a block design or a random design is improved by increasing the number of events, but for a periodic single-trial design, as the time between events is reduced, the fundamental frequency moves out from under the hemodynamic response envelope, and sensitivity is reduced.

frequencies of the stimulus pattern. For stimulus patterns dominated by low frequencies, such as the block design, more of the intrinsic variance of the stimulus pattern is preserved after the smoothing, producing a larger  $M$  value.

For the periodic single-trial design, the lowest frequency component corresponds to the fundamental stimulus frequency, and the rest of the energy is in higher harmonics of the fundamental frequency. The fundamental frequency of the stimulus pattern continues to grow as more stimuli are added and the spacing between stimuli is reduced, so more of the intrinsic variance of the stimulus pattern is attenuated by the smoothing by the hemodynamic response function. For the randomized design, the frequency spectrum is essentially flat, and as more stimuli are added, all frequency components increase, including the low frequencies. Because of this, the remaining variance after smoothing with the hemodynamic response continues to grow as more randomized events are added.

## Estimating an unknown hemodynamic response

The framework for understanding these experiments is still the general linear model. To model the hemodynamic response on a voxel-by-voxel basis, we treat the response at each



time lag  $t_i$  as a separate model function. For example, if we assume that the hemodynamic response to an event lasts for 10 s, and we want to measure this response at 1 s intervals, then we need 10 model functions. It is easiest to visualize this in the simplified case in which stimuli are presented and images are acquired on an evenly spaced grid of 1 s time intervals. That is, the stimulus pattern  $X_i$  is a series of ones and zeros at regular time intervals of 1 s, describing whether an event does or does not occur at that time point. Images also are acquired with a regular interval of 1 s. (In fact, these assumptions can be substantially relaxed, but this simple case illustrates the basic ideas.)

The most direct way to estimate the hemodynamic response is to average all the images that are made 1 s after an event, all images that are measured 2 s after an event, and so on until we have estimated the response at 10 s after an event. This selective averaging approach is much like the approach used in evoked potential recordings, in which many stimuli are presented and the responses averaged time-locked to the stimuli (Dale and Buckner 1997b). However, the problem with the naive version of this approach is that overlap of responses is not taken into account. For example, a particular image could be both 2 s after an event and 5 s after another event, and the two responses are, therefore, combined in that image.

We can analyze event-related data directly in terms of the general linear model using the formalism developed in Box 15.1 by defining a design matrix  $\mathbf{M}$  consisting of 10 model functions. The model function corresponding to a lag of 0 s is simply the stimulus pattern  $X_i$  itself, and the model function for a lag of  $n$  s is simply the pattern  $X_i$  shifted  $n$  steps to the right. Each successive column of the design matrix is then  $X_i$  shifted down by one from the previous column. (More completely, each column is a shifted version of  $X_i$  with zeroes added at the beginning and with the mean removed.) The estimated hemodynamic response to a single event then consists of a vector of amplitudes  $\mathbf{a}$ , which is calculated with the general linear model as described above. Note that if the model functions were all orthogonal to each other, the covariance matrix  $(\mathbf{M}^T \mathbf{M})^{-1}$  would simply reduce to a diagonal matrix, and the remaining term  $\mathbf{M}^T \mathbf{Y}$  in Eq. (B15.2) would be equivalent to a simple time-locked averaging of the response to individual stimuli. In other words, the correction for response overlap that is missing from the naive reordering approach is taken into account by the covariance matrix in Eq. (B15.2).

The result of the model fitting is a set of 10 amplitudes defining the local hemodynamic response. How precise is this estimate? As described in Box 15.1, the variance of any parameter or combination of parameters can be calculated with the covariance matrix. However, in the current formulation, each parameter is the amplitude of one time point of the hemodynamic response, and we are really interested in the error of the whole estimated response. A useful way to think about this is to consider the parameter space defined by the set of amplitudes  $a_i$  (i.e., each axis corresponds to one component of the vector  $\mathbf{a}$ ). The true hemodynamic response then corresponds to a point in this 10-dimensional parameter space, and our estimated hemodynamic response is another point displaced from the true point. The two points do not coincide because noise produces some variance in each of the estimates of  $a_i$ , and the distance between the estimated point and the true point is a measure of the error in the estimate of the hemodynamic response. The expected distance measured in the parameter space is simply the sum of the variances for each of the  $a_i$ -values, and this in turn is proportional to the sum of the diagonal terms of the covariance matrix, called the *trace* of the matrix (symbolized by “Tr”). So a useful measure of the efficiency ( $E$ ) of our experimental design for estimating the hemodynamic response is the inverse of the expected error measured in the parameter space (Dale 1999):

$$E = \frac{1}{\sigma \sqrt{\text{Tr}\{\mathbf{M}^T \mathbf{M}\}}} \quad (15.4)$$

Maximizing the efficiency is equivalent to minimizing the sum of the squared errors at each time point of the hemodynamic response. In practical terms, if the efficiency of one experimental design is only half that of another, then the less efficient design would have to be repeated and averaged four times to achieve the same statistical quality of the estimated hemodynamic response. The efficiency is, of course, inversely proportional to the noise standard deviation but also depends on a geometric factor through the covariance matrix. Note that the actual hemodynamic response does not enter into the expression for the efficiency. That is, the design matrix  $\mathbf{M}$  is constructed directly from the stimulus pattern, not the stimulus pattern convolved with a hemodynamic response function. Or to put it another way, for any shape of the hemodynamic response, the efficiency for estimating that response depends only on the stimulus pattern itself.

The efficiency can be used to rank the sensitivity of any pattern of stimuli (Fig. 15.9). For example, one can compare different random sequences generated with different mean interstimulus intervals. The remarkable result is that the efficiency continues to improve as the interstimulus interval is decreased (i.e., as more stimuli are included in a run of the same total duration) (Dale 1999). In other words, even though the interstimulus interval is significantly less than the width of the hemodynamic response, the efficiency is improved. However, even for a fixed average interstimulus interval, there is a wide variation in the efficiency for different random patterns.

We can understand both of these effects from the arguments developed above. In general, the larger the variance of the expected model response (i.e., the magnitude of the vector  $\mathbf{M}$  in our earlier analysis), the better the SNR will be. For this case, each model function is essentially a shifted version of the stimulus pattern  $X_p$ , so the variance of the data resulting from the response at each time point after an event (and thus the magnitudes of  $M_1, M_2, M_3$ , etc.) increases as more stimuli are added in and the interstimulus interval decreases. However, we also found earlier that non-orthogonality of the model functions can severely degrade the SNR of the amplitude estimates. So the variability of the efficiency for different random patterns with the same number of stimuli (and, therefore, the same intrinsic variance of the model vectors) results from the different degrees of non-orthogonality of the model functions. In practice, typically many stimulus patterns are generated and their efficiency calculated to find a pattern with desirable properties (Dale 1999). Buracas and Boynton (2002) introduced a useful method for finding stimulus patterns with high efficiency based on the concept of maximum length-shift-register sequences (M-sequences), specific patterns of ones and zeroes with minimum autocorrelation. These M-sequences improve on randomly generated patterns, but there are some constraints involved on the number of stimuli.

## Detecting an unknown hemodynamic response

The preceding arguments show that the best pattern of stimuli for *estimating* the hemodynamic response is found by maximizing the efficiency. However, to determine the best design for *detecting* an activation, we need to reason a little differently. Earlier in the chapter, we considered this question for the case in which we know the hemodynamic response, and then we consider this question for an event-related design in which  $h(t)$  is estimated. We return to our original geometric view of the general linear model, in which  $\mathbf{Y}_M$  is the projection of the

data into a defined model space and  $Y_E$  is the remaining error component perpendicular to the model space. In the current case, the model space has 10 dimensions and completely describes any hemodynamic response that could occur within 10 s of an event. In other words, the only assumptions we are making about the form of the hemodynamic response is that it varies slowly enough that it is fully captured by describing its value at 1 s intervals, and it does not last more than 10 s. Either of these assumptions could be relaxed by increasing the number of time points defining the hemodynamic response, which would simply increase the number of dimensions of the model space.

The important factor in determining the sensitivity for detecting activation is the magnitude of the projection  $Y_M$  compared to  $Y_E$ . As described above, this ratio defines an  $F$ -statistic that can be used to test whether the magnitude of the component of the data lying in the model space can be attributed to chance alone. The important point is that we do not care how the projection  $Y_M$  is modeled in terms of individual amplitude estimates;  $F$  is based just on the magnitude of  $Y_M$ . In contrast, for estimating the hemodynamic response, we are specifically interested in the amplitudes  $a_i$  and the errors in the estimates of each of the  $a_i$ . In both cases, we are looking at the point  $Y_M$ , but the distinction is that  $F$  is evaluated in the model space and the efficiency is evaluated in the parameter space. In addition, the added feature of the parameter space is that noise is amplified in the transformation from the model space to the parameter space if the model vectors are not perpendicular to each other in the model space. Then it is possible for two stimulus patterns to produce identical expected values of  $F$  but have radically different values for the efficiency because one pattern creates a more regular pattern of overlap of the responses and a correspondingly more severe case of non-orthogonality of the model functions.

We can further explore this distinction by estimating the magnitude we should expect for  $F$ , as we did above. For any brain region, there is a true hemodynamic response, even if we do not know its shape, and when this true response is convolved with the stimulus pattern, it produces a vector  $M$ . Then, for a true activation with amplitude  $a$ , the expected magnitude of the projection of the data into the model space is  $aM$ , and so the magnitude of  $F$  is directly determined by  $M$ . To put it another way, the true model response corresponds to a particular direction in the data space. We do not know what direction this is, but by using 10 model functions to describe a general response, we are confident that the true model vector falls within our model space. The  $F$ -statistic depends on the magnitude of the component of the data vector in the model space and so depends directly on  $M$  (plus noise contributions from the remaining dimensions of the model space). Because  $F$  is calculated just from the magnitude of the projection into a well-defined model subspace, it is independent of whether the model vectors that originally defined that space are orthogonal to each other.

## Detection and estimation sensitivity

We can consider two figures of merit for evaluating the sensitivity of a particular experimental design, as illustrated in Fig. 15.9. As before, the factor  $M$  is a measure of the sensitivity for detecting an activation and depends strongly on the hemodynamic response. The factor  $E$  is a measure of the efficiency for estimating the shape of the hemodynamic response and depends only on the stimulus pattern and not on the hemodynamic response. Both factors are affected by overlapping responses, but in different ways. The expected value of  $F$  primarily depends on the magnitude of  $M$ , the variance of the expected response. With a block design, the addition of overlapping responses produces a large variance, but for a rapidly cycled periodic single-trial paradigm, the variability of the response is damped out by

the hemodynamic response, producing a low value of  $M$ . In a similar way, the efficiency measure  $E$  depends on the intrinsic variance of the stimulus pattern, which continues to increase as the number of stimuli increases. But in addition, the factor depends on overlap through the non-orthogonality of the model functions.

Periodic single trials perform poorly by both measures of sensitivity. The smoothing of the hemodynamic response reduces  $M$ , as described above. These designs also have a low value for the efficiency factor because the regular overlap makes the model functions severely non-orthogonal and noise is strongly amplified when transformed into the parameter space. Also, for this reason, a blocked design has a poor efficiency for estimating the hemodynamic response (low efficiency) even though it has a high sensitivity for detecting a response (high factor  $F$ ). Randomized trials are generally more efficient for estimating the hemodynamic response than either periodic single trials or blocked trials, but a block design is more sensitive for detecting activations. This distinction is critical for the optimal design of event-related experiments, emphasizing that the design criteria depend on which question is being asked.

Finally, the three types of stimulus pattern described here are really three points on a continuum, and mixtures of these patterns may provide a more optimal balance. For example, one goal would be to satisfy the combined needs of making the stimulus presentation sufficiently random so that the subject cannot predict the next stimulus and also produce a sensitivity for detecting an activation that approaches that of a single-block design. Mixed designs, part way between random and block designs, can accomplish this (Friston *et al.* 1999; Liu 2004; Liu and Frank 2004; Liu *et al.* 2001).

In summary, the sensitivity of an fMRI experiment is remarkably dependent on exactly how the stimuli are presented. In this chapter, we made simple assumptions about the shape and linearity of the hemodynamic response to emphasize ideas of how the approach to analyzing the data also provides a useful tool for optimizing the design of experiments. In fact, though, the hemodynamic response is more complicated than assumed here and is still poorly understood, as discussed in Ch. 16. As our understanding of the BOLD response improves, the analysis of the data will become more sophisticated, but the basic ideas of the general linear model will still apply. It is clear that event-related paradigms will continue to be a fruitful area of research, and future developments are likely to broaden significantly the range of applications of fMRI.

## References

- Aguirre GK, Zarahn E, D'Esposito M (1998) The variability of human, BOLD hemodynamic responses. *Neuroimage* **8**: 360–376
- Bandettini PA, Jesmanowicz A, Wong EC, Hyde JS (1993) Processing strategies for time-course data sets in functional MRI of the human brain. *Magn Reson Med* **30**: 161–173
- Boynton GM, Engel SA, Glover GH, Heeger DJ (1996) Linear systems analysis of functional magnetic resonance imaging in human V1. *J Neurosci* **16**: 4207–4221
- Buckner RL, Bandettini PA, O'Craven KM, *et al.* (1996) Detection of cortical activation during averaged single trials of a cognitive task using functional magnetic resonance imaging. *Proc Natl Acad USA Sci* **93**: 14878–14883
- Buckner RL, Goodman J, Burock M, *et al.* (1998) Functional-anatomic correlates of object priming in humans revealed by rapid presentation event-related fMRI. *Neuron* **20**: 285–296
- Buracas GT, Boynton GM (2002) Efficient design of event-related fMRI experiments using M-sequences. *Neuroimage* **16**: 801–813
- Burock MA, Buckner RL, Woldorff MG, Rosen BR, Dale AM (1998) Randomized event-related experimental designs allow for

- extremely rapid presentation rates using functional MRI. *NeuroReport* **9**: 3735–3739
- Dale AM (1999) Optimal experimental design for event-related fMRI. *Hum Brain Mapp* **8**: 109–114
- Dale AM, Buckner RL (1997a) Selective averaging of rapidly presented individual trials using fMRI. *Hum Brain Mapp* **5**: 329–340
- Dale A, Buckner R. (1997b) Selective averaging of individual trials using fMRI. In *Proceedings of the Third International Conference on Functional Mapping of the Human Brain*, Copenhagen, p. S47
- Engel SA, Rumelhart DE, Wandell BA, et al. (1994) fMRI of human visual cortex. *Nature* **369**, 370 [erratum, 525, 106]
- Frank LR, Buxton RB, Wong EC (1998) Probabilistic analysis of functional magnetic resonance imaging data. *Magn Reson Med* **39**: 132–148
- Friston KJ, Jezzard P, Turner R (1994) Analysis of functional MRI time-series. *Hum Brain Mapp* **1**: 153–171
- Friston KJ, Holmes AP, Worsley KJ, et al. (1995) Statistical parametric maps in functional imaging: a general linear approach. *Hum Brain Mapp* **2**: 189–210
- Friston KJ, Josephs O, Rees G, Turner R (1998a) Non-linear event related responses in fMRI. *Magn Reson Med* **39**: 41–52
- Friston KJ, Fletcher P, Josephs O, et al. (1998b) Event-related fMRI: characterizing differential responses. *Neuroimage* **7**: 30–40
- Friston KJ, Zarahn E, Josephs O, Henson RNA, Dale AM. (1999) Stochastic designs in event-related fMRI. *Neuroimage* **10**: 607–619
- Glover GH (1999) Deconvolution of impulse response in event-related fMRI. *Neuroimage* **9**: 416–429
- Gold S, Christian B, Arndt S, et al. (1998) Functional MRI statistical software packages: a comparative analysis. *Hum Brain Mapp* **6**: 73–84
- Josephs O, Turner R, Friston KJ (1997) Event related fMRI. *Hum Brain Mapp* **5**: 243–248
- Lange N, Strother SC, Anderson JR, et al. (1999) Plurality and resemblance in fMRI data analysis. *Neuroimage* **10**: 182–303
- Liu TT (2004) Efficiency, power, and entropy in event-related fMRI with multiple trial types. Part II: design of experiments. *Neuroimage* **21**: 401–413
- Liu TT, Frank LR (2004) Efficiency, power, and entropy in event-related FMRI with multiple trial types. Part I: theory. *Neuroimage* **21**: 387–400
- Liu TT, Frank LR, Wong EC, Buxton RB (2001) Detection power, estimation efficiency, and predictability in event-related fMRI. *Neuroimage* **13**: 759–773
- Mayhew J, Zheng Y, Hou Y, et al. (1999) Spectroscopic analysis of changes in remitted illumination: the response to increased neural activity in brain. *Neuroimage* **10**: 304–326
- Price CJ, Crinion J, Friston KJ (2006) Design and analysis of fMRI studies with neurologically impaired patients. *J Magn Reson Imaging* **23**: 816–826
- Purdon PL, Weisskoff RM (1998) Effect of temporal autocorrelation due to physiological noise and stimulus paradigm on voxel-level false-positive rates in fMRI. *Hum Brain Mapp* **6**: 239–249
- Saville DJ, Wood GR (1991) *Statistical Methods: The Geometric Approach*. New York: Springer-Verlag
- Sereno MI, Dale AM, Reppas JR, et al. (1995) Functional MRI reveals borders of multiple visual areas in humans. *Science* **268**:889–893
- Smith SM (2004) Overview of fMRI analysis. *Br J Radiol* **77** (Spec Issue 2): S167–S175
- Smith SM, Jenkinson M, Woolrich MW, et al. (2004) Advances in functional and structural MR image analysis and implementation as FSL. *Neuroimage* **23** (Suppl 1):S208–S219
- Vasquez AL, Noll DC (1998) Nonlinear aspects of the BOLD response in functional MRI. *Neuroimage* **7**: 108–118
- Worsley KJ, Poline JB, Friston KJ, Evans AC (1997) Characterizing the response of PET and fMRI data using multivariate linear models. *Neuroimage* **6**: 305–319
- Zarahn E, Aguirre GK, D'Esposito M (1997a) Empirical analysis of BOLD fMRI statistics: I. Spatially unsmoothed data collected under null-hypothesis conditions. *Neuroimage* **5**: 179–197
- Zarahn E, Aguirre G, D'Esposito M (1997b) A trial based experimental design for fMRI. *Neuroimage* **5**: 179–197

# Interpreting the BOLD response

<b>Introduction</b>	<i>page</i> 400
<b>The BOLD response</b>	401
The basic BOLD measurement	401
Understanding the BOLD response	402
<b>Variability of the BOLD response</b>	403
Physiological baseline effects	403
Variability in coupling of cerebral blood flow and O <sub>2</sub> metabolism	405
<b>Neural activity and the BOLD response</b>	406
Location of BOLD signal changes	406
The relationship between the BOLD response and neural activity	408
Linearity of the BOLD response	409
Mapping resting state networks with spontaneous BOLD correlations	410
<b>Dynamics of the BOLD response</b>	411
The time scale of BOLD dynamics	411
Transients of the BOLD response	412
<b>Interpreting the BOLD response in disease</b>	418

## Introduction

Functional MRI based on the blood oxygenation level dependent (BOLD) effect is now a widely used tool for probing the working brain. The goal of fMRI studies is to map patterns of local changes in the MR signal in the brain as an indicator of neural activity associated with particular stimuli. The physical basis of the BOLD effect and how it is measured were described in [Ch. 14](#). The prototypical fMRI experiment alternates blocks of stimulus and control periods while a series of dynamic images is collected with an echo planar imaging (EPI) pulse sequence. The signal time course for each voxel of the image is analyzed to test whether there is a significant correlation of the signal with the stimulus (i.e., whether the signal increased during the stimulus). The statistical analysis of BOLD-fMRI data for reliable identification of weak changes in the MR signal is a critical component of the experiment, and the basic ideas were described in [Ch. 15](#).

In this final chapter, we turn to the physiological interpretation of the BOLD response. The BOLD response is a complex phenomenon. Although driven by neural activity, it also depends strongly on vascular and metabolic factors. The central question is just how faithfully does the BOLD response reflect neural activity. Answering this question remains an important challenge, and the goal here is to describe the current issues rather than provide definite answers.

## The BOLD response

### The basic BOLD measurement

Figure 16.1 shows an example of the BOLD signal response in the visual cortex during a simple visual stimulus. The imaging used EPI on a 3 T scanner with a repetition time of 2 s between images on the same slice and a resolution (voxel dimensions) of 3.75 mm × 3.75 mm × 5 mm (Buxton *et al.* 1998a). Subjects wore goggles that flashed a rectangular grid of red LED lights at a rate of 8 Hz, with the flashing lights on for 20 s followed by 40 s of darkness. This cycle was repeated eight times to make an 8 min run; the run was repeated four times, and the data were averaged for each of three subjects. The dynamic MR images provided a time course for the signal from each voxel, and those voxels showing a significant correlation with the stimulus pattern were selected and averaged to form the time course in Fig. 16.1.

The average response in Fig. 16.1 is fairly typical of BOLD responses to a number of stimuli. There is an initial delay of 1–3 s after the initiation of the stimulus, followed by a ramp of 5–8 s before a plateau signal change is reached (Bandettini *et al.* 1993). After the end of the stimulus, the BOLD signal ramps down over several seconds and often undershoots the original baseline. The *post-stimulus undershoot* in these data has about one-third the magnitude of the peak itself, and the undershoot takes about 20 s to resolve. Although the post-stimulus undershoot is not always evident, numerous examples can be found in the early fMRI literature (Hu *et al.* 1997; Menon *et al.* 1995; Merboldt *et al.* 1995; Ogawa *et al.* 1992; Turner *et al.* 1993). In fact, the first demonstration of the use of the BOLD effect for mapping activations shows evidence for a post-stimulus undershoot as a lowering of the baseline after the first stimulus block (Kwong *et al.* 1992). Frahm and co-workers reported examples of pronounced undershoots that took more than a minute to resolve (Frahm *et al.* 1996; Fransson *et al.* 1998, 1999; Kruger *et al.* 1996). In addition, although not apparent in Fig. 16.1, several groups have observed an *initial dip* in the BOLD signal lasting 1–2 s before the up ramp of the primary positive signal change (Ernst and Hennig 1994; Hu *et al.* 1997; Menon *et al.* 1995). The initial dip has excited considerable interest because it may map more precisely to the spatial location of the neural activity.

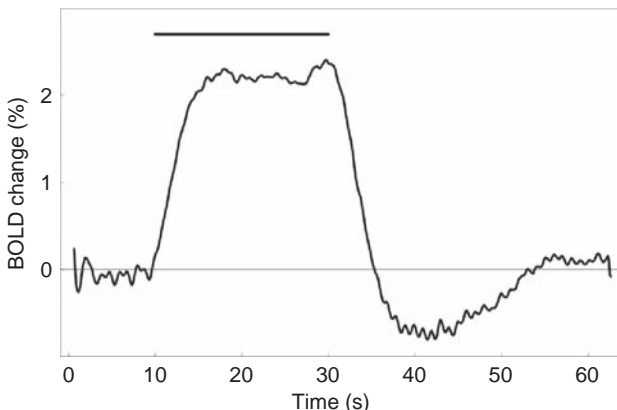


**Fig. 16.1.** The BOLD signal. This is a sample BOLD response in the visual cortex measured at 3 T. Subjects wore goggles that flashed a grid of red lights at 8 Hz. The stimulus (indicated by a horizontal bar) lasted for 20 s, followed by 40 s of darkness. The data show the average response of 32 cycles of stimulus – rest for three subjects. Characteristic features of the BOLD response are a delay of a few seconds after the start of the stimulus, a ramp of approximately 6 s up to a plateau, and a post-stimulus undershoot before the signal returns to baseline.

From an empirical viewpoint, the existence of the BOLD response is a phenomenon that can be exploited to map brain activity, and for many mapping experiments this may be sufficient. However, for a deeper interpretation of fMRI experiments, we need a better understanding of the BOLD response.

## Understanding the BOLD response

The intrinsic complexity of the BOLD response is illustrated in Fig. 16.2. A change in neural activity triggers increased cerebral energy metabolism, blood flow (CBF), and blood volume (CBV), and these physiological changes then combine to alter the MR signal. In Fig. 16.2, hypothetical responses are shown at each step to illustrate how transient or non-linear features can enter at different stages of the chain of events leading to the BOLD response. The stimulus is a simple block design with a single block, which initiates a neural response, which may decrease over time through adaptation effects. The neural response drives changes in CBF, cerebral metabolic rate of  $O_2$  metabolism ( $CMRO_2$ ), and CBV, with the CBF change much larger than the  $CMRO_2$  change, the primary physiological phenomenon creating the BOLD effect. In addition, the CBV is shown with a slower recovery at the end of the stimulus, as a reminder that the dynamics of CBF,  $CMRO_2$  and CBV may have different time constants, and this could create transient features that have nothing to do with neural activity. The relative changes in CBF and  $CMRO_2$  alter the  $O_2$  extraction fraction (OEF), and the changes in OEF and CBV create the BOLD response.

In Fig. 16.2, neural activity is presented as a single component. However, from the discussion in Chs. 1 and 2 this also is a more complex process. Synaptic activity and spiking activity are distinct aspects of neural activity, and current thinking is that the CBF change is driven directly by the synaptic activity. That is, we might have expected a simple picture in which neural activity, either synaptic or spiking, drives energy metabolism, and the change in energy metabolism then drives a change in CBF to provide more  $O_2$  and glucose. Although still a chain of actions, this simple picture would at least have the advantage of being a simple

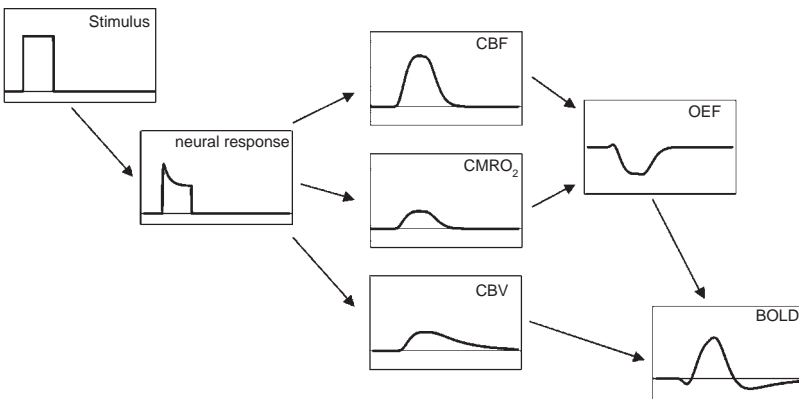


**Fig. 16.2.** The chain of events leading to the BOLD signal. A stimulus triggers local neural activity, which in turn triggers metabolic activity in the form of a large increase of cerebral blood flow (CBF), a small increase of cerebral metabolic rate of  $O_2$  ( $CMRO_2$ ), and a moderate increase of cerebral blood volume (CBV). The combined changes in CBF,  $CMRO_2$  and CBV create the BOLD signal change. The response curves at each stage suggest ways in which the stimulus shape is altered in the progression to the BOLD response. A key aspect of this chain of events is that CBF and  $CMRO_2$  are driven in parallel, rather than in series, and potentially by somewhat different aspects of the neural activity. OEF,  $O_2$  extraction fraction.



unbranched chain. However, a substantial body of work (Chs. 1 and 2) argues against this simple picture.

Instead, it appears that CBF and CMRO<sub>2</sub> are driven in parallel by neural activity. The acute CBF changes seen in brain activation studies are driven by aspects of neuronal signaling itself, such as neurotransmitter release at the synapse. We can think of this as a *feedforward* coupling of CBF and neural activity, in the sense that the CBF change is not waiting for a *feedback* signal from energy metabolism. In contrast, the change in CMRO<sub>2</sub> may simply be responding to the local energy demands of the neural activity. A large fraction of the energy cost of neural activity is thought to result from the need to pump Na<sup>+</sup>, K<sup>+</sup> and Ca<sup>++</sup> across the cell membrane against their existing electrochemical gradients (Ch. 1). This is a strongly uphill thermodynamic process, requiring consumption of ATP, and most of the ATP is recovered through oxidative metabolism. Because the required ion pumping is likely to be dominated by synaptic activity, both CBF and CMRO<sub>2</sub> are likely to increase together.

However, the idea that CBF and CMRO<sub>2</sub> are driven in parallel by neural activity has important implications for a quantitative understanding of the BOLD response. While synaptic activity dominates the energy cost, spiking activity also exacts a cost. For this reason, the CMRO<sub>2</sub> and CBF changes may be driven, in part, by different aspects of neural activity. That is, the CBF change is driven specifically by synaptic signaling, while the CMRO<sub>2</sub> responds to the overall energy cost of synaptic activity and neural activity. The balance of synaptic activity and total energy demands could vary with brain region, the type of stimulus, or even the magnitude of the stimulus. For example, if synaptic activity continued to rise as the stimulus intensity increased, but the overall neural response plateaus because of inhibitory or adaptation effects, the balance of CBF and CMRO<sub>2</sub> changes could shift. That is, such a phenomenon would directly affect the apparent CBF/CMRO<sub>2</sub> coupling index  $n$ , defined as the ratio of the fractional CBF change to the fractional CMRO<sub>2</sub> change. As described in Ch. 14, the value of this index strongly affects the magnitude of the BOLD response.

With this theoretical framework in mind, the following sections consider several practical questions important for interpreting fMRI experiments.

1. Does the BOLD signal change accurately reflect the location of neural activity change?
2. Does the magnitude of the BOLD signal change accurately reflect the magnitude of the neural activity change?
3. Do transients in the dynamic BOLD response reflect transients of neural activity or a temporal mismatch of the changes in CBF, CBV, or CMRO<sub>2</sub>?
4. How is the BOLD response altered in disease?

## Variability of the BOLD response

### Physiological baseline effects

Variability of the BOLD response, either across the brain or across subjects, could result from a number of factors. Certainly, a prominent cause could be variability of the neural activity itself. However, this type of variability is essentially what we are trying to measure, in the sense that the ability to detect subtle differences in the neural response would make fMRI a powerful tool for investigating the brain. Here we want to focus instead on sources of variability that are not related to neural activity, the effects that confound our interpretation of observed differences in the BOLD response as differences in neural activity. This question

is particularly important for interpreting the BOLD response in disease populations. If a disease group has a different BOLD response to a particular task from that of a healthy control group, what does that mean? Is it a difference in neural activity, or in some other non-neural factor that affects the BOLD signal?

In Ch. 14, the physical origins of the BOLD effect were considered. The basic picture presented was that the BOLD response is primarily driven by the change in CBF, but strongly modulated by two additional parameters,  $M$  and  $n$ . The parameter  $n$  is the apparent CBF/CMRO<sub>2</sub> coupling index mentioned above. The parameter  $M$  is an overall scaling factor that essentially defines how much deoxyhemoglobin is present in the baseline state. The BOLD effect has a ceiling, corresponding to the signal change that would result from complete removal of deoxyhemoglobin, and  $M$  defines that ceiling. Based on this picture, there are three ways in which the BOLD signal could be altered, even though the underlying neural activity is the same: a different feedforward coupling of neural activity to CBF changes, different values of  $M$ , or different values of  $n$ . The calibrated-BOLD method (Ch. 14), based on combined measurements of the BOLD response and the CBF response with arterial spin labeling (ASL), makes it possible to measure the CBF change,  $M$ , and  $n$ , as well as baseline CBF. In recent years, this has become an important tool for experimentally addressing questions related to the variability of the BOLD response.

In this section we focus on  $M$ , and how it can be altered by the baseline physiologic state. The factor  $M$  is in some ways a catch-all that includes a number of factors that affect the magnitude of the local BOLD response. That is, for the same physiological changes in CBF, CBV, and CMRO<sub>2</sub>, the BOLD response could still be different in different brain regions or subjects, and  $M$  attempts to capture the additional sources of variability. The value of  $M$  depends on the magnetic field strength, the pulse sequence used, and the echo time (TE) of the acquisition, so one needs to be careful in comparing reported values of  $M$  from different studies. In addition to this technical dependence on details of the fMRI experiment, the more important dependence is on the baseline physiological state. Because  $M$  reflects the level of deoxyhemoglobin at baseline, it depends on the local venous CBV and on the baseline OEF. If either of these are reduced, then  $M$  will be reduced, and the corresponding BOLD response will be weaker.

This phenomenon is illustrated by an experiment in which subjects performed a simple finger-tapping task before and after administration of a drug, acetazolamide (Diamox) (Brown *et al.* 2003). This drug inhibits carbonic anhydrase, an enzyme that catalyzes the conversion of CO<sub>2</sub> to bicarbonate ions, a reaction that is important for the clearance of CO<sub>2</sub> by CBF. The CO<sub>2</sub> diffuses from the brain to blood, where most of it is quickly converted to bicarbonate ions by carbonic anhydrase. This allows blood to carry a great deal of CO<sub>2</sub>, with only a modest rise in the partial pressure of CO<sub>2</sub> (pCO<sub>2</sub>) of blood. This in turn allows a strong gradient of pCO<sub>2</sub> from tissue to blood without having a high pCO<sub>2</sub> in tissue. Interfering with the activity of carbonic anhydrase is, therefore, likely to interfere with the clearance of CO<sub>2</sub> from the brain, causing tissue pCO<sub>2</sub> to rise. As described in Ch. 2, CBF is quite sensitive to CO<sub>2</sub>, so the net effect of the acetazolamide injection is to increase CBF. However, this is thought to be purely a CBF change, with no change in CMRO<sub>2</sub>. By raising CBF but not CMRO<sub>2</sub>, the baseline OEF is reduced.

In this study, subjects repeatedly performed a finger tapping paradigm, both before the acetazolamide was administered and for about 40 min after administration. During the activation, both the BOLD response and the CBF response were measured, using an arterial spin labeling (ASL) method. The results of this study were that CBF increased by

about 20% after injection of the drug, and the absolute change in CBF caused by the activation stayed about the same. However, in the altered baseline state, the magnitude of the BOLD response decreased by about 35%, consistent with a decreased  $M$  linked to the decreased baseline value of the OEF.

Note that the change in baseline CBF may also have increased baseline local blood volume which would tend to counteract the change in  $M$  resulting from the decreased baseline OEF. Theoretical calculations for the expected change in the BOLD signal when baseline CBF increases by 20%, with no change in  $\text{CMRO}_2$ , and with no difference in the absolute CBF change with activation, predict a large decrease in the magnitude of the BOLD response to activation consistent with these experimental results (Buxton *et al.* 2004). In short, when baseline CBF alone is changed, the dominant effect on  $M$  is from the change in the baseline OEF, with increased baseline CBF reducing  $M$ . However, this picture would be different if a change in baseline CBF is also accompanied by a corresponding change in  $\text{CMRO}_2$ . If baseline CBF and  $\text{CMRO}_2$  both increased by 20%, there would be no change in baseline OEF, and the increase in the baseline CBV could then lead to an increase in  $M$ . For this reason, baseline effects may be complicated, depending on the details of how the baseline is shifted.

A number of other commonly used drugs, such as caffeine and alcohol, alter baseline CBF. In studies of disease populations, other drugs with vasoactive effects could also alter the baseline state substantially and change  $M$  in a systematic way. For this reason, potential differences in the baseline state need to be considered when comparing group results, particularly in disease populations.

## Variability in coupling of cerebral blood flow and $\text{O}_2$ metabolism

The mismatch of CBF and  $\text{CMRO}_2$  changes with activation is the primary physiological source of the BOLD response. As described in Ch. 14 and above, we can characterize CBF/ $\text{CMRO}_2$  coupling by the ratio  $n$  of the fractional changes (a 20% change in CBF with a 10% change in  $\text{CMRO}_2$  would be  $n = 2$ ). Based on the theoretical discussion earlier in this chapter, with the central idea that CBF and  $\text{CMRO}_2$  are driven in parallel, rather than being mechanically coupled to each other,  $n$  is essentially an empirical index. The calibrated-BOLD method has provided a useful way to measure  $n$  under different conditions, as described in Ch. 14, and typical values of  $n$  range from approximately 1.6 to approximately 4.

The potential significance of  $n$  as a source of variability of the BOLD response is illustrated by a recent study that simultaneously measured BOLD and ASL responses in visual cortex to a visual stimulus, and in basal ganglia structures to a complex motor task (Ances *et al.* 2008). The result was that the BOLD response was approximately seven times stronger in the visual cortex than the basal ganglia. This in itself does not mean much, because the two responses were driven by different stimuli, so the different responses could just represent different effective magnitudes of the stimuli. However, the measured changes in CBF and  $\text{CMRO}_2$  suggested a different interpretation. The CBF change with activation was only approximately 2.5 times larger in visual cortex compared with basal ganglia, and the  $\text{CMRO}_2$  change was only approximately 1.8 times larger. The difference in the BOLD signal magnitudes was thus a poor reflection of the underlying difference in CBF or energy metabolism changes.

In addition, the  $M$  values for the two regions were similar (approximately 6%). Instead, the primary source of the difference in the BOLD response magnitude was the difference in  $n$ , which was approximately 2.2 in visual cortex and 1.6 in basal ganglia. In agreement with the

theoretical considerations, the BOLD response is quite sensitive to the exact value of  $n$  when  $n$  is  $\sim 2$ . The observed difference in  $n$  could be an intrinsic difference between the two brain structures. This was supported by the observation that the CBF response to  $\text{CO}_2$  also was larger in the visual cortex, suggesting the possibility that the blood vessels are simply more responsive, either to a change in neural activity or to  $\text{CO}_2$ , in visual cortex than in basal ganglia. However, another important possibility is that  $n$  depends on the magnitude of the stimulus, a possibility suggested above. In this experiment, the overall response was larger in the visual cortex. If increasing stimulus strength leads to a steady increase of the CBF change, but a rolling off of the  $\text{CMRO}_2$  response, then  $n$  will increase with increased stimulus strength.

In short, we cannot assume that  $\text{CBF}/\text{CMRO}_2$  is a fixed relationship, and more work is needed to clarify the variability of  $n$ .

## Neural activity and the BOLD response

### Location of BOLD signal changes

An important issue in the interpretation of BOLD studies is the accuracy of the localization. Because the venous vessels undergo the largest changes in deoxyhemoglobin content, the largest BOLD signal changes are likely to occur around draining veins (Lai *et al.* 1993). Such veins may be removed from the area of neuronal activation, so the location of the BOLD change could differ by as much as a centimeter or more from the area of increased neural activity. The dominant role of veins is confirmed by several experiments. In BOLD experiments, the voxel size is typically greater than  $30 \text{ mm}^3$ , and at 1.5 T the BOLD activations are a small percentage. However, when the voxel size of the images is reduced, the amplitude of the largest BOLD signal changes increases dramatically (to 20% and larger; Frahm *et al.* 1993), suggesting that the changes are localized to a region smaller than 1–2 mm. This is consistent with the much larger change in the signal of venous blood described in Ch. 14, suggesting that high spatial resolution creates voxels that are largely filled with blood. Furthermore, comparison of the locations of BOLD signal changes with MR angiograms designed to reveal the venous vasculature shows a good correspondence between the two. A study with sub-millimeter resolution concluded that the activated areas were predominantly found to be in the sulci in the location of venous vessels with diameters on the order of the pixel size (Hoogenraad *et al.* 1999).

Experiments using ASL show that the locations of the largest CBF change and the locations of the largest BOLD signal change do not always coincide. Figure 16.3 shows an example of a finger-tapping experiment performed with QUIPSS II (quantitative imaging of perfusion with a single subtraction, version II), an ASL technique that makes possible a simultaneous measurement of both the flow and BOLD signal changes (Wong *et al.* 1997; Ch. 13). The technique alternates tag images, in which the magnetization of the arterial blood is inverted before reaching the image plane, and control images, in which the blood is not inverted. Subtraction of tag from control then gives an image that directly reflects the amount of blood delivered to each voxel, and so is proportional to CBF. All images were acquired with a gradient recalled echo (GRE) EPI pulse sequence with TE of 30 ms so that each image also carries some BOLD weighting. From the raw time series for each pixel, a flow-sensitive and a BOLD-sensitive time series were constructed by calculating the difference signal (control – tag) over time and the average signal (control + tag) over time, respectively (Ch. 13). These two time series,

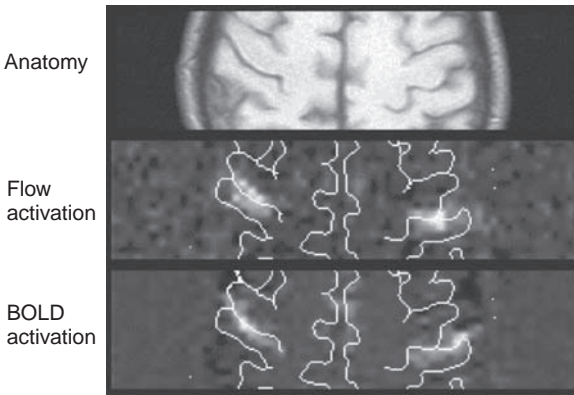


**Fig. 16.3.** The locations of BOLD and cerebral blood flow (CBF) changes. An example of an arterial spin labeling study of the sensorimotor area during a finger-tapping experiment at 1.5 T, showing an anatomical image, a map of flow activation, and a map of BOLD activation. An outline of the sulci is added to the activation maps. The foci of activation for BOLD and CBF are similar but not identical, consistent with the idea that BOLD changes are dominated by veins, and a larger draining vein may be displaced from the site of neural activity.

calculated from the same raw data, can be used to map independently the locations of the flow and BOLD changes.

Figure 16.3 shows that the peaks of the flow and BOLD changes do not precisely coincide in this example made at 1.5 T. On the left side of the image (the subject's right hemisphere), the BOLD change appears to lie directly in the sulcus, consistent with the signal being dominated by a draining vein. But the flow change appears to be displaced to either side of the sulcus, consistent with a CBF change that is more localized to the parenchyma. On the right side of the image, the focus of BOLD activity and the focus of flow activity are shifted by approximately 1 cm.

The localization of the BOLD signal changes can be improved, but at the expense of sensitivity. At higher magnetic field strengths, the voxels with the largest signal changes can simply be ignored, and only the weaker signal changes used for mapping (Menon *et al.* 1993). For experiments at 1.5–3 T, however, the signal changes are initially small enough that discarding the strongest signals would severely decrease the sensitivity. Given this constraint on fMRI at lower fields, the experimental strategy should be governed by the goals of the experiment. If the goal is simply to test whether a brain region is activated, then the displacements caused by draining veins are not likely to be critical. For detailed mapping studies in which the precise anatomical location is critical, however, an ASL experiment may be more appropriate than a BOLD experiment.

As discussed in Ch. 14, the spin echo (SE) experiment has been proposed as a better localized measurement because the extravascular signal change with SE is more sensitive to the smallest vessels owing to diffusion effects. For this reason, an SE or an asymmetric SE (which is intermediate between a standard SE and GRE signal in terms of sensitivity to small vessels) should reveal changes at the capillary level. However, the large changes in the intravascular signal in an SE experiment suggest that at 1.5 T the SE signal, like the GRE signal, is dominated by signal changes in the veins (Oja *et al.* 1999; van Zijl *et al.* 1998). For this reason, the greater selectivity of the SE pulse sequence is not effective until the main field strength is quite high so that the blood signal is suppressed by the shortened  $T_2$  (Lee *et al.* 1999; Yacoub *et al.* 2003). A recent study reporting resolution of orientation columns in human visual cortex at 7 T with high-resolution SE-BOLD imaging shows how important such methods are likely to become at higher fields (Yacoub *et al.* 2008).

A promising approach for high-resolution fMRI is based on the steady-state free precession (SSFP) pulse sequence, a method that is very sensitive to the slight resonance-frequency changes associated with changes in deoxyhemoglobin (Miller *et al.* 2006, 2007). Although the mechanisms underlying the signal changes are more complicated than for a standard  $T_2^*$ -sensitive gradient echo pulse sequence, the SSFP approach has a number of potential advantages in terms of reduced distortions and signal dropouts.

## The relationship between the BOLD response and neural activity

In most BOLD experiments for mapping activation in the brain, the investigator is interested in the pattern of neural activation rather than the pattern of blood flow and energy metabolism changes that follow. So a critical question is how reliably the BOLD effect reflects the underlying neural activity. We have already discussed the issue of the location of the BOLD activation and the problem of draining veins, and now we want to address the amplitude of the response. Does the magnitude of the BOLD response accurately reflect the magnitude of the neural activity change? In every fMRI mapping experiment, we assume that it does and that, if one area has a larger BOLD signal change than another, then the change in neural activity is correspondingly larger. The agreement of the results of numerous fMRI experiments with other techniques and with the well-established body of literature on the functional organization of the brain clearly suggests that BOLD signal changes do reflect some aspect of neural activity. However, the precise relationship between the BOLD response and neural activity remains a primary question at the heart of fMRI (Logothetis 2008).

Neural activity is often characterized in a binary way: input versus output, excitatory versus inhibitory, synaptic versus spiking, etc. While these dichotomies are sometimes useful, they are oversimplifications of the integrated complexity of neural activity (Logothetis 2008). If we think of a typical imaging voxel a few millimeters in size, there are inputs to the neurons in the voxel that originate from more distant neurons, and there are spiking outputs from the neurons in the voxel that terminate on more distant neurons. But most of the synapses within the voxel are receiving input from other neurons within the same voxel, so local processing always involves a great deal of correlated synaptic and spiking activity. In addition, local processing involves a balance of inhibitory and excitatory activity, so a direct association of a positive BOLD response with excitation and a negative BOLD response with inhibition is an oversimplification. Above, we suggested that the CBF response is primarily driven by the synaptic activity, while the CMRO<sub>2</sub> response depends on the overall energy cost, and this could also have a contribution from spiking. In addition, there is evidence that signals from inhibitory neurons can act to reduce CBF (Ch. 2). For these reasons, the BOLD response may have a complicated dependence on synaptic and spiking activity.

The beginning of understanding how different aspects of neural activity affect the BOLD response requires the combination of fMRI and direct electrode recording in the same animal, and such experiments have become feasible with the demonstration of fMRI in awake, behaving non-human primates (Dubowitz *et al.* 1998; Logothetis *et al.* 1999; Stefanacci *et al.* 1998). These important, but difficult, experiments should provide a much firmer foundation for the interpretation of BOLD signal changes in terms of the underlying neural activity.

For example, an influential paper by Logothetis and colleagues (2001) reported a study in which local field potentials (LFPs) and multi-unit activity (MUA) were recorded along with BOLD responses in the visual cortex of an anesthetized primate. The LFP and MUA signals

are both derived from the fluctuating electrical potentials recorded by the electrode based on the frequency, with the low-frequency LFPs reflecting fluctuating synaptic potentials, and the high-frequency MUA component reflecting spiking activity. Both measures were correlated with the BOLD response, with a better correlation for the LFP component. However, the time course of the BOLD response was better matched by the time course of the LFP response for a sustained stimulus, and the LFPs were a much better predictor of the BOLD response. Both the BOLD response and the LFPs continued for the duration of the stimulus, while the MUA component peaked at the beginning of the stimulus and then decreased to nearly zero. These results gave empirical support to the idea that the BOLD response primarily reflects synaptic activity rather than spiking activity.

## Linearity of the BOLD response

In the absence of any direct measure of neural activity to compare with the BOLD response, a number of investigators have examined the quantitative relationship between simple stimuli and the resulting BOLD response. One approach is to vary the stimulus duration with a constant stimulus magnitude, and the central question asked is whether the BOLD response behaves linearly with stimulus duration. For example, if the BOLD response to a 2 s stimulus is shifted and added to construct a simulated response to a 6 s stimulus, does this agree with the true response measured with a 6 s stimulus? In mathematical terms, this question is equivalent to asking whether the BOLD response is a linear convolution of the stimulus with a fixed hemodynamic response function. This idea is at the heart of most of the data-processing schemes designed to pull weak signals out of a noisy background (Ch. 15), so it is an important question.

Several studies have compared experimentally the response to brief stimuli with the response to longer stimuli, using a number of different stimuli (Birn *et al.* 2001; Boynton *et al.* 1996; Dale and Buckner 1997; Glover 1999; Miller *et al.* 2001; Robson *et al.* 1998; Vasquez and Noll 1998). The consistent result of these studies is that, even though the response is roughly linear, there is a definite non-linear component. The nature of the non-linearity is that the response to a brief stimulus (e.g., < 4 s) appears stronger than would be expected given the response to a longer stimulus.

There are several possible explanations for this non-linearity, and it is helpful to think about the process that leads from the stimulus to the BOLD response as consisting of three steps, as illustrated in Fig. 16.2. The first step is the translation of the stimulus pattern into a temporal sequence of local neural activity. The second step is the translation of the neural activity time course into changes in local CBF, CBV, and CMRO<sub>2</sub>. And the third step is the translation of the CBF, CMRO<sub>2</sub>, and CBV time courses into the BOLD response. Each of these steps could be either linear or non-linear (Miller *et al.* 2001).

The first step, from a stimulus time course to a neural activity time course is likely to be non-linear. In recordings of the electrical activity of neurons, a common pattern of response to a sustained stimulus is an initial peak of activity (firing rate) followed by a reduction to a plateau level over a few seconds. This pattern of adaptation has been observed in many systems and is a general feature of the spiking activity of neurons (Adrian 1926; Bonds 1991; Maddess *et al.* 1988). In their original study of the non-linearity of the BOLD signal, Boynton *et al.* (1996) suggested that this could be a natural explanation for the larger BOLD signal for brief stimuli. If all the non-linearity comes in during this first step, then the BOLD response could be a simple linear convolution with the neural activity.

However, non-linearities could also enter in the remaining two steps. In particular, the step from metabolic changes to BOLD changes is likely to involve two types of non-linearity. The first source comes directly from the ceiling of the BOLD effect. There is a maximum signal that could be measured in a BOLD experiment, corresponding to full oxygenation of hemoglobin. Consequently, any BOLD signal increase is an approach toward this ceiling. The result is that if we plot the BOLD change as a function of the CBF change, the curve will bend over for large flow changes (Fig. 14.8). Then any linear extrapolation of the BOLD change measured with a small CBF change will overestimate the BOLD change for a large CBF change. If the flow change in response to a brief stimulus is less than the fully developed flow change to a longer stimulus, this would produce a non-linearity in the BOLD response with the same general trend as the observed non-linearity.

A second potential source of non-linearity is that the metabolic and CBF changes may follow different time courses, with the CBV change lagging behind the CBF change (Buxton *et al.* 1998b; Mandeville *et al.* 1998). For this reason, the CBV change may be disproportionately smaller for a brief stimulus than for a more extended stimulus. Because a venous volume increase tends to reduce the BOLD signal, this effect could also contribute to making the response to a brief stimulus larger than that to a more extended stimulus.

The degree and nature of the non-linearity also may vary across the brain (Birn *et al.* 2001; Miller *et al.* 2001). In a study measuring the linearity of both the CBF and BOLD responses, the CBF was reasonably linear in primary motor cortex but non-linear in primary visual cortex (Miller *et al.* 2001). However, the BOLD response was non-linear in both regions. The BOLD non-linearity in motor cortex, without a non-linearity of the CBF response, was consistent with the non-linearity of the BOLD ceiling effect. In visual cortex, the CBF non-linearity indicates that an earlier source of non-linearity contributes, either a non-linearity of the neural response itself or a non-linearity in the step from neural activation to CBF change.

In summary, the BOLD response is non-linear with respect to stimulus duration. There are several plausible sources for this non-linearity, but the full role of each has not been established. A likely source of non-linearity is the neural response itself, which often begins with an initial peak of activity before settling down to a sustained plateau. A second likely source of non-linearity is the transformation from CBF change to BOLD signal response, owing to the flattening of the BOLD response at high flows.

Despite these non-linearities, it is common in the analysis of BOLD data to assume linearity. This undoubtedly introduces some error into the analysis, but in many applications the error is likely to be small. However, the effects are likely to be more significant for event-related experimental paradigms that involve the separation of overlapping responses. Further studies designed to pinpoint the sources of the non-linearities will be important for assessing the significance of non-linearity in typical BOLD experiments.

## Mapping resting state networks with spontaneous BOLD correlations

A promising new area of application of BOLD-fMRI is to map brain networks based on correlations between spontaneous fluctuations of the BOLD signal. The idea is to detect functional connections between spatially remote areas based on their synchronous activity (Biswal *et al.* 1995). In the standard fMRI paradigm, task and control states are carefully constructed to isolate one component of brain function, and the analysis is then to look for areas that correlate with the known stimulus. The paradigm for functional connectivity studies is rather different. There is no controlled stimulus, and indeed if this analysis is



applied to data in which there was a known stimulus applied, the specific responses to that stimulus are typically removed. The basic analysis then involves selecting a seed voxel (or an average over a small region of interest) and correlating the corresponding time course with the time course of every other voxel. Those that show a significant correlation are interpreted as being part of an extended *resting state network*. The study of resting state networks has blossomed into an active field, with these techniques applied to a number of different networks and in different disease states (Auer 2008; De Luca *et al.* 2005, 2006; Fox and Raichle 2007; Rogers *et al.* 2007; Supekar *et al.* 2008).

An important related concept is the idea of a *default mode* network in the brain (Raichle *et al.* 2001). The origin of this concept came from thinking about the significance of “deactivations,” a negative CBF or BOLD response to a task. Such deactivations were present in many studies, but often ignored because it was not clear how to interpret them. By examining a number of positron emission tomography (PET) studies, Raichle and colleagues (2001) identified a consistent pattern of regions that showed higher activity during the control state and then reduced activity during the performance of a task, and they called this a *default mode* of brain function. A later study showed that one of the resting state networks identified through BOLD fluctuations corresponds with the default mode network (Greicius *et al.* 2003).

As these methods based on resting state networks have evolved, the processing required has become more sophisticated. The spontaneous fluctuations that are used to identify the networks are low frequency ( $<0.1$  Hz), and it is essential to remove other physiological fluctuations that are not related to neural activity. These include cardiac and respiratory fluctuations, as well as vasomotion, the low-frequency spontaneous oscillations of smooth muscle. If the sampling rate (repetition time [TR]) is not fast enough, even the higher-frequency cardiac pulsations can be aliased to lower frequencies and contaminate the signals. However, there remains some skepticism about whether these non-neuronal sources of correlation are fully removed, because intrinsic vascular correlations also produce spatially extended BOLD correlation maps (Birn *et al.* 2008). A recent study comparing functional connectivity estimated with BOLD correlations with anatomical connectivity estimated from diffusion tensor imaging (DTI) found agreement, lending support to the neuronal significance of the BOLD oscillations (Greicius *et al.* 2008).

In summary, these methods present an interesting and useful alternative paradigm for fMRI studies, and the observations of network changes in disease states suggest that they may have useful clinical applications. As these methods mature, they are likely to be applied even more widely.

## Dynamics of the BOLD response

### The time scale of BOLD dynamics

The time scale of the BOLD response is much slower than the time scale of neural activity. Even a brief subsecond neural stimulus produces a BOLD response that is delayed by a few seconds and may take approximately 6 s to reach a peak. This slow response results, of course, from the slow CBF response. This time scale for the BOLD response may vary across the brain and across subjects, but a more interesting finding is that it can also vary in the same subject depending on the physiological baseline state. The basic finding is that when baseline CBF is increased, the BOLD dynamics slow down, and when CBF is decreased the BOLD dynamics speed up.

For example, Cohen and colleagues (2002) examined how the BOLD response changed when the baseline state was altered by changing the blood  $p\text{CO}_2$  levels: raising the  $p\text{CO}_2$  level (hypercapnia) by inhalation of  $\text{CO}_2$  added to air or decreasing  $p\text{CO}_2$  (hypocapnia) by having the subjects hyperventilate. The effect of  $\text{CO}_2$  on the baseline state is that CBF is elevated during hypercapnia and lowered during hypocapnia. Compared with breathing air, the BOLD dynamics slowed during hypercapnia, in the sense that the BOLD response appeared stretched in time. The results were the opposite for hypocapnia, with faster BOLD dynamics. Other studies with caffeine, which lowers baseline CBF, found faster BOLD response dynamics (Behzadi and Liu 2006; Liu *et al.* 2004).

This basic effect, of slower BOLD dynamics with increased baseline CBF, is not what one might have expected. Naively, higher CBF would suggest a shorter time constant (the inverse of CBF) and faster dynamics. A possible explanation for this phenomenon was proposed by Behzadi and Liu (2005). They considered a biomechanical model in which the compliance of the artery results from two factors: the tension of the smooth muscle and an elastic component arising when the vessel is stretched. The essential physical idea of the model is that when the vessel is constricted, so that the elastic components are not stretched, the compliance is dominated by the smooth muscle and responds more quickly to changes in smooth muscle tension. In contrast, when the artery is dilated, the elastic components make a significant contribution to the overall compliance of the vessel, and the same relaxation of the smooth muscle would not produce as large a change of the overall compliance.

## Transients of the BOLD response

In fMRI experiments, stimuli are often presented in a block design, so the temporal stimulus pattern is simply a square wave. To a first approximation, the BOLD response in many areas of the brain looks like a delayed and smoothed version of the stimulus pattern. However, one of the interesting features of the BOLD response is that a number of transient patterns have been reported to occur at the transitions between rest and active states. These dynamic aspects include signal overshoots and undershoots at both the beginning and end of the stimuli. The two features that have received the most attention are a brief *initial dip* prior to the primary BOLD signal increase, and a longer lasting *post-stimulus undershoot*.

Transients in the BOLD response could be an accurate reflection of transients in the neural activity itself. However, because the BOLD signal depends on the combined changes in CBF, CBV, and  $\text{CMRO}_2$ , such transients also can arise if the respective time courses for these physiological changes differ. For example, if the  $\text{CMRO}_2$  increases before the CBF begins to change, the BOLD response could show an initial dip through the increase of deoxyhemoglobin. A post-stimulus undershoot could occur if CBF transiently falls below the baseline level, or if the CBF returns quickly to baseline but the CBV or  $\text{CMRO}_2$  returns more slowly. Because of this dependence of the BOLD signal on multiple physiological changes, it is not possible to identify the sources of these transients from BOLD measurements alone.

A useful approach for testing whether the transients of the BOLD response are neural in origin or result from mismatches in the timing of the metabolic changes is to measure the CBF change directly with ASL techniques. If a BOLD transient is not present in the flow dynamics, then the source is likely to be in the relative time courses of the metabolic changes. If the CBF dynamics also show the transient feature, then it is more likely to be a reflection of a transient in the underlying neural activity. Such experiments combining BOLD and ASL data have been performed to investigate several of these transient features, and both types of result have been reported.

Hoge and co-workers (1999) used a range of different visual stimuli to compare the flow and BOLD responses in the visual cortex. They found that some stimuli showed initial overshoots and post-stimulus undershoots of the BOLD signal whereas other stimuli did not. For those stimuli that evoked transients, the flow signal showed a corresponding pattern of transients, although less pronounced than those in the BOLD signal. They concluded that these features represented the temporal pattern of neural activity, which differed for different stimuli, rather than time lags of the physiological changes. Other studies have found that the post-stimulus undershoot is not present (or is at least much weaker) in the CBF signal (Buxton *et al.* 1998b, 1999; Davis *et al.* 1994).

In short, we should expect that a sustained stimulus often will not elicit a uniform level of neural activity, and variations of the BOLD signal during the stimulus may reflect such variations in neural activity. A simultaneous measurement of the CBF response can provide support for such an interpretation. However, one should be cautious about interpreting transient features of the BOLD signal without also measuring the CBF response.

### The post-stimulus undershoot

The cause and significance of the post-stimulus undershoot has been a source of speculation since the beginning of fMRI, and it is still not clear whether this is a neural, vascular, or metabolic effect. Clearly one possibility is that it is driven by a lowering of the neural activity after a sustained response. Such rebound effects have been seen in electrophysiology data, and the post-stimulus undershoot of the BOLD response could simply be a coupled reflection of that lowering of neural activity. However, the observation that has driven much of the speculation is that, at least in some circumstances, the CBF response does not show a significant undershoot even though the BOLD response does. This would argue against a neural interpretation in these cases, and so the question then becomes how a BOLD post-stimulus undershoot can occur when there is no undershoot in CBF.

From the basic theory of the BOLD effect, a signal change is observed when the local deoxyhemoglobin content is altered, so there are two ways in which the BOLD signal could show an undershoot even though the flow signal does not. Either the CMRO<sub>2</sub> remains elevated after flow has returned to baseline, requiring an increased OEF (Frahm *et al.* 1996; Kruger *et al.* 1996), or the venous CBV remains elevated (Buxton *et al.* 1998b; Mandeville *et al.* 1998). Both effects would cause the deoxyhemoglobin content to remain elevated after flow has returned to the resting level. The first is metabolic, suggesting an uncoupling of CBF and CMRO<sub>2</sub> in the post-stimulus period. Alternatively, the lag of the CBV change behind the CBF change would reflect a biomechanical vascular phenomenon rather than a metabolic effect. These two hypotheses represent the two ways in which the deoxyhemoglobin content could change: a change in blood oxygenation or a change in venous blood volume.

Experiments by Mandeville and co-workers (1998) provided the initial motivation for the hypothesis that CBV recovery lags behind CBF recovery. In studies in a rat model, they used a long-lasting intravascular contrast agent (MION) to monitor the blood volume dynamics during activation and laser Doppler flowmetry to measure CBF with a similar experimental protocol. Combining these data, the dynamic curves showed a reasonably prompt return of CBF to baseline, but an elevated CBV with a time lag that matches well with the duration of the post-stimulus undershoot. In a subsequent set of experiments (Mandeville *et al.* 1998, 1999a), these investigators directly addressed the question of the dynamics of the CMRO<sub>2</sub> change using a variation of the calibrated-BOLD technique (Box 14.1). Combining dynamic measurements during activation with calibration data acquired after inhalation of CO<sub>2</sub>, the

estimated dynamic curve of  $\text{CMRO}_2$  closely followed the CBF curve, but with a smaller fractional change.

Two similar biophysical models were proposed to explain how such lags in the recovery of CBV could occur, the balloon model (Buxton *et al.* 1998b) and the delayed compliance model (Mandeville *et al.* 1999b). Both models attribute the effect to the biomechanical properties of the vessels. To illustrate how this works, we consider the balloon model. In the balloon model, the venous compartment is modeled as an expandable balloon, with an inflow rate  $F_{\text{in}}$  and an outflow rate  $F_{\text{out}}$ . At steady state,  $F_{\text{in}} = F_{\text{out}}$ . During dynamic changes, the two flows are different, and the balloon inflates when  $F_{\text{in}} > F_{\text{out}}$  and deflates when  $F_{\text{in}} < F_{\text{out}}$ . The inflow rate  $F_{\text{in}}(t)$  is taken as the driving function of the system, and the outflow rate is taken to be a function of the volume of the balloon,  $F_{\text{out}}(v)$ . As the balloon expands, the pressure inside increases, increasing the rate of outflow. The curve of  $F_{\text{out}}(v)$  is then analogous to a stress–strain curve and depends on the biomechanical properties of the balloon. The dynamic quantities of interest are the total deoxyhemoglobin content and the blood volume, and the equations for the time evolution of these quantities are derived simply from mass balance. Such a model is able to produce theoretical BOLD response curves similar to experimentally observed curves.

However, more recent studies have challenged the idea of a slow recovery of CBV. Lu and colleagues (2003) developed a novel approach for measuring CBV changes called VASO (vascular space occupancy). The method is based on the idea that when CBV increases, it must displace something else (perhaps cerebrospinal fluid). By using an inversion recovery pulse sequence with the inversion time TI carefully chosen so that the signal of blood is at its null point, the blood generates no signal. If CBV within a voxel increases and displaces water with a  $T_1$  different from blood, the net MR signal will decrease. These authors demonstrated that this method shows robust activation signals in an fMRI experiment, with signal decreases of a small percentage with activation. They then used this method in conjunction with BOLD and ASL imaging for the same stimuli (Lu *et al.* 2004). The BOLD response exhibited a strong post-stimulus undershoot, but the CBV response showed a quick return to baseline rather than a sustained elevation. More recently, Frahm and colleagues (2008) used a multiple injection contrast agent technique and found no evidence of a sustained elevation of CBV. And Schroeter and colleagues (2006), using near-infrared techniques, found evidence for an oxygenation change but not a volume change during the post-stimulus period.

A recent study by Yacoub and colleagues (2006) provides some support for a sustained CBV change, but in a way that suggests that the post-stimulus undershoot may be a rather complicated phenomenon. Using high-field imaging in a cat model, they were able to isolate responses from the middle layers of cortex and the surface layers, and they used an intravascular contrast agent (MION) to measure CBV changes in conjunction with BOLD changes. The interesting result was that BOLD undershoots occurred in both the superficial and deeper layers, and the CBV showed a sustained elevation, but only in the deeper layers. This suggests that a balloon effect may be part of the source of the undershoot in the deeper layers, but it cannot be the exclusive source. Because the blood of the deeper layers eventually reaches the veins in the upper layers, the observed dip there could be the result of transport of venous blood with altered oxygenation from the lower layers. If so, then the undershoot in the deeper layers could be a combination of an oxygenation and a volume change. In addition, this more complicated interpretation was possible only because the data were of a sufficiently high spatial resolution to reveal different patterns between deeper and superficial layers of the cortex. In human studies, we must work with averages

over these regions with different behavior, and the average results may not conform to a simple model.

As discussed in Ch. 2, a recent study with optical techniques in small animals also failed to find any evidence of venous ballooning (Hillman *et al.* 2007). Interestingly, though, they did find evidence for a sustained hematocrit change, a phenomenon that could have a similar effect on the BOLD signal as the hypothesized slow recovery of CBV. It is really the red cell density in tissue, rather than CBV itself, that is the critical factor in determining the deoxyhemoglobin content. Such a phenomenon could occur if capillaries that are poorly perfused by red cells in the baseline state dilate slightly to allow more red cells through, and then recover to baseline more slowly after the stimulus. This study suggests that more sophisticated models of the hemodynamic changes with activation are required to understand the dynamics.

Finally, it is important to remember that the undershoot could often be neural in origin, and it is only puzzling when CBF measurements fail to show an undershoot. However, the decision that there is not enough of a CBF undershoot to explain the BOLD undershoot requires some care. First, the CBF time course has more noise (Fig. 16.4), so it is possible that a weak undershoot could be present but not reach the level of statistical significance that would allow one to confidently say that it is there. Second, a more subtle factor is related to

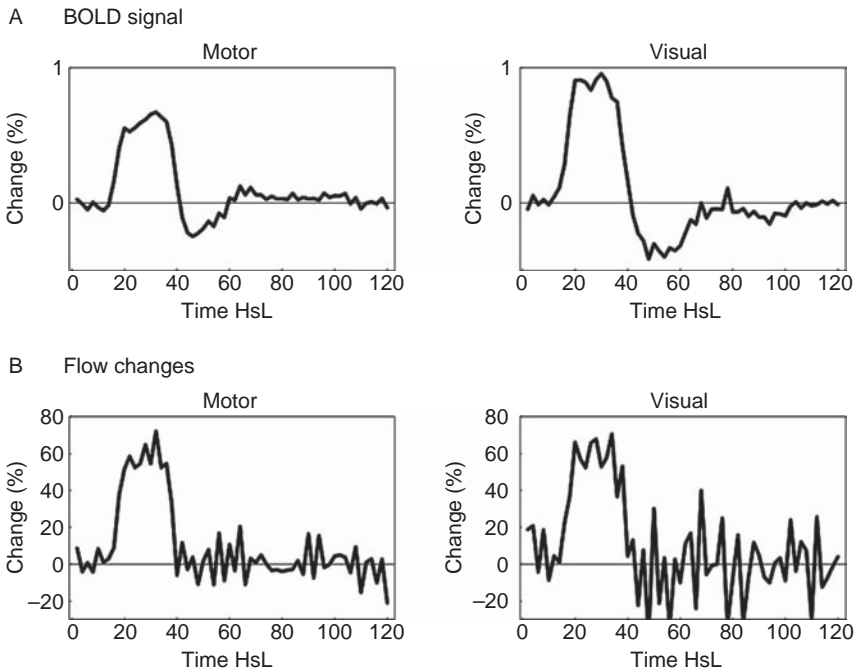


**Fig. 16.4.** The post-stimulus undershoot. A common feature of the BOLD signal is an undershoot of the baseline after the end of the stimulus. The data shown are from a study at 1.5 T of a single subject who tapped his fingers while observing a checkerboard pattern reversing at 4 Hz. The stimulus lasted 20 s, followed by a 100 s rest period to allow visualization of the undershoot. An arterial spin labeling pulse sequence (QUIPSS II) was used to measure flow and BOLD changes simultaneously in an oblique plane cutting through both the visual and motor areas of the brain. Both areas showed a pronounced post-stimulus undershoot in the BOLD signal (A), but there was no evidence of an undershoot of flow (B).

the non-linear dependence of the BOLD response on the CBF change. Because the BOLD response has a ceiling, it tends to bend over as CBF increases, approaching a plateau. For this reason, the ratio of the BOLD response to the CBF response tends to decrease as the responses grow larger. Or, put it in the opposite way, a weak CBF change will produce a proportionately larger BOLD response than a strong CBF change. Applied to the post-stimulus undershoot, this means that a relatively weak CBF undershoot may produce a comparatively large BOLD undershoot, disproportionate to the ratio of the CBF and BOLD responses in the main part of the BOLD response.

In summary, there is still no consensus on a single explanation for the post-stimulus undershoot. The post-stimulus undershoot may not have a unitary explanation, with elements of neural, vascular, and metabolic effects contributing under different circumstances.

### The initial dip

The *initial dip* (also called the *fast response*) is potentially an important aspect of the BOLD response, but it is also one of the most controversial. The interest in the initial dip stems from studies using intrinsic optical signals that are sensitive to oxyhemoglobin and deoxyhemoglobin (Malonek and Grinvald 1996). In these studies, the brain of a cat was exposed, and the reflectance spectrum from the exposed surface was measured. The reflectance spectrum is composed of several sources, including characteristic spectra for oxyhemoglobin and deoxyhemoglobin and a less-specific scattering component. The measured spectra can be modeled to extract separate signals reflecting the deoxyhemoglobin and oxyhemoglobin concentrations, and these signals are used to map local changes in the oxygenation state of hemoglobin, with a spatial resolution of 50  $\mu\text{m}$ . This study was performed with visual stimuli, oriented full-field moving gratings, designed to excite differentially the orientation columns in the cat visual cortex. Functional maps were calculated by taking the difference between the responses to moving gratings with orthogonal orientations. The resulting dynamic curves showed a biphasic response for deoxyhemoglobin, with an initial increase in deoxyhemoglobin peaking approximately 2 s after the stimulus onset, followed by a later decrease of deoxyhemoglobin that was approximately three times larger. The delayed decrease of deoxyhemoglobin corresponds to the usual BOLD effect, but the initial increase of deoxyhemoglobin should cause an initial dip of the BOLD signal.

In addition to the demonstration of an initial deoxyhemoglobin increase, a key result of this optical study was that this fast response provided a better delineation of the orientation column structure than did the later deoxyhemoglobin decrease. Malonek and Grinvald (1996) hypothesized that the explanation of this result is that CBF is controlled only on a coarse spatial scale, so that activity in one set of orientation columns nevertheless increases flow to nearby columns. They further suggested that the fast response is the result of a rapid increase in  $\text{CMRO}_2$  before the CBF has begun to increase. Because this early  $\text{CMRO}_2$  change is better localized to the activated column, the fast response yields a better map of the columnar structure. If this interpretation is correct, then the fast response of the BOLD signal could provide a much more accurate map of neural activity in fMRI experiments.

The initial dip of the BOLD response was first detected using a rapid spectroscopic acquisition in which the MR signal from a single large voxel was measured (Ernst and Hennig 1994; Hennig *et al.* 1995). The original measurements were carried out at 2 T with a  $2\text{ cm} \times 2\text{ cm} \times 2\text{ cm}$  voxel located in the visual cortex, and the data showed a weak but significant dip

in the BOLD signal at 0.5 s after the onset of a brief visual stimulus. The subsequent positive BOLD signal several seconds after the start of the stimulus was approximately 2.5 times larger in magnitude than the initial dip.

The initial dip was first observed in an fMRI imaging experiment by Menon and co-workers (1995). They used an EPI acquisition at 4 T, measuring the response in the visual cortex while subjects wore goggles that flashed red lights at a flicker rate of 8 Hz. They found that the later positive BOLD change was rather widespread in the visual cortex, including areas that could be identified as veins on higher-resolution images. However, voxels that exhibited an initial dip mapped more accurately to gray matter. The average signal time courses for voxels that showed the initial dip and those that showed only the later positive BOLD signal showed some interesting differences. For the voxels with the initial dip, the late BOLD response was approximately twice as large as the initial dip (a 2% signal increase compared with a 1% signal dip), and there was a weak post-stimulus undershoot. In contrast, the voxels without the initial dip showed a larger average late BOLD change of approximately 6% and no post-stimulus undershoot. These data suggest that the initial dip maps more accurately to the site of neural activity than does the later positive BOLD signal, which includes contributions from draining veins.

A subsequent study by Hu and co-workers (1997) at 4 T investigated the dependence of the initial dip on stimulus duration, using a similar visual stimulus. They found that both the initial dip and the post-stimulus undershoot were reduced for the shortest stimulus tested (1.5 s) but that the magnitude of the initial dip remained approximately constant for longer stimuli (3.6 and 4.8 s) despite the observation that the late BOLD response and the post-stimulus undershoot continued to increase. The initial dip reached its maximum excursion of 1–2% at 2–3 s after the stimulus onset. Additionally, the late positive BOLD response was approximately three times larger than the initial dip. These results were similar to the results of optical studies in the cat brain (Malonek and Grinvald 1996).

A much weaker initial dip has also been detected at 1.5 T, with an amplitude only approximately 10% of the amplitude of the late positive response (Yacoub and Hu 1999). This suggests that the initial dip scales much more strongly with the magnetic field than does the late positive response. Such a superlinear dependence on field strength would be expected if the BOLD effect is primarily occurring around the capillaries, where diffusion effects are important (Ch. 14).

However, the initial dip is not always seen in either optical or fMRI studies, and this led to early controversy over its existence (Buxton 2001). In an attempt to understand this elusive quality of the initial dip, many explanations have been proposed, including methodological issues (Mayhew *et al.* 1999), species differences (Marota *et al.* 1999), and the short timing intervals used (Fransson *et al.* 1998) among others. There has also been controversy over the interpretation of the initial dip, when it is seen, as a reflection of an early increase in CMRO<sub>2</sub>. Early studies with optical techniques often showed a pronounced initial increase of deoxyhemoglobin, but without a corresponding decrease of oxyhemoglobin (Malonek *et al.* 1997). If the initial dip results from an early change in CMRO<sub>2</sub> before the CBF change has begun, we would expect to see a pure exchange of oxyhemoglobin for deoxyhemoglobin. The lack of an early change in oxyhemoglobin would be more consistent with an early CBV change.

A study by Devor and colleagues (2003) has provided the best evidence of an initial dip caused by an early increase of CMRO<sub>2</sub> before the CBF increase. They used optical imaging methods with high temporal resolution in a rat model and found an early increase of

deoxyhemoglobin accompanied by a clear decrease of oxyhemoglobin. The CBV change, as estimated by the total hemoglobin signal, lagged behind these earlier changes.

By this picture, the initial dip is a transient feature resulting from the mismatch of the onset times for CMRO<sub>2</sub> and CBF, with CMRO<sub>2</sub> responding more quickly. A more recent study provides additional evidence that the sluggishness of the CBF response is a primary factor (Behzadi and Liu 2006). As noted above, one of the surprising features of BOLD dynamics is that the characteristic time scale varies with baseline CBF, although in a counterintuitive way. As baseline CBF decreases, the temporal dynamics of the BOLD response speed up. Behzadi and Liu (2006) showed that the initial dip, which they detected at 3 T in human subjects, was significantly reduced when the subjects were given caffeine. These results are consistent with the idea that the caffeine reduces baseline CBF and creates a faster CBF response.

In short, the initial dip is likely a result of an early mismatch of the onset of CMRO<sub>2</sub> and CBF changes. The variable nature of the effect likely reflects the variability of the onset kinetics of the CBF, which depend on the baseline conditions. The dip could then be varied by drugs or inhaled gases in animal studies, or potentially just by the anxiety level of the subject in human experiments. In this way, the initial dip is an interesting physiological phenomenon, particularly for probing the mechanisms that underlie fMRI. With its sensitivity to the early CMRO<sub>2</sub> change, it also could provide a more precise mapping signal that avoids the draining vein problems of the primary positive BOLD response. However, because it is a weak signal, it is not likely to replace the standard BOLD response for routine fMRI studies.

## Interpreting the BOLD response in disease

Perhaps the most difficult challenge facing the future development of fMRI is understanding how to interpret the BOLD response in disease. Many studies are applying fMRI techniques to try to shed light on disease mechanisms or to provide a means to assess the progression of disease or the response to treatment. Yet there is a fundamental ambiguity underlying these studies: if a disease group shows a different BOLD response to that of a healthy group in response to a standard task, how should this be interpreted? It could represent a difference in the neural activity associated with the task, but it could also be an effect of the disease on vascular responsiveness, or the coupling of neural activity with CBF, or a chronic change in the baseline state. Unfortunately, from the BOLD response alone, we cannot distinguish between these possible scenarios.

The essential problem is that we would like to be able to interpret the magnitude of the BOLD response in a meaningful way. That is, rather than a mapping study, where the central goal is simply to detect where activation is happening, the goal in many disease studies is to detect differences in the level of response. From the earlier discussions in this chapter, it is clear that there are many factors other than neural activity that can cause significant variations in the BOLD response. Probably the most important is the baseline state, which could be altered by the disease or by medications.

A promising approach is to use ASL techniques in addition to BOLD-fMRI to acquire measurements of baseline CBF. A more complicated study, but one that provides potentially valuable information, is to use ASL to measure the CBF response to activation as well as the baseline CBF. An example of how combined ASL and BOLD studies can provide a deeper interpretation of the BOLD response was briefly mentioned in [Ch. 13](#). This study compared subjects at risk for Alzheimer's disease, based on family history and the presence



of at least one allele of the gene *APOE4*, with a low-risk control group (Fleisher *et al.* 2008). The finding was that the high-risk group had a weaker BOLD response to a memory task, showing that the BOLD response had sufficient sensitivity to detect a difference in the high-risk group before there was any evident disease. However, from the BOLD response alone, the reason for the difference is still ambiguous. It could result from altered neural processing associated with the disease, but the CBF data suggest a different interpretation. The absolute CBF during the task was similar in the two groups, suggesting a similar level of task-related activity. Instead, the source of the reduced BOLD response was that the baseline CBF differed between the groups, being higher in the high-risk group. Rather than the disease affecting the acute processing of the task, this result suggests a chronic effect of the disease, altering the baseline state. The combination of ASL with BOLD cannot remove all of the ambiguities of the BOLD signal, but it can provide a richer context for interpreting the BOLD response.

The combination of BOLD and ASL techniques may also open new applications in the clinical setting. Functional MRI has had a relatively weak impact on clinical MRI, despite its widespread use for basic science studies and for group studies of disease (Jezzard and Buxton 2006). For a successful clinical application, one must be able to make measurements in a single individual and determine whether their responses differ from the norm. The intrinsic variability of the BOLD response discussed in earlier sections of this chapter is the primary impediment to such applications. However, the calibrated-BOLD approach, combining ASL and BOLD imaging, provides a way to move fMRI from a mapping tool to a quantitative probe of brain physiology. One approach would be to use these techniques as a kind of “stress test,” activating the brain with simple stimuli and then measuring the physiological responses. Such a study provides much more information than either a BOLD or ASL study alone. In addition to the CBF and BOLD responses, such a study would provide information on the chronic baseline state, the coupling of CBF and  $CMRO_2$ , and the vascular responsiveness to  $CO_2$ .

In summary, a promising direction for the future development of fMRI, particularly for applications in disease and clinical settings, is a close integration of BOLD and ASL methods. In general, all of the available neuroscience imaging techniques, such as electroencephalography or magnetoencephalography, have their own limitations. The combination of BOLD-fMRI with these other techniques in a multimodal approach offers the promise of overcoming limitations of the individual techniques and providing more information than either technique alone.

## References

- Adrian E (1926) The impulses produced by sensory nerve endings. *J Physiol* **61**: 49–72
- Ances BM, Leontiev O, Perthen JE, *et al.* (2008) Regional differences in the coupling of cerebral blood flow and oxygen metabolism changes in response to activation: implications for BOLD fMRI. *Neuroimage* **39**: 1510–1521
- Auer DP (2008) Spontaneous low-frequency blood oxygenation level-dependent fluctuations and functional connectivity analysis of the “resting” brain. *Magn Reson Imaging* **26**: 1055–1064
- Bandettini PA, Jesmanowicz A, Wong EC, Hyde JS (1993) Processing strategies for time-course data sets in functional MRI of the human brain. *Magn Reson Med* **30**: 161–173
- Behzadi Y, Liu TT (2005) An arteriolar compliance model of the cerebral blood flow response to neural stimulus. *Neuroimage* **25**: 1100–1111
- Behzadi Y, Liu TT (2006) Caffeine reduces the initial dip in the visual BOLD response at 3 T. *Neuroimage* **32**: 9–15

- Birn RM, Saad ZS, Bandettini PA (2001) Spatial heterogeneity of the nonlinear dynamics in the fMRI BOLD response. *Neuroimage* **14**: 817–826
- Birn RM, Murphy K, Bandettini PA (2008) The effect of respiration variations on independent component analysis results of resting state functional connectivity. *Hum Brain Mapp* **29**: 740–750
- Biswal B, Yetkin FZ, Haughton VM, Hyde JS (1995) Functional connectivity in the motor cortex of resting human brain using echo planar MRI. *Magn Reson Med* **34**: 537–541
- Bonds AB (1991) Temporal dynamics of contrast gain in single cells of the cat striate cortex. *Vis Neurosci* **6**: 239–255
- Boynton GM, Engel SA, Glover GH, Heeger DJ (1996) Linear systems analysis of functional magnetic resonance imaging in human V1. *J Neurosci* **16**: 4207–4221
- Brown GG, Eyler Zorrilla LT, Georgy B, *et al.* (2003) BOLD and perfusion response to finger-thumb apposition after acetazolamide administration: differential relationship to global perfusion. *J Cereb Blood Flow Metab* **23**: 829–837
- Buxton RB (2001) The elusive initial dip. *Neuroimage* **13**: 953–958
- Buxton RB, Luh W-M, Wong EC, Frank LR, Bandettini PA (1998a) Diffusion weighting attenuates the BOLD peak signal change but not the post-stimulus undershoot. In *Proceedings of the Sixth Meeting of the International Society for Magnetic Resonance in Medicine*, Sydney, Australia, p. 7
- Buxton RB, Wong EC, Frank LR (1998b) Dynamics of blood flow and oxygenation changes during brain activation: the balloon model. *Magn Reson Med* **39**: 855–864
- Buxton RB, Miller K, Wong E, Frank L (1999) Application of the balloon model to the BOLD response to stimuli of different duration. In *Proceedings of the Seventh Scientific Meeting of the International Society for Magnetic Resonance in Medicine*, Philadelphia, p. 1735
- Buxton RB, Uludag K, Dubowitz DJ, Liu TT (2004) Modeling the hemodynamic response to brain activation. *Neuroimage* **23** (Suppl 1): S220–S233
- Cohen ER, Ugurbil K, Kim SG (2002) Effect of basal conditions on the magnitude and dynamics of the blood oxygenation level-dependent fMRI response. *J Cereb Blood Flow Metab* **22**: 1042–1053
- Dale A, Buckner R (1997) Selective averaging of individual trials using fMRI. In *Proceedings of the Third International Conference on Functional Mapping of the Human Brain*, Copenhagen, p. S47
- Davis TL, Weisskoff RM, Kwong KK, Savoy R, Rosen BR (1994) Susceptibility contrast undershoot is not matched by inflow contrast undershoot. In *Proceedings of the Second Annual Meeting of the Society for Magnetic Resonance Imaging*, San Francisco, p. 435
- De Luca M, Smith S, De Stefano N, Federico A, Matthews PM (2005) Blood oxygenation level dependent contrast resting state networks are relevant to functional activity in the neocortical sensorimotor system. *Exp Brain Res* **167**: 587–594
- De Luca M, Beckmann CF, De Stefano N, Matthews PM, Smith SM (2006) fMRI resting state networks define distinct modes of long-distance interactions in the human brain. *Neuroimage* **29**: 1359–1367
- Devor A, Dunn AK, Andermann ML, *et al.* (2003) Coupling of total hemoglobin concentration, oxygenation, and neural activity in rat somatosensory cortex. *Neuron* **39**: 353–359
- Dubowitz DJ, Chen DY, Atkinson DJ, *et al.* (1998) Functional MR neuro-imaging in an awake behaving macaque. In *Proceedings of the Sixth Annual Meeting of the International Society for Magnetic Resonance in Medicine*, Sydney, Australia, p. 1417
- Ernst T, Hennig J (1994) Observation of a fast response in functional MR. *Magn Reson Med*:146–149
- Fleisher AS, Podraza KM, Bangen KJ, *et al.* (2008) Cerebral perfusion and oxygenation differences in Alzheimer's disease risk. *Neurobiol Aging*, in press [PMID 18325636]
- Fox MD, Raichle ME (2007) Spontaneous fluctuations in brain activity observed with functional magnetic resonance imaging. *Nat Rev Neurosci* **8**: 700–711
- Frahm J, Merboldt K-D, Hancicke W (1993) Functional MRI of human brain activation at high spatial resolution. *Magn Reson Med* **29**: 139–144
- Frahm J, Krüger G, Merboldt K-D, Kleinschmidt A (1996) Dynamic uncoupling and recoupling of

- perfusion and oxidative metabolism during focal activation in man. *Magn Reson Med* **35**: 143–148
- Frahm J, Baudewig J, Kallenberg K, *et al.* (2008) The post-stimulation undershoot in BOLD fMRI of human brain is not caused by elevated cerebral blood volume. *Neuroimage* **40**: 473–481
- Fransson P, Kruger G, Merboldt KD, Frahm J (1998) Temporal characteristics of oxygenation-sensitive MRI responses to visual activation in humans. *Magn Reson Med* **39**: 912–919
- Fransson P, Kruger G, Merboldt KD, Frahm J (1999) Temporal and spatial MRI responses to subsecond visual activation. *Magn Reson Imaging* **17**: 1–7
- Glover GH (1999) Deconvolution of impulse response in event-related fMRI. *Neuroimage* **9**: 416–429
- Greicius MD, Krasnow B, Reiss AL, Menon V (2003) Functional connectivity in the resting brain: a network analysis of the default mode hypothesis. *Proc Natl Acad Sci USA* **100**: 253–258
- Greicius MD, Supekar K, Menon V, Dougherty RF (2008) Resting-state functional connectivity reflects structural connectivity in the default mode network. *Cereb Cortex* **19**: 72–78
- Hennig J, Janz C, Speck O, Ernst T (1995) Functional spectroscopy of brain activation following a single light pulse: examinations of the mechanism of the fast initial response. *Int J Imaging Syst Tech* **6**: 203–208
- Hillman EM, Devor A, Bouchard MB, *et al.* (2007) Depth-resolved optical imaging and microscopy of vascular compartment dynamics during somatosensory stimulation. *Neuroimage* **35**: 89–104
- Hoge RD, Atkinson J, Gill B, *et al.* (1999) Stimulus-dependent BOLD and perfusion dynamics in human V1. *Neuroimage* **9**: 573–585
- Hoogenraad FGC, Hofman MBM, Pouwels PJW, *et al.* (1999) Sub-millimeter fMRI at 1.5 T: correlation of high resolution with low resolution measurements. *J Magn Reson Imaging* **9**: 475–482
- Hu X, Le TH, Ugurbil K (1997) Evaluation of the early response in fMRI in individual subjects using short stimulus duration. *Magn Reson Med* **37**: 877–884
- Jezzard P, Buxton RB (2006) The clinical potential of functional magnetic resonance imaging. *J Magn Reson Imaging* **23**: 787–793
- Kruger G, Kleinschmidt A, Frahm J (1996) Dynamic MRI sensitized to cerebral blood oxygenation and flow during sustained activation of human visual cortex. *Magn Reson Med* **35**: 797–800
- Kwong KK, Belliveau JW, Chesler DA, *et al.* (1992) Dynamic magnetic resonance imaging of human brain activity during primary sensory stimulation. *Proc Natl Acad Sci USA* **89**: 5675–5679
- Lai S, Hopkins AL, Haacke EM, *et al.* (1993) Identification of vascular structures as a major source of signal contrast in high resolution 2D and 3D functional activation imaging of the motor cortex at 1.5 T: preliminary results. *Magn Reson Med* **30**: 387–392
- Lee SP, Silva AC, Ugurbil K, Kim SG (1999) Diffusion-weighted spin-echo fMRI at 9.4 T: microvascular/tissue contribution to BOLD signal changes. *Magn Reson Med* **42**: 919–928
- Liu TT, Behzadi Y, Restom K, *et al.* (2004) Caffeine alters the temporal dynamics of the visual BOLD response. *Neuroimage* **23**: 1402–1413
- Logothetis NK (2008) What we can do and what we cannot do with fMRI. *Nature* **453**: 869–878
- Logothetis NK, Guggenberger H, Peled S, Pauls J (1999) Functional imaging of the monkey brain. *Nat Neurosci* **2**: 555–562
- Logothetis NK, Pauls J, Augath M, Trinath T, Oeltermann A (2001) Neurophysiological investigation of the basis of the fMRI signal. *Nature* **412**: 150–157
- Lu H, Golay X, Pekar JJ, van Zijl PC (2003) Functional magnetic resonance imaging based on changes in vascular space occupancy. *Magn Reson Med* **50**: 263–274
- Lu H, Golay X, Pekar JJ, van Zijl PC (2004) Sustained poststimulus elevation in cerebral oxygen utilization after vascular recovery. *J Cereb Blood Flow Metab* **24**: 764–770
- Maddess T, McCourt ME, Blakeslee B, Cunningham RB (1988) Factors governing the adaptation of cells in area-17 of the cat visual cortex. *Biol Cybern* **59**: 229–236
- Malonek D, Grinvald A (1996) Interactions between electrical activity and cortical

- microcirculation revealed by imaging spectroscopy: implications for functional brain mapping. *Science* **272**: 551–554
- Malonek D, Dirnagl U, Lindauer U, *et al.* (1997) Vascular imprints of neuronal activity: relationships between the dynamics of cortical blood flow, oxygenation and volume changes following sensory stimulation. *Proc Natl Acad Sci USA* **94**: 14826–14831
- Mandeville JB, Marota JJA, Kosofsky BE, *et al.* (1998) Dynamic functional imaging of relative cerebral blood volume during rat forepaw stimulation. *Magn Reson Med* **39**: 615–624
- Mandeville JB, Marota JJA, Ayata C, *et al.* (1999a) MRI measurement of the temporal evolution of relative CMRO<sub>2</sub> during rat forepaw stimulation. *Magn Reson Med* **42**: 944–951
- Mandeville JB, Marota JJA, Ayata C, *et al.* Weisskoff RM (1999b) Evidence of a cerebrovascular post-arteriole Windkessel with delayed compliance. *J Cereb Blood Flow Metab* **19**: 679–689
- Marota JJA, Ayata C, Moskowitz MA, Weisskoff RM, Rosen BR (1999) Investigation of the early response to rat forepaw stimulation. *Magn Reson Med* **41**: 247–252
- Mayhew J, Zheng Y, Hou Y, *et al.* (1999) Spectroscopic analysis of changes in remitted illumination: the response to increased neural activity in brain. *Neuroimage* **10**: 304–326
- Menon RS, Ogawa S, Tank DW, Ugurbil K (1993) 4 tesla gradient recalled echo characteristics of photic stimulation-induced signal changes in the human primary visual cortex. *Magn Reson Med* **30**: 380–387
- Menon RS, Ogawa S, Strupp JP, Anderson P, Ugurbil K (1995) BOLD based functional MRI at 4 tesla includes a capillary bed contribution: echo-planar imaging correlates with previous optical imaging using intrinsic signals. *Magn Reson Med* **33**: 453–459
- Merboldt KD, Kruger G, Hanicke W, Kleinschmidt A, Frahm J (1995) Functional MRI of human brain activation combining high spatial and temporal resolution by a CINE FLASH technique. *Magn Reson Med* **34**: 639–644
- Miller KL, Luh WM, Liu TT, *et al.* (2001) Nonlinear temporal dynamics of the cerebral blood flow response. *Hum Brain Mapp* **13**: 1–12
- Miller KL, Smith SM, Jezzard P, Pauly JM (2006) High-resolution FMRI at 1.5 T using balanced SSFP. *Magn Reson Med* **55**: 161–170
- Miller KL, Smith SM, Jezzard P, Wiggins GC, Wiggins CJ (2007) Signal and noise characteristics of SSFP FMRI: a comparison with GRE at multiple field strengths. *Neuroimage* **37**: 1227–1236
- Ogawa S, Tank DW, Menon R, *et al.* (1992) Intrinsic signal changes accompanying sensory stimulation: functional brain mapping with magnetic resonance imaging. *Proc Natl Acad Sci USA*. **89**: 5951–5955
- Oja JME, Gillen J, Kaupinnen RA, Kraut M, van Zijl PCM (1999) Venous blood effects in spin-echo fMRI of human brain. *Magn Reson Med* **42**: 617–626
- Raichle ME, MacLeod AM, Snyder AZ, *et al.* (2001) A default mode of brain function. *Proc Natl Acad Sci USA* **98**: 676–682
- Robson MW, Dorosz JL, Gore JC (1998) Measurements of the temporal fMRI response of the human auditory cortex to trains of tones. *Neuroimage* **7**: 185–198
- Rogers BP, Morgan VL, Newton AT, Gore JC (2007) Assessing functional connectivity in the human brain by fMRI. *Magn Reson Imaging* **25**: 1347–1357
- Schroeter ML, Kupka T, Mildner T, Uludag K, von Cramon DY (2006) Investigating the post-stimulus undershoot of the BOLD signal: a simultaneous fMRI and fNIRS study. *Neuroimage* **30**: 349–358
- Stefanacci L, Reber P, Costanza J, *et al.* (1998) fMRI of monkey visual cortex. *Neuron* **20**: 1051–1057
- Supekar K, Menon V, Rubin D, Musen M, Greicius MD (2008) Network analysis of intrinsic functional brain connectivity in Alzheimer's disease. *PLoS Comput Biol* **4**: e1000100
- Turner R, Jezzard P, Wen H, *et al.* (1993) Functional mapping of the human visual cortex at 4 and 1.5 tesla using deoxygenation contrast EPI. *Magn Reson Med* **29**: 277–279
- van Zijl PC M, Eleff SE, Ulatowski JA, *et al.* (1998) Quantitative assessment of blood flow, blood volume and blood oxygenation

- effects in functional magnetic resonance imaging. *Nat Med* **4**: 159–167
- Vasquez AL, Noll DC (1998) Nonlinear aspects of the BOLD response in functional MRI. *Neuroimage* **7**: 108–118
- Wong EC, Buxton RB, Frank LR (1997) Implementation of quantitative perfusion imaging techniques for functional brain mapping using pulsed arterial spin labeling. *NMR Biomed* **10**: 237–249
- Yacoub E, Hu X (1999) Detection of the early negative response in fMRI at 1.5 T. *Magn Reson Med* **41**: 1088–1092
- Yacoub E, Duong TQ, van de Moortele PF, *et al.* (2003) Spin-echo fMRI in humans using high spatial resolutions and high magnetic fields. *Magn Reson Med* **49**: 655–664
- Yacoub E, Ugurbil K, Harel N (2006) The spatial dependence of the poststimulus undershoot as revealed by high-resolution BOLD- and CBV-weighted fMRI. *J Cereb Blood Flow Metab* **26**: 634–644
- Yacoub E, Harel N, Ugurbil K (2008) High-field fMRI unveils orientation columns in humans. *Proc Natl Acad Sci USA* **105**: 10607–10612



# Appendix: The physics of nuclear magnetic resonance

<b>The classical physics view of NMR</b>	<i>page</i> 425
The field of a magnetic dipole	425
Interactions of a dipole with an external field	426
Equilibrium magnetization	427
Precession	428
<b>The quantum physics view of NMR</b>	429
Quantum effects	430
The rules of quantum mechanics	433
Macroscopic measurements	437

The dynamics of NMR result primarily from the interplay of the physical processes of precession and relaxation. The sources of relaxation were discussed in [Ch. 7](#), but precession has been treated more or less as a given physical fact. Precession is at the heart of NMR, and in this appendix the physical origins of precession are developed in more detail for the interested reader. The physical description of NMR presented in the earlier chapters is classical physics, but in fact the interaction of a particle possessing spin with a magnetic field is a hallmark example of quantum physics. The reader with NMR experience from chemistry may well be wondering how this classical view of NMR relates to the more fundamental quantum viewpoint. This appendix attempts to bridge that gap by describing how precession arises from both the classical and the quantum physics viewpoints.

## The classical physics view of NMR

### The field of a magnetic dipole

The physics of NMR is essentially the physics of a magnetic dipole interacting with a magnetic field. There are two basic models for a magnetic dipole that we will use: a small circular current loop and a rotating charged sphere. The dipole moment  $\mu$  has both a magnitude ( $\mu$ ) and an associated direction and so is described as a vector. For the current loop,  $\mu$  is proportional to the product of the current and the area of the loop and points in the direction perpendicular to the plane of the loop. A rotating charged sphere can be thought of as a stack of current loops, produced as the charge on the sphere is carried around by the rotation. Adding up the fields produced by all the current loops that make up the

sphere yields outside the sphere a net field that is identical to the field of a single current loop at the center. The spinning sphere is an easily visualized classical model for a proton and so is useful in thinking about NMR. The dipole moment of the sphere is proportional to three terms: the volume of the sphere, the charge  $Q$ , and the angular frequency  $\omega$ . The direction of the dipole moment is the spin axis of the sphere, defined by a right-hand rule (with the fingers of your right hand curling in the direction of rotation, your thumb points along the direction of the dipole moment  $\mu$ ).

The field produced by a magnetic dipole was illustrated in Fig. 6.2. Often in MR applications, we are interested only in the  $z$ -component of the dipole field produced by a dipole aligned along  $z$ . The form of this field ( $B_z$ ) is

$$B_z = \frac{\mu(3 \cos^2 \theta - 1)}{r^3} \quad (\text{A.1})$$

where  $r$  is radius. This field pattern recurs frequently in MRI applications (compare, for example, with Figs. 4.10 and 4.11) because it is the prototype field distortion created by a magnetized body. For example, consider a sphere of material, composed of many dipole moments, sitting in an external magnetic field along  $z$ . The action of the field on the dipoles is to cause them to align partly with the field. This creates a net dipole moment density within the sphere, and the result is that the entire sphere creates a net field that is itself a dipole field. That is, a uniformly magnetized sphere creates a dipole field outside, and the dipole moment that describes this field is proportional to the volume of the sphere and the dipole density inside. For a less symmetrical body, the field produced is more complicated, but for many shapes a good first approximation is a dipole field. For example, a sinus cavity produces a dipole-like field distortion throughout the head (Fig. 4.10) through the different magnetic susceptibilities of air and water.

## Interactions of a dipole with an external field

In the preceding discussion, we focused on the field produced by a magnetic dipole, but to understand how NMR works, we also need to know how a dipole moment  $\mu$  behaves when placed in an external field  $\mathbf{B}$ . There are three interrelated effects. First, the energy ( $E$ ) of the dipole depends on its orientation:

$$E = -\mu \cdot \mathbf{B} = -\mu B \cos \theta \quad (\text{A.2})$$

where  $\theta$  is the angle between the dipole moment vector and the magnetic field. The energy of a dipole in a magnetic field is lowest (most negative) when the dipole is aligned with the field ( $\theta = 0$ ). Second, the natural effect of this orientation dependence is that the field creates on the dipole a torque that would tend to align it with the magnetic field, just as a compass needle is twisted into alignment with the earth's magnetic field because that is its lowest energy state. The torque  $\mathbf{W}$  is the vector cross-product of the dipole moment and the field:

$$\mathbf{W} = \mu \times \mathbf{B} \quad (\text{A.3})$$

This torque acts to twist the dipole, but there is no net force if the magnetic field is uniform. But if  $\mathbf{B}$  varies with position, the third effect comes into play, and there will be a net force  $F$  tending to draw the dipole toward a region of stronger field:

$$F = \mu \frac{dB}{dz} \quad (\text{A.4})$$



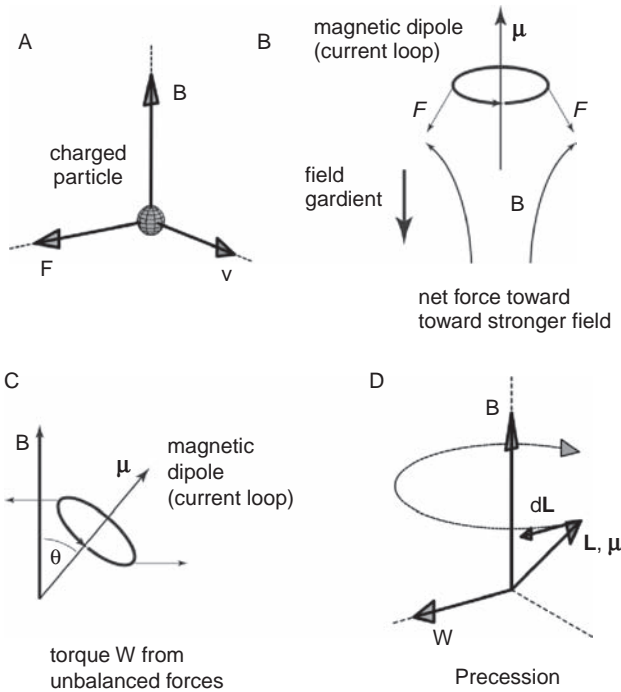


**Fig. A.1.** Classical physics view of precession: (A) A magnetic field  $B$  exerts a force  $F$  on a positive charge moving with velocity  $v$  that is proportional to  $v \times B$  and, therefore, is always perpendicular to both  $v$  and  $B$ . (B) A magnetic dipole  $\mu$  can be viewed as a small loop of current (moving charges), with the direction of  $\mu$  perpendicular to the plane of the current loop. In a non-uniform field, there is a net force on a dipole in the direction of the stronger field. (C) When  $\mu$  is at an angle to the magnetic field, unbalanced forces on the opposite sides of the loop create a torque  $W$  on the dipole. (D) For a nuclear magnetic dipole, the angular momentum  $L$  is proportional to  $\mu$ . The change in angular momentum  $dL$  in a short time  $dt$  is in the direction of  $W$ , so the change  $dL$  creates precession, a rotation of  $L$  around  $B$  without changing its magnitude or the angle it makes with  $B$ .

These physical interactions can be understood from the basic forces exerted on a current loop placed in an external magnetic field. The force  $F$  (called the Lorentz force) on a particle with charge  $Q$  moving with velocity  $v$  through a magnetic field  $B$  is

$$F \propto Qv \times B \tag{A.5}$$

Because  $F$  is proportional to the vector cross product of  $v$  and  $B$ , it is perpendicular to both. Picturing a magnetic dipole as a small loop of current (electrons in motion), the forces on opposite sides are not balanced unless the dipole moment is aligned with the external magnetic field (Fig. A.1). The energy then depends on the orientation of the dipole with respect to the field, and the moment arm between the unbalanced forces creates a torque. In a non-uniform field, the forces are not balanced even when the dipole is aligned with the field because of the curving field lines, creating a net force toward the region of stronger field.

## Equilibrium magnetization

Both the torque produced by the field and the force produced by a non-uniform field can be understood in terms of the energy of a dipole. In both cases, the effect of the external field is to push the dipole toward a lower energy state, either by aligning it with the field or moving it to a region of stronger field or both. Based on these energy arguments, we expect that the long-term behavior of a collection of dipoles will be to align with a uniform magnetic field because this is the lowest energy state. However, in any thermodynamic system, energy is constantly exchanged between different forms. For example, in a sample of pure water, the energy of the molecules is distributed between translational motions, rotational motions, and vibrational motions. If the water is also in a magnetic field, there is additional energy in the orientations

of the magnetic dipole moments. At equilibrium, the net energy is distributed among these different forms, and this prevents the dipoles from reaching their lowest energy state of complete alignment with the field. The total energy of the water molecules is reflected in the temperature, and as temperature is increased, the energy in each form increases. This means that alignment of the dipoles will be most complete at very low temperatures, but as the temperature increases, the alignment will become less pronounced.

We can quantify this dependence with a thermodynamic argument by assuming that each dipole in the magnetic field  $\mathbf{B}_0$  is either aligned with the field or opposite to the field, defining these two states as + and -. This is a very non-classical assumption, but is in accord with the quantum view described below. In any system in thermodynamic equilibrium, the ratio of the populations of two states is given by

$$\frac{n_+}{n_-} = e^{-\Delta E/kT} \quad (\text{A.6})$$

where  $\Delta E$  is the difference in energy between the two states,  $k$  is Boltzmann's constant, and  $T$  is temperature. At room temperature, the alignment of spins in a 1.5 T field is quite small, with a difference of only about 1 in  $10^5$  between those spins aligned with the field and those aligned opposite to the field. Nevertheless, this small difference creates a small equilibrium magnetization  $M_0$  in the sample. This magnetization is simply the net dipole moment density of the sample, proportional to the difference between  $n_+$  and  $n_-$ , and we can derive an expression for it from the thermodynamic equilibrium condition. For the two states of the dipole,  $\Delta E = -2\mu B_0$  (it is negative because the energy of the + state is lower than the energy of the - state). Because this energy difference is much smaller than  $kT$  at room temperature, we can expand the exponential in Eq. (A.6) to give

$$M_0 = \mu(n_+ - n_-) \approx \frac{n\mu^2 B_0}{kT} \quad (\text{A.7})$$

where  $n$  is the total spin density ( $n_+ + n_-$ ). Thus, the equilibrium magnetization, which ultimately sets the scale for the magnitude of the NMR signal, increases in proportion to the main magnetic field. This is a primary motivation for doing MRI at increasing field strengths, and human imaging systems with a main magnetic field as high as 11 T are being planned.

## Precession

The arguments so far indicate that a collection of magnetic dipoles will eventually reach a thermal equilibrium state in which they are partially aligned with the magnetic field, and this creates a uniform equilibrium magnetization of the body containing the dipoles. The time required to reach this state of equilibrium is  $T_1$ , the longitudinal relaxation time. But if this alignment of the spins was the only effect of a magnetic field acting on a dipole, there would be no NMR phenomenon and no MRI. What we have described is the final state of the spins. The additional interesting physics is what happens along the way toward this equilibrium state. The additional effect, which gives rise to the resonance of NMR, is precession of the dipole.

The source of precession is that nuclear dipoles possess angular momentum in addition to a magnetic moment. The association of a magnetic dipole moment with angular momentum is clearly seen in the prototype example of a spinning charged sphere. Both the angular momentum and the dipole moment are proportional to how fast the sphere is spinning, the

angular frequency  $\omega$ . Because of this, we can define a proportionality constant between the two called the *gyromagnetic ratio*,  $\gamma$ :

$$\gamma = \frac{\mu}{L} \quad (\text{A.8})$$

where  $L$  is the angular momentum vector (and  $L$  is the magnitude of that vector). Because the dipole moment is also proportional to the charge  $Q$ , and angular momentum is also proportional to the mass of the particle,  $m$ , we would expect that the gyromagnetic ratio would vary with the ratio  $Q/m$ . For nuclei, the largest ratio of  $Q/m$  is for hydrogen because it consists of just a single proton. For any other nucleus, the neutrons add to  $m$  without contributing to  $Q$ , so the gyromagnetic ratio is smaller. The hydrogen nucleus, therefore, has a higher resonant frequency in a magnetic field than any other nucleus. For electrons, the charge is the same as for the proton, but the mass is much smaller, so the gyromagnetic ratio is approximately three orders of magnitude larger.

The significance of the gyromagnetic ratio becomes clear when we consider the immediate behavior of a dipole when acted on by a torque and the resulting phenomenon of precession. Imagine placing a dipole  $\mu$  at an angle to a magnetic field  $B_0$ . The angular momentum  $L$  is in the direction of  $\mu$ , with a magnitude  $\mu/\gamma$ . The torque  $W$  is the rate of change of angular momentum, and with  $\gamma L$  substituted for  $\mu$  in Eq. (A3), we have

$$W = \frac{dL}{dt} = \gamma L \times B_0 \quad (\text{A.9})$$

Precession results because the change in angular momentum,  $dL$ , acquired in any brief interval  $dt$ , is always perpendicular to the current direction of  $L$ . The new angular momentum is then  $L + dL$ , but this is simply a rotation of  $L$  rather than a change in magnitude. In short, the dipole precesses around the main magnetic field  $B_0$  without changing the angle that it makes with the field. The rate of change of the phase angle in the transverse plane is the precession frequency. In a time  $dt$ , the precession angle is  $d\phi = dL/L = \gamma B_0 dt$ . The fundamental relation of NMR is then that a magnetic dipole precesses in a magnetic field with a frequency, called the Larmor frequency ( $\omega_0$ ), of

$$\omega_0 = \gamma B_0 \quad (\text{A.10})$$

Precession makes it possible to tip the net magnetization into the transverse plane and generate a detectable NMR signal. If all the dipoles are tipped, then the net magnetization also tips, and as the dipoles precess so does the net magnetization. Consequently, the net magnetization mimics the behavior of an individual dipole.

The two important processes in NMR are, therefore, precession and relaxation. Precession does not change the angle between the dipole and the field, and so does not lead to alignment, but over time relaxation does lead to a gradual alignment. The time scales for these two processes are enormously different. The precession period for a proton in a 1.5 T field is about  $10^{-8}$  s, whereas the relaxation time  $T_1$  required to reach thermal equilibrium is about 1 s.

## The quantum physics view of NMR

The previous section described a physical picture of the NMR phenomenon from the viewpoint of classical physics. With the development of quantum mechanics in the twentieth century, we know that this classical view is wrong. The correct view is much stranger, and

unfortunately quantum mechanics does not offer an easily visualized physical picture of the phenomenon in the same way that the classical view does. So important questions are: in precisely what way is the classical view wrong, and, what kind of errors will we make if we adopt the classical view in thinking about NMR? These questions are important because the behavior of a particle with spin in a magnetic field is a quintessential example of quantum mechanics. Based on the quantum view, one encounters statements suggesting that the proton's spin can only be up or down in a magnetic field. But if this is strictly true, it would seem that a transverse, precessing magnetization can never arise, and yet this is the crux of the classical view of NMR.

The answer to the question posed here is that the classical view is wrong in terms of describing the behavior of a single spin but gives an accurate description of the *average* behavior of many spins. This brings out a disturbing feature of quantum mechanics that violates our intuitive sense of logic, that the average behavior of many identical particles in precisely the same state can be so different from the behavior of any one of them. However, in a sense, it is somewhat reassuring, in that it points toward the reasons why our experience with the world on the macroscopic scale leads us to a view of physics that is so different from the fundamental picture provided by quantum mechanics. The following is a sketch of how the classical view of a precessing magnetization vector emerges from a quantum mechanical description. A much more complete description is given by Feynman *et al.* (1965).

## Quantum effects

To illustrate the fundamental strangeness of quantum mechanics, we begin with a thought experiment that is an idealization of one of the key physics experiments of the twentieth century, originally performed by Stern and Gerlach in the early 1920s. The experiment involves a simple device for measuring the component of a particle's magnetic moment along a particular spatial axis. The device is a box with an entry opening on one end and a wide exit opening on the other, and in the experiment particles are sent in one end and then observed to see whether they are deflected from their original path as they emerge from the exit (Fig. A.2). Inside the box, magnets are arranged to create a magnetic field that points primarily perpendicular to the path of the particle. From our classical ideas about the behavior of a magnetic dipole moment in a magnetic field, we would expect that the magnetic moment would precess a little while it is in the field but that, if the field is uniform, it would

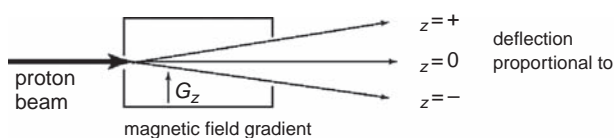


**Fig. A.2.** The Stern–Gerlach experiment to measure the magnetic dipole moment of a proton. Protons pass through a box containing a magnetic field gradient that deflects the proton in proportion to the  $z$ -component of its magnetic dipole moment,  $\mu_z$ . Classical physics predicts a continuous range of  $\mu_z$ , but experiment shows that  $\mu_z$  can take on only one of two values, corresponding to spin up or spin down relative to the field.



not be deflected. This precession is, of course, the phenomenon we are interested in for NMR, but this is not what we are after in this experiment. Here we want to explore the more fundamental concept of the spin state of a particle. The precession is a secondary effect that we will try to minimize by using a weak field and fast-moving particles that spend only a short time inside the box. We will return to precession after illustrating how different quantum effects are from our classical physics intuitions.

Our goal with this experiment is to deflect the particles by making the magnetic field non-uniform, with a strong gradient running perpendicular to the path of the particle. When a magnetic moment is placed in a non-uniform magnetic field, it feels a force in the direction of the field gradient, and the magnitude of the force is proportional to the component of the magnetic moment that lies along the gradient direction (Eq. [A.4]). The magnetic force thus deflects the particle from its initial path as it passes through the box, and the amount of deflection will be proportional to the component of the magnetic moment in the direction of the field gradient. This box can then be used to measure one component of the magnetic moment from the magnitude of the deflection, and the component along any axis can be measured by rotating the box. The original experiment measured the electron magnetic moment, but for our thought experiment we can as easily imagine doing the experiment with protons.

From a classical viewpoint, the physical picture of this experiment is clear. The magnetic moment of the proton is simply a vector in three-dimensional space, and so it has a well-defined projection on to any spatial axis. We could measure the full vector by passing the proton through three successive boxes appropriately arranged to measure the vector's components along three orthogonal directions, such as  $x$ ,  $y$ , and  $z$ . Having measured a set of three projections, we have complete information about the orientation and magnitude of the magnetic moment, and we could then predict precisely what any other experiment would yield if we measured the projection along an arbitrary axis. This classical view is so simple that it seems intuitively obvious, and yet this is not the way nature works at all, as we can see from a few experiments.

In the first experiment, we send a large number of protons through the box with the box aligned so that the field gradient is along the  $z$ -axis. Each proton is then deflected by an angle proportional to the  $z$ -component of its magnetic moment, so what would we expect to see emerging from the box? If we have done nothing to prepare the protons (i.e., nothing to align them initially), then the magnetic moment is equally likely to be pointing in any direction, and if the magnitude of the vector is  $M$ , we would expect that the  $z$ -component could fall anywhere between  $-M$  and  $+M$ . From the classical physics viewpoint, we would, therefore, expect the beam of protons to spread into a fan, with the maximum deflections corresponding to those protons whose magnetic moment is perfectly aligned or antialigned with  $z$  and so having the largest  $z$ -component.

Furthermore, from a classical view, we would expect that the angular momentum would vary among the protons. That is, if we think of the angular momentum as just another form of motion of the particle (rotational rather than translational), then we would expect for thermodynamic reasons that the total energy would divide up among the various possible forms. Then, just as there would be a distribution of translational velocities, with some particles moving rapidly and some nearly still, there would be a distribution of rotational velocities and a distribution of magnetic moments. A proton with weak spin would have a weak magnetic moment and so would suffer only a small deflection. The full classical prediction then would be that the beam of protons is spread into a fan distribution peaked at the center (no deflection).

However, when we carry out this experiment, we see the first surprise of quantum mechanics (Fig. A.2). Instead of a fan of particle paths, the beam is split cleanly into two precise beams, one deflected up and the other deflected down. By measuring the amount of deflection, the  $z$ -component of the magnetic moment is measured, and because the magnetic moment is proportional to the angular momentum, this provides a measurement of the proton's spin. The experimental result is that the spin of the proton is either  $+\hbar/2$  or  $-\hbar/2$ , where  $\hbar$  ("h-bar") is Planck's constant  $h$  divided by  $2\pi$ . This result is not at all consistent with viewing the angular momentum as a randomly oriented vector. Instead of taking on any value from the minimum to the maximum, the  $z$ -component takes on only one of two particular values, and every particle is deflected. We can refer to these two values as spin up and spin down, indicating whether the  $z$ -component is positive or negative. Suppose that we now repeat the experiment, but first we heat up the gas of protons before sending them through the box. From a classical viewpoint, each proton carries more energy; in particular, there should be more energy in rotational motions, so more large angular momenta and magnetic moments should be present. When we pass these heated protons through the box, the results are precisely as before: the beam is split in two, with angular momenta of  $+\hbar/2$  or  $-\hbar/2$ . The angular momentum is independent of the energy of the protons.

From these results, we must conclude that spin, despite the familiar sounding name, is unlike anything in classical physics. Rather than viewing it as a result of the state of the proton (i.e., how fast it is rotating), we must instead look at it as an intrinsic property of the proton, on an equal standing with the proton's mass and charge as irreducible properties. All protons carry an angular momentum and a magnetic moment, whose magnitude cannot be changed. Furthermore, there is nothing special about the particular axis we used in our experiment. If we had instead oriented our box to measure the  $x$ -component of the magnetic moment, we would have measured the same result: the  $x$ -component also takes on only the values  $+\hbar/2$  or  $-\hbar/2$ . At this basic level of fundamental particles, nature allows only discrete values for the outcomes of measurements of some physical quantities. Whatever state a proton is in, if the component of the angular momentum along any axis is measured, the measurement will yield either  $+\hbar/2$  or  $-\hbar/2$ . Angular momentum is quantized, and the measure of this quantization is  $\hbar$ . On the macroscopic scale, we are unaware of the quantized nature of angular momentum because  $\hbar$  is in fact quite small. For example, a spinning curveball in a baseball game carries more than  $10^{31}$  of these basic quanta of angular momentum, so angular momentum on the terrestrial scale appears to be a continuously varying quantity. The laws of classical physics, therefore, provide an approximate, but extremely accurate, description of macroscopic phenomena. It is only when we look closely at the behavior of individual particles that the quantum nature of the world becomes clear.

The experimental result so far is that the component of the angular momentum along any spatial axis is quantized. What happens if we try to measure several components in succession? That is, what happens when we take the output of our  $z$ -box and send it into another box? To begin with, suppose we simply measure the  $z$ -component a second time by passing the spin down beam from the first box through a second  $z$ -box (Fig. A.3A). The result is that all the protons are deflected down. In other words, all the protons that had spin down after the first box still have spin down after the second box, and the spin up protons after the first box also would still show spin up in a second  $z$ -box. This is not surprising; it is completely consistent with our classical idea that the spin has a definite  $z$ -component. The first box sorted the spins into the two states, and the second simply confirmed that the spins are still in those states. Carrying this idea further, we might naively expect that the same holds true for

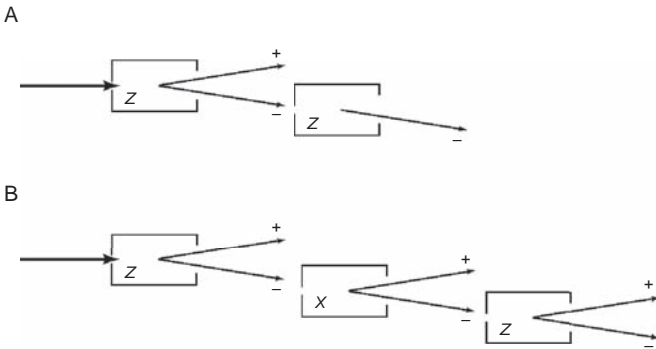


**Fig. A.3.** Quantum uncertainty. (A) After measuring the  $z$ -component of the spin with one box, sending the spin down beam through a second  $z$ -box shows that all the protons are still in the spin down state. (B) However, if another box is inserted between these two to measure the  $x$ -component of the spin, the  $z$ -component becomes unpredictable and can be either up or down with equal probability.

the other axes as well, so that, although the component along any axis is quantized and takes on only one of two values, these components nevertheless have definite values determined by the state of the particle. That is, we can imagine that it might be possible to describe the spin state of the proton in terms of the spin components of the three axes, something like  $(+, +, -)$  to indicate spin up along  $x$  and  $y$  and spin down along  $z$ . However, this idea is wrong, and the behavior of the spins is even stranger.

We can show this second surprising feature of quantum mechanics by extending our experiment. Now we replace the second box with an  $x$ -box to measure the  $x$ -component of the magnetic moment (Fig. A.3B). Specifically, we let the spin down beam from the  $z$ -box pass through the  $x$ -box. The result is that the beam is split into two beams corresponding to spin up and spin down relative to the  $x$ -axis. This result is still highly non-classical, but it is at least consistent with our earlier finding of quantization. But now we take it one step further and add a third box to re-measure the  $z$ -component of the magnetization. Based on our naive interpretation that the component of spin along any axis has a definite value, we should expect that all the protons emerging from the second  $z$ -box should be deflected into the spin down beam. Instead, the protons are split equally into the spin up and spin down beams. Somehow the measurement of the  $x$ -component of the magnetization has changed the state of the  $z$ -component. The initial  $z$ -box sorted the spins into up and down  $z$ -components, and this was confirmed by another  $z$ -box. But when an  $x$ -box is inserted between the two  $z$ -measurements, the state of the spin is jumbled so that the  $z$ -component becomes indefinite: it is equally likely to be up or down after another measurement.

## The rules of quantum mechanics

In the 1920s, physicists developed a mathematical framework for describing quantum phenomena such as those we have just sketched out. This framework can be expressed in a few rules and has proven to be highly accurate in describing the physical world. However, in the process, several ideas that were so entrenched in classical physics as to seem obviously true had to be abandoned. For example, the picture of the angular momentum as a vector with three well-defined components along the  $x$ -,  $y$ -, and  $z$ -axes must be replaced by a view in which these quantities cannot all have definite values. This introduces an uncertainty into the workings of nature that is entirely different from the classical view. The most complete description of the spin state of a proton only tells us the probabilities for measuring spin up or down along an axis. And, indeed, the role of dynamical laws of physics is not to describe how the components of the magnetic moment evolve in time but rather to describe how the *probabilities* evolve in time.

This indeterminacy is not because of ignorance on our part. Even with a classical picture, if we measured only one component of spin, there would be uncertainty about what another measurement along a different axis would yield, but this uncertainty derives from our ignorance of the full state of the spin, the three-dimensional vector. The uncertainty of quantum mechanics is wholly different and more fundamental. If we measure the component of the spin along one axis, the component along a perpendicular axis is indefinite. That is, if a spin has a definite component along  $z$ , which is how the spin is left after our initial measurement of the  $z$ -component, then it is in a state in which there is no definite value for the  $x$ -component. If we then measure the  $x$ -component, the spin will be left in a state with a definite  $x$ -component (either up or down), but now the  $z$ -component is completely indefinite.

This strange behavior can be described within the mathematical framework of quantum mechanics. For the spin state of the proton, we have the following rules of quantum mechanics.

1. A measurement of the component of the spin along any axis will yield a measurement of either  $+\hbar/2$  or  $-\hbar/2$ . The result of any one measurement is usually unpredictable, but a full description of the spin state allows us to calculate probabilities for finding spin up or spin down along any axis. After a measurement, the spin is left in a state such that a subsequent identical measurement will yield the same value.
2. The spin state can always be described as a mixture of two states, corresponding to spin up or spin down along any chosen spatial axis. The spin state is then completely described by specifying two complex numbers, the amplitudes  $a_+$  and  $a_-$ , which underlie the probabilities for measuring the spin component to be up or down. Specifically, the probability for finding the component up is  $|a_+|^2$ , the square of the magnitude of  $a_+$ , which we will write simply as  $a_+^2$ . And similarly, the probability for finding it down is  $a_-^2$ . In practice, we will call the chosen axis  $z$ , and the corresponding amplitudes  $a_{z+}$  and  $a_{z-}$ . Specifying these two complex numbers for one axis completely specifies the spin state.
3. For any other axis, there are also two associated amplitudes. For example, for the  $x$ -axis the amplitudes are  $a_{x+}$  and  $a_{x-}$ , and from these amplitudes the probabilities for the results of a measurement of the  $x$ -component of the spin are calculated using rule 2. The amplitudes for finding the spin up or down along any other axis can be expressed as a linear combination of the amplitudes for  $z$ . The transformation rules for  $x$  and  $y$  are

$$a_{x+} = \frac{1}{\sqrt{2}} (a_{z+} + a_{z-})$$

$$a_{x-} = \frac{1}{\sqrt{2}} (-a_{z+} + a_{z-})$$

$$a_{y+} = \frac{1}{\sqrt{2}} (a_{z+} + i a_{z-})$$

$$a_{y-} = \frac{1}{\sqrt{2}} (i a_{z+} + a_{z-})$$



4. The amplitudes evolve over time depending on the energy associated with the two states. Each amplitude must be multiplied by a factor  $e^{i\omega t}$ , where the angular frequency  $\omega$  is directly proportional to the energy  $E$  of the corresponding state,  $\omega = E/\hbar$ . This quantum mechanical time evolution is the source of the precession observed in NMR, as we will see shortly.

These rules are presented baldly, without any supporting argument. Each requires some amplification in order to deal with more complicated situations, but these bare rules are sufficient to describe the behavior of the spin state of a proton. However, the rules involve some subtlety. The first is the fact that the most complete specification of the spin state still does not allow one to predict the outcome of a measurement, only the probabilities for different outcomes. The only situation in which an experimental outcome *is* predictable is when one of the probabilities is equal to one (e.g., when passing a beam of protons through two successive  $z$ -boxes, as in the foregoing experiment, the result of the second box is determined with a probability of one).

An important feature of these rules is that the amplitudes from which the probabilities are calculated are complex numbers. In other words, each amplitude can be represented in the form  $ae^{i\phi}$ , where  $a$  is the magnitude and  $\phi$  is the phase. The squared magnitude is then calculated by multiplying  $ae^{i\phi}$  by  $ae^{-i\phi}$ . For the probabilities for the  $z$ -axis, the phase does not matter because it cancels out in the calculation of the probabilities. But when amplitudes are added, as in the calculation of  $a_{x+}$ , the phases of the individual amplitudes will make a difference in the calculated probabilities. Because the state of the system is described by two complex numbers, and each complex number is composed of two real numbers (a magnitude and a phase), it appears that the specification of the spin state requires four numbers. In fact, only two numbers are required, for two reasons.

First, a measurement of the  $z$ -component must yield either spin up or spin down, so the probabilities of the two outcomes must sum to one:  $a_{z+}^2 + a_{z-}^2 = 1$ . Therefore, the magnitude of one amplitude fixes the magnitude of the other. The second reason is that the absolute phase of each amplitude does not matter, only the phase difference between the two amplitudes. For example, if the phase of  $a_{z+}$  is  $\phi_+$  and the phase of  $a_{z-}$  is  $\phi_-$ , one could always factor out a phase  $e^{i\phi_+}$  in the expressions for the  $x$ - and  $y$ -amplitudes, leaving  $a_{z-}$  with a phase  $\phi_- - \phi_+$ . Then the factor involving  $\phi_+$  alone would disappear from the calculation of any of the probabilities. It is only the probabilities that are physically measurable, and these depend on the magnitude squared of the net amplitude. So, the spin state of the proton can be represented by just two numbers: one describing the magnitudes of the amplitudes and the other describing the relative phase angle. Because the sum of the squares of the magnitudes must be one, a natural choice is to describe the magnitudes in terms of the sine and cosine of an angle. A convenient form to choose is

$$\begin{aligned} a_{z+} &= \cos\left(\frac{\theta}{2}\right) e^{i\omega_+ t} \\ a_{z-} &= \sin\left(\frac{\theta}{2}\right) e^{i(\omega_- t + \phi)} \end{aligned} \tag{A.12}$$

These equations for the  $z$ -amplitudes, combined with the preceding transformation rules for calculating the  $x$ - and  $y$ -probabilities, completely describe the proton spin state. The two numbers  $\theta$  and  $\phi$  can be thought of as angles, and we will see below how this choice of representation of the spin state leads to a physical interpretation of these angles.

Note that the time dependence of the spin system depends entirely on the energy of the two states. If there is no magnetic field, then the frequencies  $\omega_+$  and  $\omega_-$  are both zero because there is no energy difference between the two states. The amplitudes are then constant, and the spin state does not change over time. Now suppose that a uniform magnetic field with magnitude  $B_0$  is turned on pointing along the  $z$ -axis. From Eq. (A.2), the energy of a magnetic dipole moment  $\mu$  in a magnetic field is  $-\mu B_0$  for the spin up state and  $+\mu B_0$  for the spin down state (the lowest energy configuration occurs when  $\mu$  is aligned with  $B_0$ ). The angular momentum of the proton is  $\hbar/2$ , and the dipole moment is proportional to the angular momentum:  $\mu = \gamma\hbar/2$ . By our rule 4, the angular frequency  $\omega$  associated with an energy  $E$  is  $\omega = E/\hbar$ , so the frequencies associated with the spin up and spin down states, respectively, are  $\omega_+ = -\gamma B_0/2$  and  $\omega_- = +\gamma B_0/2$ . Consequently, over time, the relative phases of the two amplitudes steadily change at a rate  $\omega_0 = \omega_- - \omega_+ = \gamma B_0$ , which is precisely the Larmor precession frequency we found in the classical view of precession (Eq. (A.10)). Because only the relative phase of the amplitudes matters to the physics of the state, we can write the spin state amplitudes as

$$\begin{aligned} a_{z+} &= \cos\left(\frac{\theta}{2}\right) \\ a_{z-} &= \sin\left(\frac{\theta}{2}\right) e^{i(\omega_0 t + \phi)} \end{aligned} \quad (\text{A.13})$$

From these expressions for the  $z$ -amplitudes, we can now calculate the probabilities for measuring spin up along the  $x$ -,  $y$ -, or  $z$ -axes for an arbitrary spin state specified by the numbers  $\theta$  and  $\phi$ :

$$\begin{aligned} p_{x+} &= \frac{1}{2} [1 + \sin\theta \cos(\omega_0 t + \phi)] \\ p_{y+} &= \frac{1}{2} [1 + \sin\theta \cos(\omega_0 t + \phi)] \\ p_{z+} &= \cos^2\left(\frac{\theta}{2}\right) \end{aligned} \quad (\text{A.14})$$

Figure A.4 illustrates the spin state of a proton by plotting a surface such that the length of a line drawn in any direction from the origin to this surface is the probability  $p_+$  of measuring spin up along that direction. This tomato-shaped surface comes directly from the expression above for  $p_{z+}$ , because for any chosen direction we can choose a coordinate system with the  $z$ -axis along that direction, and the probability of measuring spin up is then  $p_{z+}$ . In other words, the spin state of the proton is defined by a particular direction in space, and the probability of measuring spin up along any axis is then  $\cos^2(\theta'/2)$ , where  $\theta'$  is the angle between the measurement axis and the direction defining the spin state.

We can now describe the basic interactions of a spin in a magnetic field in terms of this quantum picture. The spin state is described by a direction defined by two angles  $\theta$  and  $\phi$ . Over time, the evolution of the spin state is a steady increase of the angle  $\phi$  with the Larmor frequency  $\omega_0$ . Only one spatial axis, the orientation direction of the spin state, has a definite component of the spin. For all other axes, we can think of the state as being a mixture of spin up and spin down states. If a component of the spin is measured along any axis, the probability for measuring spin up is defined by the surface in Fig. A.4. Furthermore, the

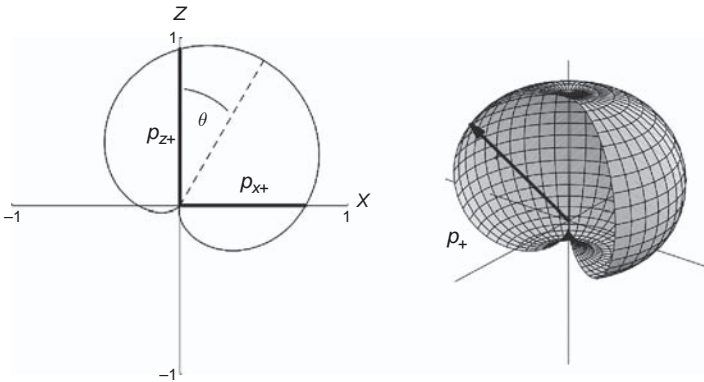


**Fig. A.4.** The spin state of the proton. The spin state of the proton describes the probability that a measurement of the spin component along a particular axis will yield spin up or spin down, the only two possible results allowed by quantum theory. This state can be visualized by plotting the surface shown on the right, such that the distance from the origin to the surface along a particular direction is the probability for measuring spin up along that axis. A two-dimensional cut through this surface is shown on the left. The spin state is described by angles  $\theta$  and  $\phi$ , which are  $30^\circ$  and  $0^\circ$  in this example. The time evolution of the spin state is a steady precession of this surface such that  $\phi = \phi_0 + \omega_0 t$ , where  $\omega_0$  is the classical Larmor frequency. (See plate section for color version.)

act of measurement causes the spin state to jump to a new orientation defined by the outcome of the measurement. If the spin is measured to be up along a particular axis, the direction defining the new spin state will be the positive direction of the measured axis, or the negative direction if the spin is down. In other words, the spin state evolves in two ways: a continuous precession described by the steady increase of the phase  $\phi$  and a discrete jump each time a measurement is made.

For example, suppose that the spin state is defined by an angle  $\theta$  of  $30^\circ$  with the  $z$ -axis. In the absence of a measurement, we can picture the tomato-shaped surface as precessing around the  $z$ -axis (the magnetic field direction). If we then measure the  $z$ -component of the spin, the spin state will jump to either pointing along  $+z$  (with probability 0.933) or pointing along  $-z$  (with probability 0.067). (Remember that our experiment with successive  $z$ -boxes showed that, when the spin down beam from the first box is passed through the second  $z$ -box, the probability of measuring spin down again is one, so the new spin state after the first box must be oriented along  $-z$ .) The spin state then continues to evolve from this new starting point until the next measurement. This dual pattern of change, combining both smooth continuous evolution and discrete jumps, is one of the deep mysteries of quantum mechanics. Nevertheless, this picture of how the world works is highly accurate.

## Macroscopic measurements

The foregoing probabilities are for the results of a measurement of one spin. But in an NMR experiment, we are measuring the net effect of many spins, the net magnetization. If the material contains identical spins, all prepared in the same state, then the net magnetization along a particular axis is simply proportional to the average value of the spin that would be measured along that axis if we measured each spin individually. And the average measured value of the spin component along the axes  $x$ ,  $y$ , and  $z$  is calculated from the probabilities for finding spin up along each of these axes: the expected value of a measurement along a particular axis is  $\hbar/2 (p_+ - p_-)$  and  $p_- = 1 - p_+$ . When the probabilities for spin up and spin

down are equal, we expect to find a zero average spin component, and when the spin is in a definite state along a particular axis, we expect to find  $\hbar/2$  along that axis. For intermediate probabilities, the average for each spin lies between zero and  $\hbar/2$ . From the expressions for the probabilities, the components of the net average magnetization are

$$\begin{aligned}M_x &\propto \sin \theta \cos (\omega_0 t + \phi) \\M_y &\propto \sin \theta \sin (\omega_0 t + \phi) \\M_z &\propto \cos \theta\end{aligned}\tag{A.15}$$

With these three equations, we have arrived at our goal of relating the phenomenon of NMR to the quantum behavior of a spin in a magnetic field. These three equations for the average components of the spin describe a vector tipped at an angle  $\theta$  to the  $z$ -axis, with the transverse component in the  $x$ - $y$  plane precessing with an angular frequency  $\omega_0$ . In other words, we have reached a crucial connection between the quantum view and the classical view: the average behavior of many quantum spins is precisely described by a classical, precessing magnetization vector  $\mathbf{M}$ . The two numbers that specify the quantum state,  $\theta$  and  $\phi$ , translate into the angle between  $\mathbf{M}$  and the  $z$ -axis and the angle between the transverse component of  $\mathbf{M}$  and the  $x$ -axis at  $t = 0$ , respectively. The precession itself arises from the time-dependent phase of the quantum amplitudes for the spin up and spin down states, with the phase changing cyclically with an angular frequency that is proportional to the energy difference of the two states.

The result of this long argument is that, despite the quantum nature of spin interactions with a magnetic field, the average behavior of many spins is accurately described by classical physics concepts. Except for the existence of spin itself, which is indeed a quantum phenomenon, the behavior of the net magnetization from protons in water is purely classical. For this reason, classical reasoning is perfectly adequate for understanding most of the NMR physics associated with MRI. However, in spectroscopy studies, and virtually all applications of NMR in chemistry, the quantum nature of NMR is critical for understanding the experimental phenomena. The reason for this is that liquid water, with only a single proton resonance, is a very simple system. In more complex molecules, protons in different chemical forms will have different resonant frequencies (chemical shift effect), and often protons will interact with one another and other nuclei. In such cases, the quantum nature of spin is evident even in a macroscopic experiment involving averaging over many spins.

For example, in many molecules, the orientation of the spin at one location affects the magnetic field in the vicinity of another spin in the same molecule, an effect called  $J$ -coupling. In the interaction of the two spins, the first spin is either up or down and so causes the local field at the second spin to be shifted either up or down by a discrete amount. As a result, the resonant frequency is shifted up or down. Averaging over many spins, the NMR signal will sample some spins whose resonance was shifted up, and some whose resonance was shifted down in frequency. In the resulting NMR spectrum, the resonance line is split into two slightly shifted lines, a direct reflection of the fact that the first spin has only two possible states. In this example, the quantum nature of spin passes through to macroscopic measurements because the precession frequency of the second spin depends on its interaction with the state of one other spin, not with the average behavior of many spins.

In conclusion, quantum mechanics is the most complete and accurate description of how the physical world works that we have, and yet the description of observable phenomena is

often rather subtle and counterintuitive. One of the most profound implications of quantum mechanics is that a physical system can exist in a kind of mixture of two states, a phenomenon called *superposition*. We encountered this phenomenon in our simple example of a spin in a magnetic field, where the spin can be in a state that is neither purely a spin up nor a spin down state, despite the fact that a measurement of the spin orientation will yield either spin up or spin down. In this case, we describe the spin state as a mixture of the spin up and spin down states, with associated amplitudes that give the probabilities for the measured orientation to be up or down. Superposition brings an intrinsic indeterminacy into the description of the world, and this is the source of the uncertainty principles of quantum mechanics. In our spin example, this uncertainty principle takes the form that, if the spin state is definite along one axis (e.g., spin up along  $z$ ), it is indefinite along all other axes. For these other axes, only probabilities can be given for what a measurement of the spin will yield. There are classical examples of physical systems, such as a compound pendulum, whose state can be described as a mixture of two more fundamental normal modes. But in a classical mixed system, any measured quantity will be found to be between the two values associated with the normal modes, not one or the other. The phenomenon of superposition has no analog in classical physics. Fortunately, for understanding MRI, we can visualize the NMR phenomenon as a classical precessing magnetization vector, and virtually all the mathematical reasoning that goes into the design of imaging pulse sequences is based on this classical view.

## Reference

Feynman RP, Leighton RB, Sands M (1965) *The Feynman Lectures on Physics*. New York: Addison-Wesley.

# Index

---

Locators for headings with subheadings refer to general aspects of that topic

Locators in **bold** refer to major entries

Locators in *italics* refer to figures/tables

- a-posteriori probability **388**
- absolute signal changes **360**
- acetazolamide 45, 404
- acetylcholine 47
- acronyms 165, 207
- action potential 8, 11; *see also*
  - spiking
- activation
  - maps **113, 376**
  - studies 25, **332**
- activity, imaging *see*
  - functional activity
  - imaging; *see also* **BOLD**
  - fMRI; fMRI
- ADC (apparent diffusion coefficient) map 178, 183–184
- adenosine; *see also*
  - thermodynamics:
    - neuronal signaling
  - diphosphate 14–15, 17, 58–59
  - monophosphate 14
  - triphosphate **14, 16, 44, 47, 403**
  - as vasoactive agent **45**
- adiabatic
  - inversion **313–314**
  - radiofrequency pulses **138, 139**
- ADP (adenosine diphosphate) 14–15, 17, 58–59; *see also*
  - thermodynamics:
    - neuronal signaling
- $A_{\text{eff}}$  (calibration factor) 310, 320, 327, 327
- agent recirculation, bolus tracking **298**
- AIF (arterial input function) 300, 312, **330**
- air–tissue interfaces 82, 98, 98
  - BOLD** effect **359**
  - distortion, magnetic field 99, **144, 144**
  - gradient echo signal 160
  - $T_2$  effects on image quality 263
- alcohol, BOLD response
  - interpretation 405
- aliasing 220, 271–273
- Alzheimer’s disease 47, 335, 418
- AMP (adenosine monophosphate) 14
- amplitude, estimating **384**
- amplitude modulated pulses 331
- analysis of variance (ANOVA) 377
- analytical chemistry **68**
- angiogram, brain vascular system 35
- angiography, magnetic resonance 95, 96, 97, 101, 103
- angular momentum 71, 72, 122, 131, 432–433; *see also* spin
- anisotropic diffusion 174, 180, 184, **184, 185, 186, 187**
- ANOVA (analysis of variance) 377
- anxiety and imaging 355, 357, 418
- APOE4* gene 419
- apparent diffusion coefficient map 178, 183–184
- arachidonic acid **46**
- arterial spin labeling (ASL) 53, 103–104, 282, **307**
  - activation studies **332**
  - adiabatic radiofrequency pulses **139**
  - advantages 407
  - amplitude modulated pulses 331
  - arterial bolus **318, 319**
  - arterial input function **330**
  - background suppression 331
  - basic ASL experiment **308, 309, 311**
  - BOLD** effect 308, 412; *see also*
    - calibrated-BOLD method
  - calibration factor 310, 320, 327, 327
  - CBF **307, 328, 404**
  - CBF/BOLD simultaneous measurement **333, 334**
  - continuous *see* continuous ASL (CASL)
  - disease 418–419
  - equations 309, 311, 312, 313, 325
  - functional activity imaging **107, 108, 110**
  - GRASE fast imaging 332
  - labeling coils 331
  - limitations 308
  - modeling **311, 320**
  - physiological noise corrections 331
  - and positron emission photometry 309
  - post-stimulus undershoot 407, 413
  - pseudo-continuous 332
  - pulsed *see* pulsed ASL (PASL)
  - QUIPSS 324, 324
  - recent innovations 330–332
  - relaxation effects 323, 326, 327
  - systematic errors 311, 320, 320, 321
  - tagged water in arteries **329**
  - transit delay effects 322, 323, 324, 324
  - vascular territory imaging 332
  - velocity sensitive imaging 332

- arteries/arterial; *see also*  
arterioles; capillaries;  
vascular system; veins  
blood delivery, measuring  
36, 38  
bolus 318, 319  
input function (AIF) 300,  
312, 330  
oxygen content 6  
pulsation, distortion effects 4,  
180, 270, 271, 272  
arterioles 39–40, 41  
arteriovenous malformation 303  
artifacts; *see also* distortion;  
Gibbs artifact; noise;  
ringing artifact; truncation  
artifact  
echo planar imaging  
261, 261  
Fourier imaging 212–213  
motion 4, 270, 272,  
274–275, 362  
ASE (asymmetric spin echo)  
pulse sequences 83,  
114, 235–236, 264,  
354, 407  
ASL *see* arterial spin labeling  
aspartate shuttle 20  
astrocytes  
blood flow control 43, 45,  
46, 48  
energy metabolism 7, 11, 13,  
16, 20, 27  
signaling 49  
asymmetric spin echo (ASE)  
pulse sequences 83,  
114, 235–236, 264,  
354, 407  
atoms  
hydrogen 65, 67, 71  
nucleus 125, 125–126  
ATP (adenosine triphosphate)  
14, 16, 44, 47, 403; *see also*  
thermodynamics: neural  
signaling  
attenuation 75, 136,  
195, 196  
curves 348, 349, 349,  
351–352, 352; *see also*  
diffusion  
decay time 234  
factor 178–179  
rates 109  
auditory noise 249  
autoradiography 23  
autoregulation 39  
axis of spin 71  
axons 8  
background suppression 331  
balloon model 414  
bandwidth 254  
basal ganglia 405–406  
battery analogy 28, 31, 59  
bicarbonate ions 404  
bicycle wheel analogy 72, 131  
biexponential diffusion  
attenuation curves 181,  
181, 182, 183, 194  
biological batteries 28,  
31, 59  
biological systems  
and diffusion 180  
and free energy 28, 29  
biophysical basis of BOLD  
effect 342, 342, 346  
bipolar gradient pulse 100,  
101–102  
BOLD effect 353  
diffusion imaging 175,  
178, 179  
diffusion tensor trace  
measurement 190, 191  
blipped gradient 267  
blips 246, 266  
blobs 35  
Bloch, Felix 67, 68  
Bloch equations 133, 133  
block-related experimental  
design 389, 390, 392–393,  
397, 398  
blood; *see also* brain blood  
supply  
delivery, measuring  
36, 38  
flow *see* cerebral blood  
flow  
oxygenation level dependent  
effect *see* BOLD  
tagging 103–104, 108, 329;  
*see also* arterial spin  
labeling  
velocity 37, 101  
vessels *see* arteries;  
capillaries; vascular  
system; veins  
blood–brain barrier 45, 282  
volume *see* cerebral blood  
volume  
blurring, image 229; *see also*  
artifacts; distortion  
burst imaging 245  
mapping the MR signal  
223, 226  
 $T_2$  effects on image quality  
263, 265  
BOLD (blood oxygenation level  
dependent) effect 7; *see*  
*also* BOLD experiment  
design/analysis; BOLD  
fMRI; BOLD response  
interpretation; BOLD  
weighting; calibrated-  
BOLD method  
activation maps 113, 376  
arterial spin labeling 308,  
333, 334, 412  
asymmetric spin echo  
pulse sequences  
235–236  
biophysical basis 342,  
342, 346  
CBF 54  
CBF/CBV relationship  
41–42  
CBF/CMRO<sub>2</sub> coupling  
347, 358  
and CMRO<sub>2</sub> 37  
contrast agents 107  
deoxyhemoglobin effects on  
MR signal 103  
diffusion effects 349, 350,  
350, 351, 352  
discovery 341  
distortion, magnetic  
field 145  
electromagnetic fields 122  
field distortions around  
magnetized cylinder 344,  
348, 348, 349  
gradient echo effect 160, 343,  
344, 354  
image acquisition  
parameters 359, 361  
image distortions 363  
intravascular contribution to  
signal 352–353, 352  
limitations 104, 107,  
281–282, 307–308, 359

- BOLD (blood oxygenation level dependent) effect (cont.)  
 magnetic field dependence 358, 361  
 magnetic susceptibility effects 342, 344, 344  
 measurement parameters 344, 352, 355  
 modeling 344  
 motion artifacts 4, 272, 274–275, 362  
 motional narrowing 200  
 MR signal changes related to agent concentration 297  
 oxygen extraction fraction 54, 55  
 physiological basis 342, 355  
 physiological changes 355  
 as signaling effect 42, 43  
 single-shot echo planar imaging 93  
 spin echo pulse sequences 83  
 spin echo-BOLD effect 351, 353
- BOLD experiment design/  
 analysis 389; *see also* BOLD fMRI; general linear model; model response function; statistical data analysis
- block/event-related designs 389, 392–393, 395, 397, 398
- detection and estimation sensitivity 392, 397
- detection power for known hemodynamic response 391, 392, 394
- detecting unknown hemodynamic response 396
- estimating model response function amplitudes/  
 variance 384
- estimating unknown hemodynamic response 384, 392, 394
- hemodynamic response 372, 373–374, 373, 377, 377, 388–389, 390–391
- BOLD fMRI 110; *see also* BOLD experiment design/  
 analysis  
 deoxyhemoglobin content 110  
 Gibbs artifact 231  
 mapping brain activation 101, 111, 112  
 statistical data analysis 101, 112–113, 112
- BOLD response interpretation 400  
 basic BOLD measurement 401, 401  
 BOLD dynamics, time scales 411  
 CBF/CMRO<sub>2</sub> coupling 405  
 disease 418  
 initial dip 401, 412, 416  
 linearity/non-linearity 387, 402, 409, 415  
 location of signal changes 406, 407  
 neural activity and BOLD effect 408  
 physiological baseline effects 403  
 post-stimulus undershoot 344, 401, 407, 412, 413, 413, 417  
 resting state networks 410  
 transient patterns 407, 412, 413, 416  
 understanding BOLD response 402, 402  
 variability of BOLD response 403
- BOLD weighting 333, 406, 407
- bolus, creating arterial 318, 319
- bolus tracking 53, 282–283, 296, 296; *see also* contrast/contrast agents  
 agent recirculation 298  
 CBF estimation 295, 300  
 CBV measurement 289, 298  
 contrast agents 238, 240  
 equations 297, 298  
 limitations 298  
 mean transit time 291, 299  
 MR signal changes related to agent concentration 297, 297
- bone, relaxation times 170  
 bone–tissue interfaces 82, 98, 98  
 BOLD effect 359  
 distortion, magnetic field 99, 144, 144  
 gradient echo signal 160  
 T<sub>2</sub> effects on image quality 263
- Bonferroni correction 372
- brain activation, and CBF 53; *see also* neural activity
- brain atlas 365
- brain blood supply 34; *see also* cerebral blood flow; cerebral blood volume  
 arterial blood delivery measure 36, 38  
 central volume principle 36, 37  
 tissue perfusion 36, 36  
 vascular system 34, 35
- brain hemorrhage 160; *see also* stroke
- brain tissue 178, 180, 181  
 diffusion mechanisms 180
- brain tumors 104, 105, 171, 282, 302, 341
- burst imaging 243, 244, 246
- caffeine 46, 355, 357, 405, 412
- calcium ions 9, 39, 43, 403; *see also* battery analogy
- calcium-activated K<sup>+</sup> channels 44
- calibrated-BOLD method 347, 357, 358  
 arterial spin labeling techniques 334  
 BOLD effect 347, 357, 358  
 BOLD response interpretation 404  
 calibration studies 343, 344  
 CBF/CMRO<sub>2</sub> coupling 358, 405  
 calibration factor ( $A_{\text{eff}}$ ) 310, 320, 327, 327



- capillaries 37, 40; *see also*  
arteries; arterioles;  
vascular system; veins  
bed 334  
diffusion 197  
plasma oxygen levels 56,  
57, 58
- carbon dioxide  
BOLD effect 357, 404  
diffusion 285  
inhalation (hypercapnia)  
335, 347, 357, 412, 413  
transport 23, 55  
as vasoactive agent 44
- carbonic anhydrase 44, 404
- cardiac motion (heart  
beat) 271, 274,  
369–370, 411
- CASL *see* continuous ASL
- cat studies 111, 414–415, 416
- cation hypothesis 45
- CBF *see* cerebral blood flow
- CBV *see* cerebral blood  
volume
- CE-FAST 165
- cell membranes 177, 182
- cellular work 28
- central volume principle  
(CVP) 36, 288,  
289, 290
- cerebral blood flow (CBF) 6, 34,  
101; *see also* brain blood  
supply  
absolute calibration  
311, 328  
arterial spin labeling 110,  
307, 328, 404  
arterioles 39–40, 41  
BOLD effect 353, 355, 358  
BOLD response  
interpretation 402, 404,  
409–410  
brain activation 53  
calibrated-BOLD method  
335, 344, 357  
capillary plasma oxygen  
levels 56, 57, 58  
and cerebral blood volume/  
velocity 37, 40, 101  
contrast agent techniques  
289, 294, 295  
control *see* cerebral blood  
flow control
- definition 36  
and disease 308  
energy metabolism 6  
function of large changes in  
43, 55  
and glucose metabolism 19,  
23, 53  
gray/white matter  
comparison 6  
hypercapnia experiment 412  
measurement *see* cerebral  
blood flow measurement  
neurovascular unit 43  
nitric oxide 39, 42,  
44, 46  
noise 407, 415  
and oxygen metabolism  
25, 26, 54, 55, 111, 358  
oxygen transport to tissue  
55, 56  
post-stimulus undershoot  
413  
tissue perfusion 36, 36  
tracers, diffusible/  
intravascular 50, 51  
transient patterns 412  
vascular system 34, 35, 45  
vasoactive agents 44,  
45, 46
- cerebral blood flow control  
cerebrovascular resistance 39  
mediation agents 42  
and neural activity 42  
neural pathways 47  
neurovascular unit 48  
research foundations 42  
smooth muscle relaxation 43  
vasoactive agents 44
- cerebral blood flow  
measurement 49; *see also*  
arterial spin labeling  
arterial blood delivery  
measure 36, 38  
BOLD effect 355  
contrast agents 282, 287, 291,  
295, 302  
estimation, bolus tracking  
295, 300  
measurement tank analogy  
49, 50  
microsphere technique 49,  
309–310, 311, 329  
MRI technique 53, 103
- nitrous oxide technique  
49, 50
- positron emission  
photometry technique  
52, 288
- radioactive xenon technique  
51, 52
- systematic errors 311, 320,  
320, 321
- cerebral blood volume (CBV) 6  
BOLD effect 41–42, 349, 349,  
353, 355  
BOLD response  
interpretation 402, 404,  
409–410  
and CBF/velocity 37,  
40, 101  
contrast agents 282, 287,  
289, 291, 294, 295,  
295, 302  
during activation 40  
energy metabolism 6  
equations 41  
measurement, bolus tracking  
289, 298  
measurement, PET  
technique 293  
transient patterns 412
- cerebral metabolic rate of  
glucose (CMRGlc) *see*  
glucose metabolism
- cerebral metabolic rate of  
oxygen (CMRO<sub>2</sub>) *see*  
oxygen metabolism
- cerebral neoplasm 303
- cerebrospinal fluid (CSF) 6  
BOLD effect 361–362  
contrast, image 154–156,  
154, 155  
gradient echo signal 162  
motion artifacts 270, 275  
T<sub>2</sub> effects on image  
quality 265
- cGMP (cyclic guanine  
monophosphate) 44
- CHARMED (composite  
hindered and restricted  
model of diffusion) 196
- chelating agents 170
- chemical shift effects 160, 161,  
266–267, 438
- chemiosmotic hypothesis 21
- chemistry 68, 438

- child on a swing analogy 75  
 chloride ion channel 9, 12  
 circularly polarized oscillating field 135  
 classical diffusion coefficient 176  
 classical physics 121–122, 425, 425, 429–430, 431–432, 433–434, 436, 439  
   quantum-classical connection 438  
 clinical applications, contrast agent techniques 303  
 clustering algorithms 260, 275  
 CMRGlC *see* glucose metabolism  
 CMRO<sub>2</sub> *see* oxygen metabolism  
 CNR (contrast to noise ratio) 78, 154, 155  
 coffee cup analogy 132  
 coincidence detections 24  
 compartmental modeling 290–291  
 compensation pulse 213  
 complex numbers 211  
 composite hindered and restricted model of diffusion (CHARMED) 196  
 computed tomography (CT) 69, 90, 183, 216, 243  
 connectivity studies, functional 410  
 continuous ASL (CASL) 310, 313, 314; *see also* arterial spin labeling  
   arterial bolus, creating well-defined 318, 319  
   CBF, absolute calibration 311, 328–329  
   CBF measurement, systematic errors 320–322, 320, 321  
   labeling coils 331  
   modeling 311, 320  
   off-resonance effects 315  
   relaxation effects 323, 326, 327  
   tagged water in arteries 329  
 techniques 310, 313, 314, 318, 319, 320–322  
 transit delay effects, controlling for 322, 323  
 contour maps 385, 387  
 contrast/contrast agents 99, 99, 302; *see also* bolus tracking; gadolinium-DTPA; relaxation;  $T_1/T_2$ -weighted images  
 BOLD effect 107  
 clinical applications 303  
 dysprosium 302  
 fMRI – diffusion effects 197  
 foundations of research 282  
 imaging functional activity 104  
 gradient echo pulse sequences 238  
 imaging functional activity 107  
 intravascular 102, 413, 414  
 measuring CBF/CBV 282, 287, 291, 295, 302  
 motion artifacts 274  
 multiple injection 414  
 NMR 67–69, 70, 78  
 perfusion imaging 281 and relaxation 104, 150, 153, 170  
 residue function 288, 289, 291, 292, 292  
 signal drop 105  
 superparamagnetic iron oxide 302–303  
 time–activity curves 283–284  
 tissue concentration–time curve 288, 289, 291, 293  
 tissue concentration–time curve interpretation 285, 286  
 tissue concentration–time curve sensitivity 289, 294, 295  
 tracer kinetics 283, 283, 289  
 volume of distribution/partition coefficient 284  
 contrast to noise ratio (CNR) 78, 154, 155  
 control images 108–109, 308, 314–315  
 control-tag signal 314, 318, 333  
 convolution *see* smoothing function  
 convolution theorem 224  
 correlation  
   analysis 113, 372  
   coefficients 112  
   times 168, 169, 169  
 cortical spreading depression (CSD) 47, 183  
 coupling 358  
 covariance matrix 395, 396  
 COX (cyclooxygenase) 47  
 CSF *see* cerebrospinal fluid  
 CT (computed tomography) 69, 90, 183, 216, 243  
 CVP (central volume principle) 36, 288, 289, 290  
 CVR (cerebrovascular resistance) 39–40  
 cyclic guanine monophosphate (cGMP) 44  
 cyclooxygenase (COX) 47  
 cytochrome oxidase 21, 35  
 cytotoxic edema 183  
 data acquisition time (TE) 236, 364; *see also*  $T_1/T_2$ -weighted images  
 Davis model 344, 346, 347, 355, 357  
 DCE (dynamic contrast enhanced) imaging 53  
 decay *see* attenuation  
 default mode networks 411  
 definitions  
   block-related experimental design 390  
   cerebral blood flow 36  
   image noise 252  
   magnetic susceptibility 142  
   precession 72  
   resolution 226  
   voxel volume 253  
 degrees of freedom 380  
 delay inversion time 108  
 delayed compliance model 414  
 ‘delicate motion’ 65, 67  
 delivery function 311  
 dendrites 8  
 density of magnetization 226–227  
 density-weighted imaging 183, 253  
 deoxyglucose (DG) technique 23

- deoxyhemoglobin/hemoglobin  
41–42, 57, 103, 171, 342,  
345–346; *see also* BOLD  
effect
- BOLD fMRI **110**
- BOLD response  
interpretation 404–405
- calibrated-BOLD method 334
- diffusion process 174
- effects on MR signal  
**102, 197**
- initial dip 416, 417
- magnetic susceptibility  
effects 342, 344, 344
- post-stimulus undershoot 413
- transient patterns 412
- diamagnetism **140, 141**
- Diamox *see* acetazolamide
- diffusible tracers **50, 51**
- diffusion **173, 197, 198**  
biexponential attenuation  
curves 181, 181, 182,  
183, 194
- biological systems **180**
- BOLD effect 349, 350, 350,  
351, 352
- display of images 178
- effects 171, 196
- fiber tract mapping 174,  
184, 192
- Fick's law 176
- field perturbations, fMRI  
176, 196, 197
- imaging 173, 174, 178,  
179, 179
- initial dip 417
- linear field gradients 175,  
176, 178, 179
- location of BOLD signal  
changes 407
- motional narrowing 198, 198
- multicompartment 178, 180,  
181, 194
- nature of 174, 175, 176
- physics of 176, 178
- process 173, 174
- random walk model 176
- restricted 176, 181, 182
- time 179
- white matter connectivity  
estimation 192, 192
- diffusion spectrum imaging  
(DSI) 176, 177, 183
- diffusion tensor imaging (DTI)  
174, 184  
anisotropic diffusion 174,  
180, 184, 184, 185,  
186, 187  
mathematics of 187, 188, 190  
model 193  
model extensions 194, 194,  
195, 196  
model limitations 193, 194  
trace 185, 186, 189, 189, 191
- diffusion-weighted imaging  
(DWI) 97, 101, 353
- diffusional kurtosis imaging 183
- dipole field 125
- disease  
arterial spin labeling  
applications 333  
BOLD effect 355, 357  
BOLD response  
interpretation 404,  
405, 418  
calibrated-BOLD method 335  
and CBF 308
- display of images 178
- distortion 98, 99, 121, 124,  
124; *see also* air–tissue  
interfaces; artifacts;  
bone–tissue interfaces;  
noise
- around magnetized cylinder  
344, 348, 348, 349
- arterial pulsation 4, 180, 270,  
271, 272
- BOLD effect 145, 342, 344,  
344, 363
- echo planar imaging 261, 261  
equation 268
- ferromagnetic materials 142
- Fourier imaging 212–213  
and geometric shape 143, 144
- ghosts 261, 261
- magnetic susceptibility  
effects 98, 99, 142
- microscopic 145
- off-resonance effects 254,  
264, 265, 267, 269
- physics of magnetism/NMR  
99, 144, 144
- physiological noise 4,  
272, 273
- $T_2$  effects on image quality  
254, 261, 262, 264
- distribution of displacements 183
- domains 142
- dopamine 12
- downstream dilation 40
- drugs, effects on initial dip 418
- DSI (diffusion spectrum  
imaging) 176, 177, 183
- DTI *see* diffusion tensor  
imaging
- DTPA 170; *see also* gadolinium  
(Gd-DTPA)
- dual-echo spiral acquisitions 333
- duration, signal 103
- DWI (diffusion-weighted  
imaging) 97, 101,  
183, 353
- dynamic contrast enhanced  
(DCE) imaging 53
- dysprosium 106, 171, 302
- echo planar imaging (EPI) 92,  
93, 113; *see also* EPSTAR
- BOLD experiment design/  
analysis 369
- BOLD response  
interpretation 400
- bolus tracking 296
- field maps 363–364
- Gibbs artifact 231
- image distortions/artifacts  
261, 261
- initial dip 417
- mapping the MR signal 206,  
206
- motion artifacts 274
- MRI techniques 243,  
243, 247
- noise associated 244
- off-resonance effects  
266–267, 270
- signal drop 106
- $T_2$  effects on image quality 265
- echo-shifted (ES) pulse  
sequences 238, 239
- echo time (TE) 81, 148, 149, 232  
BOLD effect 360
- spin echo pulse sequence  
81, 206
- echoes, generalized 149, 156
- EEG (electroencephalography)  
12–13, 13, 419
- EETs (epoxyeicosatrienoic  
acids) 47

- eicosanoids 47  
 electric dipole fields 123  
 electric fields 123, 124  
 electroencephalography (EEG) 12–13, 13, 419  
 electromagnetic fields  
   BOLD effect 122  
   field concept 122  
   gradient/radiofrequency coils 128  
   induction/signal detection 125, 126  
   magnetic fields 123  
   physics of magnetism/NMR 121, 122, 124  
 electromagnetic induction 125, 126  
 electron transfer chains 18, 19, 20  
 electrons 71  
 electrophysiology measurements 12  
 end-feet 48  
 energy equilibration 73  
 energy metabolism 6, 11, 18, 19, 42, 403; *see also* free energy  
   astrocytes 7, 11, 13, 15, 16, 20, 27  
   ATP energy budget 14, 16  
   blood flow 5, 22  
   CBV/CBF 6  
   CMRGlC/CMRO<sub>2</sub> balance 26, 27–28  
   deoxyglucose technique 23  
   electron transfer chains 18, 19, 20  
   electrophysiology measurements 12  
 fMRI – functional basis 6, 7  
 glucose metabolism 22, 24, 27  
 glycolysis, cytosolic 18, 18, 20  
 lactate production/lactate shuttle 20, 27  
 membrane potential 8, 9, 9, 18  
 mitochondria 20, 27  
 Na<sup>+</sup>/K<sup>+</sup> pump 15, 27  
 neural activity 8, 14, 15  
 neural signaling 7, 8, 14  
 physiological variables 6, 6  
 positron emission photometry measurements 23, 25, 26  
 synaptic activity 10, 11, 27–28  
 thermodynamics perspective 8, 14, 18, 28  
 tricarboxylic acid (TCA) cycle 18, 20  
 entropy concept 28  
 EPI *see* echo planar imaging  
 EPiSTAR (echo planar imaging and signal targeting with alternating radiofrequency) 292, 315–318, 316, 317, 324, 330  
 epoxyeicosatrienoic acids (EETs) 47  
 EPSP (excitatory post-synaptic potential) 9, 12  
 equations  
   A<sub>eff</sub> 309  
   agent concentration, bolus tracking 297  
   anisotropic diffusion 185, 186, 187  
   arterial spin labeling 311, 312, 313  
   Bloch equations 133, 133  
   blood volume–flow relationship 41  
   BOLD effect 344, 345, 346, 347  
   BOLD experiment design/analysis 384, 385, 395  
   CBV measurement, bolus tracking 298  
   central volume principle 38  
   contrast 288, 289, 290, 291  
   decay time 234  
   diffusion 174, 176, 177, 188, 189  
   diffusion in linear field gradient 175  
   diffusion tensor model 193  
   diffusion tensor model extensions 195  
   diffusion tensor trace measurement 191  
   equilibrium magnetization 428  
   Fick's law 176  
 fMRI diffusion effects 198  
 Fourier transform 210, 211, 212  
 Gaussian distribution 168  
 general linear model 380, 381, 389  
 k-space mapping 218, 220  
 macroscopic measurements 438  
 magnetic dipole/external field interactions 426, 427  
 magnetic dipole/magnetic field interactions 426, 430  
 model response function 384, 385  
 MR signal 151  
 multicompartment diffusion 181  
 neural signaling 30  
 NMR 73, 86  
 off-resonance effects 268  
 photosynthesis 30  
 point spread function 224  
 precession 133, 133, 429  
 quantum mechanics 434–435, 436  
 QUIPSS 325  
 random walk model 176  
 relaxation and contrast 151, 168  
 respiration 30  
 signal-to-noise-ratio 254  
 spatial noise correlations 259  
 thermodynamics of neuronal signaling 28  
 tissue concentration–time curve 288  
 tracer kinetics 289, 290, 291  
 equilibrium magnetization 73, 74, 427  
 equilibrium potential 9  
 Ernst, Richard 69  
 Ernst angle 151, 165  
 ES (echo-shifted) pulse sequences 238, 239  
 evenly spaced single trials 392–393, 392  
 event-related experimental designs 389, 390, 395, 398  
 event-related fMRI 381  
 excitation pulse 136  
 excitatory post-synaptic potential (EPSP) 9, 12

- external field interactions  
426, 427
- extracellular potentials 12, 13
- extrinsic innervation 47
- [<sup>18</sup>F]-flurodeoxyglucose (FDG) 24
- F* statistic 389, 397
- FA (fractional anisotropy)  
index 189
- facilitated diffusion 22
- FAIR (flow-sensitive alternating inversion recovery) 316–318, 317
- arterial input function 330
- modeling 311, 311
- FAST 165, 207
- fast exchange diffusion 181
- fast Fourier transform  
algorithm (FFT)  
222–223
- fast imaging techniques  
bolus tracking 296
- echo planar imaging  
243, 247
- FISP 165, 207, 236, 237
- GRASE 243, 332
- k-space sampling trajectories  
242, 242, 244
- MRI 92, 93, 242
- motion artifacts 274
- quiet imaging with burst techniques 244, 246
- safety issues 249
- fast low-angle shot *see* FLASH
- fast response *see* initial dip
- fast spin echo (FSE) 93, 242
- fat tissue 160, 161, 235, 265–266
- FDG ([<sup>18</sup>F]-flurodeoxyglucose) 24
- feed-back signal 403
- feed-forward systems 43, 403, 404
- ferromagnetism 140, 141
- fever 47
- FFT (fast Fourier transform algorithm) 222–223
- fiber tract mapping 174, 184, 192, 192
- Fick's law 176
- FID *see* free induction decay
- field concept 122
- field distortions *see* distortion
- field gradient pulses 232
- field gradients 175, 176, 178, 179, 232
- field lines 123
- field maps 363–364
- field of view *see* FOV
- filtering *k*-space 226–229, 228
- finger tapping task 112, 333, 369
- BOLD response interpretation 404–405, 406–407, 407
- post-stimulus undershoot 407, 413
- FISP (fast imaging with steady state precession) 165, 207, 236, 237
- FLASH (fast low-angle shot) 159, 165
- gradient echo (GRE) pulse sequences 236, 237
- motion artifacts 271, 273
- flip angles 80, 136
- BOLD effect 361
- burst imaging 245–246
- equations, MR signal 151, 152–153
- gradient echo signal 163, 165–166
- multiple echo pathways 158
- T*<sub>1</sub> -weighted images, control with 151, 162, 163
- flow-sensitive alternating inversion recovery *see* FAIR
- fluctuating fields 166, 173
- flux 126–127
- fMRI (functional magnetic resonance imaging) 65, 69; *see also* arterial spin labeling; BOLD fMRI; bolus tracking; contrast; nuclear magnetic resonance; perfusion
- arterial spin labeling applications 332
- diffusion effects 176, 196, 197
- energy metabolism 6, 7
- event-related 381
- research foundations 282
- mapping resting state networks 410
- signal-to-noise ratio, image 252
- Fourier analysis 373, 373
- Fourier imaging 92, 209
- phase encoding 214, 214
- pulse sequence diagram 215, 215
- as snapshot of transverse magnetization 212, 213
- Fourier transform (FT) 183, 232; *see also* *k*-space
- BOLD effect 348, 350
- BOLD experiment design/analysis 374
- convolution theorem 224
- MRI 85, 90, 91, 92
- mapping the MR signal 207, 211, 211
- motion artifacts 4, 272, 273
- noise distribution 256
- physics of diffusion 178
- properties 229
- FOV (field of view) 9.45, 206, 220, 221, 224
- echo planar imaging 248
- signal-to-noise ratio, image 254, 255
- spatial smoothing 260
- fractional anisotropy (FA)  
index 189
- free energy 14, 27
- and biological systems 28, 29
- change 28
- and neuronal signaling 30
- free induction decay (FID)  
pulse sequence 86, 88, 136, 208
- gradient echo pulse sequences 236–238, 236
- multiple echo pathways 159
- NMR 75, 75, 76
- spin echoes 148
- steady-state free precession 163
- freely diffusable agents 284
- frequency domains 374
- frequency encoding 88, 88, 90, 90, 210
- FSE (fast spin echo) 93, 242
- FT *see* Fourier transform

- functional activity, imaging  
**101, 104**; *see also* BOLD  
 fMRI; fMRI  
 arterial spin labeling **107**,  
**107, 108, 110**  
 blood velocity effects on MR  
 signal **101**  
 CBF measurement with  
 MRI **103**  
 contrast agent methods **102**,  
**104, 107**  
 deoxyhemoglobin effects **102**  
 relaxation times **104**  
 signal drop **105, 106**
- functional magnetic resonance  
 imaging; *see also* BOLD  
 fMRI *see* fMRI
- fundamental particles **432**
- G-protein-coupled receptors **11**
- GABA (gamma-aminobutyric  
 acid) **11, 12**
- gadolinium-DTPA **99, 99, 132**,  
**170**; *see also* bolus  
 tracking; contrast  
 agent recirculation **298**  
 brain activation  
 measuring **107**  
 diffusion process **174**  
 distortion, magnetic field **145**  
 foundations of research  
**282–283**
- functional activity imaging  
**102, 103, 104**  
 limitations **302**  
 magnetic susceptibility  
 effects **343**  
 mean transit time  
**291, 299**  
 relaxation/susceptibility  
 effects **104, 171**  
 signal drop **105, 106**  
 susceptibility effects **302**  
 tissue concentration–time  
 curve sensitivity **294**  
 volume of distribution/  
 partition coefficient **285**
- gamma-aminobutyric acid  
 (GABA) **11, 12**
- Gauss units **219**
- Gaussian distribution  
 diffusion imaging **175**,  
**182–183**
- diffusion tensor model  
**193, 196**  
 equation **168**  
 noise distribution **256–257**  
 spatial smoothing **257–258**
- Gaussian smoothing **229**,  
**260–261**
- Gd-DTPA *see* gadolinium-  
 DTPA
- GE *see* gradient echo
- general linear model **368, 373**,  
**376, 395, 398**  
 equations **380, 381**  
 event-related fMRI **381**  
 fitting data with known  
 model response **378, 378**  
 hemodynamic response **377**,  
**377, 381, 388–389**,  
**390–391**  
 removal of baseline trends  
**381**  
 statistical significance **378**,  
**380, 388**  
 two model functions **381**,  
**382, 383, 384**  
 two types of stimulus **381**  
 variance of parameter  
 estimates **383, 384, 385**,  
**386, 387**
- geometric analysis **378, 383**  
 BOLD experiments **368, 379**,  
**381, 382, 396**  
 and distortion **143, 144**
- ghosts; *see also* artifacts;  
 distortion  
 EPI **261, 261**  
 motion artifacts **4, 271**,  
**272–273, 272**
- Gibbs artifact **229, 229**,  
**230, 255**
- Gibbs free energy **28**
- glial cells **48**; *see also* astrocytes
- global scaling factors **298**
- glucose metabolism **18, 19**,  
**23, 53**  
 and CBF **22, 53**  
 deoxyglucose technique **23**  
 equation **22**  
 function of large  
 changes in **27**  
 and functional activity **24**
- grey/white matter  
 comparison **25**
- and neural activity **42**  
 and oxygen metabolism  
 balance **6, 26, 27–28**,  
**54, 55**  
 positron emission  
 photometry  
 measurements **23, 25**
- glutamate **11, 12, 27**
- glycolysis **18, 20**
- gradient coils **128, 128**
- gradient echo (GE) imaging  
**98, 233**  
 BOLD effect **160, 341, 343**,  
**344, 354**  
 BOLD fMRI **111**  
 diffusion process **174**  
 Fourier imaging **213, 213**  
 mapping the MR signal  
**208, 209**  
 MRI **86, 87, 97, 98**  
 terminological issues **160**
- gradient echo pulse sequence  
**86, 88, 92, 263**  
 acronyms **165**  
 CBV measurement **289, 298**  
 diffusion imaging **178**,  
**179, 180**  
 location of BOLD signal  
 changes **406, 407**  
 MR signal changes **297**  
 MRI techniques **236, 236**  
 off-resonance effects **268**,  
**269–270**  
 varieties **151, 163, 165**
- gradient echo signal **102**  
 chemical shift effects  
**160, 161**  
 relaxation and contrast **159**,  
**159, 161, 166**  
 steady-state free precession  
**163, 164**  
 $T_1$ -weighted images **151**,  
**162, 163**  
 $T_2$  effects **160, 161**
- gradient fields **129, 207, 209**
- gradient pulse **86, 233, 234**
- gradient recalled echo (GRE)  
 imaging **114, 160**
- gradient recalled echo (GRE)  
 pulse sequences  
 diffusion imaging **179**  
 fMRI – diffusion effects  
**197–198**

- mapping the MR signal 208–209  
 motional narrowing 198, 198  
 NMR 79, 79  
 gradient recalled echo (GRE)  
 signal 208  
 gradient spoiling 164  
 gradient strength 248  
 gradient switching 243, 247  
 gradient waveform 248  
 GRASE (gradient and spin echo) 243, 332  
 GRASS (gradient recalled acquisition in the steady state) 165, 207, 236, 237  
 gravitational fields 122–123  
 gray matter (GM) 361–362, 417; *see also* white/gray matter comparison  
 GRE *see* gradient recalled echo  
 guanosine triphosphate (GTP) 11  
 gyromagnetic ratio 131, 219, 429  
 half-NEX/half-Fourier acquisition 241–242; *see also* HASTE  
 HARDI (high angular resolution diffusion imaging) model 195–196  
 HASTE (half-Fourier acquisition with single-shot turbo spin echo) 93, 242  
 head  
 distortions 98, 99, 144, 144; *see also* air–tissue interfaces, bone–tissue interfaces  
 movements 270, 274, 362; *see also* motion artifacts  
 heart beat 271, 274, 369–370, 411  
 heat 30; *see also* thermodynamics perspective  
 deposition 162, 249  
 removal 23  
 Helmholtz pair 128, 129  
 hematocrit 57, 415  
 hemodynamic response 372, 373–374, 377, 377, 388–389, 390–391  
 detection of known 391, 392, 394  
 detection of unknown 396  
 estimation of unknown 384, 392, 394  
 fMRI experimental design 391, 392, 394  
 neural activity 415  
 hemoglobin *see* deoxyhemoglobin/hemoglobin  
 hemorrhage, brain 160; *see also* stroke  
 hexokinase 18  
 high angular resolution diffusion imaging (HARDI) model 195–196  
 histamine 12  
 hydrogen atoms 65, 67, 71  
 hydrogen ion gradient 21  
 hypercapnia experiment 335, 347, 357, 412, 413  
 hyperoxia 357; *see also* hypoxia  
 hypoglycemia 54  
 hypothalamus 17  
 hypoxia 20, 37, 57, 58; *see also* ischemia; stroke  
 image properties; *see also* artifacts; blurring; contrast; distortion; FOV; noise; point spread function; resolution  
 acquisition parameters, BOLD effect 359, 361  
 display 178  
 Gaussian smoothing 229  
 Gibbs artifact 229, 229, 230  
 pixels/voxels 222, 223  
 resolution 220, 221, 222, 226, 226, 228  
 as snapshot assumption 232–233, 263  
 impulse response 288  
 induction 75, 125, 126, 136  
 infarction 303  
 inflammation 47  
 inflow effect 96  
 inhibitory post-synaptic potential (IPSP) 9, 12  
 inhomogeneity effects 80, 82, 95, 233; *see also* air–tissue interfaces; bone–tissue interfaces  
 asymmetric spin echo pulse sequences 234–235  
 BOLD effect 363–364  
 contrast agents 171  
 echo planar imaging 272  
 Fourier imaging 212  
 MR signal changes related to agent concentration 297  
 off-resonance effects 267, 268–269  
 spin echoes 148–149  
 initial dip 401, 412, 416  
 interneurons 11, 48  
 intravascular  
 contrast agents 102, 413, 414  
 contribution to signal, BOLD effect 352–353, 352  
 tracers 50, 51  
 intravoxel incoherent motion (IVIM) effect 101–102, 104, 180  
 intrinsic innervation 47  
 intrinsic transverse magnetization 212, 213  
 inverse problem 14  
 inversion plane 314  
 inversion recovery (IR)  
 curve 241  
 inversion recovery (IR)  
 pulse sequence 83, 83, 151–152  
 inversion time 83  
 inward-rectifier K<sup>+</sup> channels 44  
 ion channels 9–10, 12  
 ionotropic receptors 11  
 IPSP (inhibitory post-synaptic potential) 9, 12  
 IR *see* inversion recovery  
 iron 171  
 iron oxide 302–303  
 ischemia 295, 300, 303, 307, 342, 348; *see also* hypoxia; stroke  
 isotropic diffusion 193; *see also* anisotropic diffusion  
 IVIM (intravoxel incoherent motion) effect 101–102, 104, 180

- James, William 3, 6
- k*-space 207, 210, 211, 221, 224–225, 232; *see also* Fourier transform
- fast imaging techniques 242, 242, 244
- filtering 226–229, 228
- image distortions/artifacts 261–262
- mapping the MR signal 216, 216, 217, 218
- motion artifacts 271
- MRI techniques 91, 92, 93, 241
- noise distribution 255–256, 260
- off-resonance effects 266, 267
- trajectory 247
- volume imaging 225, 240
- k*-transform 209, 210, 211, 221, 224–225
- kinetic limitations 58
- kinetic model 289, 311
- Kolmogorov–Smirnov (KS) test 374
- labeling coils 331
- lactate dehydrogenase 20
- lactate production/lactate shuttle 20, 27
- Larmor frequency 72, 131, 137, 137, 169–170, 429, 436
- laser Doppler flowmetry (LDF) 38
- Lauterbur, Paul 69
- laws of thermodynamics 28, 29
- lesions 170
- LFPs (local field potentials) 12, 408–409
- life sciences *see* biological systems
- linear field gradients 175, 176, 178
- linear regression analysis 372
- local field potentials (LFPs) 12, 408–409
- locus coeruleus 47
- longitudinal components 78
- longitudinal relaxation times 78, 132, 168, 169, 359
- low-bandwidth sequences 254
- macroscopic measurements 430, 432, 437
- magnetic dipole /external field interactions 426, 427
- field 125, 125–126, 126 /magnetic field interactions 98, 125–126, 130, 130, 425–426, 436
- moment 72
- magnetic fields 123, 124, 126
- dependence, BOLD effect 358, 361
- distortion *see* distortion
- gradients 86, 207
- /magnetic dipole interactions 98, 125–126, 130, 130, 425–426, 436
- magnetic flux 126–127
- magnetic moments 430–433, 430, 433
- magnetic properties of matter 140, 141, 145; *see also* distortion; magnetic susceptibility
- magnetic resonance angiography 95, 96, 97, 101, 103
- magnetic resonance imaging *see* MRI
- magnetic susceptibility 141, 142, 144
- BOLD effect 342, 344, 344, 359
- definition 142
- gadolinium-DTPA 171, 282–283, 302
- MRI 98, 98, 99
- off-resonance effects 267, 268, 269
- physics of magnetism/NMR 141, 142, 144
- $T_2$  effects on image quality 263
- magnetism 121
- adiabatic radiofrequency pulses 138, 139
- Bloch equations 133
- distortion, magnetic field 98, 99, 144, 144
- electromagnetic fields 122, 124, 125–126
- equations, precession/relaxation 133, 133
- field concept 122
- gradient/radiofrequency coils 128, 128
- induction 125, 126, 136
- magnetic dipole/magnetic field interactions 130, 130
- magnetic fields 123, 124, 126
- magnetic properties of matter 140
- magnetic susceptibility effects 141, 142, 144
- nuclear magnetization dynamics 130
- paramagnetism/diamagnetism/ferromagnetism 140, 141
- precession 121, 131, 133, 133
- radiofrequency excitation 134
- relaxation 121, 131, 133
- signal detection 125, 126, 129–130
- slice selection 136, 137
- magnetization density 226–227
- magnetization prepared rapid gradient echo (MP-RAGE) 94, 95, 206, 220, 240–241
- magnetization relaxation function 311
- magnetoencephalography (MEG) 13, 13, 419
- magnitude images 256, 267
- malate–aspartate shuttle 20
- Mansfield, Peter 69
- maps/mapping; *see also* MR signal mapping
- BOLD activation 113, 376
- contour 385, 387
- field distributions 363–364
- resting state networks 410
- matter, magnetic properties 140, 141; *see also* distortion; magnetic susceptibility
- maximum intensity projection (MIP) 96
- Maxwell pair 128–129, 128
- mean transit time (MTT) 291, 299



- medication and BOLD effect 355, 357
- medicine, new tool for 69
- MEG (magneto-encephalography) 13, 13, 419
- membrane potential 8, 9, 9, 18
- metabotropic receptors 11
- microsphere blood flow measurement technique 49, 309–310, 311, 329
- migraine 47
- MION (intravascular contrast agents) 413, 414
- MIP (maximum intensity projection) 96
- mitochondria 20, 27, 57
- model response function 372, 373  
amplitudes/variance, estimating 384  
BOLD experiment design/analysis 378, 378; *see also* general linear model  
non-orthogonal model functions 386, 396, 397, 398
- modeling  
arterial spin labeling techniques 311, 320  
BOLD effect 344
- monopole field 123
- Monte Carlo simulations 345, 350
- motion artifacts 4, 270, 272, 274–275, 362; *see also* head movements; physiological noise
- motion sensitivity 95, 95
- motional narrowing 198, 198
- motor cortex 407, 410
- movements, head 270, 274, 362; *see also* motion artifacts
- MP-RAGE (magnetization prepared rapid gradient echo) 94, 95, 206, 220, 240–241
- MR signal changes, and contrast agent concentration 297, 297, 297
- MR signal mapping 70, 205, 206; *see also* Fourier imaging; Fourier transform; MRI; MRI techniques  
equations 210, 211, 212, 218, 220, 224  
Gibbs artifact 229, 229, 230  
gradient echoes 208, 209  
image field of view 206, 219, 220, 221, 224  
image resolution 220, 221, 222, 226  
*k*-space mapping 216, 216, 217, 218, 226, 228  
magnetic field gradients 207  
pixels/voxels/resolution elements 222, 223  
point spread function 210, 223, 225, 226, 228, 229  
slice selection 208, 215
- MRI (magnetic resonance imaging); *see also* diffusion; MR signal mapping; MRI techniques  
CBF measurement 53, 103  
diffusion-weighted imaging 97  
fast imaging 92, 93  
Fourier transform 85, 90, 91, 92  
frequency encoding 88, 88, 90, 90  
gradient echo 86, 87, 97  
historical development 68  
*k*-space 91, 92, 93  
localization 88, 88  
magnetic field gradients 86, 207  
magnetic susceptibility effects 98, 98, 99  
non-anatomical imaging 95  
phase encoding 88, 88, 90  
principles 85  
radiofrequency coil 85  
slice selection 88, 89, 89  
terminological issues 86, 88  
volume imaging 94
- MRI techniques 161, 232, 234, 235; *see also* MR signal mapping; MRI  
echo planar imaging 243, 243, 244, 247
- echo-shifted pulse sequences 238, 239
- equations 151, 234
- fast imaging techniques 242
- gradient echo pulse sequences 236, 236
- k*-space sampling trajectories for fast imaging 242, 242, 244
- k*-space symmetry exploitation 241
- quiet imaging with burst techniques 244, 246
- safety issues 249
- spin echo imaging 233, 233  
volume imaging 225, 240
- $M_{sp}/M_{ss}^+/M_{ss}^-$  163, 165
- MTT (mean transit time) 291, 299
- MUA (multiunit activity) 12, 408–409
- multicompartment diffusion 178, 180, 181, 194
- multishot echo planar imaging 113
- multiple echo pathways 157, 158, 159
- multiple sclerosis 303
- multislice interleaving 94
- multiunit activity (MUA) 12, 408–409
- Munro–Kellie doctrine 6
- myelin sheath 170, 196
- NAD<sup>+</sup>/NADH system 19, 21, 22
- nerve stimulation 249–250
- neural activity  
BOLD response 402–403, 402, 408, 409  
CBF/CMRO<sub>2</sub> characterization 408  
energy metabolism 8, 14, 15  
feed-forward system 404  
hemodynamic response 415  
post-stimulus undershoot 415  
temporal patterns 413
- neural activity recovery 14  
astrocytes 16  
ATP energy budget 16  
ATP metabolism 14

- neural activity recovery (cont.)  
 neural signalling  
 thermodynamics 14, 15  
 Na<sup>+</sup>/K<sup>+</sup> pump 15
- neural signalling 7, 8  
 astrocytes 46  
 electrophysiology  
 measurements 12  
 and free energy 30  
 membrane potential 8, 9  
 neural activity 8  
 synaptic activity 10, 11  
 thermodynamics perspective  
 14, 28
- neuromodulatory receptors 11
- neuronal signaling *see* neural  
 signaling
- neurotransmitters 10; *see also*  
 acetylcholine;  
 norepinephrine; serotonin
- adenosine triphosphate 47  
 blood flow control 48  
 recycling 16, 17
- neurovascular unit 7,  
 43, 48
- neutrons 71
- NEX (number of excitations)  
 241–242
- nicotinamide adenine  
 dinucleotide (NAD<sup>+</sup>/  
 NADH) system 19, 21, 22
- nitric oxide 39, 42, 44,  
 46, 54
- nitric oxide synthase  
 (NOS) 46
- nitrous oxide blood flow  
 measurement technique  
 49, 50
- NMR (nuclear magnetic  
 resonance) 425; *see also*  
 magnetism; nuclear  
 magnetization dynamics;  
 quantum physics
- basic NMR experiment 70,  
 71, 77, 77
- contrast 67–69, 70, 78  
 equation 73, 86  
 equilibrium magnetization  
 73, 74, 427
- free induction decay signal  
 75, 75, 76
- gradient recalled echo pulse  
 sequences 79, 79
- historical development/  
 research foundations 67,  
 68, 70
- inversion recovery pulse  
 sequence 83, 83
- macroscopic measurements  
 430, 432, 437
- magnetic dipole/external  
 field interactions 426, 427
- magnetic dipole/magnetic  
 field interactions 98,  
 125–126, 130, 130,  
 425–426, 436
- NMR signal 70
- precession 71, 72, 425,  
 428, 436
- pulse sequence parameters 78
- pulse sequences 77–78, 78
- radiofrequency pulse 74, 75
- relaxation 73, 80, 166, 169,  
 425, 429
- spin echoes 81, 81, 82
- T<sub>1</sub>/T<sub>2</sub> -weighted images  
 67–69, 70, 75–76
- noise, image; *see also* artifacts;  
 auditory noise; distortion;  
 physiological noise
- BOLD experiment design/  
 analysis 375
- CBF 407, 415
- definition 252
- equations 254, 259
- non-uniform fluctuations  
 371
- signal-to-noise ratio 252,  
 254, 255, 255, 256
- spatial noise correlations  
 255, 258
- spatial smoothing 228, 257,  
 258, 259, 275
- spin echo signal 155
- statistical data analysis  
 369, 370
- temporal/spatial correlations  
 274–275
- non-anatomical imaging 95
- nonorthogonal model functions  
 386, 396, 397, 398
- non-steroidal anti-  
 inflammatory drugs  
 (NSAIDs) 47
- norepinephrine 47
- NOS (nitric oxide synthetase) 46
- NSAIDs (non-steroidal anti-  
 inflammatory drugs) 47
- nuclear magnetic resonance *see*  
 NMR
- nuclear magnetization  
 dynamics 130; *see also*  
 magnetism; NMR
- adiabatic radiofrequency  
 pulses 138, 139
- magnetic dipole/magnetic  
 field interactions 130, 130
- precession 131
- radiofrequency excitation 134
- relaxation 131
- slice selection, frequency  
 selective 122, 136, 137
- nuclear medicine studies 108
- nuclear spin *see* spin
- nucleus, atomic 24, 65, 67, 125,  
 125–126
- nucleus basalis 47
- null point 84
- number of excitations (NEX)  
 241–242
- Nyquist frequency 271
- off-resonance effects 212,  
 266–267
- continuous ASL 315
- distortions/artifacts 254, 264,  
 265, 267, 269
- pulsed ASL 318, 330
- T<sub>2</sub> effects on image quality
- OGI (oxygen/glucose index) 26,  
 54
- oscillation patterns 248
- oxygen diffusion 285
- oxygen extraction fraction 6, 6,  
 7, 54–55, 55
- oxygen metabolism/metabolic  
 rate 18, 36, 58, 103
- BOLD effect 37, 347, 353,  
 355, 358
- BOLD signal response 402,  
 404, 405
- calibrated-BOLD method  
 335, 344, 357
- and CBF 25, 26, 54,  
 111, 358
- energy metabolism 6
- equation 37
- and glucose metabolism  
 balance 26

- index 404
- initial dip 416, 417–418
- linearity/non-linearity of  
BOLD response 409–410
- measurement 344, 346,  
347, 355
- neural activity 42, 403
- positron emission  
photometry  
measurements 25, 111
- post-stimulus undershoot  
413–414
- transient patterns 412
- oxygen transport to tissue  
55, 56
- oxygen/glucose index (OGI)  
26, 54
- oxygen–hemoglobin binding  
curve 56–57
- oxyhemoglobin 102; *see also*  
deoxyhemoglobin
- pain 47
- parallel imaging 86, 364–365
- paramagnetism 140, 141
- parasympathetic pathway 47
- parenchyma, brain 334, 407
- Parkinson's disease 47
- partial echo acquisition  
241–242
- partial *k*-space acquisition  
241–242
- partial pressure 55
- particle physics 430–433, 430,  
432, 433
- partition coefficient 51, 284
- PASL *see* pulsed ASL
- penumbra, ischemic 303
- perfusion 36, 104, 281; *see also*  
arterial spin labeling;  
tissue perfusion
- pericytes 40
- periodic single trials 393, 394,  
397–398
- PET *see* positron emission  
photometry
- pH 44
- phase contrast 96
- phase dispersion 127, 349,  
350–351
- phase effects 96–97
- phase encoding 88, 88, 90, 214,  
214, 215
- phase shift 127
- phased array coils 127
- phosphofructokinase  
(PFK) 18
- phosphorylation potential 30
- photon spectrum 30
- photosynthesis 30
- physics  
classical *see* classical physics  
of diffusion 176, 178  
of magnetism *see* magnetism  
new tool for 68  
of NMR *see* NMR  
quantum *see* quantum  
physics
- physiological baseline  
effects 403
- physiological basis, BOLD  
effect 342, 355
- physiological changes  
BOLD effect 355  
mapping resting state  
networks 411  
transient patterns 412
- physiological noise 252, 259; *see*  
*also* motion artifacts
- arterial spin labeling  
techniques 331  
BOLD experiment design/  
analysis 369–370, 375  
image distortions/artifacts 4,  
272, 273
- physiological variables, energy  
metabolism 6, 6
- PICORE (proximal inversion  
with a control for  
off-resonance effects)  
317–318, 317
- pixels 222, 223
- point spread function  
(PSF) 210, 223, 226,  
228, 229
- volume imaging 225, 240
- positron emission photometry  
(PET) 6, 7
- arterial spin labeling  
techniques 309, 328, 329
- CBF/CMRO<sub>2</sub> coupling 25,  
26, 111, 358
- CBF measurement 52, 288
- CBV measurement 288, 293
- CMRGlc 23
- physiological basis 355
- projection reconstruction  
technique 216
- radioactive labeling 283
- residue function 293
- positron-emitting nuclei 24
- post-stimulus undershoot 42
- BOLD response  
interpretation 344, 401,  
407, 412, 413, 413, 417
- posterior probability 388
- Potassium 9, 10, 12, 44, 45, 403;  
*see also* battery analogy;  
Na<sup>+</sup>/K<sup>+</sup> pump
- PR (projection reconstruction)  
technique 91, 215, 243
- precession 121, 131, 425,  
428, 436
- characteristics 121
- equation 133, 133
- Fourier imaging 212
- Fourier transform/*k*-space 209
- frequency, NMR 232
- NMR 71, 72
- spin echo signal 156, 157
- steady-state free 163,  
164, 408
- PRESTO (principles of echo  
shifting with a train of  
observations) 240
- primate studies 16–17, 24–25,  
41, 347, 408
- principal axes of symmetry 185
- principal diffusivities 188
- principle of reciprocity 129
- principles of echo shifting with  
a train of observations  
(PRESTO) 240
- The Principles of Psychology* 3, 6
- probability 388, 433–437; *see*  
*also* quantum mechanics;  
quantum physics
- projection reconstruction (PR)  
technique 91, 215, 243
- prostaglandins 47
- proton density 74
- proton density weighting; *see*  
*also* T<sub>1</sub>/T<sub>2</sub>-weighted  
images; transverse  
relaxation time
- contrast, image 150–155,  
153, 156
- gradient echo signal 162
- spin echo signal intensity 150

- protons 71, 426, 432; *see also* magnetism; NMR
- proximal inversion with a control for off-resonance effects (PICORE) 317–318, 317
- pseudo-continuous arterial spin labeling 332
- PSF *see* point spread function
- PSIF 165 *see* steady-state free precession
- pulsation distortion, arterial 4, 180, 270, 271, 272; *see also* vasomotion
- pulse sequence diagram 233–234, 233, 243, 247
- pulse sequence parameters 78, 85, 232
- pulse sequences, NMR 77–78, 78
- pulsed ASL (PASL) 292, 309, 310, 315, 316, 317
- arterial bolus, creating well-defined 318–320
- CBF/BOLD activation – simultaneous measurement 333, 334
- CBF, absolute calibration 328
- CBF measurement – systematic errors 320–322, 320, 321
- modeling 311, 320
- off-resonance effects 330
- relaxation effects 323, 326, 327
- tagged water in arteries 329
- transit delay effects, controlling for 324, 324
- pulsed gradients 207
- Purcell, Edward M. 65, 67, 68
- pyramidal cells 11, 13
- pyruvate 20
- Q-ball imaging 196
- q-space imaging 177; *see also* diffusion spectrum imaging
- quadrature detector 127
- quantum mechanics 121–122, 438
- quantum physics 425, 428, 429
- quantum-classical connection 438
- quantum effects 430, 430, 433
- rules of quantum mechanics 433, 437
- QUASAR 330
- quiet imaging with burst techniques 244, 246
- QUIPSS (quantitative imaging of perfusion with a single subtraction) 109, 324, 324
- CBF/BOLD activation – simultaneous measurement 333
- CBF, absolute calibration 328
- location of BOLD signal changes 406–407, 407
- post-stimulus undershoot 407, 413
- tagged water in arteries 329
- radioactive labeling 51, 108, 283–284; *see also* xenon blood flow measurement technique
- radiofrequency
- radiofrequency pulse 70, 135
- adiabatic 138, 139
- frequency selective 122, 136, 137
- mapping the MR signal 205
- multiple echo pathways 157, 158, 159
- in NMR 74, 75
- spin echo signal 149, 156, 157
- steady-state free precession 163
- random walk model 166, 168, 176, 176
- randomized single trials 392–393, 392, 393, 398
- raphe nuclei 47
- rapid acquisition with relaxation enhancement (RARE) 92, 242
- rate constants, relaxation 105
- reciprocity principle 129
- rectangular windows 257
- rectilinear scanning 240
- red blood cells 38
- reduced perfusion reserve 282
- refocusing pulse 82, 87
- regression analysis 372
- relaxation 147, 232
- arterial spin labeling 321, 322, 323, 326, 327
- characteristics 121
- chemical shift effects 160, 161
- and contrast 104, 150, 153, 170
- and diffusion 174
- equations 133, 133, 151, 168
- fluctuating fields 166, 173
- Gd-DTPA 171
- generalized echoes 149, 156, 157
- gradient echo pulse sequence acronyms 165
- gradient echo pulse sequence varieties 151, 163, 165
- gradient echo signal 159, 159, 161, 166
- longitudinal relaxation times 78, 132
- longitudinal/transverse relaxation time differences 168, 169, 359
- multiple echo pathways 157, 158, 158, 159
- NMR 73
- physics of magnetism/NMR 121, 131, 425, 429
- rate constant 105, 148
- sources 166
- spin echo pulse sequence 150
- spin echo signal 148, 150, 151, 153
- steady-state free precession 163, 164
- stimulated echoes 147, 157, 159
- T<sub>1</sub>-weighted images 151, 162, 163
- T<sub>2</sub> effects 160, 161, 262–263, 265
- transverse relaxation model 167, 167
- repetition time (TR) 76, 76, 232
- BOLD effect 359
- gradient echo pulse sequences 151, 163, 165, 237
- spin echo pulse sequence 70, 206
- T<sub>1</sub>-weighted images 151, 162–163, 163

- residue function 288, **289**, 291, 292, 292, 311
- resistance, cerebrovascular **39**
- resolution, image 223  
 mapping the MR signal 226, 226, 228  
 MR image **220**, 221, 222, 222, 223  
 spatial/temporal 85, 108
- respiration 30, 270, 274–275, 411
- resting state networks (RSNs)
- restricted diffusion 176, 181, **182**
- ringing artifact 229, 230; *see also* Gibbs artifact
- rise time 248
- rodent studies 16–17, 37, 110, 341–342
- rotating reference frame 81, 135–136, 135, 156
- RSNs (resting state networks) 410–411
- safety issues, MRI **249**
- SAR (specific absorption rate) of energy 162, 249
- saturation effects 360
- saturation recovery pulse sequence 162
- SE *see* spin echo
- second messengers 11
- sensitivity patterns 129
- serotonin 12, 47
- shape, geometric 143, 144; *see also* geometric analysis
- shim coils 145
- shimming 145
- short TI inversion recovery (STIR) pulse sequence 152
- sign, phase 148
- signal detection 125, 126, 129–130
- signal drop, and contrast agents **105**, 106
- signal dropout effect 363
- signal loss 82, 198
- signal to noise ratio (SNR) 78, 108, 127  
 agent recirculation, bolus tracking 299  
 arterial spin labeling 308, 310  
 BOLD effect 359, **359**, 361, 365
- BOLD experiment design/analysis 369, 378, **380**
- burst imaging 245–246
- chemical shift effects 266
- data acquisition time 262
- fMRI experimental design, **389**, **391**, 392, 394
- general linear model 380, 383, **384**, **385**, 386, 387
- image distortion trade-offs 270
- mapping the MR signal 206–207
- noise, image 252, 254
- noise distribution 255, 255, 256
- spatial noise correlations 255, **258**
- spatial smoothing 228, **257**, 258, **259**
- volume imaging 240
- voxel volume 264–265
- signaling effect 42, 43
- signaling, neural *see* neural signaling
- single compartment model **311**, 328
- single-shot imaging 92, 93, 113, 180, 232
- sleep studies 244, 246
- slew rate 248
- slice selection  
 inversion recovery pulse sequence 333  
 mapping the MR signal **208**, 215  
 MRI 88, 89, **89**  
 physics of magnetism/NMR 122, **136**, 137  
 radiofrequency pulse 234
- smooth muscle 39, **43**, 411, 412
- smoothing function 393–394, 398; *see also* spatial smoothing
- SNR *see* signal to noise ratio
- sodium ion channel 9–10, 12; *see also* battery analogy
- sodium pump (Na<sup>+</sup>/K<sup>+</sup>) 15, 17, 27, 403
- solubility, oxygen 56–57, 56
- somatostatin 48
- spatial resolution, ASL 329
- spatial smoothing 228, **257**, 258, 259, 275
- specific absorption rate (SAR) of energy 162, 249
- spectroscopy 198, 438
- spectrum, photon 30
- SPGR (spoiled GRASS) pulse sequence 165, 236, 237, 240
- spiking 8, 408; *see also* action potential  
 ATP energy budget 16–17  
 BOLD signal response 402, 403, 409  
 and synaptic activity distinction 12
- spin 68, 71–72, 121–122; *see also* angular momentum
- spin density 74
- spin echo BOLD effect 351, **353**
- spin echo (SE) experiment 87
- spin echo (SE) imaging 233  
 diffusion imaging 173, **174**, 178, 179  
 diffusion process 174, 197–198  
 MRI techniques **148**, 149, 150, 233, **233**  
 nuclear magnetic resonance **81**, **81**, 82  
 terminological issues 160, 162
- spin echo (SE) pulse sequence 99–100, 264  
 BOLD effect 83  
 CBV measurement 298  
 linear field gradients 176, 198  
 location of BOLD signal changes 407  
 mapping the MR signal 208–209  
 motional narrowing 198, **198**  
 NMR **82**  
 off-resonance effects 269–270  
 repetition/echo time 70, 206
- spin echo signal **148**, **150**, 151, 153  
 contrast, image 150, 153  
 generalized echoes 149, 156, 157  
 multiple echo pathways 157, 158, 159  
 stimulated echoes **147**, 157, 159

- spin history, BOLD effect 363  
 spin states 431–433, 434–437;  
*see also* NMR  
 equations 436  
 quantum mechanics  
 434–435, 437, 438  
 spinal chord 231  
 spinning top analogy 72, 131  
 spiral imaging 243  
 spoiled gradient echo  
 signals 208  
 spoiled gradient recalled echo  
 pulse sequences 79, 152,  
 165–166, 236, 237  
 spoiler pulse 86, 164  
 spreading depression 47, 183  
 SSFP *see* steady-state free  
 precession  
 statistical data analysis 368  
 BOLD effect 360–361, 361  
 correlation analysis 113, 372  
 Fourier analysis 373, 373  
 interpreting BOLD  
 activation maps 113, 376  
 Kolmogorov–Smirnov  
 test 374  
 noise correlations 375  
 separating true activations  
 from noise 112, 369, 370  
*t*-test 371–372, 375, 376, 381  
 statistical parametric maps 371  
 statistical significance 378,  
 380, 388  
 status epilepticus 183  
 steady-state conditions 10  
 steady-state free precession  
 (SSFP) pulse sequences  
 165, 180  
 echo time 236, 238  
 gradient echo pulse  
 sequences 238  
 location of BOLD signal  
 changes 408  
 relaxation and contrast  
 163, 164  
 steady-state signals 165–166  
 stimulated echoes 147, 148, 157,  
 179–180  
 stimulus duration 417  
 stimulus patterns 393, 394, 396,  
 397, 398  
 stimulus–control task  
 experiment 111–112, 112
- STIR (short TI inversion  
 recovery) pulse  
 sequence 152  
 stress test 419  
 stroke 104, 160, 341  
 contrast agent techniques 303  
 diffusion imaging 173, 183  
 sulcus 407  
 superparamagnetic iron oxide  
 302–303  
 superparamagnetic particles 171  
 superposition 439  
 surface coil 86  
 susceptibility effects *see*  
 magnetic susceptibility  
 sympathetic pathway 47  
 synapses 8  
 synaptic activity 10, 12, 27–28,  
 402, 403, 408
- t*-statistic 112  
*t*-test 371–372, 375, 376, 381  
 $T_1/T_2$ -weighted images; *see*  
*also* contrast; transverse  
 relaxation time  
 image distortions/artifacts  
 261, 262, 264, 265  
 image quality 254, 262–263  
 gradient echo signal 151,  
 160, 161, 162, 163, 165  
 NMR 67–69, 70, 75–76  
 relaxation 151, 160, 161, 162,  
 163, 262–263, 265  
 repetition time 151,  
 162–163, 163  
 signal-to-noise ratio 253  
 spin echo signal 150–155, 153  
 stroke 183
- tag images 108–109, 308  
 tagging blood 103–104, 108,  
 329; *see also* arterial spin  
 labeling  
 TCA (tricarboxylic acid) cycle  
 18, 20  
 TE (data acquisition time) 236,  
 364; *see also*  $T_1/T_2$ -  
 weighted images  
 TE (echo time) *see* echo time  
 temporal noise 274  
 terminological issues 208  
 coupling 358  
 gradient echo imaging 160  
 MRI 86, 88
- mapping the MR signal 207  
 proton density weighting 156  
 spin echo/gradient echo  
 imaging distinction  
 160, 162  
 Tesla units 219  
 thermal equilibrium 132  
 thermal noise 252, 259, 274,  
 369, 375; *see also* noise;  
 image  
 thermodynamics perspective  
 equilibrium magnetization  
 428  
 laws of thermodynamics  
 28, 29  
 neural activity 8, 14, 18,  
 28, 403  
 neuronal signaling 14, 28  
 oxygen metabolism 28,  
 58–59  
 quantum effects 431  
 three-dimensional imaging 94  
 time–activity curves 24, 52,  
 283–284  
 data collection 253–254  
 diffusion 179  
 time-of-flight (TOF) effect  
 95–96, 96, 103  
 timescales, BOLD dynamics  
 411  
 tip angles 136; *see also* flip  
 angles  
 tissue concentration–time  
 curves 285, 286, 288,  
 291, 293  
 tissue interfaces *see* air–tissue  
 interfaces; bone–tissue  
 interfaces  
 tissue perfusion 36  
 TOF (time-of-flight) effect  
 95–96, 96, 103  
 tone, muscular 39  
 torque 131  
 TR *see* repetition time  
 trace, covariance matrix 395  
 tracer kinetics 283, 283, 289  
 tracers, diffusable 50, 51  
 tricarboxylic acid (TCA) cycle  
 18, 20  
 transient patterns 407, 412,  
 413, 416  
 transit delay effect 109, 322,  
 323, 324

- transmit phase 70  
 transverse components 78  
 transverse decay 152  
 transverse magnetization 69,  
   212, 213, 239–240, 253  
 transverse relaxation model  
   167, 167, 198, 263, 297  
 transverse relaxation time  
   78, 80, 168, 169; *see also*  
    $T_1/T_2$ -weighted images  
 trilaminar structures 231  
 trigeminovascular pathway 47  
 triptans 47  
 truncation artifact 230; *see also*  
   Gibbs artifact  
 tumors, brain 104, 105, 171,  
   282, 302, 341  
 tuning fork analogy 71  
 turbo SE (TSE) *see fast spin*  
   echo (FSE)  
  
 unit amplitude 391  
 upstream dilation, arteries  
   39–40  
  
 variability, BOLD response  
   interpretation 403  
 variance estimates 384, 385,  
   386; *see also ANOVA*  
 vascular space occupancy 414  
 vascular steal 40  
 vascular stenosis 303  
  
 vascular system;; *see also*  
   arteries; veins  
   brain blood supply 34, 35  
   microscopic 200; *see also*  
   arterioles, capillaries  
 vascular territory imaging 332  
 VASO (vascular space  
   occupancy) 414  
 vasoactive agents 44  
 vasomotion 370, 411; *see also*  
   pulsation distortion  
 vector fields 123  
 veins 406  
 velocity fields 126  
 velocity sensitive imaging 332  
 vesicles 10  
 vessel encoding approach 332  
 visual cortex  
   BOLD response 401, 401,  
   405–406, 407, 410  
   cat studies 416  
   initial dip 417  
   post-stimulus undershoot  
   407, 413  
 voltage-dependent  $K^+$   
   channels 44  
 volume imaging 94, 95, 225,  
   240, 240  
 volume of distribution  
   50, 284  
 voxel volume 253, 264–265, 360  
 voxels 222, 223, 411  
  
 water molecules  
   chemical shift effects 160, 161  
   diffusion 174, 175, 176, 350,  
   351, 351  
   quantum mechanics 438  
 white matter (WM)  
   connectivity estimation  
   192, 192  
   gradient echo signal 162  
 white/gray matter comparison  
   CBF 6  
   contrast 79, 154–156, 154  
   contrast to noise ratio  
   154, 155  
   glucose metabolism 25  
   gradient echo signal 162  
   MP-RAGE 240–241  
   relaxation time differences 170  
    $T_2$  effects on image  
   quality 265  
 windowing function 226–229,  
   228, 273  
 wraparound images 220, 224  
  
 x-compensation pulse 234  
 xenon blood flow measurement  
   technique 51, 52,  
   283–284, 287  
  
 z-compensation gradient pulse  
   234, 250  
 zero padding 222–223